Mechanisms of combustion dynamics of swirl-stabilised spray flames in a standing transverse acoustic field

Clement Patat

Normandie Université

THÈSE

Pour obtenir le diplôme de doctorat

Spécialité MECANIQUE DES FLUIDES, ENERGETIQUE, THERMIQUE, COMBUSTION, ACOUSTIQUE

Préparée au sein de l'Université de Rouen Normandie

Mechanisms of combustion dynamics of swirl-stabilised spray flames in a standing transverse acoustic field

Présentée et soutenue par
CLEMENT PATAT

Thèse soutenue le 16/12/2022 devant le jury composé de		
M. LAURENT GICQUEL	, CERFACS	Rapporteur du jury
M. THIERRY SCHULLER	PROFESSEUR DES UNIVERSITES, UNIVERSITE TOULOUSE 3 PAUL SABATIER	Rapporteur du jury
M. SEBASTIEN CANDEL	PROFESSEUR DES UNIVERSITES, CENTRALESUPELEC GIF SUR YVETTE	Président du jury
MME FRANÇOISE BAILLOT	PROFESSEUR DES UNIVERSITES, Université de Rouen Normandie	Directeur de thèse
M. JEAN-BERNARD BLAISOT	PROFESSEUR DES UNIVERSITES, Université de Rouen Normandie	Co-directeur de thèse

Thèse dirigée par FRANÇOISE BAILLOT (COMPLEXE DE RECHERCHE INTERPROFESSIONEL EN AEROTHERMOCHIMIE) et JEAN-BERNARD BLAISOT (COMPLEXE DE RECHERCHE INTERPROFESSIONEL EN AEROTHERMOCHIMIE)

UNIVERSITÉ DE ROUEN NORMANDIE

ED 591 PSIME

CORIA UMR 6614

Normandie Université

THÈSE

Pour obtenir le diplôme de doctorat

Spécialité MÉCANIQUE DES FLUIDES, ÉNERGÉTIQUE, THERMIQUE, COMBUSTION, ACOUSTIQUE

Préparée au sein de l'Université de Rouen Normandie

Mechanisms of combustion dynamics of swirl-stabilised spray flames in a standing transverse acoustic field

Présentée et soutenue par
Clément PATAT

Thèse soutenue publiquement le 16/12/2022 devant le jury composé de		
M. Laurent GICQUEL	Docteur HDR, CERFACS	Rapporteur
M. Thierry SCHULLER	Professeur des universités, Université Toulouse III – Paul Sabatier	Rapporteur
M. Sébastien CANDEL	Professeur des universités émérite, CentraleSupélec, Gif-sur-Yvette	Président
M. Benoit CINGAL	Ingénieur, ArianeGroup, Vernon	Membre invité
Mme Françoise BAILLOT	Professeure des universités, Université de Rouen Normandie	Directrice de thèse
M. Jean-Bernard BLAISOT	Professeur des universités, Université de Rouen Normandie	Co-directeur de thèse

Thèse dirigée par Françoise BAILLOT (UMR 6614 CNRS CORIA) et co-dirigée par Jean-Bernard BLAISOT (UMR 6614 CNRS CORIA)

UNIVERSITÉ DE ROUEN NORMANDIE

ED PSIME

CORIA UMR 6614

Remerciements

Ces travaux de thèse se sont déroulés au CORIA et à l'Université de Rouen Normandie. Je remercie tout d'abord la direction du laboratoire pour son accueil, ainsi que les organismes qui ont co-financé ces travaux : la Région Normandie et l'Agence Nationale de la Recherche (ANR), via le projet FASMIC (ANR16-CE22-0013).

J'adresse mes vifs remerciements aux membres du jury pour l'intérêt porté à mes travaux, ainsi que pour les échanges très enrichissants qui se sont tenus pendant et après la soutenance. Je suis reconnaissant envers les rapporteurs, Laurent Gicquel et Thierry Schuller, pour avoir minutieusement examiné le manuscrit et écrit d'excellents rapports, Sébastien Candel pour avoir accepté le rôle d'examinateur et présidé le jury, et Benoit Cingal pour avoir accepté l'invitation à faire partie du jury. Avoir une discussion scientifique avec autant d'experts aussi reconnus dans leur domaine a été une expérience très motivante. Leurs questions précises et leurs commentaires constructifs m'ont fourni la stimulation nécessaire à l'amélioration de la version initiale de ce manuscrit.

J'exprime également mes remerciements sincères à mes encadrants pour leur implication dans la réussite de cette thèse. Tout d'abord, à Françoise Baillot pour avoir dirigé ces travaux, et pour le temps consacré à suivre et à discuter de manière approfondie de mes avancées. Son énergie, sa persévérance et son expertise scientifique ont été non seulement une véritable force motrice tout au long de la thèse, mais sont aussi une source d'inspiration. Ensuite, à Jean-Bernard Blaisot, pour avoir co-dirigé ces travaux. Ses grandes connaissances dans le domaine des sprays et de leur analyse expérimentale ont été précieuses pour mener à bien ce processus. Son regard critique a permis d'approfondir l'interprétation des résultats. Enfin, à Éric Domingues pour son aide régulière lors des expériences, et pour ses nombreux conseils qui ont notamment largement amélioré la qualité de mes présentations scientifiques. Ses encouragements ont joué un rôle moteur tout au long de la thèse. Je leur suis grandement reconnaissant pour la confiance qu'ils m'ont témoignée durant ces années. Je remercie aussi Marcos Cáceres, qui a su me transmettre son savoir-faire acquis sur le banc TACC-Spray, et a toujours répondu de manière positive à mes sollicitations à ce sujet.

Mes remerciements vont également aux équipes du laboratoire EM2C et du CERFACS impliquées dans le projet FASMIC. J'ai beaucoup apprécié l'ensemble des discussions que j'ai pu avoir dans le cadre de cette collaboration, qui ont toujours été des moments d'échange très positifs.

Je remercie les services scolarité, audiovisuel et informatique de l'UFR Sciences et Techniques de l'Université de Rouen Normandie, qui ont permis le bon déroulement de la soutenance de thèse via la mise à disposition d'un amphithéâtre de l'Université et d'un système de visioconférence.

J'adresse également mes remerciements au personnel du CORIA, sans qui la recherche ne pourrait se dérouler dans de bonnes conditions. Tout d'abord, aux pôles administratif, bâtiment et informatique, chacun essentiel au bon fonctionnement du laboratoire, et toujours prompts à répondre aux diverses sollicitations. Puis, à l'atelier et au pôle métrologie, sans lesquels les thèses expérimentales auraient bien plus de difficultés à aboutir. Leurs compétences sont essentielles pour adapter les bancs expérimentaux, les instrumenter et pour former les doctorants à l'utilisation des diagnostics de mesure. Enfin, à celles et ceux avec qui j'ai eu l'occasion d'interagir durant ces années, en particulier les collègues de thèse, de course à pied et de vélo, sans qui l'atmosphère au CORIA ne serait pas aussi agréable ni stimulante.

Pour finir, je remercie mes parents, mon frère, mes amis, ainsi qu'Anaïs pour leur soutien indéfectible et leur implication dans la réussite de cette entreprise qu'est la thèse.

Abstract

The raising awareness of environmental issues induced by human activities is leading to the development of new combustion technologies that emit fewer pollutants and consume less energy. To ensure that combustion dynamics do not cause safety problems or affect the proper functioning of energy systems, it is important to understand how combustion instabilities can develop in order to better predict them. Due to the phenomena involved in these instabilities, they are mainly encountered in aircraft engines. In these systems, combustion is usually coupled with azimuthal acoustic modes of the combustion chamber. This research aims to contribute to the understanding of the physical mechanisms coupling combustion and acoustics in such configurations. For this purpose, a modular linear combustor of three lean swirl-stabilised spray flames, named TACC-Spray, is equipped with an acoustic forcing system, controlling the amplitude and the frequency of the standing transverse acoustic field generated in the chamber. This experimental setup located at CORIA, reproducing an unfolded sector of the laboratory-scale annular combustor MICCA-Spray located at EM2C laboratory, includes swirling aircraft-type air injectors. The combination of high-speed measurements of the acoustic pressure oscillation, $P^{'}$, flame chemiluminescence emission of CH^{*} or OH^{*} radicals, and laser diagnostics (high-speed laser tomography, Laser Doppler Anemometry and Phase Doppler Anemometry) reveals physical mechanisms coupling combustion and acoustics through the investigation of flame, spray and airflow dynamics.

We study the influence on the flame response to acoustics of the following parameters: acoustic amplitude, flame thermal power, fuel, location of the flame in the acoustic field. One important result is that the flame describing function (FDF) based on $P^{'}$ fully characterise combustion dynamics during transverse acoustic forcing performed downstream of the injectors at several locations in the standing transverse acoustic field. At an acoustic pressure antinode, space-time waves of the droplet number as well as their properties lead, after evaporation and mixing with the air during their convective propagation, to a wave of flame chemiluminescence emission intensity. Increasing the thermal power, at a fixed equivalence ratio, induces a significant increase in the amplitude of the global flame intensity oscillation, $I^{'}$, as well as a modification of the phase shift with $P^{'}$, leading to the transition from a stable combustion regime to a potentially unstable regime. The amplitude of $I^{'}$ has a linear behaviour at low forcing amplitudes, then evolves towards a saturation regime at higher amplitudes, reflecting the presence of nonlinear phenomena at sufficiently high acoustic amplitudes. A deeper analysis of the saturation phenomenon indicates that it can be induced not only by the structuring of the gas flow by acoustics, but also by the space-time organisation of the fuel spray, possibly leading to severe mixing in-

homogeneities. A study with different liquid fuels indicates that the quality of the atomisation and evaporation processes contributes to the flame dynamics: in particular, a higher proportion of small fuel droplets in the spray appears to be a factor favouring an intense flame response. At a intensity antinode, acoustic pressure effects remain dominant, while in the velocity antinode, lateral velocity effects impose a lateral displacement of the flame, facilitating its blow-out. The latter, initially observed during high-amplitude instabilities in MICCA-Spray, is reproduced in TACC-Spray for several experimental conditions, validating the development of a theoretical model initiated during previous works at the EM2C laboratory and highlighting blow-out mechanisms.

Résumé

De nouvelles technologies de combustion plus efficaces et moins polluantes sont développées pour satisfaire les objectifs de protection de l'environnement du secteur de l'énergie. Pour s'assurer que la dynamique de combustion ne cause pas de problèmes de sécurité ni n'affecte le bon fonctionnement des systèmes énergétiques, il est primordial de comprendre comment les instabilités de combustion peuvent s'y développer, afin de mieux les prédire. De par les phénomènes impliqués, ces instabilités se rencontrent notamment dans les chambres de combustion aéronautiques. Dans ces systèmes, la combustion est généralement couplées avec un mode acoustique azimutal de la chambre. Ce travail de recherche a pour but de contribuer à la compréhension des mécanismes physiques couplant la combustion et l'acoustique dans de telles configurations. Pour cela, une chambre de combustion modulable, TACC-Spray, dans laquelle sont situées trois flammes pauvres de spray stabilisées par swirl, est équipée d'un système de forçage acoustique contrôlant l'amplitude et la fréquence d'un champ acoustique transverse stationnaire généré dans la chambre. Ce dispositif expérimental situé au CORIA, reproduisant un secteur développé de la chambre de combustion annulaire MICCA-Spray située au laboratoire EM2C, comprend des injecteurs d'air swirlé de type aéronautique. La combinaison de mesures à haute cadence de l'oscillation de pression acoustique, $P^{'}$, de l'émission chimiluminescente des radicaux CH^{*} ou OH^{*} des flammes, ainsi que de diagnostics laser (tomographie haute cadence, vélocimétrie laser Doppler et vélocimétrie phase Doppler) permet de mettre en évidence des mécanismes de couplage grâce à l'examen de la dynamique de flamme, du spray et de l'écoulement d'air.

On étudie l'influence des paramètres suivants sur la réponse de flamme à l'acoustique : amplitude acoustique, puissance thermique de flamme, carburant, position des flammes dans le champ acoustique. Il est montré que la fonction descriptive de la flamme (FDF) basée sur $P^{'}$ caractérise pleinement la dynamique de flamme lors d'un forçage acoustique transverse effectué en aval des injecteurs. Au ventre de pression acoustique, des ondes spatio-temporelles du nombre de gouttes ainsi que de leurs propriétés conduisent, après évaporation et mélange avec l'air durant leur propagation convective, à une onde d'émission chimiluminescente de la flamme. L'accroissement de la puissance thermique, à richesse fixée, induit une augmentation significative de l'amplitude d'oscillation de l'intensité globale de flamme, $I^{'}$, ainsi qu'une modification du déphasage avec $P^{'}$, conduisant à une transition d'un régime de combustion stable à un régime potentiellement instable. L'amplitude de $I^{'}$ croît linéairement à faible amplitude de forçage puis évolue vers un régime de saturation à plus forte amplitude, traduisant la présence de phénomènes non-linéaires à partir d'une amplitude acoustique suffisamment élevée. L'analyse du phénomène de saturation

montre qu'il peut être induit par la structuration de l'écoulement gazeux par l'acoustique, mais aussi par l'organisation spatio-temporelle du spray, pouvant mener à de fortes inhomogénéités de mélange. L'utilisation de différents carburants liquides montre que la qualité des processus d'atomisation et d'évaporation joue un rôle dans la dynamique de flamme : en particulier, une proportion élevée de petites gouttes dans le spray favorise une réponse de flamme intense. Au ventre d'intensité, les effets de pression acoustique restent dominants tandis qu'au ventre de vitesse, les effets de vitesse latérale imposent un déplacement latéral de la flamme, facilitant son extinction. Celui-ci, initialement observé lors d'instabilités à haute amplitude dans MICCA-Spray, est reproduit dans TACC-Spray pour plusieurs conditions expérimentales, validant le développement d'un modèle théorique initié lors de travaux antérieurs au laboratoire EM2C et mettant en lumière les mécanismes d'extinction.

Contents

List of publications and communications

Peer-reviewed journal articles

1. **F. Baillot, C. Patat, M. Cáceres, J.-B. Blaisot, É. Domingues**, Saturation phenomenon of swirling spray flames at pressure antinodes of a transverse acoustic field, *Proceedings of the Combustion Institute* 38(4), 2021, pp. 5987-5995.

    - Presented at the 38th International Symposium on Combustion, 24-29 January 2021, Adelaide, Australia.

2. **C. Patat, F. Baillot, J.-B. Blaisot, É. Domingues, G. Vignat, P. Rajendram Soundararajan, A. Renaud, D. Durox, S. Candel**, Swirling spray flames dynamical blow-out induced by transverse acoustic oscillations, *Proceedings of the Combustion Institute*, available online.

    - Presented at the 39th International Symposium on Combustion, 24-29 July 2022, Vancouver, Canada.

International conferences with proceedings

1. **C. Patat, J.-B. Blaisot, É. Domingues, F. Baillot**, Response of a spray of n-heptane or dodecane at an acoustic pressure antinode in reactive conditions, *ICLASS 2021, 15th Triennial International Conference on Liquid Atomization and Spray Systems*, 29 August - 2 September 2021, Edinburgh, UK, https://hal.archives-ouvertes.fr/hal-03717229.

2. **C. Patat, F. Baillot, J.-B. Blaisot, É. Domingues**, Responses of lean swirling spray flames to acoustic pressure and transverse velocity perturbations, *Symposium on Thermoacoustics in Combustion: Industry meets Academia* (SoTiC 2021), 6 - 10 September 2021, Munich, Germany, https://hal.archives-ouvertes.fr/hal-03717261.

3. **C. Patat, F. Baillot, J.-B. Blaisot, É. Domingues, G. Vignat, P. Rajendram Soundararajan, A. Renaud, D. Durox, S. Candel**, Swirling spray flames dynamical blow-out induced by transverse acoustic oscillations, *Symposium on Thermoacoustics in Combustion: Industry meets Academia* (SoTiC 2021), 6 - 10 September 2021, Munich, Germany,

https://hal.archives-ouvertes.fr/hal-03674675

National conferences

1. **C. Patat, F. Baillot, J.-B. Blaisot, É. Domingues**, Dependence of the thermoacoustic coupling on flame power for swirling spray flames at acoustic pressure antinodes, *5ème colloque de l'Initiative sur la Combustion Avancée* (INCA), 7 - 8 April 2021, SAFRAN Paris-Saclay.
2. **C. Patat, F. Baillot, J.-B. Blaisot, É. Domingues, G. Vignat, P. Rajendram Soundararajan, A. Renaud, D. Durox, S. Candel**, Dynamical blow-out of swirling spray flames induced by transverse acoustic oscillations, *5ème colloque de l'Initiative sur la Combustion Avancée* (INCA), 7 - 8 April 2021, SAFRAN Paris-Saclay.

Nomenclature

Acronyms

CRZ	Central recirculation zone
FDF	Flame describing function
FTF	Flame transfer function
FWHM	Full width at half maximum
HRR	Heat release rate
IAN	Intensity antinode
LDA	Laser Doppler Anemometry
PAN	Pressure antinode
PDA	Phase Doppler Anemometry
PDF	Probability density function
PM	Photomultiplier
PSD	Power spectral density
PVC	Precessing vortex core
ROI	Region of interest
UV	Ultraviolet
VAN	Velocity antinode

Greek symbols

α	Phase angle during the acoustic pressure cycle
μ	Dynamic viscosity
ϕ	Equivalence ratio

Π	Rms amplitude of the acoustic pressure oscillation reduced by the bulk aerodynamic pressure
ρ	Density
φ	Phase of the flame describing function

Modifiers

$(\cdot)'(t)$	Time fluctuation
$(\cdot)^a$	Quantity relative to the air
$(\cdot)^c(t)$	Coherent oscillation at a given frequency
$(\cdot)^f$	Quantity relative to the fuel
$(\cdot)^{rms}$	Root mean square value
$(\cdot)^s(t)$	Stochastic oscillation
$\breve{(\cdot)}$	Complex amplitude
$\langle(\cdot)\rangle$	Phase-averaged value
$\overline{(\cdot)}$	Mean value
$\overline{(\cdot)}^r$	Spatial-averaged value of $(\cdot)(r,t)$
$\overline{(\cdot)}^t$	Time-averaged value of $(\cdot)(\vec{x},t)$
$\bar{\bar{\cdot}}$	Tensor
$\vec{\cdot}$	Vector

Roman symbols

$\dot{m}$	Mass flow rate
$\dot{Q}$	Global heat release rate
$\dot{q}$	Volumetric heat release rate
$\dot{q}_v$	Volumetric flow rate
$\mathcal{F}$	Flame Describing Function
$\mathcal{G}$	Gain of the Flame Describing Function
$\mathcal{R}a(t)$	Global instability index based on the classical Rayleigh criterion
$\mathcal{T}$	Temperature
$\mathfrak{R}a(x,t)$	Local instability index based on the classical Rayleigh criterion

$\mathrm{Stk_{ac}}$	Acoustic Stokes number
Stk	Stokes number
St	Strouhal number
$d(r,z)$	Fuel droplet diameter at a given location (r,z)
$d^{rms}(r,z)$	Standard deviation of the local fuel droplet diameter
$d_{10}(r,z)$	Local fuel droplet arithmetic mean diameter
D_{10}	Arithmetic mean diameter of the whole fuel spray
D_{exit}	Nozzle exit diameter
e_c	Width of the combustion chamber
f	Frequency
f_r	Acoustic excitation frequency, corresponding to the resonance frequency of the 2T1L mode of the cavity
G_θ	Axial flux of angular momentum
G_z	Axial flux of axial momentum
h_{base}	Flame standoff distance
h_{cp}	Height of the convergent part
h_c	Height of the combustion chamber
$I(t)$	Global flame intensity measured with photomultiplier
$I_{cam}(\vec{x},t)$	Local flame intensity measured with high-speed camera
L_c	Length of the combustion chamber
$P^{'}(t)$	Acoustic pressure oscillation
r	radial location
S	Swirl number
T	Acoustic period
t	Time (s)
U_θ	Tangential velocity
U_r	Radial velocity
U_z	Axial velocity

z	Vertical location

Chapter 1

Introduction

Contents

This introductive chapter begins with the contextualisation of the study. Section 1.1 provides a description of the current issues associated to the energy sector and gives the technical context of this study. In Section 1.2, the theoretical framework about thermoacoustic instabilities is introduced. The acoustic wave equation is obtained in reacting conditions, and the acoustic energy balance and the Rayleigh criterion are derived. Then, Section 1.3 deals with modelling methods to predict instabilities. An emphasis is placed on acoustic network models. The flame describing function (FDF) is also introduced, followed by a discussion of the different ways to determine it. Section 1.4 then gives a literature review about the main mechanisms by which acoustics and combustion are coupled. Finally, Section 1.5 lists the objectives of the manuscript and details its structure.

1.1 General context

1.1.1 Energy production and consequences on climate and health

In 2021, 82% of the primary energy consumed throughout the world derived from fossil fuels [1]. Among them, oil, natural gas and coal respectively accounted for 31%, 24% and 27% of the primary energy consumed. The chemical energy from these primary sources is transformed into mechanical energy and heat through combustion processes. It results in the production of several chemical species, among which greenhouse gases (GHG), leading to global warming, and pollutant emissions, directly affecting human health and biodiversity.

It is established that the human activities since the 19^{th} century's industrial revolution have led to a sharp rise of the Earth global surface temperature (see Figure 1.1). At the same period, it was already known that the absorption of the atmosphere plays an important role upon the climate [2]. In particular, Arrhenius made a model predicting that an increase of the quantity of carbon dioxide (CO_2) in the atmosphere would induce an increase of the Earth's temperature [3].

Is it now accepted that the release of greenhouses gases into the atmosphere, among which CO_2 or CH_4, is the major cause of the current global warming. However, the increase of the atmosphere temperature lags the CO_2 emission by several years. Two numerical works respectively indicate that this time lag is about ten years for a pulse of CO_2 emission of 100 GtC[1] [5], and that this time lag increases with the amount of CO_2 emitted [6]. As a consequence, a significant effort must be made to reduced GHG emissions in the shortest time possible.

It is also known that pollutant such as soots, polycyclic aromatic hydrocarbons (PAH)[2], nitrogen oxides (NO_x) and ozone affect human health and biodiversity. Contrary to GHG, which affect the climate as a whole, these forms of pollution are local and thus mainly affect living beings around their place of production. The exposure to soot and PAHs increases not only the risk of developing cancer, but also encourages respiratory diseases, which can be chronic, or acute during periods of severe air pollution [7]. The exposure to excessive amounts of NO_x [8] or ozone [9] can lead to respiratory diseases. It is worth noting that NO_x are of the main primary

[1] 1 GtC corresponds to 1 billion of tons of carbon, which is equivalent to 3.7 billions of tons of CO_2.
[2] PAHs are soot precursors.

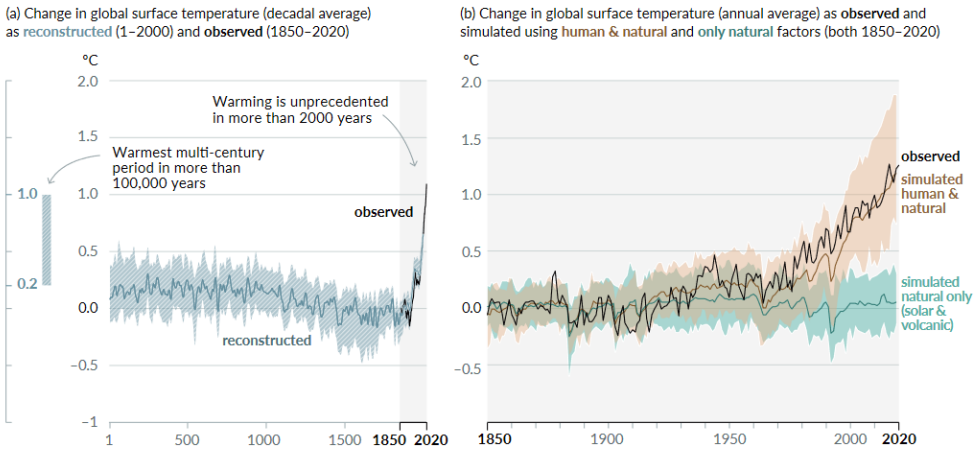

Figure SPM.1 | History of global temperature change and causes of recent warming

Panel (a) Changes in global surface temperature reconstructed from paleoclimate archives (solid grey line, years 1–2000) **and from direct observations** (solid black line, 1850–2020), both relative to 1850–1900 and decadally averaged. The vertical bar on the left shows the estimated temperature (*very likely* range) during the warmest multi-century period in at least the last 100,000 years, which occurred around 6500 years ago during the current interglacial period (Holocene). The Last Interglacial, around 125,000 years ago, is the next most recent candidate for a period of higher temperature. These past warm periods were caused by slow (multi-millennial) orbital variations. The grey shading with white diagonal lines shows the *very likely* ranges for the temperature reconstructions.

Panel (b) Changes in global surface temperature over the past 170 years (black line) relative to 1850–1900 and annually averaged, compared to Coupled Model Intercomparison Project Phase 6 (CMIP6) climate model simulations (see Box SPM.1) of the temperature response to both human and natural drivers (brown) and to only natural drivers (solar and volcanic activity, green). Solid coloured lines show the multi-model average, and coloured shades show the *very likely* range of simulations. (See Figure SPM.2 for the assessed contributions to warming).

Figure 1.1: Reproduced from [4].

precursor of ozone. In light of these elements, it is important to mitigate as possible the pollutant emissions from fossil-fueled devices. Since the discovery of the effects of these pollutants on health, a considerable effort has been made to reduce these emissions [10–12]. The thermal-NO mechanism discovered by Zeldovich [13] indicates that NO_x production strongly increases with the temperature. Therefore, controlling the flame temperature appears as a solution to limit the NO_x emissions. Reduction in NO_x emissions can be achieved by using non-stoichiometric mixtures, either lean or rich. However, rich mixtures promote the production of soots and PAHs as well as the release of unburnt fuel at the combustor outlet, which goes against the objectives of reducing fuel consumption. Conversely, lean combustion allows to reduce NO_x, PAH and soot production as well as fuel consumption, which makes it a promising solution to reach the above-mentioned objectives. Nevertheless, lean flames are sensitive to combustion instabilities [14]. Such phenomena are detrimental to the combustion efficiency, and, in extreme cases, can lead to combustor damage. In light of these elements, it is important to gain a deeper understanding of combustion instabilities.

1.1.2 Combustion instabilities in industrial devices

Combustion instabilities can be separated in three categories, according to Barrère & Williams [15]: (i) instabilities associated to the combustion chamber; (ii) instabilities associated to the entire system; (iii) instabilities intrinsic to the reactants. In all this work, we focus on thermoacoustic instabilities, which are classified in the first category. This kind of instabilities involves a coupling between acoustics and combustion. In essence, a loop is established between combustion and acoustics under certain conditions: combustion feeds acoustics and in return, acoustics

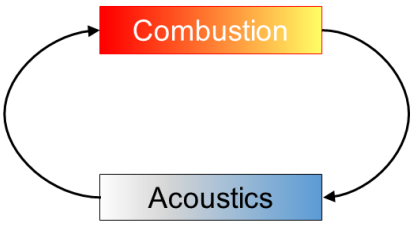

(a) Basic representation

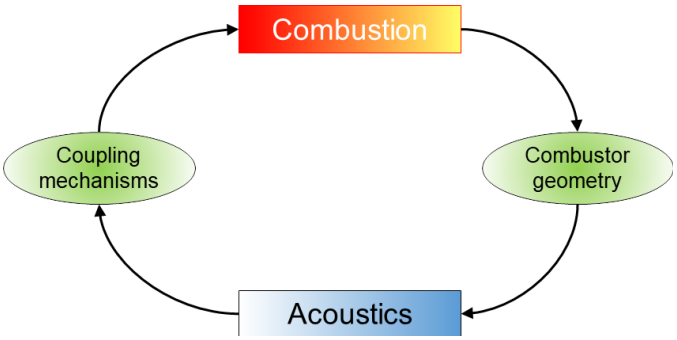

(b) Coupling between acoustics and combustion depends on the combustor geometry and is driven by physical mechanisms.

Figure 1.2: Representation of the coupling loop at the basis of thermoacoustic instabilities.

disturbs combustion. This very basic principle is illustrated in Figure 1.2 (a). This corresponds to the more simple representation of the loop at the basis of thermoacoustic instabilities. A more complete representation[3], shown in Figure 1.2 (b), emphasises that the thermoacoustic coupling depends on the combustor geometry, which determines the natural modes of oscillation, and requires driving mechanisms to link the acoustic perturbation to the combustion oscillation. Combustion instabilities can therefore be seen as an energy transfer between combustion and acoustics. In practical devices, such as rocket engines, ramjets, gas turbines and aicraft engines, furnaces or boilers, this energy transfer is facilitated by the ability of acoustic waves to propagate with very low attenuation in compact and confined geometries, and by the high energy density in such systems.

Although 'singing flames' [16] are observed since the 18th century, leading to the famous explanation of Rayleigh [17], the interest in the subject growed considerably in the middle of the 20th century. At this time, the works on the subject were mainly motivated by the development of the aerospace and military sectors, in which the engines were characterised by a extremely high power in a relatively compact area[4]. During tests, engines suffered from unexpected levels of oscillation resulting from the interaction between combustion and acoustics. In the worst cases, this led to the destruction of the engine. The most known example is that of the F-1 engine from the Apollo program, for which combustion instabilities were found during tests since 1959, and

[3] However, far from being exhaustive.

[4] This is illustrated by noting that in the F-1 engine, five of which equipped the Saturn V rocket from the NASA Apollo program, the nominal pump mass flow rates were 796 kg/s for the fuel (liquid kerosene) and 1,754 kg/s for the oxidizer (liquid oxygen), and the whole assembled engine can be included in an hollow cylinder of length 6.1 m and diameter 3.7 m [18].

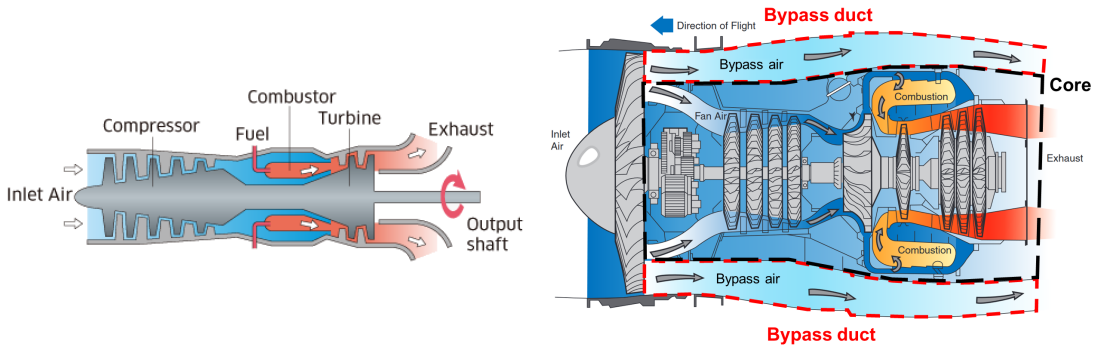

(a) (b)

Figure 1.3: Sketches of longitudinal cuts of: (a) a single-shaft gas turbine (Kawasaki Heavy Industries); (b) a turbofan, adapted from [20].

injector stability was finally demonstrated in 1965 [18]. These issues led to the creation, in 1962, of a committee dedicated to combustion instabilities, called 'Project First', whose mission ended in 1966 [19].

In the context of high-performance gas turbines and aircraft engines, combustion instabilities are linked to the fact that lean combustion, which is promising to meet the environmental goals of the aeronautical industry, is more conducive to such instabilities. This can be explained by several reasons [14]: first, lean flames are more easily extinguished by turbulent fluctuations than stoichiometric ones. Secondly, they can reignite later and generate pressure waves that can couple with an acoustic mode of the chamber. Finally, the higher air flow rate through the injector increases the probability of exciting hydrodynamic instabilities. The high compactness of lean-burn systems also reduces the acoustic damping, and the increasing air flow rate dedicated to combustion results in a reduction of the air flow rate affected to secondary dilution holes, therefore enhancing the acoustic reflectivity of the chamber.

In light of these considerations, it is worth developing new methods to predict combustion instabilities in high-performance combustion systems as soon as possible during the design stage. For this purpose, the understanding of the physical mechanisms driving combustion instabilities is required. This thesis aims at giving deeper insight about the physical mechanisms governing the dynamics of swirl-stabilised spray flames, which combine several characteristics of the flames that are found in industrial combustors such as gas turbines or aircraft engines.

1.1.3 Gas turbines and aircraft engines

Gas turbine engines are used for power generation or propulsion. For all the applications, the three main steps are:

- compression of the inlet air flow by a set of compressors;
- combustion of the air-fuel mixing inside the combustor, leading to a rise in pressure and temperature;

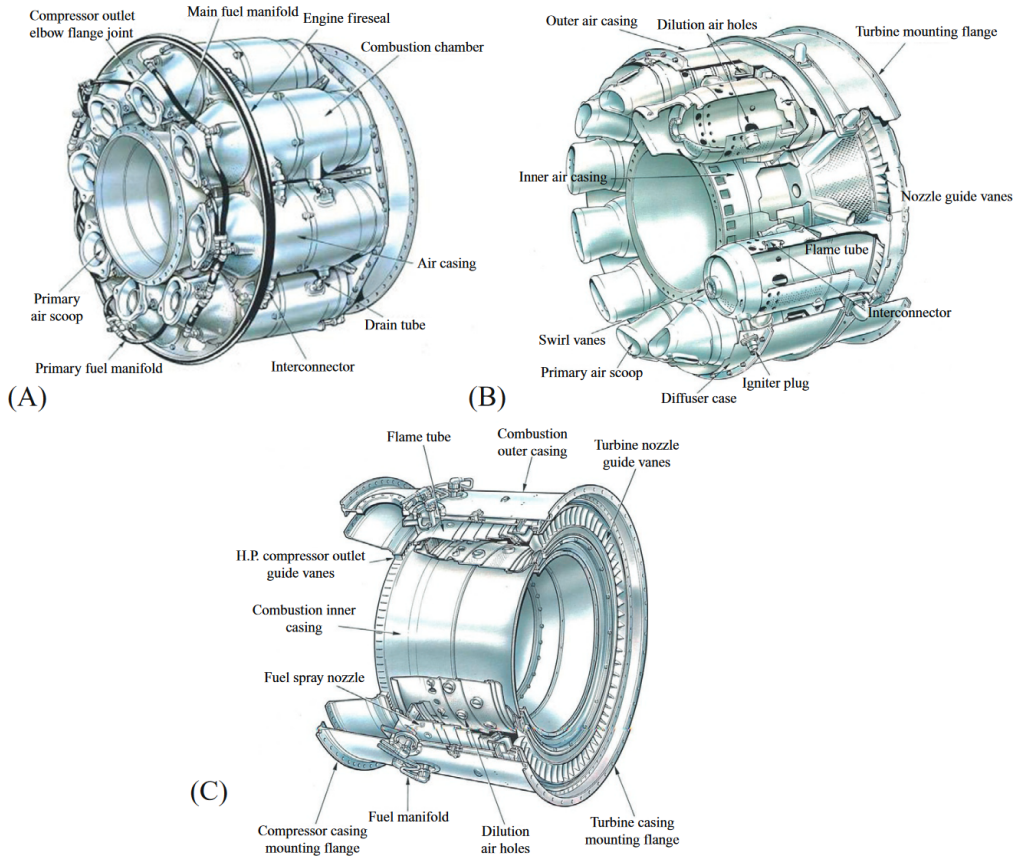

Figure 1.4: Three types of gas turbines combustion chambers: (a) can-type combustor; (b) can-annular (or tubo-cannular) combustor; and (c) annular combustor. Adapted from [22].

- expansion of the hot gases by one or several turbines.

Rotation of the turbines by the hot gas expansion always leads to the rotation of the compressors via one or several shafts. For power generation or propeller propulsion, a shaft also link the turbine to a generator or to a propeller (see Figure 1.3 (a)). For turbojet aircraft engines, the exhaust gases are expanded downstream of the turbine to produce the necessary thrust for movement. For civil aircraft applications, turbojet engines are now mostly supplanted by turbofan engines (see Figure 1.3 (b)), in which most of the thrust is provided by the air sent to the bypass duct due to the large air mass flow passing through this duct compared to that passing through the core[5]. In such engines, the energy released by combustion is mostly used to drive the fan rather than to generate thrust by expanding the hot gases. The reader can find more details in [21].

1.1.4 Combustion chambers

Several types of combustion chambers are found in gas turbines [21]. Three of them are illustrated in Figure 1.4. In **can-type combustors**, combustion occurs in a number of separate tubular combustion chambers, called *cans*. The air flow exiting the compressors is split into

[5]The ratio of the mass flow passing through the bypass duct to that passing through the core is named **bypass ratio** (BPR). Some recent turbofan engines can have a BPR up to 12.

separate streams, each directed to a separate can. Each can has its own fuel injection system, with fuel supplied by a common line. In each can, the combustion process is thus independent of the other cans. Such a feature is advantageous in the design phase as, except for processes related to the fuel supply line, the combustion process can be optimised by considering only one can. However, can-type combustors are relatively heavy and large, limiting their range of application to land-based systems. **Can-annular combustors** are also based on separate combustion chambers, but compared to can-type combustors, all the cans are interconnected, limiting the overpressure in the cans. In **annular combustors**, the flames are distributed along an annular ring with no rigid boundaries between them, and the air and fuel supply lines are common to all the injectors. However, the disadvantages include the propensity of such combustors to develop combustion instabilities, due to their large azimuthal dimension that can lead to the coupling between combustion and low-frequency acoustic modes of the combustor, and the low damping associated with these combustors. Annular combustors are lighter and more compact than can-annular combustors and especially than can-type combustors, which explains their widespread use in aircraft and helicopter engines. The interested reader can refer to [21–23] for further details.

1.1.5 Swirling flows

Swirling flows are widely used in industrial combustion systems [24, 25]. They were originally designed to improve and control fuel-oxidizer mixing [26, 27]. The swirling motion is obtained by imparting a tangential component to the velocity of a flow. In this manner, a centrifugal force is induced by the tangential flow velocity, which leads to a radial pressure gradient $\partial p/\partial r \sim \rho U_\theta^2/r$ and hence a low pressure region near the injector axis. The expansion of the flow through a nozzle induces an axial decay of the tangential velocity, and thus of the radial pressure gradient. As a consequence, the pressure near the injector axis increases with the axial direction, leading to a reverse axial pressure gradient, in turn resulting in the recirculation of the flow near the injector axis [28]. This recirculation is sought after in many industrial burners, as it increases flame stability and compactness by allowing hot combustion products and active chemical species to recirculate close to the injector exit, thereby facilitating the ignition of the incoming fresh mixture. The typical structure of a swirling flow is illustrated in Figure 1.5. The central region in which recirculation takes place is often denoted as central recirculation zone (CRZ)[6]. In practice, recirculation is observed when the level of swirl exceeds a given level. If the condition is fulfilled, vortex flows undergo major structural changes [29], among which the vortex breakdown. According to Leibovich [29], vortex breakdown *'refers to a disturbance characterized by the formation of an internal stagnation point on the vortex axis, followed by reversed flow in a region of limited axial extent'*.

The level of swirl is quantified by the swirl number S, which corresponds to the ratio of the time-averaged axial flux of angular momentum G_θ to the time-averaged axial flux of axial momentum RG_z, where R is a characteristic radius. S is expressed by:

[6]It is sometimes called inner on internal recirculation zone (IRZ) or central toroidal recirculation zone (CTRZ).

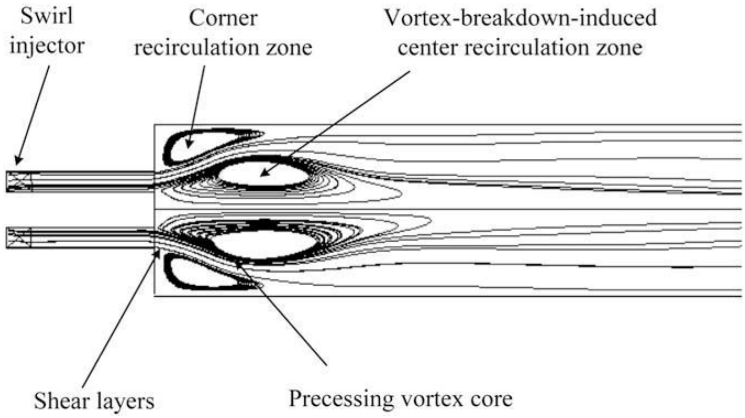

Figure 1.5: Structure of a typical swirling flow. Reproduced from [30].

$$S = \frac{G_\theta}{RG_z} \tag{1.1}$$

$$= \frac{\int_A \rho U_z(r,\theta) U_\theta(r,\theta) r dA}{R \int_A (P + \rho U_z^2(r,\theta)) dA} \tag{1.2}$$

$$= \frac{\int_0^{2\pi} \int_0^{r_{max}} \rho U_z(r,\theta) U_\theta(r,\theta) r^2 dr d\theta}{R \int_0^{2\pi} \int_0^{r_{max}} (P + \rho U_z^2(r,\theta)) r dr d\theta} \tag{1.3}$$

In this expression, A corresponds to the integration surface area, ρ is the flow density, U_z and U_θ the flow instantaneous axial and tangential velocities, P the pressure and r_{max} the upper radial integration limit. This expression can be simplified with the following considerations and assumptions:

- the pressure is neglected [25], as it is difficult to determine in experiments;
- ρ is constant;
- The flow is axisymmetric. This implies that $U_z(r)$ and $U_\theta(r)$ do not depend on θ.

Equation (1.3) thus reads:

$$S = \frac{2\pi \int_0^{r_{max}} U_z(r) U_\theta(r) r^2 dr}{2\pi R \int_0^{r_{max}} U_z^2(r) r dr} \tag{1.4}$$

Although the role of the swirl motion is to stabilise the flames, hydrodynamic instabilities are inherently present in swirling flows. One well-known instability is the precessing vortex core (PVC), illustrated for an isothermal flow in Figure 1.6. The instantaneous 2D velocity field in a horizontal plane just above the injector exit, obtained with Particle Image Velocimetry (PIV), shows that the vortex core is not located on the central axis of the burner exit. With time, the vortex core rotates around the central axis. At a given mass flow rate, Manoharan et al. [31]

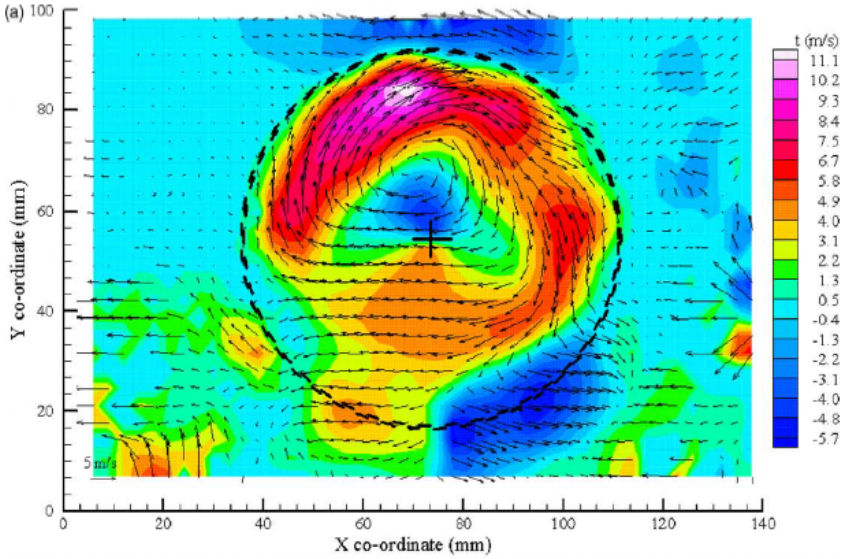

Figure 1.6: Instantaneous 2D velocity field in a horizontal plane just above the swirl burner exit for an isothermal flow, obtained with PIV. Colours indicates the velocity magnitude. The black cross indicates the central axis of the burner exit. The swirl number is $S = 2.6$. Reproduced from [28].

showed with a weakly nonlinear analysis that the frequency of the PVC scaled linearly with $S - S_c$, where S_c was a critical swirl number above which the PVC was observed. The PVC frequency is in general linearly related to the flow rate in non-reacting flows [28, 32, 33], and in reacting flows [34, 35], leading to a constant value of the Strouhal number based on the PVC frequency and the flow velocity. With combustion, Steinberg et al. [34] showed in a single-injector setup that the value of this Strouhal number is 0.78 for all the non-reacting conditions they examined, while it was 0.88 for reacting conditions that display a PVC. Indeed, they also showed that combustion could prevent the appearance of the PVC which was observed for their lower flame powers (10 - 15 kW, $\phi = 0.7$) and higher equivalence ratio ($\phi = 0.8$, for a power of 30 kW).

1.1.6 Spray combustion

To reach the environmental goals, lean premixed combustion is preferable as it reduces GHG and pollutant emissions. However, perfect premixing leads to safety issues, which are often reduced by injecting the gaseous fuel closely upstream of the combustion chamber. In such cases, gaseous fuel and oxidiser often do not have time to produce a homogeneous mixture before combustion: this is referred to as **partially-premixed combustion**, also called **technically-premixed flames**. The quality of the air-fuel mixing then mainly depends on diffusion and turbulence.

For aircraft engine and gas turbine applications, liquid fuels are usually more convenient than gaseous fuels, due to the excellent trade-off they offer between volumetric energy density, safety and ease of use. But, this introduces the evaporation process to the mixing mechanisms already producing a reacting mixture, which may lead to a decrease of the mixture quality and therefore

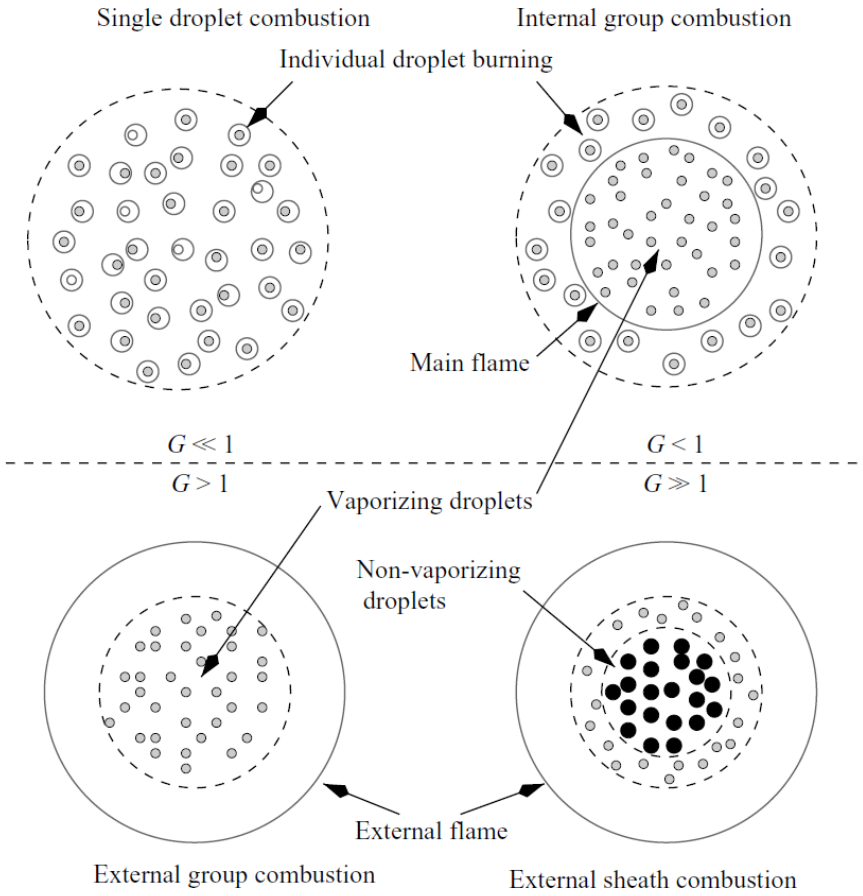

Figure 1.7: Spray combustion modes highlighted by Chiu et al. [36, 37]. Adapted from [38].

of the combustion efficiency, while increasing pollutant emissions. To decrease the evaporation time as much as possible, the liquid fuel is injected in the chamber in the form of a spray, thus increasing the evaporation surface for a given liquid volume.

Chiu et al. [36,37] highlighted four modes of droplet group combustion, illustrated in Figure 1.7:

- single droplet combustion, in which each droplet is surrounded by an envelope flame;
- internal group combustion, in which the core of the droplet cloud, constituted of evaporating droplets, is surrounded by a unique flame front, while droplets outside the core burn in the single droplet combustion mode;
- external group combustion, in which the flame front surrounds the whole droplet cloud, constituted of evaporating droplets;
- external sheath combustion, in which a unique flame front surrounds the cloud, which is made of a central region consisting of non-evaporating droplets surrounded by a region of evaporating droplets.

The combustion is a function of physical parameters gathered in the *group combustion number*, G. The combustion mode of a spray is controlled by mechanisms such as convective transport,

thermal diffusivity, mass diffusivity, and momentum diffusivity. In addition, it depends on the number of droplets in the cloud, N, and on the non-dimensional separation distance equal to the ratio of the interdrop spacing to the droplet radius, S_d, such that G is proportional to $N^{2/3}/S_d$ [36].

Such an analysis indicates that the combustion of a spray depends on the spatial distribution of the droplets. Droplet transport in the carrier flow therefore impacts the combustion process. For instance, coherent structures can engulf the weakly inertial droplets [39, 40], leading to droplet clustering [41] through preferential segregation of the droplets [42]. Droplet inertia is usually examined through a Stokes number (Stk here) which relates the relaxation time of the droplets, τ_{drop}, to a characteristic time τ_{flow} associated to the carrier flow, such that:

$$\mathrm{Stk} = \frac{\tau_{drop}}{\tau_{flow}} \tag{1.5}$$

By assuming that the particle motion is dominated by Stokes' drag, such that other effects are negligible[7], the droplet relaxation time is $\tau_{drop} = \rho^f d^2/18\mu^a$, where ρ^f is the fuel droplet density, d its diameter and μ^a the air dynamic viscosity. By defining the flow characteristic time by $\tau_{flow} = D_{exit}/U$, where D_{exit} is the nozzle exit diameter and U the flow velocity, the Stokes number reads:

$$\mathrm{Stk} = \frac{\rho^f d^2 U}{18\mu^a D_{exit}} \tag{1.6}$$

This Stokes number thus indicates the ability of the droplets to follow the air flow. Droplets with a high Stk have a ballistic behaviour and may cross turbulent structures of the air flow while those with a small Stk are entrained by the structures and concentrated in low-vorticity regions. Nevertheless, as indicated in [42], preferential droplet segregation is not maximum for the smaller droplets of a spray, as turbulent micro-mixing tends to homogeneise the mixture. Therefore, optimal segregation is obtained for a Stokes number such that turbulent micro-mixing is weak and droplet inertia is low enough, leading to a higher droplet concentration in low-vorticity regions.

In an oscillating flow, such as a flow subjected to acoustic forcing, it is useful to define a second Stokes number which relates τ_{drop} to a characteristic time of the oscillation, τ_{oscil}. This Stokes number is defined by:

$$\mathrm{Stk_{ac}} = \frac{\tau_{drop}}{\tau_{oscil}} \tag{1.7}$$

In conclusion, spray combustion involves very specific phenomena, which complicate the search for an optimum in terms of performance, energy efficiency and pollutant emissions. Spray dynamics and evaporation can lead to spatial equivalence ratio inhomogeneities, affecting the combustion efficiency and pollutant emissions. To increase the former and diminish the latter, one seeks to form a homogeneous air-fuel mixture in the shortest time possible. It is thus understandable to combine spray combustion with a swirling air flow, which allows hot gases to recirculate close to the injector, subsequently increasing the evaporation rate ot the spray.

[7] The motion of a particle in an incompressible flow at low Reynolds number is described by the Basset-Boussinesq-Oseen (BBO) equation.

1.2 Theoretical framework for combustion instabilities

A flame is a noise generator and can be assimilated to a pulsating sphere. Local perturbations of the flow influence the local heat release rate (HRR), producing a periodic succession of compressions and expansions, which is reflected by the propagation of acoustic waves through the medium. While perturbations generated by turbulence generally have a large spectrum and small amplitudes, leading to a broadband combustion noise of acceptable amplitude[8], organised oscillations can reach significant amplitudes, especially in confined systems where acoustic waves are easily reflected by rigid walls. Subsequently, the flame is considerably perturbed at one or several specific frequencies related to the excited acoustic modes, and flame intensity oscillations in turn generate acoustic waves. Since the sound speed is, in the practical cases of interest here, much higher than the flow speed, the acoustic perturbation propagates upstream the flame. As a consequence, the noise generated by the flame is able to perturb the inlet flow at a later instant, exciting mechanisms which in turn disturb the flame with an additional delay. A loop is thus established. This is basically how thermoacoustic instabilities arise in a combustor.

1.2.1 Acoustic wave equation in reacting conditions

An inhomogeneous acoustic wave equation in reacting flows can be established using the conservation equations for mass, momentum, energy and species, and the ideal gas law. Here, we present the main steps leading to the establishment of the inhomogeneous wave equation. More details can be found in [43, 44]. By assuming negligible body forces and radiative heat transfer, an equation for the logarithm of pressure is obtained:

$$\begin{aligned}\vec{\nabla}\cdot(\frac{c^2}{\gamma}\vec{\nabla}\ln(P)) - \frac{d}{dt}\left(\frac{1}{\gamma}\frac{d}{dt}\ln(P)\right) &= \vec{\nabla}\cdot(\frac{1}{\rho}\vec{\nabla}\cdot\overline{\overline{\tau}}) \\ &- \frac{d}{dt}\left\{\frac{1}{\rho c_p \mathcal{T}}\left[\vec{\nabla}\cdot\lambda\vec{\nabla}\mathcal{T} + \overline{\overline{\tau}} : \overline{\overline{\nabla}}\vec{u} - \sum_{k=1}^{N} h_k\dot{\omega}_k - \sum_{k=1}^{N}(\rho Y_k c_{pk} V_k^D\cdot\vec{\nabla}\mathcal{T})\right]\right\} \\ &- \frac{d^2\ln(r)}{dt^2} - \overline{\overline{\nabla}}\vec{u} : \overline{\overline{\nabla}}\vec{u} \end{aligned} \tag{1.8}$$

In this expression, the parameters are:

- c: speed of sound
- γ: adiabatic index
- P: pressure
- $\overline{\overline{\tau}}$: viscous stress tensor
- ρ: density
- $\mathcal{T}$: temperature
- λ: thermal conductivity
- $c_p = \sum_k c_{pk}$: constant-pressure specific heat capacity

[8] acceptable in the sense that it does not affect combustion or system integrity.

- c_{pk}: specific heat capacity of species k
- h_k^0: enthalpy per unit mass of species k
- $\dot{\omega}_k$: mass production rate of species k
- Y_k: mass fraction of species k
- V_k^D: diffusion velocity of species k
- r: specific molar gas constant

Kotake [43] proposed a simplification of this equation by using an order-of-magnitude analysis. He only retained the terms associated to the chemical reactions and the velocity fluctuations, which are the dominant sources of the pressure fluctuations. Equation (1.8) can be further simplified under the hypothesis of low Mach number and low convection velocity, which allows to neglect the convective component of the material derivative, and the hypothesis of constant adiabatic index. This leads to:

$$\vec{\nabla}\cdot(c^2\vec{\nabla}\ln(P)) - \frac{\partial^2\ln(P)}{\partial t^2} = \frac{\partial}{\partial t}\left(\frac{\gamma}{\rho c_p \mathcal{T}}\sum_{k=1}^{N} h_k\dot{\omega}_k\right) - \gamma\overline{\overline{\nabla}}\vec{u} : \overline{\overline{\nabla}}\vec{u} \tag{1.9}$$

In the framework of small perturbations, the pressure is expressed by the sum of its time-averaged and its time-fluctuating component: $P = \overline{P} + P'$, with $P' \ll \overline{P}$. Therefore, $\ln(P) \simeq \ln(\overline{P}) + P'/\overline{P}$ and Equation (1.9) reads

$$\vec{\nabla}\cdot(c^2\vec{\nabla}P') - \frac{\partial^2 P'}{\partial t^2} = \frac{\partial}{\partial t}\left(\frac{\gamma\overline{P}}{\rho c_p \mathcal{T}}\sum_{k=1}^{N} h_k^0\dot{\omega}_k\right) - \gamma\overline{P}\,\overline{\overline{\nabla}}\vec{u} : \overline{\overline{\nabla}}\vec{u} \tag{1.10}$$

$$= \frac{\partial}{\partial t}\left((\gamma-1)\sum_{k=1}^{N} h_k^0\dot{\omega}_k\right) - \gamma\overline{P}\,\overline{\overline{\nabla}}\vec{u} : \overline{\overline{\nabla}}\vec{u} \tag{1.11}$$

In reacting flows, the first right-hand side term is generally dominant since noise generation is mainly due to the chemical reactions [43]. This source term can be reformulated for a given reaction defined by $\sum_{k=1}^{N_{sp}} \nu_k^u E_k \rightarrow \sum_{k=1}^{N_{sp}} \nu_k^b E_k$, where N_{sp} is the number of chemical species, ν_k^u is the quantity (in mole) of the chemical species E_k in the unburnt gases and ν_k^b is the quantity of E_k in the burnt gases. By writing $\nu_k = \nu_k^b - \nu_k^u$, the source term is expressed by:

$$\sum_{k=1}^{N_{sp}} h_k^0\dot{\omega}_k = \sum_{k=1}^{N} h_k^0\nu_k\dot{\omega} \tag{1.12}$$

$$= \Delta h_r^0\dot{\omega} \tag{1.13}$$

$$= \dot{q} \tag{1.14}$$

where $\dot{\omega}$ is the reaction rate, $\Delta h_r^0 = \sum_k \Delta h_k^0\nu_k$ is the standard enthalpy of reaction (also called heat of reaction) per unit mass, $\dot{q}$ the volumetric HRR, expressed by the sum of its time-averaged

and time-fluctuating components $\dot{q} = \overline{\dot{q}} + \dot{q}^{'}$, and $\dot{q}^{'} \ll \overline{\dot{q}}$.

$$\frac{\partial^2 P^{'}}{\partial t^2} - c^2 \Delta P^{'} = (\gamma - 1)\frac{\partial \dot{q}^{'}}{\partial t} \tag{1.15}$$

In this expression, $c = c(\mathcal{T}(x))$ is inhomogeneous inside the combustor. By assuming a constant sound speed $c = c_0$[9], Equation (1.15) reads:

$$\frac{\partial^2 P^{'}}{\partial t^2} - c_0^2 \Delta P^{'} = (\gamma - 1)\frac{\partial \dot{q}^{'}}{\partial t} \tag{1.16}$$

Compared to the linearised acoustic wave equation for non-reacting flows, the only difference is found in the right-hand side term, which here corresponds to a source term. While it is zero for non-reacting flows, it only depends on the combustion process in reacting conditions. Equations (1.15) and (1.16) express how the volumetric HRR fluctuations feed the acoustic pressure. But, how acoustic pressure impacts the volumetric HRR is still an open question. Bringing more knowledge to this subject is an objective of this manuscript.

1.2.2 Acoustic energy balance and Rayleigh criterion

To determine whether the oscillations will grow or decay in a system, it is worth examining the acoustic energy balance in all the system. The volumetric acoustic energy e_{ac} is expressed as the sum of the volumetric potential acoustic energy and volumetric kinetic acoustic energy:

$$e_{ac} = \frac{1}{2}\frac{P^{'2}}{\overline{\rho} c_0^2} + \frac{1}{2}\overline{\rho}\vec{U}^{'} \cdot \vec{U}^{'} \tag{1.17}$$

Under the hypotheses of low Mach number, negligible convection and constant sound speed, a local equation for the acoustic energy balance can be obtained:

$$\frac{\partial e_{ac}}{\partial t} + \vec{\nabla} \cdot \vec{j}_{ac} = s_{ac} - d_{ac} \tag{1.18}$$

Here, $\vec{j}_{ac} = P^{'}\vec{U}^{'}$ is the surface acoustic energy flux, $s_{ac} = ((\gamma - 1)/\overline{\rho} c_0^2) P^{'}\dot{q}^{'}$ the source term and $d_{ac} \geq 0$ a volumetric damping term associated to the energy loss processes [46]. This equation indicates that locally, the volumetric acoustic energy grows if the source term exceeds the divergence of the surface acoustic flux and the volumetric damping. However, the volumetric acoustic energy does not fluctuate in a homogeneous manner in the whole combustor, justifying an integrated approach in all the volume. Using the divergence theorem, the balance of the global acoustic energy in the whole system is expressed:

$$\frac{\partial}{\partial t}\left(\int_{\mathcal{V}} e_{ac} d\mathcal{V}\right) = \int_{\mathcal{V}} (s_{ac} - d_{ac}) d\mathcal{V} - \oint_{\partial \mathcal{V}} \vec{j}_{ac} \cdot \vec{n} dS \tag{1.19}$$

$$\Leftrightarrow \qquad \frac{\partial E_{ac}}{\partial t} = S_{ac} - D_{ac} - J_{ac} \tag{1.20}$$

[9] A justification of this approach in a laboratory-scale configuration was given by Cáceres with numerical simulations of the acoustic field. He showed that considering a uniform temperature across a cavity can give results close to those with a non-uniform temperature (see Figure 5.11 in [45]).

There, $\vec{n}$ is the normal vector to the surface, and E_{ac}, S_{ac}, D_{ac} and J_{ac} the volume-integrated expression of e_{ac}, s_{ac}, d_{ac} and $\vec{\nabla} \cdot \vec{j}_{ac}$. Equation (1.20) indicates that the periodic heat release adds energy to the acoustic motion if S_{ac} is positive, which means that heat release and pressure oscillations are in phase. Mathematically, this corresponds to:

$$S_{ac} = \int_{\mathcal{V}} \frac{\gamma - 1}{\overline{\rho} c_0^2} P^{'} \dot{q}^{'} d\mathcal{V} > 0 \tag{1.21}$$

Due to the oscillation of $P^{'}(t)$ and $\dot{q}^{'}(t)$, S_{ac} oscillates with time. Hence, it may alternate between positive and negative values. To estimate if an instability is susceptible to grow, one must therefore consider a time-integrated approach. By integrating Equation (1.21) over a time interval, say $[t, t + \Delta t]$, with Δt much greater than the acoustic period, we obtain the Rayleigh source term:

$$\boxed{\mathscr{S}_{ac} = \frac{1}{\Delta t} \int_t^{t+\Delta t} \int_{\mathcal{V}} \frac{\gamma - 1}{\overline{\rho} c_0^2} P^{'} \dot{q}^{'} d\mathcal{V} dt > 0} \tag{1.22}$$

This criterion, sometimes called **classical Rayleigh criterion** [47], is a necessary but not sufficient condition to drive an instability. To drive an instability, $\mathscr{S}_{ac}$ must not only be positive, but also counteract the acoustic energy loss processes and the global algebraic acoustic flux transfer through the boundaries of the domain. The criterion indicating that the driving process must surpass the damping processes for the system to be unstable, sometimes called **extended Rayleigh criterion**, is expressed by:

$$\boxed{\mathscr{S}_{ac} = \frac{1}{\Delta t} \int_t^{t+\Delta t} \int_{\mathcal{V}} \frac{\gamma - 1}{\overline{\rho} c_0^2} P' \dot{q}' d\mathcal{V} dt > \frac{1}{\Delta t} \int_t^{t+\Delta t} D_{ac} dt + \frac{1}{\Delta t} \int_t^{t+\Delta t} J_{ac} dt} \tag{1.23}$$

Both the classical and extended Rayleigh criteria, constructed on the acoustic energy balance, state that the driving process involves a positive coupling between the acoustic pressure and HRR oscillations. The limitation of the Rayleigh criterion to isentropic flows was highlighted by Chu [48] and discussed by Poinsot & Veynante [47] (8.3.8).

1.2.3 Acoustically compact flames

In the case where the flame dimensions are much smaller than the acoustic wavelength, flames are acoustically compact. In this case, $P^{'}$ is considered uniform in the small domain occupied by the flame, thus it comes out of the volume integral and the Rayleigh source term reads:

$$\mathscr{S}_{ac} = \frac{1}{\Delta t} \int_t^{t+\Delta t} P^{'} \int_{\mathcal{V}} \frac{\gamma - 1}{\overline{\rho} c_0^2} \dot{q}^{'} d\mathcal{V} dt \tag{1.24}$$

$$\boxed{\mathscr{S}_{ac} = \frac{1}{\Delta t} \int_t^{t+\Delta t} \frac{\gamma - 1}{\overline{\rho} c_0^2} P^{'} \dot{Q}^{'} dt} \tag{1.25}$$

In this expression, $\dot{Q}^{'}$ is the global HRR of the flame.

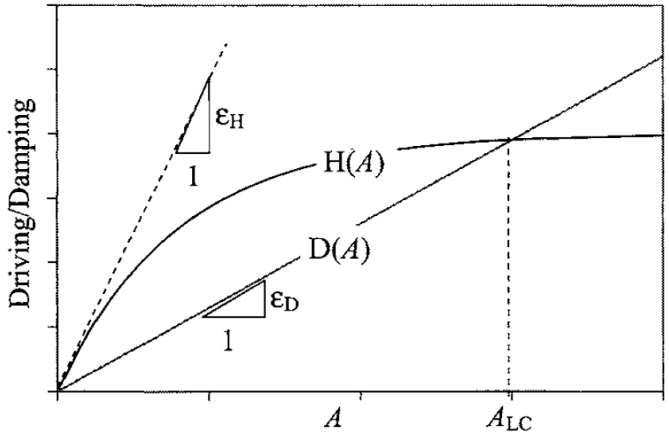

Figure 1.8: Hypothetical evolution of the magnitude of the driving and damping processes, $H(A)$ and $D(A)$, with the acoustic amplitude, A. A_{LC} indicates the limit cycle amplitude, where driving and damping processes compensate. Reproduced from [46].

1.2.4 Stability of a system

Compliance with the extended Rayleigh criterion does not mean that the instability amplitude will grow to infinity. Indeed, the driving and damping processes do not evolve linearly with the acoustic amplitude. This is illustrated in Figure 1.8 by the hypothetical evolution of the magnitude of these processes with the acoustic amplitude, A. In this example, the damping processes grow linearly with A, with a slope ε_D, while the driving processes evolve nonlinearly with the amplitude. Due to the steep initial slope $\varepsilon_H > \varepsilon_D$, driving mechanisms exceeds the damping ones, but the saturation of ε_H as A increases leads to the intersection of the two curves at $A = A_{LC}$. At this point, a stable equilibrium is reached between driving and damping mechanisms, leading to the establishment of a limit cycle. This illustrative example is however not representative of all the instabilities that can be found in various systems.

1.3 Modeling thermoacoustic oscillations

To predict combustion instabilities, it is necessary to know the effects of combustion dynamics on acoustics, but also the effects of acoustics on combustion dynamics, thus closing the thermoacoustic loop. All the loop can be modelled analytically [49, 50], but in most cases, the effects of the acoustic perturbation on combustion dynamics are obtained experimentally or numerically in reference configurations, and the results are injected into semi-analytical models, in which the acoustic wave propagation inside the geometry is modelled [51–53]. Such models are called **acoustic network models**. Another family of models, extensively studied by Culick [54], is based on the projection of the acoustic pressure oscillation on the system's eigenmodes.

In this section, we firstly focus on the acoustic network models. The method is briefly described. In a second time, we introduce the flame describing function (FDF), which relates the HRR oscillation to the acoustic fluctuations. The measurement of the FDF is finally discussed.

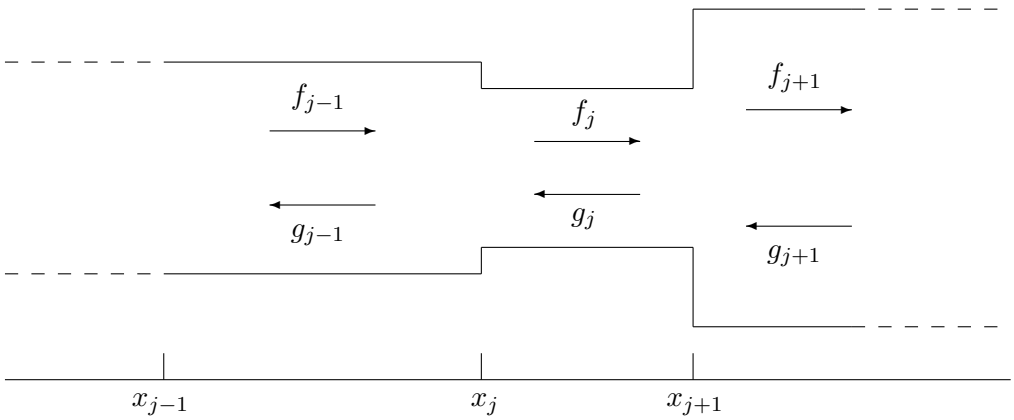

Figure 1.9: Illustration of an acoustic network model without combustion. Acoustic elements j are numbered from 1 to N_j, where N_j is the number of acoustic elements in the model. Location x_j indicates the position of the interface between elements $j-1$ and j. f_j and g_j represent characteristic waves travelling respectively downstream and upstream in element j.

1.3.1 Acoustic network models

Acoustic network models describe the system as a set of one-dimensional acoustic elements through which harmonic acoustic waves travel (see Figure 1.9). This approach is thoroughly detailed in [47,55]. The elements are connected via interfaces at which are defined jump conditions. These models have been widely used in the literature [51, 56–64]. In essence, thermoacoustics is treated as a pure acoustic problem with a source term. The knowledge of the acoustic fields upstream and downstream of each interface is required, which can be expressed by a relationship between the acoustic variables in acoustic elements j and $j+1$ separated by the interface located at x_j.

$$\begin{pmatrix} P'_{j+1} \\ U'_{j+1} \end{pmatrix} = \begin{pmatrix} T_{11} & T_{12} \\ T_{21} & T_{22} \end{pmatrix} \begin{pmatrix} P'_j \\ U'_j \end{pmatrix} \tag{1.26}$$

In the frequency domain, acoustic variables P' and U' are considerered as harmonic acoustic quantities of frequency $\omega/2\pi$ and can be expressed via the characteristic waves in acoustic element j, $f_j = \frac{1}{2}(\frac{P'}{\rho c} + U) = A_j^+ e^{ik(x-x_j)-i\omega t}$ and $g_j = \frac{1}{2}(\frac{P'}{\rho c} - U) = A_j^- e^{-ik(x-x_j)-i\omega t}$, propagating downstream and upstream respectively. In the acoustic element j, acoustic pressure and velocity are thus expressed by:

$$P'_j(x,t) = \rho_0 c_0 (f_j + g_j) = A_j^+ e^{ik(x-x_j)-i\omega t} + A_j^- e^{-ik(x-x_j)-i\omega t} \tag{1.27}$$

$$U'_j(x,t) = f_j - g_j = \frac{1}{\rho_j c_j}\left(A_j^+ e^{ik(x-x_j)-i\omega t} - A_j^- e^{-ik(x-x_j)-i\omega t}\right) \tag{1.28}$$

Without combustion, $\rho_j c_j$ is assumed to be equal in all the acoustic elements. As long as the flow is non-reacting and does not encounter any obstacle other than the change in cross section[10],

[10] More complex cases can be found in [55] (Chapter 7).

jump conditions are:

$$P'_{j+1} - P'_j = 0 \tag{1.29}$$

$$S_{j+1}U'_{j+1} - S_jU'_j = 0 \tag{1.30}$$

Considering that $P'_j = \rho_0 c_0(f_j + g_j)$ and $U'_j = f_j - g_j$, a relationship between the characteristic wave amplitudes in upstream and downstream acoustic elements j and $j+1$ can be derived, yielding:

$$\begin{pmatrix} A^+_{j+1} \\ A^-_{j+1} \end{pmatrix} = \frac{1}{2}\begin{pmatrix} e^{ikl_j}(1+\Lambda_j) & e^{-ikl_j}(1-\Lambda_j) \\ e^{ikl_j}(1-\Lambda_j) & e^{-ikl_j}(1+\Lambda_j) \end{pmatrix}\begin{pmatrix} A^+_j \\ A^-_j \end{pmatrix} \tag{1.31}$$

where $\Lambda_j = \frac{S_j}{S_{j+1}}$. **With combustion**, jump conditions across a reacting region are generally derived under the hypothesis of an infinitely thin flame front, which is valid as soon as the flame is compact relatively to the acoustic wavelength [47]. Consequently, jump conditions read:

$$P'_{j+1} - P'_j = 0 \tag{1.32}$$

$$S_{j+1}U'_{j+1} - S_jU'_j = \frac{\gamma - 1}{\rho c^2}\dot{Q}' \tag{1.33}$$

where $\dot{Q}$ is the HRR of the flame, which is assumed to be harmonic too, $\dot{Q}' = A_{\dot{Q}}e^{-i\omega t}$. A subsequent matrix relationship as Equation (1.31) can be obtained, but it is now expressed:

$$\begin{pmatrix} A^+_{j+1} \\ A^-_{j+1} \end{pmatrix} = \frac{1}{2}\begin{pmatrix} e^{ikl_j}(1+\Lambda_j) & e^{-ikl_j}(1-\Lambda_j) \\ e^{ikl_j}(1-\Lambda_j) & e^{-ikl_j}(1+\Lambda_j) \end{pmatrix}\begin{pmatrix} A^+_j \\ A^-_j \end{pmatrix} + \frac{\Lambda_j}{2S_j}\begin{pmatrix} \frac{\gamma-1}{\rho_j c_j^2}A_{\dot{Q}} \\ -\frac{\gamma-1}{\rho_j c_j^2}A_{\dot{Q}} \end{pmatrix} \tag{1.34}$$

where $\Lambda_j = \frac{S_j}{S_{j+1}}\frac{\rho_{j+1}c_{j+1}}{\rho_j c_j}$. From this expression, it appears that calculating the acoustic velocity downstream of a flame requires to know the unsteady HRR. This issue is now addressed.

1.3.2 The Flame Describing Function (FDF)

1.3.2.1 Definition

Equation (1.33) raises the issue of flame modelling. Without heat release (see Equation (1.30)), the downstream velocity U_{j+1} is predictable by knowing the upstream velocity and the sections of the upstream and downstream acoustic elements. But, with combustion, Equation (1.33) points out that $\dot{Q}'$ must be obtained to close the problem and predict U_{j+1}. A first attempt to model flames was done by Crocco and Cheng [65] with the $n-\tau$ model linking the global HRR oscillation to the velocity perturbation at a reference position.

$$\frac{\dot{Q}'(t)}{\overline{\dot{Q}}} = n\frac{U'(t-\tau)}{\overline{U}} \tag{1.35}$$

This time-domain representation reveals two parameters: the interaction index n, which quantifies the strength of the coupling, and τ, the time delay between the velocity perturbation and the HRR oscillation. This representation is at the basis of the flame transfer function (FTF) and flame describing function (FDF), which are now largely used to model combustion dynamics. Compared to the $n-\tau$ model, the FTF and the FDF are frequency domain representations. The FTF is expressed by:

$$\mathcal{FTF}(\omega) = \frac{\breve{\dot{Q}}/\overline{\dot{Q}}}{\breve{U}'/\overline{U}} = \mathcal{G}(\omega)e^{i\varphi(\omega)} \tag{1.36}$$

$\breve{\dot{Q}}' = A_{\dot{Q}}e^{i\varphi_{\dot{Q}}}e^{-i\omega t}$ and $\breve{U}' = A_U e^{i\varphi_U}e^{-i\omega t}$ are the (complex) harmonic oscillations of HRR and velocity respectively, in which $A_{\dot{Q}}$ and A_U correspond to the amplitudes of the HRR and velocity oscillations, and $\varphi_{\dot{Q}}$ and φ_U to their phase constant. The gain of the FTF, $\mathcal{G}$, is analogous to the interaction index n in the $n-\tau$ model, while the phase φ expresses the phase shift between the oscillations of velocity and the HRR. The FTF depends on the acoustic frequency through $\omega = 2\pi f$, but not on the acoustic amplitude. It is useful for linear stability analyses [66], which is valid at low acoustic amplitudes corresponding to the linear growth of the driving processes (see Figure 1.8). However, the FTF is not able to capture the nonlinear evolution of the driving processes with the acoustic amplitude, which is observed in all practical systems (see, for example [67, 68]). Since the limit cycle amplitude is generally determined by the nonlinear processes [46], the latter must be considered for predicting the instability amplitude. This leads to the definition of the FDF, a tool originating from control theory which is mostly used in low-order models [52, 53, 69–71]. The FDF reads:

$$\mathcal{FDF}(\omega, U^{rms}/\overline{U}) = \frac{\dot{Q}'/\overline{\dot{Q}}}{U'/\overline{U}} = \mathcal{G}(\omega, U^{rms}/\overline{U})e^{i\varphi(\omega, U^{rms}/\overline{U})} \tag{1.37}$$

Due to its dependence on the the velocity amplitude, $U^{rms}/\overline{U}$, it is able to capture the nonlinear evolution of the driving processes.

1.3.2.2 Determination of the FDF

The FDF, as the FTF, contains the physical mechanisms linking the input signal to the output signal without necessarily describing them. In low-order models, the knowledge of the FDF is necessary to predict instabilities but the mechanisms may remain unknown. The FDF can be obtained through experiments, numerical simulations or analytical models. Understanding the physical mechanisms driving the HRR oscillation can allow to develop analytical flame models, with the aim of predicting the HRR oscillation at lower cost.

Analytical flame models have been extensively developed for laminar premixed flames without swirl, due to the relative simplicity of these flames. These models are widely based on flame front kinematics, studied through the G-equation [72]. The early models predicted the flame intensity oscillation by considering linear effects [73–75], while other ones also took into account nonlinear effects [49, 76–78]. With swirl, linear [79] and nonlinear [80] premixed flame response was modelled. However, the complexity of the reacting flows encountered in practical applications (due to, *e.g.,* non-premixed combustion, spray, turbulence, flame-wall or

flame-flame interactions...) has led to the development of academic configurations which share several characteristics of practical combustors: flame-flame interaction has been reproduced in laboratories [81–83] and simulated [84], turbulent flames are very common [67, 85, 86], non-premixed [87] or partially-premixed [88] flames have been studied, and spray flames are widely investigated, both experimentally [45, 89–91] and numerically [92]. However, the complexity of much of these flames is such that, at present, analytical models to describe their HRR oscillation in response to acoustics do not exist. Therefore, low-order models are often fed by the FDF obtained from experiments or numerical simulations [53].

By definition, the determination of the FDF requires to control the acoustic driving amplitude and frequency. In self-excited systems, these quantities cannot be controlled as they are determined by the coupling between combustion and acoustics. Therefore, it is needed to use configurations in which flames are forced by an external acoustic field. For instance, large eddy simulations (LES) of premixed non-swirling [93] and swirling flames [94, 95] were performed to obtain the FDF computationally. In these studies, the acoustic excitation was simulated by imposing a single-frequency velocity oscillation at the inlet of the computational setup. Simulations were run for various excitation frequencies and amplitudes, and the results were compared with experimental ones, showing that the nonlinear saturation of the FDF was well captured by the LES. The FDF can also be obtained experimentally on setups designed for acoustic forcing experiments. In these setups, the acoustic excitation is performed with loudspeakers [96–100]. Nevertheless, some points must be considered with care to accurately determine the FDF.

Acoustic forcing method

A first point concerns the acoustic forcing method. In unstable annular combustors, the instability is generally coupled by an azimuthal mode of the chamber, which can be of various types: standing [98, 101], spinning [102, 103], or a combination between different azimuthal and axial modes [104]. In a standing mode, the flames are subjected to pressure or transverse velocity fluctuations according to their location in the chamber. The ability of linear combustors forced with a standing transverse acoustic wave to reproduce fundamentally the flame behaviour during a self-excited standing-wave instability found in annular model combustor at a pressure antinode and a pressure node was shown by O'Connor et al. [98]. Moreover, a linear array of three injectors was used to conduct a study at a pressure antinode (PAN) for an operating point originally unstable in an annular combustor [99][11]. It highlighted the positive sign of the Rayleigh source term, which is consistent with the instabilities found in the annular combustor. However, in most configurations allowing FDF measurements, longitudinal acoustic excitation is performed by using one or several loudspeakers placed in the supply lines upstream of the chamber [105–107]. This longitudinal excitation induces an axial flow modulation.

It is often admitted that flames placed in an azimuthal/transverse acoustic field mainly respond to the indirect axial flow perturbation induced by the pressure oscillation [108]. In particular, the response of a rod-stabilised premixed V-flame to upstream longitudinal forcing or downstream transverse forcing at a pressure antinode (PAN) was studied by the CORIA team [109]. They highlighted two different mechanisms for the two forcing cases, at frequencies in the range 500-

[11] This work is included in the present manuscript, in Chapter 7.

1000 Hz. With upstream longitudinal forcing, the increase of the pressure pushed the jet out of the burner, leading to the jet acceleration. This mechanism was called 'pumping effect'. With downstream transverse forcing at a PAN, the pressure decrease induced the suction of the jet, leading to the jet acceleration. This mechanism was called '**plugging effect**'. In spite of these two different mechanisms, both forcing methods led to the same dynamics of the jet and flame. Investigations on a swirling premixed flame subjected to longitudinal or transverse forcing were performed by Saurabh & Paschereit [110]. Longitudinal forcing was performed in the frequency range 20-250 Hz while transverse forcing was performed in the range 30-160 Hz. Transverse forcing corresponded to symmetric forcing (like at a pressure antinode) for all frequencies except for those in the range 100-120 Hz, which was attributed to the interaction with anti-symmetric forcing of the test rig. For two swirl numbers and two mass flow rates, they observed the same phase of the FDF with both forcing methods, except in the range 100-120 Hz due to the anti-symmetric transverse forcing. On the contrary, the gain was much higher with transverse forcing for frequencies lower than 120 Hz. By performing Proper Orthogonal Decomposition (POD) analysis on flame intensity images captured at an excitation frequency of 80 Hz, they found that the mode corresponding to symmetric flame fluctuations has a similar structure with both forcing methods, suggesting the presence of vortical structures at the outer shear layer. Nevertheless, the contribution to the fluctuating energy contained in the dominant POD mode pair was found to be 67% higher with transverse forcing than with longitudinal while normalised velocity fluctuations only varied by 15 %. They concluded that the difference between the flame response to longitudinal or transverse forcing could be linked to the vortical disturbances. While these studies indicate similarities between the flame response to longitudinal forcing and axisymmetric transverse forcing (*i.e.*, forcing at PAN), the flame response can result from different effects at other locations inside a standing transverse acoustic field. The work of Acharya et al. [79] on swirl-stabilised premixed flames indicates that the global response of such flames is very little affected by transverse velocity fluctuations. Nevertheless, Lespinasse & Baillot [111] showed that the symmetry of a laminar premixed V-flame in the TACC setup was affected by the cross contribution of the local pressure and pressure gradient, leading to a stationary deviation of the flame when the flame was placed between PAN and a velocity antinode. This feature was also found for a swirl-stabilised spray flame characterised by a low power in TACC-Spray [45], an upgraded version of TACC.

Choice of the reference signal for the FDF

A second point concerns the location at which the input signal is measured. In most cases, the input signal is the velocity fluctuation. Truffin & Poinsot [112] showed that the axial location at which it was measured can affect the FTF. Their numerical work, performed on a forced laminar Bunsen flame, showed that the velocity fluctuation must be measured very close to the burner exit to avoid the dependence on the boundary conditions, and therefore to give a robust FTF that could be extrapolated to other burners, which have different boundary conditions. Another study by Gaudron *et al.* [52], who investigated a swirl-stabilised premixed flame subjected to longitudinal forcing, either upstream or downstream the injection system, showed that the FDFs measured in both forcing cases were comparable for $f < 220$ Hz only when the velocity fluctuation was measured close to the injector exit. When the FDF was based on velocity or pressure

fluctuations measured at other locations, acoustic models of the injector were needed to link the different FDFs together. With downstream forcing, a linear acoustic model was sufficient to link the acoustic quantities (pressure and velocity) upstream and downstream of the injector. With upstream acoustic forcing, the acoustic model had to be modified to include the pressure drop across the swirler to accurately link the acoustic quantities on both sides of the swirler. These results indicate that the acoustic pressure field inside the system differs depending on whether the forcing system is located upstream or downstream. Although the velocity fluctuation is often taken as the input signal of the FDF, it is sometimes difficult to measure it while respecting the abovementioned condition for practical reasons. In addition, the velocity fluctuation amplitude can strongly depend on the radial location in realistic flows such as swirling flows [53]. This motivates the study of an FDF based on a quantity less sensitive to the location. The downstream acoustic pressure could be an adequate quantity due to its low sensivity to the location (under the assumption of compact flames), but also due to its relation with the velocity fluctuation in downstream forcing, through the abovementioned 'plugging' effect. This is the subject of Chapter 4 of the present manuscrit.

1.4 Mechanisms of flame dynamics

In this section, a literature review on the mechanisms by which combustion is coupled to acoustics, previously identified by 'coupling mechanisms' (see Figure 1.2b), is made. The proposed approach in the manuscript first emphasises the physical quantities which control the HRR for premixed flames. Such an approach is justified by the fact that n-heptane swirl-stabilised spray flames have been shown to behave primarily like premixed flames for an injection unit very similar to the one used in the present work [53, 113]. Then, mechanisms that can modulate the physical quantities controlling the HRR, and therefore lead to the HRR oscillation are described on the basis of a literature review.

1.4.1 Physical quantities controlling the heat release rate: application to a laminar premixed plane flame front

To understand which mechanisms can lead to HRR fluctuations, it is first interesting to observe which physical quantities affect the HRR. A chemical reaction such as combustion is represented by:

$$\sum_k \nu_k^u E_k \rightarrow \sum_k \nu_k^b E_k \tag{1.38}$$

Subscript k refers to the chemical species, superscripts u and b to the unburnt mixture and burnt combustion products respectively, and ν_k indicates the quantity (in mole) of the chemical species E_k. The global HRR of a flame $\dot{Q}$ is expressed by:

$$\dot{Q} = \int_{\mathcal{V}} \sum_k \Delta h_k^0 \nu_k \dot{\omega} d\mathcal{V} \tag{1.39}$$

In this expression, Δh_k^0 is the standard enthalpy of formation per unit mass of species k, $\nu_k = \nu_k^b - \nu_k^u$ and $\dot{\omega}$ the reaction rate. Then, the standard enthalpy of reaction (also called heat of

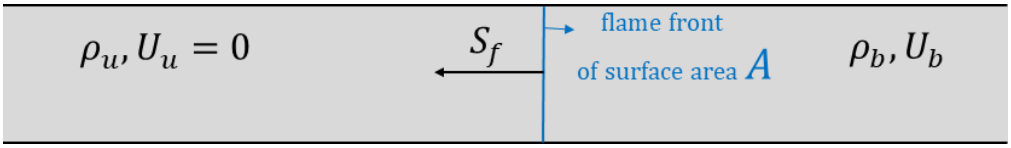

Figure 1.10: Sketch of the one-dimensional propagation of a premixed flame front in a tube. The unburnt mixture is characterised by a density ρ_u and a velocity $U_u = 0$, and the combustion products by a density ρ_b and a velocity U_b. The flame front of surface area A_f propagates at its displacement speed S_f towards the unburnt mixture.

reaction) per unit mass, expressed by $\Delta h_r^0 = \sum_k \Delta h_k^0 \nu_k$, is introduced in Equation (1.39). This gives:

$$\dot{Q} = \int_{\mathcal{V}} \Delta h_r^0 \dot{\omega} d\mathcal{V} \tag{1.40}$$

Let us now consider the one-dimensional propagation of a perfectly-premixed turbulent flame front inside a tube (see Figure 1.10). Δh_r^0 is known and does not depend on the volume and $\int_{\mathcal{V}} \dot{\omega} = \rho_u S_c A$, where ρ_u is the density of the unburnt mixture, S_c the consumption velocity and A_f the flame surface area. For laminar adiabatic unstretched plane flames, $S_c = S_f$. Therefore, the global HRR is expressed by:

$$\dot{Q} = \Delta h_r^0 \rho_u S_f A_f \tag{1.41}$$

This expression reveals that the global HRR depends on several parameters:

- the flame surface area A_f can be affected by velocity oscillations of the inlet flow;
- The burning velocity can be affected by several factors. First, it is modified by turbulence. For a turbulent premixed flame with negligible strain and curvature effects, the turbulent burning velocity S_T can be expressed as a function the laminar burning velocity S_f, the cross-sectional area of the tube, A, and A_f [114]. In this approach, the turbulent burning velocity is obtained by assimilating the turbulent flame front of area A to a wrinkled laminar flame front of surface A_f. As the mass flow rate across these two flame fronts is similar, it follows that $\rho_u S_T A = \rho_u S_f A_f$, thus $S_T = S_f(A_f/A)$. Secondly, the burning velocity depends on the equivalence ratio. For laminar premixed flames, the greater burning velocity is generally reached for an equivalence ratio slightly greater than 1 [115]. For turbulent premixed flames, the relationship between the burning velocity and the equivalence ratio strongly depends on the turbulence intensity [116]. For low turbulence, the maximum burning velocity is reached for an equivalence ratio slightly greater than 1, as for laminar premixed flames, but for high turbulence levels, the burning velocity continues to increase at higher equivalence ratios.
- Δh_r^0 is sensitive to the equivalence ratio. The equivalence ratio is constant in perfectly-premixed flames, but a modification of Δh_r^0 may influence the HRR of partially-premixed flames.

In the following of this section, we review the main mechanisms by which the abovementioned physical quantities can be modified, leading to the fluctuation of the HRR.

1.4.2 Modulation of the flame surface area

As noted by Schuller *et al.* [117], the fluctuations of the HRR in the absence of mixture composition inhomogeneities are governed by the fluctuations of the flame surface area. Therefore, many studies focused on the mechanisms leading to a modulation of the flame surface area. For simplicity, the first works were made on laminar premixed flames. By combining experimental analysis of a laminar premixed conical flame to upstream longitudinal acoustic forcing and theoretical modelling, Baillot *et al.* [74] highlighted that at a given height z above the burner exit, the deformation of the flame front results from two separate perturbations: (i) the local instantaneous disturbance near the flame front and (ii) disturbances originating from the flame base, which are convected along the flame front. Wrinkles were dependent on a velocity proportional to the flow velocity and related to the flame angle. These features were also noted in [73]. Baillot *et al.* also noticed the presence of curvature and stretching effects at the flame base and top, which leads to small discrepancies between the experimental and theoretical flame fronts at these specific locations, as they are not taken into account in the theoretical model.

Laminar conical premixed flames act as low-pass filters of axial flow perturbations, as illustrated in Figure 1.12 (a). In this figure, reproduced from [97], the gain of the FDF tends to unity at low frequencies but suddenly decreases when the reduced frequency ω^*[12] increases [77, 97, 118]. Characteristic rebounds are found at $\omega^* \simeq 8n$, where $n = 1, 2, 3$, but the gain progressively vanishes as ω^* increases. At low frequencies ($\omega^* \leq 4$), the gain is independent of the acoustic velocity oscillation, which reinforces the low-pass filter character of the system at high acoustic amplitudes. At higher ω^*, the flame can be significantly affected by the acoustic level, indicating the presence of nonlinear phenomena. Such a behaviour was attributed to the increase of the curvature of the flame wrinkles, leading to an increase of the flame velocity due to stretch effects. These processes, illustrated in Figure 1.11, are known as 'kinematic restoration processes' [77].

Flame geometry has a substantial impact on its dynamics. A typical FDF of V-flames subjected to upstream longitudinal forcing is shown in Figure 1.12b, reproduced from [97]. Contrary to conical flames, their gain can reach values higher than unity. The overshoots indicate that such flames amplify flow perturbations in a certain range reduced frequencies. Therefore, they are more susceptible to drive combustion instabilities than conical flames.

In the presence of swirl motion, flame front wrinkles are not only transported by the axial component of the flow, but also by the azimuthal component specific to swirling flows [79]. While these effects are not significant in axisymmetric flames subjected to axisymmetric perturbations (like at a pressure antinode of a standing transverse acoustic field), they can affect the flame shape with non-axisymmetric perturbations (like at a velocity antinode), leading to interferences between wrinkles created at the flame base and transported by the swirling flow, and wrinkles due to the local flow perturbation at another azimuthal location above the burner.

[12] $\omega^* = \omega R / S_1 cos(\alpha)$, in which $\omega = 2\pi f$ is the angular frequency, R a characteristic dimension of the flame base, S_1 the laminar burning velocity and α the flame half-angle at the flame tip.

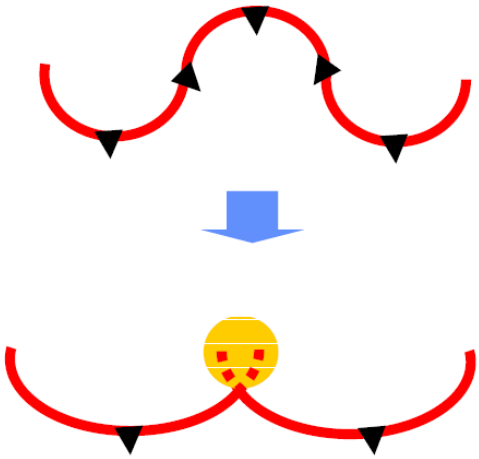

Figure 1.11: Illustration of the reduction of the surface area of a wrinkled flame due to kinematic restoration processes. Reproduced from [77].

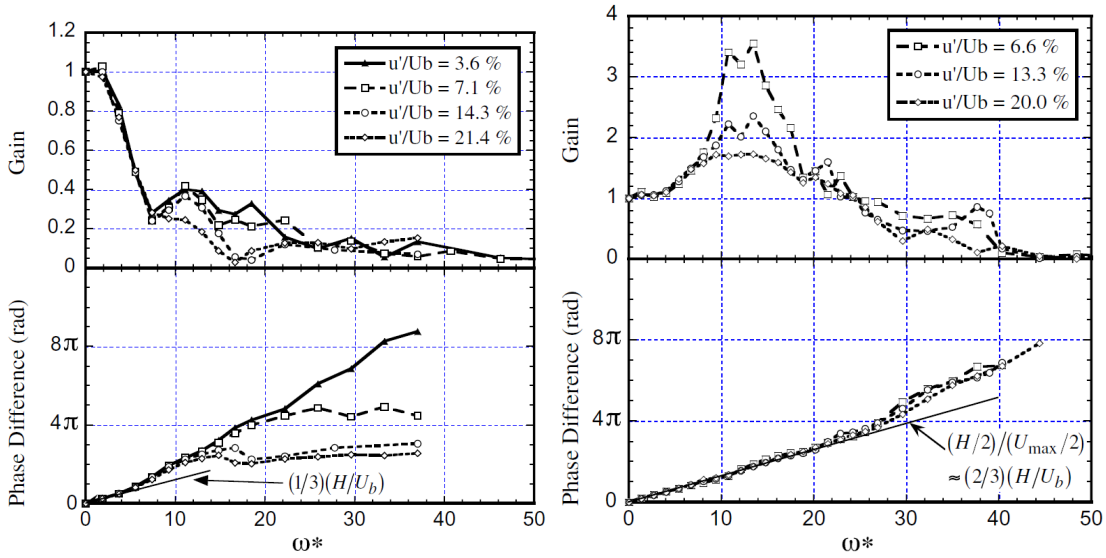

Figure 1.12: Flame describing functions of laminar premixed conical (left) and V-shape (right) flames. Figures reproduced from [97].

1.4.3 Flame-vortex interaction

Vortices develop along shear layers and, depending on their receptivity to input disturbances, can grow during their transport [66]. These coherent structures engulf fresh reactants and can lead to a significant increase of the HRR when they reach the flame front. Nevertheless, it can also lead to local flame extinctions due to high strain rates [119–121]. The interactions between coherent structures and the flame are recognised as a key mechanism in many combustion instabilities [122]. For instance, Poinsot *et al.* [123] identified a self-excited instability involving a strong vortex periodically formed in a multiple-inlet dump combustor. The instability was coupled with an eigenmode of the system of length $L \sim 3.7$ m, which includes a cylindrical tube ($L \sim 1.5$ m), a diverging section ($L \sim 1$ m), a test duct ($L \sim 1$ m) and the combustor. Propane is injected radially at the end of the cylindrical tube, corresponding to about 2 m upstream of the combustor. Their experiment shows the initiation of a vortex at each inlet of the combustor, its growth during convection, producting small-scale turbulence and intense mixing, and the significant C_2 radical emission (linked to the HRR) in the wake of the vortices side branches. This mechanism led to a self-sustained instability that meets the Rayleigh criterion (see Equation (1.22)).

Vortex-flame interactions have been observed in many flames subjected to upstream longitudinal acoustic forcing [67, 86, 124, 125]. Balachandran *et al.* [67] showed the significant roll-up of the flame front induced by the vortex for a lean premixed bluff-body stabilised turbulent flame, resulting in a modulation of the flame surface area and subsequently in a HRR oscillation. Nevertheless, vortex roll-up was also identified as a nonlinear mechanism at high acoustic amplitudes, as indicated by Preetham and Lieuwen [77] and observed with non-swirling [67] and swirling [124] premixed flames. The mechanisms involved include local extinctions of the flame, linked to the high strain rate when the vortex hits the flame front, or kinematic restoration processes due to curvature and stretch effects (see Figure 1.11).

Vortex-flame interactions have also been observed with downstream transverse acoustic forcing, resulting from the axial velocity oscillation induced by the acoustic pressure oscillation in the chamber [109]. Baillot *et al.* [126] highlighted experimentally that the response of a laminar premixed V-flame at a pressure antinode of a standing transverse acoustic field was strongly related to the vortices, particularly to those formed in the outer shear layer. In their work, the flame was stabilised on a rod, leading to the presence of an inner shear layer between the jet and the wake of the rod, and an outer shear layer between the jet and the surrounding medium. They noticed a strong flame response at half the forcing frequency for one specific case, which resulted from the pairing of two successive vortices.

1.4.4 Swirl number fluctuations and precessing vortex core

By definition (see Equation (1.3)), the swirl number is affected by modulation of the axial and tangential velocities. In an experimental and theoretical investigation of a turbulent premixed swirl-stabilised V-flame, Palies *et al.* [127] noticed two separate mechanisms participating to the flame intensity oscillation. The first one was the vortex shedding induced by the axial velocity oscillation, and the second one was attributed to the combined axial and tangential velocity oscillations, leading to the swirl number modulation. While vortex shedding resulted in a significant

flame intensity oscillation at the flame tip, swirl number oscillations affected the flame base angle, subsequently inducing an oscillation of the turbulent burning velocity, and therefore of the HRR at the flame foot. These two mechanisms combined either constructively or destructively, depending on the excitation frequency, to induce a global flame intensity oscillation.
With upstream longitudinal acoustic forcing, the axial and tangential velocity oscillations giving rise to the swirl number oscillation result from the impingement of the incident acoustic wave on the swirler. On the downstream side of the swirler, the axial velocity oscillation propagates at the sound speed while the tangential velocity oscillation corresponds to a vorticity wave propagating at a convective velocity [127]. Due to the different propagation velocities of these two waves, it is possible to control swirl number oscillations at the injector exit by changing the recess of the swirler with respect to the injector exit [128]. Since vortex roll-up at the flame tip and swirl number fluctuations both control the flame intensity oscillation in such configurations, the FTF/FDF is affected by a modification of the distance between the swirler and the injector exit [128, 129].

Other structures linked to swirling flows may be involved during thermoacoustic instabilities, such as the PVC. Caux-Brisebois *et al.* [130] indicate that the HRR oscillation during the thermoacoustic cycle was induced by the deformation of the PVC at the thermoacoustic frequency, which was different to the frequency of rotation of the PVC. Therefore, the PVC can drive an instability. On the contrary, results in isothermal flow by Frederick *et al.* [131] indicate the PVC can suppress the receptivity of the shear layer to external longitudinal forcing, thereby suppressing the flow response to the forcing frequency. Under self-excited conditions for which the PVC was naturally suppressed, Lückoff *et al.* [132] performed upstream longitudinal acoustic excitation at a frequency chosen to excite the PVC. With this method, the self-excited instability amplitude was significantly reduced, which they attribute to the mitigation of equivalence ratio fluctuations (see Section 1.4.5) induced by PVC-enhanced mixing.

1.4.5 Equivalence ratio fluctuations

In the cases where mixture composition inhomogeneities are present, they can be a driving mechanism for instabilities. Lieuwen *et al.* [133] developed a method to study combustion instabilities induced by fluctuations of the equivalence ratio ϕ in a lean premixed combustor. They derived a stability criterion based on the time lag between the fluctuation of ϕ at the injector and the HRR oscillation for several inlet boundary conditions. They found a good agreement between the instability regions predicted by the model and experimental results obtained with three different combustors. Ćosić *et al.* [88] examined the effect of simultaneous velocity and equivalence ratio perturbations on the response of a swirl-stabilised flame. Their experimental setup allows to modify the degree of premixedness by splitting the gaseous fuel injection between a location far upstream of the burner, at which the air is injected, and a location immediately upstream of the burner. They defined a fuel-split ratio parameter $\varepsilon = \dot{m}^f_{burner}/\dot{m}^f_{tot}$, where $\dot{m}^f_{burner}$ is the fuel mass flow rate injected immediately upstream of the burner and $\dot{m}^f_{tot}$ is the total fuel mass flow rate. To distinguish between the effects of the velocity fluctuation and those of the equivalence ratio fluctuation on the flame response, they separated the contribution of each mechanism to the

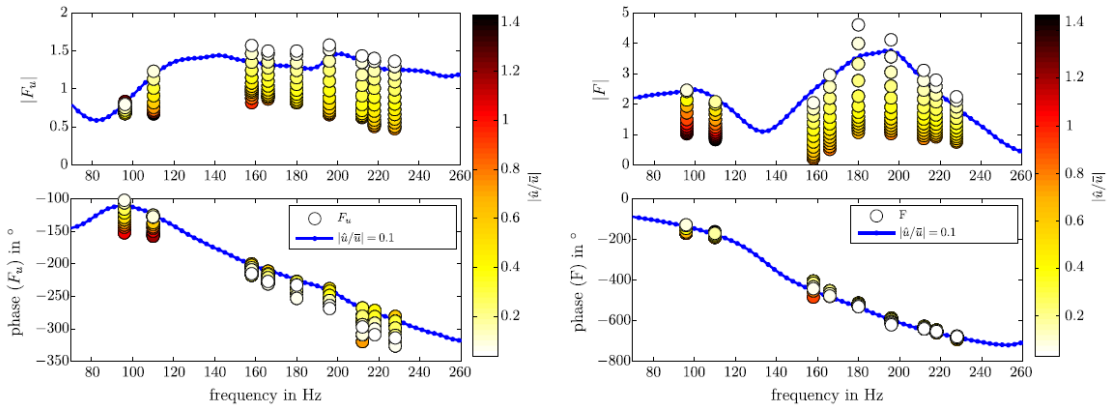

(a) Flame describing function at premixed conditions.

(b) Flame describing function at partially premixed conditions. ε = 1

Figure 1.13: Flame describing functions (FDF) for various acoustic amplitudes and frequencies. The left column shows the FDF for a fuel-split ratio $\varepsilon = 0$, corresponding to perfectly premixed conditions. F_u is the FDF resulting from the velocity perturbation. The right column shows the FDF for $\varepsilon = 1$, corresponding to partially premixed conditions. $F = F_u + F_\phi$ is the FDF resulting from perturbations in velocity and in equivalence ratio. Reproduced from [88].

HRR fluctuation for small acoustic amplitudes:

$$\frac{\hat{\dot{q}}}{\overline{\dot{q}}} = F_u(\omega)\frac{\hat{u}}{\overline{u}} + G_\phi(\omega)\frac{\hat{\phi}}{\overline{\phi}} \tag{1.42}$$

where $\hat{(\cdot)}$ and $\overline{(\cdot)}$ indicates Fourier transforms and mean quantities respectively. This model requires two inputs and gives one output. This approach, called multiple-input single-output (MISO) system [134], is an extension of single-input single-output (SISO) systems, such as the classical FTF. However, the authors assumed a stiff fuel injection and a short distance between the injector and the burner; therefore, the equivalence ratio fluctuation only depended on the velocity fluctuation, and by extending Equation (1.42) to the FDF framework, they obtained:

$$\frac{\hat{\dot{q}}}{\overline{\dot{q}}} = \left[F_u(\omega, |\hat{u}/\overline{u}|) + F_\phi(\omega, |\hat{u}/\overline{u}|)\right]\frac{\hat{u}}{\overline{u}} \tag{1.43}$$

$$= F(\omega, |\hat{u}/\overline{u}|)\frac{\hat{u}}{\overline{u}} \tag{1.44}$$

In this way, the FDF was reduced to a SISO system. $F(\omega, |\hat{u}/\overline{u}|)$ corresponds to the FDF that was measured. $F_u(\omega, |\hat{u}/\overline{u}|)$ was measured in perfectly premixed conditions ($\varepsilon = 0$), for which $F(\omega, |\hat{u}/\overline{u}|) = F_u(\omega, |\hat{u}/\overline{u}|)$. $F_\phi(\omega, |\hat{u}/\overline{u}|)$ was then deduced from the measurement of $F(\omega, |\hat{u}/\overline{u}|)$ for a given $\varepsilon \neq 0$, and $F_u(\omega, |\hat{u}/\overline{u}|)$ obtained for $\varepsilon = 0$. Their results (see Figure 1.13) indicate that the FDF can be significantly affected by equivalence ratio fluctuations, as the latter interfere with the mechanisms driving the premixed flame response.

1.4.6 Mechanisms linked to the fuel spray

It is now interesting to focus on the driving mechanisms related to the fuel spray. Giuliani *et al.* [135] investigated a non-reacting polydisperse spray generated by a swirling airblast injector. The authors simulated the air velocity modulation associated to acoustics by using a rotating cogged wheel, and the fuel flow rate modulation with a solenoid valve. With air flow modulation or fuel flow modulation, they identified an oscillation of the local spray density during the modulation cycle, leading to a periodic fuel feeding to the flame. With air flow modulation only, they also observed a periodic modulation of the droplet size distribution, although they indicate that the atomisation mechanism should be very little affected by fluctuations of the air velocity or of the liquid velocity. In this case, droplets accumulate near the injector at low air velocity and are ejected with the flow acceleration. A numerical investigation of the non-evaporating spray transport by the gaseous flow using the Basset-Boussinesq-Oseen equation showed that the response of the droplet velocity to the flow modulation was strongly dependent on the droplet size. They concluded that the modulation of the droplet size distribution was induced by the sensitivity of the small droplets to the air flow velocity: small droplets were close to each other near the injector exit during the low-velocity phase, while they were more distant during the high-velocity phase. On the contrary, the density of the largest droplets was quite constant during the acoustic cycle, due to their low reactivity to the air flow modulation. The same team later identified (see [136]) a second mechanism on a swirling airblast injector for the formation of the droplet density wave, which was linked to disintegration of the liquid fuel sheet by the oscillating airflow. This mechanism, also identified by Eckstein *et al.* [71], relies on the sensitivity of the fuel droplet size upon the airflow velocity. In addition, Gajan *et al.* [136] showed that the droplet density wave, which mainly concerned the small droplets, was amplified during its propagation towards the chamber exit. Due to the axial velocity oscillation, faster particles could catch up with slower particles, leading to a sharp peak of droplet density downstream of the injector. This phenomenon had previously been identified as a potential driving mechanism of combustion instability in liquid fuel rocket engines (see [137] or 3.3.1 in [138]). The droplet number density wave generated by this mechanism could lead to equivalence ratio oscillations and subsequently to HRR oscillations. Nevertheless, droplet number density waves may also lead to droplet clustering [139], which might slow down the evaporation process [38].

A recent numerical work using LES [140] showed that thermoacoustic instabilities can be sustained by the coupling between a liquid fuel film created at the wall inside the injector and the acoustic perturbation. In particular, the important of the film treatment at the injector wall was identified.

1.5 Objectives and organisation of the manuscript

1.5.1 Objectives of the present work

The present work aims at providing an experiment-based analysis in order to better understand the mechanisms through which swirl-stabilised spray flames couple with acoustics. It is part of

the ANR FASMIC[13] program ANR-16-CE22-0013, a collaboration between CERFACS, CORIA and EM2C laboratories coordinated by Professor Françoise Baillot from CORIA. In light of the above considerations, the manuscript proposes to answer to the questions listed below:

- One question concerns the **influence of the flame location in a standing transverse acoustic field on its coupling with acoustics**. For that purpose, the injector array is placed at several positions of interest in the TACC-Spray chamber, such that the position of the central swirl-stabilised spray flame coincides with a pressure antinode (PAN), an intensity antinode (IAN)[14] or a velocity antinode (VAN) of the forced acoustic field. Although it is known that pressure fluctuations effects (at PAN) have a greater impact on the heat release rate oscillation of the flame than the transverse velocity fluctuations (at VAN), it is worth examining the response to simultaneous fluctuations of both these quantities (at IAN), which was shown to result in a stationary deviation of a swirl-stabilised spray flame characterised by a low power in a previous study on TACC-Spray [45]. An intriguing phenomenon found in MICCA-Spray, consisting in the **dynamical blow-out of the flames located around the velocity antinodal line** is reproduced and examined in TACC-Spray.

- One item pertains to the **experimental determination of the flame describing function (FDF)**. In low-order models, this relation is used to link an input signal, which is the velocity fluctuation induced by acoustics, to an output signal, which is the heat release rate fluctuation of the flame. All the mechanisms linking the input to the output are contained in this 'black-box'. One issue is related to the measurement of the velocity fluctuation, which may be challenging in experimental setups for practical reasons. Moreover, strong velocity gradients due to the presence of shear layers are found in realistic flows, which require to perform very accurate measurements, potentially leading to increased uncertainties. In the case of standing transverse acoustic forcing, the velocity fluctuation is induced by the pressure fluctuation inside the chamber. Therefore, an FDF based on the pressure fluctuation is defined and compared with the classical FDF based on velocity fluctuation. It is shown that the pressure-based FDF is as suitable as the velocity-based FDF to describe the evolution of the gain and phase with the acoustic amplitude. This feature arises from the linear relationship between the amplitudes of the pressure and velocity fluctuations, and the quasi-constant phase shift between them.

- One remarkable feature of thermoacoustic instabilities is their dependence on the operating point. To elucidate this, the **influence of the flame thermal power** is examined in this manuscript. This study is motivated by the fact that instabilities in annular combustors are strongly dependent on the flame thermal power, as shown by instability maps obtained in an annular combustor [141]. This work is performed by selecting three operating points with different flame powers but the same equivalence ratio. Among them, one operating point corresponds to an unstable point in MICCA-Spray annular combustor introduced just below, which allows to investigate the mechanisms driving the instability.

- It is also interesting to know how the **the nature of the fuel influences the flame response**.

[13] FASMIC for Flames/Acoustics coupling in Swirling spray Multi-Injection Chambers.
[14] IAN corresponds to the location of the maximum surface acoustic flux.

This study is motivated by the need of an increased fuel flexibility for future combustors, for instance, due to the recent interest about drop-in fuels. Therefore, it is important to identify fuel properties that play a significant role in the flame response. To this end, the response of spray flames of n-heptane or dodecane is examined. The former fuel is more volatile and more easily atomised than the latter. It is thus expected to better understand how fuel atomisation and evaporation processes affect the flame response.

The abovementioned analyses are based on the identification of the dominant mechanisms behind the response to acoustics of these swirl-stabilised spray flames.

1.6 Structure of the manuscript

To address the points mentioned above, the manuscript proposes a development of the methods, results and analyses in three parts and nine chapters.

Part I deals with the experimental setup and methods used.

In Chapter 2, the experimental setup TACC-Spray, the diagnostics and the post-processing methods used are presented. The acoustic cavity represents an unfolded sector of three swirl-stabilised spray flames of the self-excited annular combustor MICCA-Spray, located at EM2C laboratory [101], in which a controlled standing transverse acoustic field can be generated by an acoustic forcing system. Experimental diagnostics can be used to investigate the physical mechanisms driving the flame response to acoustics for a set of chosen operating conditions. For this purpose, the flame, the spray and the air flow are examined with adequate diagnostics. The main post-processing methods used in the manuscript are then introduced.

In Chapter 3, the central flame is characterised in steady conditions, as well as the fuel spray of n-heptane and the air flow in reacting conditions. A reference operating condition, named $\mathbb{P}_{59}$, characterised by a thermal power of 5.9 kW/flame and an equivalence ratio $\phi = 0.85$, is chosen. Emphasis is firstly placed on the description of the fuel spray. We then focus on the conditions that must be fulfilled to describe the flow from measurements made on the fuel droplets. As expected, one must focus on small droplets, due to their greater ability to follow air flow fluctuations. Finally, the steady flame is characterised using the emission CH^* or OH^* radicals.

In Chapter 4, the flame describing function (FDF) is the focus of interest. A comparison is performed between the FDF based on the axial velocity oscillation measured at a well-chosen location at the central burner exit, defined on the basis on previous works [52, 53, 112], and the FDF based on the acoustic pressure oscillation at the central flame location. This study is motivated by the fact that (i) the measurement of axial velocity oscillation is sensitive to the measurement location due to strong gradients at the burner exit, which could lead to increased uncertainties, and that (ii) axial velocity oscillation is often more difficult to measure experimentally than acoustic pressure oscillation. It is shown that the pressure-based FDF can suitably describe combustion dynamics in the present configuration. This finding is used throughout the following of the manuscript to investigate combustion dynamics.

Part II investigates the flame response when the central injection unit is placed at the central PAN of the 2T1L mode. Due to the dimensions of the cavity and the acoustic wavelength, the flame is acoustically compact.

In Chapter 5, the global flame intensity oscillation and the FDF are firstly characterised with n-heptane for operating condition $\mathbb{P}_{59}$ as a function of the non-dimensional parameters Π, corresponding to the acoustic pressure amplitude reduced by the aerodynamic bulk pressure. It is shown that both CH^* and OH^* radicals are able to describe the evolution of the global flame intensity oscillation with the reduced acoustic amplitude Π, and thus that of the FDF. The coupling between global flame intensity oscillation and acoustic pressure oscillation is then examined using an instability index based on the Rayleigh criterion. Space-time analyses of the flame intensity oscillation, air flow modulation and fuel spray modulation are then carried out to understand the physical mechanisms leading to the global flame intensity. It is found that a flame-intensity wave propagates with convection, and that its amplitude evolves during the propagation, leading to a remarkable oscillation of the flame intensity in the middle region of the flame. The peak of flame intensity is induced by the simultaneous ejection of a large droplet amount and a coherent vortex, which allows to periodically supply the flame with a large fuel amount properly mixed with the oxidizer. Finally, some insights into the saturation of the flame intensity oscillation at high values of Π are given.

In Chapter 6, the influence of the flame power on the flame intensity oscillation is investigated with two additional operating points, characterised by a flame power lower or higher than for $\mathbb{P}_{59}$, and the same equivalence ratio. For all the powers, the evolution of the flame intensity oscillation reduced by the mean flame intensity with Π presents three zones: (i) a linear growth, up to $\Pi = 0.3$; (ii) a transition zone characterised by a lesser slope up to $\Pi = 0.5$; and (iii) a saturation zone beyond $\Pi = 0.5$. However, the flame intensity oscillation increases notably when the flame power is augmented. By using high-speed flame images, it is shown that at low power, the global flame intensity oscillation is reduced by destructive interferences between the local oscillation of the flame intensity emitted by different regions of the flame, due to the low convective propagation velocity of the flame intensity wave. The flame power is also influenced by the characteristics of the fuel spray, which is constituted by droplets whose mean diameter decreases as the flame power increases, accelerating the evaporation process.

In Chapter 7, an analysis of the saturation of the flame intensity oscillation is carried out in the case of the three flame powers. This chapter reproduces a work published in Proceedings of the Combustion Institute 38 (2021) after peer-review, under the title 'Saturation phenomenon of swirling spray flames at pressure antinodes of a transverse acoustic field', by Françoise Baillot, Clément Patat, Marcos Cáceres, Jean-Bernard Blaisot and Éric Domingues. It follows a work presented by C. Patat with the same title and the same co-authors at the 38th International Symposium on Combustion, which was held on 24 - 29 January 2021 in Adelaide, Australia. An operating point characterised by a lower flame power than $\mathbb{P}_{59}$ is chosen, allowing to reach large values of Π. It is shown that saturation is characterised by a loss of the flame structure, leading to a reduction of both its mean intensity and its intensity oscillation. The saturation process may be explained by the generation of strong droplet number waves at the injector exit, which could lead to a decrease of the evaporation rate due to droplet clustering effects.

In Chapter 8, the impact of the liquid fuel on the flame intensity oscillation is evaluated. To this end, the fuel lines are fed either by n-heptane or by dodecane while keeping all the other operating parameters unchanged. An analysis of the hollow-cone sprays in reacting conditions without acoustic forcing highlights that droplets are larger with dodecane. The radial droplet distribution at the injector is identical for the two fuels, but the flame base angle is more open with dodecane. With acoustic forcing, the flame intensity oscillation is higher with n-heptane at a given Π, leading to a greater gain of the pressure-based FDF. In addition, the FDF phase is slightly higher with dodecane at low Π, indicating a longer time delay between the acoustic pressure oscillation and the flame intensity oscillation, but it is equal at $\Pi = 0.5$, corresponding to the beginning of the saturation zone. Analyses of the spray modulation induced by acoustics indicate the the gain of the FDF is linked to the proportion of small droplets. Thus, the lower gain with dodecane should be linked to the shift of the drop size distribution towards higher diameters.

Part III investigates the flame response when the central injection unit is placed at various locations inside the 2T1L mode: a pressure antinode (PAN), an intensity antinode (IAN) and a velocity antinode (VAN).

In Chapter 9, the flame intensity oscillation is compared when the central flame is placed at PAN, at IAN or at VAN. The central flame intensity oscillation is stronger at PAN and progressively decreases as the local acoustic pressure amplitude decreases, until it reaches negligible levels at VAN. Local analyses of the central flame at the three locations indicate that its intensity oscillation is dominated by effects of the acoustic pressure oscillation. Nevertheless, they also show that the gaseous phase is sensitive to the transverse velocity oscillation at IAN and particularly at VAN. On the contrary, the spray at the injector exit is unaffected by the transverse motion of the flow. This suggests that the flame could be destabilised due to the transverse velocity oscillation.

In Chapter 10, the dynamical blow-out (DBO) of the flames at VAN, observed in MICCA-Spray during high-amplitude self-excited instabilities coupled by a standing azimuthal acoustic mode, is reproduced in TACC-Spray for three air mass flow rates and various acoustic amplitudes. This chapter is the result of a joint work between EM2C and CORIA laboratories through the ANR FASMIC program. It has been published as a journal article in Proceedings of the Combustion Institute (2022) after peer-review, under the title 'Swirling spray flames dynamical blow-out induced by transverse acoustic oscillations', by Clément Patat, Françoise Baillot, Jean-Bernard Blaisot, Éric Domingues, Guillaume Vignat, Preethi Rajendram Soundararajan, Antoine Renaud, Daniel Durox and Sébastien Candel. It follows a work presented by C. Patat with the same title and the same co-authors at the 39$^{\text{th}}$ International Symposium on Combustion, which was held on 24 - 29 July 2022 in Vancouver, Canada. This study exploits the complementarity between the self-unstable sixteen-injector annular combustor MICCA-Spray and the acoustically-forced three-injector linear array TACC-Spray. The experimental data obtained in TACC-Spray show a very good accordance with a theoretical model, originating from a previous work [142] but further developed here. An analysis of the space-time OH*-intensity of the flames gives deeper insight into the physical phenomena leading to the DBO.

In conclusion, the main outcomes of this work and the perspectives for future works are given.

Part I

Experimental setup and methods

Chapter 2

Experimental setup, diagnostics and post-processing methods

Contents

This chapter first describes the experimental setup TACC-Spray used for all the experiments reported in this manuscript. TACC-Spray is a combustion test rig equipped for acoustic forcing experiments. It consists in a rectangular-shaped cavity in which three swirling spray injectors are placed, corresponding to an unwrapped sector of the annular combustor MICCA-Spray. This setup allows to investigate mechanisms of flame response to a variety of acoustic perturbations consisting in a combination of pressure and transverse velocity oscillations. The diagnostics used for temperature and acoustic pressure measurements, flame front emission analysis and two-phase flow investigation, and the associated experimental configurations are described. The post-processing methods are also introduced.

2.1 Experimental setup

All the experimental works presented in this manuscript are carried out on the TACC[1]-Spray experimental facility. This setup consists in an acoustic cavity, five injection units and an acoustic forcing system. TACC-Spray is an open-loop system designed for studying mechanisms leading to thermoacoustic combustion instabilities, especially those associated to downstream transverse acoustic waves. Its design was chosen to reproduce some basic elements of the annular combustor MICCA-Spray constituted of sixteen injectors developed at EM2C laboratory, which can be self-excited under some operating conditions (see Figure 2.1). In the FASMIC program, TACC-Spray is part of an ensemble of experimental facilities having the same injection units, which includes two facilities designed and operated at EM2C laboratory in addition to MICCA-Spray [113]: (i) SICCA-Spray, a single-injector chamber which can be operated under self-excited instabilities or upstream longitudinal forcing; and (ii) TICCA-Spray setup, a new linear array of three injectors that can be subjected to upstream longitudinal forcing. The acoustic field is generated by the acoustic forcing system and the facility is not operated at conditions leading to self-excited instabilities.

2.1.1 Acoustic cavity

The CORIA TACC-Spray acoustic cavity is a chamber with a rectangular cuboid shape equipped with driver units, as shown in Figures 2.1 and 2.2. The dimensions of the TACC-Spray cavity are adjustable, allowing to select the resonance frequency of the cavity. The cavity length, L_c, can be modified by moving the two side walls along rails and by combining a set of front plates of various sizes to form the front walls. In this work, two chamber lengths $L_c = 800$ mm and $L_c = 880$ mm are used in reacting conditions, while $L_c = 520$ mm is set in non-reacting conditions. The chamber height is set to $h_c = 200$ mm. It can be increased by adding two sets of steel plates of height 100 mm on top of the cavity. The cavity is surmounted by a convergent part of height $h_{cp} = 60$ mm and exit width $e_{cp} = 10$ mm, which prevents the entrainment of surrounding air and allows to increase the acoustic level and to homogeneise the temperature field inside the cavity, as shown in [45]. The chamber width, e_c, is 55 mm, similar to that of the MICCA-Spray combustor. The origin of the coordinate system (O, x, y, z) is at the center of the cavity base.

2.1.2 Injection system

A five-injector linear array, designed to generate three swirling spray flames at the center and two swirling air jets at its extremities is located at the cavity base, as shown in Figure 2.2. As combustion takes place inside the cavity, the names *acoustic cavity* and *combustion chamber* are equivalently used throughout this manuscript. The objective of this setup is to place the central flame in an environment reflecting that of MICCA-Spray, as illustrated in Figure 2.1. The five injectors are fixed independently of each other to a steel plate, which is the cavity base. Several plates with different inter-injector distances a_{inj} are available, allowing to modify the degree of interaction between flames. The cavity can be continuously displaced, such that the injector array

[1]Transverse Acoustic Combustion Chamber

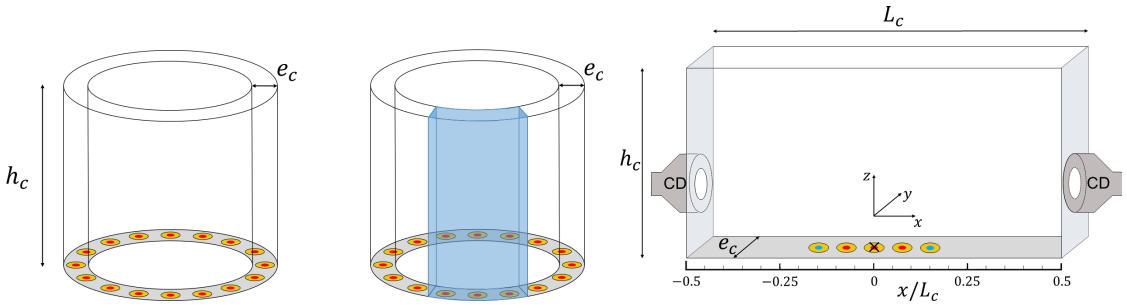

(a) MICCA-Spray

(b) Isolating and unfolding a three-injector sector

(c) TACC-Spray

Figure 2.1: Relationship between the annular combustor MICCA-Spray (EM2C laboratory) and the linear array TACC-Spray (CORIA laboratory). The latter setup consists in a unfolded sector of three flames of the annular combustor, equipped with lateral compression drivers (CD). The black cross indicates the location of the origin of the reference frame in (c).

and consequently the flames can be placed at several locations of interest into the acoustic field. All the five injectors feature a distinct plenum, to which air is supplied from a compressor before entering in a tangential swirler and a distributor, on top of which is located an outlet cup which creates a convergent nozzle exit, as depicted in Figure 2.3. While the plenum and the distributor of the three central injectors are identical for all the experiments, two sets of swirlers and outlet cups are used here. The first one, called K modified set, corresponds to that used by Cáceres [45] and Prieur [91]. The second one, called 716 set, is used to focus on characteristics observed in the MICCA-Spray combustor [53]. The two side swirling injectors act as stabilizers of the lateral flames. The three central injectors each include an additional liquid fuel feeding system through which either n-heptane or dodecane is injected in the cavity via a simplex atomiser set before the nozzle exit of diameter $D_{exit} = 8$ mm. The atomiser is located with a recess from the nozzle exit of $0.67D_{exit}$ with the K modified set and $0.8D_{exit}$ for the 716 set. This original solution proposed in [45] allows to keep the three flames anchored far from the side walls, and thus the injector array to be placed freely at any location inside the cavity.

2.1.3 Acoustic field

Acoustic forcing is performed with a system composed of a Hameg HM8150 signal generator, an IMG Stageline frequency filter to suppress frequencies lower than 500 Hz, which can damage the compression drivers, a Peavey PV 900 power amplifier and two Beyma CP850ND compression drivers, which are fixed face to face on the side walls of the acoustic cavity. The same sinusoidal signal is sent to both compression drivers in order to excite a standing mode of the cavity, which is here the 2T1L mode (see Figure 2.4). The theoretical resonance frequency of the three-dimensional TACC-Spray cavity, which presents closed-closed ends in the $\vec{x}$ and $\vec{y}$ direction and open-closed ends in the $\vec{z}$ direction, is expressed by Equation (2.1), in which m_x, m_y and m_z characterise the normal modes in each direction. Here, $m_x = 2$, $m_y = 0$ and $m_z = 0$, indicating that the second transverse mode in the $\vec{x}$ direction and the first longitudinal mode (in

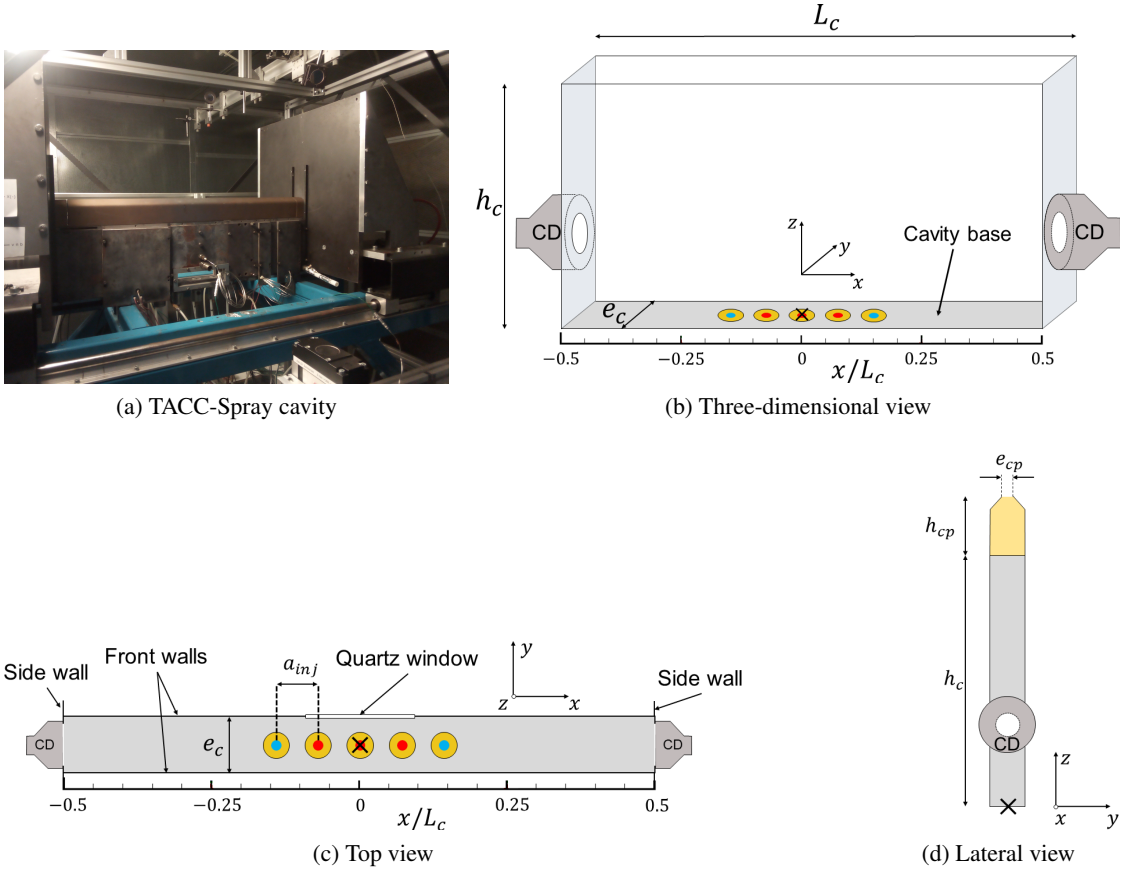

(a) TACC-Spray cavity

(b) Three-dimensional view

(c) Top view

(d) Lateral view

Figure 2.2: Pictures and sketches of the TACC-Spray acoustic cavity. Red injectors are supplied with liquid fuel and air, blue injectors are only supplied with air. All the injectors feature a swirling air flow. The black cross indicates the location of the origin in the reference frames associated to (b,c,d). Here, the movable injector array is placed to locate the central injector at the center of the cavity. The convergent part is shown on the picture (a) and on the lateral view of the cavity (d). CD: compression drivers.

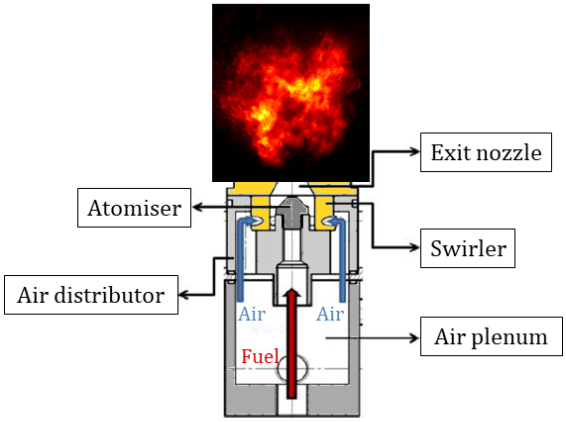

Figure 2.3: Sketch of a radial cut of a liquid fuel/air injector with an instantaneous flame image in false colours. The flame and the injector are at the same scale.

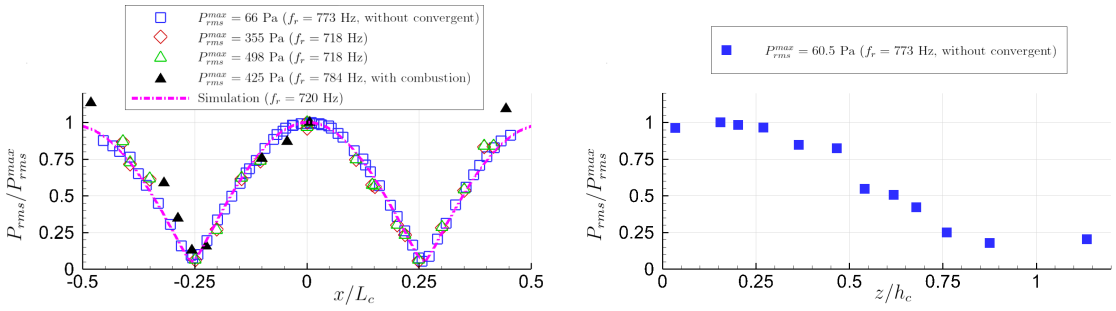

(a) 2T mode of the cavity

(b) 1L mode of the cavity at $x = y = 0$

Figure 2.4: Characterisation of the 2T1L mode of the acoustic cavity. In the absence of combustion, $L_c = 520$ mm to remain in the frequency range 700-780 Hz. With combustion, $L_c = 800$ mm. Measurements are obtained without combustion and with convergent part, unless otherwise stated. The simulation is performed with $L_c = 800$ mm and with an inhomogeneous temperature field, characterised by a local temperature varying between 623 and 800 K inside the cavity.

the $\vec{z}$ direction) are excited.

$$f = c_0(T)\left[\left(\frac{m_x}{2L_c}\right)^2 + \left(\frac{m_y}{2e_c}\right)^2 + \left(\frac{2m_z+1}{4(h_c+h_{cp})}\right)^2\right]^{1/2} \tag{2.1}$$

In this expression, $c_0(T)$ corresponds to the sound speed. In the present work, the frequency of the 2T1L mode is set in the range 700-780 Hz by adjusting the dimensions of the cavity. It is ensured that the acoustic forcing excites the 2T1L mode of the cavity by measuring the acoustic field for various amplitudes with the acoustic pressure measurement method described below (see Section 2.2.2). Measurements are performed without and with combustion and results are shown in Figure 2.4. In this figure, L_c is set to 800 mm with combustion, while it is reduced to 520 mm without combustion to obtain resonance frequencies in the same range. The 2T component of the acoustic field is well identified without combustion for three acoustic pressure amplitudes (see Figure 2.4a). When the convergent part is removed from the top of the cavity, the resonance frequency $f_r = 773$ Hz (for $P_{rms}^{max} = 66$ Pa). With the convergent part placed at the top of the cavity, the resonance frequency $f_r = 718$ Hz (for $P_{rms}^{max} = 355$ Pa and 498 Pa). The theoretical resonance frequencies obtained from Equation (2.1) by considering $c_0 = 340$ m/s are 778 Hz and 731 Hz without and with the convergent part respectively, which is not far from to the experimental values. With combustion, the 2T component of the acoustic field is retrieved. A modal analysis of the acoustic cavity is performed using Comsol Multiphysics software. The temperature is set to 623 K at $x/L_c = \pm 0.5$ and 800 K at $x/L_c = 0$, simulating the temperature field when the central flame is placed at the center of the cavity of length $L_c = 800$ mm. Results indicate the second transverse mode is associated to a numerical resonance frequency of 720 Hz, which is consistent with the experimental value of 718 Hz and the theoretical value of 731 Hz. The 1L component of the acoustic field is measured in the absence of combustion and an illustration at $z = y = 0$ is shown in Figure 2.4b. It is interesting to note that the acoustic pressure level is constant between $z = 0$ and $z = 0.3h_c$.

2.1.4 Operating points

Several operating points are used throughout this manuscript. These points are identified by the following parameters: fuel, equivalence ratio ϕ, flame power, air mass flow rate $\dot{m}^a$ and the set of swirler and outlet cup. The flame power is a theoretical value, calculated by multiplying the fuel mass flow rate $\dot{m}^f$ by the fuel lower heating value. The lower heating values for n-heptane and n-dodecane are taken as the values at 25°C, which are respectively 44.925 MJ/kg and 44.574 MJ/kg [143]. The characteristics of the operating points are summarised in Table 2.1.

2.2 Diagnostics

2.2.1 Temperature measurements

Temperature measurements are performed by 7 type K thermocouples fixed flush to the front walls, connected to an ALMEMO 5690-2M data acquisition system operating at a frequency of 0.83 Hz. The thermocouple probes are inserted through the perforated front plates, allowing to

Name	Fuel	ϕ	Flame power (kW)	$\dot{m}^f$ (g/s)	$\dot{q}_v^a$ (SLM)	$\dot{m}^a$ (g/s)	U_b (m/s)	Excitation frequency range (Hz)	Swirler name	L_c (mm)	Chapters
$\mathbb{P}_{43}$	n-heptane	0.85	4.3	0.097	80.2	1.72	28.5	703-720	K modified	800, 880	6, 7
$\mathbb{P}_{59}$			5.9	0.133	109.4	2.35	38.9	714-766			3, 5, 6, 7, 8, 9
$\mathbb{P}_{59d}$	dodecane							725-735		880	8
$\mathbb{P}_{75}$	n-heptane		7.5	0.168	138.6	2.99	49.3	732-778		800, 880	6, 7
DBO50	n-heptane	variable	variable	variable	50	1.08	17.8	745-760	716	800	10
DBO63					63	1.36	22.4	755			10
DBO75					75	1.62	26.7	750-762			10
$\mathbb{P}_{74}$	n-heptane	0.95	7.4	0.165	122	2.63	43.4	745-762	716	880	4
$\mathbb{P}_{74d}$	dodecane			0.167				737-763			4

Table 2.1: Operating points and experimental characteristics. U_b and $\dot{q}_v^a$ are defined at the burner exit of diameter $D_{exit} = 8$ mm for the air flow at 20°C.

characterise the gas temperature field at multiple locations along the $\vec{x}$ and $\vec{z}$ directions.

2.2.2 Acoustic pressure measurements

Pressure fluctuations $P^{'}(t)$ are measured with three Brüel & Kjaer Type 4182 microphones placed flush to the front walls, connected to Brüel & Kjaer Nexus Type 2690 conditioner amplifiers. The microphone signals are sent to a National Instruments (NI) acquisition card PCI-6123, recording data at high samples rates, typically 100 times the acoustic frequency (which is in the range 700-780 Hz). All the microphones are equipped with a probe tube of diameter 1.2 mm and length 100 mm, in order to put the sensor away from the heat of the combustor walls. The microphone probe tube is inserted through the perforated front plates and can thus be placed at several positions into the acoustic field, as for the thermocouples. **When the central flame is placed at IAN or at VAN**, one microphone is placed at ($x = x_{cf}, y = -e_c/2, z = 60$ mm $= 0.3h_c$), where x_{cf} is the x-location of the central flame; another one is placed at the central PAN ($x = 0, y = +e_c/2, z = 55$ mm $= 0.275h_c$); and the last one close to a lateral PAN ($x = 415$ mm, $y = -e_c/2, z = 8$ mm $= 0.04h_c$). **When the central flame is located at the central PAN**, one microphone is placed at the central PAN at $z = 60$ mm ($z/h_c = 0.3$) and the two others at the two lateral PANs at $z = 8$ mm. As shown in Figure 2.4 (b), the acoustic pressure level at the central PAN is the same from $z/h_c = 0$ to $z/h_c = 0.3$. Therefore, the acoustic pressure level measured at the central PAN ($z/h_c = 0.3$) gives the same level as the one at the injector exit ($z/h_c = 0$).

The tube at the extremity of the microphone probe introduces a delay between the acoustic pressure in the chamber and that measured by the sensor, which corresponds to the propagation time of the acoustic wave inside the tube. For the range of frequencies used here, this delay is not negligible and must be considered to correct the pressure measurements. Admittedly, the temperature decreases from the wall to the sensor. Nevertheless, as shown by Cáceres [45], taking the assumption of a constant temperature or a constant heat flux inside the probe tube does not significantly affect the calculated value of the tube delay. Therefore, the phase delay introduced by the tube, φ_{tube}, is here estimated by supposing a constant temperature inside the probe tube.

$$\varphi_{tube} = \frac{\omega L}{c(\mathcal{T})} \tag{2.2}$$

where $c = \sqrt{\gamma r \mathcal{T}}$ is the sound velocity, $\gamma = 1.4$ the adiabatic index, $r = 287$ J.kg^{-1}.K^{-1} the mass-specific gas constant and $\mathcal{T}$ the wall temperature measured with a thermocouple placed less than 25 mm from to the microphone probe. The acquisition system introduces a phase inversion of the microphone signals which is added to φ_{tube}. Consequently, the phase of the signal obtained from the acquisition chain, φ_{mic} and the phase of the pressure signal in the chamber at the extremity of the probe tube, $\varphi_{P'}$, are linked via the relationship: $\varphi_{P'} = \varphi_{mic} + \varphi_{tube} + \pi$. The signal amplitude is not corrected to account for the attenuation induced by the probe tube. The reader can refer to [45, 144] for more details.

2.2.3 Chemiluminescence emission from the flame front

Determination of the flame HRR is important in experimental works. While this quantity is directly available in numerical works, it cannot be directly measured experimentally. Therefore,

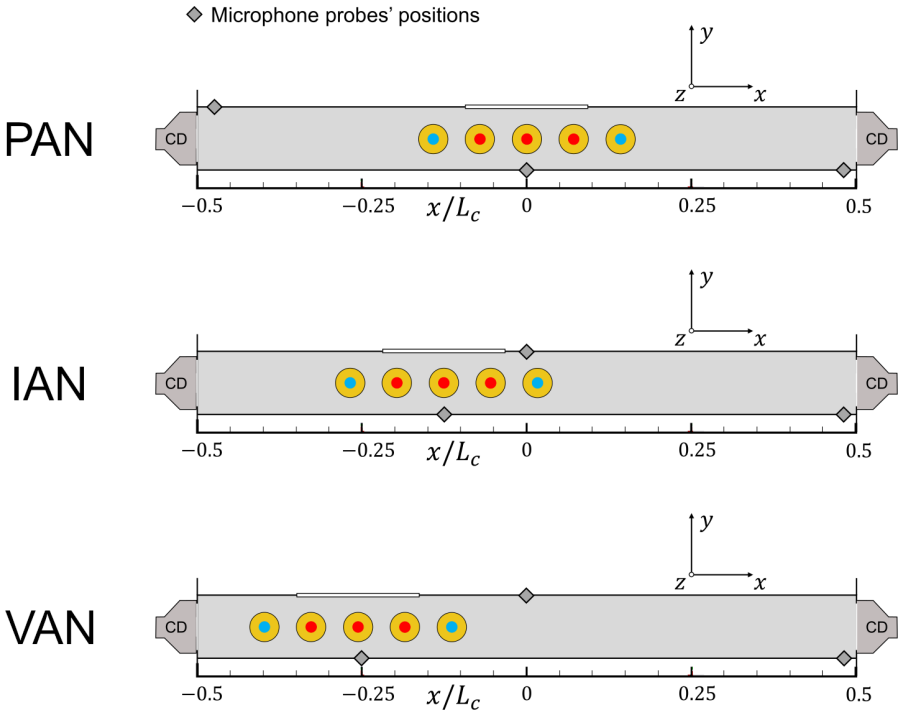

Figure 2.5: Positions of the three microphone probes flush-mounted to the front walls for the three locations of the injector array.

indirect measurements are required in cases of experimental flames. As discussed in Chapter 1, a widespread method consists in measuring the chemiluminescence signals of one or several chemical radicals, *e.g.* CH^*, OH^*, $C_2{}^*$ or $CO_2{}^*$ [85, 145–151]. This technique is relatively simple to set up. The relevance of the method to estimate the HRR in the present configuration is discussed in Section 5.2.2 and Section 6.3.2. In the present work, two methods are used to measure the chemiluminescence emission intensity of one specified radical (OH^* or CH^*), either integrated on the whole flame or spatially-resolved. The first method uses a photomultiplier tube (PM) and gives a time signal of the light emitted by the chosen radical in the whole flame while the second method uses a high-speed camera and intensifier, allowing to obtain series of two-dimensional flame images. Theses setups, shown in Figure 2.6, are described below.

2.2.3.1 Spatially-integrated measurements

In the present work, spatially-integrated chemiluminescence signals of CH^* or OH^* radicals are measured on the whole central flame only, using a Hamamatsu H10721-210 photomultiplier tube, connected to Hamamatsu C10709 power supply unit and a Hamamatsu C7319 amplifier unit. The light from the central flame is focused on the PM sensor with a lens treated to let UV rays through and filtered with an interference filter to observe the emission either from CH^* or OH^*. The filter for CH^* is centered around $\lambda = 430$ nm, with a full width at half maximum (FWHM) of 20 nm, whereas that for OH^* is centered around $\lambda = 305$ nm with a FWHM of 24 nm. The gain of the PM is chosen as constant as possible between different experiments. Sometimes, some adjustments are necessary to avoid saturation of the sensor while

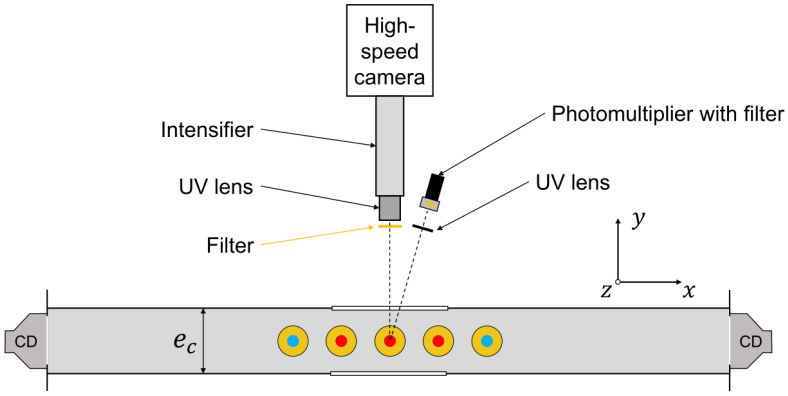

Figure 2.6: Sketch of the experimental setup for flame emission images. The photomultiplier tube captures the light emission from OH* or CH* radical integrated on the whole central flame. The camera captures two-dimensional images of the intensified light emission from OH* or CH* radical. The filters in front of the devices serve to select the radical whose light emission is to be observed. CD: compression drivers.

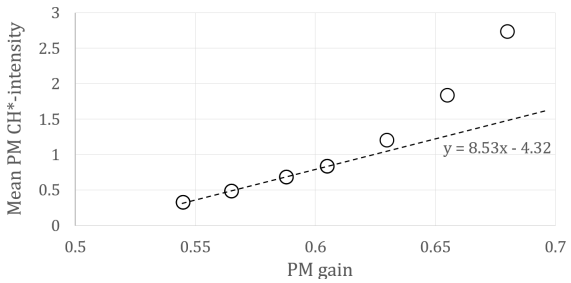

Figure 2.7: Relationship between the gain applied to the photomultiplier tube signal and the mean CH* intensity of the central flame measured by the photomultiplier

keeping a sufficient signal level when the flame power is changed. But, the PM gain, always chosen between 0.55 V and 0.6 V, shows a linear relationship with the mean radical intensity, as illustrated with CH* radical in Figure 2.7. This allows to correct the PM signals in order to compare them as if they are acquired with the same gain by using the empirical law $I_{PM} = aG_{PM} + b$, where G_{PM} is the gain of the PM, $a = 8.53$ and $b = -4.32$. Here, the correction applied is of the form: $I_{PM}^{corr}(t) = I_{PM}^{exp}(t) + a(G_{PM}^{corr} - G_{PM}^{exp})$, where I_{PM}^{corr} and I_{PM}^{exp} are the corrected and uncorrected PM signals respectively, G_{PM}^{corr} is the target gain after correction and G_{PM}^{exp} is the gain of the direct PM chosen during experiments. This correction is applied to compare signals presented in Chapter 6, in which the response of the energy system for various flame powers $\mathbb{P}$ is examined.

2.2.3.2 High-speed spatially-resolved measurements

Capturing high-speed images from CH* or OH* radicals allows to obtain a two-dimensional distribution of the radical light intensities, here in the (O, x, z) space. Due to the positioning of the camera, chemiluminescence signals are integrated over $\vec{y}$ direction. High-speed OH* and CH* images are recorded at 10,000 frames per second (fps) or 20,000 fps with a Phantom V2012

camera equipped with a Lambert HiCATT 25 intensifier, a lens treated to let UV rays through with a focal distance of 105 mm (or 100 mm)[2] and bandpass filters. The emission from the OH^* radical is obtained using a UG11 filter of thickness 3 mm, centered around $\lambda = 325$ nm and with a FWHM of 90 nm. The emission from the CH^* radical is measured using a BG12 filter of thickness 3 mm, centered around $\lambda = 400$ nm and with a FWHM of 110 nm. Three measurement campaigns have been carried out. The objective of each campaign and the chosen acquisition settings are written in Table 2.2. The settings will be recalled in the following if appropriate. Flame image acquisition is synchronised with acoustic pressure measurements and PM signal acquisition. For that purpose, a Berkeley Nucleonics (BNC) Model 575 delay/pulse generator with eight outputs is used. The experimental setup for synchronisation is described in Section A.1.

2.2.4 Phase and Laser Doppler Anemometry (PDA/LDA)

Laser Doppler Anemometry (LDA) is a measurement technique that allows to characterise velocity components of seeding particles introduced into a carrier fluid flow. Under certain conditions discussed in Chapter 3, the particle velocity can be assimilated to that of the flow. The principle of LDA is briefly described. More details can be found in [152]. To obtain one velocity component, two coherent laser beams with different directions of propagation intersect at a particular location, creating a measurement volume, which consists in a pattern made of a succession of interference fringes. When particles cross the measurement volume, they are alternatively illuminated as they cross the bright and dark fringes, and then diffuse light, resulting in modulated light intensity signals captured afterwards by photomultiplier tubes. Since the fringe spacing is known, as it depends on the laser wavelength and the angle between the two beams, it is possible to calculate the velocity of the particles in a direction perpendicular to that of the fringes. To disambiguate the direction of the particle movement, a Bragg cell is used to shift the frequency of one of the laser beams by f_{Bragg}, making the fringe pattern move across the measurement volume. A validation process based on the particle velocity and signal-to-noise ratio then ensures that signals actually correspond to real seeding particles and are not measurement artefacts. One important feature about LDA is that signals are not uniformly sampled, as data are acquired each time a droplet passes across the measurement volume. The consequences of the nonuniform data sampling on post-processings are developed in Section 2.3.

Phase Doppler Anemometry (PDA), also called Phase Doppler Interferometry (PDI)[3], extends the LDA technique to measure the diameter of spherical particles. PDA uses the fact that the phase of the Doppler signal, induced by the passage of the particle through the measurement volume, depends on the particle diameter. Compared to LDA, an additional validation step is performed to reject non-spherical particles. Hence, the data rate with PDA is lower than with LDA.

For this work, a two-component Dantec Dynamics LDA/PDA system is used, allowing to measure two velocity components simultaneously (see Figure 2.8). It is constituted of a source emit-

[2] Two lenses were used for the experimental campaigns.

[3] The associated measurement system is sometimes called Phase Doppler Particle Analyser (PDPA).

Campaign n°	Objective	Chapter	Exposure time (µs)	Intensifier gain (V)	Spatial resolution (mm/pixel)	Acquisition rate (Hz)
1	Influence of thermal power and flame location on the flame response with n-heptane	3,5,6,7,9	45	660	0.143	20,000
2	Influence of the fuel on the flame response	8	49	590-630	0.167	20,000
3	Dynamical blow-out at the velocity antinode	10	99	660	0.148	10,000

Table 2.2: Experimental campaigns of flame image acquisition and the associated settings.

ting two laser beams at λ = 488 nm and two other ones at λ = 532 nm, coupled with a 250 mm focal length lens, and a reception probe equipped with a 500 mm focal length lens that is placed at 30° with respect to the axis of the source. One set of two laser beams are rotated of 90° relative to the other set, so that two orthogonal velocity components are simultaneously measured. The LDA/PDA system is placed on a Bosch Rexroth motion control system. Measurements per-

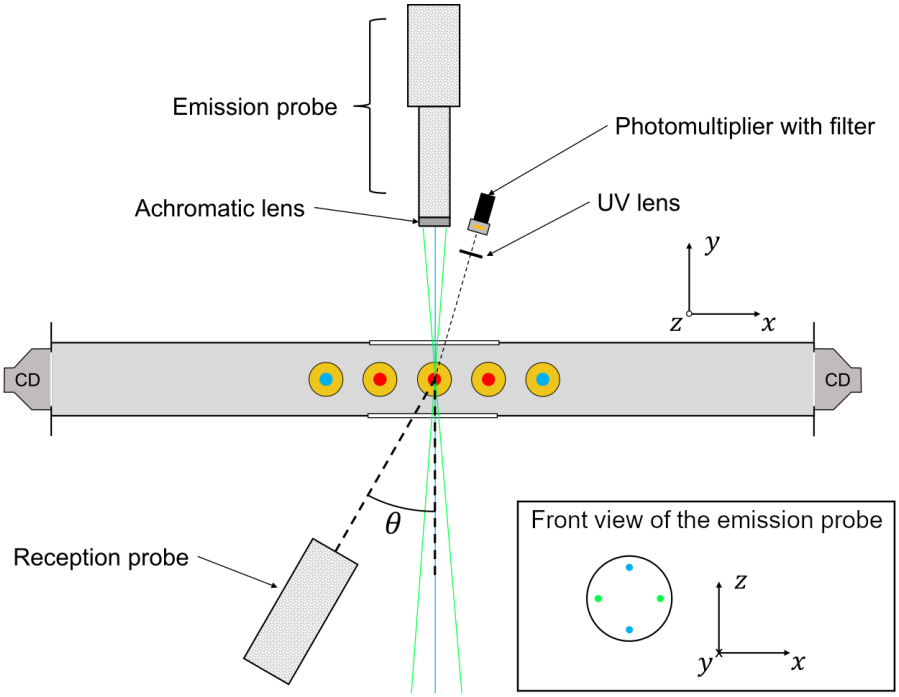

Figure 2.8: Sketch of the setup for Laser/Phase Doppler Anemometry. The emission probe emits two sets of two laser beams, which illuminate seeding particles. The reception probe, placed at $\theta = 30°$ with respect to the beam axis, receives the light scattered by the particles. These two probes are displaced together in the $\vec{x}$ or $\vec{y}$ direction to obtain data profiles. The CH^* or OH^* radical light intensity from the flame is simultaneously captured by the PM equipped with the adequate filter. The origin of the reference frame $(x, y, z) = (0, 0, 0)$ is located at the center of the central injector, on the cavity base. CD: compression drivers.

formed on lines defined by $y = 0$ and $z = z_{meas}$ give the fuel droplet vertical velocity, U_z^f and radial velocity, U_r^f. Measurements performed on lines defined by $x = 0$ and $z = z_{meas}$ give U_z^f and the fuel droplet tangential velocity, U_θ^f. At each location (x, y, z), measurements are performed during 2 to 10 seconds to collect enough data. The measurement duration depends on the operating mode (LDA or PDA), since the data rate is lower with PDA.

2.2.5 High-speed laser tomography

High-speed laser tomography technique allows to capture the motion of seeding particles in a flow. To this end, a laser sheet is formed and directed to illuminate the seeding particles in a plane, the normal direction of which is parallel to the line of sight of a camera which records the light diffused by the particles. In the absence of combustion, the air flow is seeded with DEHS droplets generated by a seeding system. As shown by Cáceres [45], DEHS droplets are good tracers of the air flow. Nevertheless, the high evaporation rate of DEHS makes it unsuitable in reacting conditions. In this case, the air flow is seeded with olive oil droplets. However, due to the use of a liquid fuel spray in TACC-Spray, fuel droplets are also illuminated by the laser sheet. This leads to one limitation of this technique, which arises if the seeding particle-size distribution is polydisperse. As the intensity of the light scattered by a spherical particle depends

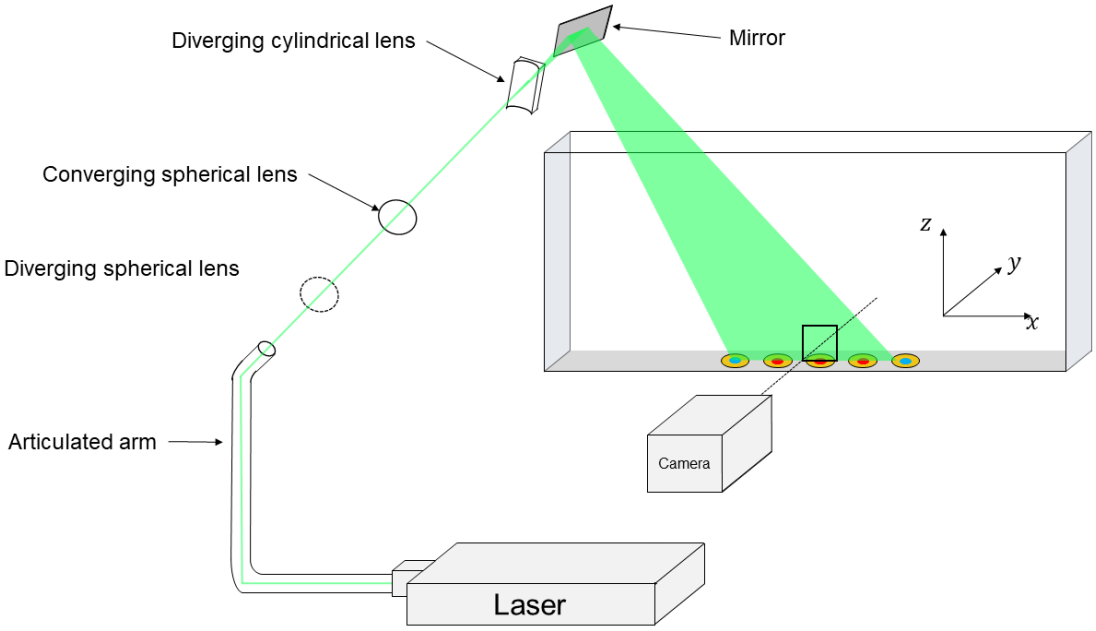

Figure 2.9: Sketch of the setup for high-speed tomography images. The camera captures the light diffused by the seeding particles, which are illuminated by the laser sheet. The square at the central injector exit illustrates the size of the field of view.

on the square of its diameter [153], a bias towards larger particles can be easily introduced. The larger particles have a greater inertia and subsequently a lower reactivity to fluctuations of the carrier fluid flow, so their motion can be very different from that of the carrier fluid. Therefore, a distinction between the motion of the seeding particles and that of the carrier flow may be needed in such cases. The ability of the seeding particles to follow the carrier fluid should thus be carefully assessed before assimilating their motion to that of the carrier fluid. This ability is evaluated with PDPA measurements in Chapter 3 of this manuscript.

High-speed laser tomography technique is here performed using a laser with a high repetition rate, an optical system to produce a laser sheet from the laser beam, a high-speed camera and a device to synchronise laser pulse, image acquisition and acoustic pressure measurements. The laser is a Photonics Industries DM100-532 DH laser, with two laser heads emitting at a wavelength $\lambda = 532$ nm. At 10 kHz, the average power is 200 W and the pulse energy is 20 mJ when the two lasers heads are combined. Each individual head delivers a pulse with a width of about 130 ns. Repetition rates are fixed in the range 20,000 Hz - 35,000 Hz. The average power and pulse of each laser head in this range of repetition rates are reported in Table 2.3. The optical system is made of an articulated arm connected to the laser exit, allowing to direct the laser beam more easily and more safely, a beam expander made of a converging spherical lens and a diverging spherical lens, a cylindrical lens which creates the laser sheet and a mirror to direct the sheet to the cavity. The laser sheet of width about 500 µm is in the plane defined by $y = 0$ mm. The camera is a Phantom V2512, which can be operated up to 25,700 frames per second at a resolution of 1280x800 pixels, or up to 39,100 frames per second with an image size of 768x768 pixels. It is here operated with a size of 768x768 pixels at rates comprised between 20,000 Hz

	Average power (W)		Pulse width (ns)	
Rate (kHz)	Head 1	Head 2	Head 1	Head 2
20	98.6	100.4	235	251
25	93.3	96.5	269	272
30	89.4	92	298	287
35	86.1	86.2	310	288

Table 2.3: Characteristics of the Photonics Industries DM100-532 DH laser heads used for high-speed tomography imaging

and 35,000 Hz. The field of view is a square of side 30.3 mm, resulting in a spatial resolution of 0.039 mm/pixel. The laser pulse emission, the image acquisition and the acoustic pressure measurements are synchronised with a Berkeley Nucleonics (BNC) Model 575 delay/pulse generator with eight outputs. The experimental setup for synchronisation is sketched in Section A.2.

2.3 Post-processing methods

This section gathers the basic elements of the post-processing methods for ease of reading. However, when a post-processing method is used in the following chapters, some of its characteristics are recalled in the text and some extensions of this method could be explained.

2.3.1 Post-processing of time signals

2.3.1.1 Signal decomposition

A signal $s(t)$ can be decomposed into a mean value, $\overline{s}$, and a fluctuating component, $s'(t)$. For a system excited at a given frequency f_r, $s'(t)$ is composed of a coherent oscillation, $s^c(t)$, and a stochastic fluctuation, $s^s(t)$ [154], such that:

$$s(t) = \overline{s} + s'(t) \tag{2.3}$$

$$= \overline{s} + s^c(t) + s^s(t) \tag{2.4}$$

This decomposition method is illustrated with a CH* signal, $I_{CH^*}(t)$, captured by the PM with acoustic forcing at $f_r = 722$ Hz in Figure 2.10 (a). $I_{CH^*}(t)$ clearly presents a coherent oscillation at f_r at the beginning of this example signal, but the coherent oscillation is drastically reduced at other times, *e.g.*, for $0.47 \text{ s} < t < 0.48$ s. To capture this coherent oscillation at f_r, and particularly its changing amplitude over time, $I_{CH^*}(t)$ is filtered with a 4th-order (bandpass) Butterworth filter with cutoff frequencies $f_r \pm 100$ Hz, giving $I^c_{CH^*}(t)$. Filtering with a tolerance around f_r is necessary to capture the changes in amplitude of $I^c_{CH^*}(t)$. The bandwidth of 200 Hz, applied to all the filtered signals in this manuscript, is carefully chosen by ensuring that the signals do not present any significant information at frequencies other than f_r in this frequency range. The power spectral densities (PSD) of $I'_{CH^*}(t)$, $I^c_{CH^*}(t)$ and $I^s_{CH^*}(t)$, shown in Figure 2.10 (b), indicate that $I^c_{CH^*}(t)$ does capture the oscillation at f_r of $I'_{CH^*}(t)$ while $I^s_{CH^*}(t)$ has a larger frequency content.

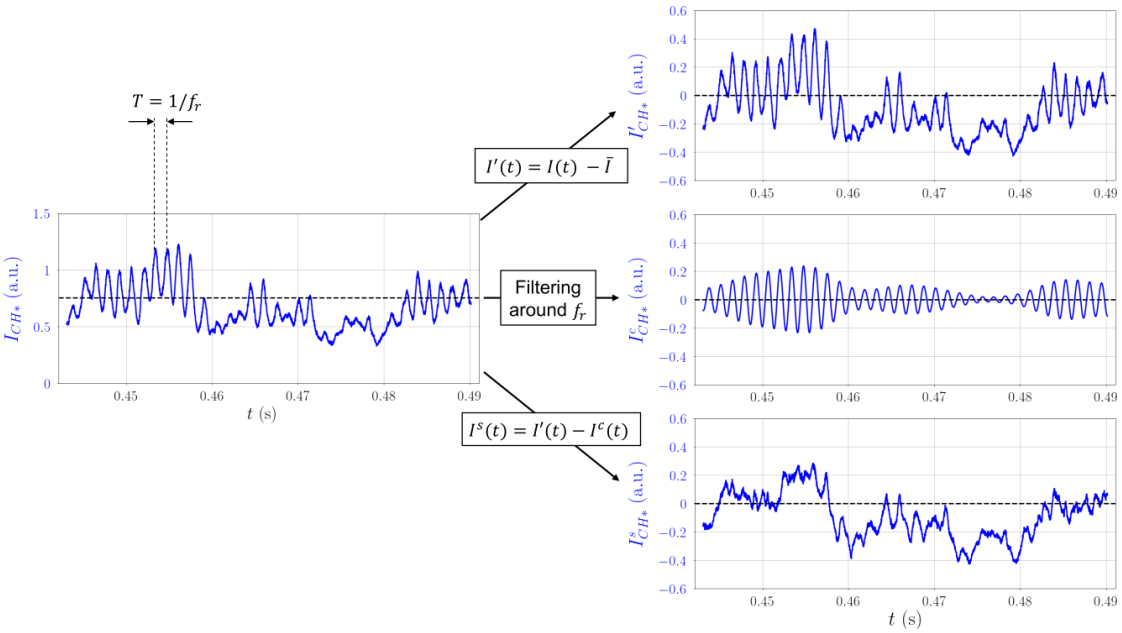

(a) Raw and filtered time-averaged CH*-intensity signals

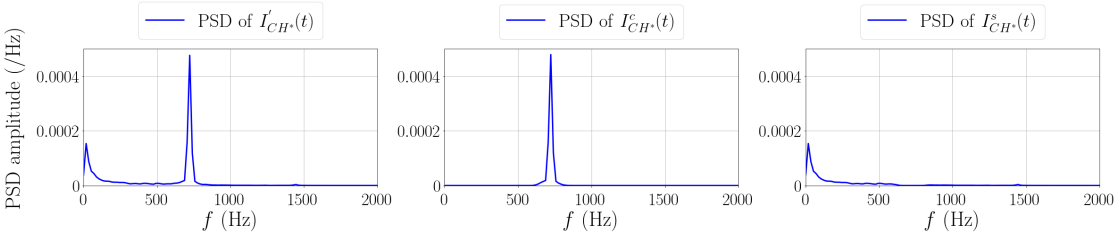

(b) PSDs of the raw and filtered CH*-intensity signals

Figure 2.10: (a) Decomposition of a signal, here $I_{CH^*}(t)$, into a fluctuation $I'_{CH^*}(t)$, a coherent oscillation $I^c_{CH^*}(t)$ obtained by filtering $I_{CH^*}(t)$ with a 4th-order Butterworth filter with cutoff frequencies $f_r \pm 100$ Hz (f_r = 722 Hz), and a stochastic oscillation $I^s_{CH^*}(t)$. $I'_{CH^*}(t)$, $I^c_{CH^*}(t)$ and $I^s_{CH^*}(t)$ have a zero mean. (b) power spectral density (PSD) of $I'_{CH^*}(t)$, $I^c_{CH^*}(t)$ and $I^s_{CH^*}(t)$, calculated from whole CH*-intensity signals of duration 1.4 s, whose excerpts are shown in (a).

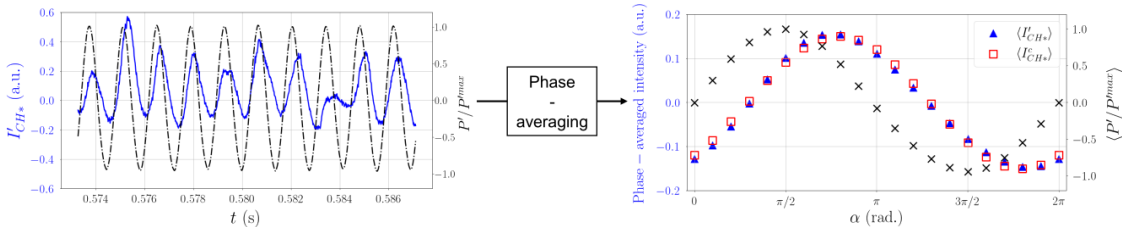

Figure 2.11: Illustration of the results given by the phase-averaging process performed at the acoustic frequency f_r = 722 Hz. On the left are shown extracts of the fluctuating CH* intensity signal and acoustic pressure signal reduced by its maximum value. On the right are shown the results of the phase-averaging process carried out on $I'_{CH^*}(t)$ (filled blue triangles), on $I^c_{CH^*}(t)$ (empty red squares) and on the simultaneous reduced acoustic pressure P'/P'^{max} (black crosses) for post-synchronisation. These signals have a total duration 1.39 s, corresponding to about 1000 acoustic cycles.

The rms oscillation amplitude of $s(t)$ at f_r or, equivalently, the rms oscillation amplitude of $s^c(t)$, is calculated around f_r by integrating the PSD of $s(t)$ obtained with the Welch's method. This method, restricted to uniformly-sampled signals, first consists in dividing a signal into N_{seg} segments, with a 50% overlap here, and in applying a Hann window to each of them. The PSD is then calculated in each segment. Finally, the PSD of the whole signal is estimated by averaging the PSD in each overlapping segment. A detailed description of the method can be found in [155]. For nonuniformly-sampled signals such as PDA/LDA data, the oscillation amplitude is obtained via phase-averaging, described below.

2.3.1.2 Phase-averaging and post-synchronisation

In some cases, it is interesting to reconstruct a periodic signal during an average oscillation cycle. For example, this allows to visualise the average oscillation amplitude of PM signals and the phase shift with a reference signal (see Figure 2.11). These reconstructed signals can be obtained by phase-averaging the instantaneous data. Phase-averaging a signal $s(t)$ at f_r is performed by decomposing an oscillation cycle in N_{bins} bins of equal duration $1/(N_{bins}f_r) = T/N_{bins}$, where T is the oscillation period. The procedure is illustrated in Figure 2.12. Bin n is centered around phase angle $\alpha = 2\pi(n/N_{bins})$, and all the data for which $2\pi\frac{(n-0.5)}{N_{bins}} \leq \alpha < 2\pi\frac{(n+0.5)}{N_{bins}}$ are stored into bin n. This gives the phase-averaged signal at f_r, $\langle s \rangle(\alpha)$. With this method, the average value of the stochastic fluctuations is not significant provided that enough samples are acquired, thus $\langle s \rangle(\alpha) = \overline{s} + \langle s^c \rangle(\alpha)$.

Phase-averaging is also performed when sampling is non-uniform, as with PDA/LDA data. This is particularly interesting as it produces a uniformly-sampled signal from nonuniformly-sampled data, allowing to use the Welch's method. It is verified that the oscillation amplitude and the phase of the signal are the same when calculated directly from a uniformly-sampled raw signal, or from a phase-averaged signal reconstructed from this raw signal.

The phase-averaged signals presented in all this manuscript are post-synchronised with the acoustic pressure measured at the flame location, with correction for the probe tube delay. This phase-averaged acoustic pressure signal thus serves as a reference for all the measurements per-

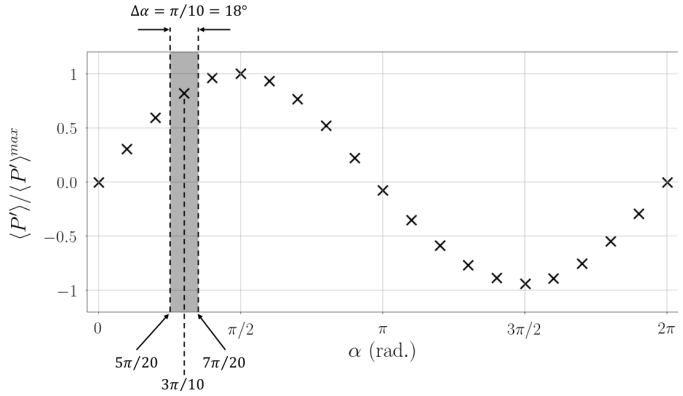

Figure 2.12: Illustration of the phase-averaging process with a phase-averaged acoustic pressure cycle. The oscillation cycle is split into $N_{bins} = 20$ bins. Bin n ($n \in [0, 20[$) is centered around phase angle $\alpha_n = 2\pi(n/N_{bins})$. Instantaneous data acquired around α_n, with a tolerance of $\pm\pi/20$ depicted by the grey rectangle, are put into bin n. The phase-averaged acoustic pressure cycle presented here, defined by $\langle P' \rangle = A_{P'} \sin(\alpha)$, serves as a reference for all the phase-averaged results in this manuscript.

formed here. It is of the form $\langle P' \rangle(\alpha) = A_{P'} \sin(\alpha)$ where $A_{P'}$ is the acoustic pressure amplitude. An illustration of the reference acoustic pressure cycle is shown in Figure 2.12.

2.3.1.3 Flame describing function based on pressure signals

In all this work, the flame is considered compact relatively to the acoustic field (see Section 1.2.3). The response of the flame to the acoustic perturbation is characterised in the flame describing function (FDF) framework. The FDF is a function of both frequency and amplitude, allowing to describe nonlinear responses. Moreover, it can be parameterised by several quantities, such as the flame power, equivalence ratio or fuel nature, among others. In this work, the evolution of the FDF with the acoustic amplitude is investigated, but the evolution with the frequency is not examined, as the dimensions of the acoustic cavity are kept nearly identical for all experiments. As acoustic pressure and PM flame intensity signals are uniformly sampled, the FDF at a given frequency f_r can be directly calculated from the raw signals in the frequency domain:

$$\mathcal{F}(f_r, \Pi) = \frac{\breve{I}/\overline{I}}{\breve{P}/\rho^a U_b^2} = \mathcal{G}_{P'-I'}(\Pi) e^{i\varphi_{P'-I'}(\Pi)} \tag{2.5}$$

where $\breve{I}$ and $\breve{P}$ are complex amplitudes of the flame intensity and pressure oscillations respectively. The FDF can also be expressed through a gain $\mathcal{G}_{P'-I'}$ and a phase $\varphi_{P'-I'}$. The gain indicates the efficiency of the coupling between acoustics and combustion and the phase expresses the phase delay of the light intensity oscillation of the flame with respect to the pressure perturbation.

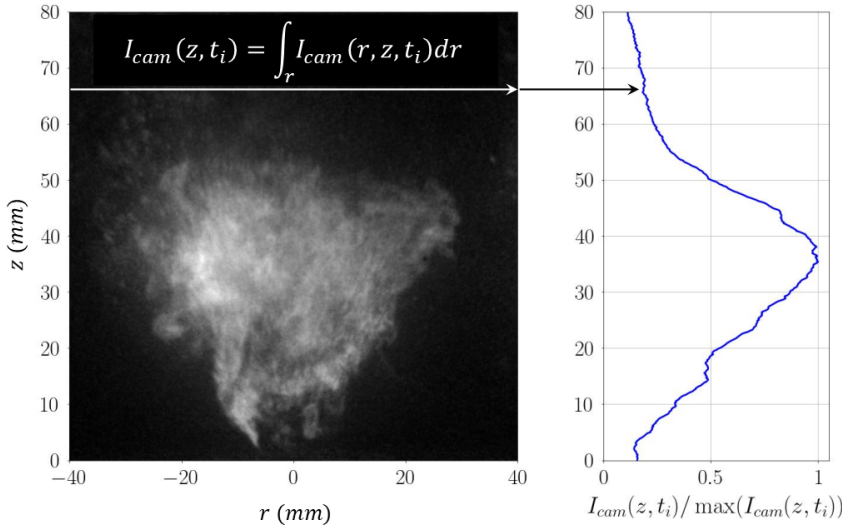

Figure 2.13: Illustration of the conversion of a flame intensity image, $I_{cam}(r,z,t)$, into a two-dimensional signal, $I_{cam}(z,t)$, by integration along $\vec{r}$ direction. The image corresponds to an instantaneous OH* image at a given time $t = t_i$.

2.3.2 Post-processing of chemiluminescence images

2.3.2.1 Induced longitudinal flame intensity wave

It is known that longitudinal oscillations of the HRR are often a dominant mechanism of combustion dynamics [108]. To extract information about the longitudinal flame intensity wave, a relevant approach, proposed in [156] to analyse combustion instabilities, consists in integrating the flame intensity over a cross section of the combustor. This approach can be applied to high-speed experimental flame chemiluminescence images of the central flame here. These images give a light emission intensity signal, $I_{cam}(r,z,t)$, which is firstly thresholded to minimise the influence of the background noise. $I_{cam}(r,z,t)$, which is line-of-sight-integrated, is then integrated along $\vec{r}$ direction to result in a function of z and t only, as shown with an instantaneous image in Figure 2.13. The radial integration of $I_{cam}(r,z,t)$ allows to simplify a multidimensional problem by considering only the longitudinal dimension, thus preserving the ability to characterise the longitudinal flame intensity wave and the spatial structure of the flame intensity oscillation, the knowledge of which is valuable for a better understanding of the global flame response. The radially-integrated signal, $I_{cam}(z,t)$ is then phase-averaged by putting the instantaneous flame emission images in N_{bins} bins (as described in Section 2.3.1.2), each one being constructed with around 100 instantaneous images. This gives the phase-averaged signal $\langle I_{cam}\rangle(z,\alpha)$. $\langle I_{cam}\rangle(z,\alpha)$ is then reduced by the mean intensity of a whole reference flame without acoustic forcing. This post-processing method allows to characterise the flame intensity oscillation over the acoustic cycle at each z, and thus to show how different parts of the flame respond to the acoustic perturbation. An example of $\langle I_{cam}\rangle(z,\alpha)$ is given in Figure 2.14.

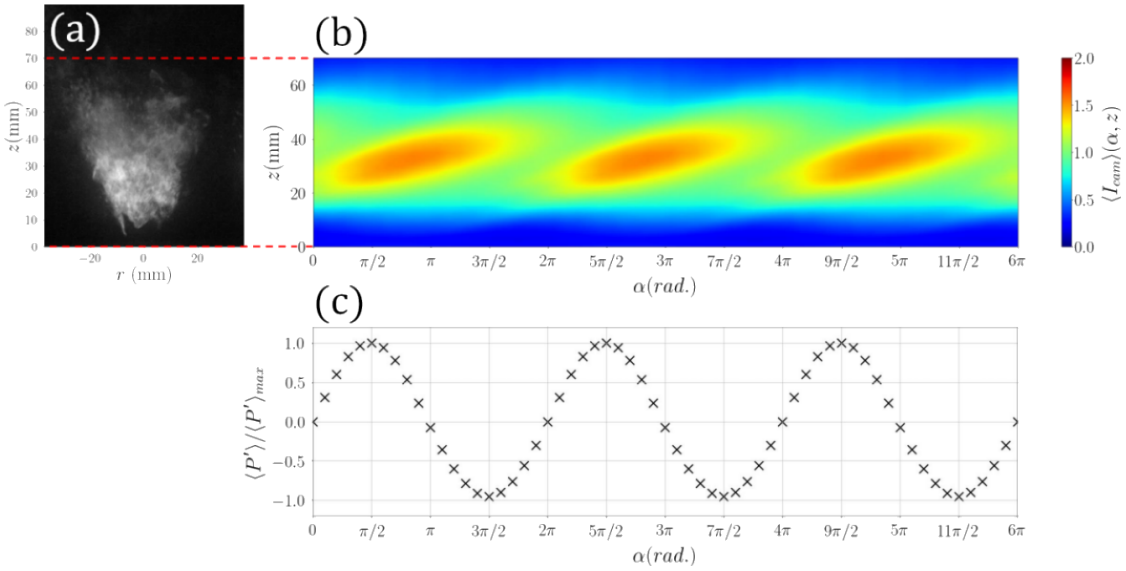

Figure 2.14: Phase-averaged spatially-resolved OH*-intensity signal in the presence of acoustics. This signal is obtained from instantaneous flames images with the method described in Section 2.3.2.1. Here we see: (a) an instantaneous OH* image; (b) phase-averaged spatially-resolved OH*-intensity signal $\langle I_{cam} \rangle(z, \alpha)$; (c) associated phase-averaged pressure cycle $\langle P' \rangle / \langle P' \rangle_{max}$. Both $\langle I_{cam} \rangle(z, \alpha)$ and $\langle P' \rangle / \langle P' \rangle_{max}$ are reproduced three times for the sake of clarity. Phase-averaging is performed at the acoustic frequency $f_r = 722$ Hz.

2.3.2.2 Flame standoff distance and flame length

Flame emission images are also used to obtain time signals for the flame standoff distance and flame length. The associated post-processing methods, illustrated in Figure 2.15, is described here. Images are firstly cropped to isolate the central flame, which is the object of the analysis. The cropped images are then filtered with a Gaussian blur to remove the high spatial frequencies generated by the noise. The resulting images are binarised using a threshold method. In the binarised image, the flame is identified by white pixels in Figure 2.15b. From the binarised images, the flame standoff distance h_{base} is obtained by finding the lowest row at which a flame presence condition is verified. The flame tip position is obtained from the same images. It corresponds to the highest row at which a flame presence condition is fulfilled. Flame presence conditions are adjusted to distinguish between the flame and very small and isolated pockets. This is performed by setting a minimum number of white pixels on a given row. At the flame base, this number is set to 8 but at the flame tip, it is set to 16 due to the presence of small reacting pockets isolated from the main reaction zone (see Figure 2.15b).

2.3.2.3 Barycentre of the radical light intensity

The response of the central flame to acoustics is also evaluated through the displacement of the barycentre of the OH* or CH* light intensities during the acoustic cycle. For that purpose, instantaneous images are first cropped to isolate the central flame. Then, images are thresholded in order to retain only the pixels with a grey level higher or equal than 10% of the maximum

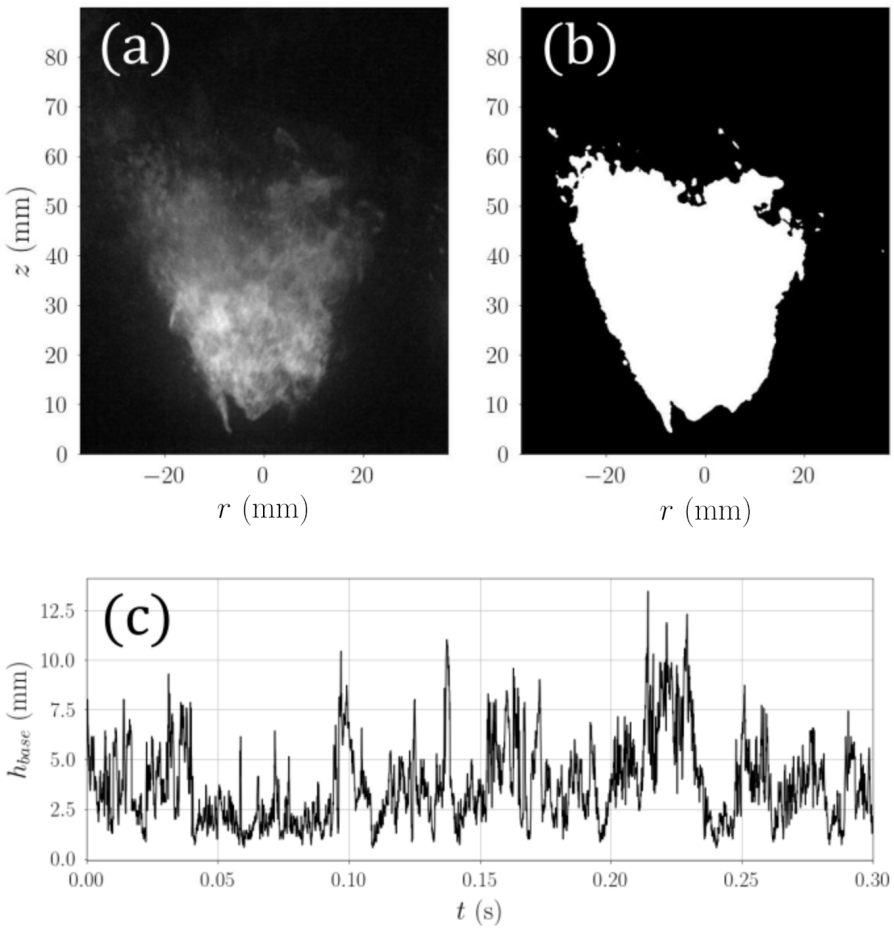

Figure 2.15: Illustration of the main steps of the post-processing method for finding the flame standoff distance and flame length: (a) cropped raw instantaneous OH* image; (b) same image after filtering and binarisation; (c) signal for the flame standoff distance h_{base} calculated with 6,000 images acquired at 20,000 Hz.

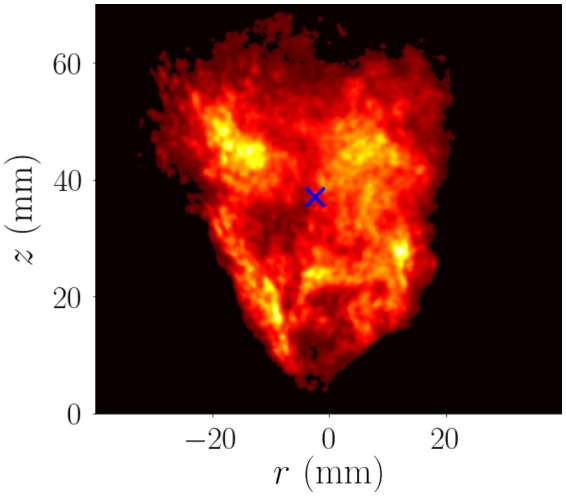

Figure 2.16: Instantaneous image of the CH*-intensity from the central flame in false colours, with the barycentre of CH*-intensity located at the center of the blue cross. The image is thresholded such that only the pixels with a grey level $I_{cam}(r_i, z_j, t)$ higher than or equal to 10% of the maximum value in the image are retained.

level in the image. In the resulting images, the grey level is projected onto the (O, r) and (O, z) axes and averaged, giving $\overline{I}^r_{cam}$ and $\overline{I}^z_{cam}$ respectively.

$$\overline{I}^z_{cam}(r_i, t) = \frac{1}{N_{rows}} \sum_{j=1}^{N_{rows}} I_{cam}(r_i, z_j, t) \tag{2.6}$$

$$\overline{I}^r_{cam}(z_j, t) = \frac{1}{N_{cols}} \sum_{i=1}^{N_{cols}} I_{cam}(r_i, z_j, t) \tag{2.7}$$

In these expressions, N_{rows} and N_{cols} are respectively the number of rows and columns of the images. The barycentre of flame light intensity is then calculated by using these quantities, with the following expressions:

$$r_{bary}(t) = \frac{\sum_{i=1}^{N_{cols}} \overline{I}^z_{cam}(r_i, t) r_i}{\sum_{i=1}^{N_{cols}} \overline{I}^z_{cam}(r_i, t)} \tag{2.8}$$

$$z_{bary}(t) = \frac{\sum_{j=1}^{N_{rows}} \overline{I}^r_{cam}(z_j, t) z_j}{\sum_{j=1}^{N_{rows}} \overline{I}^r_{cam}(z_j, t)} \tag{2.9}$$

The location of the barycentre on an instantaneous CH*-intensity image is identified by a blue cross in Figure 2.16. Then, phase-averaging is applied on r_{bary} and z_{bary} to evaluate the motion of the barycentre of flame light intensity during the acoustic cycle.

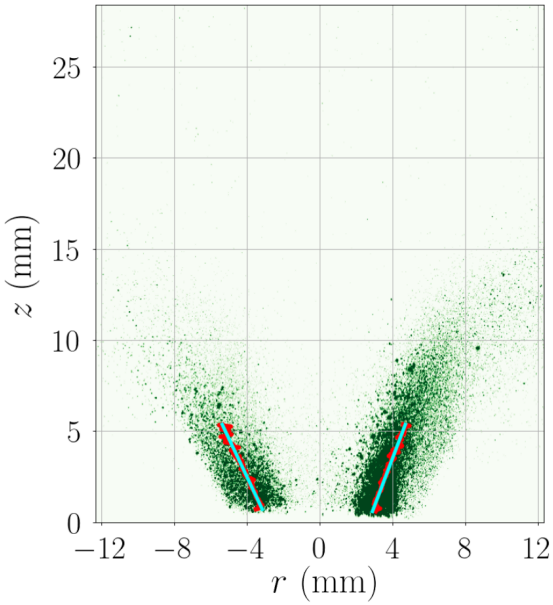

Figure 2.17: Calculation of the spray injection angle on a phase-averaged fuel spray image. A short region of interest (ROI) above the injector exit is isolated on both sides of the injector axis. The red curves correspond to the barycentre of light intensity at each z-location in the ROI. The cyan lines are first-order polynomial fittings of the red lines. These are used to calculate the spray injection angle.

2.3.3 Post-processing of spray measurements

2.3.3.1 Spray injection angle

The vertical spray tomography images give a signal $I_{tomo}(r, z, t)$ of the light scattered by the particles in the flow. When these seeding particles are the fuel droplets, information on the spray injection angle can be obtained. In this manuscript, this quantity is measured on averaged spray images. In the absence of acoustic forcing, a time-averaged image is obtained from all the instantaneous images while with acoustic forcing, phase-averaged images are obtained by reconstructing an acoustic cycle at the forcing frequency. The method for calculating the spray injection angle is illustrated in Figure 2.17. The injection angle is defined by the angle of the spray in a short region of interest (ROI) of about 5 mm above the nozzle exit. By doing this, the influence of the processes occurring downstream on the calculation is limited, therefore the response of injection angle to the acoustic forcing can be better captured. On each side of the injector axis ($r < 0$ or $r > 0$), the r-location of the local barycentre of light intensity (red points in Figure 2.17) is calculated at each height z in the ROI with the expression:

$$\langle r_{bary} \rangle (z_i, \alpha) = \frac{\sum_{i=1}^{N_{cols}} \langle I_{tomo} \rangle (r_i, z_j, \alpha) r_i}{\sum_{i=1}^{N_{cols}} \langle I_{tomo} \rangle (r_i, z_j, \alpha)} \tag{2.10}$$

where $\langle \cdot \rangle$ indicates phase-averaged quantities, $\langle r_{bary} \rangle (z_j, \alpha)$ is the barycentre at axial location z_j and phase angle α, and N_{col} is the number of columns in the ROI. $\langle r_{bary} \rangle (z, \alpha)$ shown for phase angle α corresponds to the red curves in Figure 2.17. The injection angle is then obtained

with a first-order polynomial fitting of $\langle r_{bary} \rangle(z, \alpha)$, indicated by the cyan lines.

2.3.3.2 Phase Doppler Anemometry (PDA) / Laser Doppler Anemometry (LDA)

The PDA/LDA system gives several quantities characterising the droplets. When it is operated in LDA mode, quantities such as the velocity components, droplet count or data rates are measured. In PDA mode, the fuel droplet diameter is also measured. These data are obtained from measurements performed on the droplets passing through the measurement volume. As a consequence, the data are nonuniformly sampled and analysis techniques for uniformly-sampled signals cannot be used. However, it is possible to turn these data into uniformly-sampled signals through the phase-averaging process. Phase-averaging is here performed at the acoustic frequency f_r to extract from the signals the modulation induced by acoustics.

Measurement of the swirl number

The swirl number S, which quantifies the rate of rotation of a flow, is calculated from radial profiles of fuel droplet axial and tangential velocities, U_z^f and U_θ^f respectively. At each radial location, the fuel droplet velocity components are time-averaged, hence, the swirl number is obtained by using the equation:

$$S = \frac{\int_{r_0}^{r_1} \overline{U_z^f}\, \overline{U_\theta^f} r^2 dr}{R \int_{r_0}^{r_1} \left(\overline{U_z^f}\right)^2 r dr} \tag{2.11}$$

In this expression, derived in Section 1.1.5, $\overline{(\,\cdot\,)}$ indicates time-averaged quantities, r is the radial location, $R = 4$ mm the radius of the nozzle exit, and r_0 and r_1 are the integration boundaries. Here, r_0 = 0 and $r_1 = +\infty$. However, at the closest vertical location at which PDA/LDA measurements are performed in this work ($z = 2.1$ mm), no droplets are generally found beyond $r = 1.5R$, thus $r_1 \simeq 1.5R$.

With acoustic forcing at f_r, the phase-averaged swirl number $\langle S \rangle(\alpha)$ is calculated from phase-averaged radial profiles of fuel droplet axial and tangential velocities, $\langle U_z^f \rangle(\alpha)$ and $\langle U_\theta^f \rangle(\alpha)$ respectively, which are obtained with the method described in Section 2.3.1.2. At a given phase angle α, the value of the phase-averaged swirl number is given by:

$$\langle S \rangle(\alpha) = \frac{\int_{r_0}^{r_1} \langle U_z^f \rangle \langle U_\theta^f \rangle r^2 dr}{R \int_{r_0}^{r_1} \langle U_z^f \rangle^2 r dr} \tag{2.12}$$

Transfer function to examine swirl number fluctuations

The conversion of the pressure perturbation into a swirl number oscillation is described by the transfer function $\mathcal{H}_{P'-S'}$, defined in the frequency domain:

$$\mathcal{H}_{P'-S'}(f_r) = \frac{\widetilde{\langle S \rangle} / \overline{S}}{\widetilde{\langle P \rangle} / \rho^a U_b^2} = \mathcal{G}_{P'-S'} e^{i\varphi_{P'-S'}} \tag{2.13}$$

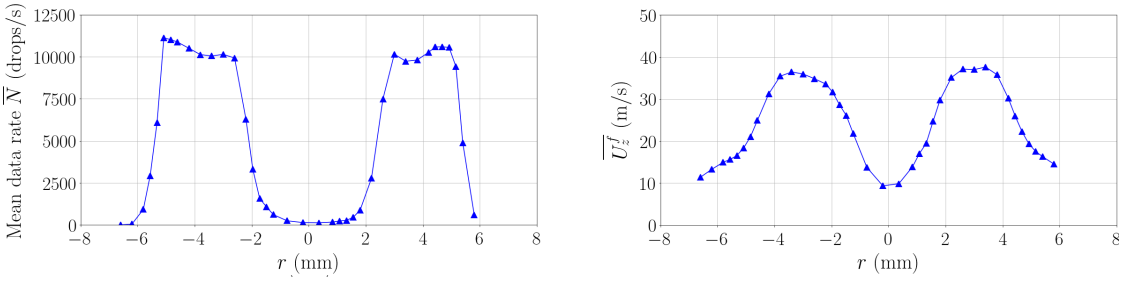

Figure 2.18: Radial profile of: (left) mean data rate $\overline{N}$ and (right) mean fuel droplet axial velocity $\overline{U_z^f}$ measured with PDA at $z = 2.1$ mm above the nozzle exit.

where $\overline{\langle S \rangle}$ and $\overline{\langle P \rangle}$ are the complex amplitudes at f_r of the phase-averaged oscillations of swirl number and pressure and $\overline{S}$ is the cycle-averaged swirl number. As mentioned above, calculating the phase-averaged swirl number and pressure signals at f_r before computing the transfer function allows to turn nonuniformly sampled signals (obtained with PDA/LDA) into uniformly-sampled signals, with a sampling frequency equal to $N_{bins} \times f_r$, wtith N_{bins} the number of bins in the acoustic cycle (see Figure 2.12). The gain of the transfer function, $\mathcal{G}_{P'-S'}$, indicates the ratio of the amplitude of the reduced swirl number oscillation to that of the reduced pressure perturbation, and the phase, $\varphi_{P'-S'}$, expresses the phase delay of the swirl number oscillation with respect to the pressure perturbation.

Measurement of the droplet amount injected into the chamber

Among the many quantities measured when a droplet crosses the measurement volume of the PDA/LDA system, the time at which each droplet enters the measurement volume can be exploited to estimate the droplet amount at a given location measured during a given time interval, also called data rate. Radial profiles of the data rate give an indication about the spatial distribution of the droplets in a spray. An illustration is given with a radial profile measured with PDA in Figure 2.18. With acoustic forcing, the data rate can also be obtained as a function of the phase angle, in order to highlight a periodic modulation of droplet injection. Here, this is performed with the phase-averaging technique, *i.e.* by dividing the acoustic cycle into N_{bins} bins of equal width, as described in Section 2.3.1.2. The droplets are then put into the bins depending on the time at which they enter the measurement volume. This method is applied to the measurements performed at each location in the (r, z) space. In bin m corresponding to phase angle α_m, the phase-averaged droplet count at a location (r, z), $\langle N \rangle(r, z, \alpha_m)$, is expressed as follows:

$$\langle N \rangle(r, z, \alpha_m) = \frac{1}{N_{cycles}} \sum_{n=1}^{N_{cycles}} N^{m,n}(r, z) \tag{2.14}$$

In this expression, $N^{m,n}(r, z)$ corresponds to the droplet count measured in bin m during the n-th acoustic cycle. $\langle N \rangle(r, z, \alpha_m)$ thus corresponds to the droplet count measured during a time interval of width $\Delta\tau = T/20$ around phase angle α_m, where T is the acoustic period. By using the acoustic pressure signal as the same reference signal for all the radial locations, it is possible to consider the modulation of the droplet amount integrated over a whole radial line passing by

the injector axis, at a given height above the injector exit, expressed by:

$$\langle N \rangle(z, \alpha_m) = \frac{1}{N_{loc}} \sum_{p=1}^{N_{loc}} \frac{1}{N_{cycles}} \sum_{n=1}^{N_{cycles}} N^{m,n}(r_p, z) \tag{2.15}$$

In this expression, N_{loc} is the number of radial locations at which measurements are performed, for a given height z.

Chapter 3

Energy system in the absence of acoustic forcing

Contents

This chapter introduces the characteristics of the energy system in the absence of acoustic forcing. These characteristics are explored for one operating point, namely $\mathbb{P}_{59}$ (see Table 2.1), considered as the reference operating point throughout the manuscript. The injection system generates a hollow-cone liquid fuel spray [157]. Particular attention is paid to the sensitivity of the fuel droplets motion to the carrier flow. To this end, an analysis based on the Stokes number is performed and shows that the velocity of the fuel droplets with a diameter lower than 5 µm can be well assimilated to the air flow velocity. The swirl number is nonetheless equivalent when calculated with these small fuel droplets only or with all the fuel droplets. The flame is characterised via CH^* and OH^* radicals, both of which capture the flame features equally well. The CH^* and OH^* light emission signals from the flame have a noisy broadband frequency content, with no particular frequency standing out from the background noise.

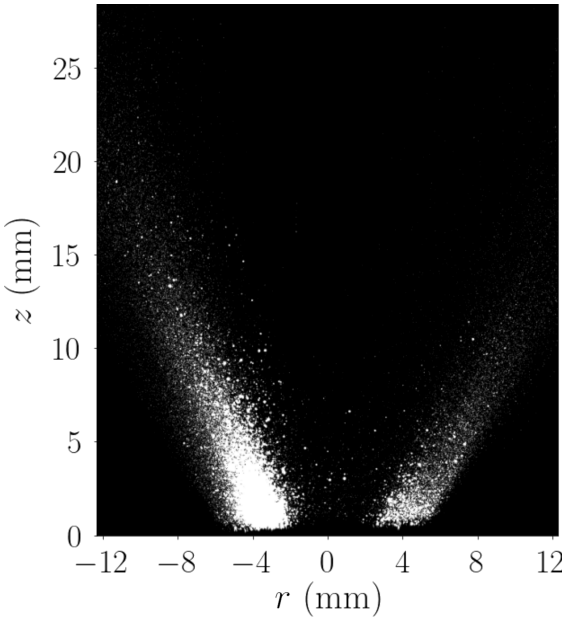

Figure 3.1: Time-averaged high-speed tomography image of the n-heptane spray in the absence of acoustic forcing.

3.1 Characterisation of the fuel spray in reacting conditions

The characteristics of the liquid n-heptane fuel spray for the operating point $\mathbb{P}_{59}$ are presented in this section. The operating point is characterised by a fuel mass flow rate of 0.133 g/s and a swirling air flow with a mass flow rate of 2.35 g/s, corresponding to a bulk velocity $U_b = 38.9$ m/s, calculated at $20°$C at the injector exit. A time-averaged spray image obtained with high-speed tomography is presented in Figure 3.1, showing the hollow-cone shape of the spray and the strong evaporation occurring in a few millimeters. The spray is not totally axisymmetric due to inherent features of the injection system. This asymmetry could be linked to differences in the droplet amount as well as in the droplet size distribution. Indeed, the light intensity scattered by a spherical particle depends on the square of its diameter. The spray base angle, calculated with the method described in Section 2.3.3.1, is $\theta_{spray} = 51°$. This angle is obtained by considering only the z-location in the range 0.39 mm - 5.37 mm.

3.1.1 Spatial distribution of the fuel droplets

Mean radial profiles of the fuel droplet data rate averaged over 4 seconds, $\overline{N}(r, z)$, are presented at three heights above the injector exit in Fig. 3.2. As expected, the radial distribution of the fuel droplets is typical of a hollow-cone spray, with a very few droplets measured near the injector axis ($r = 0$) at all heights z. In particular, at $z = 2.1$ mm, the data rate for -2 mm $\leq r \leq 2$ mm is lower than 15% of the maximum local data rate. In the following, this region almost empty of droplets is defined as *core region*. As z increases, the core region widens due to the conical shape of the spray. At all z locations, it is surrounded by an annular-shaped region with a higher data rate, the maximum value of which is strongly z-dependent. Indeed, while the maximum data rate

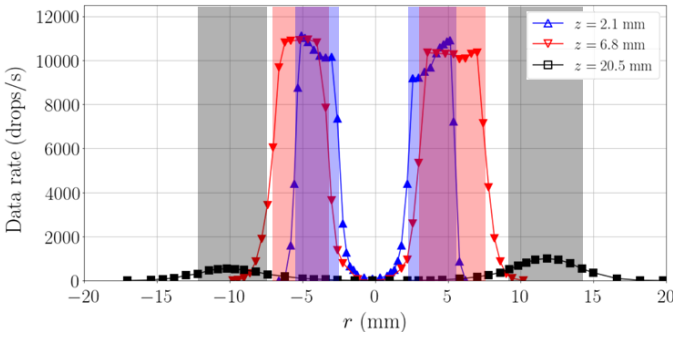

Figure 3.2: Mean radial profiles of the fuel droplet data rate, $\overline{N}(r, z)$ at $z = 2.1$ mm, $z = 6.8$ mm and $z = 20.5$ mm. The coloured bands indicate the radial locations at which $\overline{N}(r, z)$ is higher than half its maximum value for each height.

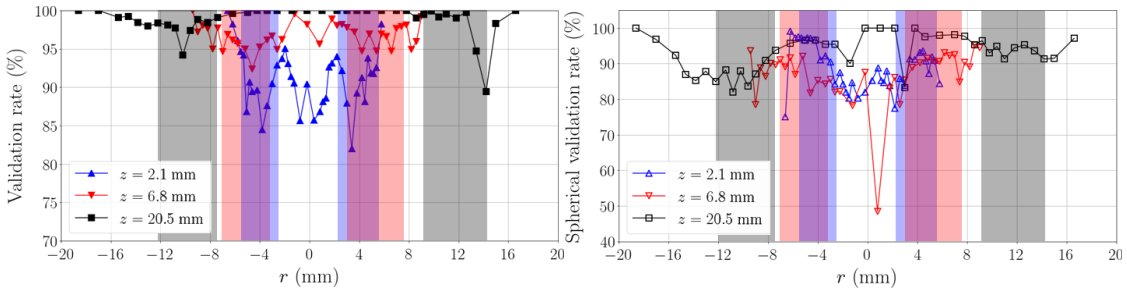

(a) (b)

Figure 3.3: Radial profiles at $z = 2.1$ mm, $z = 6.8$ mm and $z = 20.5$ mm: (left) fuel droplet validation rate; (right) fuel droplet spherical validation rate. The validation rate includes conditions on the droplet velocity and signal-to-noise ratio. The spherical validation rate measured the amount of spherical droplets. The coloured bands, reported from Figure 3.2, indicate the radial locations at which $\overline{N}(r)$ is higher than half its maximum value for each height.

is about 11,000 drops/s both at $z = 2.1$ mm and $z = 6.8$ mm, it decreases to about 1000 drops/s at $z = 20.5$ mm. It shows the impact of the evaporation process, especially due to the presence of the flame, the base of which is stabilised at $\overline{h_{base}} = 3.3$ mm (with $h_{base}^{rms} = 1.2$ mm) (see Section 3.3). This analysis is supported by the radial profiles of fuel droplet validation rate and spherical validation rate (see Figure 3.3). The validation rate indicates the proportion of droplets measured by the system that are validated based on criteria relating to drop velocity and the signal-to-noise ratio of the Doppler signal. The spherical validation rate indicates the proportion of droplets measured by the system that are validated on the basis of a droplet sphericity criterion (see, for example, [158]). Although the validation rate increases with z, it is larger than 85% at almost all the radial locations at $z = 2.1$ mm. The spherical validation rate is also higher than 85% in the regions with a high droplet data rate, identified by the coloured band, at all heights. Therefore, the proportion of validated droplets, quite similar at $z = 2.1$ mm and $z = 6.8$ mm and at $z = 20.5$ mm (although a little higher) validates the analysis made on the data rate profiles. At $z = 20.5$ mm, asymmetries of the spray can be observed: the maximum data rate is lower for $r < 0$ than for $r > 0$; in addition, it is located near $r = -10.2$ mm and near $r = +11.8$ mm.

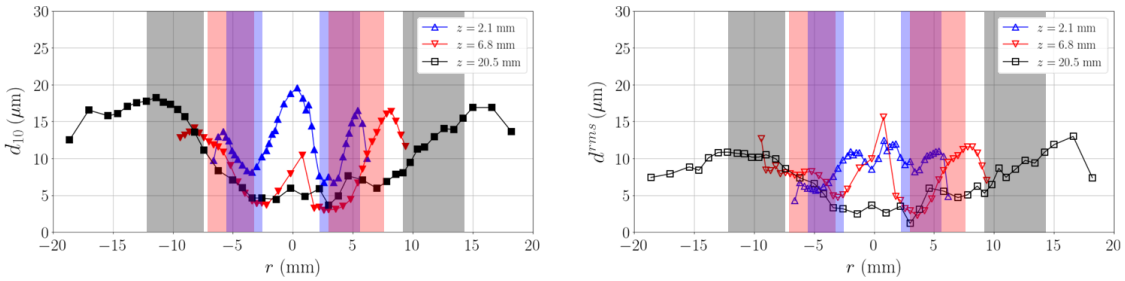

Figure 3.4: Radial profiles of the local mean droplet diameter, $d_{10}(r, z)$, and standard deviation of the droplet diameter, $d^{rms}(r, z)$, at $z = 2.1$ mm, $z = 6.8$ mm and $z = 20.5$ mm. The coloured bands, reported from Figure 3.2, indicate the radial locations at which $\overline{N}(r, z)$ is higher than half its maximum value for each height.

3.1.2 Fuel droplet size

The arithmetic mean droplet diameter, $d_{10}(r, z)$ depends on the radial and axial location, as does the droplet count. At $z = 2.1$ mm, the arithmetic mean diameter d_{10} is maximum in the core region, reaching values of 20 μm (see Figure 3.4). Its minimum values are about 6-8 μm around $|r| = 3$-4 mm, which corresponds to the center position of the data rate plateau around 10,000 drops/s (see Figure 3.2). It is worth noting that this plateau is characterised by a low d_{10} in its inner part (3 mm $\lesssim r \lesssim 4$ mm) and a higher d_{10} in its outer part (4 mm $< r \lesssim 5$ mm). This feature is further described below. The standard deviation, which is of the order of d_{10}, suggests the polydisperse nature of the spray. At $z = 6.8$ mm, the profile of d_{10} has a similar shape compared to $z = 2.1$ mm but it is widened over the radial direction as droplets are found at a larger radial distance from the injection axis. Also, d_{10} is generally smaller, showing that evaporation has already significantly occurred. At $z = 20.5$ mm, where most of the droplets are already evaporated, the very few droplets remaining in $|r| \leq 7$ mm are quite small, but the main part of the droplet population, located at $|r| > 10$ mm, is characterised by a d_{10} higher than 10 μm or even 15 μm. This population results from the larger droplets found at lower locations.

3.1.2.1 Drop size distribution of the spray

The polydisperse nature of the spray is clearly shown by the drop size distributions at the three heights, which are obtained by integrating the droplets measured at all the radial locations for a given height (see Figure 3.5). At all the radial locations, the integration time is 4 seconds. At $z = 2.1$ mm, 60% of the droplets have a diameter lower than 10 μm, while they are 73% at $z = 6.8$ mm and 39% at $z = 20.5$ mm. This supports the assumption deduced from the data rate profiles, *i.e.* droplets have partially evaporated at $z = 6.8$ mm, while most of them have completely evaporated at $z = 20.5$ mm. As a consequence, the proportion of large droplets ($d > 20$ μm) is reduced at $z = 6.8$ mm and significantly increased at $z = 20.5$ mm. According to Cáceres [45][1], droplets with an initial diameter lower than 10 μm may evaporate in less than ~ 0.55 ms. If we suppose that the droplets are transported at the bulk velocity[2], this gives an evaporation

[1] In Section 3.6.2.1 of his manuscript.
[2] This assumption is justified below.

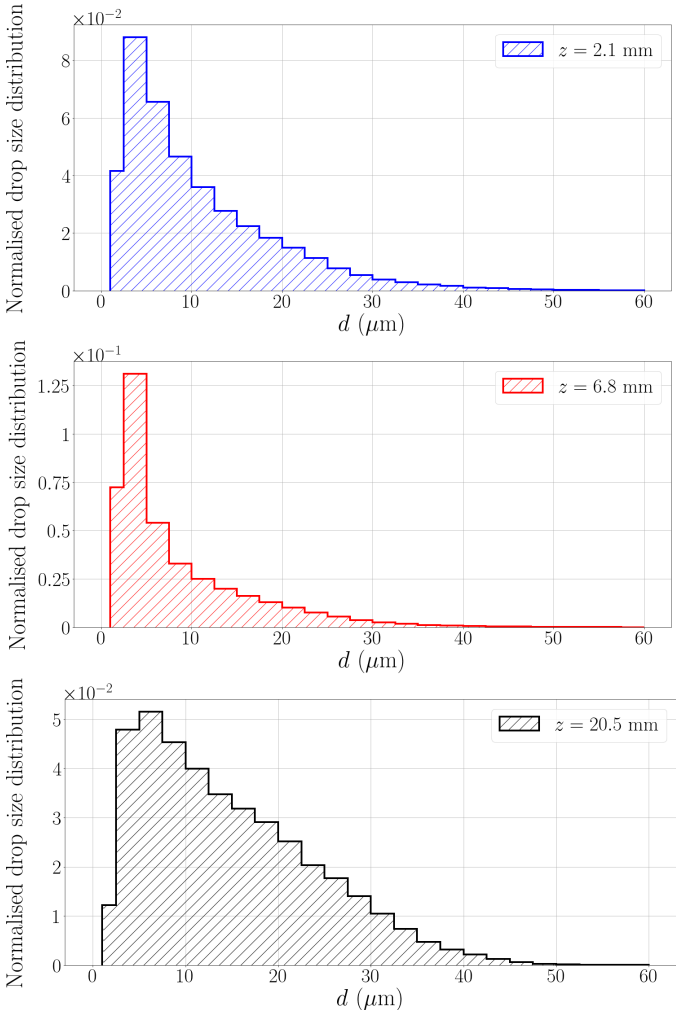

Figure 3.5: Droplet size distribution measured all along a radial profile at $z = 2.1$ mm, $z = 6.8$ mm and $z = 20.5$ mm. The bin width is 2.5 µm except for the first bin, which includes droplets of diameter in the range $1 - 2.5$ µm.

distance of $\sim$ 21 mm. This simple analysis suggests the droplet amount at $z = 20.5$ mm may be about 40% of that at $z = 2.1$ mm. Nevertheless, Cáceres [45] obtained evaporation times for an operating point characterised by a flame power of 4.3 kW/flame, compared to 5.9 kW/flame in the present study, thus leading to lower temperatures than here. Hence, this participates to explain why the amount of droplets measured at $z = 20.5$ mm is much lower than 40% of the amount measured at $z = 2.1$ mm.

3.1.2.2 Consequence of spray polydispersity on instability modelling

The spray polydispersity is an important feature as it implies that the droplet evaporation time is not unique and suggests that droplet segregation may occur due to their inertial response. The evaporation time, τ_{evap}, is part of the conversion time $\tau_c = \tau_{evap} + \tau_{mix} + \tau_{ch}$, where τ_{mix} and τ_{ch} correspond to the characteristic mixing and chemical times respectively. The conversion time therefore includes the physico-chemical processes that turn the two-phase flow into a burning mixture. As the spray is polydisperse here, the conversion time may be expressed as a distribution depending on the evaporation time, which in turn is a function of the droplet diameter. This suggests the hypothesis of a single time delay between the droplet injection and the fuel consumption may be too strong for such spray flames. An interesting approach could be to represent the conversion time as a distribution. Such distributed time-lag models were used to include the spatial dispersion of equivalence ratio waves with convection [57], or to model the FTF of a lean premixed hydrogen-methane-air flame which is non-compact relatively to the convective wavelength [159].

3.1.2.3 Spatial segregation of the droplets

As indicated in Figures 3.2 and 3.4, the droplets present in the outer part of the high data rate plateau are larger than those in the inner part of this plateau. This is highlighted with the drop size distributions for each of these parts, given for the three heights in Figure 3.6. For $z = 2.1$ mm and $z = 6.8$ mm, the inner and outer parts are separated by the center location of the quasi-plateau around 10,000 drops/s (see Figure 3.2), *i.e.* $r = \pm 4$ mm and $r \pm 5.3$ mm respectively. For $z = 20.5$ mm, the two parts are separated by the location of the highest data rate, *i.e.* the inner part is such that -10.2 mm $\leq r \leq 11.8$ mm. For the three heights, the smallest droplets are mainly found in the inner part of the spray. This is remarkable at the two lowest vertical locations: at $z = 2.1$ mm, 70% of the droplets in the inner part have a diameter lower than 10 µm compared with 52% in the outer part; at $z = 6.8$ mm, 90% of the droplets have a diameter lower than 10 µm while they are 57% in the outer part. Therefore, large droplets are more easily found in the outer part of the spray. This is an important feature as it may lead to differentiated responses of these two parts to acoustics and to different evaporation rates.

3.1.3 Fuel droplet velocity

The radial profiles for the three mean velocity components and their standard deviation are shown at the three heights $z = 2.1$ mm, $z = 6.8$ mm and $z = 20.5$ mm in Figure 3.7. These profiles are obtained by including all the droplets validated by the acquisition system. As shown in the axial

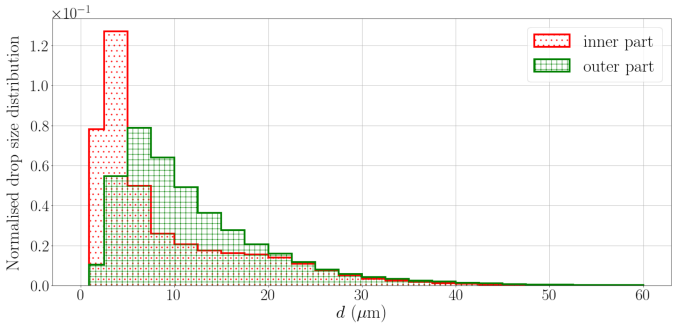

(a) $z = 2.1$ mm

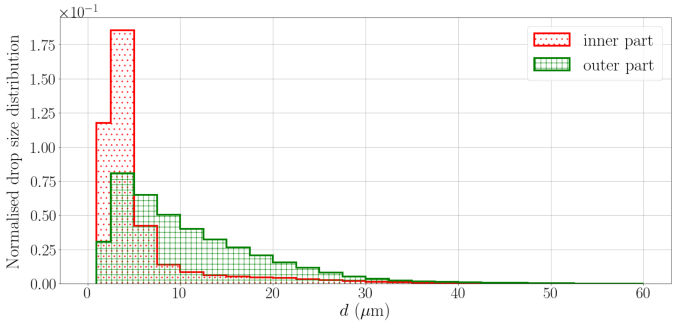

(b) $z = 6.8$ mm

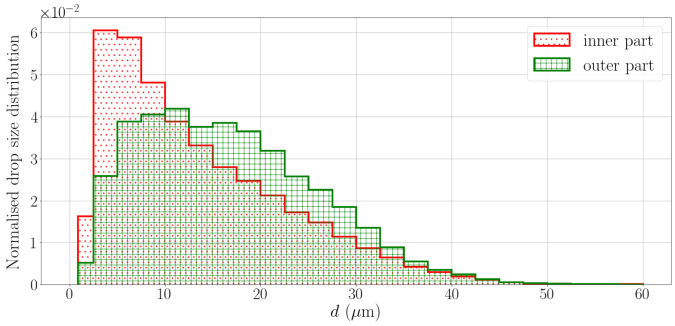

(c) $z = 20.5$ mm

Figure 3.6: Drop size distributions in the inner part and the outer part of the spray, which are separated by the location of the maximum data rate. The inner part corresponds to -4 mm $\leq r \leq 4$ mm for $z = 2.1$ mm, 5.3 mm $\leq r \leq 5.3$ mm for $z = 6.8$ mm and -10.2 mm $\leq r \leq 11.8$ mm for $z = 20.5$ mm; the outer part is the complement.

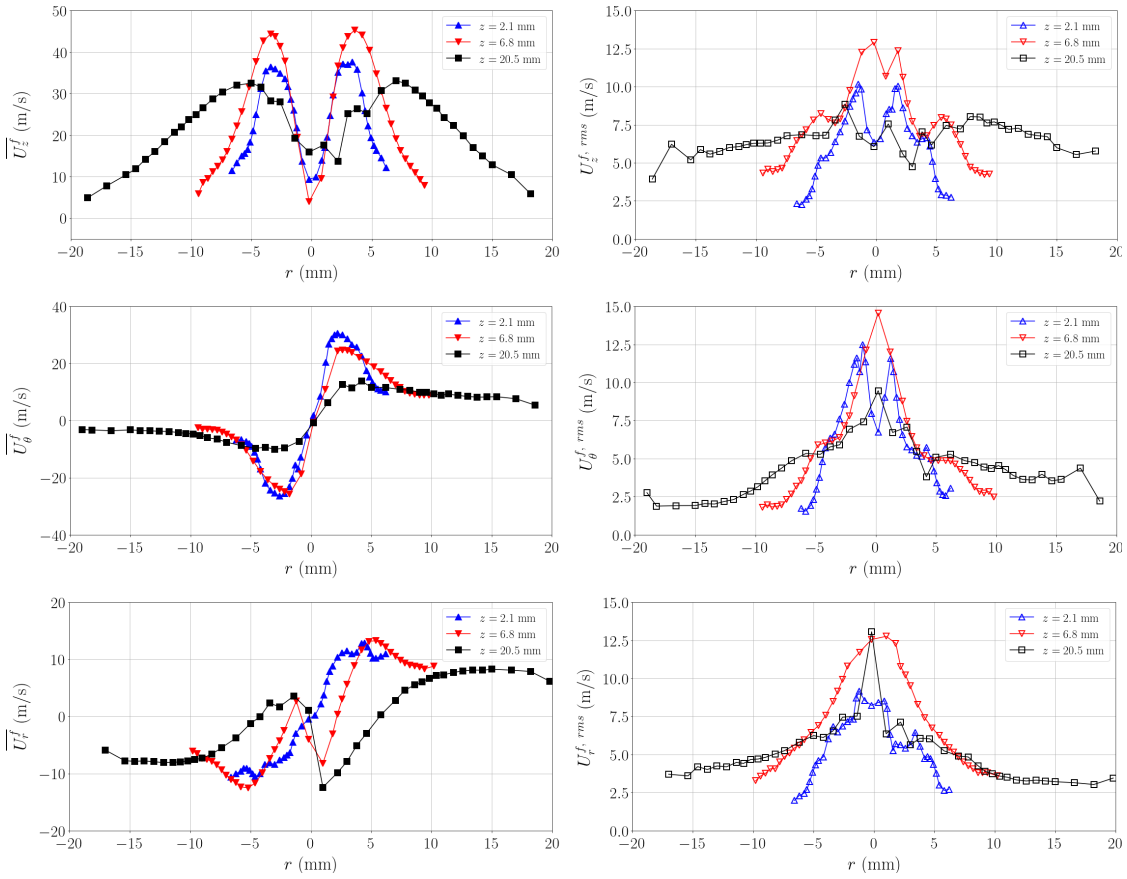

Figure 3.7: Radial profiles of fuel droplet mean velocity $\overline{U^f}$ and velocity standard deviation $U^{f,rms}$ at $z = 2.1$ mm, $z = 6.8$ mm and $z = 20.5$ mm. Top: axial velocity ($\overline{U_z^f}, U_z^{f,\,rms}$); middle tangential velocity ($\overline{U_\theta^f}, U_\theta^{f,\,rms}$); bottom: radial velocity ($\overline{U_r^f}, U_r^{f,\,rms}$). The profiles are obtained using all the validated droplets.

velocity ($\overline{U_z^f}$) profiles, the central region of the flow is characterised by low velocities typical of swirling flows. At $z = 2.1$ mm, the standard deviation $U_z^{f,rms}$ is close to the mean velocity $\overline{U_z^f}$ but at $z = 6.8$ mm, it becomes about twice higher. This indicates the presence of a central recirculation zone (CRZ). It is admitted in the literature that the presence of the CRZ occurs when the swirl number exceeds a threshold value of 0.6 [28], but it was also observed for a swirl number as low as 0.45 [160]. Here, the swirl number calculated either at $z = 2.1$ mm or at $z = 6.8$ mm is 0.58. At $z = 20.5$ mm, $\overline{U_z^f}$ is about 15 m/s near the injector axis, which is much higher than $U_z^{f,rms}$. This shows that the presence of the CRZ is no further detected at this height. The mean axial velocity profiles also show peaks near $r \pm 4$ mm for the two lowest z-locations. Peak velocities are about 7 m/s more rapid at $z = 6.8$ mm than at $z = 2.1$ mm due to thermal expansion induced by the presence of the flame. At $z = 20.5$ mm, the peak of fuel droplet mean axial velocity is about 30% lower than that at $z = 6.8$ mm and it is found at radially outward location, due to the shape of the flow. For both $z = 2.1$ mm and $z = 6.8$ mm, the highest axial velocities are mostly located at 3 mm $\lesssim r \lesssim$ 4 mm, while $\overline{U_z^f}$ drastically decreases for 4 mm $\lesssim r \lesssim$ 5 mm, which corresponds to the inner and outer parts of the high data rate plateau highlighted above. Hence, it is interesting to visualise correlations between droplet diameters and axial velocities to see whether there exists a clear relation between these quantities.

This correlation obtained on all the radial profile at $z = 2.1$ mm is displayed in Figure 3.8, by showing the probability to measure a droplet with an axial velocity U_z^f and a diameter d, $P(U_z^f, d)$. The large majority of the droplets of diameter $d > 30$ µm have an axial velocity comprised between 10 m/s and 30 m/s, with some rare exceptions. For $d \leq 30$ µm, the smaller the fuel droplets, the wider the range of droplet axial velocities. For droplets in the range 1-5 µm, their axial velocity is comprised between -20 m/s and 70 m/s. In addition, the most-probable droplet axial velocity decreases as the droplet diameter increases: for $d = 1 - 5$ µm, $\mathcal{P}(U_z^f, d)$ is maximum around $U_z^f = 40$ m/s while for $d \geq 30$ µm, $\mathcal{P}(U_z^f, d)$ is maximum around $U_z^f = 20$ m/s.

Small droplets have indeed a better reactivity to carrier flow fluctuations such as those induced by turbulence, whereas larger droplets tend to have a ballistic behaviour, so their velocity may be unaffected by small structures present in the carrier flow. As the spray is mostly constituted of small droplets at low vertical locations, one can wonder whether the air flow velocity profiles may be estimated from measurements performed on fuel droplets. This is the subject of the next section.

3.2 Can we characterise the air flow using fuel droplets?

To characterise local velocity components of an air flow, widely-used methods in experimental fluid dynamics use seeding particles as tracers. In this way, air flow characteristics can be measured by assimilating the air flow motion to the particles' motion. However, it is first necessary to verify that the particles' motion is able to describe the air flow motion. This section aims at answering the following question: can we reasonably use the fuel droplets as seeding particles to assess the air flow characteristics? To this end, the fuel droplets are sorted into classes according to their diameter. The mean droplet axial velocity is then examined in all the classes. The Stokes

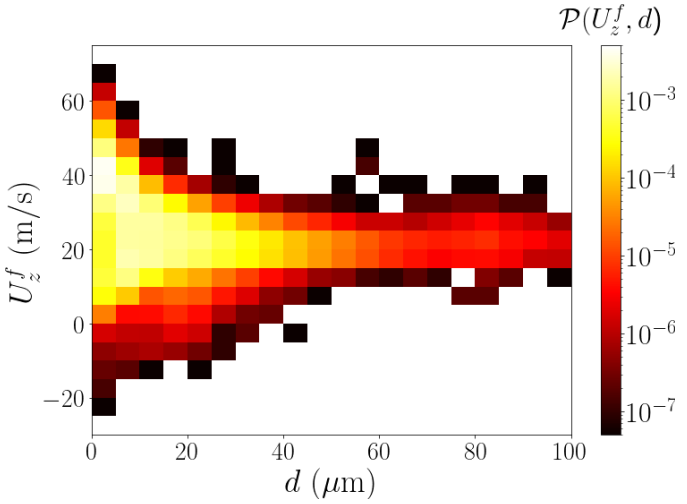

Figure 3.8: Normalised correlation between fuel droplet diameter and fuel droplet axial velocity obtained on all the radial profile at $z = 2.1$ mm. The colorbar indicates the probability $\mathcal{P}(U_z^f, d)$ to measure a droplet with an axial velocity U_z^f and a diameter d.

Droplet-diameter class	C_1	C_2	C_3	C_4	C_5
Minimum diameter d_{min} (µm)	1	5	10	15	20
Minimum diameter d_{max} (µm)	5	10	15	20	100

Table 3.1: Definition of the droplet-diameter classes

number, which indicates the ability of a spherical particle to follow the carrier flow, guides the choice of the diameter-based droplet filter able to capture the air flow behaviour. A comparison between measurements obtained with LDA and PDA (without and with droplet filtering) is finally performed to ensure that both measurement techniques give the same results.

3.2.1 Diameter-based droplet filtering

Due to the polydispersity of the fuel spray underlined in the previous section, all the fuel droplets do not behave in the same manner in the carrier flow. This was clearly highlighted by the droplet axial velocity - diameter correlation in Figure 3.8. The diameter-dependent axial velocity profiles of the fuel droplets are here obtained for five classes of droplet diameter, defined in Table 3.1.

The radial profiles of mean value and standard deviation of the axial velocity are shown at $z = 2.1$ mm for each droplet-diameter class and compared with the values obtained without droplet diameter-filtering in Figure 3.9. For all the diameter classes, the global shape of the mean axial velocity profile is similar to that obtained without filtering, showing a central region of low velocity for $|r| < 2$ mm surrounded by an annular-shaped region of higher velocity for 2 mm $\lesssim |r| \leq 4$ mm, beyond which the axial velocity decreases. Near the injector axis, all the droplets have almost the same mean axial velocity $\overline{U_z^f}$, but this is not anymore true in the other regions. In the annular-shaped region, the mean axial velocity of C_1 droplets reach a maximum of 41 m/s while it is about 26 m/s for C_5 droplets. The highest mean axial velocities for C_1 droplets are about 10% higher than the values for all droplets as well as for the C_2 droplets. For larger

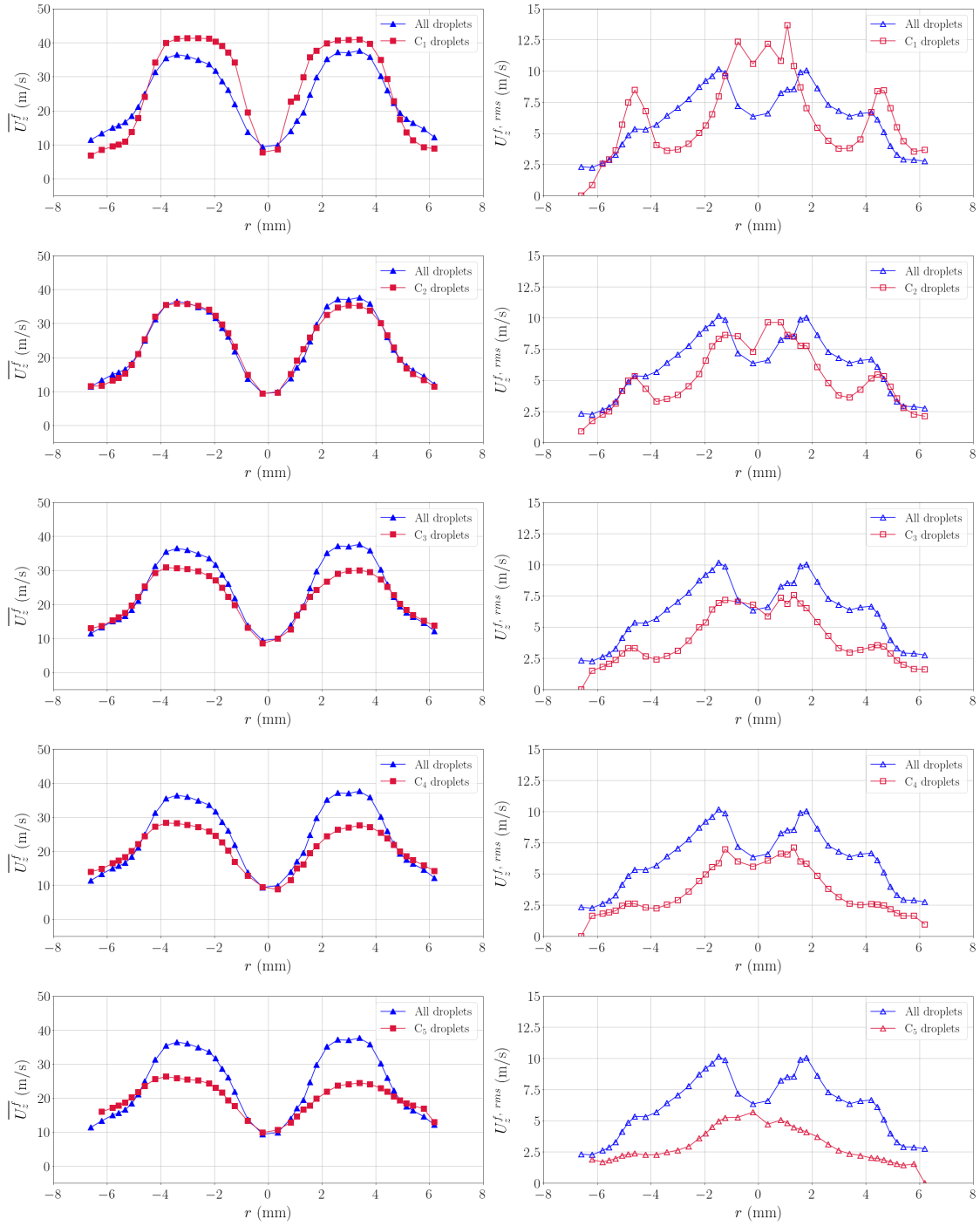

Figure 3.9: Comparison between the radial profiles of fuel droplet axial velocity at $z = 2.1$ mm calculated by including all the measured droplets or diameter-filtered droplets, as defined in Table 3.1. Left column: mean axial velocity, $\overline{U_z^f}(r)$; right column: standard deviation of the axial velocity, $U_z^{f,rms}(r)$. From the top row to the bottom row, the axial velocity profiles obtained from all the measured droplets are compared with those obtained from C_1 to C_5 droplets.

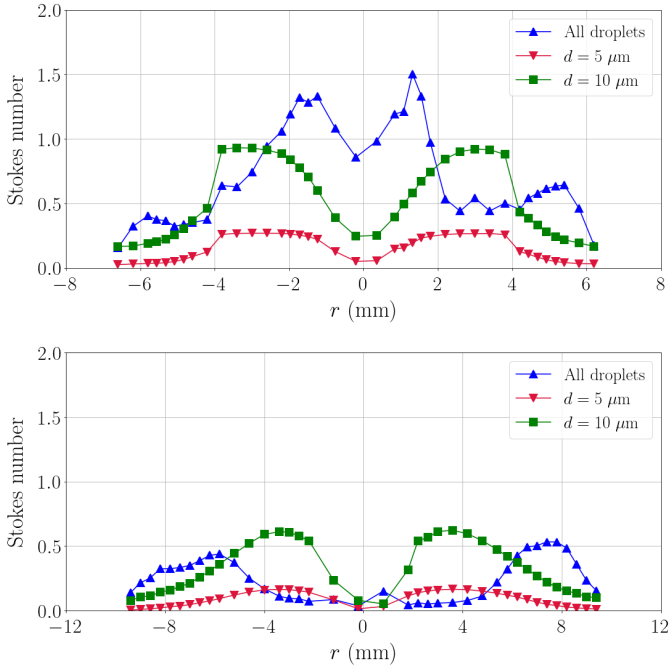

Figure 3.10: Radial profiles of the fuel droplets Stokes number at $z = 2.1$ mm (top) and at $z = 6.8$ mm (bottom) calculated for all droplets by using the mean axial velocity of all the droplets, for a droplet of diameter 5 µm by using the mean axial velocity of C_1 droplets and for a droplet of diameter 10 µm by using the mean axial velocity of C_2 droplets.

droplets, the highest mean axial velocities are lower by at least 15% compared to that for all droplets. Since the fuel droplet velocity depends significantly on their diameter, one should focus on the smallest droplet to analyse the air flow motion.

Some indications about the physics of the flow are also given by the plots in Figure 3.9. The notable decrease of $\overline{U_z^f}$ with the droplet diameter indicates that small fuel droplets are more likely to be entrained by the air flow than the bigger ones. For $|r| > 4$ mm, low axial velocities are observed for C_1 droplets, potentially indicating the presence of an outer recirculation zone in the inter-flame domains. Further information about the air flow is obtained by analysing the standard deviation of the axial velocity, $U_z^{f,\,rms}$ for each droplet-diameter class. At all the radial locations, $U_z^{f,\,rms}$ decreases as the mean droplet diameter increases. It is maximum near the injector axis: for C_1 and C_2 droplets, the negative axial velocity of some droplets results in values of $U_z^{f,\,rms}$ of the order of $\overline{U_z^f}$. The main difference between profiles of $U_z^{f,\,rms}$ for the droplet-diameter classes lies around $|r| = 4.5$ mm: a local peak, which is all the more significant as the droplets are small, is found at this location. This peak coincides with a strong gradient of $\overline{U_z^f}$, indicating the presence of the outer shear layer. As noted by Cáceres [45] in the TACC-Spray cavity, three-dimensional Kelvin-Helmholtz type vortices were observed in this region. The high standard deviation of the axial velocity of small droplets might be linked to these vortices. Consequently, they are only captured by C_1 droplets, and C_2 droplets to a lesser extent, in the present flow.

3.2.2 Stokes number

To verify if C_1 and C_2 droplets have a good ability to follow the air flow, the Stokes number is evaluated:

$$\mathrm{Stk} = \frac{\rho^f d^2 \overline{U_z^f}}{18 \mu^a D_{exit}} \tag{3.1}$$

ρ^f is the fuel density, d the fuel droplet diameter, $\overline{U_z^f}$ the mean fuel droplet axial velocity, μ^a the air dynamic viscosity and D_{exit} the injector exit diameter. Radial profiles of the Stokes number are presented at $z = 2.1$ mm and $z = 6.8$ mm for three droplet diameters and axial velocities in Figure 3.10. It is first calculated by taking $d_{10}(r)$ as d in Equation (3.1) and the mean axial velocity calculated from all the droplets. Two other estimations are made by taking $d = 5$ µm (respectively $d = 10$ µm) and by considering the mean axial velocity of C_1 (respectively C_2 droplets). The air dynamic viscosity is calculated by considering an inhomogeneous temperature distribution. At $z = 2.1$ mm, the temperature is assumed to be 293 K for $|r| \leq 4$ mm and 700 K for $|r| > 4$ mm. At $z = 6.8$ mm, it is assumed to be 700 K at every radial location.

At $z = 2.1$ mm, the Stokes number of a 5-µm droplet does not exceed 0.28 at all radial locations while that of a 10-µm droplet is almost 1 in the annular-shaped region, where the axial velocity is maximum. When all droplets are considered, Stk is about 0.5 in the annular-shaped region but it reaches values higher than unity in the core region. This shows that at $z = 2.1$ mm, only C_1 droplets should be considered to examine the air flow dynamics. **At $z = 6.8$ mm**, the Stokes number obtained by including all the droplets does not exceed 0.5 while that based on a 10-µm droplet reaches slightly higher values for r in the range $2 - 4$ mm. This means that at $z = 6.8$ mm, the air flow motion obtained by including all the droplets gives a reasonable estimate of the air flow dynamics. Nevertheless, the lower Stokes number for a 5-µm droplet at all radial locations, coupled with the high data rate of these small droplets, makes the analysis of the air flow based on C_1 droplets preferable. In the following of the manuscript, the ability of these fuel droplets to follow air flow oscillations induced by the acoustic excitation is also estimated by using an *acoustic* Stokes number (introduced in Equation (1.7)).

3.3 Characterisation of the swirl-stabilised spray flame using CH* or OH* radicals

In this section, the main characteristics of the swirling spray flame in the absence of acoustic forcing are presented for the operating point $\mathbb{P}_{59}$. For that purpose, the emission signals from CH* or OH* radicals are captured with a PM, giving signals $I_{CH^*}(t)$ or $I_{OH^*}(t)$ integrated in the three dimensions of space, or with high-speed cameras, giving two-dimensional signals $I_{cam}^{CH^*}(r, z, t)$ and $I_{cam}^{OH^*}(r, z, t)$ that are line-of-sight-integrated in the $\vec{y}$ direction. A complete description of the acquisition systems associated to these devices is provided in Section 2.2.

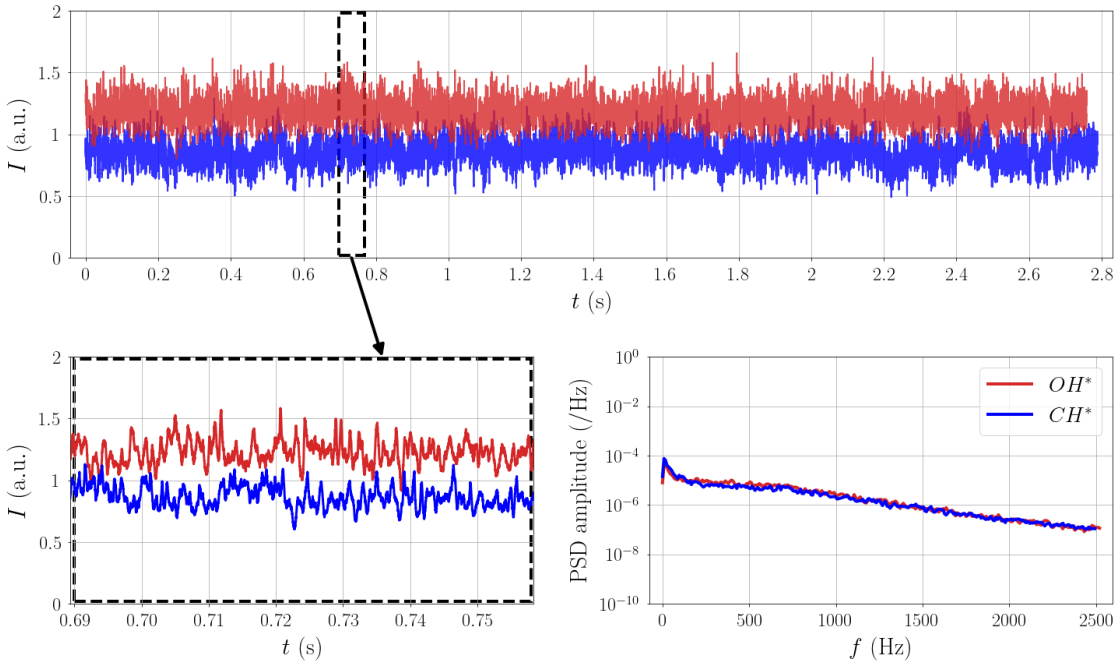

Figure 3.11: Signals from OH* and CH* emission of the central flame for power $\mathbb{P}_{59}$ without acoustic forcing. Whole raw signals are shown on top, zoomed-in raw signals on the bottom left and power spectral densities on the bottom right. Both measurements are acquired with the same PM gain. The mean value with OH* is 40% higher than with CH*.

3.3.1 Time-varying flame emission intensity

Whole raw CH* and OH* intensity signals are presented together with a zoomed-in view and the power spectral density (PSD) of the whole signals in Figure 3.11, The PSD is estimated using Welch's method, described in Section 2.3.1.1. A more complete description is found in [155]. CH* and OH* intensity signals fluctuate in a tight range around their mean value, which is about 40% higher with OH* than with CH*. Their power spectra do not show any dominant frequency, in particular in the range 700-800 Hz, which is the range of excitation frequencies used in the next chapters.

3.3.2 Flame shape

The flame shape is here described using time-averaged CH* and OH*-intensity images, which provide the average spatial repartition of the radical intensities. These characteristics are obtained using 6,000 images for each radical, acquired at 20,000 fps. To compensate for the lower signal with CH*, the gain of the intensifier is increased to obtain a mean pixel intensity in the flame region similar to that with OH*. Horizontal and vertical intensity profiles are obtained by summing the grey level values of all pixels at a given r or z respectively. As shown in Section 3.3.2, the V-shape of the flame is identically found with the two radicals. The flame is slightly asymmetric with respect to the plan $z = 0$, as shown by the higher intensities found for $r < 0$. In particular, the maximum light intensity found at $z = 30 - 35$ mm is perfectly captured by the two radicals. The flame base angle, estimated from Abel-transforms of the time-averaged

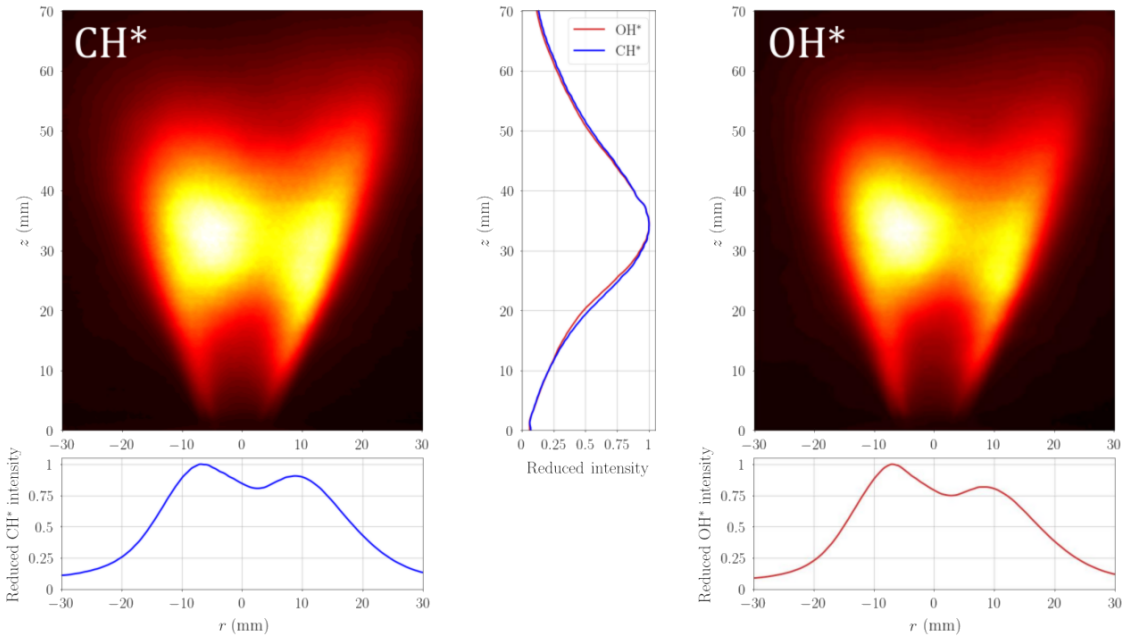

Figure 3.12: Time-averaged flame shapes with CH* and OH* radicals and associated horizontal-integrated and vertical-integrated profiles of the radical intensities. The operating point $\mathbb{P}_{59}$ is characterised by a flame power of 5.9 kW and a equivalence ratio of 0.85.

images is $62° \pm 2°$. The mean flame standoff distance is 3.3 mm $\pm$1.2 mm, and the mean flame length is 63.5 mm $\pm$1.9 mm. This is obtained identically from CH* and OH* images.

Chapter 4

Comparison between flame describing functions using acoustic pressure or axial velocity oscillations as a reference signal

Contents

Predicting thermoacoustic instabilities requires to know how the flame responds to acoustic perturbations. This response is usually described by the flame describing function (FDF), which uses the velocity oscillation at the burner exit as a reference signal. However, FDFs are often determined from single-burner experiments with upstream longitudinal acoustic forcing, while in annular combustors, combustion can couple with an azimuthal mode of the cavity, for which the axial velocity oscillation at the injector exit is driven by the pressure oscillation inside the chamber. To give further insight into such configurations, this study makes use of the TACC-Spray setup, a linear array of three swirling spray flames subjected to a controlled standing transverse acoustic wave. It is representative of an unfolded sector of the annular combustor MICCA-Spray (EM2C laboratory) in the presence of an azimuthal standing mode. In this chapter, combustion dynamics is described by using two FDFs, one defined with the acoustic pressure oscillation in the chamber at the central flame, $P^{'}$, as the reference signal, and the other defined with the air flow axial velocity oscillation, $U_z^{a'}$, measured at a well-chosen location at the central injector exit as the reference signal. Both FDFs are compared for a variety of acoustic amplitudes at a given frequency $f_r \simeq 750$ Hz, corresponding to a self-sustained instability frequency in MICCA-Spray. This comparison is performed for two fuels, n-heptane and dodecane, at two locations inside the standing transverse acoustic field: a pressure antinode (PAN) and an intensity antinode (IAN). It is found that the determination of the velocity-based FDF requires an accurate knowledge of the air flow as $U_z^{a'}$ is very sensitive to the radial location at the injector exit. On the contrary, $P^{'}$ is less sensitive to the radial location. Here, the two FDFs behave in a similar way as the acoustic amplitude increases for both PAN and IAN. The similarity between them is explained by the linear relationship between $P^{'}$ and $U_z^{a'}$. When the central flame is placed at IAN, both the gain and the phase of the FDFs match with the results obtained at PAN, showing that the flame response is mainly driven by acoustic pressure effects. When the fuel is dodecane, the FDF gain is lower while the phase is higher. These results agree with the lower instability amplitude found with dodecane than with n-heptane in MICCA-Spray at the same operating conditions. In addition, an analysis based on the Rayleigh criterion indicates a constructive interference between combustion and acoustics for all the studied cases, which is consistent with instabilities observed in the annular combustor. These results show that the pressure-based FDF can be suitably used to characterise the evolution of combustion dynamics with the acoustic amplitude in this configuration, and that information about the combustor stability in the annular combustor operating at the same conditions may be directly inferred from this FDF.

4.1 Introduction

Low-order models are being developed to predict self-excited instabilities at a low computational cost while keeping the fundamental mechanisms at the basis of the instabilities. In such models, combustor acoustics and combustion dynamics are included. For simple geometries, the combustor acoustics can be modelled analytically by representing the combustor as a succession of acoustic cavities [61], while for more complex geometries, acoustic solvers are generally

needed [161]. In many low-order models, combustion dynamics is represented by the flame describing function (FDF, see Section 1.3.2), which is able to predict limit cycle oscillations due to its dependence on the disturbance amplitude. While the output signal of the FDF is always the HRR oscillation, the input signal can be the velocity oscillation or the acoustic pressure oscillation [162–164].

As highlighted in Section 1.3.2, the determination of the FDF is a major question to predict instabilities. Points to consider carefully include the reference signal to take and the location at which it should be considered. It is generally admitted that the velocity in the fresh gases as close as possible to the burner exit is the best option, due to its independence from boundary conditions [112] and its reliability for both upstream and dowstream longitudinal forcing [52]. In addition, its radial location should be chosen such that the velocity oscillation reduced by its mean value corresponds to the volumetric flow rate oscillation reduced by its mean value [53]. However, complex flows such as swirling ones have velocity gradients which may lead to significant differences in axial velocity oscillation for a small change of the measurement location. In addition, it may be difficult to measure the velocity oscillation in combustors for practical reasons. Therefore, using a reference signal that is less sensitive to the measurement location and more convenient to measure could facilitate the FDF measurement, especially when a large number of FDFs have to be acquired.

In addition, the acoustic forcing method used may have an influence on the FDF measurement. A comparison between FDFs of swirl-stabilised premixed flames obtained with longitudinal or transverse acoustic forcing at a pressure antinode highlighted that, at low frequencies, the gain of the FDF depends on the acoustic forcing method [110]. In spite of the quantitative difference, the authors noticed that the flame response mechanisms were identical with both forcing methods. A previous work on a laminar premixed flame showed that the longitudinal acoustic field induced by downstream transverse forcing at a pressure antinode was identical to the direct longitudinal acoustic field induced by usptream longitudinal acoustic forcing, although the mechanism by which the velocity oscillation is generated is different in each case [109]. Furthermore, the authors noticed that jet and flame dynamics have the same properties for both forcing cases. While the mechanisms driving the flame response are qualitatively the same for upstream longitudinal forcing and downstream transverse forcing at a pressure antinode, this might not be the case when the flame are subjected to a transverse velocity perturbation. During instabilities coupled by a standing transverse acoustic mode, a flame is subjected to pressure and transverse velocity perturbation depending on its position in the acoustic field. This kind of phenomena can only be reproduced in setups equipped to perform transverse acoustic forcing.

The environment of the flames must also be considered. FDFs are generally obtained on single-injector setups (experimental or numerical), or derived from analytical models considering a single flame, while in annular combustors, effects linked to the presence of neighbouring flames are found. For instance, the thermal environment is not the same as in a single-injector setup, or effects such as flame-flame interactions can affect the flame response [81,84,165]. A recent work indicates that a single-injector setup would approximately represent a multiple-injector setup if flame-flame and flame-wall interactions are weak [53]. It may therefore be important to account for these effects.

This chapter aims at giving elements of response to elucidate whether combustion dynamics can be described by an FDF based on the acoustic pressure oscillation inside the chamber for a standing transverse acoustic field. The chosen configuration includes several characteristics found in industrial annular combustors: swirling flows, spray combustion, neighbouring flames. In addition, a transverse acoustic field, which is most likely to develop in such combustors, is excited. In this study, the nonlinear response of a swirl-stabilised spray flame to a standing transverse acoustic forcing is examined via two FDFs, based either on the velocity fluctuation measured at the injector exit or on the acoustic pressure fluctuation. The central flame, which is the object of the study, is part of a linear array of three identical flames, and is thus located in an environment similar to that of a flame in a model self-unstable annular combustor presenting oscillations coupled with an azimuthal mode. The FDF, which is originally a function of both the acoustic amplitude and frequency, is here parameterised by changing the fuel (n-heptane or dodecane) and the location of the central flame in the standing transverse acoustic field (PAN or IAN). The acoustic amplitude is varied while the excitation frequency is kept constant.

In Section 4.2, the experimental setup, diagnostics and post-processing methods are presented, after which a description of the velocity measurement method is given in Section 4.3. The two FDFs are then presented and examined in Section 4.4 for all the operating conditions explored here. In Section 4.5, the injector response, which provides the link between acoustic pressure and velocity fluctuations measured close to the injector exit, is characterised. Finally, the ability of the pressure-based FDF to evaluate the thermoacoustic coupling is discussed in Section 4.6. The impact of the fuel and the flame location is briefly discussed in this work. Nevertheless, more detailed analysis about the influence of these parameters is developed in Chapter 8 and Chapter 9 of this manuscript.

4.2 Experimental setup and diagnostics

4.2.1 Acoustic cavity and injection system

We give here the major features of the acoustic cavity and the operating conditions for this specific study. The acoustic cavity TACC-Spray and the injection system are presented with more detail in Section 2.1. Forcing of the 2T1L standing mode (see Figure 4.1 (a)) is performed for various acoustic amplitudes at frequencies $f_r = 752 \pm 15$ Hz, corresponding to frequencies at which instabilities are observed in MICCA-Spray [141]. Thus, TACC-Spray is set to a length $L_c = 880$ mm. In this study, the five-injector array is shifted inside the acoustic field to place the central flame either at PAN or at IAN (see Figure 4.1 (a)). The five injection units are similar to that used in [53], each one consisting of a plenum, a distributor and a radial swirler of type 716 for the air flow (see Figure 4.1 (b)). The choice of the type 716 swirler is guided by the strong instabilities observed in MICCA-Spray with this swirler [101]. The three central injectors also comprise a fuel atomiser set at $0.8D_{exit}$ usptream the nozzle exit of diameter $D_{exit} = 8$ mm. The system is operated with n-heptane or dodecane. The choice of these two fuels is guided by their different physico-chemical properties, modifying atomisation and evaporation. Air mass flow rate is 2.63 g/s and fuel mass flow rates are 0.165 g/s for n-heptane and 0.167 g/s for dodecane, corresponding to a global equivalence ratio $\phi = 0.95$ and resulting in the same flame power

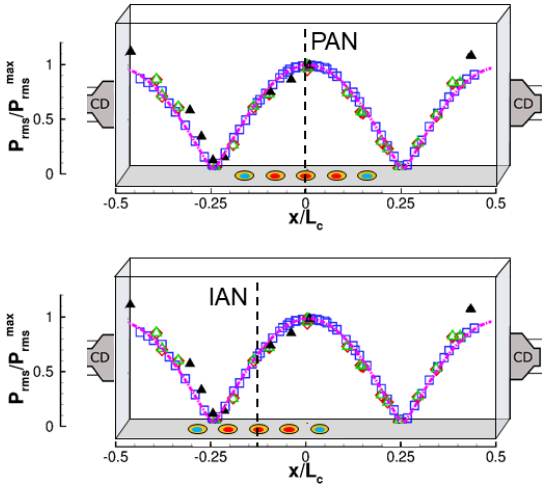

(a) Acoustic cavity, acoustic field and location of the injection array

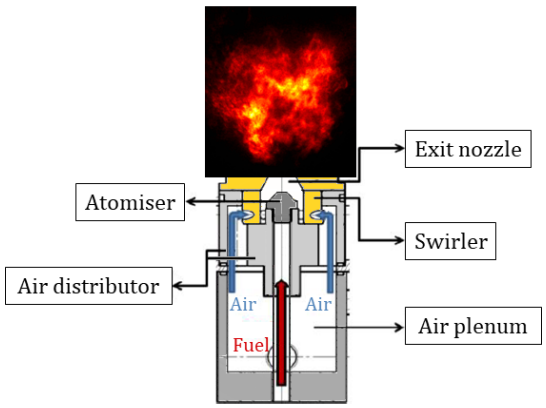

(b) Injection system

Figure 4.1: Details of the experimental setup: (a) Acoustic cavity TACC-Spray with the acoustic pressure field measured. Red dots: air and liquid fuel injection; blue dots: air injection only. Left top: central flame at PAN; left bottom: central flame at IAN. CD: compression drivers. Blue squares: $P_{max}^{rms} = 66$ Pa, $f_r = 773$ Hz; red diamonds: $P_{max}^{rms} = 355$ Pa, $f_r = 718$ Hz; green triangles: $P_{max}^{rms} = 498$ Pa, $f_r = 718$ Hz; black filled triangles: $P_{max}^{rms} = 425$ Pa, $f_r = 784$ Hz, with combustion; magenta dash-dotted line: simulation; (b) sketch of the injection system and flame. In (b), the flame and the injector are at the same scale.

$\mathcal{P} = 7.4$ kW for both fuels. These conditions correspond to the operating points $\mathbb{P}_{74}$ and $\mathbb{P}_{74d}$ (see Table 2.1).

4.2.2 Diagnostics

The acoustic pressure is measured using the setup described in Section 2.2.2. In this chapter, one microphone is placed at the central flame location, giving the acoustic pressure $P^{'}(t)$, and another is placed at a reference position which is the central PAN, giving $P^{'}_{ref}(t)$. Thus, when the central flame is located at PAN, $P^{'}(t) = P^{'}_{ref}(t)$. The maximum attainable value of $\Pi = P^{rms}/\rho^a U_b^2$ is imposed by the acoustic forcing system and thus depends on the position inside the acoustic field. It is about $\Pi = 0.5$ at PAN while at IAN, it is about 55-60% of this value (see Figure 4.1 (a)).

Flame dynamics is analysed through the OH*-intensity signal I measured with the setup described in Section 2.2.3.1. A Dantec Dynamics 2-component Laser/Phase Doppler Anemometry (LDA/PDA) system is used to measure fuel droplet axial (U_z^f), tangential (U_θ^f) and radial (U_r^f) velocity components with and without acoustic forcing. When the system is operated in PDA mode, the fuel droplet diameter d is also measured. The data rate can reach values of 20-25,000 droplets/s with LDA and 10,000 droplets/s with PDA at some radial locations (see Appendix 4.A). Measurements with LDA and PDA are performed during 4 seconds and 10 seconds respectively, in order to obtain a similar droplet count. Pressure and OH* signals are simultaneously

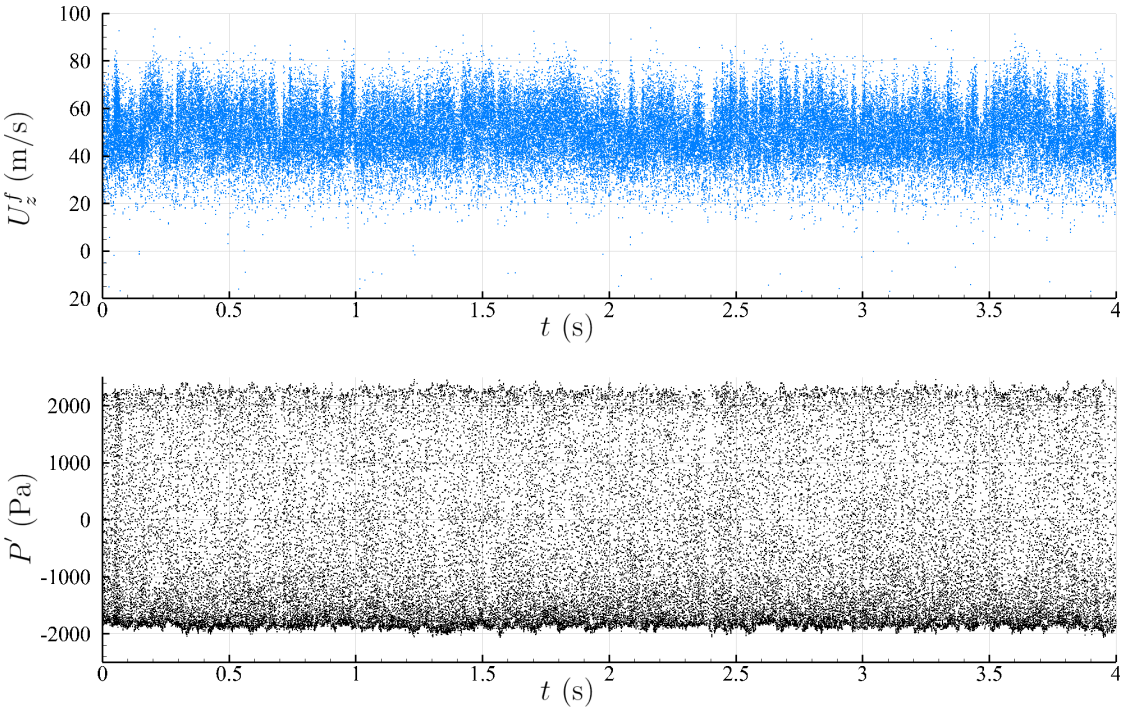

Figure 4.2: Time signals obtained by LDA with dodecane fuel for $\Pi = 0.48$. Top: axial velocity, U_z^f, measured at $z = 2.5$ mm and r = 4 mm; bottom: acoustic pressure oscillation, $P^{'}$, measured at the central flame location. The acoustic forcing frequency f_r is 748 Hz. Measurements are shown for about 3,000 acoustic cycles.

acquired with the Labview software at a sampling frequency of $100 f_r$, and with the LDA/PDA system, the latter system giving a sample each time a fuel droplet is measured.

Four-second time signals of axial velocity measured with LDA at ($z = 2.5$ mm, r = 4 mm), and acoustic pressure oscillation measured at the central flame location and acquired with the LDA system are illustrated for $\Pi = 0.48$ in Figure 4.2, with dodecane fuel. Each data point corresponds to one fuel droplet validated by the LDA system. Due to the forcing frequency $f_r = 748$ Hz, these plots show the instantaneous values during about 3,000 acoustic cycles. Most of the validated fuel droplets have a velocity $U_z^f(t)$ between 20 m/s and 80 m/s, centered around 50 m/s. $P^{'}(t)$ oscillates between -2000 Pa and 2000 Pa. The dark line drawn by the numerous data points around $P^{'} = -2000$ Pa, which is darker than the line around $P^{'} = 2000$ Pa, indicates that more droplets are measured at the pressure minimum than at the pressure maximum. It highlights the modulation of the droplet count at the injector exit during the acoustic cycle. Droplet count oscillation is further studied in Part II of this manuscript.

4.3 Velocity measurements

Measurement of the air flow velocity oscillation is a crucial point to estimate the FDF. The location of the velocity measurement should fulfill two conditions: (i) the air flow velocity oscillation is measured very close to the burner exit; (ii) the air flow velocity oscillation reduced by the mean

velocity is representative of the volumetric air flow rate oscillation reduced by the mean volumetric air flow rate [53]. In the present study, the first condition is dealt with by performing velocity measurements (with LDA or PDA) at $z = 2.5$ mm (corresponding to $z/R = 0.625$), which is the closest location to the burner at which the LDA/PDA measurement volume can be placed. The second condition is addressed by seeking the most adequate radial location for the velocity measurement in the plane defined by $z = 2.5$ mm. Due to the axisymmetry of the velocity profile, the most adequate measurement location is actually sought on a radial line which is comprised in this plane.
In this work, velocity measurements are performed by using the fuel droplets as tracer particles. It is thus necessary to examine beforehand the ability of these droplets to give the air flow velocity for these specific operating conditions. In the following, the two fuel sprays are first characterised in steady conditions; then, the velocity oscillation measured as close as possible to the injector exit is given.

4.3.1 Characterisation of the sprays of n-heptane or dodecane in steady conditions

The radial profiles of the mean and rms fuel droplet velocity components at $z = 2.5$ mm are examined with n-heptane or dodecane as a fuel, without acoustic forcing and in reacting conditions in Figure 4.3. The profiles with n-heptane are obtained with PDA while those with dodecane include LDA and PDA measurements[1]. The radial profiles of the mean and rms values of the three velocity components are identical for n-heptane and dodecane. The only exception is found around $r = 0$ mm, where negative mean axial velocities are about 5-10 m/s higher with n-heptane than with dodecane.

It is worth investigating whether the fuel droplet velocity is representative of the air flow velocity. For this purpose, we first evaluate the radial profile of the local mean arithmetic droplet diameter, $d_{10}(r)$ at $z = 2.5$ mm. Indeed, as shown in Section 3.2.1, there is a relationship between the mean velocity of a fuel droplet population and the mean diameter of this population. The radial profile of $d_{10}(r)$ at $z = 2.5$ mm is shown in Figure 4.4 (a). For the two fuels, $d_{10}(r)$ is similar at all locations, except in the range $r = 2 - 6$ mm, where $d_{10}(r)$ is a little higher with n-heptane. Nevertheless, it remains lower than 7 µm, except around $r = 6$ mm. The ability of the fuel droplets to follow the air flow is measured with the local Stokes number $\mathrm{Stk}(r) = \rho^f d_{10}^2(r)\overline{U_z^f}(r)/18\mu^a D_{exit}$, with ρ^f the fuel density and μ^a the air dynamic viscosity[2]. It is worth noting that $d_{10}(r)$ and $\overline{U_z^f}(r)$ are obtained by including all the droplets measured with PDA. For $|r| \leq 5$ mm, the Stokes number is everywhere lower than 0.45 with the two fuels (see Figure 4.4 (b)). At most locations, it is even lower than 0.3, indicating that the air flow velocity can be well estimated from statistical velocity measurements performed on both the n-heptane and dodecane fuel droplets.

To conclude, the air flow velocity, $\overline{U_z^a}(r)$, corresponds to $\overline{U_z^f}(r)$. Therefore, $\overline{U_z^a}(r)$ can be ob-

[1] A detailed comparison of the measurements with PDA and LDA is given in Appendix 4.A.

[2] To calculate μ^a, the air temperature is assumed to be 700 K for $|r| \leq 4$ mm due to the presence of the flame and 293 K at other locations.

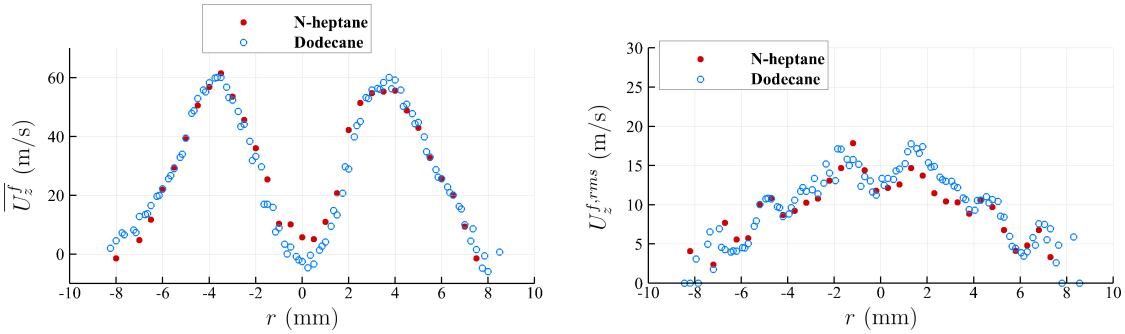

(a) Axial velocity

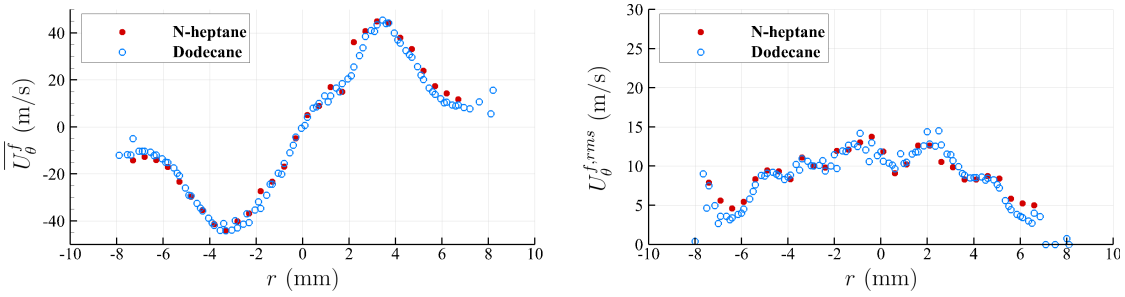

(b) Tangential velocity

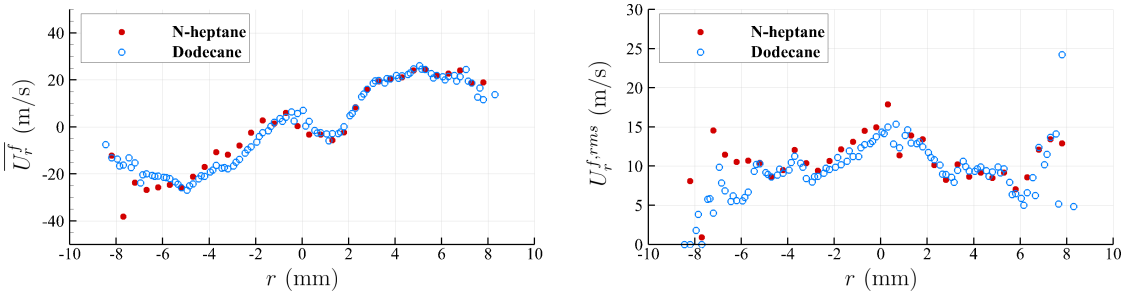

(c) Radial velocity

Figure 4.3: Radial profiles of the mean and rms fuel droplet velocity components at $z = 2.5$ mm without acoustic forcing, in reacting conditions, with n-heptane or dodecane, $U_b = 43.4$ m/s, $\phi = 0.95$. The profiles are measured with PDA or LDA, both of which provide the same velocity profiles.

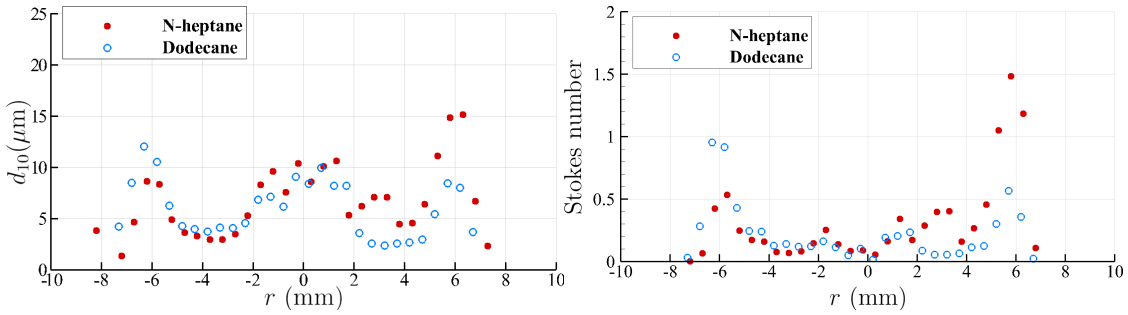

(a) Arithmetic mean diameter $d_{10}(r)$ (b) Stokes number

Figure 4.4: Radial profiles of arithmetic mean diameter r_{10} and Stokes number without acoustic forcing in reacting conditions, with n-heptane or dodecane, $U_b = 43.4$ m/s, $\phi = 0.95$. The Stokes number is calculated by assuming an air temperature of 700 K for $|r| \leq 4$ mm and 293 K at other locations.

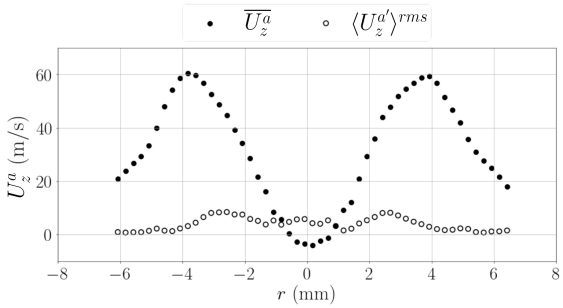

Figure 4.5: Radial profiles of air flow mean axial velocity, $\overline{U_z^a}$, and coherent oscillation amplitude at f_r, $\langle U_z^{a'} \rangle^{rms}$. The fuel is dodecane. Reduced acoustic amplitude: $\Pi = 0.29$.

tained with LDA as well as with PDA, without filtering the droplets according to on their diameter. This is valid for both n-heptane and dodecane.

4.3.2 Air flow velocity oscillation induced by acoustics

Since the air flow velocity can be equally obtained from measurements performed on n-heptane or dodecane fuel droplets (except for $|r| < 0.5$ mm), we investigate here the air flow axial velocity oscillation at $z = 2.5$ mm induced by the acoustic pressure oscillation in the chamber for dodecane only. The radial profile of axial velocity oscillation amplitude is illustrated with dodecane together with the mean axial velocity for $\Pi = 0.29$ in Figure 4.5. As mentioned above, the reduced velocity oscillation that serves as an input signal for the FDF must be as close as possible to the reduced volumetric flow rate oscillation at the injector exit. By using the radial profiles of Figure 4.5, it is possible to calculate the reduced volumetric flow rate oscillation, $\langle \dot{q}_v^{'} \rangle^{rms} / \overline{\dot{q}_v}$. For this purpose, the phase-averaged axial velocity signals obtained at $z = 2.5$ mm and at various radial locations are post-synchronised with the acoustic pressure at the central flame location and integrated along a radial profile. This method gives $\langle \dot{q}_v^{'} \rangle^{rms} / \overline{\dot{q}_v} = 0.055$. We now compare this value with $\langle U_z^{a'} \rangle^{rms}(r) / \overline{U_z^a}$ in Figure 4.6 (a). At $r = \pm 4$ mm and $r = \pm 5$ mm,

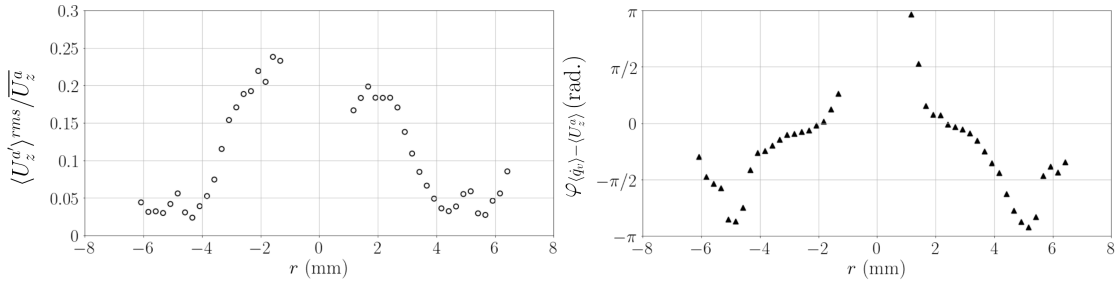

(a) Normalised oscillation of $\langle U_z^{a'} \rangle^{rms} / \overline{U_z}$

(b) Phase shift between $\langle \dot{q_v'} \rangle$ and $\langle U_z^{a'} \rangle$

Figure 4.6: Radial profiles of normalised oscillation amplitude of the air flow coherent axial velocity, $\langle U_z^{a'} \rangle^{rms} / \overline{U_z^a}$ and phase shift between the mass flow rate oscillation $\langle \dot{q_v'} \rangle$ and $\langle U_z^{a'} \rangle$. The fuel is dodecane. Reduced acoustic amplitude: $\Pi = 0.29$.

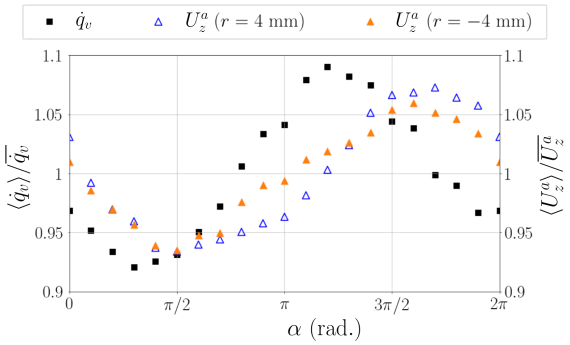

Figure 4.7: Phase-averaged normalised mass flow rate oscillation at the injector exit and normalised axial velocity oscillation at $r \pm 4$ mm along a reconstructed acoustic cycle. The fuel is dodecane.

a good match is found between $\langle U_z^{a'} \rangle^{rms}(r)/\overline{U_z^a}$ and $\langle \dot{q}_v' \rangle^{rms}/\overline{\dot{q}_v}$, which is consistent with the observations of the EM2C team [53] in the single-injector SICCA-Spray combustor, subjected to upstream longitudinal acoustic forcing. One must now considers the phase shift between $\langle \dot{q}_v \rangle$ and $\langle U_z^a \rangle(r)$. The radial profile of this phase shift, $\varphi_{\langle \dot{q}_v \rangle - \langle U_z^a \rangle}$, is shown in Figure 4.6 (b). At $r = \pm 4$ mm, $\varphi_{\langle \dot{q}_v \rangle - \langle U_z^a \rangle} \simeq -\pi/4$ while at $r = \pm 5$ mm, $\varphi_{\langle \dot{q}_v \rangle - \langle U_z^a \rangle} \simeq \pi$. Therefore, it is chosen to retain the location ($r = \pm 4$ mm, $z = 2.5$ mm) to perform the velocity measurements, as it gives the closest measurement to the volumetric flow rate oscillation. This is illustrated with phase-averaged signals in Figure 4.7. To ensure that the fuel droplets correctly follow the air flow oscillations induced by acoustics at this specific location, an *acoustic* Stokes number, $\mathrm{Stk_{ac}} = \omega \tau_{drop}$ (see Equation (1.7), with $\tau_{oscil} = \omega = 2\pi/T$), is introduced. At the location ($r = \pm 4$ mm, $z = 2.5$ mm), $\mathrm{Stk_{ac}}$ is in the range 0.06 - 0.17 for both fuels, indicating the ability of the method used here to capture the axial velocity oscillation at f_r.

It is worth noting that the axial velocity oscillation is nonetheless highly sensitive to the radial location. In addition, the optimal location is specific to a given injector, and could be affected by the acoustic amplitude or the fuel, which can make the work difficult to perform for a variety of configuration. This justifies the search for a quantity that is less sensitive to the location. In the present setup, the wavelength $\lambda = L_c$ is such that the injector exit of diameter 8 mm is compact with respect to the acoustic pressure field. Therefore, acoustic pressure is a quantity whose robustness is ensured by its low sensitivity to a small displacement.

4.4 Flame describing functions (FDFs)

The thermoacoustic loop can be roughly decomposed in three steps: (i) the pressure perturbation induces axial velocity oscillations; (ii) axial velocity oscillations perturb the flame, leading to HRR oscillations; (iii) HRR oscillations generate pressure oscillations. The FDF based on the downstream acoustic pressure oscillation, $\mathcal{F}_{P'}$, contains the first two steps, *i.e.* the injector response to the acoustic pressure perturbation and the flame response to the velocity oscillation, whereas $\mathcal{F}_{U'}$ includes the second step only, *i.e.* the flame response to the velocity oscillation. Therefore, $\mathcal{F}_{P'}$ does not allow the decoupling of the injector response and the flame response. A recent work by the EM2C team [53] showed that changing the swirler induces both a change in flame response and a change in injector response. In other words, the injector acts on the system's response not only via the conversion of the pressure perturbation into a velocity oscillation, but also because it affects the flame geometry and so the flame response. However, it will be shown below that the evolution of the flame response as the acoustic amplitude increases is equally described by $\mathcal{F}_{P'}$ and $\mathcal{F}_{U'}$ in the present case. In this section, these two FDFs are compared as a function of acoustic amplitude for the two fuels (n-heptane and dodecane) at the two locations in the standing acoustic field (PAN and IAN). The global trends of the FDFs are first outlined, then the influence of the flame location inside the acoustic field and that of the fuel are briefly discussed.

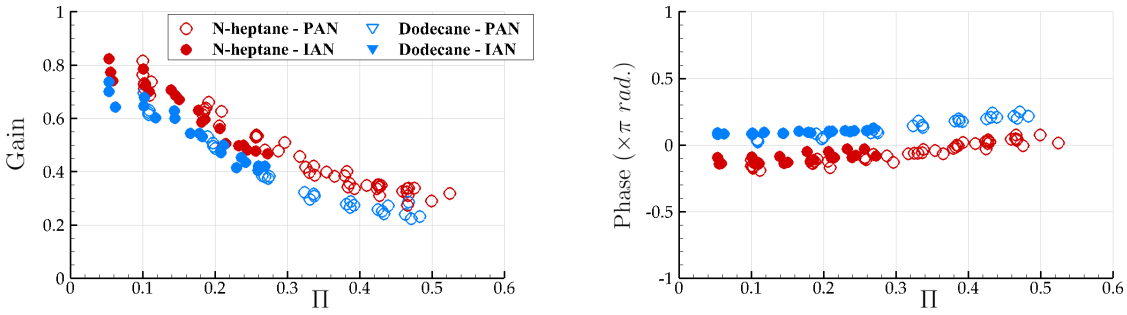

Figure 4.8: FDF $\mathcal{F}_{P'}$ defined in eq. (4.1) evaluated at $f_r = 752 \pm 15$ Hz, at PAN and IAN for n-heptane and dodecane. Left: gain $\mathcal{G}_{P'}$; right: phase $\varphi_{P'-I'}$.

4.4.1 Calculation of the FDF

Two flame describing functions are defined in the frequency domain, one based on the acoustic pressure fluctuation and the other on the axial velocity fluctuation. First, the pressure-based FDF is expressed by:

$$\mathcal{F}_{P'}(f_r, \Pi) = \frac{\breve{I}\,/\overline{I}}{\breve{P}\,/\rho^a U_b^2} = \mathcal{G}_{P'}(\Pi) e^{i\varphi_{P'-I'}(\Pi)} \tag{4.1}$$

where $\breve{(\cdot)}$ indicates complex amplitudes, $\overline{(\cdot)}$ mean values, $\mathcal{G}_{P'}$ the gain and $\varphi_{P'-I'}$ the phase of this FDF. $\mathcal{F}_{P'}$ corresponds to the ratio of the cross-power spectral density between the reduced pressure oscillation $P'/\rho^a U_b^2$ and the reduced OH*-intensity oscillation $I'/\overline{I}$ to the power spectral density of the reduced pressure oscillation. The acoustic pressure and OH*-intensity signals are obtained via the Labview software by using the Welch's method. This method is easily applicable as these signals are uniformly sampled.

Velocity signals obtained with LDA/PDA are non-uniformly sampled, as data are acquired each time a droplet crosses the measurement volume. A uniformly-sampled signal is nonetheless reconstructed by phase-averaging the axial velocity signal at f_r, such that the data are put into bins of equal width $1/(20 f_r)$, which gives reconstructed signals with a sampling rate of $20 f_r$ (as described in Section 2.3.1.2). It is shown in Section 4.B that FDFs at a given frequency f_r calculated with raw signals and phase-averaged signals give the same results. By defining $A = \langle U_z^a \rangle^{rms} / \overline{U_z^a}$ and indicating phase-averaged signals in square brackets, the velocity-based FDF at f_r is expressed by ;

$$\mathcal{F}_{U'}(f_r, A) = \frac{\breve{\langle I \rangle}\,/\overline{I}}{\breve{\langle U_z^a \rangle}\,/\overline{U_z^a}} = \mathcal{G}_{U'}(A) e^{i\varphi_{U'-I'}(A)} \tag{4.2}$$

4.4.2 Pressure-based FDF

The flame response is first investigated with the FDF based on acoustic pressure, shown in Figure 4.8 with n-heptane and dodecane at PAN and IAN. For the two fuels and the two flame locations, the gain $\mathcal{G}_{P'}$ decreases when the acoustic amplitude increases, indicating a nonlinear flame response. This indicates that the processes converting the pressure perturbation into an

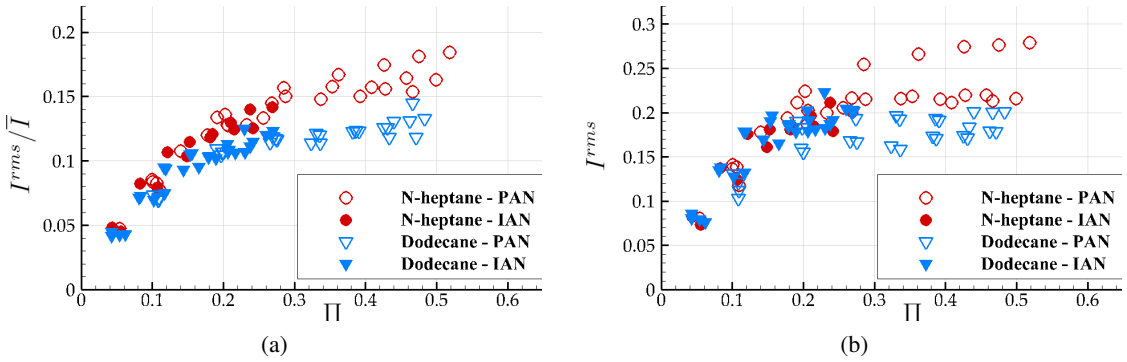

(a) (b)

Figure 4.9: Evolution of the flame intensity with Π. Left: $I^{rms}/\overline{I} = f(\Pi)$; right: $I^{rms} = f(\Pi)$

OH*-intensity oscillation become less efficient as the acoustic amplitude increases. This is a major characteristic feature of the energy system, as the HRR oscillation in turn drives the pressure oscillation [85]. It is therefore interesting to see whether the OH*-intensity oscillation amplitude continues to grow above a certain acoustic level or not. This is investigated by plotting the relationship $I^{rms}/\overline{I} = f(\Pi)$, which is an alternative representation of the gain, in Figure 4.9 (a). At low acoustic amplitudes, $I^{rms}/\overline{I}$ increases significantly with Π. On the contrary, at high acoustic amplitudes, $I^{rms}/\overline{I}$ increases very little when Π increases. The nonlinearity here found in the flame response is important as it is known that finite amplitude oscillations are controlled by nonlinear processes [46].

The phase of the FDF is also of substantial importance for the establishment of instabilities, as stated by the Rayleigh criterion. Here, $\varphi_{P'-I'}$ is quite constant as Π increases up to a value of 0.3, above which it slightly increases with Π. It is interesting to note that I^{rms} saturates above the same value of $\Pi = 0.3$ whereas it increases with Π at lower amplitudes (see Figure 4.9 (a)). This could indicate that the saturation of the flame response affects the phase of the FDF. Nevertheless, it is always comprised between $-\pi/2$ and $+\pi/2$ for all the reduced acoustic amplitudes Π, for the two fuels (n-heptane and dodecane) and for the two locations (PAN and IAN), suggesting that these flames could potentially drive an instability at f_r, as stated by the Rayleigh criterion (see Equation (1.22)).

4.4.3 Velocity-based FDF

The flame response is now investigated with the FDF based on axial velocity, $\mathcal{F}_{U'}$. Figure 4.10 shows results at PAN and at IAN, for n-heptane and dodecane. For the two fuels and the two flame locations, the gain $\mathcal{G}_{U'}$ decreases when the Π increases in a similar manner to $\mathcal{G}_{P'}$. However, for a given acoustic amplitude, values are more scattered than those of $\mathcal{G}_{P'}$, especially at low acoustic amplitudes. The scatter of the FDF gain at low acoustic amplitudes was also observed by Nygård et al. [100] for lean premixed combustion in a forced annular combustor. In the present work, this may originate from the sensitivity of the axial velocity oscillation to the radial location, shown in Figure 4.6. A sensitivity analysis (see Section 4.C) indicates that a displacement of 0.2 mm of the velocity measurement location around $r = 4$ mm affects the amplitude of the axial velocity oscillation by 30%, and therefore modifies the gain of the FDF

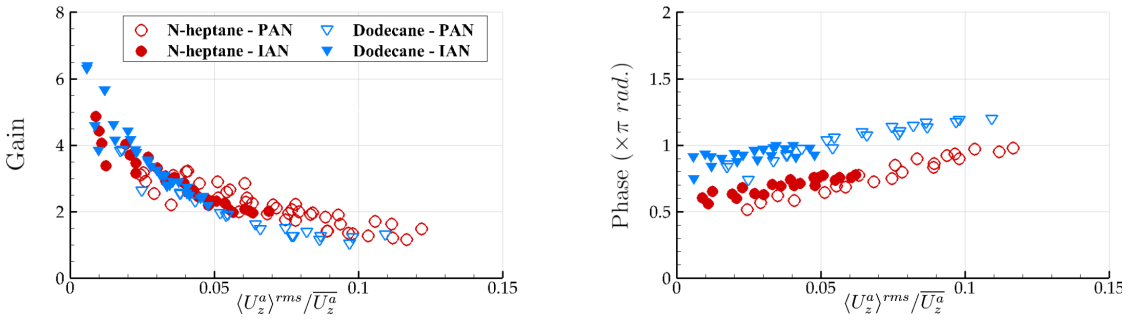

Figure 4.10: FDF $\mathcal{F}_{U'}$ defined in eq. (4.2) evaluated at $f_r = 752 \pm 15$ Hz, at PAN and IAN and for n-heptane and dodecane. Left: The gain $\mathcal{G}_{U'}$; right: phase $\varphi_{U'-I'}$.

in the same proportion. It must also be noted that at low forcing amplitudes, coherent velocity oscillations at f_r are more easily perturbed by the stochastic noise. This shows the high gain values of $\mathcal{F}_{U'}$ should be considered with caution for low $\langle U_z^{a'} \rangle^{rms}/\overline{U_z^a}$.

The phase $\varphi_{U'-I'}$ increases more than $\varphi_{P'-I'}$ when Π is modified. At the highest acoustic amplitudes reached, the phase is about 0.4π higher than at the lowest acoustic amplitudes. The increase of the phase is important to consider in low-order models as it could indicate the transition from an unstable system to a stable system or vice versa. Like the nonlinear evolution of the gain, it plays an essential role in the establishment of a limit cycle.

4.4.4 Effects of the flame location and fuel

Location in the acoustic field

When a standing mode is excited into an annular combustor, flames located at PAN are theoretically subjected to acoustic pressure oscillations only while flames located at IAN are subjected to mixed acoustic pressure and transverse velocity oscillations. In addition, the acoustic pressure oscillation is less intense at IAN than at PAN. As shown in Figures 4.8 and 4.10 for both fuels, the gain curves at PAN and IAN are superimposed, indicating the OH*-intensity oscillation amplitude mainly depends on acoustic pressure effects, whereas it is not significantly affected by the transverse velocity oscillation at IAN. For both fuels, the phase curves at PAN and IAN are also superimposed, which shows that the acoustic pressure effects are also driving the phase of the FDF. The flame response as a function of the location in the acoustic field is further analysed in Chapter 9.

Fuel type

For both fuels, the gain curves have the same shape, indicating that nonlinearity is dominated by processes independent of the fuel. It is known, for example, that the roll-up of a strong vortex or the unsteady flame lift-off can induce nonlinear flame responses [67, 124]. However, the fuel influences the intensity of the gain of both $\mathcal{F}_{P'}$ and $\mathcal{F}_{U'}$, which is lower with dodecane than with n-heptane for the two FDFs. The only exception concerns low axial velocity amplitudes ($\langle U_z^{a'} \rangle^{rms}/\overline{U_z^a} \leq 0.03$), but the higher gain $\mathcal{G}_{U'}$ with dodecane must be considered with care due to the large scatter of the FDF gain at low axial velocity amplitudes, as mentioned above. The

lower gain with dodecane may explain why stronger instabilities were found with n-heptane than with dodecane by the EM2C team [53] for the same operating conditions as here. Nevertheless, this is not the only parameter that must be considered, as the FDF phase also plays a major role in the development of instabilities. The lower gain with dodecane might be linked to the coarser atomisation, which produces a lower amount of small droplets. The influence of the fuel on the flame response is investigated in Chapter 8.

Comparison of the phase curves for the two fuels is particularly insightful. At all acoustic amplitudes, the phase of both FDFs obtained with dodecane is shifted by $\sim 0.3\pi$ compared to that obtained with n-heptane. For both fuels, the phase of the FDF evolves linearly with $\langle U_z^{a'} \rangle^{rms} / \overline{U_z^a}$. One can thus write $\varphi_{U'-I'} = \omega_r \tau_{U'-I'} = a(\langle U_z^{a'} \rangle^{rms} / \overline{U_z^a}) + b$, where $a \simeq 3.2\pi$ for the two fuels and $b \simeq 0.55\pi$ for n-heptane and 0.85π for dodecane. Hence, a, independent of the fuel, could be linked to the unsteady aerodynamics, whereas b could depend on the fuel evaporation. The difference of b leads to an additional time delay of 0.2 ms for dodecane, which agrees with characteristic fuel evaporation times obtained with a theoretical model droplet evaporation based on heat transfer [45]. A change of b can modify combustor stability, as pressure and HRR must oscillate in phase to drive an instability.

To conclude, the evolution of the FDF with Π is retrieved by both the pressure-based FDF and the velocity-based FDF. This indicates that the acoustic pressure oscillation measured at the central flame location can be used as a reference signal of the FDF to describe the nonlinear FDF evolution.

4.5 Injector response to acoustics

The present section aims at investigating the link between the acoustic pressure oscillation and the axial velocity oscillation. The relation between these two quantities, also named 'injector impedance', characterises the injector response to the acoustic pressure oscillation. This relation was shown to depend on the injector geometry and the frequency under self-sustained longitudinal oscillations [53]. The mechanisms linking the acoustic pressure oscillation and the axial velocity oscillation were investigated experimentally by the CORIA team [109] with upstream longitudinal forcing or downstream transverse forcing. With transverse downstream forcing, they showed that the axial velocity oscillation at PAN results from the pressure oscillation in the chamber, a feature named 'plugging effect'. However, their analysis dealt with a laminar premixed flame, while in the present case, the reacting flow is turbulent and has a swirl motion.

In the present study, the relationship between Π and the relative axial velocity oscillation amplitude $\langle U_z^{a'} \rangle^{rms} / \overline{U_z^a}$ is evaluated for a given injector, a given frequency but for various acoustic amplitudes. Results are presented in Fig. 4.11. In the range of acoustic amplitudes investigated here, $\langle U_z^{a'} \rangle^{rms} / \overline{U_z^a}$ and Π are linked by a proportionality relationship. This important feature explains the similar shapes of the gain curves of $\mathcal{F}_{P'}$ and $\mathcal{F}_{U'}$ and therefore demonstrates that the flame response is equally captured by these two FDFs in the present case. The proportionality relationship is independent of the flame location up to $\Pi = 0.3$, showing that the axial velocity oscillation only depends on the downstream pressure oscillation in this range. The phase of

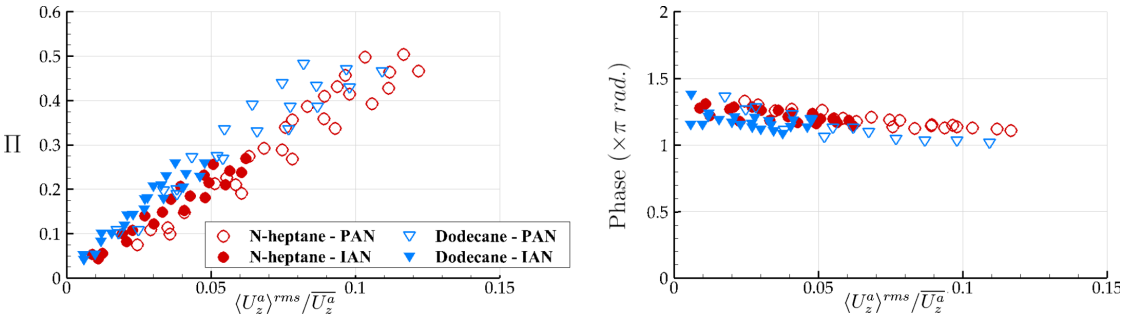

Figure 4.11: Injector response at PAN and IAN with n-heptane and dodecane. Left: $\Pi = f(\langle U_z^a \rangle^{rms}/\overline{U_z^a})$; right: phase $\varphi_{P'-U'} = f(\langle U_z^a \rangle^{rms}/\overline{U_z^a})$.

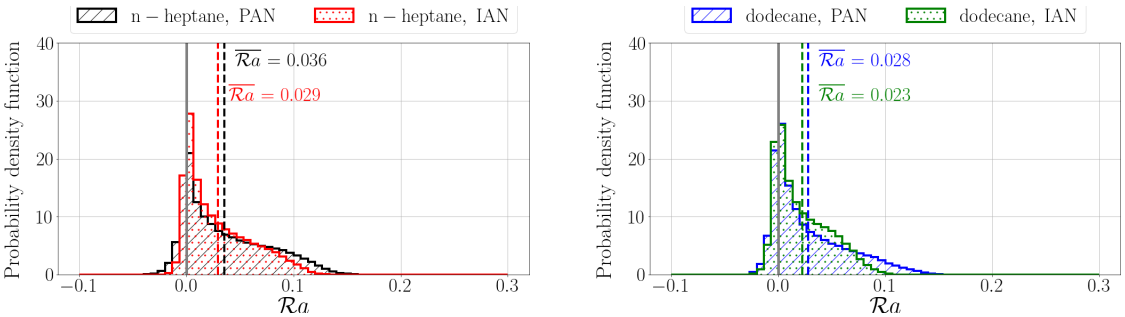

(a) N-heptane (b) Dodecane

Figure 4.12: Probability density function of the coupling index $\mathcal{R}a_2(t)$ for a similar local pressure perturbation $\Pi = 0.26 - 0.27$ when the central flame is located at PAN and IAN. Vertical grey solid line: $\overline{\mathcal{R}a_2} = 0$.

the injector response is similar for both fuels as well as for both locations. It is close to $5\pi/4$ at low acoustic amplitudes and π at high amplitudes. It is verified that the phase of $\mathcal{F}_{P'}$ (see Fig. 4.8) can be obtained from the phase of $\mathcal{F}_{U'}$ (see Fig. 4.10) by means of the relationship: $\varphi_{P'-I'} = \varphi_{P'-U'} + \varphi_{U'-I'}$.

4.6 Thermoacoustic coupling

The information about combustor stability given by the FDF can be analysed through the Rayleigh criterion. For acoustically-compact flames, this criterion states that a positive Rayleigh source term indicates the propensity of an energy system to drive instabilities (see Section 1.2.2). We define the time-varying instability index $\mathcal{R}a_2(t)$[3] expressed by:

$$\begin{aligned} \mathcal{R}a_2(t) &= \frac{P^c(t)}{\rho^a U_b^2} \times \frac{I^c(t)}{\overline{I}} \\ &= \xi \times P^c I^c(t) \end{aligned} \tag{4.3}$$

[3]This notation is justified in Section 5.2.3.

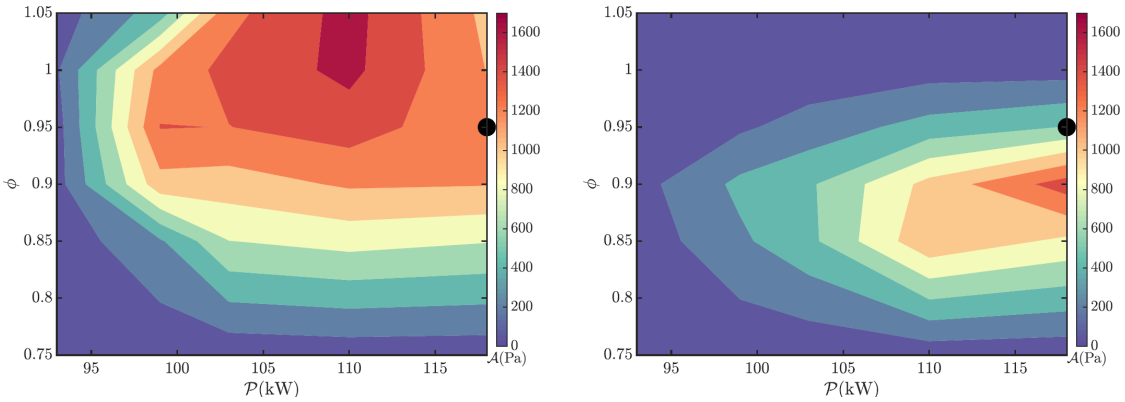

(a) N-heptane

(b) Dodecane

Figure 4.13: Maps of instability amplitude as a function of thermal power and equivalence ratio in the sixteen-injector annular combustor MICCA-Spray, with n-heptane or dodecane as a fuel. The black dot corresponds to the operating condition investigated in the present chapter. Reproduced from [141].

In this expression, $\xi = 1/\rho^a U_b^2 \overline{I}$. The sign of its time-averaged value, $\overline{\mathcal{R}a_2}$, corresponds to the sign of the Rayleigh source term. $P^c(t)$ and $I^c(t)$ are the coherent oscillation of $P^{'}(t)$ and $I^{'}(t)$ filtered around f_r, as expressed in the triple decomposition method (presented in Section 2.3.1.1).

The probability density functions (PDFs) of $\mathcal{R}a_2(t)$ for a same Π at the central flame location are shown at PAN and IAN for the two fuels in Figure 4.12. For all flame locations and fuels studied, $\mathcal{R}a_2(t)$ is mostly positive over time, resulting in a positive time-averaged value. This shows that these have the potential to drive an instability, which is consistent with the instability maps of MICCA-Spray obtained for n-heptane and dodecane (see Figure 4.13).

4.6.1 Effect of the flame position

4.6.1.1 Response to a same Π

We now compare the flame at PAN with that at IAN, both subjected to a same Π, *i.e.* a same acoustic pressure amplitude at the central flame location. For a given fuel, the thermoacoustic coupling is expected to be comparable since $\mathcal{F}_{P'}$ is similar at PAN and IAN (see Figure 4.8). As shown in Figure 4.12, the shape of the pdf of $\mathcal{R}a_2$, and the time-averaged value $\overline{\mathcal{R}a_2}$ for a given fuel are close at PAN and at IAN: $\overline{\mathcal{R}a_2} = 0.029$ at IAN and $\overline{\mathcal{R}a_2} = 0.036$ at PAN; for dodecane, $\overline{\mathcal{R}a_2} = 0.023$ at IAN and $\overline{\mathcal{R}a_2} = 0.028$ at PAN. This feature supports that thermoacoustic coupling is mainly linked to the acoustic pressure level at the flame location.

4.6.1.2 Response in a same acoustic field

It is also interesting to examine $\mathcal{R}a_2(t)$ for flames placed in a same acoustic field, characterised by different acoustic pressure amplitudes at PAN and at IAN. In such case, the acoustic pressure amplitude at IAN is about 55% of that at PAN (see Figure 4.1 (a)), and the OH^*-intensity of the flame oscillates with a greater amplitude at PAN than at IAN (see Figure 4.9 (a)). Consequently,

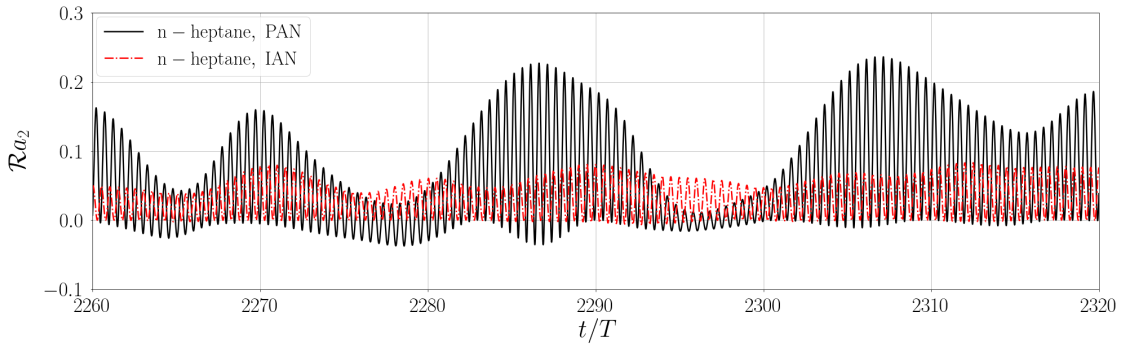

Figure 4.14: Excerpts of the instantaneous Rayleigh index signal, $\mathcal{R}a_2(t)$, with n-heptane for the same acoustic field characterised by $\Pi = 0.39$ at PAN and $\Pi = 0.21$ at IAN. $\mathcal{R}a_2(t)$ is plotted against the time reduced by the acoustic period T. These excerpts have been obtained during two separate measurements. The acoustic forcing frequency is 748 Hz at PAN and 762 Hz at IAN.

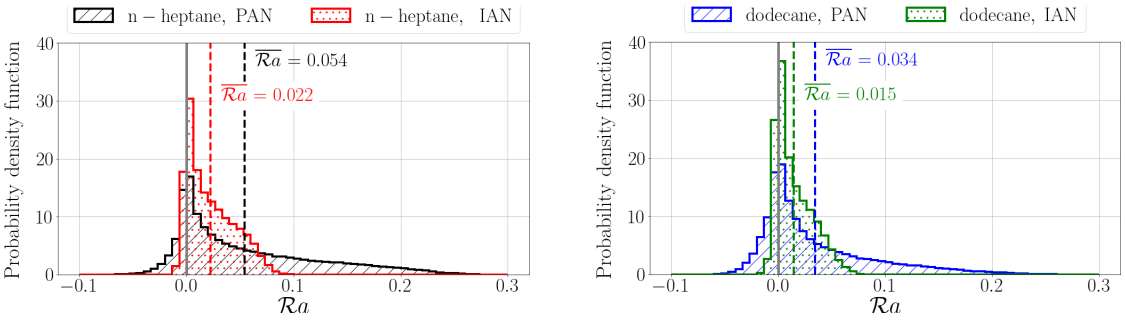

(a) N-heptane

(b) Dodecane

Figure 4.15: Probability density function of the coupling index $\mathcal{R}a_2(t)$ for the same acoustic field characterized by $\Pi = 0.39$ at PAN and $\Pi = 0.21$ at IAN. Vertical grey solid line: $\overline{\mathcal{R}a_2} = 0$.

$\mathcal{R}a_2(t)$ corresponds to the product between two quantities that oscillate with a higher amplitude at PAN than at IAN.

In Figure 4.14, instantaneous excerpts of $\mathcal{R}a_2(t)$ with n-heptane are shown when the central flame is placed at PAN or at IAN in the same acoustic field, characterised by $\Pi = 0.39$ at PAN and $\Pi = 0.21$ at IAN. As expected, $\mathcal{R}a_2(t)$ oscillates with a higher amplitude at PAN than at IAN: as a result, the values of $\mathcal{R}a_2(t)$ are more spread out at PAN.
In Figure 4.15, the distribution of $\mathcal{R}a_2(t)$ for a whole signal of length 3,000 acoustic cycles is illustrated for the two locations, in this case characterised by $\Pi = 0.39$ at PAN and $\Pi = 0.21$ at IAN The time-averaged value $\overline{\mathcal{R}a_2}$ is higher for the flame located at PAN, which results from stronger oscillation amplitudes of P^c and I^c. With n-heptane, $\overline{\mathcal{R}a_2}$ at PAN is 145% greater than at IAN. This value is directly linked to the increase of Π and $I^{rms}/\overline{I}$. Indeed, as shown with n-heptane in Figure 4.9 (a), $I^{rms}/\overline{I} \simeq 0.13$ for $\Pi = 0.21$ and $I^{rms}/\overline{I} \simeq 0.165$ for $\Pi = 0.39$. Thus, for $\Pi = 0.39$, corresponding to the flame at PAN, the product of Π and $I^{rms}/\overline{I}$ is about 135% higher than for $\Pi = 0.21$, corresponding to the flame at IAN. This is consistent with the value of 145% found above.

These results indicate that both flames, at PAN and at IAN, contribute to maintaining the coupling, although those at PAN contribute more strongly than those at IAN.

4.6.2 Effect of the fuel

With dodecane, $\overline{\mathcal{R}a_2}$ is a little lower than for n-heptane. This is consistent with $\mathcal{F}_{P'}$, as the lower gain with dodecane for a given Π indicates a weaker OH*-intensity oscillation. It is also interesting to note that the proportion of negative values is higher with dodecane than with n-heptane (28% vs. 19% for $\Pi = 0.39$, see Figure 4.15). Negative values of $\mathcal{R}a_2(t)$ are only found when instantaneous pressure and OH*-intensity are of opposite signs. This is quite scarce with n-heptane since the phase $\varphi_{P'-I'}$ of the $\mathcal{F}_{P'}$ is close to $0[2\pi]$, while with dodecane, the phase is about $0.2\pi[2\pi]$ (see Figure 4.8). Thus, the total time during which $\mathcal{R}a_2(t) < 0$ is increased with dodecane. Nevertheless, when integrated over time, the coupling remains positive with dodecane. This analysis therefore indicates that both n-heptane and dodecane flames are potentially able to drive an instability at f_r, agreeing with instabilities found in MICCA-Spray for the same operating points [53].

4.7 Conclusion

This chapter examines the response of swirling spray flames in a linear array of three swirling spray flames representing an unwrapped sector of the annular combustor MICCA-Spray. For that purpose, two flame describing functions (FDFs) are used, a first one using the acoustic pressure oscillation as a reference signal and a second one using the axial velocity oscillation measured at the injector exit as a reference signal. This analysis is performed for two fuels, n-heptane and dodecane at two locations in the standing transverse acoustic field, pressure antinode (PAN) and intensity antinode (IAN). The measurement location of the axial velocity is chosen such that its local oscillation represents the mass flow rate oscillation at the whole injector exit. It is shown that the axial velocity oscillation is highly sensitive to the radial location, making the accurate determination of the velocity-based FDF challenging. On the contrary, the acoustic pressure level is less sensitive to the radial location, ensuring the lower uncertainty of the pressure-based FDF. The two FDFs here present the same evolution when the acoustic ampliude increases, characterised by a decrease of the gain and a slight increase of the phase. This similarity is explained by the injector impedance, which shows a proportionality relationship between the oscillation amplitudes of the normalised axial velocity and acoustic pressure, in addition to a little change of the phase when the acoustic amplitude increases. The thermoacoustic coupling is then examined with an instability index based on the Rayleigh criterion. Information about the system stability derived from the pressure-based FDF is well recovered with the instability index, *i.e.*, a positive thermoacoustic coupling for all the studied conditions. Moreover, the higher coupling obtained with n-heptane with dodecane is consistent with instabilities observed in the annular combustor MICCA-Spray. Finally, this study shows the the coupling is driven by the flames around PAN, but flames located at IAN also contribute to the positive coupling, albeit to a lesser extent, as the flame intensity oscillation result from local acoustic pressure effects. These results show that the pressure-based FDF can be suitably used to characterise the evolution of

the flame response with the acoustic amplitude in this configuration, and that information about the combustor stability may be directly inferred from this FDF.

Appendices

4.A Are LDA and PDA equivalent to measure the fuel droplet velocity?

Fuel droplets of diameter lower than 5 µm can be considered as good indicators of the air flow velocity for the operating point $\mathbb{P}_{59}$, which is characterised by the use of the K modified set of swirler and outlet cup and $U_b = 38.9$ m/s (see Chapter 3). In this case, droplet-diameter filtering is necessary to examine the air flow behaviour as fuel droplets larger than 5 µm are present in non-negligible amounts. Therefore, it is needed to measure the fuel droplet velocity with PDA and to retain only the velocity of the smallest droplets during post-processing. In the case where the great majority of the droplets are small enough to represent the motion of the carrier flow, it could be unnecessary to filter droplets by their diameter. Diameter measurements would therefore not be required and the LDA technique could be used instead of PDA to obtain the velocity. As the atomisation process depends on the operating conditions[4], the need for droplet-diameter filtering may depend on the operating conditions. The comparison between velocity measurements with LDA and PDA is here performed by using the 716 set of swirler and outlet cup operated with a bulk velocity $U_b = 43.4$ m/s, with dodecane fuel injected with a mass flow rate of 0.165 g/s. This analysis is motivated by the fact that velocity fluctuations are measured for these operating conditions in order to obtain the FDF based on velocity fluctuations.

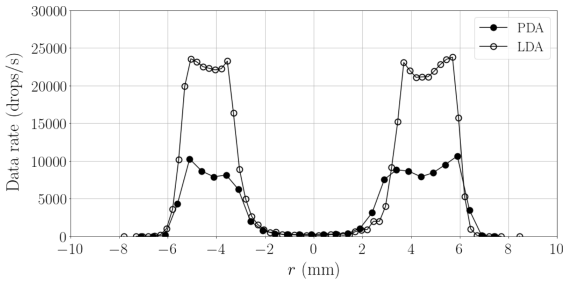

Figure 4.16: Radial profiles of data rate with LDA or PDA for operating condition $\mathbb{P}_{74d}$, $U_b = 43.4$ m/s, 716 set of swirler and outlet cup and dodecane as a fuel.

The mode of operation of the measurement system (LDA or PDA) strongly affects the data rate, which shows a threefold increase with LDA compared with PDA (see Figure 4.16). This increase is not entirely due to the spherical validation process specific to PDA, as the spherical validation rate lies between 67% and 100% depending on the radial location. Radial profiles of the mean value and the standard deviation of the axial, tangential and radial velocity components of the fuel droplets are measured with LDA and PDA and a comparison between these two techniques is shown in Figure 4.17 (a-c). The axial velocity measured with PDA is presented by including all the measured droplets and by considering only C_1 droplets (1 µm $\leq d \leq$ 5 µm). All the velocity profiles obtained with LDA and PDA by including all the measured droplets are superimposed, showing the data rate of PDA measurement is sufficient to ensure statistical convergence of the results at all radial locations. The axial velocity profiles are very similar to those obtained with

[4]In a general way, the higher the bulk velocity, the smaller the droplets, as shown in Chapter 6.

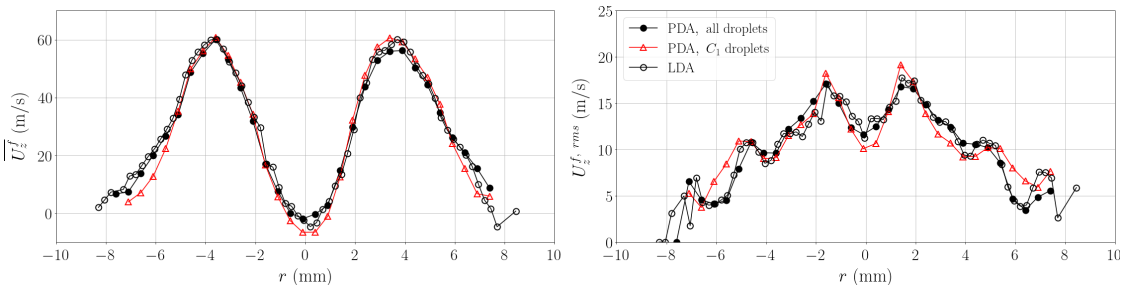

(a) Mean and rms axial velocity

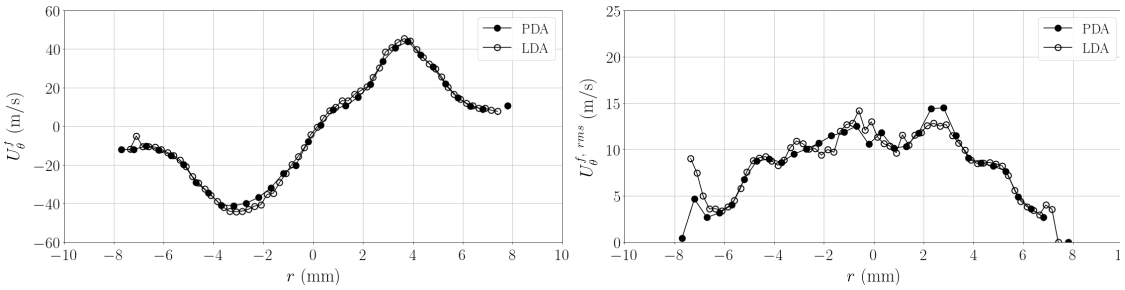

(b) Mean and rms tangential velocity

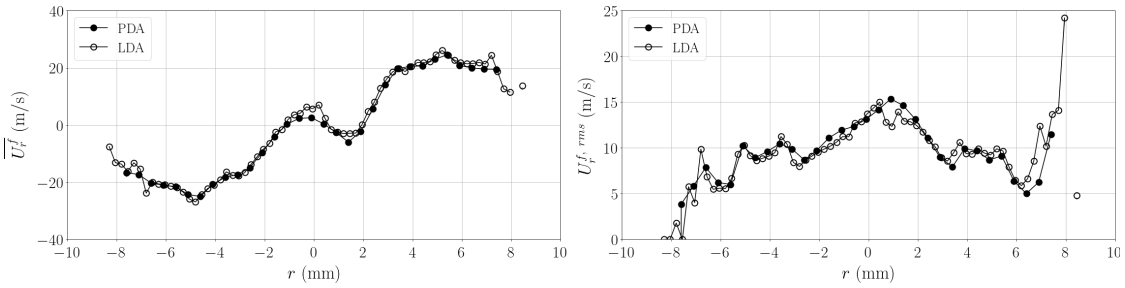

(c) Mean and rms radial velocity

Figure 4.17: Radial profiles of the mean value (left) and standard deviation (right) of the three velocity components: axial velocity U_z^f (top), tangential velocity U_θ^f (top), radial velocity U_r^f (top), for $\mathbb{P}_{74d}$, $U_b = 43.4$ m/s, the 716 set of swirler and outlet cup and dodecane as a fuel. Continued on next page.

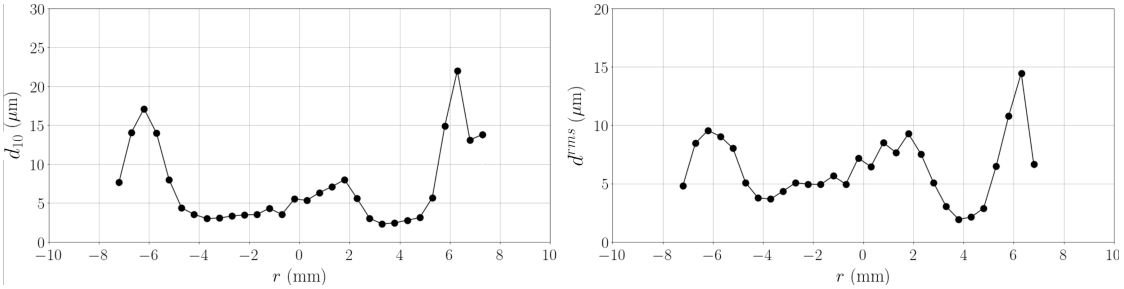

(d) Mean and rms diameter

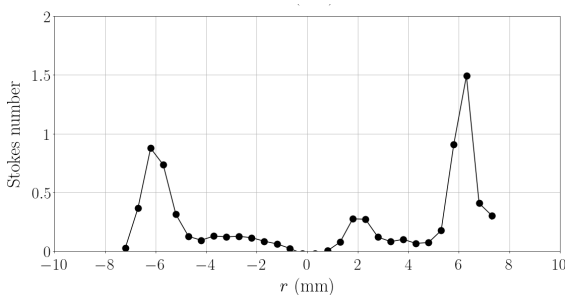

(e) Stokes number Stk

Figure 4.17: (continued) Radial profiles of the arithmetic mean droplet diameter $d_{10}(r)$ (top left), standard deviation of the droplet diameter $d^{rms}(r)$ (top right) and Stokes number (bottom), for $\mathbb{P}_{74d}$, $U_b = 43.4$ m/s, the 716 set of swirler and outlet cup and dodecane as a fuel.

C_1 droplets. One can notice that the negative velocities around the injector axis are lower when measured on C_1 droplets, but the difference between the profiles for all droplets is small. This indicates that droplet-diameter filtering of the PDA data is not necessary to obtain the air flow velocity. This is made possible by the very small diameter of the fuel droplets at almost all radial locations (see Figure 4.17 (d)), resulting in very low values of the Stokes number $\mathrm{Stk}(r)$ calculated on all droplets, which is significantly lower than 1 at most locations. Therefore, the fuel droplets are adequate seeding particles to examine the air flow motion in these conditions. As no droplet-diameter filtering is necessary for this specific case, PDA may be replaced by LDA to measure the air flow velocity here, which is a simpler to operate and gives higher data rates.

4.B Calculation of the flame describing function (FDF) with raw signals and with phase-averaged signals

In this manuscript, both the acoustic pressure signal and the radical intensity signal have a uniform sampling, *i.e.* the samples are acquired at a constant frequency, when the signals are acquired with the Labview software. On the contrary, the droplet velocity signals measured with PDA or LDA necessarily have a non-uniform sampling, which is intrinsic to the PDA/LDA method. It is nonetheless possible to reconstruct a uniformly-sampled velocity signal through the phase-averaging method (see Section 2.3.1.2). In this appendix, we investigate whether the FDF at a given frequency f_r calculated from phase-averaged signals is equal to that calculated from raw signals. The system is operated at condition $\mathbb{P}_{74}$ (see Table 2.1).

The FDF relates an input signal to an output signal in the frequency domain. It is a function of the excitation frequency, f_r, and of the excitation amplitude, here denoted Π, corresponding to the ratio of the rms amplitude of the acoustic pressure oscillation to the aerodynamic pressure. In this example, the input signal is the acoustic pressure oscillation reduced by the aerodynamic pressure, and the ouput signal is the OH^* or CH^* radical intensity oscillation reduced by its mean value. For the purpose of this study, two FDFs are defined, one based on the raw acoustic pressure and radical intensity signals, $\mathcal{F}_{P'}(f,\Pi)$, and the other based on the associated phase-averaged signals, $\mathcal{F}_{\langle P'\rangle}(f,\Pi)$:

$$\mathcal{F}_{P'}(f,\Pi) = \frac{\breve{I}\,/\overline{I}}{\breve{P}\,/\rho^a U_b^2} = \mathcal{G}_{P'}(f,\Pi)e^{i\varphi_{P'-I'}(f,\Pi)} \tag{4.4}$$

$$\mathcal{F}_{\langle P'\rangle}(f,\Pi) = \frac{\breve{\langle I\rangle}\,/\overline{\langle I\rangle}}{\breve{\langle P'\rangle}\,/\rho^a U_b^2} = \mathcal{G}_{\langle P'\rangle}(f,\Pi)e^{i\varphi_{\langle P'\rangle-\langle I'\rangle}(f,\Pi)} \tag{4.5}$$

$\breve{(\cdot)}$ and $\overline{(\cdot)}$ respectively indicate the complex amplitude and the mean value of $(\cdot)$, and ρ^a and U_b are the air density and the air flow bulk velocity at 20°C. These FDFs can be expressed by a gain $\mathcal{G}$, which quantifies the ratio of the oscillation amplitude of the output signal to that of the ipnut signal, and a phase φ, which corresponds to the phase delay between these two signals. The raw signals are constituted of 320,000 samples obtained with a sampling frequency equal to 100 times the acoustic forcing frequency f_r. Phase-averaging of the raw signals is performed by dividing the acoustic cycle in 20 bins of equal width, as explained in Section 2.3.1.2. Thus, phase-averaged signals are constituted of 20 samples, corresponding to a sampling frequency of $20f_r$. Phase-averaged signals are identified by $\langle(\cdot)\rangle$.

The gain and the phase, calculated from raw or phase-averaged signals for two series of measurements, are shown in Figure 4.18. A very good accordance is found between the two FDFs. Therefore, phase-averaging the raw input and output signals allows to calculate the FDF based on non-uniformly-sampled raw signals with the same tools as for uniformly-sampled signals.

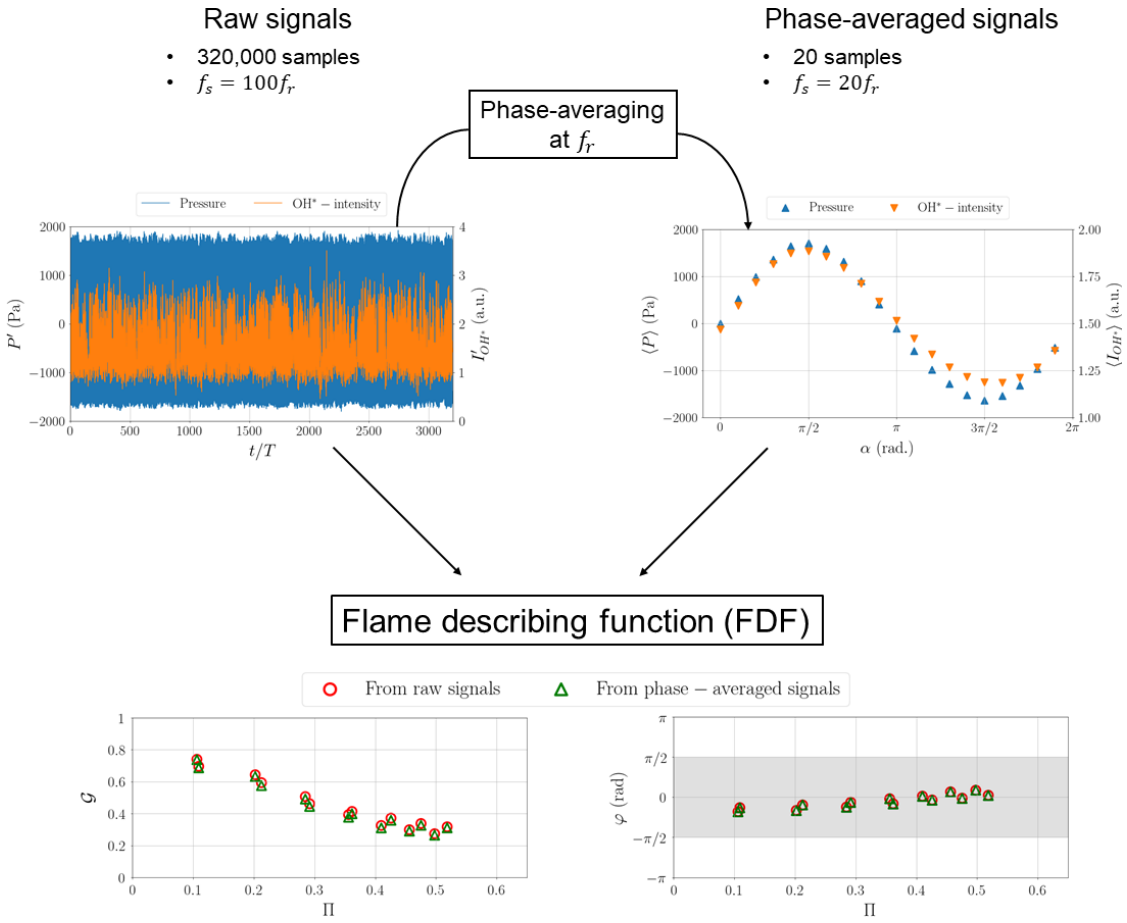

Figure 4.18: The flame describing function (FDF) is calculated (i) from raw signals of the acoustic pressure and of the CH^* or OH^* radical intensity and (ii) from phase-averaged signals at f_r of the same quantities, which are obtained from the raw signals. In this example, the FDF is obtained for two series of measurements, for which $f_r = 743$ Hz and $f_r = 748$ Hz respectively. f_s corresponds to the sampling frequency and T to the acoustic period.

4.C Sensitivity of the velocity-based flame describing function on the velocity measurement location

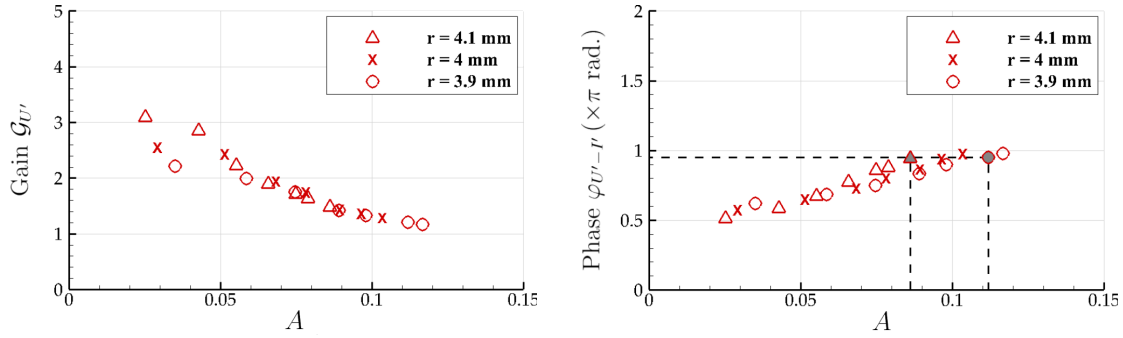

(a) Gain (b) Phase

Figure 4.19: Flame describing function $\mathcal{F}_{U'}(f_r, \Pi)$, obtained from the axial velocity oscillation measured at three different locations, $r = 3.9$ mm, $r = 4$ mm and $r = 4.1$ mm. The meaning of the grey-filled symbols is indicated in the text. The acoustic forcing frequency f_r is 748 Hz.

For a given vertical location z above the injector, the amplitude and the phase of the axial velocity oscillation are dependent on the radial location at which the axial velocity is measured (see Figures 4.6 and 4.7). Therefore, the gain and the phase of the velocity-based flame describing function (FDF) depends on the velocity measurement location.

In this appendix, a sensitivity analysis of the velocity-based FDF at the excitation frequency f_r, $\mathcal{F}_{U'}(f_r, A = \langle U_z^{a'} \rangle^{rms} / \overline{U_z^a})$, to the radial location of the velocity measurement is carried out. The velocity-based FDF is expressed by:

$$\mathcal{F}_{U'}(f_r, A) = \frac{\widetilde{\langle I \rangle} / \overline{I}}{\widetilde{\langle U_z^{a'} \rangle} / \overline{U_z^a}} = \mathcal{G}_{U'}(f_r, A) e^{i\varphi_{U'-I'}(f_r, A)} \tag{4.6}$$

$U_z^{a'}$ the air flow axial velocity oscillation and I the OH*-intensity from the central flame. $\overline{(\cdot)}$ indicates time-averages quantities, $\widetilde{(\cdot)}$ complex amplitudes at f_r and $\langle (\cdot) \rangle$ phase-averaged quantities at f_r. $\langle U_z^{a'} \rangle^{rms}$ is the amplitude of the air flow axial velocity oscillation at f_r. The FDF is also expressed in terms of a gain $\mathcal{G}_{U'}$ and a phase $\varphi_{U'-I'}$. The FDF is obtained by measuring the axial velocity at three radial locations: $r = 3.9$ mm, $r = 4$ mm and $r = 4.1$ mm, and for various acoustic amplitudes. Flame dynamics measured with the OH* radical, and acoustic pressure at the central flame location are acquired simultaneously with the fuel droplet axial velocity. The vertical measurement location is $z = 2.5$ mm above the injector exit. The system is operated in the conditions of the point $\mathbb{P}_{74}$ (see Table 2.1).

The velocity-based FDF plotted against $A = \langle U_z^{a'} \rangle^{rms} / \overline{U_z^a}$ is shown in Figure 4.19. For the lowest acoustic amplitudes ($A < 0.05$), the gain is sensitive to the velocity measurement location. For higher values of A, a 0.2 mm-displacement around $r = 4$ mm does not affect the gain. The phase of the FDF grows linearly with A. It is slightly affected by the measurement location, particularly for A in the range $0.06 - 0.09$: for $A \simeq 0.09$, a difference of 0.13π is found between

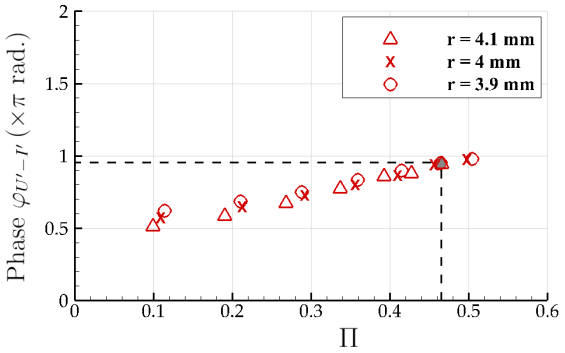

Figure 4.20: Phase $\varphi_{U'-I'}$ of the velocity-based flame describing function plotted against Π. The acoustic pressure is measured at the central flame location simultaneously with the axial velocity measurement at $r = 3.9$ mm, $r = 4$ mm and $r = 4.1$ mm. The meaning of the grey-filled symbols is indicated in the text. The acoustic forcing frequency f_r is 748 Hz.

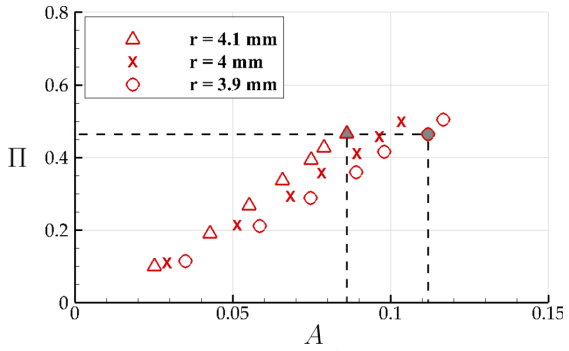

Figure 4.21: Relationship between $\langle U_z^{a'} \rangle^{rms} / \overline{U_z^a}$ measured at $r = 3.9$ mm, $r = 4$ mm and $r = 4.1$ mm, and Π. The meaning of the grey-filled symbols is indicated in the text. The acoustic forcing frequency f_r is 748 Hz.

the phase obtained with the axial velocity measured at $r = 3.9$ mm and the phase obtained with the axial velocity measured at $r = 4.1$ mm. It is worth noting that $\varphi_{U'-I'}$ is equal to 0.95π for both ($r = 4.1$ mm, $A \simeq 0.085$) and ($r = 3.9$ mm, $A \simeq 0.11$), as indicated by the symbols filled with greys.

$\varphi_{U'-I'}$ is now plotted against the reduced acoustic pressure Π[5], which is measured at the central flame location simultaneously with the axial velocity (see Figure 4.21). The grey-filled symbols correspond to the same data as in Figure 4.19 (right column). The same value of $\varphi_{U'-I'}$ abovementioned now corresponds to the same Π. This indicates that the relationship between A and Π depends on the velocity measurement location, which is confirmed by Figure 4.21. For a given measurement series, the relationship between these two quantities is linear. For the series corresponding to the velocity measurement at $z = 4.1$ mm, $A \simeq 0.085$ corresponds to $\Pi = 0.46$. For the series corresponding to the velocity measurement at $z = 3.9$ mm, $A \simeq 0.112$ corresponds to $\Pi = 0.46$. Therefore, for a same value of Π, A is increased by 30% when the axial velocity is measured at $r = 3.9$ mm compared to $r = 4.1$ mm.

[5] $\Pi = P^{rms}/\rho^a U_b^2$, where P^{rms} is the rms amplitude of the acoustic pressure oscillation and $\rho^a U_b^2$ is the aerodynamic pressure calculated at the injector exit at 20°C.

Part II

Response of the energy system at PAN

Chapter 5

Reference flame response and basic mechanisms

Contents

This chapter investigates the dynamics of the central flame when it is placed at a pressure antinode of the forced standing transverse acoustic field. Both CH^* and OH^* radicals describe the evolution of the flame dynamics with the acoustic amplitude, characterised by a linear response at low acoustic amplitudes, followed by a non-linear transition leading to the saturation. Therefore, the two radicals capture the physical mechanisms driving the flame emission intensity oscillation. The analysis of the sign of a global instability index, based on the classical Rayleigh criterion, indicates that the flames have the potential to drive self-excited instabilities. The mechanisms at the origin of the flame response are then explored. The convective axial propagation of a flame intensity wave and the simultaneous evolution of its amplitude result in the

strong response of the middle region of the flame, in which a constructive interference between combustion and acoustic pressure is found. This indicates that the middle flame region drives the combustion-acoustics coupling. The axial velocity modulation at the injector exit, induced by the acoustic pressure oscillation in the chamber, leads to the swirl number oscillation, the occurrence of a periodic disruption of the CRZ and the formation of a coherent vortex, which grows during its convection. These features lead to the modulation of the flame base angle and flame standoff distance, as well as the modulation of the spray base angle. A periodic droplet number wave is also generated at the injector exit, such that a high droplet amount is injected simultaneously with the coherent vortex, resulting in the engulfment of the reactants followed by an effective air-fuel mixing. At the beginning of the flame middle region, the high droplet amount is correlated to the maximum of flame intensity oscillation, showing the link between the droplet number wave generated at the injector exit and the flame intensity wave. This shows that the coupling between the fuel spray and the acoustic pressure oscillation in the chamber is a potential mechanism of combustion instabilities. Finally, some insights are given to introduce the saturation of the flame emission intensity oscillation, which are highlighted at high acoustic amplitudes. They show that the occasional destabilisation of the flame anchoring point participates in the saturation. A detailed analysis of the saturation phenomenon is given in Chapter 7.

5.1 Introduction

In low-order models, the flame response to acoustics is represented by the flame describing function (FDF), which links the input acoustic perturbation to the flame HRR oscillation. In order to enhance the prediction of thermoacoustic instabilities in industrial combustors, the knowledge of the flame response mechanisms in configurations having similar characteristics to industrial combustors is required, such as swirling flows, spray combustion, and multiple injectors. Such characteristics are reproduced at laboratory scale in TACC-Spray (see Section 2.1). The main mechanisms through which combustion is coupled with acoustics are reviewed in Section 1.4.

In this chapter, the flame response is examined for the operating point $\mathbb{P}_{59}$, which was investigated without acoustic forcing in Chapter 3. The operating conditions, described in Table 2.1, are briefly reminded here. The system is operated with n-heptane as a fuel, a flame thermal power of 5.9 kW per flame and an equivalence ratio $\phi = 0.85$. This corresponds to a fuel mass flow rate of 0.133 g/s and an air mass flow rate of 2.35 g/s. The bulk velocity, calculated by diving the volumetric air flow rate by the area of the injector exit, is $U_b = 38.9$ m/s. The K modified swirler is used here, giving a swirl number of 0.58 without acoustic forcing.

This chapter starts with the description of the global flame response in Section 5.2. The reliability of CH^* and OH^* radicals is then discussed. In Section 5.3, the mechanisms leading to the flame response are explored. To this end, the spatially-resolved flame response is investigated with high-speed flame emission images. Then, the behaviour of the air flow is examined by using PDA measurements and high-speed tomography images, allowing to obtain spatially-resolved measurements. The same diagnostics are used to analyse the response of the fuel spray to acoustics, which is then correlated with the spatially-resolved flame response. Finally, in Section 5.4, some insights are given to introduce the saturation of the flame response, which is

further developed in Chapter 7.

5.2 Global characteristics of the flame response

Combustion feeds acoustics as the unsteady HRR produces pressure waves that travel across the medium. In some cases, these pressure waves in turn impact the ingoing flow and thereafter combustion, giving rise to a self-sustained instability under certain conditions. In this section, the characteristics of the flame response are examined globally, *i.e.* spatially-averaged, using the PM setup described in Subsection 2.2.3.1. The global flame response is first described. Then, the relevance of measuring the flame intensity with CH^* and OH^* radicals in the present configuration is dicussed. Finally, the thermoacoustic coupling is evaluated by using an instability index based on the Rayleigh criterion.

5.2.1 Flame response to acoustics

Figure 5.1 presents the responses of CH^* and OH^* emission signals of the central flame, as well as zoomed-in views on signal excerpts and the power spectral density (PSD) of the whole signals for $\Pi = P^{rms}/\rho^a U_b^2 = 0.33$. Both I_{CH^*} and I_{OH^*} signals clearly oscillate at the excitation frequency f_r. It is not a natural frequency of the reacting flow (see Figure 3.11), hence, this oscillation at f_r can be unambiguously attributed to the acoustic forcing. The presence of oscillations at $2f_r$ is also visible in the PSDs, but their amplitude is much weaker than that at f_r. It should be noted that a peak at $2f_r$ is also observed in the acoustic pressure spectrum, but it is negligible compared to the peak at f_r . Therefore, it is highly probable that the very weak flame response at $2f_r$ results from the acoustic pressure oscillation at the same frequency, and not from mechanisms leading to a frequency bifurcation. The radical-intensity response to acoustics is estimated by integrating the peak of the PSDs in a frequency band around f_r, giving the rms oscillation amplitude, I^{rms}.

The evolution of $I^{rms}(\Pi)$ with the reduced acoustic pressure amplitude Π is presented in Fig. 5.2, together with the mean intensity reduced by its value without forcing, $\overline{I}(\Pi)/\overline{I}^0$, and the reduced rms oscillation amplitude, $I^{rms}/\overline{I}(\Pi)$. All these quantities are obtained with CH^* or OH^* radicals. When Π increases, $\overline{I}(\Pi)$ decreases very little for low Π, while the decrease is a little more discernible at higher acoustic amplitudes. $I^{rms}(\Pi)$ increases almost linearly up to a value of $\Pi \simeq 0.35$, but it shows a lesser increase at higher amplitude, indicating the presence of nonlinear processes inhibiting the flame response. As a result, the ratio $I^{rms}/\overline{I}(\Pi)$ follows a linear growth up to $\Pi = 0.35$ which is dominated by the increase of $I^{rms}(\Pi)$, while for higher acoustic amplitudes, its growth, less strong than at low Π, results from the decrease of $\overline{I}(\Pi)$ and the little increase of $I^{rms}(\Pi)$. Therefore, $\Pi = 0.35$ marks the threshold between linear and non-linear flame responses. This threshold is well detected by CH^* and OH^* radicals, indicating that both of them capture the physical mechanisms of flame response. The values of $I^{rms}/\overline{I}(\Pi)$ are about 40% higher with CH^* than with OH^*, which is consistent with observations on another swirling spray flame [166].

The relationship between acoustic pressure oscillation and flame intensity oscillation is also

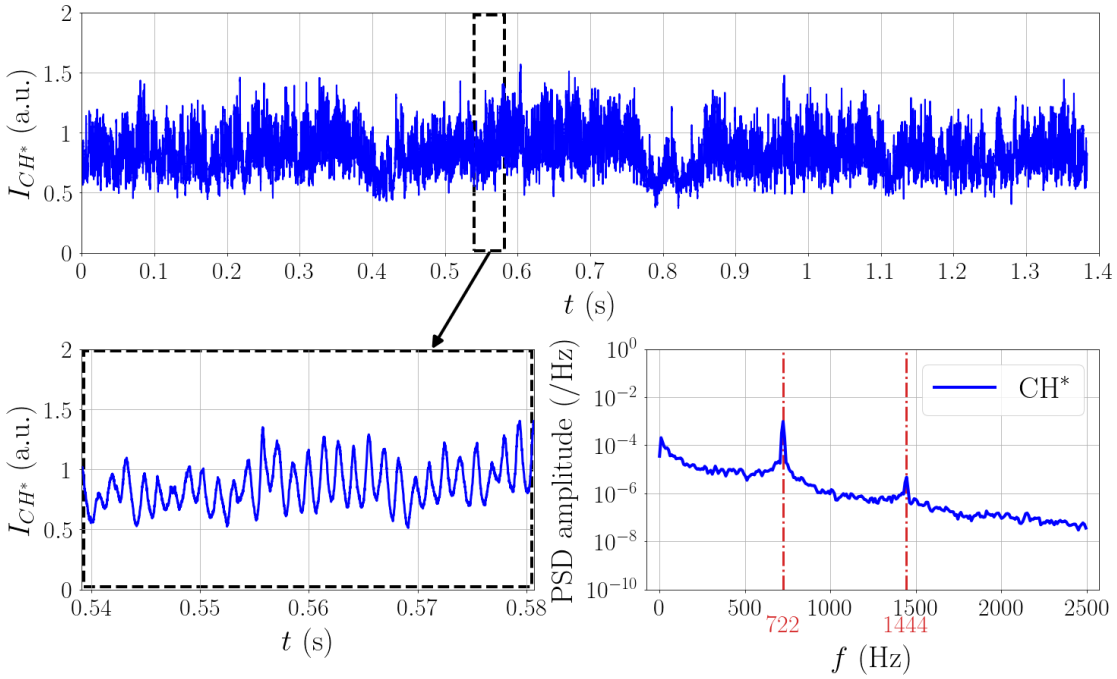

(a) CH*, $f_r = 722$ Hz, $\Pi = 0.33$

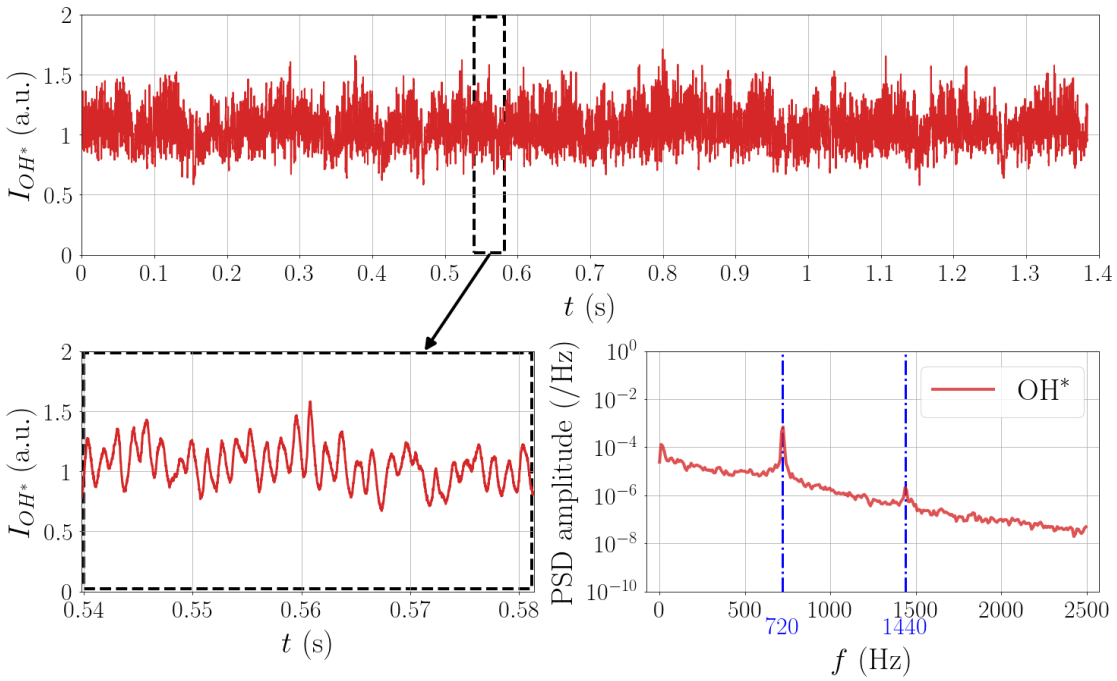

(b) OH*, $f_r = 720$ Hz, $\Pi = 0.33$

Figure 5.1: Examples of CH* and OH* emission signal of the central flame with acoustic forcing. For both (a) and (b), the top row shows a whole raw signal and the bottom row shows a zoomed-in view of the raw signal on the left and the power spectral density of the whole raw signal on the right.

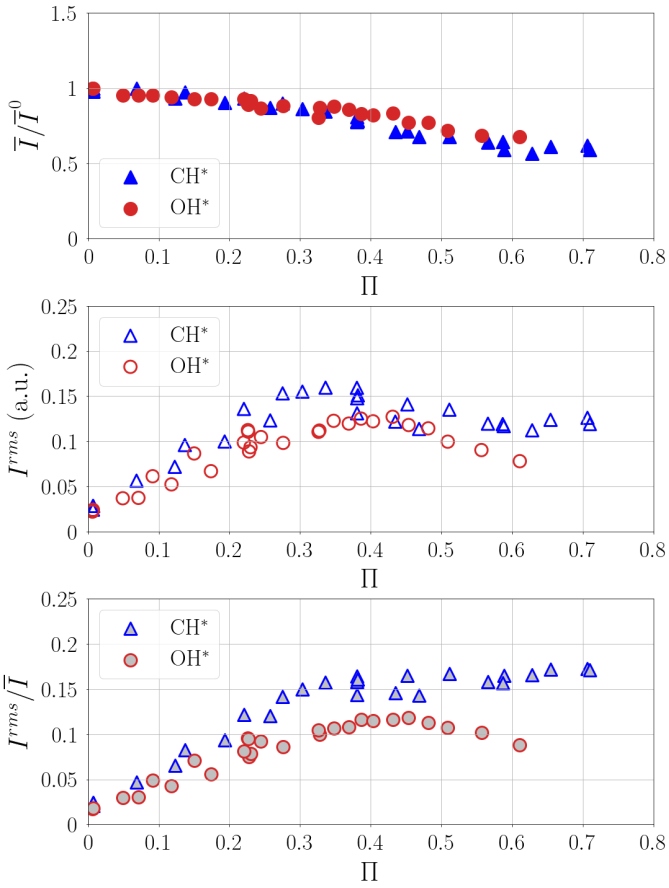

Figure 5.2: Response of the flame CH* and OH* intensities as a function of the reduced acoustic amplitude Π. Top: mean intensity, $\overline{I}/\overline{I}^0$; middle: rms oscillation amplitude, I^{rms}; bottom: reduced rms oscillation amplitude: $I^{rms}/\overline{I}$. The acoustic frequency f_r here lies in the range $714 - 722$ Hz.

evaluated with the pressure-based FDF, $\mathcal{F}_{P'}(f_r, \Pi)$:

$$\mathcal{F}_{P'}(f_r, \Pi) = \frac{\breve{I}/\overline{I}}{\breve{P}/\rho^a U_b^2} = \mathcal{G}_{P'}(f_r, \Pi) e^{i\varphi_{P'}(f_r, \Pi)} \tag{5.1}$$

In the following of this chapter, $\mathcal{F}_{P'}$, $\mathcal{G}_{P'}$ and $\varphi_{P'}$ are respectively called $\mathcal{F}$, $\mathcal{G}$ and φ for the sake of clarity. $\breve{I}$ and $\breve{P}$ are the complex amplitudes of the flame chemiluminescence emission from CH^* or OH^* radicals and acoustic pressure signals respectively, $\mathcal{G}$ the gain of the FDF, which indicates the efficiency of the coupling between combustion and acoustics, and φ the phase of the FDF, corresponding to the phase shift between pressure and radical emission signals. As shown in Chapter 4, this FDF based on downstream transverse acoustic pressure oscillations is equivalent to the FDF based on axial velocity oscillations measured at the burner exit for the present energy system.

The FDFs obtained with CH^* or OH^* radicals are presented in Fig. 5.3. $\mathcal{F}(f_r, \Pi)$ is estimated for a set of acoustic amplitudes at one particular acoustic frequency f_r correponding to the resonance frequency of the chamber. The value of f_r is selected to investigate the mechanisms leading to self-excited instabilities in MICCA-Spray, which occur at frequencies in the range 700-800 Hz [101]. The gain decreases as the reduced acoustic amplitude increases with both CH^* and OH^*, indicating the presence of non-linearities even for $\Pi \leq 0.35$. The phase of the FDF is identical with both radicals. It evolves slightly with Π, indicating a little modification of the time interval between pressure and radical intensity oscillations. But, at all acoustic amplitudes studied here, it remains in the theoretical instability region based on the Rayleigh criterion, represented by the grey band in Fig. 5.3. This indicates the positive coupling between combustion and acoustics in all the amplitude range here, which is further investigated below.

These results show that both CH^* and OH^* allow to capture the main characteristics of the flame response, *i.e.* (i) the linear growth of the flame response up to $\Pi \simeq 0.35$ and its saturation at higher levels; (ii) the positive coupling between combustion and acoustics at all acoustic amplitudes studied here. The only difference between these two radicals concerns the amplitude of $I^{rms}/\overline{I}$, which is a about 40% higher with CH^*. It is now worth discussing the relevance of these radicals to estimate the HRR.

5.2.2 Measurement of the flame response with CH^* or OH^* radicals

The measurement of the HRR is important to quantify the flame response to the acoustic perturbation. However, it cannot be directly measured in experimental flames. Therefore, several studies focused on methods to determine the HRR in flames, first without acoustic forcing. In premixed flames, the HRR is often obtained by measuring the chemiluminescence emission of chemical radicals, such as CH^*, OH^* or CO_2^* [146,148,167]. The basic idea is to focus on chemical radicals that are confined to the reaction zone [85]. Usually, the HRR scales linearly with the chemiluminescence emission intensity of a well-chosen radical. But, an issue concerns the HRR estimation in non-premixed flames, which emerges as the chemiluminescence intensity not only depends on the HRR but also on the local equivalence ratio. Other dependences can also appear, such as that of the CH^*-intensity to the soot proportion [166], which is not considered

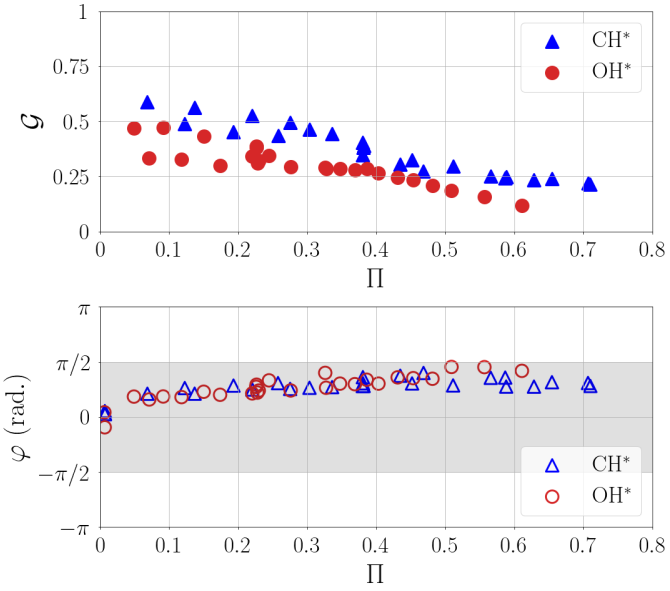

Figure 5.3: Flame describing function $\mathcal{F}$ as a function of reduced acoustic pressure amplitude, Π. The gain is shown on top, the phase on bottom. The grey band indicates the region of potential instability predicted by the Rayleigh criterion. The acoustic frequency f_r here lies in the range $714 - 722$ Hz.

in this manuscript as the flames investigated do not present soot emission. Works have been carried out on spray flames to assess the validity of CH* or OH* radicals for estimating HRR in steady conditions [166, 168, 169]. In particular, the works from Muruganandam et al. [168] on a swirl-stabilised n-heptane/air flame show that CH* is a good indicator of steady-state HRR when the equivalence ratio ϕ is comprised in the range 0.75 - 0.9, while OH* is valid in a wider range ($0.6 < \phi < 1$). Other authors express the HRR of spray flames as a function including the chemiluminescence emission intensities of several radicals, *e.g.*, CH*, OH* and CO_2^* [150, 151]. Recent studies were also performed on a injection system very close to that used in the present study by the EM2C team [53, 113, 169]. Using a quasi-steady approach [169], they first concluded that the relationship between CH* (or OH*) intensity and HRR featured a slight deviation from linearity, which was not larger for a liquid n-heptane spray flame than for a premixed propane-air flame; and secondly that OH* was a better marker of HRR compared to CH* due to a lesser deviation from linearity.

In the presence of acoustic forcing, chemiluminescence is widely used to estimate the HRR fluctuation in laminar [118, 126] or turbulent premixed flames without swirl [67, 85, 86] or with swirl [68, 106]. In technically-premixed flames, the potential presence of equivalence ratio fluctuations complicates the matter, as the chemiluminescence emission intensity depends on both the HRR and the equivalence ratio. As a consequence, no general trend can be obtained for this type of flames, which implies the need to study the presence of equivalence ratio fluctuations on a case-by-case basis.

One method to measure the equivalence ratio in steady flames is based on the ratio of chemi-

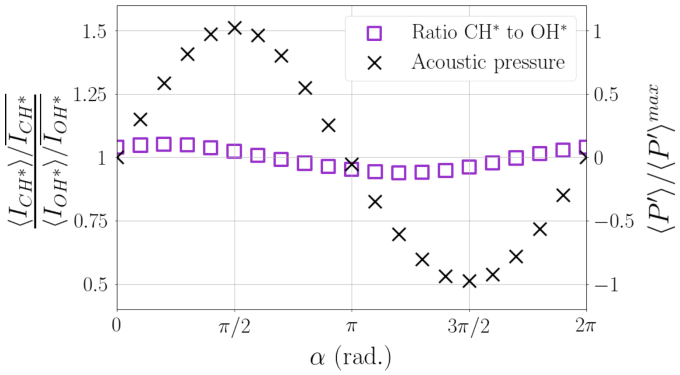

Figure 5.4: Ratio between normalized CH* and OH* oscillations of the central flame at PAN for $\Pi = 0.26$.

luminescence emission intensities of two species, *e.g.*, OH*/CH* in a premixed counterflow flame [167] but also in a swirl-stabilised n-heptane/air flame [168], or CO_2^*/CH* in a technically premixed swirl flame [170]. Docquier et al. [171] used these two ratios to build an optical sensor to control the equivalence ratio of a lean premixed flame. In their configuration, the intensity ratio CO_2^*/CH* monotonically decreases with the equivalence ratio but it has a low dynamical range. Conversely, OH*/CH* has a larger dynamical range but a non-monotonic behaviour: for very lean mixtures ($0.5 \leq \phi < 0.75$), it increases with the equivalence ratio while for $0.75 \leq \phi$, it decreases with it. With acoustic forcing, the EM2C team measured equivalence ratio inhomogeneities in space and time by using phase-averaged CH* and OH* images [53] by means of the single-injector SICCA-Spray setup. It was shown that the equivalence ratio oscillations are mostly lower than 10% of the mean equivalence ratio in the flame zone. They concluded that these fluctuations are weak enough to consider that OH* can be reasonably used to measure the HRR fluctuations in their specific configuration, which has specificities close to our configuration concerning the injectors. They attributed the weakness of the spatial and temporal equivalence ratio inhomogeneities with acoustic forcing to the impact of the injected fuel spray on the inner conical injector wall induced by the recessed position of the atomiser inside the air duct (see Figure 2.3). This configuration led to the formation of a secondary liquid fuel film on the wall, which is then atomised by the swirling air flow, as highlighted by the numerical work of Lo Schiavo *et al.* [140] on the same injector.

In the present work, equivalence ratio fluctuations are examined by using the ratio of the phase-averaged oscillation of the global CH*-intensity, $\langle I_{CH^*} \rangle$, to that of the global OH*-intensity, $\langle I_{OH^*} \rangle$, each reduced by their cycle-averaged value, $\overline{I_{CH^*}}$ and $\overline{I_{CH^*}}$ respectively. Results are presented in Figure 5.4 for $\Pi = 0.26$. The quantity $(\langle I_{CH^*} \rangle / \overline{I_{CH^*}}) / (\langle I_{OH^*} \rangle / \overline{I_{OH^*}})$ oscillates slightly during the acoustic cycle: it oscillates with an amplitude of about 5%, suggesting that equivalence ratio fluctuations are weak. Therefore, fluctuations of the CH* and OH*-intensities are assumed to give a reasonable estimate of the HRR fluctuations in this configuration.

5.2.3 Thermoacoustic coupling

In acoustically compact flames, the Rayleigh source term $\mathscr{S}_{ac}$ is proportional to the time integral of $P^{'}\dot{Q}^{'}$, where $P^{'}$ is the acoustic pressure oscillation at the flame location and $\dot{Q}^{'}$ is the global HRR oscillation of the flame (see Section 1.2.3). In thermoacoustically self-unstable systems, $\mathscr{S}_{ac}$ exceeds the sum of the acoustic flux divergence and the damping term, fulfilling the extended Rayleigh criterion characteristic of the occurrence of instabilities (see Section 1.2.2). Since the acoustic flux divergence and the damping term are in practice difficult to measure, it is challenging to determine whether the extended Rayleigh criterion is fulfilled or not. Nevertheless, some deductions can be made from the classical Rayleigh criterion, *i.e.* by knowing the sign of $\mathscr{S}_{ac}$:

- a negative Rayleigh source term indicates that combustion is necessarily stable;
- a positive Rayleigh source term suggests that the system could lead to instabilities.

Nothing more can be said as long as the acoustic flux divergence and damping terms are unknown. For the central flame, the sign of $\mathscr{S}_{ac}$ is estimated under the hypothesis of compact flame (see Equation (1.25)) through the instability index $\mathcal{R}a_1(t) = \xi P^{'}(t)I^{'}(t)dt$, where $I^{'}(t)$ is the global CH^* or OH^* emission intensity from the flame and $\xi = 1/(\rho^a U_b^2 \overline{I})$.

In the following, our first goal is to determine the sign of the Rayleigh source term, which depends on the phase of the FDF but not on the gain. $\mathcal{R}a_1(t)$ is expected to be positive when the phase is located inside the instability zone, identified by the grey band in Figure 5.3, and negative outside. As shown on the same figure, the phase is identical with CH^* or OH^*; therefore, the sign of $\mathcal{R}a_1(t)$ is the same with both radicals. This shows that both of them are reliable to indicate whether the system is necessarily stable or potentially unstable. Our second goal is to assess how the instability index should be defined.

5.2.3.1 Decomposition of flame intensity signals

The decomposition method presented in Section 2.3.1.1 is here applied to the radical intensity signals $I(t)$, giving:

$$I(t) = \overline{I} + I^{'}(t) \tag{5.2}$$

$$= \overline{I} + I^{c}(t) + I^{s}(t) \tag{5.3}$$

As observed in Figure 5.5, the CH^* intensity oscillation does not have a constant amplitude over time. For instance, the signal oscillates weakly for $t > 0.328$ s (see Figure 5.5 (a)) while the oscillation at f_r is well established for $0.014 \text{ s} \leq t \leq 0.027$ s (see Figure 5.5 (b)). So, the coherent oscillation can be modelled as $I^c(t) = A^c(\lfloor t/T \rfloor)\sin(\omega t + \varphi^c)$. In this expression, $\omega = 2\pi/T$ is the angular frequency, φ^c the phase constant and $A^c(\lfloor t/T \rfloor)$ an amplitude specific to each acoustic cycle. $\lfloor t/T \rfloor$ is the integer part of t/T and T is the acoustic period.

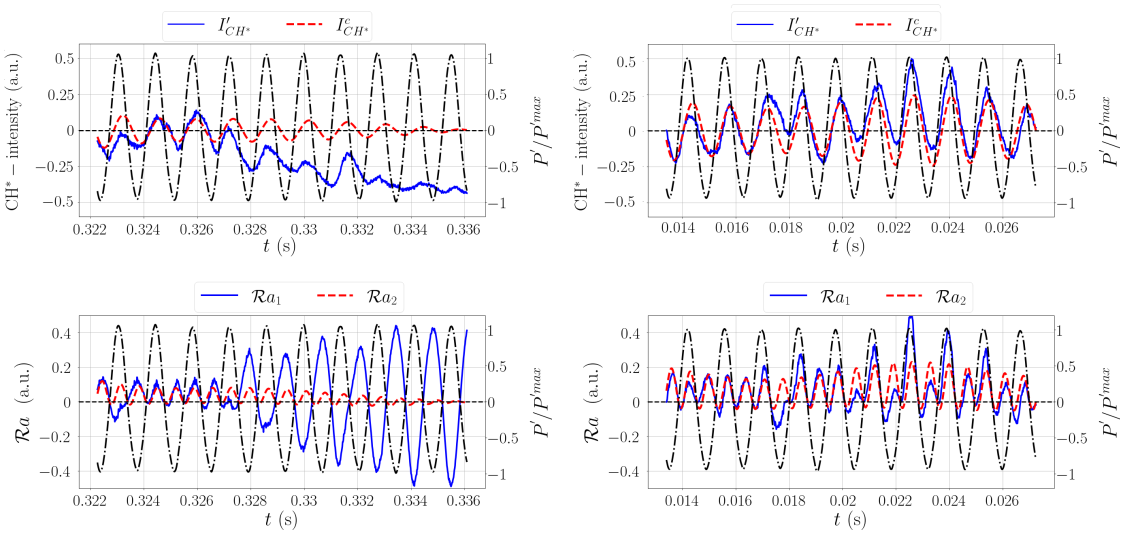

(a) Weak instantaneous flame response and notable decrease of I'_{CH^*}

(b) Well-established instantaneous flame response

Figure 5.5: Excerpts of instantaneous fluctuating CH*-signal ($I'_{CH^*}(t)$), coherent CH*-signal ($I^c_{CH^*}(t)$) and simultaneous reduced acoustic pressure at the flame location during two time intervals (top row); associated instantaneous instability indices $\mathcal{R}a_1(t) = \xi P' I'(t)$ and $\mathcal{R}a_2(t) = \xi P^c I^c(t)$, and simultaneous reduced acoustic pressure at the flame location (bottom row). Left: weak CH*-intensity oscillation followed by a notable decrease of the CH* signal; right: well-established instantaneous CH*-intensity oscillation . $I^c_{CH^*}(t)$ is obtained by filtering $I'_{CH^*}(t)$ at $f_r \pm 100$ Hz. The reduced acoustic amplitude is $\Pi = 0.59$.

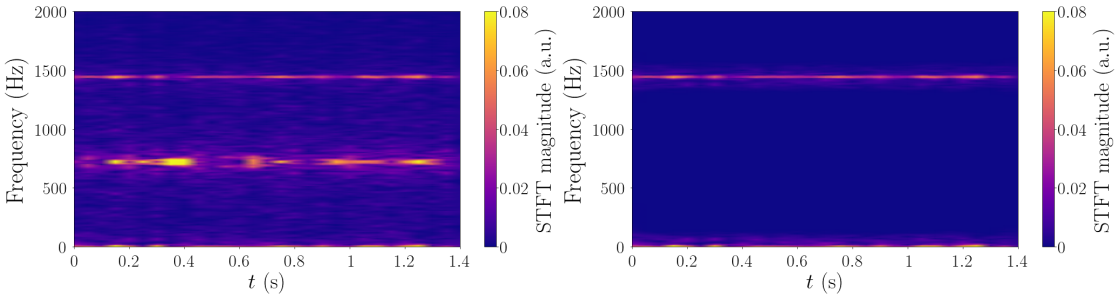

(a) STFT of the raw instability index, $\mathcal{R}a_1(t)$

(b) STFT of the filtered instability index, $\mathcal{R}a_2(t)$

Figure 5.6: Short-time Fourier transform of the instability indices for $\Pi = 0.59$, $f_r = 722$ Hz. The flame intensity oscillation is measured through CH* radical. $\mathcal{R}a_1(t)$ is calculated from the fluctuations of the acoustic pressure and CH*-intensity signals and $\mathcal{R}a_2(t)$ is obtained by filtering both the acoustic pressure and the CH*-intensity signals at f_r.

5.2.3.2 Global instability index based on the Rayleigh criterion

The abovementioned decomposition methods of radical intensity signals raises two possibilities to calculate the instability index. The first one is based on the fluctuating signals containing both coherent and stochastic components, which gives $\mathcal{R}a_1(t)$, while the second method is based solely on the coherent oscillations at f_r, giving $\mathcal{R}a_2(t) = \xi P^c(t) I^c(t)$. For the pressure signal, both decompositions yield the same results, as the stochastic fluctuation and the harmonics of f_r are negligible compared to the coherent oscillation at f_r. On the contrary, the flame intensity signals $I^{'}(t)$ and $I^c(t)$ can be significantly different, as illustrated in Figure 5.5. $I^{'}(t)$ and $I^c(t)$ are obtained from Equation (5.3), in which the mean intensity $\overline{I}$ is calculated on a whole signal of duration 1,000 acoustic cycles, corresponding to 1.39 s.
In Figure 5.5 (b), $I^{'}(t)$ (solid blue curve) oscillates around 0, indicating that $I(t)$ is modulated around $\overline{I}$. This oscillation, clearly at frequency f_r, is such that the phase shift between $P^{'}(t)$ and $I^{'}(t)$ is between 0 and $\pi/2$. As a result, $\mathcal{R}a_1(t)$ (bottom) is mostly positive. In addition, it oscillates at a frequency $2f_r$, as expected for the product of two signals oscillating at f_r. But, $I(t)$ can also suffer sudden decreases, such that it becomes less than the average value calculated over the entire length of the signal, $\overline{I}$, during several acoustic cycles. This case is illustrated in Figure 5.5 (a). For $t > 0.328$ s, $I(t)$ is lower than $\overline{I}$, hence, $I^{'}(t)$ is negative during several acoustic cycles. In addition, its fluctuation at f_r is barely discernible. Simultaneously, $\mathcal{R}a_1(t)$ starts to oscillate with a large amplitude at frequency f_r.
We now analyse the oscillation of $I^c(t) = I^{'}(t) - I^s(t)$. In Figure 5.5 (b), $I^c(t)$ (red dash curve) oscillates similarly to $I^{'}(t)$. This indicates that $I^s(t)$ is weak. Therefore, $\mathcal{R}a_2(t)$ is similar to $\mathcal{R}a_1(t)$: it fluctuates at $2f_r$ and its values are mostly positive. In Figure 5.5 (a), this is different: $I^c(t)$ oscillates weakly and, for $t > 0.328$ s, it becomes significantly different from $I^{'}(t)$, indicating that the latter signal is polluted by the stochastic noise. $\mathcal{R}a_2(t)$ oscillates at $2f_r$, but very weakly due to small amplitude of $I^c(t)$. Nevertheless, it does not show the significant fluctuation at f_r undergone by $\mathcal{R}a_1(t)$.

The time evolution of the frequency content of $\mathcal{R}a_1(t)$ and $\mathcal{R}a_2(t)$ is further explored by per-

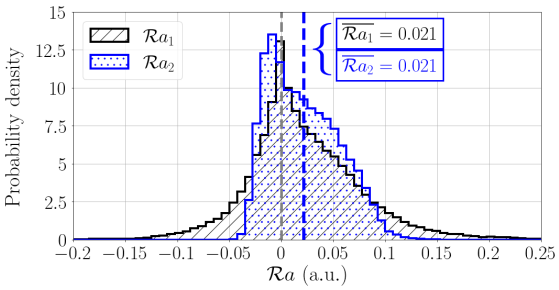

(a) Probability density functions of $\mathcal{R}a_1$ and $\mathcal{R}a_2$ for $\Pi = 0.33$. I is measured with CH*. The grey dash line indicates $\mathcal{R}a_1 = \mathcal{R}a_2 = 0$.

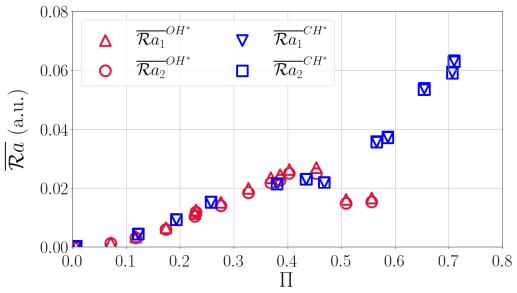

(b) Time-averaged values of $\mathcal{R}a_1$ and $\mathcal{R}a_2$ for I measured with CH* and OH*.

Figure 5.7: Probability density function of the instability indices $\mathcal{R}a_1(t)$ and $\mathcal{R}a_2(t)$ for $\Pi = 0.33$ and time-averaged values of the indices as a function of Π measured at the flame location. The acoustic frequency is 714 Hz for OH*-intensity measurements and 722 Hz for CH*-intensity measurements.

forming a short-time Fourier transform (STFT). For that purpose, the CH* signal is divided in segments of equal length, 0.1 s, with an overlap of 50%. The Fourier transform is then computed in each segment. Results are shown in Figure 5.6 for a whole CH* signal of duration 1.39 s, whose excerpts are shown in Figure 5.5. As $\mathcal{R}a_1(t)$ is calculated with the non-filtered raw CH* signal, it contains all the frequencies present in this raw signal. A quasi-continuous response is detected at $2f_r$, but its amplitude changes over time. The oscillation at f_r is present through high-amplitude spots, which are found at times when $I(t)$ undergoes the sudden decreases illustrated in Figure 5.5 (a). Simultaneously with these spots at f_r, the oscillation amplitude at $2f_r$ is relatively low. The STFT of $\mathcal{R}a_2(t)$, plotted for comparison, shows that the oscillation of $\mathcal{R}a_1(t)$ at frequency $2f_r$ is well extracted and oscillations at other frequencies are cut out.

To measure the discrepancy between the two instability indices, their probability density functions (PDFs) are shown in Figure 5.7 (a) for $\Pi = 0.33$. These distributions show a higher scattering for $\mathcal{R}a_1(t)$ than for $\mathcal{R}a_2(t)$, expressing the effect of the stochastic fluctuations. Instantaneous values of $\mathcal{R}a_1(t)$ and $\mathcal{R}a_2(t)$ can be either positive or negative, but they are more likely to be positive, indicating the potential of the flames to drive instabilities. It is possible to obtain indications about the ability of the flame to drive instabilities by considering the time-averaged value of the instability indices. Interestingly, the positive time-averaged values of $\overline{\mathcal{R}a_1}$ and $\overline{\mathcal{R}a_2}$ are identical. This is found for all acoustic amplitudes explored here, both with CH* and OH*, as shown in Figure 5.7 (b). To conclude, both $\overline{\mathcal{R}a_1}$ and $\overline{\mathcal{R}a_2}$ can be used to calculate the ability of a system to drive self-excited instabilities. In addition, this analysis indicates that the swirl-stabilised spray flames investigated here have the potential to drive such instabilities.

5.3 Mechanisms of swirl-stabilised spray flame response at PAN

In this section, the energy system is more deeply investigated to understand the mechanisms at the origin of the flame response and the positive sign of the Rayleigh source term indicated by

the mean values of the global instability indices $\mathcal{R}a_1$ and $\mathcal{R}a_2$ in Section 5.2. The formation and evolution of an axial flame intensity wave is firstly described. A local instability index is then defined to understand which parts of the flame are susceptible to couple with acoustics. By using CH* and OH* images, the appearance of local equivalence ratio fluctuations is also examined. The response of the flame base to the acoustic modulation is also explored. The air flow axial velocity modulation is then highlighted and its effects on the swirl number and vortex roll-up are investigated. Finally, the modulation of the fuel spray is shown and correlated with the flow aerodynamics and the flame response. This investigation is made for a reduced acoustic amplitude Π in the linear zone (see Figure 5.2) to limit the influence of nonlinear effects.

5.3.1 Flame intensity wave

The axial propagation of a flame intensity wave is highlighted with phase-averaged images of the flame OH* emission intensity post-synchronised with the acoustic pressure and presented for a reduced acoustic pressure amplitude $\Pi = 0.35$ in Figure 5.8. At a phase angle $\alpha_0 = -\pi/2$, a perturbation is initiated at the flame base. It is identified by a high flame base angle and a high OH*-intensity level close to the injector. This perturbation then propagates and, at $\alpha_1 = 0$, the flame base angle is less open while the flame displays a 'bulb' at mid-height, suggesting the roll-up of a strong vortex, as that observed in [67]. It is interesting to note the roughly-axisymmetric shape of the flame, as expected for flames at a pressure antinode [108]. This shows that the modulation of the flame shape is dominated by axisymmetric acoustic pressure effects rather than asymmetric swirl effects. It is interesting as large-scale vortices are known to control air-fuel mixing [122], thus promoting faster combustion. As it further propagates downstream, the 'bulb' becomes less protuberant but the OH*-intensity level grows to reach a maximum near $\alpha_2 = \pi/2$. These images show that axial flame intensity waves are a major feature of the flame response at a pressure antinode. This is confirmed by the evolution of the CH*-intensity barycentre in the (r, z) space[1], which displays a purely vertical motion, as illustrated for $\Pi = 0.26$ in Figure 5.9.

5.3.2 Projection of space-time signals onto the vertical axis

To examine the propagation and growth of the OH*-intensity wave, the approach described in Section 2.3.2.1, previously applied to numerical simulations by the EM2C and CERFACS teams to analyse self-sustained oscillations in [156], can be applied to the experimental flame images. It is briefly recalled here. The two-dimensional intensity signal obtained from the instantaneous images, $I_{cam}(r, z, t)$, is firstly thresholded to minimise the influence of the background noise. Then, it is integrated along horizontal lines to give the total intensity at given heights, and phase-averaged, giving $\langle I_{cam}\rangle(\alpha, z)$. Finally, $\langle I_{cam}\rangle(\alpha, z)$ is reduced by a reference value, which corresponds to the product of the mean OH*-intensity of the flame without acoustic forcing by the number of pixels of a horizontal line.

Results are shown in Figure 5.10 for $\Pi = 0.35$. The flame can be separated in three regions. In the lower region, called R_1, $\langle I_{cam}\rangle(\alpha, z)$ is relatively low and quite constant during the acoustic cycle. In the middle region, R_2, $\langle I_{cam}\rangle(\alpha, z)$ increases; in addition, it oscillates significantly

[1] The associated post-processing method is described in Section 2.3.2.3.

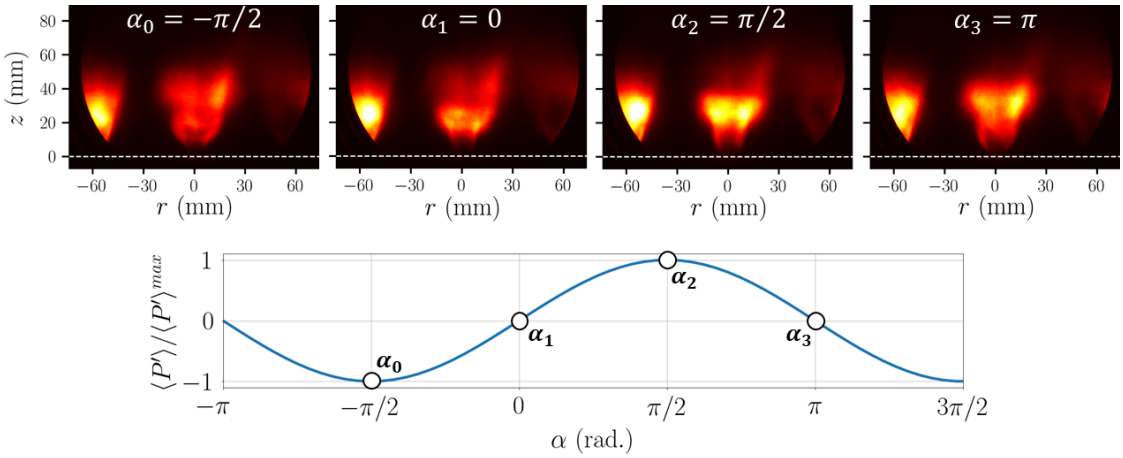

Figure 5.8: Phase-averaged OH*-intensity images represented in false colors for $\Pi = 0.35$, $f_r = 722$ Hz. The white dash line indicates the injector exit, located at $z = 0$. Each phase-averaged image is obtained from about 100 instantaneous images. Post-synchronisation with the phase-averaged pressure cycle at the bottom row (here reproduced twice) is performed. $\langle P' \rangle$ corresponds to the phase-averaged acoustic pressure at the pressure antinode.

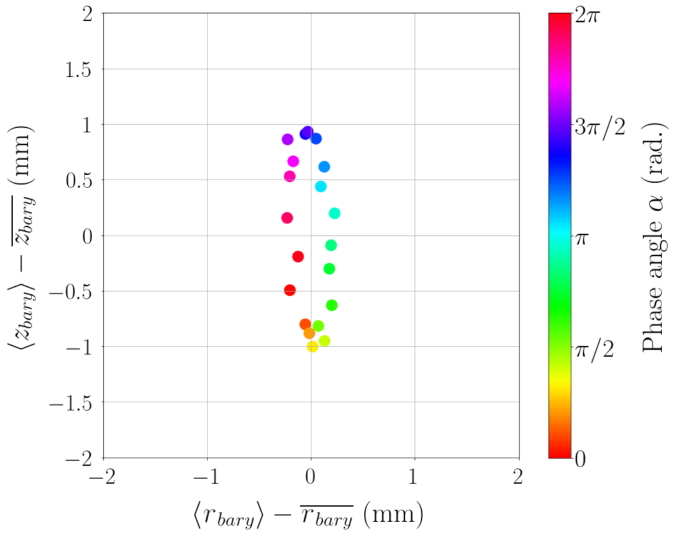

Figure 5.9: Phase-averaged location in the (r, z) plane of the CH*-intensity barycenter for $\Pi = 0.26$ post-synchronised with the acoustic pressure.

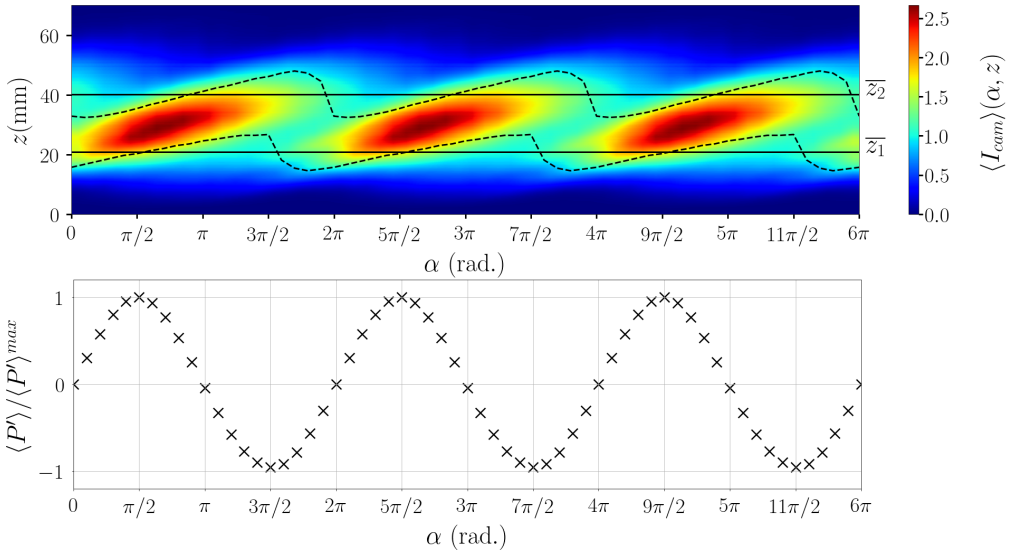

Figure 5.10: Phase-averaged normalised OH*-intensity level $\langle I_{cam}\rangle(\alpha, z)$ at $\Pi = 0.35$ post-synchronised with the acoustic pressure reproduced three time for clarity. The dash lines are defined by $\langle I_{cam}\rangle(z, \alpha)/\max(\langle I_{cam}\rangle(z, \alpha)) = 0.65$ and the two horizontal solid lines indicate the cycle-averaged vertical locations of the two dash lines, $\overline{z_1}$ and $\overline{z_2}$.

Boundary name	$\overline{h_{base}}$	$\overline{z_1}$	$\overline{z_2}$	$\overline{h_{tip}}$
z (mm)	5.34	20.9	40.3	68.1

Table 5.1: Vertical locations of the flame boundaries. $\overline{h_{base}}$ and $\overline{h_{tip}}$, the time-averaged vertical location of the flame base and flame tip, are obtained with a threshold method to detect the flame front, while $\overline{z_1}$ and $\overline{z_2}$ correspond to the time-averaged location of the lower and upper isolines defined by $\langle I_{cam}\rangle(\alpha, z)/\max(\langle I_{cam}\rangle(\alpha, z)) = 0.65$.

during time and over the longitudinal dimension of space, indicating the downstream axial propagation of an OH*-intensity wave. In the upper region, R_3, $\langle I_{cam}\rangle(\alpha, z)$ is relatively low and quite constant during the acoustic cycle. The regions are formally defined by using four boundaries: the flame standoff distance, $\overline{h_{base}}$, the time-averaged z-location of the two isolines defined by $\langle I_{cam}\rangle(\alpha, z)/\max(\langle I_{cam}\rangle(\alpha, z)) = 0.65$, $\overline{z_1}$ and $\overline{z_2}$, and the time-averaged vertical location of the flame tip, $\overline{h_{tip}}$. $\overline{h_{base}}$ and $\overline{h_{tip}}$ are obtained by using a threshold method to detect the flame front. The separation of an instantaneous flame image into these three regions is illustrated in Figure 5.11. The lower region, R_1, corresponds to $\overline{h_{base}} \leq z < \overline{z_1}$. The middle region, R_2, is defined by $\overline{z_1} \leq z < \overline{z_2}$. Finally, the upper region, R_3 corresponds to $\overline{z_2} \leq z < \overline{h_{tip}}$. The z-locations of the four boundaries are given in Table 5.1.

It is interesting to examine the propagation velocity of the OH*-intensity wave particularly observed in R_2. This velocity obtained from the evolution along the z-direction of the phase delay between the acoustic pressure oscillation at the flame location and the oscillation of $\langle I_{cam}\rangle(\alpha, z)$, $\varphi_{\langle P'\rangle - \langle I'_{cam}\rangle(z)}$, which is shown in Figure 5.12. In R_2, the OH*-intensity wave propagates at a velocity equal to 0.78 U_b, thus it is closely linked to convection.

$\langle I_{cam}\rangle(\alpha, z)$ can be seen as a set of 'local' signals, each corresponding to a z-location, which

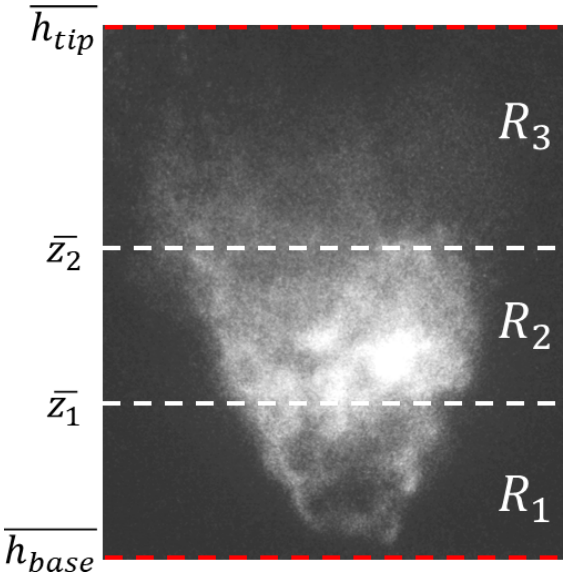

Figure 5.11: Illustration of the separation of the flame into three regions for post-processing.

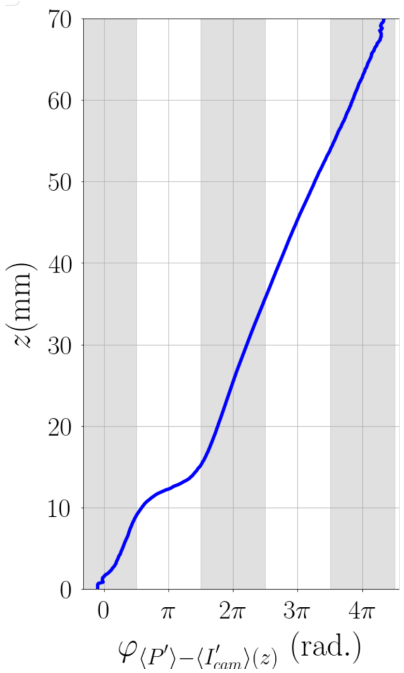

Figure 5.12: Phase shift between the phase-averaged acoustic pressure oscillation and local OH*-intensity oscillation as a function of z. Acoustic forcing: $\Pi = 0.35$, $f_r = 722$ Hz.

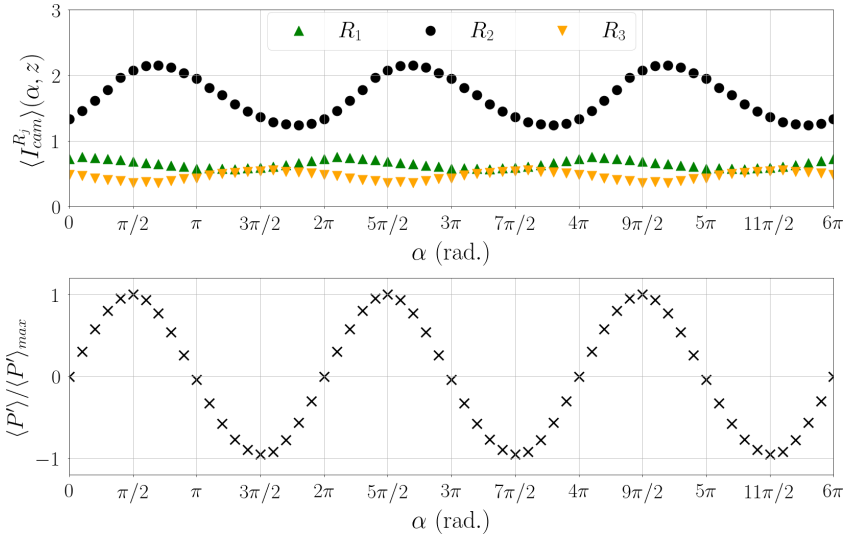

Figure 5.13: Phase-averaged OH*-intensity integrated in regions R_j, $\langle I_{cam}^{R_j} \rangle(\alpha)$ for $\Pi = 0.35$.

oscillate with a phase linked to convection. It is then interesting to integrate $\langle I_{cam} \rangle(\alpha, z)$ in each region to see how the 'local' signals interfere. $\langle I_{cam} \rangle(\alpha, z)$ is thus integrated in each region $R_j, j = 1, 2, 3$, giving:

$$\langle I_{cam}^{R_j} \rangle(\alpha) = \int_{z \in R_j} \langle I_{cam} \rangle(\alpha, z) dz \tag{5.4}$$

The signals $\langle I_{cam}^{R_j} \rangle(\alpha)$ corresponding to the results presented in Figure 5.10 are shown in Figure 5.13. The resulting oscillation in the whole R_2 is significantly stronger than those in R_1 and in R_3. In addition, the OH*-intensity in R_2 oscillates with a phase delay $\sim \pi/4$ with the acoustic pressure. This phase delay is very similar to the phase of the FDF, which is calculated with the global OH*-intensity (see Figure 5.3). This shows that the flame response is mostly linked to that of its middle region R_2, while the contribution of the flame base and flame tip to the flame response are much weaker.

5.3.2.1 Local coupling between combustion and acoustics

From the phase-space diagram in Figure 5.10, a local instability index based on the Rayleigh criterion is defined by:

$$\langle \mathfrak{Ra} \rangle(\alpha, z) = \frac{\langle P' \rangle}{\rho^a U_b^2} \frac{\langle I_{cam} \rangle(\alpha, z) - \overline{I_{cam}}^t(z)}{\overline{I_{cam}}} \tag{5.5}$$

where $\overline{I_{cam}}^t(z)$ is the cycle-averaged value of $\langle I_{cam} \rangle(\alpha, z)$ and $\overline{I_{cam}}$ the mean cycle and space-averaged value of $\langle I_{cam} \rangle(\alpha, z)$. $\langle \mathfrak{Ra} \rangle(\alpha, z)$ thus describes the coupling between the reduced acoustic pressure and the reduced local flame intensity oscillation. The phase-space distribution of this instability index is shown for $\Pi = 0.35$ in Figure 5.14 (left). It emphasises the mainly-positive contribution of region R_2, located between the two horizontal solid black lines, to the coupling between combustion and acoustics, which is not counterbalanced by the weakly-

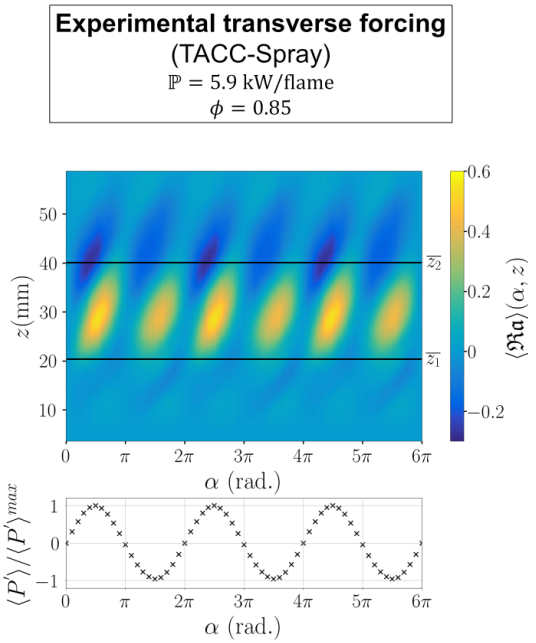

(a) Experimental results in TACC-Spray with transverse acoustic forcing

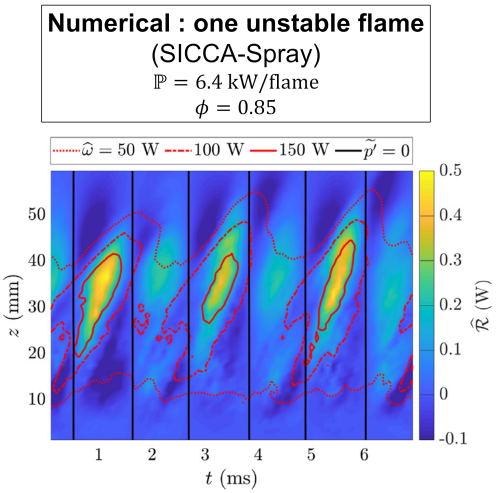

(b) Numerical results in SICCA-Spray with self-excited longitudinal oscillations. Results from EM2C and CERFACS teams, reproduced from [156]

Figure 5.14: **Left**: Phase-averaged local instability index $\langle \mathfrak{Ra} \rangle(\alpha, z)$ based on the Rayleigh criterion for $\Pi = 0.35$, $f_r = 722$ Hz. The associated reconstructed acoustic pressure cycle, reproduced three times for clarity, is shown at the bottom. The two horizontal solid lines indicate $\overline{z_1}$ and $\overline{z_2}$, defined in Figure 5.10. **Right**: Evolution of the Rayleigh source term during three acoustic cycles, obtained from a numerical simulation performed on the SICCA-Spray setup under self-excited longitudinal oscillations at a frequency of 461 ± 42 Hz [156]. The black vertical lines indicate $P^{'}(t) = 0$, and $t = 1$ ms corresponds to a pressure maximum.

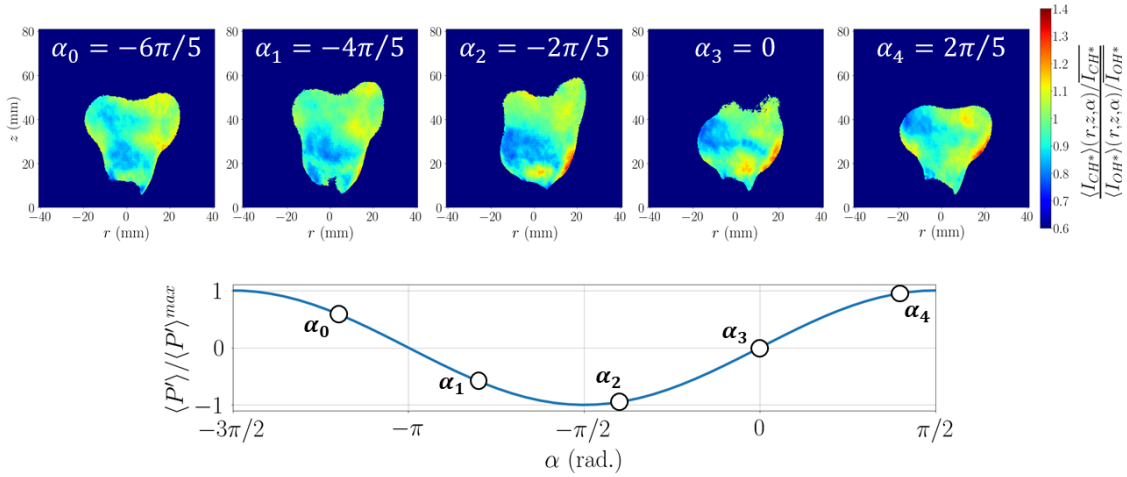

Figure 5.15: Ratio between the reduced phase-averaged CH* and OH* intensities in the (r, y) plane. $f_r = 713$ Hz for CH* and 722 Hz for OH*, $\Pi = 0.31$.

negative contribution of R_3 to this coupling. Due to its negligible OH*-intensity oscillation, region R_1 does not participate to the coupling here. These features explain the positive value of the global instability index observed in Section 5.2.3.2 and indicate that the middle region of the flame is the largest contributor to the thermoacoustic coupling.

In [156], the Rayleigh source term was calculated from numerical simulations of the single-injector SICCA-Spray setup in the presence of self-excited longitudinal oscillations, with an injection unit similar to those used in TACC-Spray. Results of this study, shown in Figure 5.14 (right), show the convective transport of the Rayleigh source term and the significant positive contribution to the Rayleigh source term located in the same region of the flame ($z \simeq 20 - 45$ mm) as in the TACC-Spray setup. The excellent accordance between the experimental results in TACC-Spray and the numerical results in the unstable SICCA-Spray indicate that $\langle \mathfrak{Ra} \rangle(\alpha, z)$ is able to provide a qualitative description of the local Rayleigh source term here.

5.3.2.2 Local equivalence ratio fluctuations

As discussed in Section 5.2.2, the ratio of the CH* intensity to the OH* intensity is linked to the equivalence ratio. It is thus possible to estimate the presence of local equivalence ratio fluctuations by using images of the CH* and OH* radical intensities. To this end, phase-averaged images for the reduced radical intensities, $\langle I_{cam} \rangle / \overline{I_{cam}}$ are obtained from 6,000 instantaneous images for each radical. These phase-averaged images are filtered to retain only the pixels with a grey level higher than 20% of the maximum intensity. The ratio of the reduced CH*-intensity to the reduced OH*-intensity is then calculated for each pixel having a grey level obtained by both radicals. The resulting images are illustrated for $\Pi = 0.31$ in Figure 5.15. For this acoustic level in the linear zone, the intensity ratio in the flame zone oscillates within the range $\sim 0.8 - 1.1$. Near the flame edge, values outside this range can be found due to the lower light intensity, as noted in [53]. By taking the relationship $\Delta(\langle I_{CH^*} \rangle / \overline{I_{CH^*}}) / (\langle I_{OH^*} \rangle / \overline{I_{OH^*}}) = 1.17 \Delta\phi$ established for a very similar flame [113], local values of ϕ in the flame zone can be estimated between

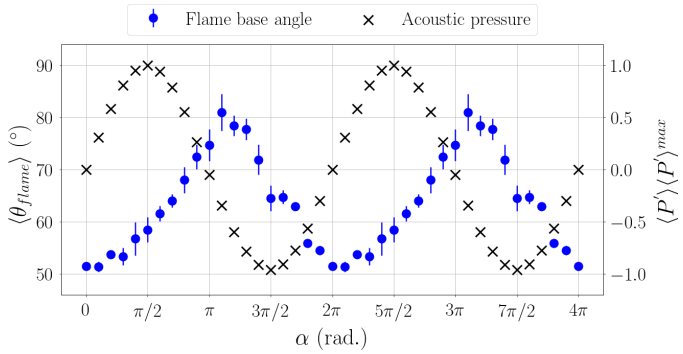

Figure 5.16: Phase-averaged flame base angle for $\Pi = 0.22$, $f_r = 722$ Hz, reproduced during two reconstructed acoustic cycles for clarity.

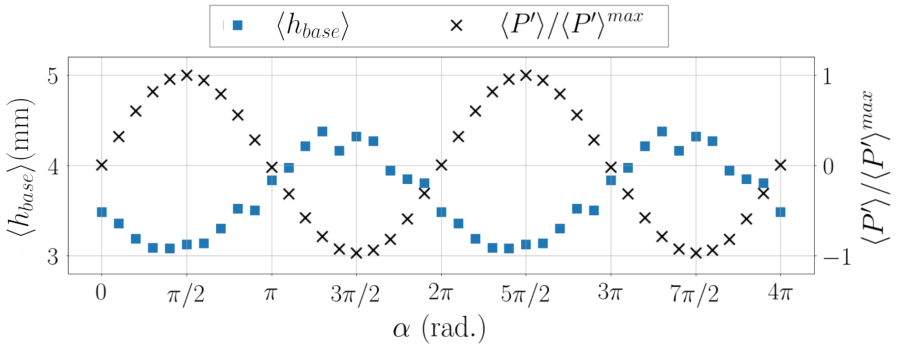

Figure 5.17: Phase-averaged flame standoff distance for $\Pi = 0.22$, $f_r = 722$ Hz, reproduced during two reconstructed acoustic cycles for clarity.

83% and 109% of the global equivalence ratio, 0.85. These equivalence ratio fluctuations may explain the higher gain of the FDF measured with CH* than with OH* (see Figure 5.3) and indicate that only a qualitative estimate of the HRR oscillation amplitude can be provided by the CH* or OH* radicals in this configuration. Nevertheless, this does not invalidate the fact that the flame response mechanisms are properly captured by both radicals, which is highlighted by the same evolution of the flame response with the acoustic amplitude and that of the FDF phase with CH* and OH*.

5.3.2.3 Perturbation of the flame base

Here, we focus on the behaviour of the flame near its stabilisation point by investigating the response of the flame base to the acoustic perturbation. For that purpose, the phase-averaged spreading angle of the flame base, $\langle\theta_{flame}\rangle$ is measured from the contour of the flame front for an acoustic amplitude $\Pi = 0.22$, and shown in Figure 5.16. $\langle\theta_{flame}\rangle$ oscillates in phase quadrature with the pressure, with values comprised between 55° and 80°. This oscillation is accompanied by that of the flame standoff distance, $\langle h_{base}\rangle$, shown in Figure 5.17. It oscillates in phase opposition with the acoustic pressure. As shown in the next section, this implies that $\langle h_{base}\rangle$ fluctuates in phase with the axial velocity of the air flow at the injector exit. Therefore, the flame base is pushed away by the high axial velocities, while it is able to go closer to the

burner when the axial velocity decreases.

5.3.3 Modulation of the air flow in reacting conditions

The previous section has highlighted the axial modulation of the flame intensity and the importance of the air flow convective processes on the flame response to acoustics. It is therefore natural to focus on the fluid-dynamic processes that may affect the flame during the acoustic cycle. The modulation of the air flow axial velocity is first examined, as it is known to affect flame wrinkling and thus HRR in premixed and non-premixed flames. The focus is then placed on swirl number oscillations, which arise from a competition between axial and tangential velocity oscillations. It is particularly relevant to study this quantity as a weakening of the swirling flow may induce a disruption of the central recirculation zone (CRZ), which could weaken proper flame stabilisation. The appearance of a coherent vortex at the injector exit is then investigated. Vortex roll-up is indeed a major feature that can occur in pulsating flows, both axially [39] and transversely [126, 172]. In premixed flames, this phenomenon leads to the periodic modulation of the flame surface area, inducing HRR oscillations, but it can also lead to saturation of the flame response at high acoustic amplitudes, both in non-swirling [67] and swirling flames [124]. In non-premixed flames, it is also known to promote air-fuel mixing and subsequently a high reactivity.

5.3.3.1 Air flow velocity modulation

We examine here the fuel droplet coherent axial velocity oscillation at f_r and the phase shift between acoustic pressure and fuel droplet coherent axial velocity oscillations, by using PDA measurements performed on the fuel droplets. As explained in Section 3.2 without acoustic forcing, the fuel droplet axial velocity can be assimilated to the air flow axial velocity by selecting fuel droplets with a Stokes number small enough. With acoustic forcing, the *acoustic* Stokes number $\mathrm{Stk_{ac}} = \tau_{drop}/\tau_{oscil} = \omega\tau_{drop}$ should also be quantified to estimate whether the droplets are able to follow the air flow fluctuations induced by the acoustic excitation. In the present case (acoustic forcing at $f_r \simeq 720$ Hz), $\mathrm{Stk_{ac}}$ does not exceed 0.25 for droplets of diameter $d \leq 5$ µm, while it can reach unity for droplets of diameter $d = 10$ µm. Therefore, the axial velocity oscillation of the air flow is here obtained by means of the fuel droplets of class C_1, *i.e.* with a diameter $d \leq 5$ µm, which are able to follow the air flow oscillations induced by acoustics. The rms amplitude of the phase-averaged axial velocity oscillation of the air flow, $\langle U_z^{a'} \rangle^{rms}(r, z)$, and the phase shift between $\langle P' \rangle(r, \alpha)$ and $\langle U_z^{a'} \rangle(r, z, \alpha)$ are obtained at each radial location of measurement. The method is reliable and avoids difficulties introduced by the non-uniform sampling of PDA. $\langle U_z^{a'} \rangle^{rms}(r, z)$, and the phase shift mentioned above are investigated with combustion for three heights $z = 2.1$ mm, $z = 6.8$ mm and $z = 20.5$ mm in Figure 5.18. The injector exit edge is located at $r \pm 4$ mm. It is worth noting that the scale of r-axis is changed as z is increased in this figure.

At $\mathbf{z = 2.1}$ mm, the amplitude of the axial velocity oscillation is highly dependent on the radial location. No oscillation is measured for $|r| < 1.25$ mm due to the very low droplet count. At $|r| = 1.3$ mm, $\langle U_z^{a'} \rangle^{rms}(r, z) = 6 - 8$ m/s, but it decreases to 4-5 m/s at $|r| = 2$ mm, showing a

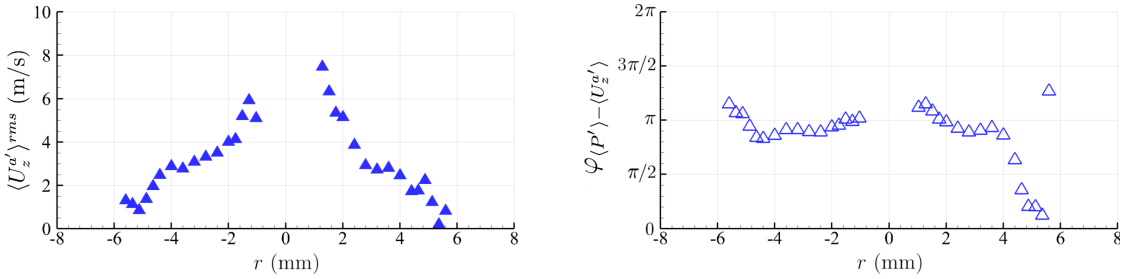

(a) $z = 2.1$ mm

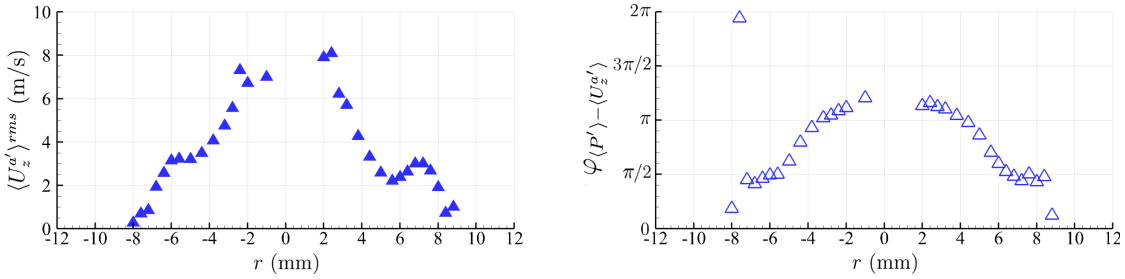

(b) $z = 6.8$ mm

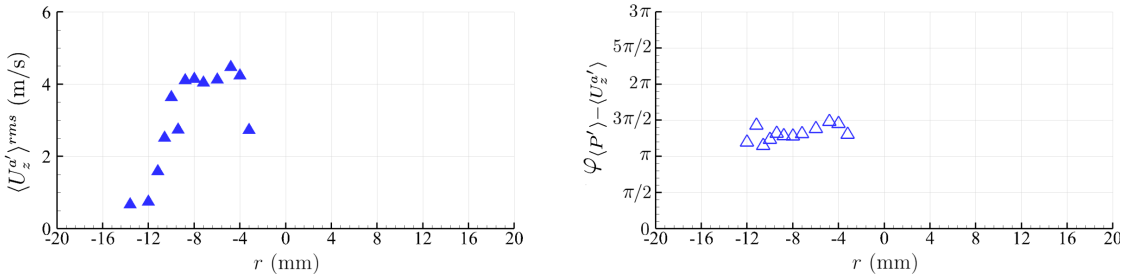

(c) $z = 20.5$ mm

Figure 5.18: Amplitude of the air flow axial velocity oscillation at $f_r = 720$ Hz, $\langle U_z^{a'} \rangle^{rms}$, and phase shift between the pressure oscillation $\langle P' \rangle$ and $\langle U_z^{a'} \rangle$. $\langle U_z^{a'} \rangle$ is obtained from the fuel droplets of classes C_1. The amount of C_1 droplets for $z = 20.5$ mm, $r > 0$ is too low to obtain results. $\Pi = 0.22$.

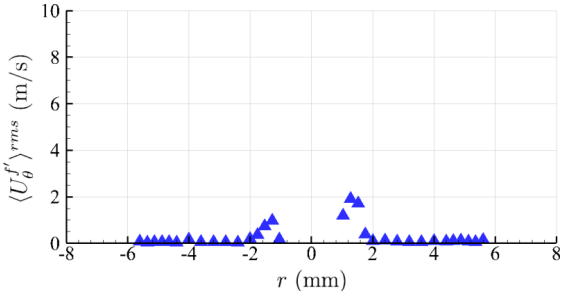

Figure 5.19: Amplitude of the air flow tangential velocity oscillation at $f_r = 720$ Hz, $\langle U_\theta^{f'} \rangle^{rms}$. $\langle U_\theta^{f'} \rangle^{rms}$ is obtained from all the fuel droplets. The acoustic amplitude is $\Pi = 0.22$.

region of strong gradient. Between $|r| = 2$ mm and $|r| = 4$ mm, $\langle U_z^{a'} \rangle^{rms}(r, z)$ decreases more smoothly, from 4-5 m/s at the inner radial location to 2.5 m/s at the outer one. Beyond $|r| = 4$ mm, $\langle U_z^{a'} \rangle^{rms}(r, z)$ decreases more sharply and reaches almost zero for 5 mm $\leq |r| \leq 6$ mm, beyond which no axial velocity oscillation is measured due to the low droplet count.
The axial velocity oscillates in phase opposition with the acoustic pressure oscillation within the chamber at most radial locations, except for $r > +4$ mm, where it is almost in phase with the pressure. This must nonetheless be nuanced by the fact that the axial velocity oscillation amplitude is very low at these radial locations, reducing the signal-to-noise ratio and therefore increasing the uncertainty about the result.

At z = 6.8 mm, $\langle U_z^{a'} \rangle^{rms}(r, z)$ reaches 7-8 m/s for $|r| \simeq 2$ mm. It decreases to $2 - 3$ m/s at $|r| = 5 - 6$ m/s, again showing a region of strong gradient. Around $|r| = 6$ mm, $\langle U_z^{a'} \rangle^{rms}(r, z)$ stabilises (for $r < 0$), or even increases a little (for $r > 0$) at $|r|$ increases, which might be linked to Kelvin-Helmholtz vortices, shown in [45]. From $|r| = 7$ mm to $|r| = 8$ mm, $\langle U_z^{a'} \rangle^{rms}(r, z)$ decreases to zero. Above $|r| = 8$ mm, the droplet count is too low to calculate $\langle U_z^{a'} \rangle^{rms}(r, z)$.
The oscillations of acoustic pressure and axial velocity are in phase opposition around $|r| = 2$ mm and in phase quadrature around $|r| = 7$ mm. Between these two locations, the phase delay progressively decreases, in a symmetric manner with respect to the injector axis.

At z = 20.5 mm, data are only given for $r < 0$ as the C_1 droplet amount for $r > 0$ is too low to give phase-averaged signals. For -4 mm $\leq r \leq -10$ mm, $\langle U_z^{a'} \rangle^{rms}(r, z) \simeq 4$ mm. Beyond $r = -10$ mm, is decreases to reach zero at $r = 12$ mm to $r = 14$ mm, beyond which the droplet count is too low. At the locations where $\langle U_z^{a'} \rangle^{rms}(r, z)$, it oscillates with a phase delay between $5\pi/4$ and $3\pi/2$.

The fuel droplet tangential velocity oscillation is also examined in Figure 5.19. Contrary to the axial velocity, the tangential velocity is measured by including all the droplets. The results show that the fuel droplet tangential velocity does not exhibit a particular response at f_r.

5.3.3.2 Swirl number oscillations

The axial velocity modulation is known to affect the HRR through flame wrinkling, as highlighted by studies carried out on laminar premixed flames [73, 74, 78, 173]. The matter is complexified for swirling flows, for which axial velocity fluctuations modify the swirling strength

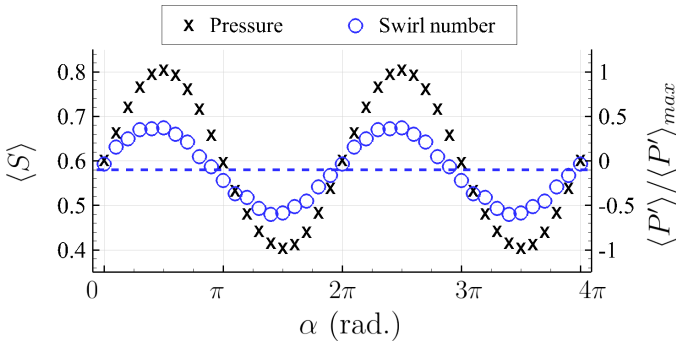

Figure 5.20: Phase-averaged swirl number oscillation at $f_r = 720$ Hz measured at $z = 2.1$ mm, post-synchronised with the acoustic pressure for $\Pi = 0.2$. The acoustic cycle is reproduced twice for the sake of clarity. The dash line indicates the mean swirl number, which is 0.58 here.

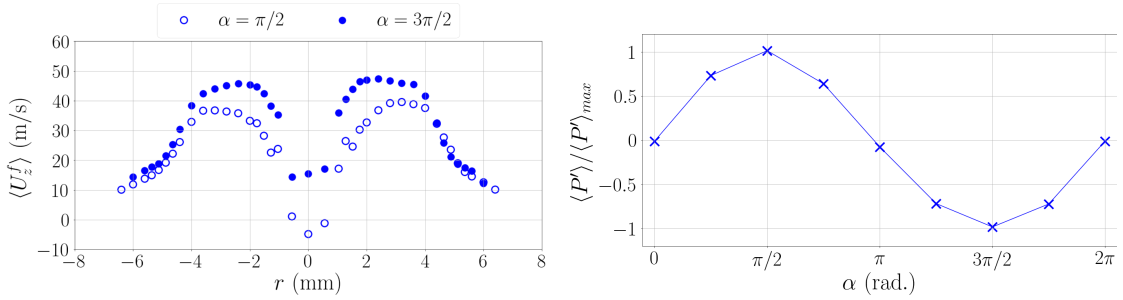

(a) Phase-averaged axial velocity profiles

(b) Phase-averaged acoustic pressure cycle

Figure 5.21: Phase-averaged axial velocity profiles calculated on droplets of diameter d in the range $1 - 15$µm for two phase angles $\alpha = \pi/2$ and $\alpha = 3\pi/2$ on the left, and the associated phase-averaged acoustic pressure cycle on the right. Acoustic forcing is performed at a reduced amplitude $\Pi = 0.2$ and a frequency $f_r = 720$ Hz. The acoustic cycle is divided into 8 bins of equal width $\pi/4$.

and may disrupt the CRZ, thus weakening the proper flame stabilisation. It is generally admitted that the CRZ establishes when the swirl number exceeds a value of about 0.6 [28]. In the present configuration, its value without acoustic excitation is 0.58 and the presence of the CRZ is suggested by the low mean axial velocity and high rms axial velocity found near the injector axis (see Figure 3.9). With acoustic forcing at an amplitude $\Pi = 0.2$, the swirl number $\langle S \rangle$ measured at $z = 2.1$ mm, shown in Figure 5.20, periodically oscillates in phase with the acoustic pressure, hence, in phase opposition with the axial velocity. This indicates that the oscillation of the swirl number is mainly induced by the axial velocity oscillation. One effect of swirl number fluctuations is the modification of the flame base angle, shown in the present configuration in Figure 5.16. The oscillation of the flame base angle lags behind that of the swirl number by about $\pi/4$, which is close to the convective propagation time of the flame surface disturbance. This indicates a close link between the swirl number and the flame base angle. During its oscillation, $\langle S \rangle$ reaches values as low as 0.48 when the pressure is minimum and as high as 0.67 when the pressure is maximum. The swirl level reached at the pressure minimum is 20% lower than the value of 0.6 admitted for the appearance of the CRZ. To examine whether the weakening of the swirl level leads to the disruption of the CRZ or not, phase-averaged axial velocity profiles are shown for two phase angles $\alpha = \pi/2$ and $\alpha = 3\pi/2$, corresponding to the acoustic pressure maximum and minimum respectively, in Figure 5.21. These phase-averaged profiles are obtained from droplets of diameter in the range $1 - 15$ µm by dividing the acoustic cycle into 8 bins of equal width of $\pi/4$ radians. The choice of the bin amount is a trade-off between the width of the bins and the amount of data collected in each of them. Indeed, due to the hollow-cone shape of the spray, the bin width must be large enough to include a sufficient amount of data near the injector axis. The results, presented in Figure 5.21, show a notable modulation of the axial velocity near the injector axis, reaching negative values at the pressure maximum while it is about 15 m/s at the pressure minimum. This indicates that the CRZ is not present during all the acoustic cycle: near the pressure maximum, the CRZ is reinforced due to the decrease of the axial velocity while near the pressure minimum, it disappears because of the increase of the axial flow velocity. Simultaneously with its disappearance, the flame standoff distance increases (see Figure 5.17), showing the influence of the CRZ on the flame stabilisation.

5.3.3.3 Vortex roll-up

The roll-up of a coherent toroidal vortex suggested by the phase-averaged flame emission images (see Figure 5.8) is now examined by using instantaneous high-speed vertical tomography images. A total of 2,750 images are obtained at an acquisition rate of 27,500 Hz. These images are obtained in reacting conditions by illuminating olive oil droplets, used to seed the air flow, with a laser sheet, and by capturing the Mie scattering signals of these droplets with a Phantom V2512 high-speed camera. The experimental setup is described in Section 2.2.5. The images are thresholded to zero[2] to remove the background noise and to limit the signal from the fuel droplets.

Results are illustrated for $\Pi = 0.38$, $f_r = 716$ Hz in Figure 5.22. The coherent toroidal vortex

[2]Pixels with a grey level greater or equal than a threshold are retained and their grey level is unchanged while the other pixels are set to zero, *i.e.* they appear black.

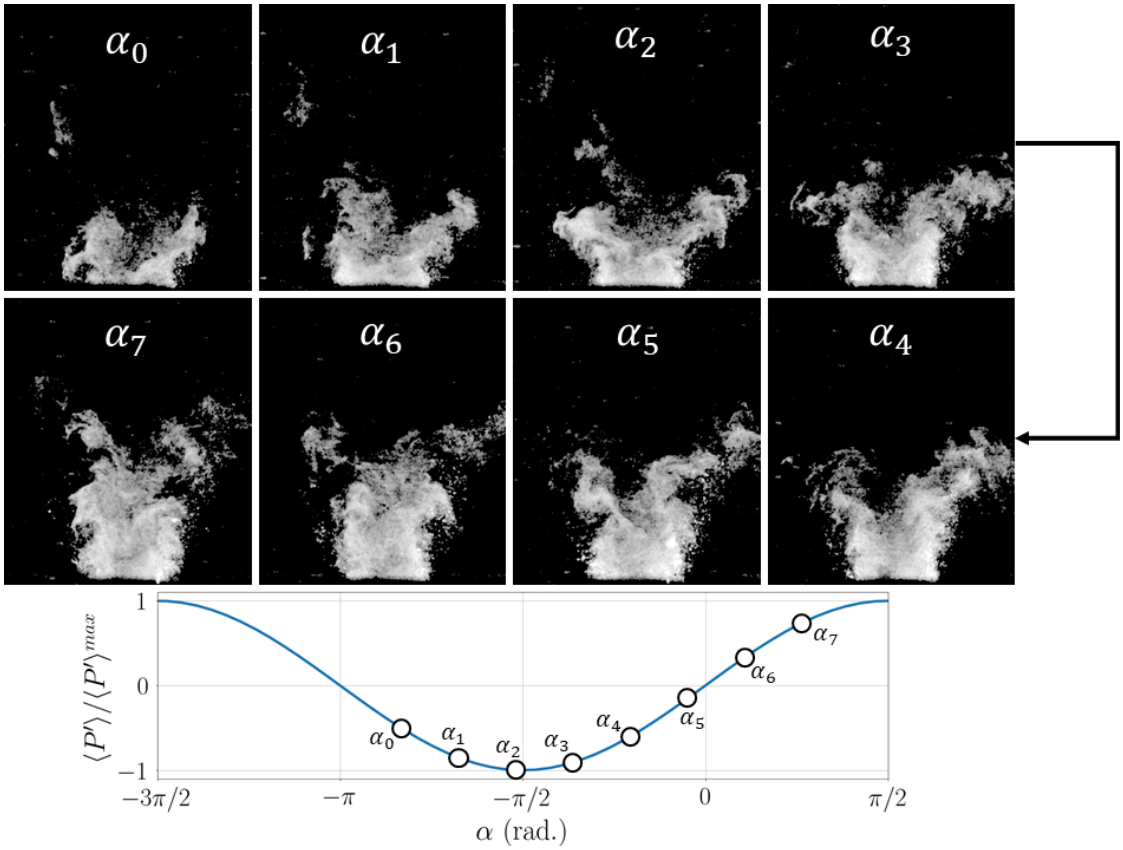

Figure 5.22: Instantaneous vertical tomography images of olive oil droplets used as seeding particles of the air flow in reacting conditions for $\Pi = 0.38$, $f_r = 716$ Hz. The images are acquired at an acquisition rate of 27,500 Hz, allowing to follow the formation and development of a toroidal vortex, here from phase angles α_0 to α_7. The vortex appears at the injector exit near $\alpha_2 \simeq 3\pi/2$ and is then convected by the air flow. Olive oil droplets disappear because of the evaporation due to the presence of the flame. Images have a size of 24.6×28.6 mm^2.

is identified by the symmetric roll-up of olive oil droplets, first noticed close to the injector at $\alpha_2 = 1.51\pi$. After its ejection, the coherent structure grows as it is transported by the mean flow to higher locations, but the growth is somewhat difficult to estimate because of the simultaneous oil droplet evaporation occurring due to the presence of the flame. It is known that coherent structures formed by forcing a swirling flow grow with downstream transport until vertical locations equal to several times the nozzle exit diameter [66]. As shown above on the flame images (see Figure 5.8), the 'bulb', and thus the coherent vortex, correlate with a high CH*-intensity level at high locations, indicating the important role of this vortex in the flame response.

5.3.4 Modulation of the fuel spray

Mechanisms associated with the spray are now investigated, especially as they are not well documented in reacting conditions. To this end, Mie scattering imaging of the fuel spray only and PDA measurements are performed in reacting conditions. These techniques are here used to visualise the instantaneous spray injection and to estimate the variation of the droplet amount

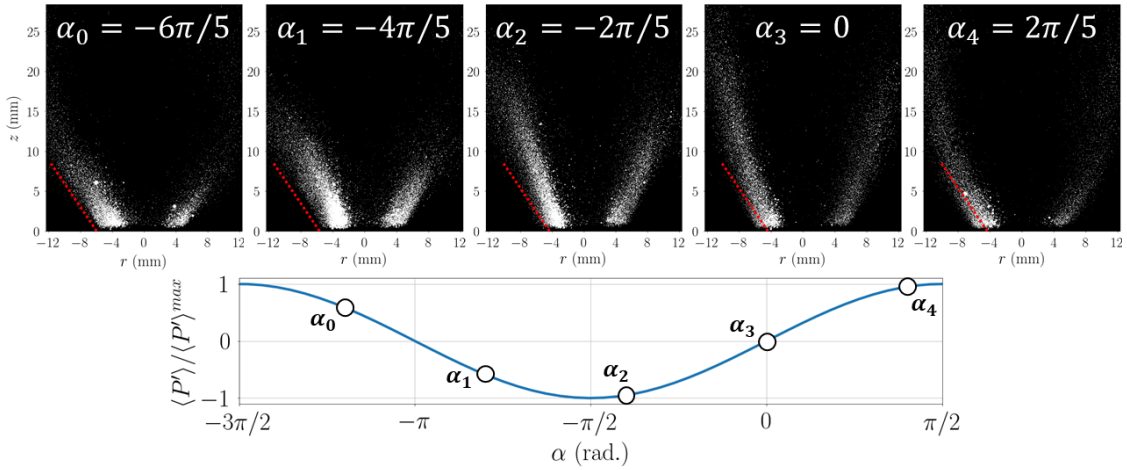

Figure 5.23: Phase-averaged spray images. $\Pi \simeq 0.38$, $f_r = 716$ Hz. At the bottom, the phase-averaged acoustic pressure cycle is represented with five dots indicating the phase angle at which the images are obtained. The red line, identical on all the images, helps to appreciate the modification of the spray angle.

during the acoustic cycle.

Mie scattering imaging of the spray is performed using high-speed laser tomography, as described in Section 2.2.5. A total of 2,750 images are obtained at an acquisition rate of 27,500 Hz. To remove the background noise, the instantaneous spray images are first filtered such that pixels with a grey level higher than a threshold value keep their grey level while the other pixels are set to zero. Then, the filtered images are phase-averaged and post-synchronised with the acoustic pressure measured at the central flame location. Here, the acoustic cycle is divided in 20 phase-averaging bins, thereby giving about $137 - 138$ images to reconstruct one phase-averaged image.

Phase-averaged spray images are shown in Figure 5.23 for an acoustic frequency $f_r = 716$ Hz and a reduced acoustic amplitude $\Pi = 0.38$. The spray undergoes an oscillatory motion characterised by an unsteady amount of fuel injected and an oscillating injection angle. The evolution of the amount of fuel injected into the chamber is illustrated by the modification of the scattered light intensity during the acoustic cycle. Thus, near the injector exit, the liquid fuel amount is maximum around $\alpha_2 = -2\pi/5$, close to the pressure minimum. This large amount is injected with a low injection angle and a high axial velocity. It is then transported by the air flow to higher locations and, in spite of the simultaneous evaporation, some droplets reach vertical locations up to $z = 25$ mm (around $\alpha_3 = 0$). On the contrary, the amount of liquid fuel injected is reduced around the pressure maximum and the spray injection angle increases. Coupled to the low velocities at these phase angles, the penetration length of the liquid fuel diminishes until $\alpha \simeq \pi$. From these images, it clearly appears that the spray injection angle and the amount of liquid fuel injected into the chamber are coupled to the pressure oscillation. The oscillations of the spray injection angle and injected droplet amount are now further investigated.

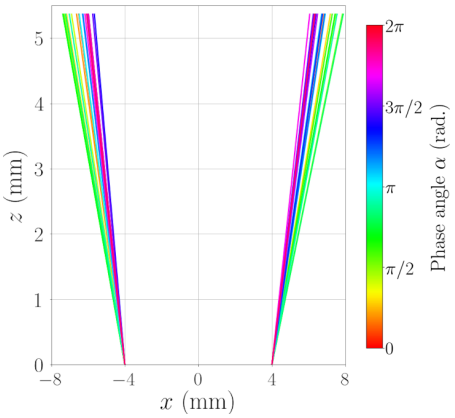

(a) Representation of the phase-averaged spray base opening by using a first-order approximation based on $\langle\theta_{spray}\rangle$

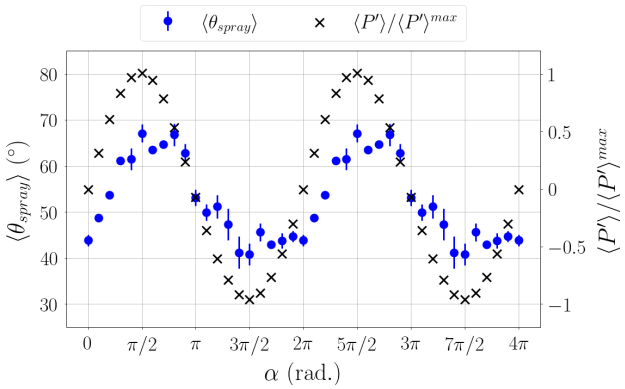

(b) Phase-averaged angle of the spray base

Figure 5.24: Oscillation of the fuel spray base injection angle $\langle\theta_{spray}\rangle$. The reduced acoustic amplitude and frequency are $\Pi = 0.38$, $f_r = 716$ Hz. Right: the acoustic cycle is reproduced twice for clarity.

5.3.4.1 Modulation of the spray injection angle

As the tomography images are obtained in the (r, z) plane and the spray has a hollow cone shape, it is easy to examine the injection angle of the spray. For this purpose, a post-processing method based on the barycentre of the light scattered by the spray, described in Section 2.3.3.1, is applied to the 20 phase-averaged spray images. For this study, the barycentre for each side of the spray image is obtained for each row in the region of interest (ROI) defined by 0.43 mm $\leq z \leq 5.37$ mm, giving a curve $x = f(z(\alpha))$ for each side of the spray. The ROI is chosen to isolate the spray base, in order to minimise the convective effects on the spray angle. A first-degree polynomial then fits the data, giving a relation $x(z, \alpha) = a(\alpha)z + b(\alpha)$. The spray angle is finally calculated from the value of $a(\alpha)$. Due to the shape of the spray (see Figure 5.23), $a(\alpha) < 0$ for $r < 0$ and $a(\alpha) > 0$ for $r > 0$ at all phase angles. The relation $x(z, \alpha) = a(\alpha)z + b$ is illustrated at various phase angles in Figure 5.24a (left column). In this plot, parameter b is assumed to be independent of α, in order to focus on the modulation of the spray base angle.
The phase-averaged spray base angle, $\langle\theta_{spray}\rangle$, is then calculated from the values of $a(\alpha)$ obtained for $r < 0$ and for $r > 0$. The evolution of $\langle\theta_{spray}\rangle$ during the acoustic cycle is shown in Figure 5.24 (left column) for $f_r = 716$ Hz, $\Pi = 0.38$. It oscillates between 40° and 70°, in phase with the acoustic pressure, and thus in phase with the swirl number too (see Figure 5.20). The cycle-averaged spray base angle is 53°, which is similar to the time-averaged spray base angle without acoustic forcing, which is 51° (see Section 3.1).

5.3.4.2 Droplet number waves

The modulation of fuel droplet amount is now examined more finely by counting the fuel droplets passing through the measurement volume of the PDA system. PDA measurements are performed on radial lines at three heights above the injector. For each height, the droplet count is phase-

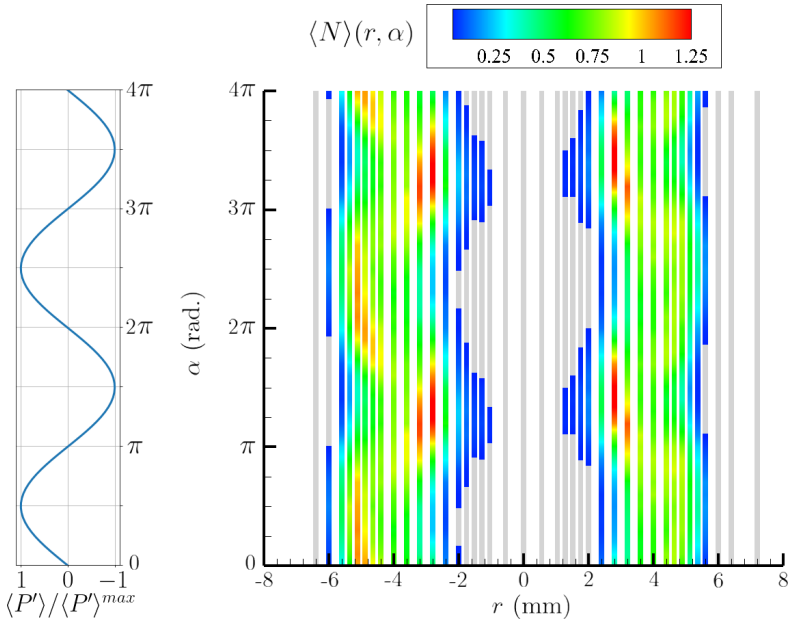

Figure 5.25: Phase-averaged droplet number $\langle N \rangle(r, z, \alpha)$ at $z = 2.1$ mm on the right, post-synchronised with the acoustic pressure represented on the left. The acoustic cycle is reproduced two times. The reduced acoustic amplitude is $\Pi = 0.2$. The grey zones indicate regions where $\langle N \rangle < 0.04$ drops/$\Delta\tau$.

averaged at each radial location. All the phase-averaged signals are post-synchronised using a same reference signal, namely the acoustic pressure at the central flame location. The phase-averaged droplet count $\langle N \rangle(r, z, \alpha)$ is thus presented as a function of radial location r, vertical location z and phase angle α, allowing to examine space-time oscillations.

$\langle N \rangle(r, z, \alpha)$ is firstly represented in Figure 5.25 at $z = 2.1$ mm for $\Pi = 0.2$, $f_r = 713$ Hz during two reconstructed acoustic cycles. The grey zones indicate regions where the droplet count is too low to be validated, *i.e.* the 'hollow' part of the spray cone. It corresponds to the *core region* identified in the absence of acoustic forcing (see Chapter 3). The modulation of the droplet amount is shown to be space-dependent:

- Near the pressure maximum ($\alpha = \pi/2$), the droplet count in the inner part of the spray ($|r| \lesssim 4$ mm) is minimum. Droplets are absent from the core region ($|r| \leq 2$ mm), as without acoustic forcing. At the same time, droplets are mainly located in the outer part of the spray ($|r| > 4$ mm).
- Conversely, at the pressure minimum ($\alpha = 3\pi/2$), the droplet count is maximum in the inner part of the spray. Simultaneously, the core region is reduced and, in the outer part of the spray, the droplet count reaches a minimum value.

We now focus on the phase-averaged droplet count integrated over all a radial profile, $\langle N \rangle_{spray}(\alpha)$, shown in Figure 5.26 (a) for three heights. We first emphasise the cycle-averaged droplet count. Consistently with observations made without acoustic forcing (see Figure 3.2), the cycle-averaged droplet count decreases very little between $z = 2.1$ mm and $z = 6.8$ mm, while it is

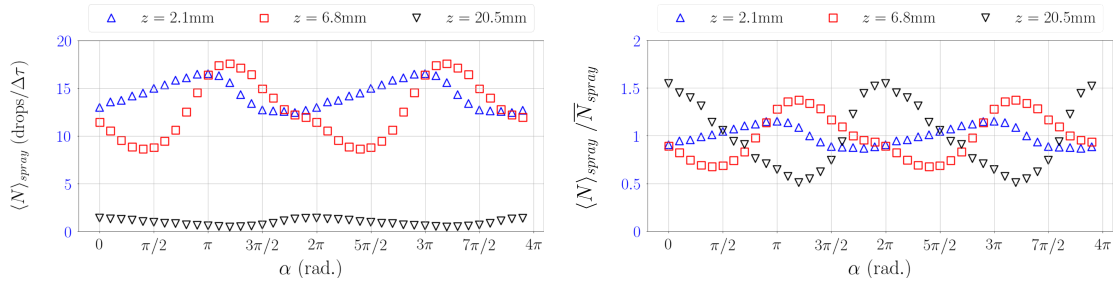

(a) (b)

Figure 5.26: Phase-averaged fuel droplet number over all a radial line, $\langle N \rangle_{spray}(\alpha, z)$ at three heights above the burner, post-synchronised with the acoustic pressure cycle as in Figure 5.25. Left: absolute values. Right: reduced values $\langle N \rangle_{spray}(\alpha, z)/\overline{N}_{spray}(z)$. The acoustic cycle is reproduced two times. The acoustic forcing frequency is $f_r = 713$ Hz and the reduced amplitude $\Pi = 0.2$.

significantly reduced at $z = 20.5$ mm, roughly by a factor 10. This indicates that most droplets have only partially evaporated at $z = 6.8$ mm while they have mostly completely evaporated at $z = 20.5$ mm, suggesting that the fuel is mainly in gaseous form at the latter vertical location. It can thus be easily engulfed by the coherent vortex, together with the oxidizer. In addition, as forced coherent structures in swirling flows first grow during transport up to vertical locations equal to several times the injector exit diameter [66], the coherent vortex is stronger than at the injector exit, and is therefore able to lead to a more effective air-fuel mixing. This mechanism may explain why the highest flame intensity levels are reached above $z = 20$ mm.
We now focus on the oscillation amplitude of $\langle N \rangle_{spray}(\alpha)$. At $z = 6.8$ mm, the maximum count is found at $\alpha \simeq 5\pi/4$. But, at this point the fuel droplets still need to evaporate and to mix with the air before combustion. These processes are improved by the coherent vortex, which was shown to reach similar vertical locations at $\alpha \simeq 3\pi/2$, *i.e.* quasi simultaneously with the maximum droplet count. However, the increase of the oscillation amplitude of the droplet count reduced by its cycle-averaged value, $\langle N \rangle_{spray}/\overline{N}_{spray}$, with the vertical location may indicate the segregation of the droplets by the velocity field, observed in non-reacting sprays in [135,136]. This feature might lead to the formation of droplet clusters, potentially affecting the evaporation rate [42], modifying the spray combustion regime [36, 38] and so flame dynamics [139].

It is also interesting to compare the oscillation of $\langle N \rangle_{spray}$ to the air flow velocity oscillation (see Figure 5.18) to understand the reason why the equivalence ratio fluctuations are weak (see Figure 5.4 and Figure 5.15). At $z = 6.8$ mm, where both $\langle N \rangle_{spray}$ and the air flow axial velocity $\langle U_z^{a'} \rangle$ oscillate remarkably, these two quantities roughly oscillate in phase, *i.e.* in phase opposition with the acoustic pressure oscillation at the flame location. This indicates that near the pressure minimum, the high amount of fuel is accompanied by a high air flow rate, whereas near the pressure maximum, the lower amount of fuel is accompanied by a lower air flow rate. This mechanism can explain the low equivalence ratio fluctuations observed despite the presence of droplet number waves.

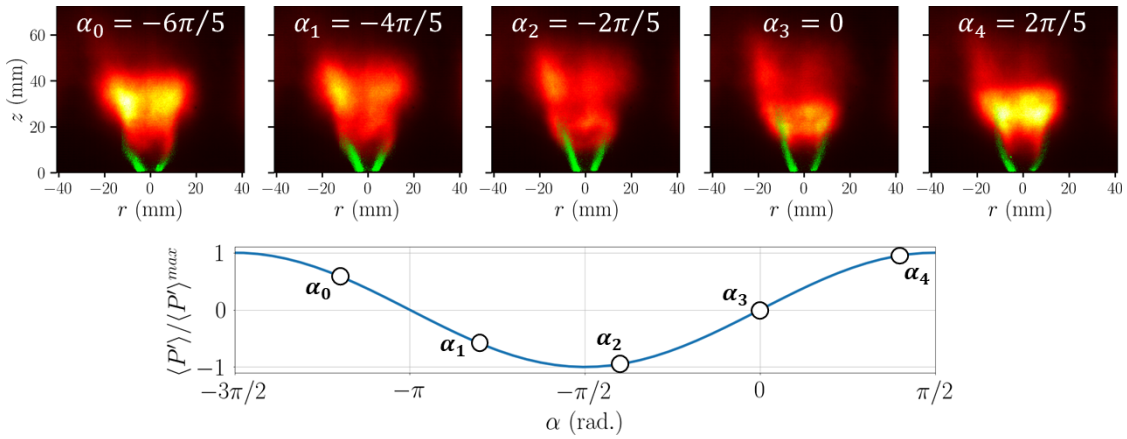

Figure 5.27: Superposition of phase-averaged OH*-intensity and spray images in false colours. $\Pi = 0.35$, $f_r = 722$ Hz for the flame images and $\Pi = 0.38$, $f_r = 716$ Hz for the spray images. At the bottom, the phase-averaged acoustic pressure cycle is represented with five dots indicating the phase angle at which the images are obtained.

5.3.4.3 Correlation between spray and flame-intensity oscillations

It is now interesting to observe how the spray and the flame behave simultaneously during an acoustic cycle. To this end, the abovementioned phase-averaged spray images obtained for $\Pi = 0.38$, $f_r = 716$ Hz (see Figure 5.23) are superimposed on phase-averaged OH*-intensity images obtained for $f_r = 722$ Hz and $\Pi = 0.35$. Results are given in Figure 5.27 during a reconstructed acoustic cycle. At $\alpha_0 = -6\pi/5$, which is slightly after the pressure maximum, the spray base angle is large near the injector exit. In addition, the light intensity scattered by the spray is low, indicating the injection of a small droplet amount. When the pressure decreases, the spray base angle decreases and the droplet amount increases. Then, a spot with a high OH*-intensity is formed at the flame base at $\alpha_2 = -2\pi/5$ around $z = 15 - 20$ mm. As mentioned above, the spray has already significantly evaporated at this vertical location. Since the fuel is mainly in gaseous form, it is more easily engulfed by the coherent vortex and turbulent mixing with the air is thus achieved more effectively. This allows the formation of a reacting mixture, which induces a notable increase of the OH*-intensity until the pressure maximum, beyond which the amount of reacting mixture available significantly reduces.

These observations are supported by comparing the phase shift between the oscillations of droplet number $\langle N \rangle_{spray}(\alpha)$ and OH*-intensity, $\langle I_{cam} \rangle(z, \alpha)$, at various vertical locations, as shown in Figure 5.28. Local oscillations of the OH*-intensity are obtained for each z in the range $14 - 49$ mm, while those of the droplet number are obtained from PDA measurements at three heights $z = 2.1$ mm, $z = 6.8$ mm and $z = 20.5$ mm. The respective phase angles at which these local oscillations reach their maximum value are retained. In Figure 5.28, black points indicate the vertical locations of the local maxima of $\langle I_{cam} \rangle(z, \alpha)$, and white crosses represent the phase angles at which $\langle N \rangle_{spray}(\alpha)$ is maximum at $z = 2.1$ mm, $z = 6.8$ mm and $z = 20.5$ mm. The associated lines are obtained by fitting a first-degree polynomial to the data. The coincidence between the maxima of the axial waves of OH*-intensity and droplet number at $z \simeq 20$ mm is evidenced. Consequently, the peak of OH*-intensity is induced by a peak of fuel feeding

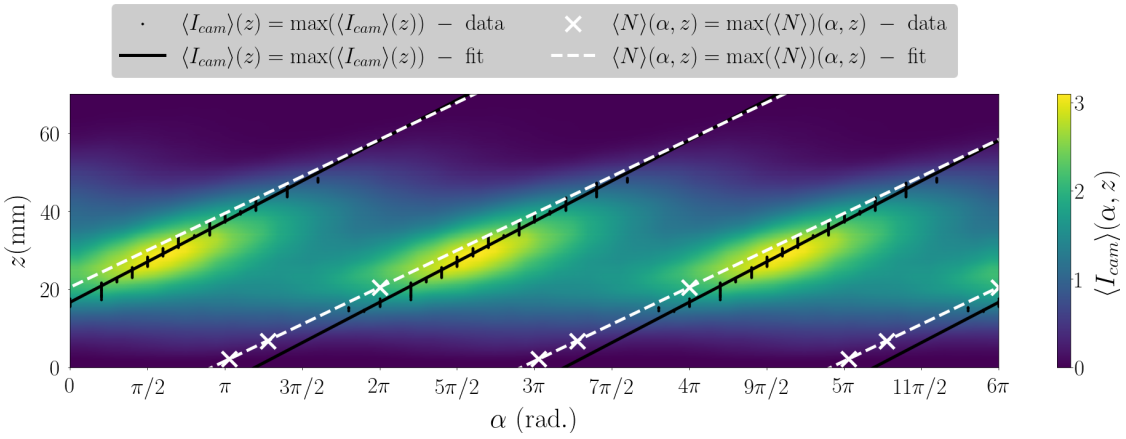

Figure 5.28: Analysis of space-time OH*-intensity wave and droplet number wave. The colormap gives the radical light intensity level $\langle I_{cam}\rangle(\alpha, z)$. For each z_i, the black dots indicate the phase angle at which $\langle I_{cam}\rangle(\alpha, z_i)$ is maximum for z_i in the range 14 mm - 49 mm; the solid black line draws a linear extrapolation of these experimental data points. White crosses give the phase angle at which the maximum droplet count is measured at three locations z; the white dashed line corresponds to a linear extrapolation of the experimental data points. The space-time OH*-intensity is evaluated for $\Pi = 0.2$, $f_r = 722$ Hz and the droplet number wave for $\Pi = 0.2$, $f_r = 715$ Hz.

to the flame. Using the best-fit lines, the propagation velocity of the waves are calculated. For the droplet number, it is $0.83U_b$, while for the OH*-intensity, it is U_b, indicating that the waves propagate at a convective velocity.
The generation of a strong spot of OH*-intensity is therefore allowed by two mechanisms acting simultaneously: (i) the injection of a high liquid fuel amount and (ii) the increase of the air-fuel mixing effectiveness due to the ejection of a coherent vortical structure.

5.4 Response at high acoustic amplitudes: insights into the saturation phenomenon

In this section, we focus on the flame response at high acoustic amplitudes. While for $\Pi \leq 0.35$, the flame response is linearly related to the acoustic pressure amplitude, this is no longer true at higher acoustic amplitudes due to the presence of nonlinear phenomena. Some elements are given to understand the features at the origin of the nonlinear evolution of the flame response. This phenomenon is analysed more thoroughly in Chapter 7, in which the flame power is decreased, allowing to reach higher values of Π.

5.4.1 Global features of the flame response

In the absence of acoustic forcing, radical intensity signals fluctuate in a limited range around their mean value $\overline{I}$, as illustrated with CH* signals measured with PM in Figure 5.29 (a). At low acoustic amplitudes (see Figure 5.29 (b) for $\Pi = 0.2$), radical intensities oscillate at f_r due to the acoustic modulation, with a reduced amplitude $I^{rms}_{CH^*}/\overline{I_{CH^*}} \simeq 0.16$ (see Figure 5.2), but the

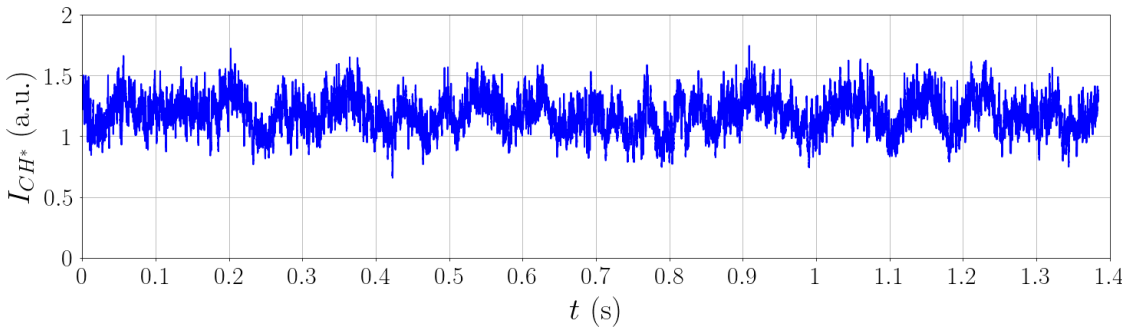

(a) $\Pi = 0$ (no acoustic forcing)

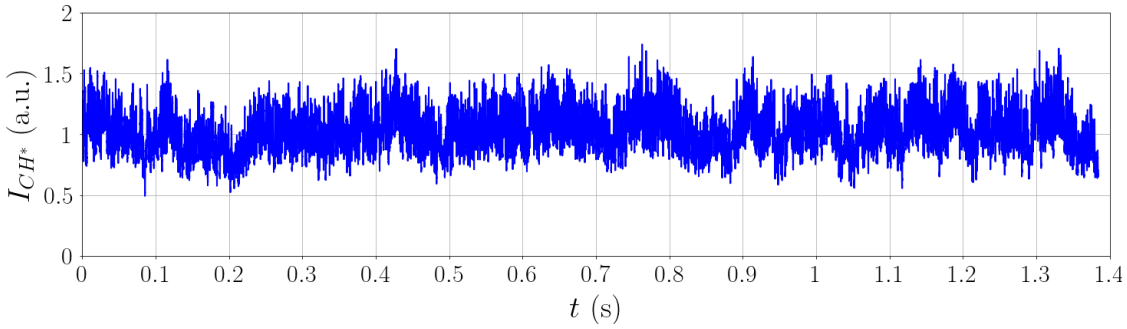

(b) $\Pi = 0.22$; $f_r = 722$ Hz

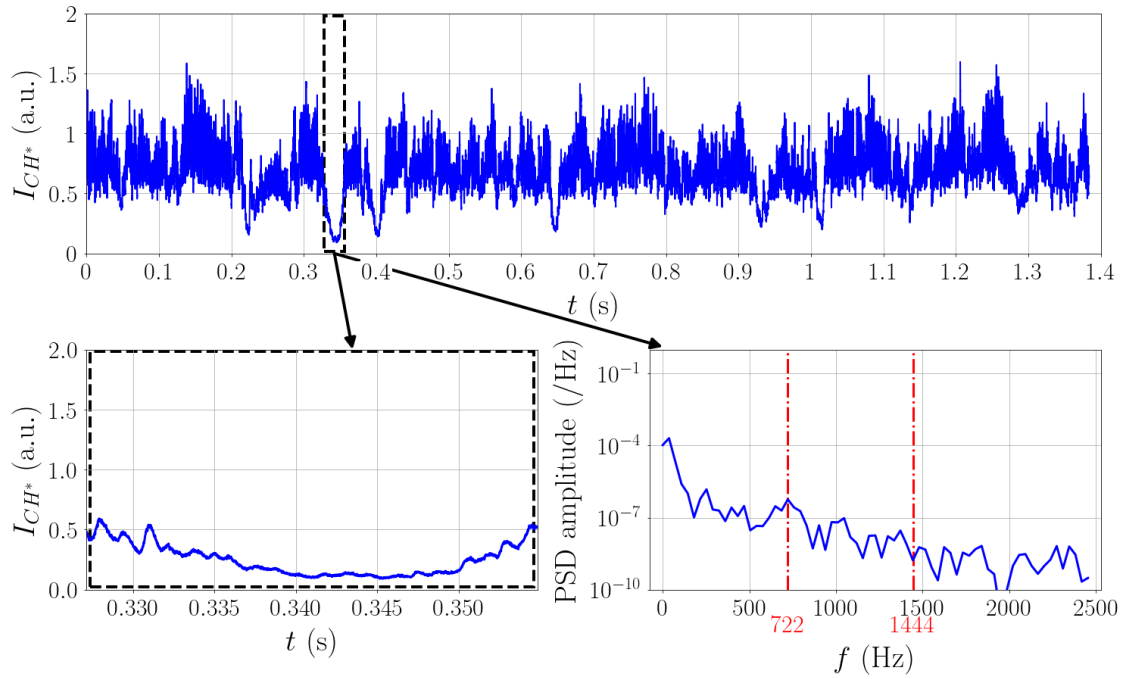

(c) $\Pi = 0.59$; $f_r = 722$ Hz. An excerpt of the CH^* signal and the PSD of this excerpt are shown on the bottom raw.

Figure 5.29: CH^* emission signals of the central flame captured with PM: (a) without acoustic forcing; (b) in the linear zone and (c) in the saturation zone of the flame response.

radical intensity remains in a tight range around its time-averaged value. In these two cases, the intensity level does not exhibit any significant increase or decrease, which would indicate flame extinction or reignition. Therefore, the main effect of the pressure perturbation in the chamber is the modulation of the global flame intensity at the excitation frequency.
In the saturation zone, this is not true anymore: radical emission signals indicate that the flame intensity undergoes severe variations that are not locked around a particular frequency. An example is given for $\Pi = 0.59$ in Figure 5.29 (c), in which events characterised by a notable drop of the CH*-intensity are found at several times. From these events, the strong decrease of the CH* intensity occurring around $t = 0.35$ s is further studied. During the time interval from $t = 0.34$ s to $t = 0.35$ s, $I_{CH^*}(t)$ does not exceed 24% of the mean CH* intensity of the whole signal. Simultaneously with the lowest intensities, the flame does not respond at the acoustic frequency, as shown by the PSD of the shortened signal, which does not exhibit a notable peak at f_r. This example suggests a correlation between $I^{rms}_{CH^*}/\overline{I_{CH^*}}$ and $\overline{I_{CH^*}}$, calculated during time intervals of a few acoustic periods.

To analyse this, the CH* signal of length 100,000 samples and duration 1.39 s is divided into 100 shortened signals with a 50% overlap, each one encompassing about 20 acoustic cycles. In each shortened signal, the time-averaged CH*-intensity, $\overline{I_{CH^*}}$ is calculated and the PSD is obtained with Welch's method. The PSD is then integrated in a frequency band around f_r to obtain the oscillation amplitude at the excitation frequency, $I^{rms}_{CH^*}$. The correlation between flame intensity and flame response is evaluated for the signals by plotting $I^{rms}_{CH^*}$ as a function of $\overline{I_{CH^*}}$. Figure 5.30 shows the correlation for the signal presented in Figure 5.29c, corresponding to $\Pi = 0.59$. Each symbol represents a shortened signal. The black dash line indicates the best-fit line. The coefficient of determination[3], R^2, is 0.75. The correlation between the mean flame intensity and its oscillation amplitude at f_r is revealed by the positive slope of the best-fit line. In particular, events characterised by a low $\overline{I_{CH^*}}$ and a low $I^{rms}_{CH^*}$ (called 'LILR' events) highlight that the flame is almost unable to respond to acoustics when its mean intensity is significantly reduced.

The same analysis is performed for various acoustic amplitudes, as shown in Figure 5.31. The case without acoustic forcing is shown for reference. R^2 increases with Π up to $\Pi = 0.3$, above which it remains between 0.65 and 0.8. For instance, $R^2 = 0.16$ for $\Pi = 0.09$ and $R^2 = 0.65$ for $\Pi = 0.29$. For $\Pi = 0.14$, the cluster of data points remains almost as compact as in the absence of acoustic forcing, but it is much more spread out along the best-fit line as Π increases. The dispersion of the scatter plots is investigated by calculating the standard deviations of $\overline{I_{CH^*}}$ and $I^{rms}_{CH^*}$, $\sigma_{\overline{I_{CH^*}}}$ and $\sigma_{I^{rms}_{CH^*}}$ respectively. Up to $\Pi \simeq 0.4$, $\sigma_{\overline{I_{CH^*}}}$ remains similar when the acoustic amplitude grows, but it suddenly increases at higher Π, which corresponds to the partial extinctions identified above. This indicates that from $\Pi \simeq 0.4$, a transition occurs towards a behaviour characterised by strong variations of the flame intensity that are not directly linked to acoustics, as those illustrated by the signal in Figure 5.29c. Compared to $\sigma_{\overline{I_{CH^*}}}$, $\sigma_{I^{rms}_{CH^*}}$ presents a linear increase with Π, showing that the flame response during short time intervals can present higher disparities at higher acoustic amplitudes.

[3] $R^2 = 1 - \frac{\sum_i (y_i - \tilde{y}_i)^2}{\sum_i (y_i - \overline{y})^2}$, in which y_i is the i-th experimental value of $I^{rms}_{CH^*}$, $\tilde{y}_i$ the value of y_i predicted by the best-fit line, and $\overline{y}$ the mean value of all the y_i.

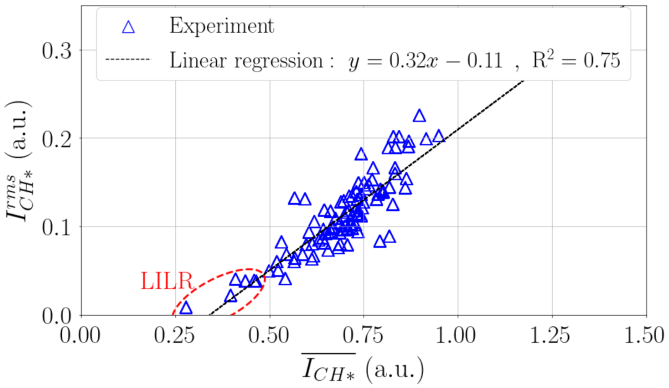

Figure 5.30: Correlation between the mean OH*-intensity and its rms oscillation amplitude at $f_r = 704$ Hz for 100 signals of duration ~ 28 ms, corresponding to about 20 acoustic cycles. Reduced acoustic pressure amplitude: $\Pi = 0.59$. LILR: low-intensity-low-response.

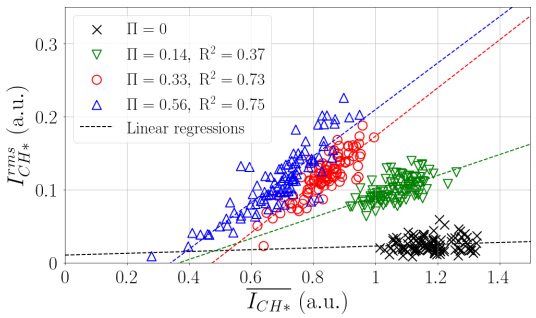

(a) Correlation between $\overline{I_{CH*}}$ and I^{rms}_{CH*}

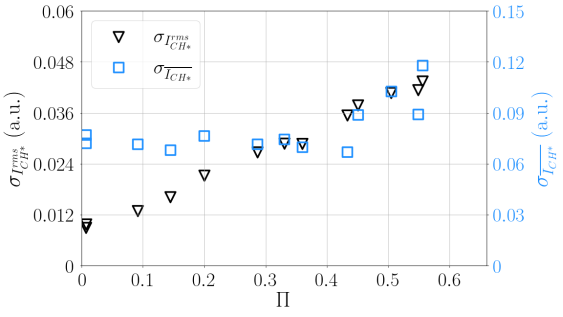

(b) Standard deviation of $\overline{I_{CH*}}$ and I^{rms}_{CH*} versus Π

Figure 5.31: Correlation between the mean and rms CH*-intensities of the central flame measured with PM for four acoustic amplitudes (left), and standard deviation of $\overline{I_{CH*}}$ and I^{rms}_{CH*} as a function of the reduced acoustic pressure amplitude Π (right).

5.4.2 Correlation between flame intensity oscillation and flame anchoring

To understand how the flame behaves with high-amplitude forcing, line-of-sight OH* emission images are captured at 20,000 Hz, simultaneously with PM acquisition of CH* emission for $\Pi = 0.59$. Four instantaneous images are compared in Figure 5.32, each one being captured slightly before a local minimum of the function $I_{cam} = f(t)$, which coincides with a local minimum of the function $I_{CH^*} = f(t)$, measured by PM. The zoomed-in view of the CH* intensity signal highlights that the flame intensity oscillation can drastically change in a few acoustic cycles: while the CH* intensity oscillation amplitude is large immediately before time t_A, it suddenly decreases to become two times weaker around t_B, which is only two acoustic periods after t_A. In addition, the CH* intensity oscillation is almost inexistent during two acoustic periods before t_C and increases afterwards to become discernible around $t_D = t_C + 2T$. At time t_A, around which the flame intensity oscillation is strong and the radical intensities averaged over one acoustic cycle are quite high, the flame is anchored close to the burner exit. At t_B, the cycle-averaged radical intensities and the flame response are weaker and the corresponding OH* image indicates a disorganisation of the flame base. The cycle-averaged radical intensities are even weaker at t_C and the flame response at f_r is inexistent, which is correlated to the substantial increase of the flame standoff distance. Two acoustic periods later, at t_D, the flame is anchoring closer to the burner exit as its foot propagates towards the burner. In the same time, the cycle-averaged radical intensities is higher and the flame response at the acoustic frequency becomes more intense.

The importance of flame anchoring on the flame intensity oscillation is further examined with the correlation between the simultaneous time-averaged flame standoff distance, $\overline{h_{base}}$, and flame intensity oscillation amplitude, $I^{rms}_{CH^*}$. For that purpose, post-synchronised simultaneous signals of the flame standoff distance $\overline{h_{base}}$ (determined from OH* images) and of CH* intensity, I_{CH^*} (measured with PM), are split into 15 shortened signals with a 50% overlap. All the shortened signals have an equal duration 0.013 s, corresponding to about 9.5 acoustic cycles. In each shortened signal of $\overline{h_{base}}$, the time-averaged value $\overline{h_{base}}$ is calculated and in each shortened signal of I_{CH^*}, the mean intensity, $\overline{I_{CH^*}}$, the rms oscillation amplitude at f_r, $I^{rms}_{CH^*}$, and the ratio between these two quantities is calculated.
Results for $\Pi = 0.59$ are given in Figure 5.33. $\overline{I_{CH^*}}$ globally decreases when $\overline{h_{base}}$ increases. This may be linked to the weakening of the propagative flame edge. Indeed, $\overline{I_{CH^*}}$ is a global quantity, which corresponds to the volume integration of the time-averaged volumetric CH*-intensity, $\overline{I_{v,CH^*}}$. The increase of the mean flame standoff distance may thus result in a decrease of the volume occupied by the flame, thus if $\overline{I_{v,CH^*}}$ remains constant, $\overline{I_{CH^*}}$ decreases. $I^{rms}_{CH^*}$ also diminishes when $\overline{h_{base}}$ increases. However, as shown in Section 5.3.2, the flame base participates negligibly to the flame intensity oscillation. One might therefore expect that the weakening of the flame edge would result in a decrease of $\overline{I_{CH^*}}$, but that $I^{rms}_{CH^*}$ would remain identical. This is obviously not the case. In addition, the ratio $I^{rms}_{CH^*}/\overline{I_{CH^*}}$ also decreases, indicating that the reduction of the level of $I^{rms}_{CH^*}$ is more pronounced than that of $\overline{I_{CH^*}}$.

This analysis highlights the importance of flame anchoring on its response to acoustics and suggests that the occasional destabilisation of the flame anchoring point participates to the saturation of the flame intensity oscillation. This destabilisation may be facilitated by the periodic oscillation of the swirl number, which is significantly modified during the acoustic cycle, illustrated for

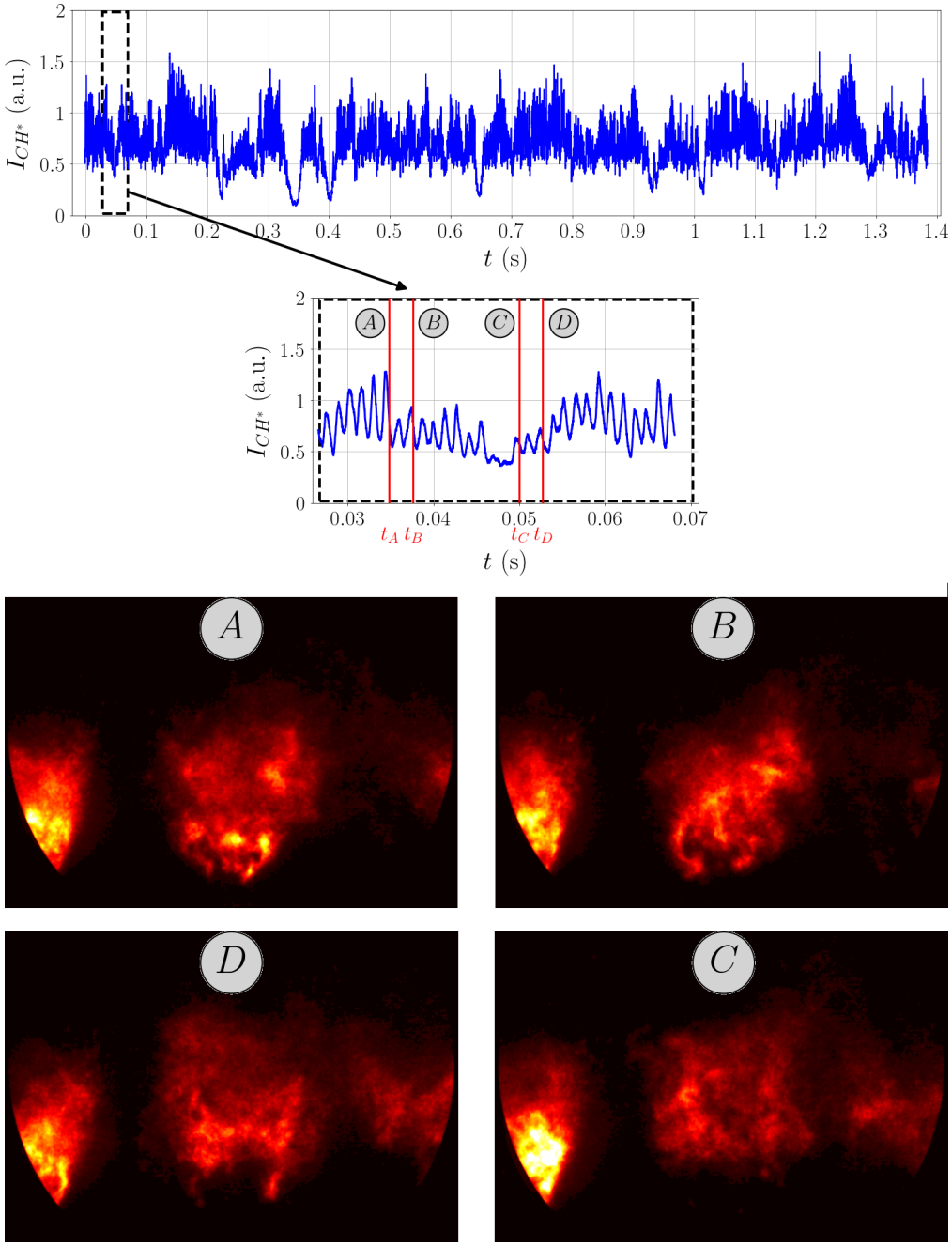

Figure 5.32: CH* emission signal of the central flame and OH* images for $\Pi = 0.59$. Top: CH* emission signal of the central flame captured by PM. A portion of the CH* signal is presented in the middle, in which vertical lines identified by A and B indicate the times corresponding to the OH* images shown at the bottom.

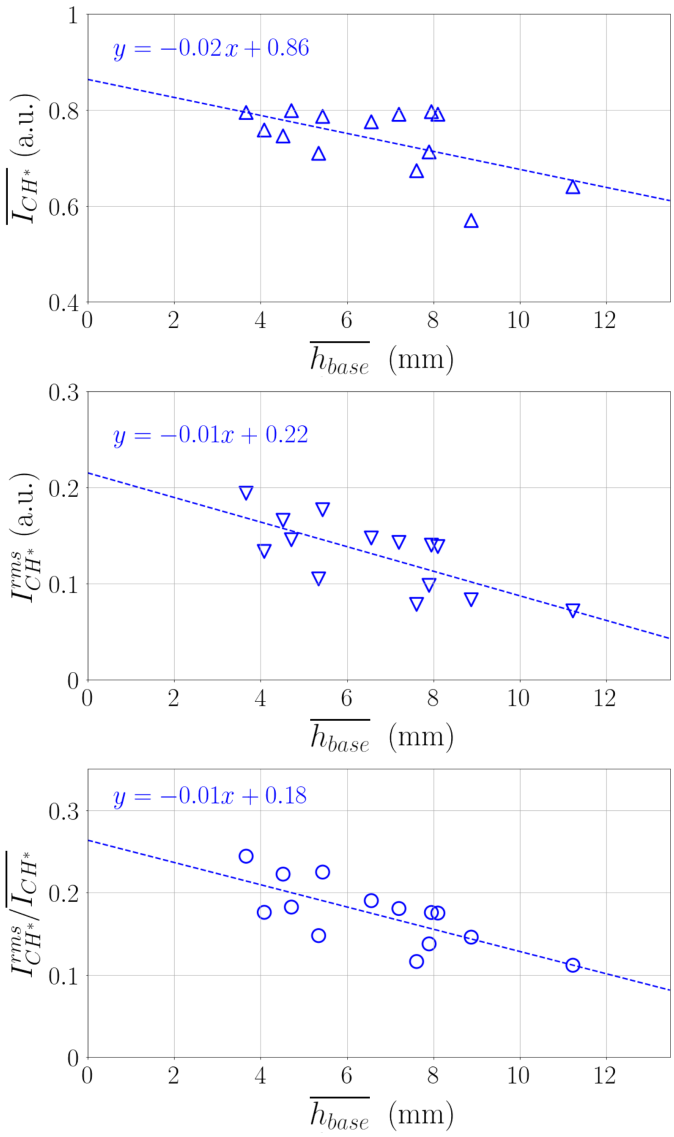

Figure 5.33: Correlation between the simultaneous mean flame standoff distance, $\overline{h_{base}}$, obtained from OH* images, and: top: mean CH*-intensity of the central flame, $\overline{I_{CH^*}}$; middle: rms oscillation amplitude at $f_r = 722$ Hz, $I^{rms}_{CH^*}$; bottom: $I^{rms}_{CH^*}/\overline{I_{CH^*}}$. The CH*-intensity is measured with a PM. This correlation is obtained for 15 signals of equal duration 0.013 s, corresponding to about 9.5 acoustic cycles. The reduced acoustic amplitude is $\Pi = 0.59$.

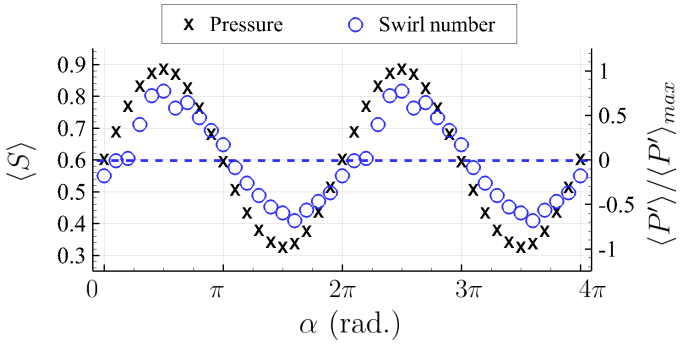

Figure 5.34: Phase-averaged swirl number oscillation at f_r measured at $z = 2.1$ mm post-synchronised with the acoustic pressure for $\Pi = 0.42$, $f_r = 716$ Hz. The oscillations are reproduced twice for the sake of clarity. The dash line indicates the mean swirl number, which is 0.6 here.

$\Pi = 0.42$ in Figure 5.34. The swirl number reaches values as low as 0.41 around the pressure minimum, leading to the periodic disruption of the CRZ.

5.5 Conclusion

This chapter presents the response of a linear array of swirling spray flames to acoustic pressure oscillations and the underlying mechanisms. This is made possible by placing the three-flame array such that the central flame is located at a pressure antinode of the standing transverse acoustic field. The global response of the energy system is characterised by using CH^* and OH^* radicals. Both of them capture the evolution of the flame response as the acoustic amplitude increases, characterised by a linear growth and a nonlinear behaviour. Therefore, the two radicals capture the underlying physical mechanisms. Although the response of the system is about 40% higher with CH^* than with OH^*, the phase shift between acoustic pressure and radical intensity oscillations is unchanged, showing that both radicals can be reasonably used to indicate the sign of the Rayleigh source term and thus the potential of the system to drive an instability. Two global Rayleigh indices, based on the broadband or the coherent oscillations, indicate that the Rayleigh source term is positive.

The mechanisms at the origin of the flame response are then explored. Spatially-resolved images of the CH^* or OH^* radicals highlight the convective propagation of a radical-intensity wave. This wave evolves during its propagation such that the flame response is mainly linked to the response of the flame middle region, which is also found to be the origin of the positive Rayleigh source term. Analyses of the air flow show the presence of axial velocity modulation at the injector exit in phase opposition with the acoustic pressure at the flame location. This modulation produces a periodic disorganisation of the swirling flow, highlighted by the periodic disruption of the CRZ, and the formation of a coherent vortex at the injector exit, which grows during its convection and is reflected by periodic changes of the flame shape. The axial velocity modulation also affects the spray, generating droplet number waves. The amount of droplets injected into the chamber oscillates in phase with the air flow axial velocity. Near the pressure minimum, the high amount of fuel is accompanied by a high air flow rate, whereas near the pressure max-

imum, the lower amount of fuel is accompanied by a lower air flow rate. This mechanism can explain why equivalence ratio fluctuations are weak here. In addition, the high droplet amount is injected quasi-simultaneously with the vortex shedding at the injector exit, *i.e.* near the pressure minimum. As a result, an effective air-fuel mixing is produced, giving rise to a strong spot of flame intensity at higher locations. Due to the convective processes, this high-intensity spot occurs in phase with the acoustic pressure and induces a positive thermoacoustic coupling.
An analysis of the flame response at high acoustic amplitudes indicates that saturation of the flame response is linked to the occasional destabilisation of the flame anchoring point, which might be facilitated by the strong oscillation of the swirl level during the acoustic cycle. These results provide new insights into the mechanisms coupling acoustics and swirl-stabilised spray flames at a pressure antinode of a standing transverse acoustic field.

Chapter 6

Influence of the thermal power on the flame response at a pressure antinode

Contents

This chapter examines the dynamics of the central flame placed at a pressure antinode for three operating conditions, characterised by different flame powers but the same equivalence ratio. For all the powers, CH and OH* radicals capture the mechanisms driving the evolution of the flame dynamics with the acoustic amplitude. The amplitude of the reduced flame intensity oscillation, $I^{rms}/\overline{I}$, transitions from a linear growth to a nonlinear evolution at the same value of the parameter Π for all the powers, where Π corresponds to the rms acoustic pressure amplitude reduced by the bulk aerodynamic pressure. This shows that the nonlinearities are governed by the balance between acoustics and aerodynamics. The gain of the flame describing function (FDF) increases with the flame power and its phase tends to zero, indicating that combustion is necessarily stable at the lowest power while it is potentially unstable at higher powers, consistently with an analysis of the thermaocoustic coupling based the Rayleigh criterion. The evolution of the phase with the flame power $\mathbb{P}$ is mainly linked to the modification of the convective processes. An analysis of the air flow modulation indicates that the vortex roll-up may be linked to swirl number oscillations rather than axial velocity oscillations. Analyses of the generation and transport of droplet number waves indicate that the high droplet amount is quite well correlated to the maximum of flame intensity oscillation. These results help in understanding mechanisms at the origin of the response of swirl-stabilised spray flames to a downstream acoustic pressure oscillation.*

6.1 Introduction

The previous chapter has shed light on the basics of flame response mechanisms to the acoustic pressure oscillation. This knowledge is important to give more insight about the main parameters driving thermoacoustic instabilities. One parameter of interest is the flame thermal power. In a recent study performed in the MICCA-Spray annular combustor inside which sixteen swirl-stabilised spray flames similar to those used in the present study are located, the EM2C team [141] drew up stability maps for a variety of flame thermal powers and equivalence ratios. In particular, they observed that at a given equivalence ratio, changing the flame power can modify the stability of the system (see Figure 6.1). A mechanism explaining the frequency shift of a self-excited oscillation in a swirl-stabilised kerosene spray flame was proposed by de la Cruz García et al. [89]. In this study, a combustor was operated at two conditions, named A and B, characterised by a same equivalence ratio $\phi = 0.75$ but two thermal powers of 54.5 kW and 76.4 kW respectively. When the flame power was increased, the peak frequency of the instability shifts from 220 Hz to 323 Hz, with the notable presence of harmonics at 440 Hz (for operating point A only) and 646 Hz. Using spray analysis, the authors noticed a decrease of the Sauter mean diameter (SMD) at a given location when the flame power increases, and even the disappearance of fuel droplets far from the injector, showing the enhancement of spray evaporation due to the higher air mass flow rate. They concluded that the spray evaporation plays a role in the appearance of self-sustained instabilities.

The purpose of this chapter is to provide elements to understand how changing the flame power while keeping a constant equivalence ratio influences the flame response and the thermoacoustic

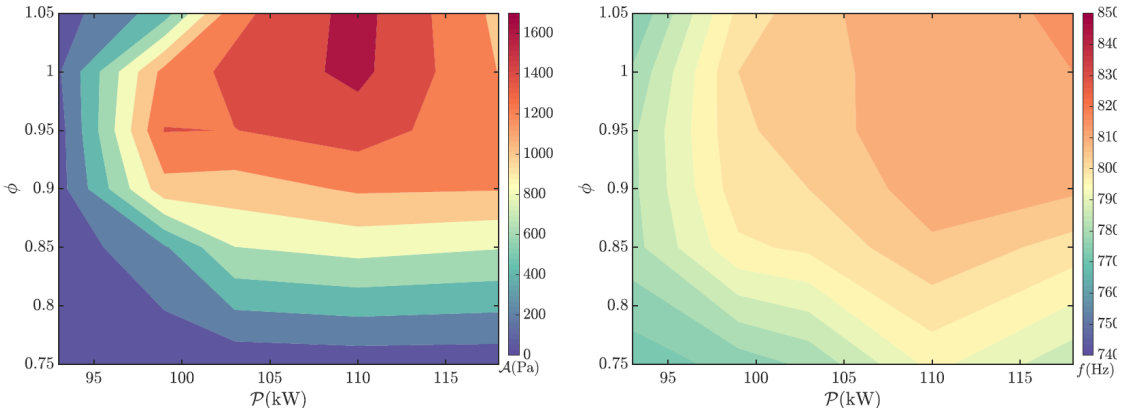

Figure 6.1: Stability maps as a function of thermal power $\mathbb{P}$ and equivalence ratio ϕ in the sixteen-injector annular combustor MICCA-Spray, with n-heptane as a fuel. The left column indicates the instability amplitude and the right column the instability frequency. Reproduced from [141].

coupling. Three operating points, whose characteristics are reported in Table 6.1 are used. Details about the experimental methods are found in Chapter 2. In Section 6.2, the energy system is described without acoustic forcing to highlight the fundamental differences to which it is submitted when the flame power is varied. In Section 6.3, the global flame response measured by PM to acoustic forcing is investigated, and the potential presence of equivalence ratio fluctuations is discussed. The coupling between combustion and acoustics is examined. Section 6.4 gives a spatially-resolved analysis of the flame response by means of high-speed flame imaging, in order to understand the longitudinal spatial structure of the flame subjected to a transverse acoustic forcing for various flame powers. In Section 6.5, the modifications of the air flow characteristics due to the power variations are examined. Finally, Section 6.6provides an analysis of the fuel spray modulation, giving elements to link the spray behaviour to the flame response to acoustics.

Name	$\mathbb{P}_{43}$	$\mathbb{P}_{59}$	$\mathbb{P}_{75}$
Flame power (kW)	4.3	5.9	7.5
ϕ		0.85	
$\dot{m}^f$ (g/s)	0.097	0.133	0.168
$\dot{m}^a$ (g/s)	1.72	2.35	2.99
U_b (m/s)	28.5	38.9	49.3
f_r (Hz)	704-720	714-722	732-740

Table 6.1: Operating points and experimental characteristics.

6.2 Energy system in the absence of acoustic forcing

6.2.1 Swirl-stabilised spray flame

The swirl-stabilised spray flames are first examined without acoustic forcing via OH*-chemiluminescence with a high-speed Phantom V2012 camera operated at 20,000 Hz. More details about the setup can be found in Section 2.2.3.2.

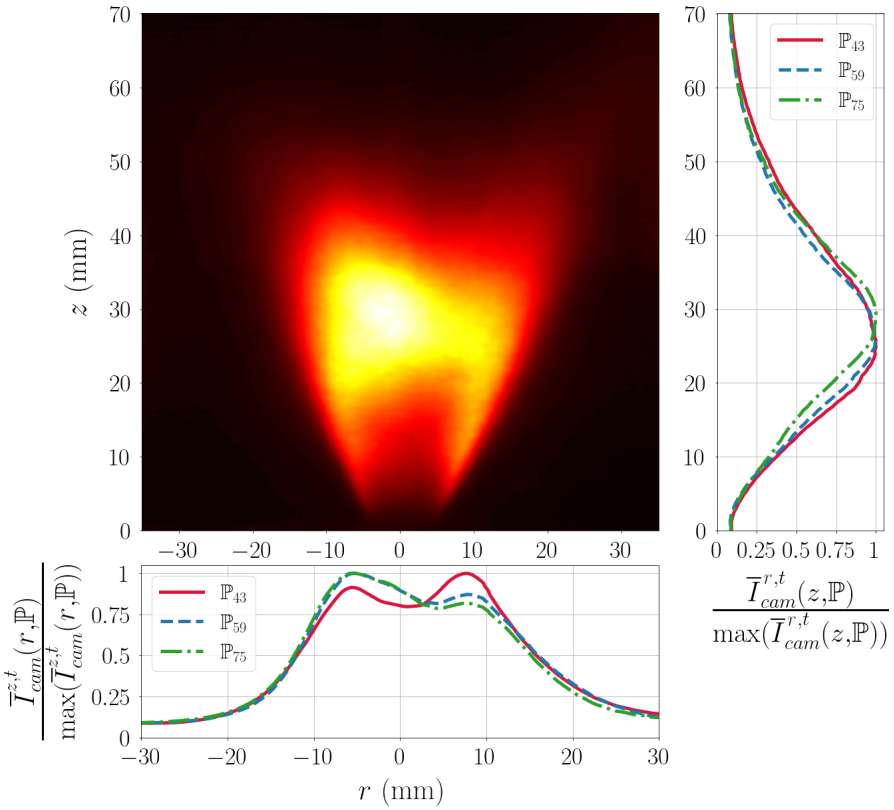

Figure 6.2: Time-averaged OH* intensity image from the central flame without acoustic forcing for $\mathbb{P}_{75}$; right side: reduced time-averaged vertical OH* intensity distribution, $\overline{I}^{r,t}_{cam}(z,\mathbb{P})/\max(\overline{I}^{r,t}_{cam}(z,\mathbb{P}))$ for the three flame powers; bottom: reduced time-averaged radial OH* intensity distribution $\overline{I}^{z,t}_{cam}(r,\mathbb{P})/\max(\overline{I}^{z,t}_{cam}(r,\mathbb{P}))$ for the three flame powers.

Flame extremity position	$\mathbb{P}_{43}$	$\mathbb{P}_{59}$	$\mathbb{P}_{75}$
$\overline{h}_{base}$ (mm)	3.3	2.9	2.2
$\overline{h}_{tip}$ (mm)	64.2	67.7	66.8
$\overline{L}_{flame}$ (mm)	60.9	64.8	64.6

Table 6.2: Mean flame standoff distance, $\overline{h}_{base}$, mean location of the flame tip, $\overline{h}_{tip}$, and flame length $L_{flame} = \overline{h}_{tip} - \overline{h}_{base}$ in the absence of acoustic forcing for the three flame powers.

The swirl-stabilised spray flames are characterised by an inverted conical shape, here called a V-shape, illustrated in Figure 6.2 with a time-averaged flame image for flame power $\mathbb{P}_{75}$. The time-averaged OH*-intensity image, given by the signal $\overline{I}^t_{cam}(r, z, \mathbb{P})$, where $\mathbb{P}$ is the flame power, is also integrated along $\vec{r}$ direction to give the time-averaged vertical OH* distribution, $\overline{I}^{r,t}_{cam}(z, \mathbb{P})$, or along $\vec{z}$ direction to give the time-averaged radial OH* distribution, $\overline{I}^{z,t}_{cam}(r, \mathbb{P})$. These distributions are expressed by:

$$\overline{I}^{z,t}_{cam}(r, \mathbb{P}) = \frac{1}{N_{rows}} \sum_{j=1}^{N_{rows}} \overline{I}^t_{cam}(r, z_j, \mathbb{P}) \tag{6.1}$$

$$\overline{I}^{r,t}_{cam}(z, \mathbb{P}) = \frac{1}{N_{cols}} \sum_{i=1}^{N_{cols}} \overline{I}^t_{cam}(r_i, z, \mathbb{P}) \tag{6.2}$$

Both of them are reduced by their maximum value, which is specific to each flame power. Figure 6.2 shows the flame power has no significant influence on the reduced longitudinal OH*-distribution, showing that the main flame intensity is found around $z = 30$ mm. The time-averaged flame standoff distance, $\overline{h}_{base}$, and the position of the flame tip, $\overline{h}_{tip}$, are calculated with the same threshold method applied to the images for the three flame powers (see Section 2.3.2.2 for more details about the method). Results are presented in Table 6.2. When the flame power increases, $\overline{h}_{base}$ gets slightly closer to the injector exit, which indicates a better flame stabilisation. The time-averaged flame length $\overline{L}_{flame} = \overline{h}_{tip} - \overline{h}_{base}$ remains similar for all the flame powers.

6.2.2 Characterisation of the fuel spray

The fuel spray is characterised for the three flame powers with the PDA system presented in Section 2.2.4. Figure 6.3 presents radial profiles of mean droplet data rate averaged over 4 seconds, $\overline{N}(r, \mathbb{P})$, arithmetic mean droplet diameter $d_{10}(r, \mathbb{P})$, and mean and rms velocity components of fuel droplet axial, tangential and radial velocities for $\mathbb{P}_{43}$, $\mathbb{P}_{59}$ and $\mathbb{P}_{75}$ at the burner exit ($z = 2.1$ mm).

The data rate profiles highlight the hollow-cone shape of the spray for the three powers. In the following of this chapter, the sparsely-populated region defined by $|r| < 2$ mm will be referred to as 'core region'. For all the flame powers, most of the droplets are located in an annular-shaped region.

Profiles of mean droplet diameter, $d_{10}(r, \mathbb{P})$, show a high sensitivity of the droplet size to the

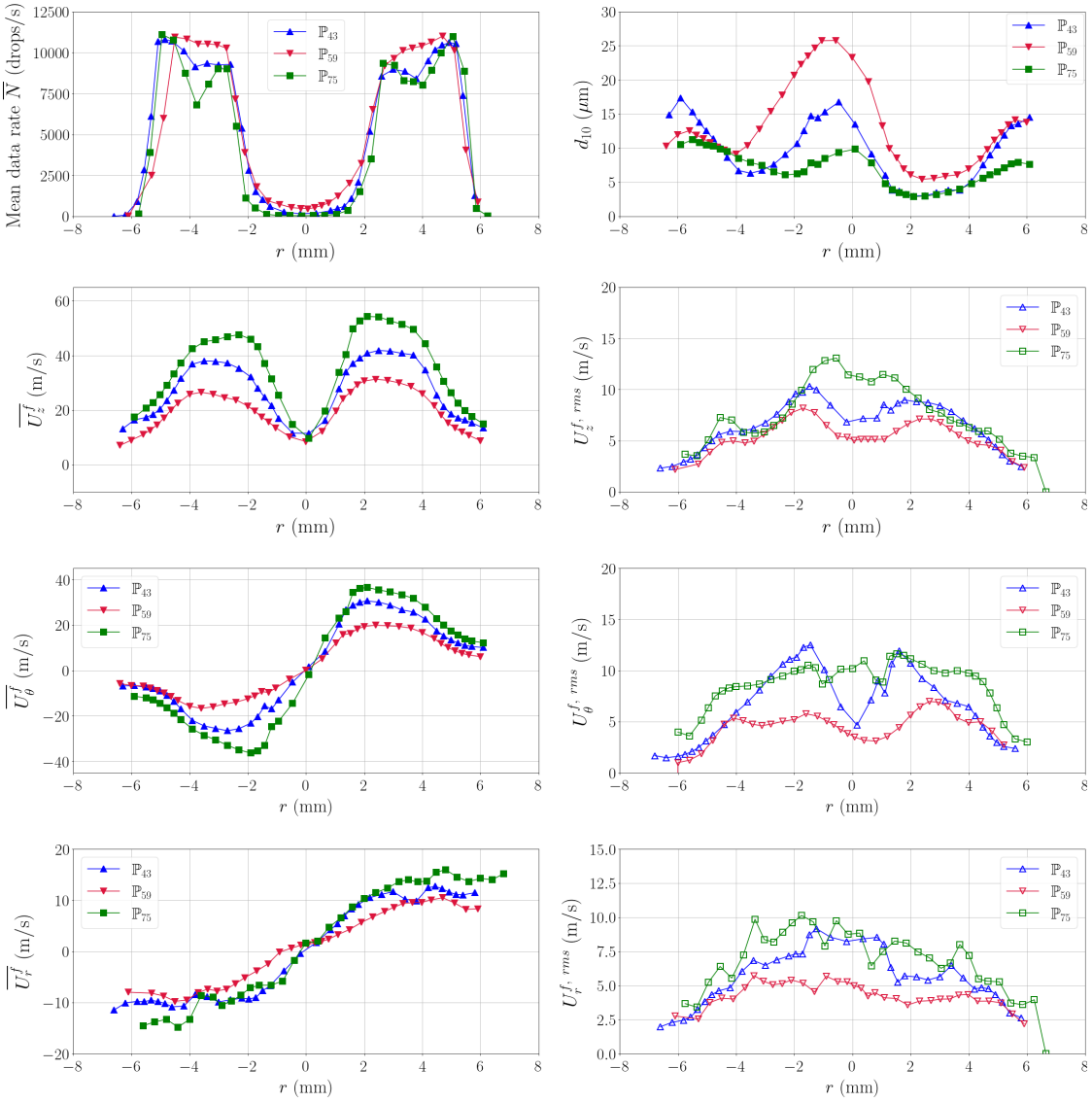

Figure 6.3: Fuel droplet radial profiles in the absence of acoustic forcing at $z = 2.1$ mm for flame powers $\mathbb{P}_{43}$, $\mathbb{P}_{59}$, and $\mathbb{P}_{75}$. The top row shows the profiles of $\overline{N}$ on the left and d_{10} on the right. The three lower rows show, from top to bottom, the profiles of axial velocity, tangential velocity and radial velocity respectively. The mean values are shown on the left column and the standard deviation on the right.

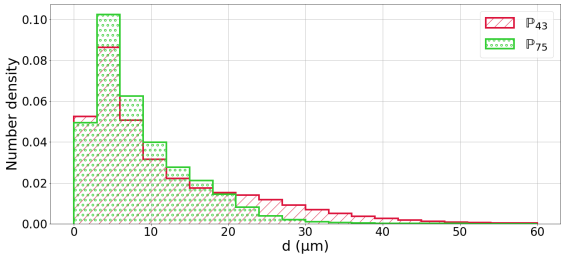

Figure 6.4: Normalised fuel drop size distribution in the absence of acoustic for operating points $\mathbb{P}_{43}$ and $\mathbb{P}_{75}$ along a radius at the injector exit ($z = 2.1$ mm).

mass flow rate in the core region, in which the mean diameter is about 2.5 times higher for $\mathbb{P}_{43}$ than for $\mathbb{P}_{75}$, while the mass flow rate is 1.73 times lower. Outside of the core, d_{10} profiles for the three flame powers get closer, particularly in the annular-shaped region where most of the droplets are injected. The drop size distribution of the whole spray is shown in Figure 6.4, for $\mathbb{P}_{43}$ and $\mathbb{P}_{75}$ only, for the sake of clarity. It shows the higher proportion of small droplets and the quasi-disappearance of droplets of $d \geq 30$ µm for $\mathbb{P}_{75}$, compared to $\mathbb{P}_{43}$ for which they remain clearly present. The reduction in the mean droplet diameter and the higher proportion of small droplets when the flame power increases, showing a better atomisation and suggesting an early evaporation, participate to the decrease of the flame standoff distance mentioned above.

We now focus on the radial fuel droplet velocity profiles at a fixed $z = 2.1$ mm shown in Figure 6.3. Profiles of mean fuel droplet axial velocity, $\overline{U_z^f}(r)$, are typical of swirling flows: they highlight a region of low velocity near the injector axis for the two flame powers, surrounded by an annular region of high axial velocity, with a maximum at $|r| \simeq 3$ mm. In the annular region, $\overline{U_z^f}(r)$ is proportional to the mass flow rate. At further radial locations, $\overline{U_z^f}(r)$ decreases. When the flame power changes, the mean axial velocity near the injector axis remains similar, but its rms is much changed. For $\mathbb{P}_{43}$, $U_z^{f,\,rms}$ is close to $\overline{U_z^f}$, suggesting that negative axial velocity components are sometimes measured. For $\mathbb{P}_{75}$, $U_z^{f,rms}$ is higher than $\overline{U_z^f}$ near the injector axis, indicating negative axial velocity values, characteristic of a CRZ. Nevertheless, in the core region, d_{10} is about 25 µm for $\mathbb{P}_{43}$ compared to 15 µm for $\mathbb{P}_{59}$ and 10 µm for $\mathbb{P}_{75}$, indicating that the lowest power is characterised by more ballistic droplets, which would have more difficulty to recirculate. This is admittedly a limitation to the current measurement, but it is restricted to the core region for $\mathbb{P}_{43}$, as shown in 6.2.3. Profiles of $\overline{U_\theta^f}$ and $\overline{U_r^f}$ show that for the two flame powers, the core region also feature low tangential and radial velocities. In $2\ \mathrm{mm} \leq |r| \leq 4\ \mathrm{mm}$, the high mean axial velocities are accompanied by high mean tangential velocities due to the swirling motion, whereas the mean radial velocities are lower.

6.2.3 Analysis of the air flow motion through measurements on the fuel spray

Some additional precautions must be taken to characterise the air flow from measurements performed on the fuel droplets. In this section, we evaluate the ability of the fuel droplets to follow the carrier air flow for flame powers $\mathbb{P}_{43}$ and $\mathbb{P}_{75}$. For this purpose, the local Stokes number is now introduced, $\mathrm{Stk}(r) = \frac{\rho^f d_{10}^2(r)\overline{U_z^f}(r)}{18\mu^a(r)D_{exit}}$, where d_{10} and U_z^f are calculated by including all the

droplets measured[1]. The lower the value of Stk, the better the air flow features are captured by the fuel droplets. Radial profiles of mean and rms axial velocity and of Stokes number of the fuel droplets for all the flame powers are given in Figure 6.5 at the injector exit ($z = 2.1$ mm) both with no drop size discrimination and for 1 µm $\leq d \leq$ 5 µm.

Near the injector axis ($|r| \leq 0.5$ mm), low mean axial velocities are well measured both without and with drop size discrimination for all the flame powers, in spite of the high Stk and d_{10} in this region for $\mathbb{P}_{43}$ (see Figure 6.3). $U_z^{f,rms}$ is almost twice higher with smaller droplets than with no drop size discrimination, and becomes higher than $\overline{U_z^f}$, indicating the occurrence of negative axial velocities. On the contrary, for $\mathbb{P}_{75}$, $U_z^{f,rms}$ is only about 20% higher with smaller droplets than with no drop size discrimination. This is consistent with profiles of Stk, as the values without or with drop size discrimination are closer for $\mathbb{P}_{75}$ than for $\mathbb{P}_{43}$. For $1\ \mathrm{mm} \leq r \leq 4\ \mathrm{mm}$, $\overline{U_z^f}$ is higher when calculated with the smaller droplets for the two flame powers. The difference between profiles obtained without and with drop size discrimination is more pronounced at locations where Stk is the higher with no drop size discrimination. Therefore, drop size discrimination has a bigger impact for $\mathbb{P}_{43}$, due to the higher d_{10}. A better accordance between $U_z^{f,rms}$ calculated without and with drop size discrimination is found than near the injector axis. For $r \geq 4\ (\mathrm{mm})$, both $\overline{U_z^f}$ and $U_z^{f,rms}$ are almost independent of the drop size discrimination.

These results show the main features of the air flow (*i.e.*, CRZ in the core region, annular jet) are fairly well captured with no drop size discrimination. This assumption is further investigated by comparing the swirl number calculated without and with drop size discrimination. When all the droplets are considered, it is 0.58 for $\mathbb{P}_{43}$ and for $\mathbb{P}_{75}$, identical to the value found for $\mathbb{P}_{59}$ (see Section 3.1.3). Measurements are also performed with coincident PDA for the lowest flame power, allowing to obtain the tangential velocity of C_1 fuel droplets. Considering only the C_1 fuel droplets leads to a swirl number value 3% higher. Therefore, it is reasonable to estimate the swirl number through measurements on all fuel droplets here.

6.3 Global flame response

6.3.1 Spatially-integrated flame response

In this subsection, the focus is on the response of the whole central flame to the transverse acoustic forcing. Flame dynamics is investigated with the PM equipped with a filter to capture either the OH*-radical intensity or CH*-radical intensity (see Section 2.2.3.1). The time-averaged intensity signals for CH* or OH* are first compared for the three flame powers. Then, the link between combustion and acoustics is further assessed with an instability index based on the Rayleigh criterion.

The mean chemiluminescence intensity of the flame, $\overline{I}(\Pi, \mathbb{P})$, the rms oscillation amplitude at f_r, $I^{rms}(\Pi, \mathbb{P})$, and the reduced rms intensity $I^{rms}/\overline{I}(\Pi, \mathbb{P})$ are compared for CH* or OH* as functions of the non-dimensional parameter Π for the three flame powers.

[1] ρ^f is the fuel droplet density and $\mu^a(r)$ the air dynamic viscosity, here calculated at 300 K for $|r| \leq 4$ mm and at 750 K for $|r| > 4$ mm.

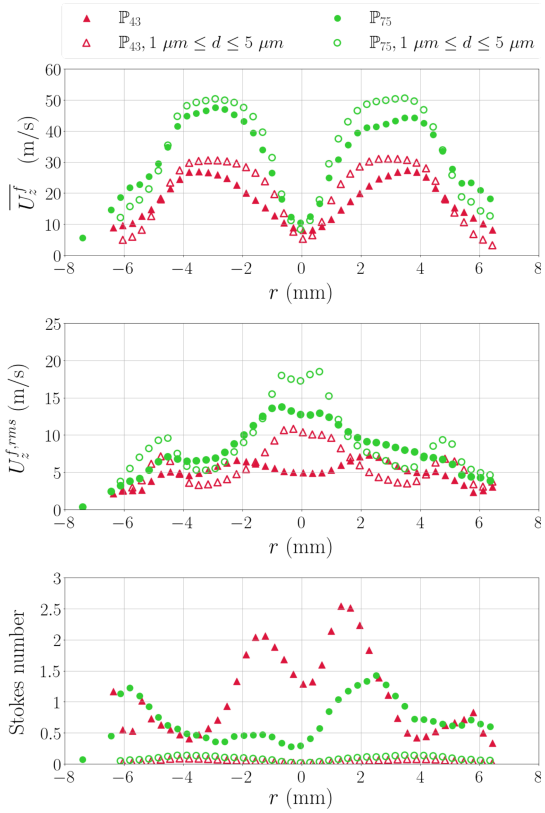

Figure 6.5: Fuel droplet radial profiles obtained from all the fuel droplets and for droplets of diameter d in the range $1 - 5$ µm at $z = 2.1$ mm for flame powers $\mathbb{P}_{43}$ and $\mathbb{P}_{75}$. Top: mean axial velocity, $\overline{U_z^f}$; middle: standard deviation of the axial velocity, $U_z^{f,\,rms}$; bottom: mean Stokes number. For clarity, data are plotted for $\mathbb{P}_{43}$ and $\mathbb{P}_{75}$ only.

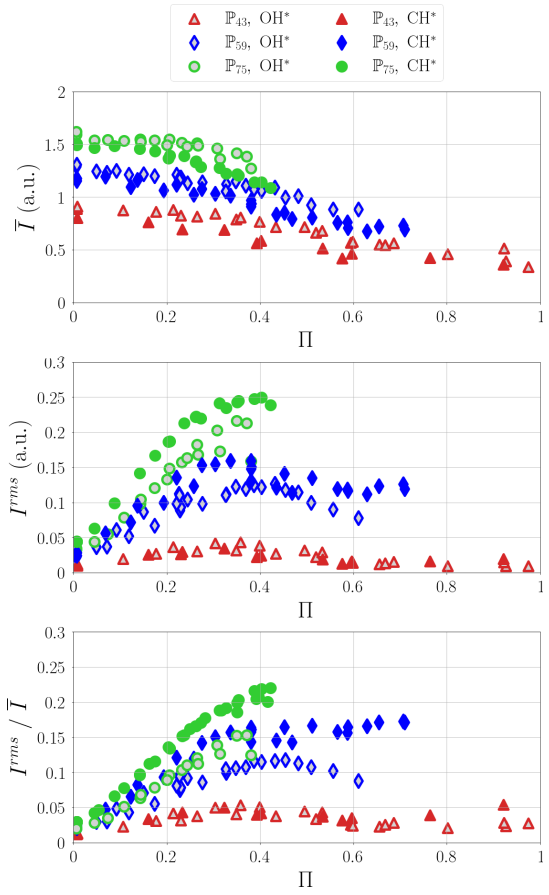

Figure 6.6: Response of the flame as a function of $\Pi = P^{rms}/\rho^a U_b^2$ for the three flame powers, and for CH* and OH* radicals. Top: Mean radical light intensity $\overline{I}(\Pi, \mathbb{P})$; middle: rms radical emission intensity ay f_r, $I^{rms}(\Pi, \mathbb{P})$; bottom:$I^{rms}/\overline{I}(\Pi, \mathbb{P})$.

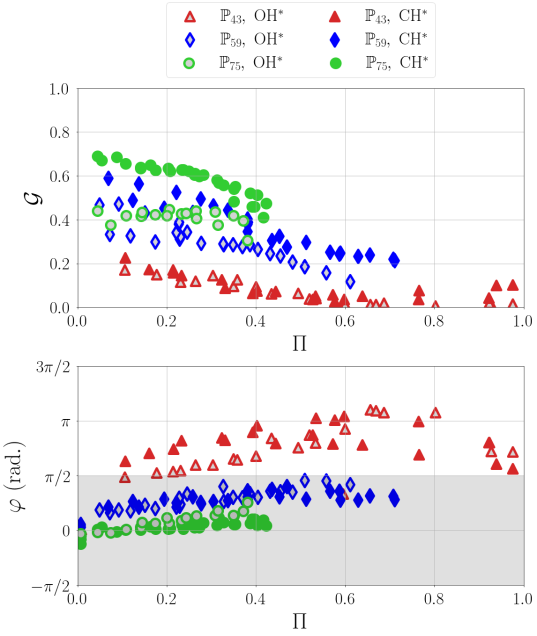

Figure 6.7: Flame describing function $\mathcal{F}$ vs. $\Pi = P^{rms}/\rho^a U_b^2$ for the three flame powers for CH* and OH* radicals. Top: gain, bottom: phase. The grey zone indicates the region of potential instability.

Results are reported in Figure 6.6. For all the flame powers and for both radicals, the flame response to acoustics is characterised by the following features. First, when Π increases up to $\Pi \simeq 0.3$, $\overline{I}$ decreases slightly and I^{rms} grows almost linearly. Secondly, for higher acoustic amplitudes, $\overline{I}$ presents a sharper decrease when Π increases and I^{rms} increases non-linearly, then saturates. As a result, $I^{rms}/\overline{I}(f_r, \Pi, \mathbb{P})$ grows quasi-linearly up to $\Pi = \Pi_{trans} \simeq 0.35$, then enters a transition zone up to $\Pi = \Pi_{sat} \simeq 0.45$, above which it saturates. The same values of Π_{trans} and Π_{sat} found for all the flame powers indicate that Π is a relevant parameter to describe the flame response to acoustics. This indicates that the linear, transition and saturation zones are controlled by a balance between acoustics and aerodynamics. These results also show that both CH* and OH* are capable to capture the mechanisms driving the flame response for a variety of flame powers in these non-sooty flames. This is consistent with results obtained in [45, 166].

The flame response to acoustics can also be investigated in the FDF framework at frequency f_r. The expression of the FDF in the complex space is recalled:

$$\mathcal{F}(f_r, \Pi) = \frac{\breve{I}/\overline{I}}{\breve{P}/\rho^a U_b^2} = \mathcal{G}_{P'}(\Pi) e^{i\varphi_{P'-I'}(\Pi)} \tag{6.3}$$

In the following, $\mathcal{G} = \mathcal{G}'$ and $\varphi = \varphi_{P'-I'}$ for clarity. Results for the three flame powers are shown in Figure 6.7 (top), where I is measured with CH* or OH*. The gain of the FDF is another representation of the relationship between $I^{rms}/\overline{I}$ to Π. For all values of Π, the gain $\mathcal{G}$ increases when the flame power increases, as well as $I^{rms}/\overline{I}$. In the linear zone ($\Pi \leq 0.35$),

the gain decreases a little, indicating that the relationship between the amplitudes of the radical intensity oscillation and acoustic pressure oscillation is roughly proportional, although small nonlinearities are present. Above Π_{trans}, the gain clearly decreases, showing the presence of nonlinear mechanisms. When Π exceeds Π_{sat}, the gain has already significantly reduced but continues to decrease with Π. For $\mathbb{P}_{43}$, the gain is close to 0 for $0.6 \leq \Pi \leq 0.8$, showing that the coherent oscillation of the flame intensity at f_r is insignificant. The insights about the saturation given in Section 5.4 have demonstrated the role of flame anchoring on its intensity oscillation. Further investigation about the saturation process is done in Chapter 7 for $\mathbb{P}_{43}$.

The FDF also contains the information about the phase shift between $P^{'}(t)$ and $I^{'}(t)$ through the variable φ. This quantity is of primary interest to determine whether a system is prone to drive an instability, according to the Rayleigh criterion (see Section 1.2.2). For an acoustically compact flame (see Section 1.2.3), the system could drive an instability if acoustic pressure and global HRR oscillations of the flame are in phase, which corresponds to $-\pi/2 < \varphi < \pi/2$. Nevertheless, this is not a sufficient condition, as in practice, the Rayleigh source term must also exceeds the sum of the damping terms and the acoustic flux terms. However, knowing the sign of the Rayleigh source term can give first insights about the ability of the system to drive an instability, as indicated in Section 5.2.3. In Figure 6.7 (bottom), the potential instability region, defined by $-\pi/2 < \varphi < \pi/2$, is depicted by a grey band.
The flame power has a substantial impact on the phase. While for the lowest power, combustion and acoustics interfere destructively, the phase progressively tends to zero when the flame power increases, leading to a constructive interference. Moreover, the increase of the phase with Π is observed for all the flame powers. This suggests that, when the acoustic amplitude increases, the limit cycle amplitude can be affected not only by the gain drop, but also by the change of the phase, the combination of which could strengthen or weaken the thermoacoustic coupling.
For $\Pi > 0.6$, only observed for $\mathbb{P}_{43}$ due to limitations of the acoustic forcing system, the phase stops increasing and even decreases with increasing acoustic amplitudes. However, while the coherence function between acoustic pressure and radical intensity signals at f_r is higher than 0.8 for $\Pi \leq 0.3$, it can reach values as low as 0.4 at higher acoustic amplitudes for the lowest flame power. The latter case indicates that the radical intensity oscillation is admittedly perturbed at the highest acoustic amplitudes, but essentially by noise and that acoustics and combustion are now not strongly related. Although the phase varies with Π, $\mathbb{P}_{43}$ is characterised by a phase following $+\pi/2 < \varphi < +\pi$ for almost all acoustic amplitudes, showing a destructive interference between combustion and acoustics. For the two highest flame powers, the modification of φ with Π is less pronounced than for $\mathbb{P}_{43}$. The phase remains in the potential instability region both for $\mathbb{P}_{59}$ and $\mathbb{P}_{75}$, indicating that the constructive combustion-acoustics interference is kept in all the range of amplitudes studied.

To conclude, these results strongly suggest that the thermoacoustic coupling increases with the flame power, which stems from two different mechanisms, namely: i) the higher gain of the FDF and ii) the progressive phasing between acoustic pressure and HRR oscillations.

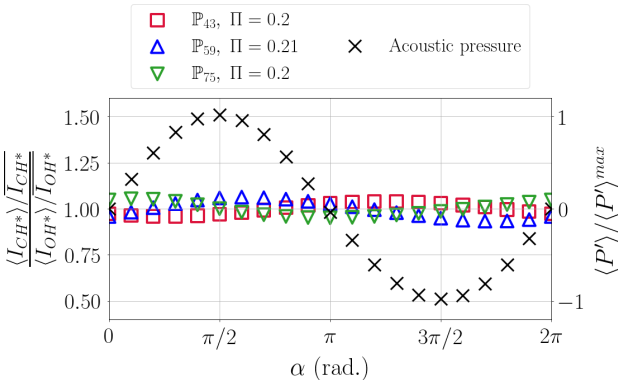

Figure 6.8: Relative equivalence ratio fluctuations estimated with the ratio between the reduced phase-averaged CH* and OH* intensities measured with PM.

6.3.2 Equivalence ratio fluctuations

The ratio of the chemiluminescence intensity from two species has been used to determine equivalence ratio fluctuations in partially-premixed flames, as discussed in Section 5.2.2. As shown above, both CH* and OH* are able to capture the physical mechanisms of flame response. Nevertheless, it is interesting to examine the presence of equivalence ratio fluctuations due the difference of $I^{rms}/\overline{I}$ measured with these two radicals. The phase-averaged ratio between the reduced rms intensity measured with CH* and with OH*, $(\langle I_{CH^*}\rangle/\overline{I_{CH^*}})/(\langle I_{OH^*}\rangle/\overline{I_{OH^*}})$, is illustrated for the three flame powers and $\Pi = 0.2$ in Figure 6.8. For all the flame powers, $(\langle I_{CH^*}\rangle/\overline{I_{CH^*}})/(\langle I_{OH^*}\rangle/\overline{I_{OH^*}})$ remains within the range 93-107 %, similar to the value found for a perfectly premixed flame with a similar injector [53]. This supports that the energy system operates close to a premixed regime with n-heptane for all the flame powers.

6.3.3 Thermoacoustic coupling

The stability of the operating points can be estimated by evaluating an instability index based on the Rayleigh criterion. As indicated by the Rayleigh criterion, the potential of a flame to drive an unstable behaviour can be estimated by the sign of $P'\dot{Q}'$, where $\dot{Q}'$ is the global HRR oscillation (see Section 1.2.3). The higher the value of $P'\dot{Q}'$, the greater the probability of the flame to drive an instability, since it can surpass stronger damping processes. A good estimate of the phase of $\dot{Q}'(t)$ can be obtained by means of $I'_{CH*}(t)$ or $I'_{OH*}(t)$ for $\mathbb{P}_{59}$ and $\mathbb{P}_{75}$, as shown by the similar value of the FDF phase φ with both radicals (see Section 6.3.1) and the negligible equivalence ratio fluctuations shown above. This is a priori different for $\mathbb{P}_{43}$, for which φ has little different values with CH* and OH* (see Figure 6.7 (bottom)). Nevertheless, with both radicals, φ remains outside the instability region, and it is shown below that for $\mathbb{P}_{43}$, the choice of the radical does not modify the following analysis.

As the intensity $I(t)$ is obtained from the whole flame and $P'(t)$ is measured at the location of the acoustically-compact flame, an instability index based on the Rayleigh criterion is here

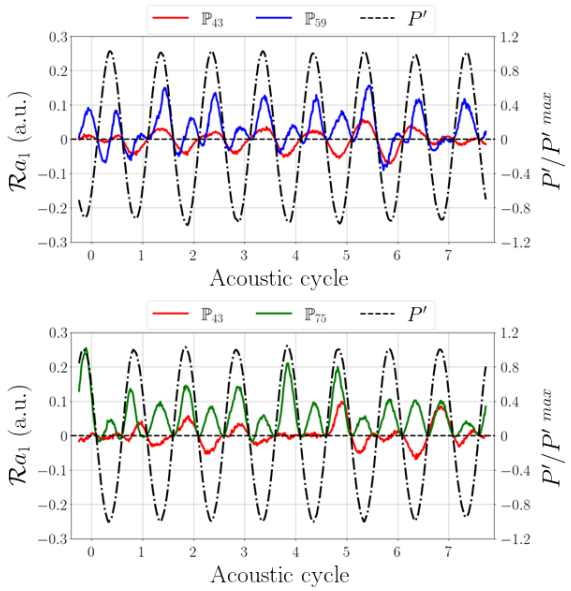

Figure 6.9: Instantaneous instability index $\mathcal{R}a_1(t) = \xi P^{'} I^{'}(t)$ synchronised with the acoustic pressure for $\Pi \simeq \Pi_{trans}$. On the top plot, $\mathcal{R}a_1(t)$ is obtained with $I^{'}(t)$ measured with CH* for $\mathbb{P}_{43}$ ($f_r = 704$ Hz, $\Pi = 0.26$) and $\mathbb{P}_{59}$ ($f_r = 722$ Hz, $\Pi = 0.29$). On the bottom plot, $\mathcal{R}a_1(t)$ is obtained with $I^{'}(t)$ measured with OH* for $\mathbb{P}_{43}$ ($f_r = 707$ Hz, $\Pi = 0.24$) and $\mathbb{P}_{75}$ ($f_r = 732$ Hz, $\Pi = 0.28$).

defined by:

$$\begin{aligned} \mathcal{R}a_1(t) &= \frac{P^{'}(t)}{\rho^a U_b^2} \times \frac{I^{'}(t)}{\overline{I}} \\ &= \xi P^{'} I^{'}(t) \end{aligned} \tag{6.4}$$

In this expression, the product between acoustic pressure and radical light intensity oscillations is multiplied by a factor $\xi = 1/(\rho^a U_b^2 \overline{I})$ which is inversely proportional to the aerodynamic bulk pressure, making the instability index insensitive to the increase of P^{rms} necessary to reach the same Π when the flame power increases. The time evolution of $\mathcal{R}a_1(t)$ is illustrated in Figure 6.9 during several acoustic cycles, for the three flame powers at $\Pi \simeq \Pi_{trans}$, with CH* (top) and OH* (bottom). When two signals oscillate at a same frequency f_r, their product oscillates at $2f_r$. Therefore, $\mathcal{R}a_1(t)$ is expected to oscillate at $2f_r$. For $\mathbb{P}_{43}$, $\mathcal{R}a_1(t)$ oscillates weakly around 0 with both CH* and OH*. This weak oscillation mainly occurs at frequency f_r. For $\mathbb{P}_{59}$ and $\mathbb{P}_{75}$, $\mathcal{R}a_1(t)$ reaches higher positive values, whereas negative values are more scarce, indicating a reinforcement of the coupling between combustion and acoustics. Moreover, $\mathcal{R}a_1(t)$ mainly oscillates at $2f_r$.

To investigate how $\mathcal{R}a_1(t)$ oscillates over the whole signal duration, its time-resolved frequency content is explored for the three flame powers at $\Pi \simeq \Pi_{trans}$ by using the short-time Fourier transform (STFT). Results are displayed in Figure 6.10. For the three flame powers, the oscillation of $\mathcal{R}a_1(t)$ at $2f_r$ is detected but, for $\mathbb{P}_{43}$, its magnitude is so weak that it barely stands out from the background noise: at some instants, *e.g.* $t \simeq 0.9$ s and $t \simeq 1.2$ s, it even has a

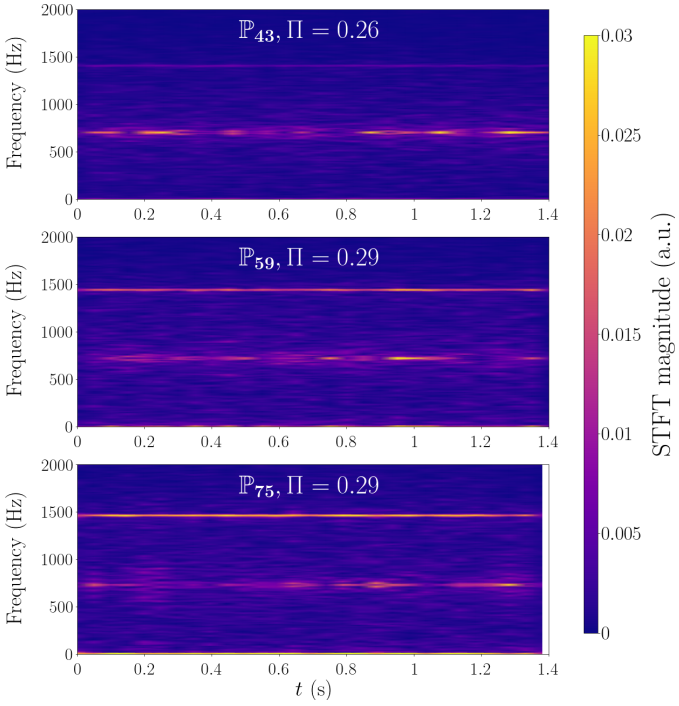

Figure 6.10: Short-Time Fourier Transform of $\mathcal{R}a_1(t) = \xi P^{'} I^{'}(t)$ for the three flame powers and $\Pi \simeq \Pi_{trans}$. $I^{'}(t)$ is measured with CH*-chemiluminescence.

level similar to that of the background noise. In addition, an oscillation at f_r is sometimes remarked, as indicated by brighter spots in the STFT. Although these spots have a short duration, they can reach higher magnitudes than at $2f_r$. It is remarkable that the strong spots at f_r occur simultaneously with notable decreases of the STFT magnitude at $2f_r$. At the two higher flame powers, a continuous oscillation of $\mathcal{R}a_1(t)$ at $2f_r$ is clearly detected, showing a well-established coupling between combustion and acoustics, which is all the more strong as the flame power is high. Moreover, the response at f_r decreases as the flame powers grows, such that $\mathcal{R}a_1$ oscillates mainly at $2f_r$ at $\mathbb{P}_{59}$ and $\mathbb{P}_{75}$. This difference in frequency response is explained in the following.

As seen in Section 5.2.3.1, the radical intensity signal $I(t)$ corresponds by the sum of a mean component $\overline{I}$, a coherent oscillation at f_r, $I^c(t)$ and a stochastic fluctuation, $I^s(t)$, following the decomposition of Hussain & Reynolds [154]. In this framework, $I'(t) = I^c(t) + I^s(t)$. It was shown in Section 5.2.3.2 that a notable oscillation of $\mathcal{R}a_1(t)$ at frequency f_r was linked to stochastic fluctuations that become significant compared to coherent oscillations. For $\mathbb{P}_{43}$, the weak flame response at f_r highlighted above indicates that coherent oscillations are small. As a consequence, $I(t)$ is easily perturbed by the stochastic fluctuations contrary to the intensity for the two higher flame powers, and the instability index $\mathcal{R}a_1(t)$ features a clear oscillation at f_r (see Figure 6.10). This component at f_r can be removed from the instability index by defining a

new index:

$$\mathcal{R}a_2(t) = \frac{P^c(t)}{\rho^a U_b^2} \times \frac{I^c(t)}{\overline{I}} \tag{6.5}$$

$$= \xi P^c I^c(t) \tag{6.6}$$

$\mathcal{R}a_2(t)$ is based only on the coherent oscillation at f_r of the acoustic pressure and radical intensity signals. The difference between the STFT of $\mathcal{R}a_1(t)$ and that of $\mathcal{R}a_2(t)$ was highlighted in Figure 5.6: $\mathcal{R}a_2$ only oscillates in a tight range around $2f_r$.
It is now interesting to observe how $\mathcal{R}a_1(t)$ and $\mathcal{R}a_2(t)$ behave for the three flame powers investigated in this chapter, by means of their probability density function (PDFs) illustrated for $\Pi \simeq \Pi_{trans}$ in Figure 6.11. For the three flame powers, the PDF of $\mathcal{R}a_1(t)$ is more spread out than that of $\mathcal{R}a_2(t)$, which results from the inclusion of the stochastic fluctuations. When the flame power increases, the discrepancy between the PDFs of $\mathcal{R}a_1(t)$ and $\mathcal{R}a_2(t)$ is reduced. This arises from the stronger contribution of $I^c(t)$ to $I'(t)$. In other words, $I'(t)$ resembles more and more $I^c(t)$ when the flame power increases.

Although the PDFs of the two instability indices are different, their respective mean values $\overline{\mathcal{R}a_1}$ and $\overline{\mathcal{R}a_2}$ are identical for the three flame powers, as illustrated in Figure 6.11. This confirms the observation made with $\mathbb{P}_{59}$ in Section 5.2.3.2. It is a good indicator of the fulfillment of the Rayleigh criterion: for a positive value of $\overline{\mathcal{R}a}$, the system could potentially drive an instability while for a negative value, combustion is stable. As shown in Section 6.3.3, $\overline{\mathcal{R}a_1}$ is negative for $\mathbb{P}_{43}$ while it is positive for $\mathbb{P}_{59}$ and $\mathbb{P}_{75}$. Hence, $\mathbb{P}_{43}$ should lead to stable combustion, whereas the two higher flame powers could drive an instability. In addition, the higher $\overline{\mathcal{R}a}$ is, the more likely the system is to be unstable, which means that $\mathbb{P}_{75}$ is more likely than $\mathbb{P}_{59}$ to lead to self-excited instabilities. This is consistent with results found in the MICCA-Spray annular combustor, in which instabilities were found at operating conditions very close to those of $\mathbb{P}_{75}$ [141, 174].

6.4 Local flame response to acoustics

The space-time flame response is now more deeply investigated by using high-speed image sequences to get time-resolved chemiluminescence intensity distributions from OH* radical. Camera and intensifier settings remained unchanged for all the flame powers, allowing quantitative comparisons. The analysis performed for the three flame powers focuses on the response for $\Pi \simeq \Pi_{trans}$. Phase-averaged vertical profiles $\langle I_{cam} \rangle(z, \alpha, \mathbb{P})$ are obtained from the image series by radial integration of the OH*-images. This method, presented in Section 2.3.2.1, allows to focus on the longitudinal OH*-intensity wave induced by the acoustic perturbation, which is a major mechanism of flame response (see Section 5.3.2). Results are shown for $0 < z < 71$ mm along a reconstructed acoustic cycle repeated three times for the sake of clarity in Figure 6.13.
For all the flame powers, the following features can be noted. First, at a given z_j, $\langle I_{cam} \rangle(z_j, \alpha, \mathbb{P})$ oscillates during the acoustic cycle. Secondly, the local maximum of $\langle I_{cam} \rangle(z, \alpha, \mathbb{P})$ propagates downstream. The OH*-intensity oscillation can thus be seen as a wave propagating towards the increasing z-locations. Finally, the oscillation of $\langle I_{cam} \rangle(z, \alpha, \mathbb{P})$ is weak in the lower region of the flame and the flame tip region, whereas stronger oscillations are found in the middle region

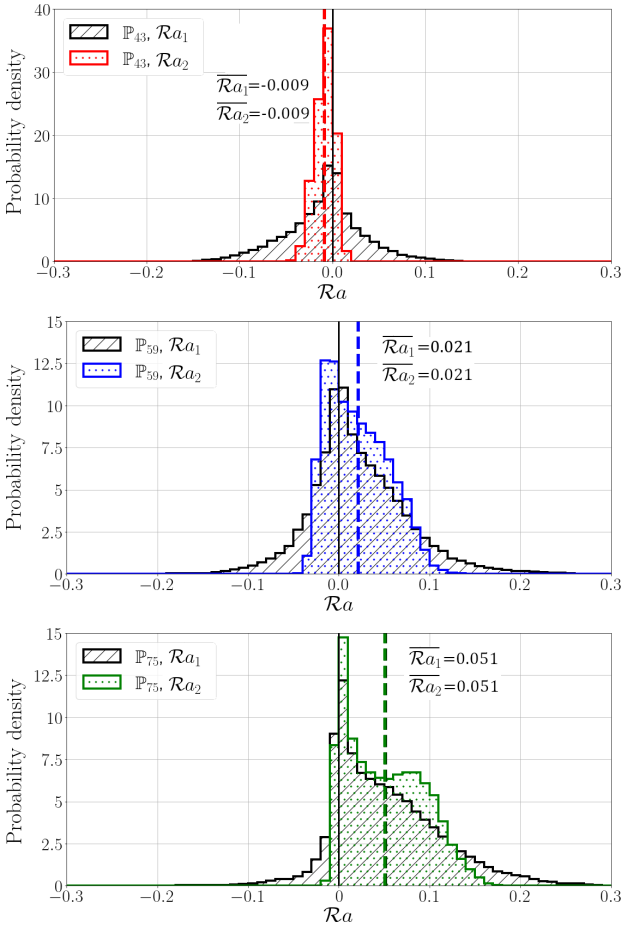

Figure 6.11: Probability density functions of the instability indices $\mathcal{R}a_1(t)$ and $\mathcal{R}a_2(t)$. Top: $\mathbb{P}_{43}$, $f_r = 704$ Hz, $\Pi = 0.26$; middle $\mathbb{P}_{59}$, $f_r = 722$ Hz, $\Pi = 0.29$; bottom $\mathbb{P}_{75}$, $f_r = 732$ Hz, $\Pi = 0.29$. $I'(t)$ is measured with CH*. The mean values of the distributions are indicated on each subfigure and marked by the vertical dash lines. For each flame power, coloured and black dash lines are superimposed.

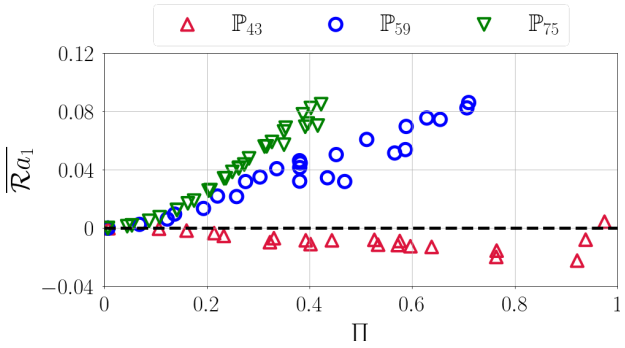

Figure 6.12: Time-averaged value $\overline{\mathcal{R}a_1}$ for the three flame powers, with $I'(t)$ measured with CH*. The horizontal black dash line indicates $\overline{\mathcal{R}a_1} = 0$.

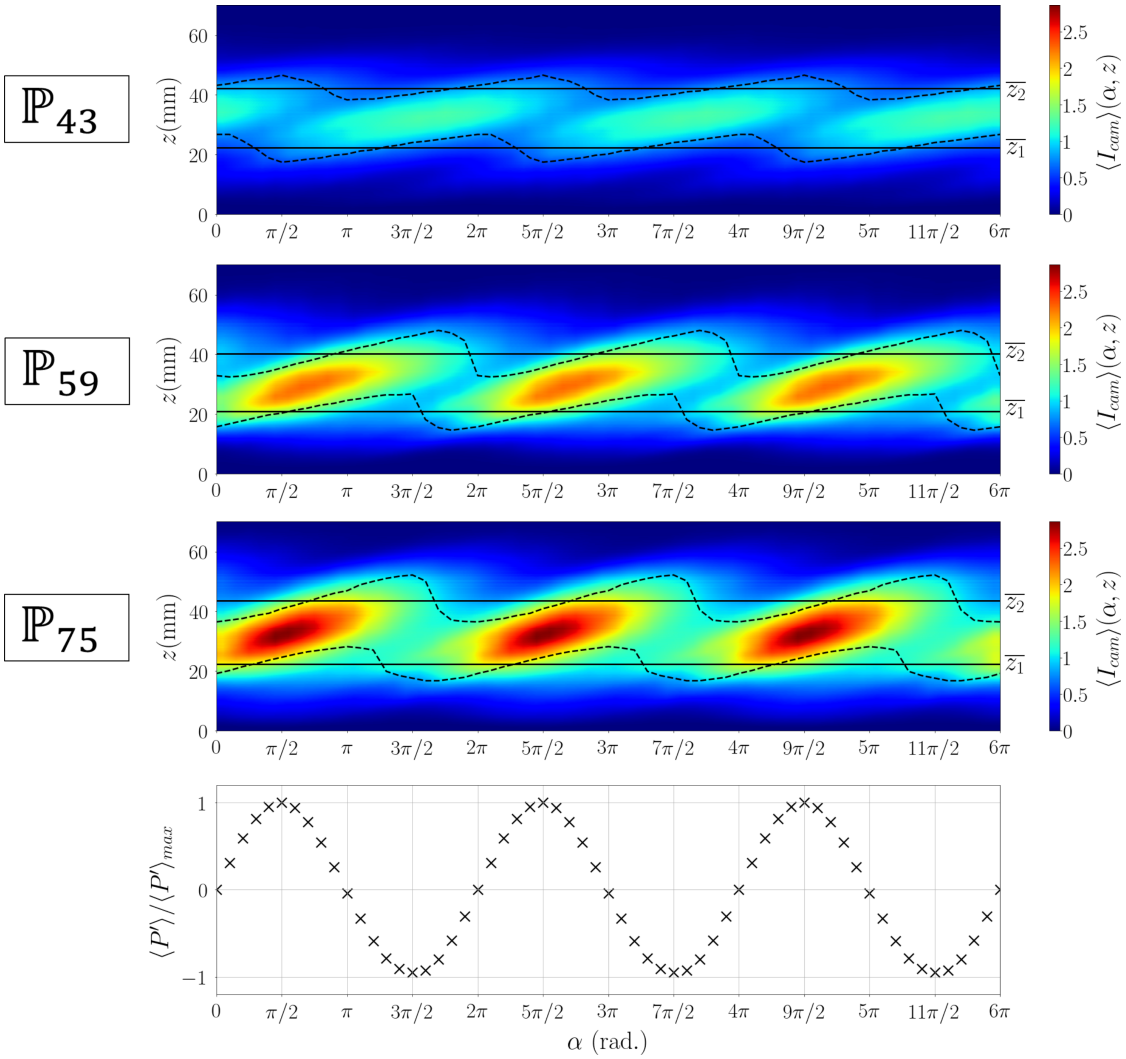

Figure 6.13: Phase-averaged OH*-intensity level $\langle I_{cam}\rangle(z, \alpha)$ for $\Pi = 0.35 \simeq \Pi_{trans}$ post-synchronised with a reconstructed acoustic cycle reproduced three times. For $\mathbb{P}_{43}$, $f_r = 704$ Hz; for $\mathbb{P}_{59}$, $f_r = 722$ Hz; for $\mathbb{P}_{75}$, $f_r = 732$ Hz. The associated reconstructed acoustic pressure cycle is shown at the bottom. The dash lines are defined by $\langle I_{cam}\rangle(z, \alpha, \mathbb{P})/\max_{z_0 \leq z \leq z_3}(\langle I_{cam}\rangle(z, \alpha, \mathbb{P})) = 0.65$ and the two horizontal solid lines indicate the cycle-averaged vertical locations of the two dash lines, z_1 and z_2.

Height	$\mathbb{P}_{43}$	$\mathbb{P}_{59}$	$\mathbb{P}_{75}$	$\mathbb{P}_{75}(\Pi = 0)$
$\overline{z_0}$ (mm)	5.5	5.3	3.2	2.2
$\overline{z_1}$ (mm)	22.3	20.9	22.3	-
$\overline{z_{1.5}}$ (mm)	32.2	30.6	32.9	-
$\overline{z_2}$ (mm)	42.2	40.3	43.6	-
$\overline{z_3}$ (mm)	66.7	68.1	71	66.8

Table 6.3: Location of the boundaries of the flame regions for $\Pi = 0.35$. For each flame power, $\overline{z_0}$ is the mean flame standoff distance above the burner and $\overline{z_3}$ is the mean location of the flame tip. $\overline{z_1}$ and $\overline{z_2}$ are the mean positions of the two isolines defined by $\langle I_{cam}\rangle(z,\alpha)/\max(\langle I_{cam}\rangle(z,\alpha)) = 0.65$.

of the flame. To separate the flames into regions, two isolines are defined by $\langle I_{cam}\rangle(z,\alpha,\mathbb{P})/\max_{\overline{z_0}\leq z\leq \overline{z_3}}(\langle I_{cam}\rangle(z,\alpha,\mathbb{P})) = 0.65$, where $\overline{z_0}$ is the time-averaged flame standoff distance and $\overline{z_3}$ the time-averaged location of the flame tip. The phase-averaged locations of the two isolines are represented by the dash lines, while their cycle-averaged locations, $\overline{z_1}$ and $\overline{z_2}$ respectively, are indicated by the solid lines. In the following, only the solid lines are considered to separate the flames into regions, so that each region keeps the same size during the cycle. The lower region, called R_1, is defined by $\overline{z_0} \leq z < \overline{z_1}$, the middle region R_2 by $\overline{z_1} \leq z \leq \overline{z_2}$ and the flame tip region R_3 by $\overline{z_2} < z \leq \overline{z_3}$. Quantities $\overline{z_0}$, $\overline{z_1}$, $\overline{z_2}$, $\overline{z_3}$ and $\overline{z_{1.5}} = \overline{z_1} + (\overline{z_2} - \overline{z_1})/2$, specific to each flame power, are defined in Table 6.3.

When the flame power is increased, both the cycle-averaged value $\overline{I_{cam}}(z,\alpha,\mathbb{P})$ and the oscillation amplitude of $\langle I_{cam}\rangle(z,\alpha,\mathbb{P})$ are enhanced in the middle region. This is further examined by investigating $\langle I'_{cam}\rangle^{rms}(z,\mathbb{P})$ in Figure 6.14 (left), which corresponds to the rms amplitude of $\langle I'_{cam}\rangle(z,\alpha,\mathbb{P}) = \langle I_{cam}\rangle(z,\alpha,\mathbb{P}) - \overline{I_{cam}}(z,\mathbb{P})$. For $\mathbb{P}_{43}$, the maximum value is about 0.3, compared to 0.6 for $\mathbb{P}_{59}$ and 0.65 for $\mathbb{P}_{75}$. This indicates the strengthening of the OH*-intensity wave when the power increases. But, the greater values of $\langle I'_{cam}\rangle^{rms}(z,\mathbb{P})$ are found around $z = 30$ mm for the three flame powers.
The phase between $\langle P'\rangle(\alpha)$ and $\langle I'_{cam}\rangle(z,\alpha,\mathbb{P})$ is also modified, as shown in Figure 6.14 (right). It is worth noting that the value of $\varphi_{\langle P'\rangle-\langle I'_{cam}\rangle(z)}$ at the maximum of $\langle I'_{cam}\rangle^{rms}(z,\mathbb{P})$ is found at $\alpha = 3\pi/2[2\pi]$ for $\mathbb{P}_{43}$, while for $\mathbb{P}_{59}$ and $\mathbb{P}_{75}$, it is found at $3\pi/4[2\pi]$ and $\pi/2[2\pi]$ respectively. In the plot, the grey bands indicate the potential instability regions corresponding to in-phase oscillations of acoustic pressure and local OH*-intensity. It is observed that for $\mathbb{P}_{43}$, the maxima of $\langle I'_{cam}\rangle^{rms}(z,\mathbb{P})$ are mostly outside of the grey bands, contrary to $\mathbb{P}_{59}$ and $\mathbb{P}_{75}$ for which the response at most it lies inside the grey bands, particularly for the highest power. Therefore, the increase of the flame power leads to a progressive phasing between the OH*-intensity oscillation in the middle region and the acoustic pressure oscillation. Combined with the increase of the OH*-intensity oscillation amplitude, this shows the increased ability of the middle region of the flame to couple with acoustics. This is further investigated below.

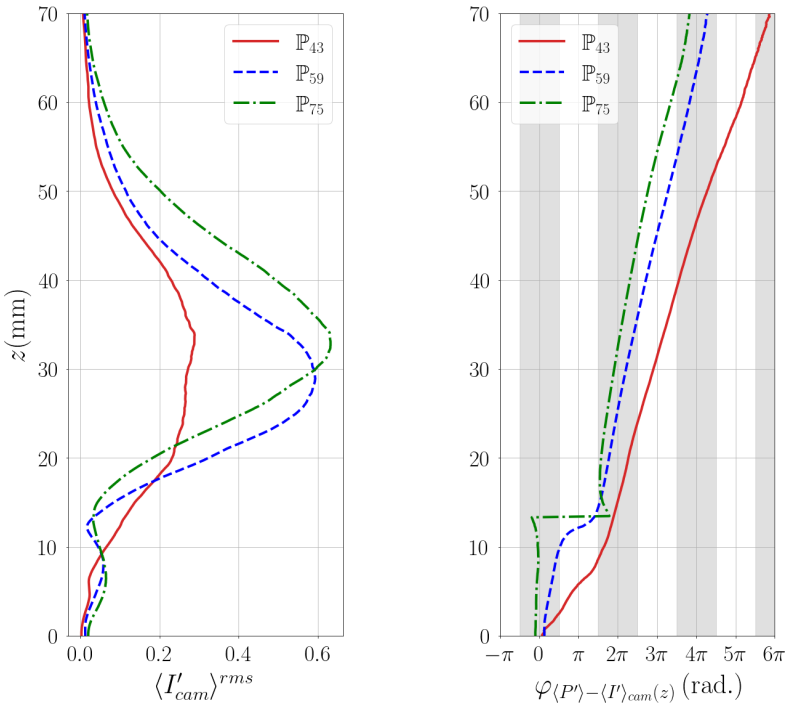

Figure 6.14: Rms fluctuation amplitude of $\langle I_{cam}\rangle(z,\alpha,\mathbb{P})$ filtered at f_r for $\Pi = 0.35$ and for the three flame powers. $\mathbb{P}_{43}$: $f_r = 704$ Hz; $\mathbb{P}_{59}$: $f_r = 722$ Hz; $\mathbb{P}_{75}$: $f_r = 732$ Hz.

6.4.1 Spatial structure of the OH*-intensity oscillation

The quantity $\langle I_{cam}^{R_j}\rangle(\alpha,\mathbb{P})$ is now introduced. It corresponds to the space integration into region R_j of the phase-averaged OH* signals, $\langle I_{cam}\rangle(z,\alpha,\mathbb{P})$ (see Equation (5.4)). Results are shown in Figure 6.15 for the three flame powers, for $\Pi = 0.35$.

For all the flame powers, the cycle-averaged level of $\langle I_{cam}^{R_2}\rangle(\alpha,\mathbb{P})$ is about twice as that of $\langle I_{cam}^{R_1}\rangle(\alpha,\mathbb{P})$ and that of $\langle I_{cam}^{R_3}\rangle(\alpha,\mathbb{P})$. Moreover, $\langle I_{cam}^{R_1}\rangle(\alpha,\mathbb{P})$ and $\langle I_{cam}^{R_3}\rangle(\alpha,\mathbb{P})$ oscillate very weakly.

When the flame power is increased, the cycle-averaged level of $\langle I_{cam}^{R_j}\rangle(\alpha,\mathbb{P})$ increases for all regions R_j. In addition, the oscillation amplitude of $\langle I_{cam}^{R_2}\rangle(\alpha,\mathbb{P})$ is more and more significant, whereas those of $\langle I_{cam}^{R_1}\rangle(\alpha,\mathbb{P})$ and $\langle I_{cam}^{R_3}\rangle(\alpha,\mathbb{P})$ remain weak, even though they are greater than for the low power. Therefore, the energy system transitions from a flame power ($\mathbb{P}_{43}$) characterised by a weak oscillation amplitude of $\langle I_{cam}^{R_j}\rangle(\alpha,\mathbb{P})$ in all the regions, to flame powers ($\mathbb{P}_{59}$ and $\mathbb{P}_{75}$) at which the response of R_2 is dominant compared to those of R_1 and R_3. In addition, the progressive phasing between acoustic pressure and $\langle I_{cam}^{R_2}\rangle(\alpha,\mathbb{P})$ signals when the flame power increases is clearly identified. Indeed, the phase shift between $\langle P'\rangle(\alpha)$ and $\langle I_{cam}^{R_2}\rangle(\alpha,\mathbb{P})$ is equal to π for $\mathbb{P}_{43}$, $\sim \pi/4$ for $\mathbb{P}_{59}$ and 0 for $\mathbb{P}_{75}$. For the two higher flame powers, this phase delay is identical to that of the FDF (see Figure 6.7), which is calculated over the whole flame, while it is different for $\mathbb{P}_{43}$. One can therefore conclude that the whole flame response mainly arises from its middle region, R_2, for $\mathbb{P}_{59}$ and $\mathbb{P}_{75}$, whereas for $\mathbb{P}_{43}$, the flame response is not strongly linked to one particular region of the flame.

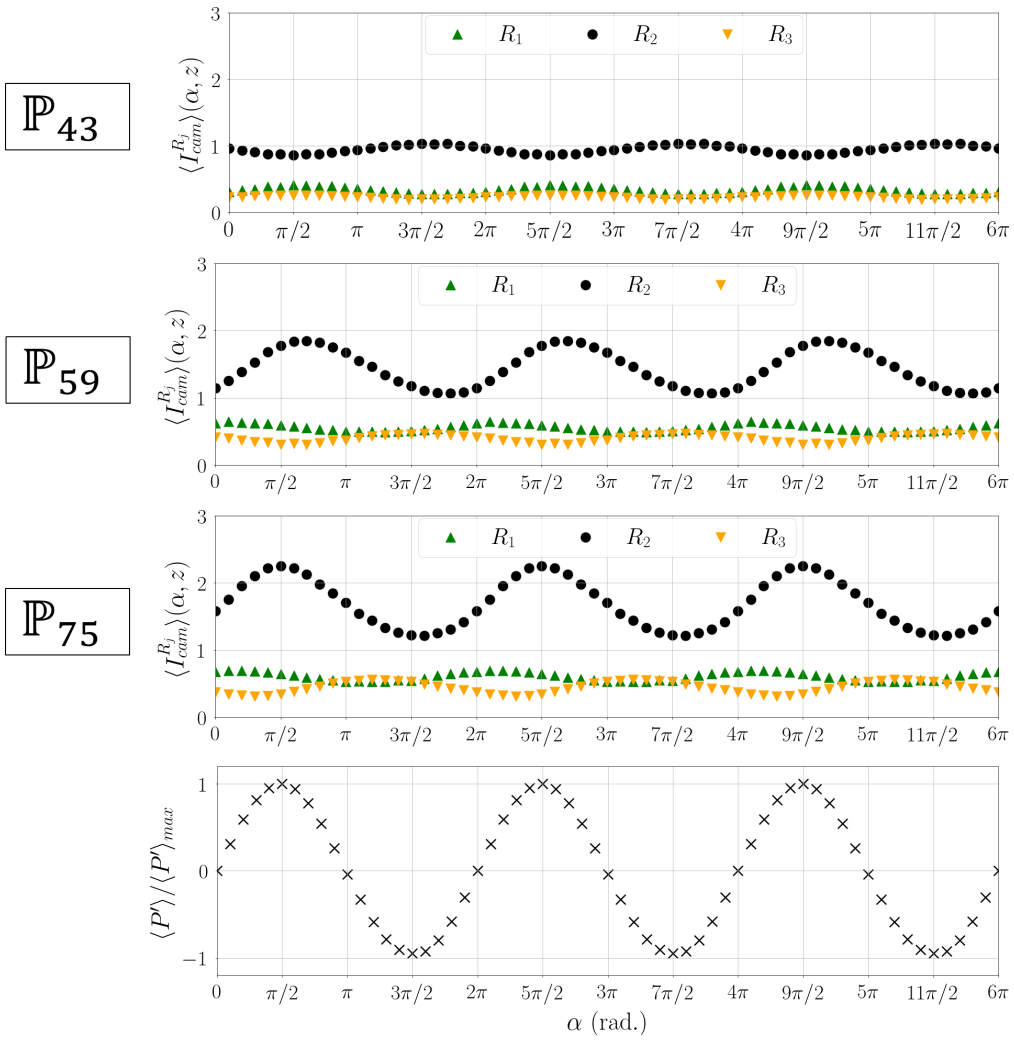

Figure 6.15: Oscillation of the phase-averaged OH*-intensity integrated in regions R_1, R_2 and R_3 for the three flame powers post-synchronised with the reconstructed acoustic pressure cycle reproduced three times for $\Pi \simeq 0.35$. For $\mathbb{P}_{43}$, $f_r = 704$ Hz; for $\mathbb{P}_{59}$, $f_r = 722$ Hz and for $\mathbb{P}_{75}$, $f_r = 732$ Hz. The reconstructed acoustic pressure cycle is shown at the bottom.

6.4.2 Propagation of the OH*-intensity wave

As shown in Figure 6.13, the middle region of the flame undergoes a strong modulation of $\langle I_{cam}\rangle(\alpha, z)$ for $\mathbb{P}_{75}$, characterised by large peaks around $\alpha = \pi/2$ and troughs around $\alpha = 3\pi/2$. In particular, the high-intensity spot propagates faster when the power increases. The propagation velocity of the OH*-intensity wave is obtained from $\varphi_{P'-I'_{cam}(z)}$ (see Figure 6.14). The linear evolution of $\varphi_{P'-I'_{cam}(z)}$ found at most z locations, except at the flame extremities where the OH*-intensity oscillation is weak, indicates the OH*-intensity wave propagates at $U_{prop} \sim 0.7U_b$ for the three flame powers. From these elements, the convective compactness [70] can be quantified by means of the Strouhal number $L_{R_2}/L_{prop} = f_r L_{R_2}/U_{prop} = \mathrm{St}$. $L_{R_2} = \overline{z_2} - \overline{z_1}$, the length of region R_2, is quite unchanged with $\mathbb{P}$ (see Table 6.3), and $L_{prop} = U_{prop}/f_r$ is the distance traveled by the propagating OH* wave during an acoustic period. Here, $\mathrm{St} = 0.83$, 0.56 and 0.47 for $\mathbb{P}_{43}$, $\mathbb{P}_{59}$ and $\mathbb{P}_{75}$ respectively. The decrease of St indicates that region R_2 is more and more compact relatively to the convective wavelength when the power increases.

The impact of the relative weight between L_{R_2} and L_{prop} is highlighted by quantifying the OH* wave in the two sub-regions R_2^{low} and R_2^{up}, which are separated by location $\overline{z_{1.5}}$ (see Table 6.3). The former sub-region corresponds to the lower half of R_2 while the latter corresponds to its upper part. For $\mathbb{P}_{43}$, $\langle I_{cam}^{R_2^{low}}\rangle(\alpha, \mathbb{P})$ and $\langle I_{cam}^{R_2^{up}}\rangle(\alpha, \mathbb{P})$ oscillate with a comparable amplitude, but, as their length is about $L_{prop}/2$, these two sub-regions oscillate almost in phase opposition, leading to a very weak fluctuation in the whole R_2. For $\mathbb{P}_{59}$, $\langle I_{cam}^{R_2^{low}}\rangle(\alpha, \mathbb{P})$ and $\langle I_{cam}^{R_2^{up}}\rangle(\alpha, \mathbb{P})$ oscillate more strongly in the two sub-regions than for the lowest flame power. In addition, they oscillate almost in phase quadrature, resulting in a significant fluctuation in R_2. For $\mathbb{P}_{75}$, the oscillation amplitude in the two sub-regions further increased and the phase delay between these signals is reduced, as U_{prop} is higher. These characteristics lead to enhanced values of $\langle I_{cam}^{R_2}\rangle(\alpha, \mathbb{P})$ compared to $\mathbb{P}_{59}$.

6.4.3 Thermoacoustic coupling

A phase-averaged local coupling index, $\langle \mathfrak{Ra}\rangle(z, \alpha)$, based on the Rayleigh criterion, is now examined in order to find the locations that participates the most in the thermoacoustic coupling. It is expressed in Equation (5.5) but reminded here for clarity:

$$\langle \mathfrak{Ra}\rangle(\alpha, z) = \frac{\langle P'\rangle}{\rho^a U_b^2} \frac{\langle I_{cam}\rangle(\alpha, z) - \overline{I_{cam}}^t(z)}{\overline{I_{cam}}} \tag{6.7}$$

where $\overline{I_{cam}}^t(z)$ is the cycle-averaged value of $\langle I_{cam}\rangle(\alpha, z)$ and $\overline{I_{cam}}$ the mean cycle and space-averaged value of $\langle I_{cam}\rangle(\alpha, z)$. As shown in Figure 6.17, for $\mathbb{P}_{43}$, the slow propagation of the OH* wave results, at a given phase angle, in a superimposition of positive and negative contributions of equal strength to the thermoacoustic coupling. In R_1 and R_3, $\langle \mathfrak{R}\rangle(z, \alpha)$ always oscillates in phase with the acoustic pressure, while in R_2, it mainly oscillates in phase opposition with the acoustics pressure. These regions annihilate themselves when considering the thermoacoustic coupling of the whole flame, which explains the very weak value of the instability index $\mathcal{R}a_1(t)$ found above (see Fig. 6.11). The negative mean value of $\mathcal{R}a_1(t)$ indicates that negative contribu-

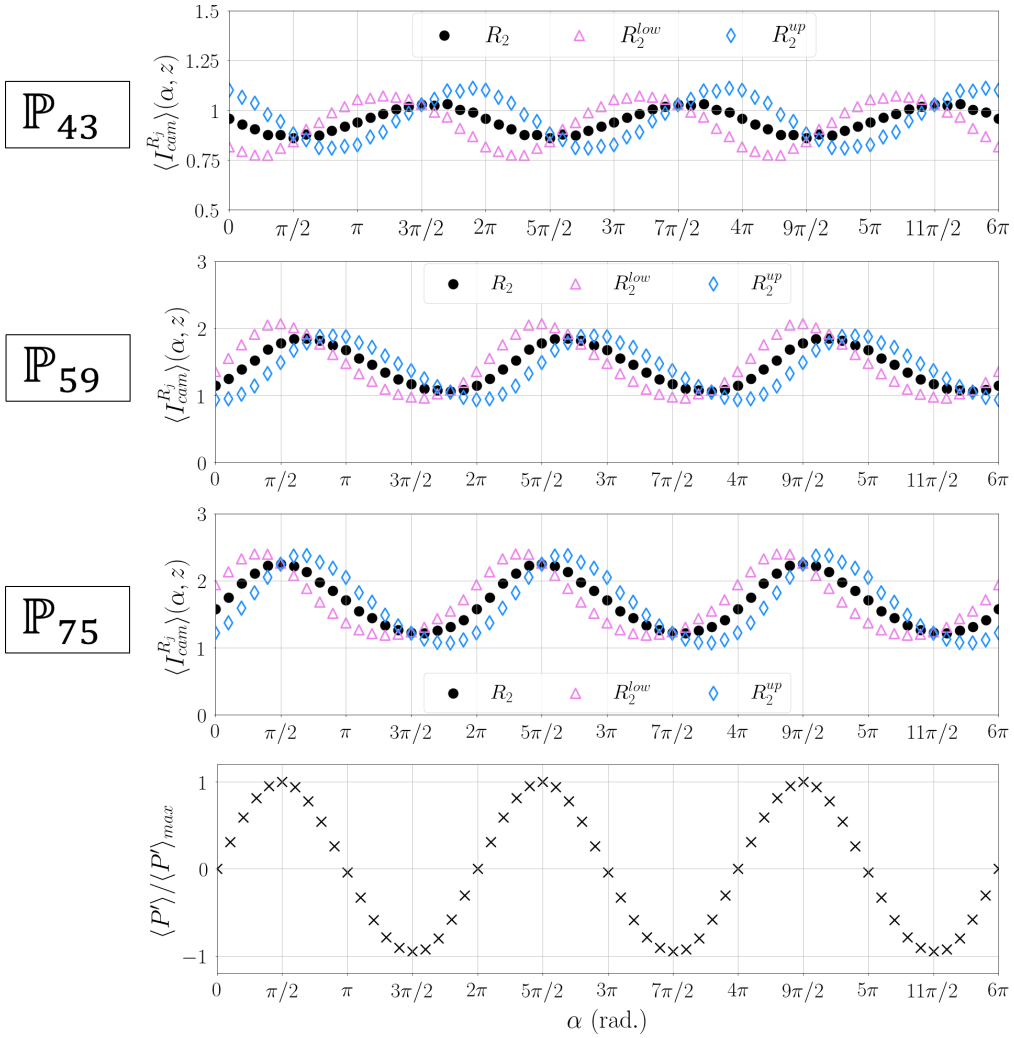

Figure 6.16: Oscillation of the phase-averaged OH*-intensity integrated in regions R_2, R_2^{up} and R_2^{low} for the three flame powers post-synchronised with the reconstructed acoustic cycle reproduced three times for $\Pi \simeq 0.35$. For $\mathbb{P}_{43}$, $f_r = 704$ Hz; for $\mathbb{P}_{59}$, $f_r = 722$ Hz and for $\mathbb{P}_{75}$, $f_r = 732$ Hz. The reconstructed acoustic pressure cycle is shown at the bottom. The scale associated to $\langle I_{cam}^{R_j} \rangle (\alpha, z)$ is reduced for $\mathbb{P}_{43}$ to highlight the oscillation.

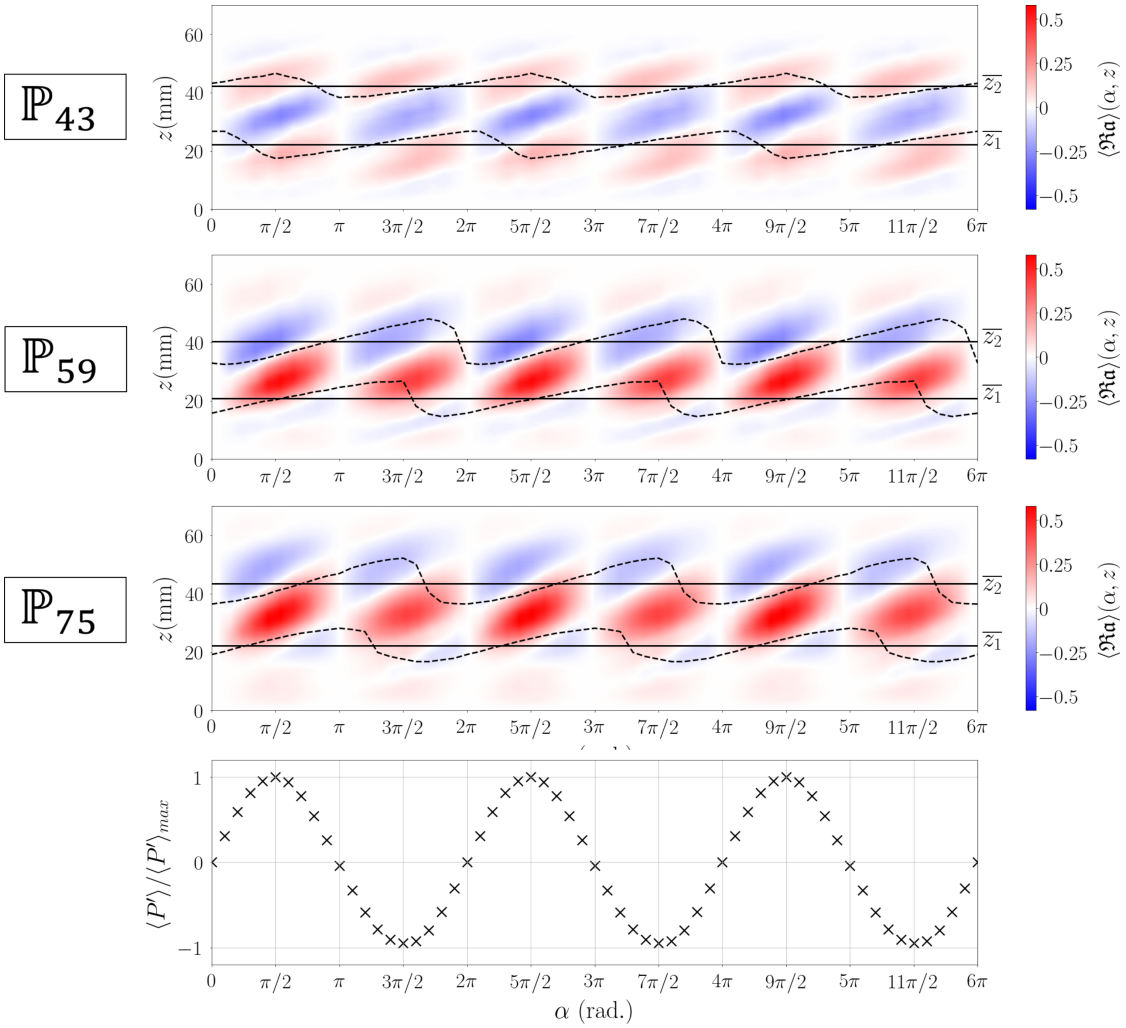

Figure 6.17: Phase-averaged Rayleigh index $\langle \mathfrak{Ra}(z, \alpha) \rangle$ as a function of height above the burner z and phase angle, post-synchronised with a reconstructed acoustic cycle reproduced three times, for Π = 0.35. (a) $\mathbb{P}_{43}$, $f_r = 704$ Hz; (b) $\mathbb{P}_{59}$, $f_r = 722$ Hz; (c) $\mathbb{P}_{75}$, $f_r = 732$ Hz; (d) associated reconstructed acoustic pressure cycle. The dash lines are defined by $\langle I_{cam} \rangle(z, \alpha, \mathbb{P}) / \max(\langle I_{cam} \rangle(z, \alpha, \mathbb{P})) = 0.65$ and the solid lines indicate the cycle-averaged vertical location of the two dash lines, z_1 and z_2 respectively.

tions to the thermoacoustic coupling are stronger than positive ones for $\mathbb{P}_{43}$. For $\mathbb{P}_{59}$ and $\mathbb{P}_{75}$, the thermoacoustic coupling is strongly positive in R_2 for both pressure minimum and maximum, reflecting the constructive interference induced by the in-phase oscillations of acoustic pressure and local OH*-intensity. This positive coupling is furthermore increased with the flame power. In R_3, a negative coupling, which is all the more weak as the power grows, is found for $\mathbb{P}_{59}$ and $\mathbb{P}_{75}$. This negative coupling does not counterbalance the strong positive coupling found in R_2. Consequently, the thermoacoustic coupling is mainly positive, with higher values reached for $\mathbb{P}_{75}$. This is consistent with results obtained with PM acquisition.

6.4.4 Discussion

These results underline the importance of convective processes on the increasing global response of swirling spray flames with the flame power. However, they do not explain the increase of the OH* wave amplitude at a given height observed in Figure 6.14. Mechanisms that can lead to this feature are discussed here. In non-reacting swirling flows, the mass flow rate oscillation reduced by the mean mass flow rate necessary to induce vortex formation was shown to decrease when the Strouhal number increases [86]. Here, this feature is obtained when the flow velocity is decreased. In our case, this would suggest that coherent vortices created by acoustics are more likely to be formed at the lowest flame power. Vortex roll-up is known to be a mechanism of HRR oscillation at the flame tip [66, 127], but it was also identified as a saturation mechanism for premixed swirling flames [67, 124]. On the contrary, swirl number oscillations generally alter the flame angle and therefore the HRR at the flame foot, through the modulation of the size of the central recirculation zone [127]. Although the weak OH* intensity oscillations in R_1 presented above suggests that swirl number fluctuations do not participate strongly to the flame response, it is interesting to evaluate the fluctuating swirling flow since it takes part into the stabilisation process and can then affect flame dynamics indirectly, as shown in Section 5.4. Other mechanisms, linked to the generation of a droplet number density wave [136, 175] and to the conversion of air and liquid fuel into a reactive mixture are at stake, since liquid-fuel atomisation, evaporation and air-fuel mixing must occur before combustion. The time delay τ between the acoustic perturbation and the flame response can be expressed as follows:

$$\tau = \tau_{inj} + \tau_{evap} + \tau_{mix} + \tau_{ch} \tag{6.8}$$

where τ_{inj}, τ_{evap}, τ_{mix}, τ_{ch} are the characteristic times for injector response, evaporation of the fuel, air-fuel mixing and chemical reactions respectively. In particular, the duration of the evaporation process is linked to the flow and its structure (*e.g.,* turbulence intensity or droplet clustering), thermal environment and physico-chemical characteristics of the fuel. Here, the temperature is increased when the flame power is enhanced, and the lower flame standoff distance implies that high temperatures are reached closer to the burner exit, facilitating the evaporation process. Moreover, higher air mass flow rates are associated to higher turbulence levels, enhancing the evaporation rate [176]. The evaporation rate may also be modified due to the modulation of the drop size distribution [135, 175, 177]. For a pressure-swirl atomiser having a given flow number, increasing the liquid flow rate results in the decrease of the Sauter mean diameter (SMD) [157]. While a first atomisation stage is produced by the pressure-swirl atomiser,

a second stage comes from the fragmentation of a liquid-fuel film that forms at the injector wall due to the backward position of the atomiser [140]. This second atomisation stage is controlled by the air flow, the velocity of which is modulated by acoustics. For a plain-jet airblast atomiser, the higher the air velocity, the smaller the SMD [157]. All these features tend to indicate that conversion processes of the two-phase flow into a reactive mixture should be accelerated when increasing the power. This assumption is *a priori* supported by results shown in this section, in particular the similar position of region R_2 for all powers, which shows that, in spite of the reduction of the travelling time to reach R_2 with increasing mass flow rate, the flame can stabilise closer to the burner exit and keeps the same length. However, evaporation can be slowed down by droplet clustering, which can occur locally due to the presence of regions of high droplet concentration [139]. In this limit case, evaporation is drastically reduced and relies on diffusion of fuel vapour towards fresh gases, on the ability of fuel droplets to leave saturated regions and on the turbulence level [42]. It is thus interesting to examine how the spray properties are modified during the acoustic cycle for various flame powers and how they evolve during convection. In the following sections, the responses of the air flow and the fuel spray to acoustics are evaluated to give insights into mechanisms leading to the variation of the flame response with the flame power.

6.5 Modulation of the air flow

In this section, the modulation of the air flow induced by the acoustic pressure oscillation in the cavity, highlighted for $\mathbb{P}_{59}$ in Section 5.3.3, is investigated for the three flame powers. A same reduced acoustic pressure amplitude, $\Pi = 0.2$, is chosen. First, the modulation of the axial velocity is examined at the injector exit. Then, the formation of a vortex is depicted. It was shown in Section 5.3.3.3 that this vortex plays a role in the flame intensity oscillation by engulfing fuel droplets, leading to an efficient turbulent mixing. Finally, the oscillation of the swirl number during the acoustic cycle is quantified for the three flame powers.

6.5.1 Axial velocity modulation

The modulation of the axial air flow induced by the acoustic pressure oscillation in the chamber is investigated by considering fuel droplets of classes C_1 only, *i.e.* having a diameter d comprised in the range $1 - 5$ µm. As shown in Figure 6.5, considering these droplets only allows to obtain an accurate description of the air flow behaviour due to their low Stokes number Stk. To capture the velocity oscillation induced by acoustics, it is interesting to calculate the *acoustic* Stokes number $\mathrm{Stk_{ac}}$ (see Section 1.1.6 and Section 5.3.3.1). For the droplets of class C_1, it does not exceed 0.3 for the three flame powers, indicating that these droplets does capture the air flow oscillations induced by acoustics. Results at $z = 2.1$ mm are shown in Figure 6.18 for $\Pi = 0.2$.

The radial profiles of mean axial velocity, $\overline{U_z^a}$, plotted for the three flame powers, have the same shape as without acoustic forcing (see Figure 6.3), characterised by a central region of low axial velocity surrounded by an annular region of high axial velocity, about 10% higher than the bulk velocity, around which the axial velocity decreases towards further radial locations. When the flame power is modified, the mean axial velocity at a given position is changed approximately in

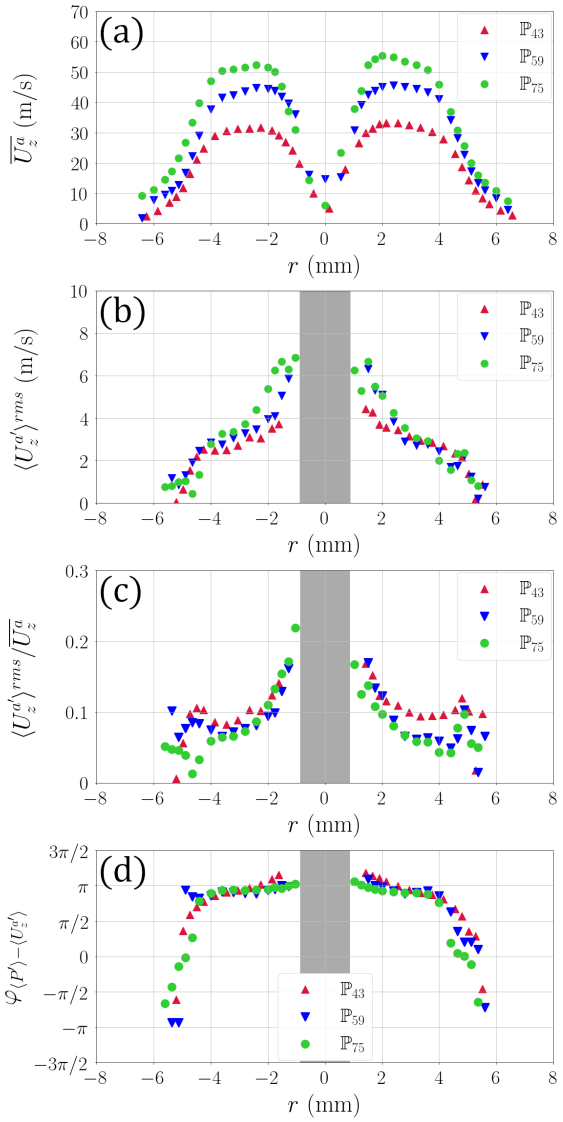

Figure 6.18: Radial profiles of air flow axial velocity with acoustic forcing ($\Pi = 0.2$), measured on fuel droplets of classes $C_1(1\ \mu\text{m} \leq d < 5\ \mu\text{m})$. (a) mean axial velocity $\overline{U_z^a}(r)$; (b) rms oscillation amplitude at f_r, $\langle U_z^{a'} \rangle^{rms}(r)$; (c) $\langle U_z^{a'} \rangle^{rms}(r)/\overline{U_z^a}(r)$; (d) Phase shift between $\langle P' \rangle$ and $\langle U_z^{a'} \rangle$. The phase-averaged quantities are calculated by dividing the acoustic cycle in 12 bins of equal width. The grey zone in (b,c,d) indicates the region where the less-populated bin contains less than 8 droplets, which is assumed too low to calculate the phase-averaged quantities.

proportion to the bulk velocity, except around the injector axis.
The phase-averaged axial velocity oscillation at f_r, $\langle U_z^{a'} \rangle$, is examined through its rms amplitude, $\langle U_z^{a'} \rangle^{rms}$, and the phase shift between the phase-averaged acoustic pressure oscillation, $\langle P' \rangle(\alpha)$, and $\langle U_z^{a'} \rangle(\alpha)$. The phase-averaged signals are calculated by dividing the acoustic cycle in 12 bins of equal width. Close to the injector axis, the droplet count in some of the 12 bins is too low to validate the phase-averaged quantities: the radial locations at which the count in the less-populated bin is lower than 8 droplets, equivalent to 3.2 droplets every 100 acoustic cycles, are indicated by the grey band in Figure 6.18 (b-d) and correspond to $|r| < 0.9$ mm.
As shown in Figure 6.18 (b), $\langle U_z^{a'} \rangle^{rms}$ increases with the flame power for $|r|$ in the range $1-3.5$ mm. At $|r| \simeq 1$ mm, $\langle U_z^{a'} \rangle^{rms}$ reaches its maximum values, which are about 7 m/s for $\mathbb{P}_{75}$, 6 m/s for $\mathbb{P}_{59}$ and 4 m/s for $\mathbb{P}_{43}$. These values equal to 15% of the bulk velocity whatever the power. It then decreases as the radial location increases, until it reaches 3 m/s for the three flame powers at $|r| = 3.5$ mm, breaking the proportionality relation with the bulk velocity. At further radial locations, corresponding to the zone between adjacent flames, $\langle U_z^{a'} \rangle^{rms}$ decreases to 0 in an identical manner for all the flame powers.
In Figure 6.18 (c), it appears that the reduced oscillation amplitude $\langle U_z^{a'} \rangle^{rms} / \overline{U_z^a}$ is the same for all the powers only for $|r|$ in the range $1-2$ mm. At further radial locations, the value of $\langle U_z^{a'} \rangle^{rms} / \overline{U_z^a}$ obtained at a given r decreases, although the diminishing is less pronounced as the flame power increases. These results indicate that the relative modulation of the volumetric flow rate passing by the injector exit is less intense when the flame power increases. In light of the observations made in Section 6.3 and Section 6.4, this indicates that the global flame intensity oscillation is more sensitive to smaller relative modulations of the volumetric air flow rate when the flame power increases.
Figure 6.18 (d) shows that the phase shift between $\langle P' \rangle$ and $\langle U_z^{a'} \rangle$ is quite unchanged unaffected by a change of the flame power: at most locations, the air flow axial velocity is modulated in phase opposition with the acoustic pressure in the chamber.

6.5.2 Vortex generation

It is worth focusing on the vortex generation at the injector exit. The roll-up of the flame front due to the vortex is higlighted in the present configuration for flame power $\mathbb{P}_{59}$ for $\Pi = 0.35$, in Section 5.3.3.3. In this case, the location of the vortex is correlated with a significant curvature of the flame front (see Figure 5.8).

In the present subsection, the air flow motion is highlighted with high-speed laser tomography visualisations of olive oil seeding droplets in a vertical plane. The experimental setup is described in Section 2.2.5. The image acquisition rate, f_s^{cam} depends on the flame power: it is 20,000 fps for $\mathbb{P}_{43}$, 27,500 fps for $\mathbb{P}_{59}$ and 35,000 fps for $\mathbb{P}_{75}$. This choice is guided by the bulk velocity associated to each power. By increasing the acquisition rate proportionally to the bulk velocity[2], one can expect to follow the convection of the vortex equally well for all the powers. Vortex roll-up at the injector exit is illustrated for flame powers $\mathbb{P}_{43}$ and $\mathbb{P}_{75}$ in Figure 6.19, for Π in the linear zone (see Figure 6.6).. For each power, the images displayed are separated by a power-

[2]For simplicity, the acquisition rate is increased by 1.375 from $\mathbb{P}_{43}$ to $\mathbb{P}_{59}$, while the bulk velocity ratio is 1.36; and by 1.75 from $\mathbb{P}_{43}$ to $\mathbb{P}_{75}$, while the bulk velocity ratio is 1.73.

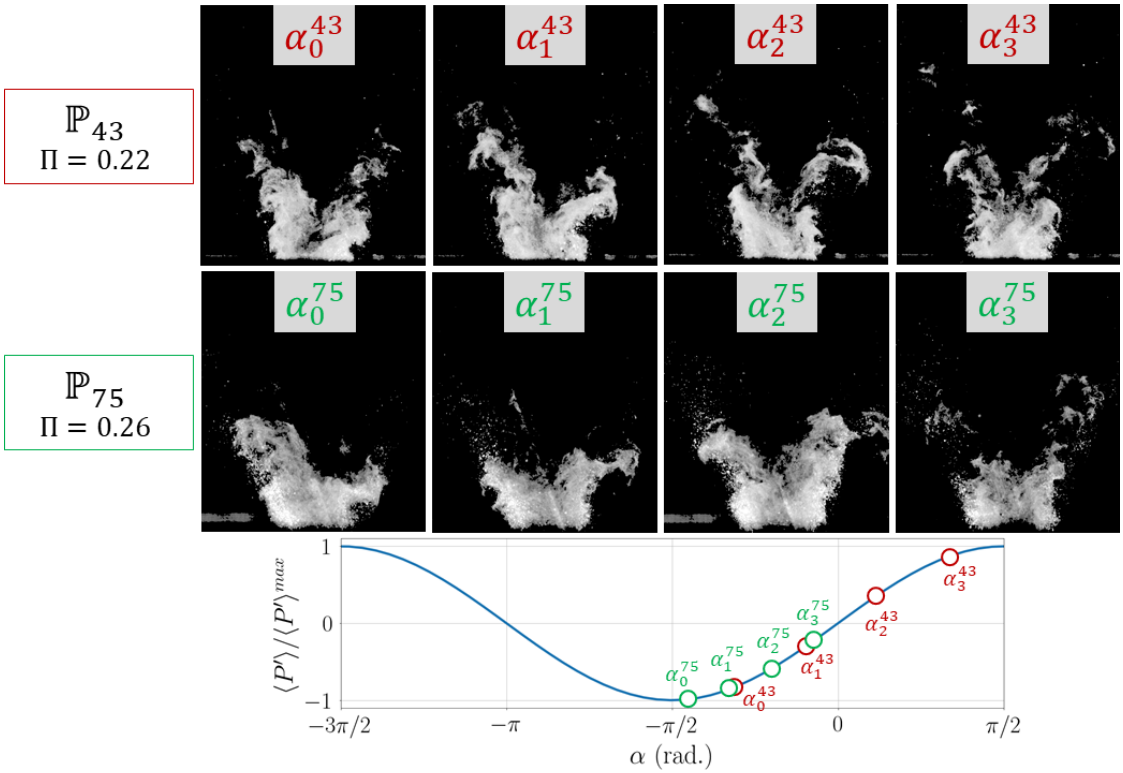

Figure 6.19: Vertical tomography views of the spray and seeded air flow with combustion post-synchronised with the pressure at the center of the cavity for Π in the linear zone. Top row: $\mathbb{P}_{43}$, $f_r = 710$ Hz; middle row: $\mathbb{P}_{75}$, $f_r = 758$ Hz; bottom row: Reconstructed acoustic pressure cycle. Images have a size of 24.6×28.6 mm^2.

dependent time gap $\Delta\tau = 3T_s^{cam}$, where $T_s^{cam} = 1/f_s^{cam}$ is the sampling period. $\Delta\tau$ also depends on the flame power in such a way that it is inversely proportional to the bulk velocity. Therefore, convective phenomena can be observed with the same relative time resolution for the two powers.

The periodic ejection of a vortex is observed for all the powers, but at slightly different phase angles of the acoustic pressure cycle. For $\mathbb{P}_{43}$, the initiation of the vortex roll-up around $z = 3$ mm is observed at $\alpha = \alpha_0^{43} \simeq -\pi/3$. For $\mathbb{P}_{75}$, it is observed at the same z-locations at $\alpha = \alpha_0^{75} \simeq -\pi/2$, *i.e.* with a phase advance of $\sim \pi/6$ compared to $\mathbb{P}_{43}$. The vortex becomes more difficult to identify as it propagates downstream, due to the evaporation of the seeding olive oil droplets. Nevertheless, one can distinguish that between α_0^{43} and α_3^{43}, the vortex for $\mathbb{P}_{43}$ has travelled the same distance as between α_0^{75} and α_3^{75} for $\mathbb{P}_{75}$, highlighting that it is carried by the mean flow.

The phase advance of $\simeq \pi/6$ of the vortex ejection for $\mathbb{P}_{75}$ can $\mathbb{P}_{43}$ cannot be explained by the axial velocity modulation, whose phase shift with the acoustic pressure oscillation is independent of the flame power (see Figure 6.18 (d)). It is now interesting to examine the swirl number oscillation to see its link with the vortex roll-up.

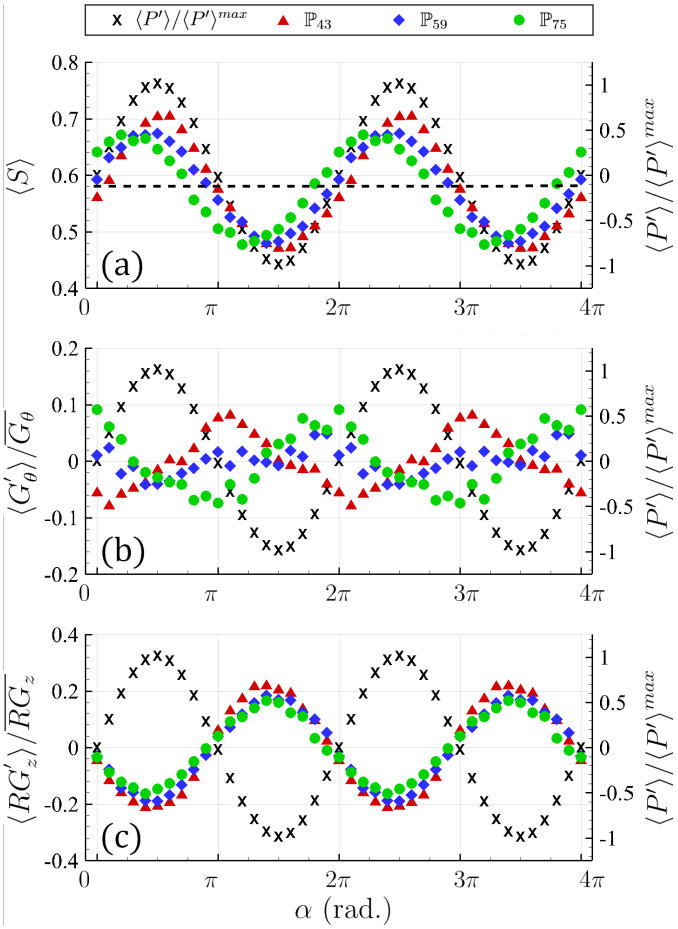

Figure 6.20: Phase-averaged oscillations at $z = 2.1$ mm of: (a) swirl number $\langle S\rangle$; (b) reduced axial flux of angular momentum $\langle G'_\theta\rangle/\overline{G_\theta}$; (c) reduced axial flux of axial momentum $\langle RG'_z\rangle/\overline{RG_z}$. For the three flame powers, the time-averaged swirl number is 0.58, indicated by the horizontal dash line in (a).

6.5.3 Swirl number oscillation

It is interesting to focus on swirl number oscillations as they can interfere with other mechanisms of flame response. In particular, large swirl number oscillations can weaken the vortex formation and growth at low frequencies, thus decreasing the response of gaseous-fuelled premixed flames stabilised both by swirl and by a bluff-body [127, 178]. Nevertheless, Gatti *et al.* [178] also showed that for a swirl-stabilised gaseous-fuelled premixed flame (without bluff-body), large vortices develop even in the presence of swirl number oscillations, leading to a significant flame response.

The comparison between the phase-averaged swirl number $\langle S\rangle$, calculated at $z = 2.1$ mm for the three flame powers and for $\Pi = 0.2$, is presented in Figure 6.20 in addition to the reduced phase-averaged oscillations of the axial flux of angular momentum, $\langle G'_\theta\rangle/\overline{G_\theta}$, and of the axial flux of axial momentum multiplied by the injector exit radius, $\langle RG'_z\rangle/R\overline{G_z}$ (see Equation (1.3)). For all the flame powers, the swirl number has a mean value $\overline{S}$ of 0.58, which is comparable to

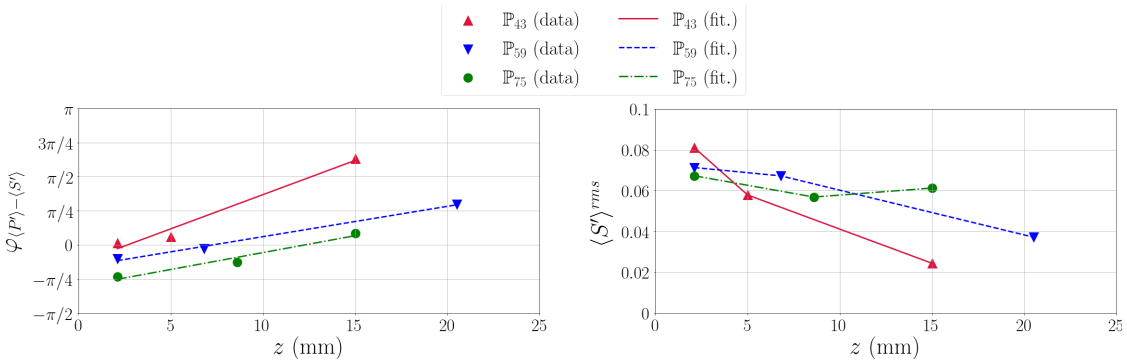

Figure 6.21: Evolution of the swirl number fluctuations with the z-location and with the flame power. Left: rms amplitude of the phase-averaged swirl number oscillation at f_r, $\langle S^{'}\rangle^{rms}$; right: Phase shift between the oscillations at f_r of the acoustic pressure, $\langle P^{'}\rangle$, and of the swirl number $\langle S^{'}\rangle$.

the value without acoustic forcing. $\langle S\rangle$ oscillates with a slightly larger amplitude for $\mathbb{P}_{43}$ than for the two higher powers, but for all the powers, it reaches during the cycle values lower than 0.5 and other higher than 0.65, which might indicate the periodic appearance and disappearance of the CRZ, potentially disorganising flame stabilisation. At the burner exit, for all Π, $\langle S\rangle$ oscillates roughly in phase with the acoustic pressure for the three flame powers, but one can notice a phase advance for $\mathbb{P}_{59}$ ($\simeq \pi/10$, as shown in Figure 6.21) and for $\mathbb{P}_{75}$ ($\simeq \pi/4$), while for $\mathbb{P}_{59}$, $\langle S\rangle$ and $\langle P^{'}\rangle$ oscillate in phase.
The origin of the phase shift in the swirl oscillation between the different powers is related to $\langle G'_\theta\rangle$, whose oscillations for the three powers are clearly out-of-phase. On the contrary, RG_z oscillates in phase opposition with the acoustic pressure for the three flame powers. On the basis of the swirl number definition (see Equation (1.3)), this means that the phase of the axial velocity oscillation integrated over all the radial location, and thus the phase of the volumetric air axial flow rate oscillation, $\dot{q}_v$, is unaffected by a change in flame power. It is interesting to note that the amplitude of $\langle RG_z^{'}\rangle/\overline{RG_z}$ decreases with the flame powers, which is consistent with the observation made on the radial profiles of the reduced amplitude of the axial velocity oscillation (see $\langle U_z^{a'}\rangle^{rms}/\overline{U_z^{a'}}$ in Figure 6.18 (c)). This indicates that the relative modulation of the axial flow rate is decreased with the flame power for a given Π.

To understand the role of the swirl number in the vortex roll-up, we now focus on the phase shift $\varphi_{\langle P'\rangle-\langle S'\rangle}$ between the acoustic pressure oscillation and the swirl number oscillation, $\langle S^{'}\rangle$. $\varphi_{\langle P'\rangle-\langle S'\rangle}$ is quantified by using the transfer function framework (see Section 2.3.3.2) and shown in Figure 6.21 (left column). The first-degree polynomials fit the experimental data. At $z = 2.1$ mm, $\varphi_{\langle P'\rangle-\langle S'\rangle}$ indicates the swirl number oscillation is advanced of $\pi/4$ for $\mathbb{P}_{75}$ compared with $\mathbb{P}_{43}$, which is quite close to the phase shift of $\pi/6$ for the vortex ejection found between the two present powers. This suggests that vortex roll-up may be driven by swirl number oscillations rather than axial velocity oscillations.
$\langle S^{'}\rangle$ then propagates downstream. Its propagation velocity is examined with the best-fit lines. $\langle S^{'}\rangle$ is carried at a constant velocity for the z-locations at which measurements were performed. The slopes indicate propagation velocities of $1.03U_b$, $1.7U_b$ and $1.19U_b$ for $\mathbb{P}_{43}$, $\mathbb{P}_{59}$ and $\mathbb{P}_{75}$

respectively.

In Figure 6.21 (right column), the amplitude of the swirl number oscillation is calculated at various z-locations for the three flame powers. At $z = 2.1$ mm, the swirl number oscillation is stronger when the flame power is lower. However, it vanishes rapidly as it propagates downstream for $\mathbb{P}_{43}$. For $\mathbb{P}_{59}$, $\langle S' \rangle^{rms} \simeq 0.07$ up to $z = 6.8$ mm while it is 0.04 at $z = 20.5$ mm. For $\mathbb{P}_{75}$, it keeps a similar value up to $z = 15$ mm. The persistence of the swirl number oscillation at higher locations implies that swirl waves are susceptible to perturb the flames much more for $\mathbb{P}_{75}$. This may participate to the increase of the global OH*-intensity oscillation as the flame power increases, in spite of a weaker modulation of the axial flow rate.

6.6 Modulation of the fuel spray

It is now worth investigating how the flame power affects the fuel spray behaviour with acoustic forcing. An interesting aspect pertains to the generation of droplet number waves, observed for $\mathbb{P}_{59}$ in Section 5.3.4.2, and their transport by the flow. A second aspect concerns fuel evaporation. Indeed, the time delay between the acoustic pressure oscillation and the OH*-intensity is reduced as the flame power increases. This time delay includes characteristic times for several physical mechanisms, namely injector response, evaporation, mixing and combustion (see Equation (6.8)). It is therefore important to understand how physical mechanisms are modified when the flame power is changed.

6.6.1 Droplet number waves

It is first interesting to examine the space-time modulation of the local phase-averaged droplet count, $\langle N \rangle(\alpha, r)$ as a function of flame power, in a similar manner to what is done in Figure 5.25 for $\mathbb{P}_{59}$. This is here illustrated in Figure 6.22 for $\mathbb{P}_{43}$ and $\mathbb{P}_{75}$, for a reduced acoustic amplitude $\Pi = 0.2$. For all the flame powers, $\langle N \rangle(\alpha, r)$ oscillates during the acoustic cycle at all the radial locations in the range $2 - 6$ mm. In this annular-shaped region, the droplet count is always comprises between 0.5 and 1.4 droplets per duration $\Delta\tau = T/20$. This region can be separated in an internal part and an external part, which are separated at $r = 4$ mm. In these two parts, the droplet count roughly oscillates in phase opposition; This is further discussed below. When the flame power is changed, the effects of acoustics on the spray modulation is modified too. In the annular-shaped region, the minima of $\langle N \rangle(\alpha, r)$, as well as the maxima, are not found at the same phase angles for the differnt flame powers This is further developed below. In addition, the empty core region ($r < 2$ mm without acoustic forcing) is periodically suppressed for $\mathbb{P}_{43}$, near the pressure minimum, while it remains clearly established for $\mathbb{P}_{75}$.

6.6.1.1 Generation of droplet number waves

Droplet number waves are first investigated at the burner exit ($z = 2.1$ mm) by integrating the local phase-averaged droplet count, $\langle N \rangle(\alpha, r)$, over all the radial locations, giving the quantity $\langle N \rangle_{spray}(\alpha)$. This post-processing method allows to simplify the problem by retaining only the longitudinal space dimension, allowing to describe longitudinal droplet number waves. The

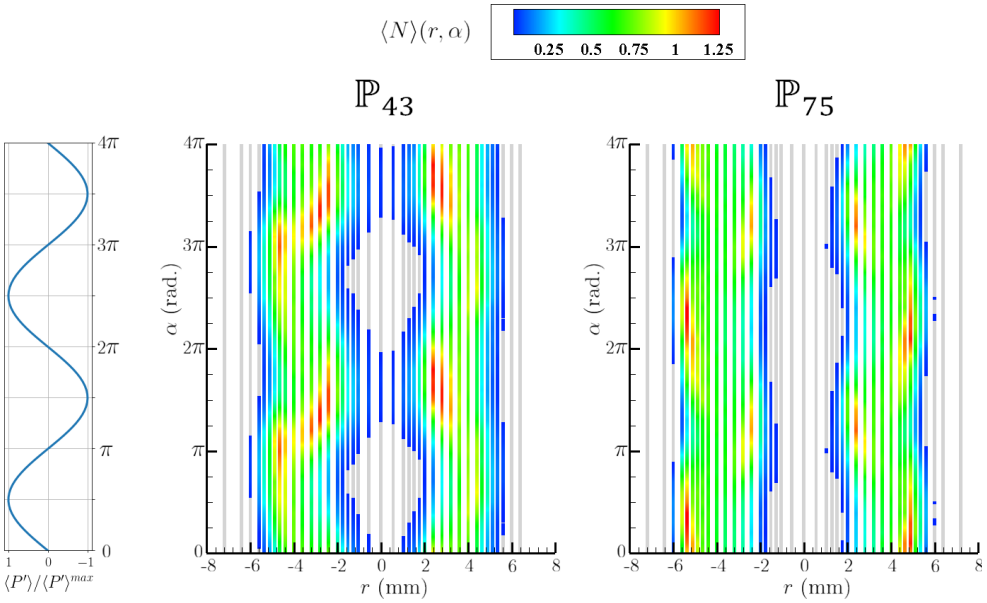

Figure 6.22: Phase-averaged local droplet count $\langle N \rangle(r, \alpha)$ illustrated for operating conditions $\mathbb{P}_{43}$ and $\mathbb{P}_{75}$ for $\Pi = 0.2$, and reproduced during two reconstructed acoustic cycles.

essence of this method, previously applied to describe flame intensity waves, is explained in Section 2.3.2.1. This method was also applied to numerical results in order to estimate the space-time evolution of the mass flow rate during self-excited longitudinal oscillations [156]. In the present work, the spray is also separated into an internal part and an external part by a fictitious boundary located at r_{sep}[3]. At $z = 2.1$ mm, $|r_{sep}|$ is equal to 4 mm. The behaviour of the spray in each part is examined by calculating the phase-averaged droplet count in each of these regions, giving $\langle N \rangle_{int}(\alpha)$ and $\langle N \rangle_{ext}(\alpha)$. Formally, the quantities introduced here are expressed by:

$$\langle N \rangle_{spray}(\alpha) = \sum_{i} \langle N \rangle(\alpha, r_i) \tag{6.9}$$

$$\langle N \rangle_{int}(\alpha) = \sum_{i | r_i \leq r_{sep}} \langle N \rangle(\alpha, r_i) \tag{6.10}$$

$$\langle N \rangle_{ext}(\alpha) = \sum_{i | r_i > r_{sep}} \langle N \rangle(\alpha, r_i) \tag{6.11}$$

Results are plotted in Figure 6.23 at a reduced acoustic amplitude $\Pi = 0.2$ for the three operating points. **In the whole spray**, $\langle N \rangle_{spray}(\alpha)$ differs significantly when the power is changed. For $\mathbb{P}_{43}$, it oscillates in a quasi-sinusoidal manner between 11 and 16 drops per duration $\Delta\tau$, in phase opposition with the pressure. For $\mathbb{P}_{59}$, it oscillates much weaker and for $\mathbb{P}_{75}$, $\langle N \rangle_{spray}(\alpha)$ is even less modulated and can be considered as roughly constant during the acoustic cycle. **In**

[3] r_{sep} is the radial location at which the droplet data rate without acoustic forcing is maximum. See Section 3.1.2.3 for more details.

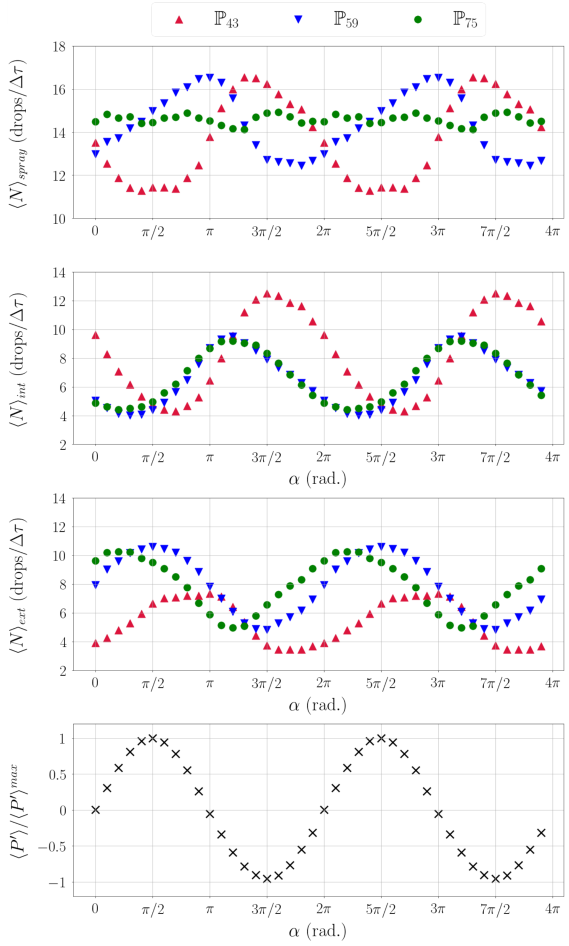

Figure 6.23: Phase-averaged droplet data rate, $\langle N \rangle(\alpha)$ integrated in the internal part, external part, and in the whole spray for the three flame powers at $z = 2.1$ mm. Top: droplets integrated in the whole spray; middle up: droplets integrated in the internal part ($|r| \leq |r_{sep}|$); middle bottom: droplets integrated in the external part ($|r| > |r_{sep}|$); bottom: phase-averaged acoustic pressure. $|r_{sep}| = 4$ mm. The acoustic cycle is reproduced twice for clarity.

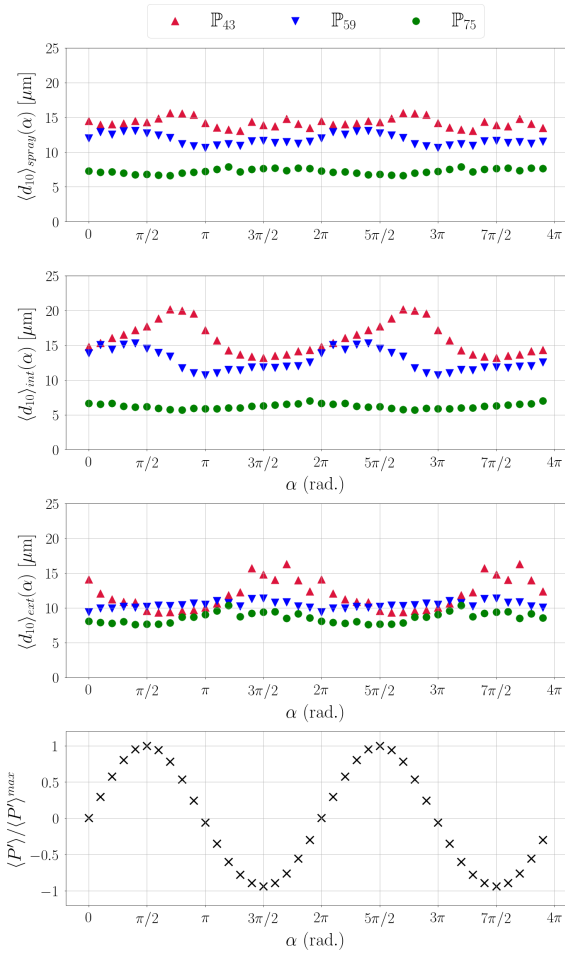

Figure 6.24: Phase-averaged droplet diameter integrated in the internal part, external part, and in the whole spray for the three flame powers at $z = 2.1$ mm. Top: droplets integrated in the whole domain, giving $\langle N\rangle_{spray}(\alpha)$; middle up: droplets integrated in the internal part ($|r| \leq |r_{sep}|$), giving $\langle N\rangle_{int}(\alpha)$; middle bottom: droplets integrated in the external part ($|r| > |r_{sep}|$), giving $\langle N\rangle_{ext}(\alpha)$; bottom: phase-averaged acoustic pressure. $|r_{sep}| = 4$ mm. The acoustic cycle is reproduced twice for clarity.

the internal part of the spray, $\langle N\rangle_{int}\ (\alpha)$ oscillates at f_r for the three flame powers, but its oscillation, stronger for $\mathbb{P}_{43}$, decreases as the flame power grows. The phase delay of $\langle N\rangle_{int}(\alpha)$ with respect to $\langle P^{'}\rangle(\alpha)$ is close to π for the three flame powers, but a slight shift is observed from a value little higher than π for $\mathbb{P}_{43}$ to a value of about $3\pi/4$ for $\mathbb{P}_{59}$ and $\mathbb{P}_{75}$. **In the external part of the spray**, $\langle N\rangle_{ext}(\alpha)$, oscillating at f_r for the three flame powers, is in phase opposition with $\langle N\rangle_{int}\ (\alpha)$. For $\mathbb{P}_{43}$, the oscillation amplitude of $\langle N\rangle_{ext}\ (\alpha)$ is much lower than that of $\langle N\rangle_{int}\ (\alpha)$, resulting in an oscillation of $\langle N\rangle_{spray}\ (\alpha)$ dominated by the internal part. For $\mathbb{P}_{59}$, the droplet number oscillation in the internal part is only slightly stronger than in the external part, resulting in a weaker oscillation of $\langle N\rangle_{spray}\ (\alpha)$ than for $\mathbb{P}_{43}$. For $\mathbb{P}_{75}$, the droplet number oscillation has a similar amplitude in the two parts, leading to a minor oscillation of $\langle N\rangle_{spray}\ (\alpha)$.

To appreciate the fuel amount oscillation during the periodic cycle, the phase-averaged droplet diameter is plotted in the same regions as the droplet count. Therefore, Equations (6.9) to (6.11) are applied to the local phase-averaged droplet diameter, $\langle d_{10}\rangle(\alpha, r)$. The resulting values $\langle d_{10}\rangle_{spray}\ (\alpha)$, $\langle d_{10}\rangle_{int}\ (\alpha)$ and $\langle d_{10}\rangle_{ext}\ (\alpha)$ respectively apply to the whole spray, the internal part and the external part. Results at $z = 2.1$ mm are shown in Figure 6.24 for the three flame powers. **In the whole spray**, $\langle d_{10}\rangle_{spray}\ (\alpha)$ oscillates weakly for the three flame powers. **In the internal part**, a remarkable oscillation is noticed for $\mathbb{P}_{43}$. For this power, $\langle d_{10}\rangle_{int}\ (\alpha)$ roughly oscillates in phase with the acoustic pressure, and thus in phase opposition with the droplet count. As noticed in Figure 6.18 (d), the air flow axial velocity[4] mostly oscillates in phase opposition with the acoustic pressure. Therefore, this leads to an alternation between the injection of a great amount of rapid smaller droplets followed by a lower amount of slow larger droplets. When the flame power is increased, the values of $\langle d_{10}\rangle_{int}\ (\alpha)$ decrease at all phase angles, and its oscillation amplitude is reduced too. **In the external part**, the oscillation of $\langle d_{10}\rangle_{ext}\ (\alpha)$ is weaker for $\mathbb{P}_{43}$ but remains more intense than for the two higher powers, for which it can be considered as negligible. The higher values of $\langle d_{10}\rangle_{ext}\ (\alpha)$ are correlated with the lower droplet count and vice-versa, but the axial velocity modulation is weak in this part of the spray. Therefore, the external region is characterised by a modulation of the droplet count, but droplet properties like axial velocity and diameter are not much modified during the acoustic cycle.

6.6.1.2 Propagation of the droplet number wave and correlation with the OH*-intensity wave

The propagation of the droplet number wave is addressed by measuring the evolution of the droplet number during the acoustic cycle at an axial location further away from the injector, here $z = 15$ mm. The comparison with the previous results, obtained at $z = 2.1$ mm, indicates how the droplet number wave evolve during transport. $\langle N\rangle_{spray}\ (\alpha)$, $\langle N\rangle_{int}\ (\alpha)$ and $\langle N\rangle_{ext}\ (\alpha)$ obtained at $z = 15$ mm, for which the separation between the internal and the external parts is located at $|r_{sep}| = 8.25$ mm, are illustrated for $\mathbb{P}_{43}$ and $\mathbb{P}_{75}$ in Figure 6.25.

At $z = 15$ mm, $\langle N\rangle_{spray}\ (\alpha)$ is significantly lower than at $z = 2.1$ mm, due to evaporation. In addition, $\langle N\rangle_{spray}\ (\alpha)$ clearly oscillates for $\mathbb{P}_{43}$ and $\mathbb{P}_{75}$, but now, its oscillation amplitude is stronger for $\mathbb{P}_{75}$ than for $\mathbb{P}_{43}$. For both powers, this oscillation is dominated by that of $\langle N\rangle_{int}\ (\alpha)$, in which the droplet number is strongly modulated during the cycle. The propagation velocities of the maximum as well as the minimum of $\langle N\rangle_{int}\ (\alpha)$ can be obtained by comparing the phase angle at which they are found at $z = 2.1$ mm and $z = 15$ mm. The propagation velocity of the maximum is about 36 m/s for $\mathbb{P}_{43}$, corresponding to 1.25 U_b, while for $\mathbb{P}_{75}$ it is 58 m/s, corresponding to 1.2 U_b. The propagation velocity of the minimum is 26 m/s for $\mathbb{P}_{43}$, corresponding to 0.9 U_b, while for $\mathbb{P}_{75}$ it is 47 m/s, corresponding to 0.95 U_b. The maximum of the droplet number wave is transported at a higher velocity since it is ejected simultaneously with the maximum of the axial velocity oscillation. In other words, the pocket with a higher droplet density is faster than the pocket with a lower droplet density. This leads to the deformation of $\langle N\rangle_{int}(\alpha)$, which has a sinusoidal shape at $z = 2.1$ mm while it characterised by a steep increase and a

[4] calculated by focusing on the smallest fuel droplets.

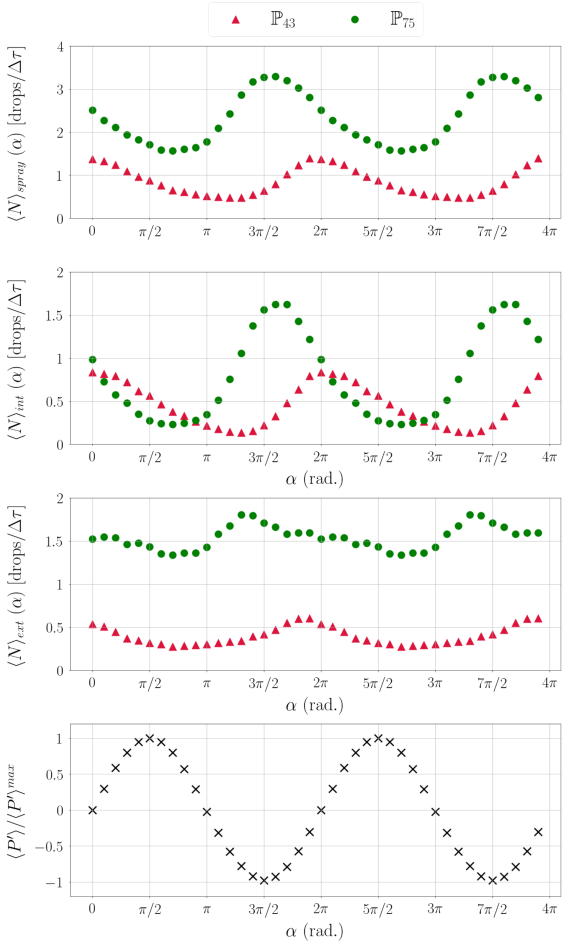

Figure 6.25: Phase-averaged droplet count integrated in the internal part, external part, and in the whole spray spray for $\mathbb{P}_{43}$ and $\mathbb{P}_{75}$ at $z = 15$ mm. The separation between the internal part and the external part is defined at $|r_{sep}| = 4$ mm. Top: droplets integrated in the whole domain, giving $\langle d_{10} \rangle_{spray}(\alpha)$; middle: droplets integrated in the internal part, giving $\langle d_{10} \rangle_{int}(\alpha)$; bottom: droplets integrated in the externa part, giving $\langle d_{10} \rangle_{ext}(\alpha)$.

smoother decreaser at $z = 15$ mm. This effect, identified in a non-reacting spray [136], tends to amplify the droplet number wave as the faster droplets catch up with the slower ones.

To correlate the droplet number wave with the OH*-intensity wave, the phase angle corresponding to the maximum of $\langle N \rangle_{spray}$ is obtained at several z-locations and compared with the z-location of the highest values of $\langle I_{cam} \rangle(\alpha, z)$ at a given α, obtained from Figure 6.13. At a given flame power, $\langle I_{cam} \rangle(\alpha, z)$ is reduced by the mean intensity of a reference flame specific to each power[5] (see method in Section 2.3.2.1). This is identical to the method used in Section 5.3.4.3 (see Figure 5.28). In Figure 6.26, this analysis is illustrated for $\mathbb{P}_{43}$ and $\mathbb{P}_{75}$ at a reduced acoustic amplitude $\Pi = 0.2$. For $\mathbb{P}_{43}$, the maximum of $\langle N \rangle_{spray}$ is obtained at $z = 2.1$ mm, $z = 5$ mm and $z = 15$ mm while for $\mathbb{P}_{75}$, it is only obtained at $z = 8.6$ mm and $z = 15$ mm due to the insignificant oscillation at $z = 2.1$ mm.
For all the flame powers, the phase angle at which the maximum of $\langle N \rangle_{spray}$ enters the region R_2, corresponding to $z \simeq 20$ mm for all the powers, coincides relatively well with the phase angle at which the OH* becomes discernible at the same location. The maximum of $\langle N \rangle_{spray}$ also coincides with the strong coherent vortex, leading to the engulfment of the great amount of fuel injected, and subsequently to an efficient air-fuel mixing.

6.7 Conclusion

Acoustic forcing is carried out on a configuration of three lean swirl-stabilised spray flames aligned in a cavity, where the central flame is placed of a pressure antinode of a standing transverse acoustic field. Three flame thermal powers, sharing the same equivalence ratio, are examined. For each power, the global flame response is similar for both CH* and OH* radicals. When the power is increased, the flame response becomes stronger and a progressive phasing appears with the acoustic pressure perturbation, resulting in an increased thermoacoustic coupling. The flame response and subsequent thermoacoustic coupling are governed by the middle region of the flame, whose location is unchanged for all flame powers. When the power increases, the OH*-wave propagates more rapidly in this region, limiting local anti-phase oscillations that reduce the flame response. Measurements performed on fuel droplets with a PDA system are able to give a good approximation of air flow velocities and swirl number. This latter quantity indicates that the swirl level is here sufficient to generate a central recirculation zone (CRZ). With acoustics, the periodic oscillation of the swirl number may induce periodic disappearance of the CRZ, resulting in the weakening of the flame stabilisation. As the flame powers grows, the swirl number oscillation can reach further downstream locations, allowing it to disturb the flame front in the strongly-responding middle region of the flame. Acoustics also generates the space-time modulation of droplet properties (count, diameter and velocity) at the injector exit. Separating the spray in an internal part and an external part shows the out-of-phase oscillation of the droplet number wave between these two regions. However, due to their different propagation velocity in each part, they oscillate nearly in phase slightly upstream of the middle region of the flame ($z \simeq 20$ mm), inducing a strong droplet count modulation at this location. Analyses indicate that the high droplet count is quite well correlated to the maximum of flame intensity oscillation.

[5] Here, the reference flame for a power $\mathbb{P}$ is the flame at the same power $\mathbb{P}$ without acoustic forcing.

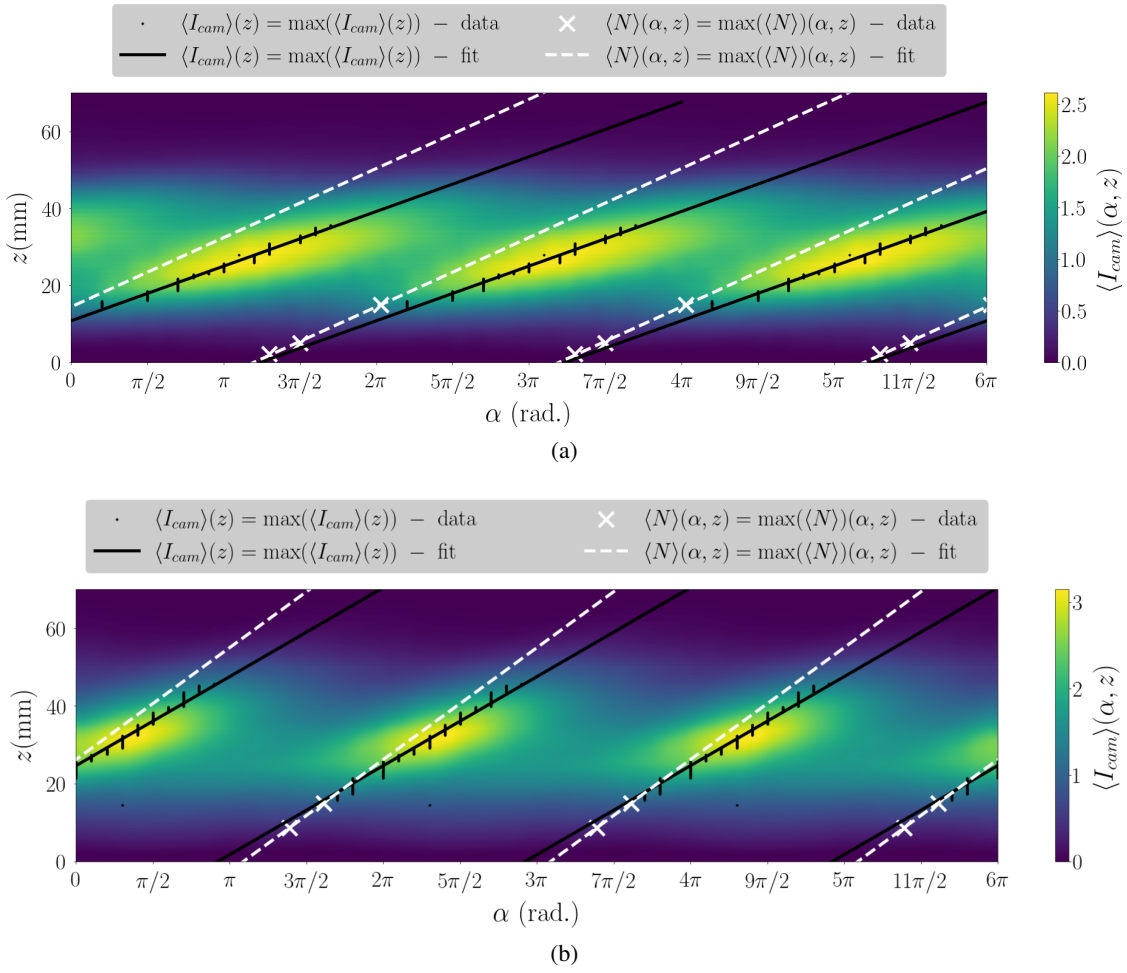

Figure 6.26: Analysis of space-time OH*-intensity wave and droplet number wave for $\mathbb{P}_{43}$ and $\mathbb{P}_{75}$, for $\Pi = 0.2$. The colormap gives the radical light intensity level $\langle I_{cam}\rangle(\alpha, z)$. For each z_i, the black dots indicate the phase angle at which $\langle I_{cam}\rangle(\alpha, z_i)$ is maximum; the solid black line draws a linear extrapolation of these experimental data points. White crosses give the phase angle at which the maximum droplet count is measured at three locations z; the white dashed line corresponds to a linear extrapolation of the experimental data points.

These results help in understanding mechanisms at the origin of the response of swirl-stabilised spray flames to downstream acoustic pressure oscillations.

Chapter 7

Saturation phenomenon of swirling spray flames at pressure antinodes of a transverse acoustic field

Contents

This chapter reproduces a work published in Proceedings of the Combustion Institute 38 (2021) after peer-review, under the title 'Saturation phenomenon of swirling spray flames at pressure antinodes of a transverse acoustic field', by Françoise Baillot, Clément Patat, Marcos Cáceres, Jean-Bernard Blaisot and Éric Domingues. It follows a work presented with the same title by C. Patat at the 38th International Symposium on Combustion, which was held on 24 - 29 January 2021 in Adelaide, Australia. This paper describes an experimental investigation of a linearly-arranged multiple-injection system of three swirling spray flames, simulating an unfolded sector of an annular combustor. Here we focus on the central flame placed in the basin of a pressure-antinode (PAN) of a standing transverse wave. Its response, quantified by means of the rms CH* amplitude filtered at the forcing frequency f_r, is studied as a function of the acoustic pressure rms amplitude reduced by the bulk aerodynamic pressure, Π, and parameterised by the flame power $\mathbb{P}$. As Π increases, three zones are identified: a linear growth, a transition zone and a saturation zone. Data in the linear growth and transition zone reIduced by an adequate parameter merge

into a unique self-similar curve whatever $\mathbb{P}$. In the saturation zone, the time-frequency analysis applied to photomultiplier signals shows that the frequency signal at f_r degrades in intensity level and uniformity, showing a loss of robustness in the flame response to the acoustic forcing over time. The gas phase displays strongly oscillating aerodynamics that can disrupt the central recirculation zone and destructure the mixing process. The liquid-phase shows a severe space-time modulation in droplet distribution and properties at high Π. Droplets are mainly found in an annular domain, characterised by a large time-dependence and inhomogeneity: a few quite big and slow fuel droplets are detected when the acoustic pressure $P^{'}(t)$ is positive, while a large population of small and rapid droplets is found when $P^{'}(t)$ is negative. In contrast, a little populated central core widens at positive $P^{'}(t)$ and fills up with big and slow droplets at negative $P^{'}(t)$. Such a periodic clustering might thus slow down the evaporation process.

7.1 Introduction

Environmental issues for limiting pollution are in the spotlight. Among the disruptive technologies, lean-burn combustor technology is a key element in bringing sustainable solutions while satisfying energy needs. Moreover flame stabilisation is often ensured by swirling flows to keep flames sufficiently far from solid elements while reducing the energy system size and increasing the power density. Unfortunately, this technology also induces weaknesses by diminishing damping and enhancing compacity, making the system more sensitive to combustion instabilities with possible flashback, extinction or structural damages [179]. Essential properties describing the physics of instabilities have been investigated to develop analysis tools, such as Flame Transfer Functions (FTF) and Flame Describing Functions (FDF), as well as low order models by performing numerous experimental and numerical studies on mono-injector premixed flames in response to longitudinal acoustic modes (*e.g* [50, 70, 74, 180, 181]) Nevertheless swirling flows complicate the matter due to flow instabilities likely to couple with longitudinal or azimuthal acoustic modes [25, 108]. Moreover the annular combustor geometry usually used in practical applications leads to preferential couplings between heat release rate and azimuthal acoustic chamber modes [104, 182–184].

Furthermore in engines and combustion chambers, energy systems are commonly powered by liquid-fuel injectors [185]. Coupling mechanisms involved in such combustors still need basic investigations to propose models able to predict the onset of instabilities. Indeed, studies concerning thermo-acoustic instabilities are found for gaseous non-premixed swirling flames (*e.g* [88]), but few deal with liquid-fuel spray combustion. Among those are the experiments of de la Cruz Garcia et al. [89] and Eckstein et al. [71] in the presence of longitudinal modes or the numerical work of Ghani [186] in the case of azimuthal modes. The spray introduces a supplementary complexity due to the impact of both fuel evaporation and air-fuel mixing times on the phase delay that characterises the coupling between combustion waves and acoustics. There are still fewer studies on the response of a complete energy system such as the annular multi-injection configuration of the academic MICCA-Spray combustor (MSC) [91, 101].

Identifying mechanisms responsible for instabilities is facilitated by using forcing methods. Forced flames present a linear response at low forcing levels, but nonlinear and complex be-

haviours at higher levels, resulting from the superposition, even the interference, of several physical mechanisms involving flames, flows and acoustics. In particular, a saturation phenomenon for gaseous flames, possibly linked to the appearance of limit-cycles in self-excited instabilities processes has been emphasised [67,68,88]. The different time scales characterising mixing inhomogeneities, oscillatory vortical flow structures, vortex breakdown and unsteady flame standoff distance can enhance or dampen the oscillating response of (partially) premixed swirling flames. But there is still a lack of knowledge on swirling spray flames submitted to azimuthal disturbances, especially for multiple injections.

The present study concerns a linearly-arranged multiple-injection system of three swirling spray flames, simulating an unfolded sector of the annular MSC likely to develop thermo-acoustic azimuthal instabilities [91, 101]. Here we focus on the response to a standing transverse wave of the central flame placed in the basin of a pressure-antinode (PAN), while each lateral flame is at about mid-distance between PAN and an intensity antinode (IAN). This investigation is an essential milestone in highlighting the basic mechanisms involved, and will also serve as a reference for future works at IAN and VAN (velocity antinode). The paper is composed of four sections in addition to the introduction and concluding remarks. In section 2, the experimental facility (acoustic cavity and instrumentation) is presented. In section 3, the physical and aerodynamic properties of the energy system (two-phase swirling flow and swirling flames) are introduced without acoustics. The transverse acoustic field is characterised in section 4. The flame response is discussed in section 5 where the highlighted saturation phenomenon is quantified.

7.2 Experimental facility

Acoustic cavity: The cavity design derives from the MSC, in which azimuthal standing instabilities are found to develop at a frequency varying in the range 700-780 Hz [91], which leads to the forcing values chosen here. The cavity is formed by a fixed base, two side plates separated by an adjustable length, L_c, and two front walls $e = 55$ mm apart of height $h_c = 200$ mm, that can be equipped with quartz windows. A convergent part (exit width of 10 mm, height of 60 mm) sits on top of the front walls, avoiding outer air to go inside and increasing resonance level. The coordinate system (O_c, x, y, z) is at the base's center (see Figure 7.1). Two compression drivers Beyma CP850ND are set face to face on the side walls to force a 2T1L mode.

Injection system: Three independent swirl injectors are flush with the base and separated by an interaxis $a_{inj} = 65$ mm, identical to that in the MSC. Each injector comprises a plenum, a distributor and a radial swirler for the air, and an atomiser set at 0.67D before the nozzle exit of diameter $D_{exit} = 8$ mm. The fuel is n-heptane. Experiments were performed at two global equivalence ratios ϕ and four powers per flame $\mathbb{P}$ (see table 7.1). A subscript is associated to the symbol $\mathbb{P}$, peculiar to a flame power value. For example, $\mathbb{P}_{75}$ corresponds to 7.5 kW, which is an unstable MSC condition in the presence of azimuthal standing waves. In the following, superscripts "a" and "f" denote air and fuel respectively.

Stabilisation system: The linearly-arranged flames were stabilised by adding a swirling air-jet next to each outer injector at the interaxis a_{inj} [45]. The two non-reactive jets prevent overheat-

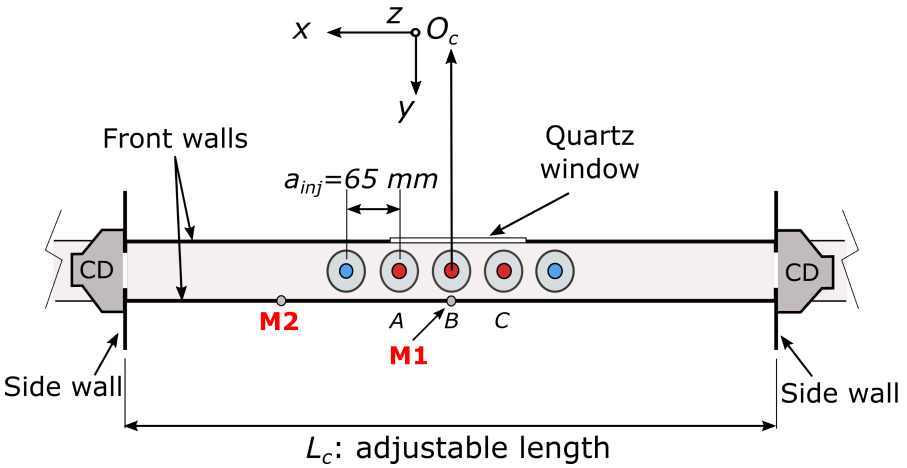

Figure 7.1: Acoustic cavity top view: compression drivers (CD), injectors: red (fuel/air), blue (air). M1 and M2: microphones. A, B, C: position of the flames.

ϕ	0.85			0.95
Flame power	$\mathbb{P}_{43}$	$\mathbb{P}_{59}$	$\mathbb{P}_{75}$	$\mathbb{P}_{48}$
(kW)	4.3	5.9	7.5	4.8
$\dot{m}^f$ (g/s)	0.097	0.132	0.168	0.108
$\dot{m}^a$ (g/s)	1.72	2.35	2.99	1.72
$I_{CH^*}^{rms,trans}/\overline{I_{CH^*}}^0(\%)$	6.1 ± 0.6	18 ± 0.7	24.3 ± 1.2	-

Table 7.1: Operating points and experimental characteristics. *Parameters defined in section 5.

ing of the side-walls and compression drivers to keep their performances unchanged compared to ambient temperature conditions. The two swirlers are the same as the swirlers used for the injection system.

Cavity instrumentation and flame diagnostics: Basic instrumentation was composed of type K thermocouples and B&K type 4182 microphones. High-speed laser tomography was used to describe the swirling gas flow. Either DEHS or oil particles were used to seed the air-flow for experiments without or with combustion respectively. In the latter case, the spray was characterised with fuel droplets as tracers. Images were recorded by a Phantom V2512 camera equipped with a 200 mm-focal-length lens and a 20 mm extension-tube. For horizontal views the camera was tilted at $45°$ from the $x-y$ plane and equipped with a Scheimpflug mount set at $20°$. Horizontal views were recorded at $35,000$ fps (exposure time $t_e = 10$ µs; 768×768 pixels; 0.031 mm/pix) and vertical views at $20,000$ fps ($t_e = 40$ µs; 976×1024 pixels; 0.036 mm/pix). To quantify gas and spray dynamics, 4W argon-ion laser-based LDA or PDA systems were used. Flame dynamics was analysed through OH* or CH* radical emissions which give similar results [45]. Indeed, $I_{OH^*}(t)$ signal is considered as an adequate indicator of the combustion heat release rate as well as $I_{CH^*}(t)$ signal in the absence of soot [166]. These signals were recorded by a Hamamatsu H6779 photomultiplier (PM) coupled with a UV-visible lens and an interference filter for CH* or

OH^*. OH^* emission images (0.19 mm/pix) were recorded with or without forcing by a Phantom V2512 camera at $20,000$ fps ($t_e = 40$ µs), and without acoustics by a Phantom V10 camera at $2,773$ fps ($t_e = 160$ µs), both equipped with a Lambert HiCATT 25 intensifier, a UV-100 mm lens and the adequate filter.

Here, the investigated flow and flame are those associated to the central burner. Measurements performed from its exit are specified in a local coordinate system (O_c, r, θ, z). O_c is also the center of the burner exit cross-section.

7.3 Energy system without acoustics

Air flow: Velocity components of the air flow (U_z^a, U_r^a, U_θ^a) were measured by LDA by means of seeding particles for $0.375 \leq z/D_{exit} \leq 1.125$ and $\dot{m}^a = 1.72$ g/s. A number of droplets between 10,000 and 200,000 with a maximum acquisition time of 4s ensured the mean values converged. The swirl number, given by $S^a(z) = \frac{\int_0^R \overline{U_z^a}\ \overline{U_\theta^a} r^2 dr}{R \int_0^R (\overline{U_z^a})^2\, r dr}$, with $R = D_{exit}/2$, is 0.68. A central recirculation zone (CRZ) was detected, as expected for flows with a swirl number higher than 0.6 [28]. The jet structure was investigated by time-resolved laser tomography. In the outer layer, Kelvin-Helmholtz type vortices, described by a helical mode turning with the swirl flow, are periodically shed at a frequency between 2.2 and 2.5 kHz. Streamwise structures, ejected laterally, were also detected. The cross-observation of vertical and horizontal views indicates the presence of a double helix turning in the swirl flow direction and identified as the Precessing Vortex Core (PVC). This turns around the CRZ at a frequency, f_{pvc} between 2.25 and 2.5 kHz. f_{pvc} is also verified to vary quasi-linearly with the flow-rate [28].

Reactive flow with combustion: Characterisation of the spray by laser diffraction without combustion showed that the Sauter-mean diameter D_{32} decreased from about 30 µm to 19 µm when $\dot{m}^a$ increased but changed little with $\dot{m}^f$ for the conditions studied here. With combustion, the spray was characterised by PDA. Four droplet size classes of 5 µm width, labeled C_1 to C_4, were defined in the range 0-20 µm with a fifth class, C_5, for droplets larger than 20 µm. Figure 7.2 reports the mean velocity field measured in the vertical axial plane ($O, \boldsymbol{r}, \boldsymbol{z}$) for classes C_1 and C_4. The most numerous droplets are in the smallest size class and the least numerous in the largest size class, as given by the data rates reported in Table 7.2. The biggest droplets show

Class of fuel drops	C_1	C_2	C_3	C_4	C_5
Max. data rate (drops/s)	7758	2349	1879	1409	1269
Mean data rate (drops/s)	1304	429	331	245	196

Table 7.2: Droplet numbers per second for the 5 fuel classes

ballistic behaviour (straight streamlines) whereas streamlines of smallest droplets suggest that they are likely to follow the air flow (curved streamlines). To evaluate this, the local Stokes number $\mathrm{Stk}(r) = \frac{\rho^f d_{10}^2(r)\, \overline{U_z^f}(r)}{18 \mu^a(r)\, D_{exit}}$ was determined at $z/D_{exit} = 0.625$ above the central injector. The air dynamic viscosity $\mu^a(r)$ was estimated in the low (near the burner axis) and high (near

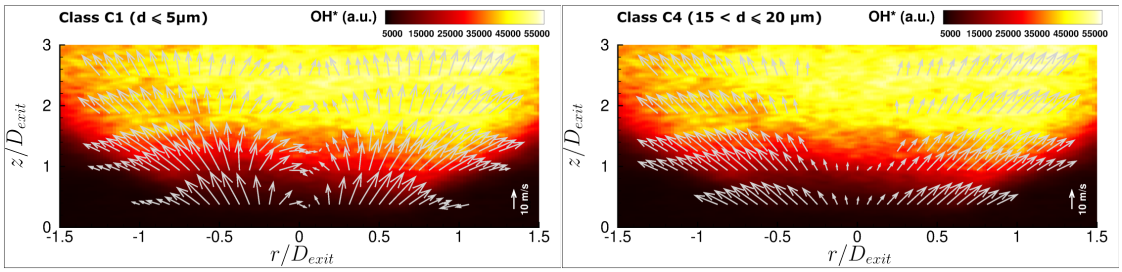

(a) (b)

Figure 7.2: N-heptane droplets velocity field sorted by droplet size classes and mean OH* intensity field ($\phi = 0.95$).

the wall) velocity domains, from the temperature measurements $\mathcal{T}_{low} = 338$ K and $\mathcal{T}_{high} = 750$ K respectively. S_t, estimated from data of Figure 7.2, is about 0.1 and 0.3 for classes C_1 and C_2 respectively, which confirms that gas phase dynamics can be characterised by these droplets. The negative axial velocity component for the smallest droplets highlights the CRZ, which is actually present with or without combustion. The radial velocity profiles extracted from PDA measurements also look similar with or without combustion, but for all diameter classes. Fuel droplet velocities, U_r^f, U_θ^f and U_z^f, were also obtained by LDA without discriminating between droplet sizes. Except in the CRZ domain, the shape of the mean velocity profiles at $z/D_{exit} = 0.375$ differ little from the shape of the profiles for droplet class C_1 or for seeding particles without combustion, leading to the same order of magnitude for the swirl number, $S^f = 0.76$ (cf [45]).

Swirling flames: The mean OH*-intensity field obtained from high-speed visualisation is reported in Figure 7.2. The mean flame standoff distance measured on image series is 2.6 mm (with a rms of 1.2 mm and a maximum distance of 7.4 mm) for the conditions of the figure.

7.4 Transverse acoustic field

The acoustic field was first validated without flow. For a given length L_c, the forcing frequency f_0 was adjusted at the acoustic 2T mode. Acoustic fields obtained for $L_c = 522$ mm, are presented for $f_r = 718$ Hz with the convergent part and without it for $f_r = 773$ Hz in Figure 7.3 where data are normalised by the maximum value recorded at the mid point ($x = 0$). Measurements made along the z-direction ($x = 0$, $y = 0$) indicate a quarter wavelength behaviour, typical of a 1L mode. It is noted that the pressure amplitude varies very little from $z = 0$ to $z = 0.3h_c$. Whatever the operating conditions, the domain is much wider than the space occupied by the compact flames. Finally it was verified that pressure amplitude does not vary in the y-direction. The acoustic mode identification was completed by a finite element analysis achieved with COMSOL Multiphysics©; the results, reported in Figure 7.3, agree well with experimental data. From this analysis a quick identifying procedure through verifying both the following conditions was set up: (i) the pressure amplitude measured at $x = 0$ is maximum; (ii) the phase of the pressure fluctuations $\varphi_p(f_r, x)$ measured along a segment located in the vicinity of $x = 0.25L_c$ must vary from 0 to π. This procedure succeeds with combustion (see Figure 7.3 for $L_c = 800$ mm

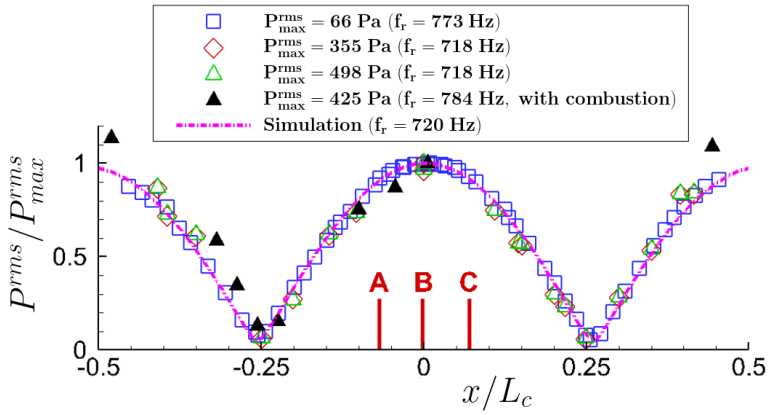

Figure 7.3: Pressure amplitude along the x-axis ($y = 0$, $z = 0.12h_c$). W/o combustion: $L_c = 522$ mm, $f_r = 773$ Hz (w/o the convergent part (c.p.), $f_r = 718$ Hz (with c.p.). With combustion: $L_c = 800$ mm, $f_r = 784$ Hz (with c.p.). Red lines and letters A, B and C: position of flames.

and $f_r = 784$ Hz).

7.5 The saturation phenomenon

The forcing frequency f_r is chosen in the instability frequency basin of the MSC (see table 7.3). At PAN, the acoustic rms amplitude P^{rms} was increased from 100 to 1600 Pa. P^{rms} is then reduced by the bulk aerodynamic pressure, introducing the non-dimensional parameter $\Pi = P^{rms}/(\rho^a U_b^2)$. ρ^a and U_b (defined at the burner exit) are calculated at 293 K. The central flame at PAN is placed in a small gradient environment at the highest acoustic level, while a lateral flame depends not only on the acoustic amplitude which remains high in that position, but also on the local acoustic pressure gradient. This leads to a different response to the forcing [45, 111]. An illustration is reported in Figure 7.4 presenting images at the dominant mode of frequency f_r obtained by Dynamic Mode Decomposition (DMD). There the behaviour of the central flame is axisymmetrical on average, contrary to that of the lateral flame. In the following, the results concern the central flame response.

The power of all flames was simultaneously changed while keeping $\phi = 0.85$. Three powers are used: $\mathbb{P}_{43} = 4.3$ kW, $\mathbb{P}_{59} = 5.9$ kW and $\mathbb{P}_{75} = 7.5$ kW (see table 7.1). Superscript "0" denotes no forcing conditions and overline indicates time-average mean quantities.

L_c (mm)	f_r at $\mathbb{P}_{43}$ (Hz)	f_r at $\mathbb{P}_{59}$ (Hz)	f_r at $\mathbb{P}_{75}$ (Hz)
800	-	760, 762, 766	776, 778
880	704, 709	-	742

Table 7.3: Forcing frequency corresponding to the results of section 7.5.

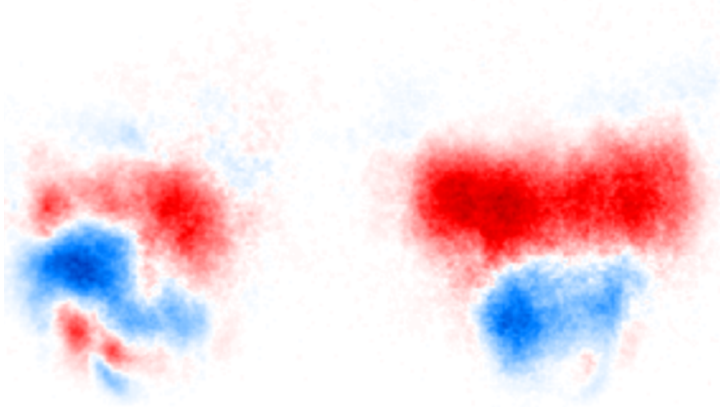

Figure 7.4: DMD images for $\mathbb{P}_{48}$, $\phi = 0.95$, $L_c = 800$ mm. Right flame: at PAN, left flame: at about mid-distance between PAN and IAN.

7.5.1 Flame dynamics analysis with PM

The post-processing of PM signals $I_{CH^*}(t)$ is the same for all the data. The rms amplitude $I^{rms}_{CH^*}$ is estimated at frequency f_r from the Welch's method. Figure 7.5 shows that $\overline{I_{CH^*}} \,/\, \overline{I_{CH^*}}^0$ diminishes as a unique function of Π whatever $\mathbb{P}$. At low Π, the decrease remains small; it can be ascribed to a preferential dilution of the reactants by burnt gases due to three-dimensional acoustic-pumping-enhanced recirculation flows that are shown in our high-speed laser tomography images (not illustrated here). Beyond $\Pi \sim 0.3$, the slope becomes steeper. In addition to the recirculation effects, a loss of ordered and periodic flame response leads to weakening of the flame stabilisation as shown below. Unlike $\overline{I_{CH^*}}/\overline{I_{CH^*}}^0$, the data for $I^{rms}_{CH^*}/\overline{I_{CH^*}}$ do not merge on a unique function of Π whatever $\mathbb{P}$ (see Figure 7.5). This is also the case for the data reported for $I^{rms}_{CH^*}/\overline{I_{CH^*}}^0$, which evolve in a similar manner to those for $I^{rms}_{CH^*}/\overline{I_{CH^*}}$ (not reported here). Whatever the profile ($I^{rms}_{CH^*}/\overline{I_{CH^*}}$, $I^{rms}_{CH^*}/\overline{I_{CH^*}}^0$ and $I^{rms}_{CH^*}$ versus Π), the rms intensity increases with $\mathbb{P}$ as a strictly monotone function: the more the thermal power in the system, the greater the flame instability. At a fixed $\mathbb{P}$, $I^{rms}_{CH^*}/\overline{I_{CH^*}}$ first increases linearly up to $\Pi \sim 0.3$ before reaching a saturation zone. Such behaviours were noted in gaseous partially-premixed swirling flames [88]. Reducing $I^{rms}_{CH^*}$ by $I^{rms,trans}_{CH^*}$, a value corresponding to $\Pi = \Pi^{trans} = 0.32$ leads to a (partial) self-similarity behaviour with $\mathbb{P}$. As seen in Figure 7.5 three zones are clearly identifed: a self-similarity linear growth until Π^{trans}, then a self-similar transition until $\Pi^{sat} \sim 0.5$ and finally a saturation zone. These features suggest that the relative balance between the mechanisms driving the instability, even mechanisms themselves, is modified by passing from the linear growth to the saturation zone. The robustness of the flame response was then characterised in the three identified zones by a time-frequency analysis applied to PM signals through Short-Time Fourier Transform (STFT). In all the cases, the driving frequency f_r is well detected. In the linear growth, the signal becomes uniform as Π increases. In addition, the greater the flame power, the more uniform the signal. In the transition zone, the signal reveals that the flame response is established: the intensity level is the highest. But at the same time it becomes less uniform, showing fluctuations over time. These features are accentuated by the flame power increase. Finally in the saturation zone, the signal degrades in intensity level, but also in uniformity. It

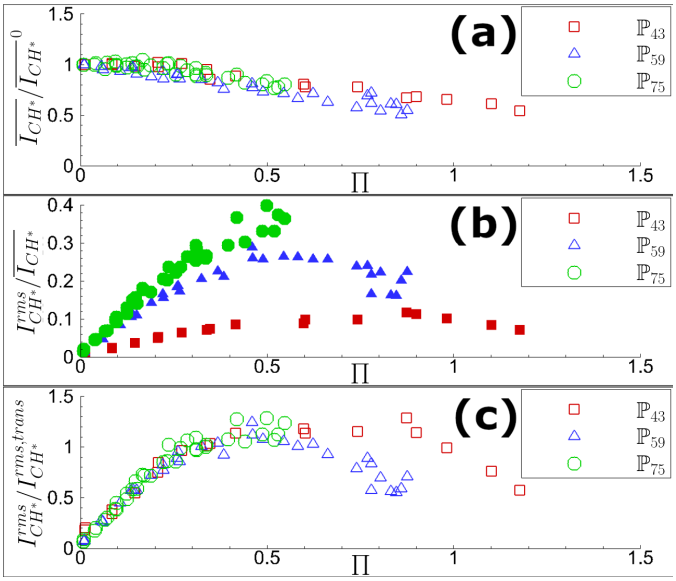

Figure 7.5: Response of the flame vs. $\Pi = P^{rms}/\rho^a U_b^2$ for three flame powers $\mathbb{P}$: (a) normalised mean intensity $\overline{I_{CH^*}}/\overline{I_{CH^*}}^0$; (b) reduced rms intensity $I^{rms}_{CH^*}/\overline{I_{CH^*}}$ filtered at f_r; (c) reduced rms intensity $I^{rms}_{CH^*}/I^{rms,trans}_{CH^*}$ filtered at f_r.

strongly fluctuates, even revealing interruptions specified by an intensity lower than the detected noise. Thus the saturation zone is marked by a loss of robustness in the ordered response of the flame to the acoustic forcing over time.

However these features cannot be taken as indicators of the "efficiency" of the energy system in producing periodic heat release rate fluctuations at f_r. This can be obtained by the use of the concept of FDF. In the case of a downstream forcing applied to premixed flames, Gaudron et al. [52] showed that there was an equivalence between the FDF based on pressure fluctuations and that on velocity fluctuations. Here, the downstream forcing of the standing 2T1L mode generates pressure fluctuations $P^{'}(t)$ at PAN which are at the origin of velocity fluctuations as well as of equivalence ratio fluctuations coming from a complex process from atomisation to mixing via evaporation phenomenon. Thus $P^{'}(t)$ may be introduced as a "global input" on which velocity and equivalence ratio fluctuations depend. It is proposed, on the basis of the previous elements, to formulate $(\breve{I}_{CH^*}/\overline{I_{CH^*}})$, in the frequency domain, at f_r by the relation $(\breve{I}_{CH^*}/\overline{I_{CH^*}}) = \mathcal{F}_{P'}\ (f_r, \Pi; \mathbb{P})(\breve{P}/(\rho^a U_b^2)$. Here, $\mathcal{F}_{P'}$, parameterised by $\mathbb{P}$, is a meaningful inclusive FDF. The gain $\mathcal{G}$ and phase delay φ are reported in Figure 7.6 as functions of the reduced acoustic amplitude Π. The decrease of $\mathcal{G}$ with Π clearly shows a nonlinear amplitude dependence. It also indicates that the flame loses some ability to convert acoustic fluctuations into CH*-intensity fluctuations. In the saturation zone, the gain is quite small, showing a weak coupling at f_r. In addition, $\mathcal{G}$ augments with $\mathbb{P}$ increase in a nonlinear manner in agreement with previous results giving the dependency of $I^{rms}_{CH^*}/\overline{I_{CH^*}}$ with $\mathbb{P}$ (see Figure 7.5). The phase delay φ is nearly independent of Π, so it cannot be used to discriminate between the three zones. But it strongly depends on $\mathbb{P}$. The phase delay tends to zero while $\mathbb{P}$ increases, which suggests a stronger coupling between acoustics and combustion. This is consistent with the presence of

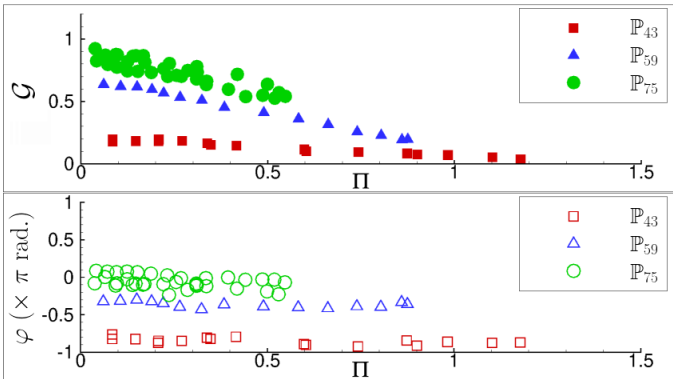

Figure 7.6: FDF $\mathcal{F}_{P'}$ at f_r vs. Π: gain $\mathcal{G}$ and phase φ for three flame powers $\mathbb{P}$.

instabilities observed in the MSC at flame powers close to $\mathbb{P}_{75}$ [91]. So, the system sensitivity to instabilities can be crucially modified by the change of φ, a key-element to predict self-instability via the Rayleigh criterion, according to $\mathbb{P}$.

7.5.2 Flame dynamics analysis with high-speed camera

To explore the underlying mechanism leading to saturation, the response of the middle flame for $\mathbb{P}_{43}$ was investigated by 2,000 OH* emission images recorded at 20,000 fps. It is quite higher than the value of about 500 images that ensures signal statistical convergence. Three series of images were considered, two with forcing and one without forcing. The PSD of $I_{OH^*}(t)$ signal was extracted from each series. Two forcing conditions are presented with similar intensities $I^{rms}_{CH^*}/\overline{I_{CH^*}}$: $\Pi = 0.45$ (transition zone) and $\Pi = 1.27$ (established-saturation zone) (see Figure 7.5). In both forcing cases, PSDs highlight a peak at f_r, but in the transition zone the peak is strong, 2.7 times greater than that obtained in the established-saturation zone. This confirms that the flame responds very weakly at the forcing frequency in the established-saturation zone. The DMD method was used here to complete the analysis. Results are obtained for a reconstructed $P^{'}(t)$ cycle and illustrated in Figure 7.7 at the cycle phase angles α equal to 0 and $3\pi/4$ for both $\Pi = 0.45$ and 1.27. A longitudinal intensity-wave propagating downstream at a speed of about 26 m/s, the order of magnitude of U_b, is highlighted in both cases. No significant phase delay between them is noted, which agrees with data given in Figure 7.6. But the blurred aspect of the flame response for the established-saturation zone shows a weaker link between combustion and acoustics. Stabilisation being also a key-element to sustain combustion, the flame foot from each series was investigated. Without acoustics, the mean standoff distance $\overline{H}^0$ is about 3.6 mm and its standard deviation δ^0 is 1.9 mm. However the flame foot may reach downstream distances up to 10.5 mm. For $\Pi = 0.45$ the standoff distance differs little compared to the unforced configuration: its mean value $\overline{H}$ is about 1.1 $\overline{H^0}$ and its standard deviation only increases by about 16%. While the maximum locations are similar, the minimum values are lower than those without acoustics, diminishing by about 40%. The flame thus has the capacity to go nearer the burner. For $\Pi = 1.27$, $\overline{H}$ is 2.5 $\overline{H}^0$ and the standard deviation is 2.1 δ^0. While the flame never stabilises at lower positions than those of the unforced flame, it may reach distances twice as great as those without forcing. So the flame can be pushed far away downstream; its

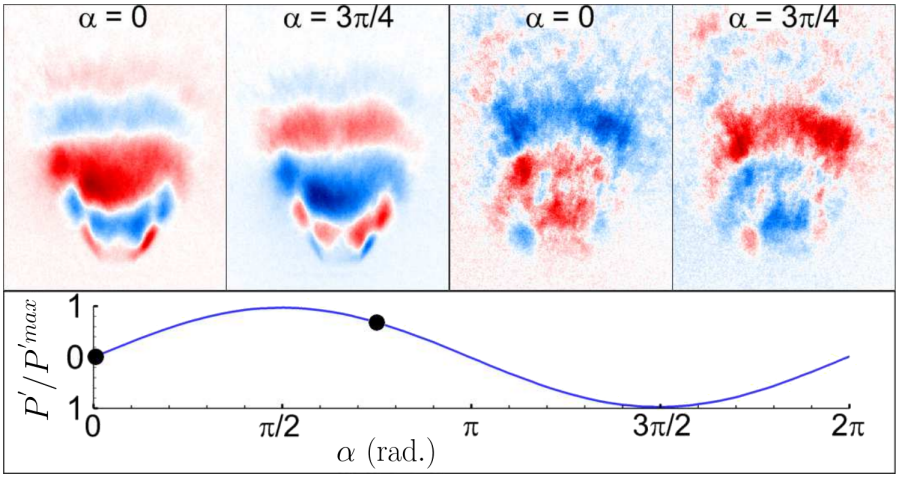

Figure 7.7: DMD images of 2000 instantaneous flame front OH* emission images for $\Pi = 0.45$ (left) and 1.27 (right), post-synchronised with the acoustic pressure. $\mathbb{P}_{43}$, $\phi = 0.85$. Points: values of the phase angle α associated to the images.

stabilisation, greatly weakened, becomes more sensitive to blowout. This feature, as well as elements extracted from the DMD investigation, confirms that the periodic spray-flame response is drastically "destructured" at high perturbation amplitudes.

7.5.3 Saturation mechanism in spray combustion

In the saturation zone, the higher flame stabilisation position associated to the "destructured" flame behaviour should lead to a weak combustion intensity, which might precede blowout. The perturbed gas-phase dynamics can play a specific role in the instability process. In particular, the periodic shedding of a very energetic vortex linked to successive strong flow accelerations/decelerations, is able to push the flame far downstream. The CRZ observed in vertical tomography views appears dramatically disturbed, even destroyed, over time. This agrees with results without combustion showing swirl number values for the air flow much lower than 0.6 during most of each forcing cycle [45]. The disruption of the CRZ should induce a modification in the flame aerodynamic environment, which leads the flame to find adequate stabilisation conditions farther downstream (see section 7.5.2).

In order to understand the spray impact on the energy system under forcing, phase-averaged radial distribution quantities obtained from PDA measurements of all the droplets were determined: the droplet count $\langle N \rangle(r/D_{exit}, \alpha)$, Sauter-mean diameter $\langle D_{32} \rangle(r/D_{exit}, \alpha)$ and axial velocity $\langle U_z^f \rangle(r/D_{exit}, \alpha)$. Measurements are recorded over 2s to 4s ($N_{cycles} = 1400$ to 2800). Each cycle is divided in 20 bins of duration $\Delta\tau = T/20$ (*i.e.* $\Delta\alpha = \pi/10$), with T the acoustic period. The phase-averaged values are then calculated in each bin. The reference counting without acoustics $N^0(r/D_{exit}, \alpha)$ is obtained by averaging the droplet count during the same duration $T/20$) over the same equivalent recording duration, *i.e.* from 2s to 4s.

Figure 7.8 illustrates $N^0(r/D_{exit}, \alpha)$ and $\langle N \rangle(r/D_{exit}, \alpha)$ measured near the burner exit at $z/D_{exit} = 0.27$ without acoustics and $z/D_{exit} = 0.26$ for $\Pi = 0.35$ and 1. The droplet

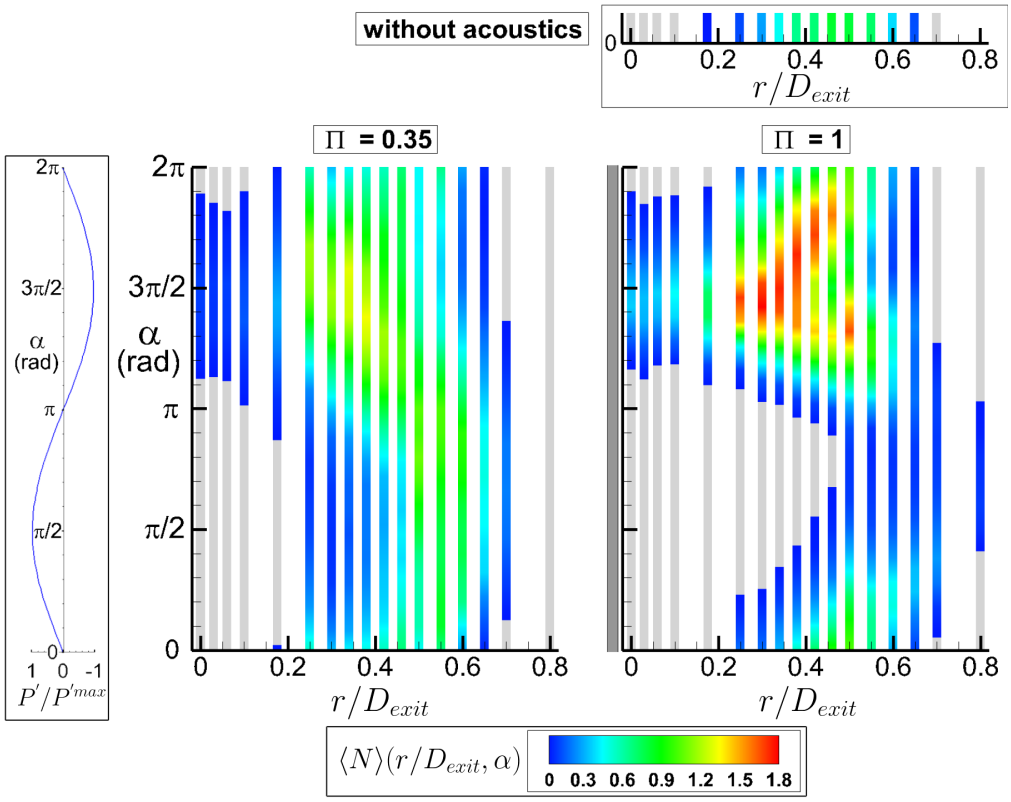

Figure 7.8: Phase-averaged droplet number $\langle N \rangle (r/D_{exit}, \alpha)$ over a reconstructed cycle and along a radius at $z \simeq 0.26 D_{exit}$. $f_r = 703$ Hz, $\mathbb{P}_{43}$, $\phi = 0.85$. Grey: $\langle N \rangle \leq 0.04$ droplet/$\Delta\tau$.

count gives information about the populated region of the space. ***Without acoustics***, this region appears as a ring delimited by $r_{in} = 0.2D$ and $r_{out} = 0.7D$. $N^0(r/D_{exit})$ inside the ring is quasi-homogeneous. The core region ($r < r_{in}$) and the external region ($r > r_{out}$) where the droplet count is too low to be validated ($< 1/25$ droplet per $\Delta\alpha$) are colored in grey. Profiles of $U_z^{f,0}$ along r/D_{exit} are almost bell-shaped with a maximum of about 24.5m/s centered at $r/D_{exit} = 0.45$ and reach 13 m/s at the periphery of the ring. D_{32}^0 is in the range 25-35 µm for $r_{in}/D_{exit} < r/D_{exit} < 0.45$ and in the range 15-25 µm for $r/D_{exit} > 0.45$, showing that the smallest droplets are located at the periphery of the ring. ***With acoustics***, the droplet distribution is time-dependent and is no longer homogeneous inside the ring.

For $\Pi = 0.35$ (transition zone), when $P'(t)$ is positive, the ring distribution begins to be spatially inhomogeneous with droplets spreading over the outer region. Their diameters $\langle D_{32} \rangle$ and velocities $\langle U_z^f \rangle$ vary between 25-40 µm and 13-26 m/s respectively. In addition, the core is sparsely populated, so no count validation is possible. But when $P'(t)$ is truly negative for $1.2\pi < \alpha < 1.8\pi$, the core is now populated by more droplets, which are characterised by $\langle D_{32} \rangle$ in the range 30-35 µm and velocities $\langle U_z^f \rangle$ between 11-20 m/s; simultaneously, the droplet count in the ring increases, reaching a maximum about 1.5 times greater than the maximum for $N^0(r/D_{exit})$, and $\langle D_{32} \rangle$ and $\langle U_z^f \rangle$ vary in the ranges 20-30 µm and 25-32 m/s respectively.

For $\Pi = 1$ (established saturation zone), when $P'(t)$ is negative, the ring domain is filled by

more droplets than for $\Pi = 0.35$ (in particular the maximum count is about 1.33 times greater). Moreover, its droplets are quite small (15 µm $\leqslant \langle D_{32} \rangle \leqslant$ 30 µm) and rapid (30 m/s $\leqslant \langle U_z^f \rangle \leqslant$ 38 m/s). Simultaneously, the core is also more populated, but with droplets which are still fewer, larger (25 µm $\leqslant \langle D_{32} \rangle \leqslant$ 42 µm) and slower (14 m/s $\leqslant \langle U_z^f \rangle \leqslant$ 20 m/s) than those in the ring. In the remainder of the cycle, the droplet count in the core, which widens up to $r/D_{exit} = 0.46$, is so small that it cannot be validated. The droplet population in the ring diminishes drastically and these droplets are quite slow (10 m/s $\leqslant \langle U_z^f \rangle \leqslant$ 15 m/s) and large (30 µm$\leqslant \langle D_{32} \rangle \leqslant$ 45 µm). So, the features of the spray identified for $\Pi = 0.35$ are strongly amplified, *i.e.* time-dependence of droplet-population in the ring, inhomogeneity of this population, widening of the non-populated core at positive $P^{'}(t)$ and filling-up of the core at negative $P^{'}(t)$.

The saturation zone is thus characterised by a severe space-time modulation in droplet distribution and properties, which leads to the concentration of many small and rapid droplets during negative $P^{'}(t)$ delivered in a delimited spatial domain, namely the ring. This occurs simultaneously to the ejection of the large energetic vortex, which promotes the disorganisation of the CRZ. In contrast, a few quite big and slow droplets are in the ring when $P^{'}(t)$ is positive. This generates a spatial-gradient of fuel, varying with time, which is strengthened as Π increases. This process, based on large inhomogeneities, should not benefit either efficient fuel evaporation or mixing. In particular, evaporation might be slowed down due to droplet clustering [139].

7.6 Conclusion

This chapter concerns an original configuration of an energy system constituted of three swirl-stabilised spray flames, which simulates an unfolded sector of an annular combustor. These results characterise the central flame placed in the vicinity of the pressure antinode of a 2T1L acoustic mode. The flame response quantified by the fluctuating CH*-intensity is studied as a function of Π, the acoustic pressure rms amplitude reduced by the bulk aerodynamic pressure. The normalised mean CH*-intensity $\overline{I_{CH^*}}/\overline{I_{CH^*}}^0$ is shown to decrease as a self-similarity function with Π. The fluctuations $I_{CH^*}^{'}(t)$ at f_r are characterised by three zones: a linear growth followed at $\Pi \sim 0.3$ by a transition that ends at $\Pi \sim 0.5$, followed in turn by a saturation zone. The flames, crossed by a periodic flame-emission intensity wave that weakens in the saturation zone, are then pushed away as Π increases. All these features can be explained not only by the gas phase aerodynamics structured by acoustics, but also by the new space-time organisation of the spray over acoustic cycles. At high Π, a few quite big and slow fuel droplets are detected when the acoustic pressure $P^{'}(t)$ is positive, while a large population of small and rapid droplets is found when $P^{'}(t)$ is negative. This pattern constitutes the initiation of droplet waves which are amplified with Π. It might be induced by the formation on the wall, upstream from the burner exit, of a film that undergoes oscillatory pull, as shown numerically on a similar injector in [140]. Severe inhomogeneities in equivalence ratio together with strongly oscillating aerodynamics that can disrupt the CRZ and destructure the mixing process can both interfere to produce those flame responses described by a FDF gain diminishing towards zero at high Π and a typical quasi-constant power-dependent phase-delay.

Chapter 8

Influence of the liquid fuel on the flame response to pressure fluctuations

Contents

Part of this chapter is based on works presented by C. Patat at ICLASS 2021[1] *and published in the conference proceedings under the title 'Response of a spray of n-heptane or dodecane at an acoustic pressure antinode in reactive conditions', by Clément Patat, Jean-Bernard Blaisot, Éric Domingues and Françoise Baillot. The impact of the liquid fuel characteristics on the swirl-stabilised spray flame response at a pressure antinode is investigated here. To this end, n-heptane or dodecane flames are established in TACC-Spray. These two fuels are chosen due to*

[1] 15^{th} Triennial International Conference on Liquid Atomization and Spray Systems, Edinburgh, UK, 29 August - 2 September 2021.

their physico-chemical characteristics leading to different atomisation properties and evaporation times. Without acoustic forcing and with combustion, the dodecane spray is characterised by a lower proportion of small droplets (diameter $d \leq 5$ µm) and a higher proportion of large droplets ($d > 30$ µm). With acoustic forcing, the classical Rayleigh criterion is fulfilled at all the acoustic amplitudes explored here with the two fuels, indicating the potential of these fuels to drive self-excited instabilities at the chosen operating conditions. In the linear zone, n-heptane flames have a greater potential to drive instabilities due to the higher FDF gain than dodecane and the FDF phase close to 0. The difference of the FDF phase may result from the higher evaporation time with dodecane. The higher gain with n-heptane can be explained by a modification of the space-time fuel spray modulation with the fuel: the higher count of small droplets and its stronger modulation with n-heptane than with dodecane indicates that the flame response may be dominated by the modulation of the fuel amount provided by small droplets.

8.1 Introduction

One proposed solution to reduce the environmental impact of gas turbines and aircraft engines is to replace fossil fuels with others produced from renewable sources such as biomass. However, 82% of the primary energy consumed in 2021 derived from fossil sources [1], which necessarily implies a gradual transition. Therefore, there is a significant interest in (i) developing fuel-flexible systems and (ii) improving the processes based on fossil fuel combustion to help in reducing pollutant and greenhouse gas (GHG) emissions in the short to medium term. A promising path to address the latter point is lean-burn combustion, which could allow a reduction of nitrogen oxides (NO_x) and carbon monoxide (CO) emissions, soot production and an increase in combustion efficiency. However, this technology has the disadvantage of being more prone to combustion instabilities, which complicates the development of lean-burn engines. Developing fuel-flexible systems is also a challenging task, especially because of the dependence of dynamic flame stability on the fuel [141, 187]. Therefore, combustion instabilities are a major issue for both these technological solutions.

Real aircraft engines are operated with liquid fuels, which have a higher volumetric energy density than gaseous fuels. The presence of a spray introduces the need for the fuel to evaporate and to mix with the air before the combustion process. To increase the combustion efficiency, these processes are accelerated by injecting a fine spray in the combustion chamber. However, coupling mechanisms involving the fuel spray were identified (see Section 1.4.6). The importance of considering the response of the spray to acoustics was already shown in the literature. As droplet size is known as a parameter determining for fuel transport and evaporation [71], a modulation of the drop size distribution, observed in non-reacting conditions [135, 177], could drive a self-excited instability in reacting conditions. In a study from De la Cruz García et al. [89], the modification of the spray Sauter mean diameter (SMD) with the increase of the air mass flow rate was identified as a cause for a shift in the frequency of a self-excited instability, from 220 Hz to 323 Hz. In addition, the formation of droplet number density waves, observed experimentally in non-reacting [136] and reacting conditions (see Chapters 5 to 7), and numerically [140], leads to a periodic modulation of the fuel amount reaching the flame front and can therefore result in

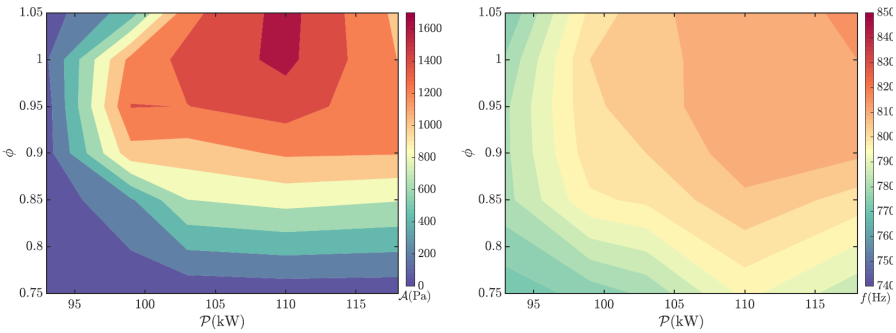

(a) N-heptane

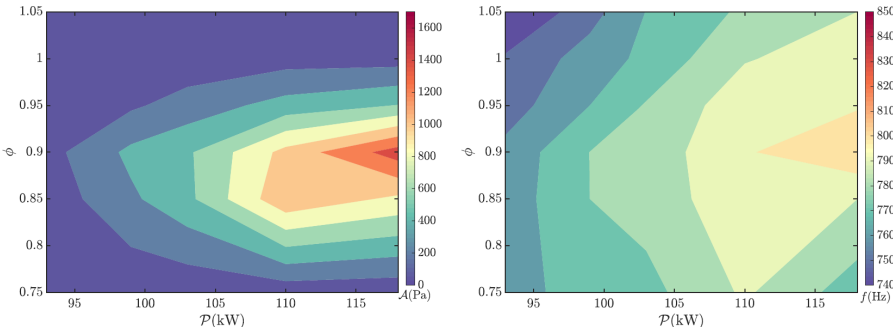

(b) Dodecane

Figure 8.1: Stability maps as a function of thermal power $\mathcal{P}$ and equivalence ratio ϕ in the sixteen-injector annular combustor MICCA-Spray, with n-heptane or dodecane as a fuel. The left column indicates the instability amplitude and the right column the instability frequency. Reproduced from [141].

an oscillation of the HRR.

Deeper insight of the role of the spray-acoustics coupling in self-excited instabilities was brought by a recent numerical work from Lo Schiavo et al. [140], developed in the FASMIC project. They showed, in a system equipped with an airblast injector, that thermoacoustic instabilities at a frequency around 500 Hz can be sustained by the coupling between a liquid fuel film created at the wall inside the injector and the acoustic perturbation. The authors performed simulations at the same operating conditions as those giving rise to a self-excited instability in the single-injector burner SICCA-Spray [91]. They assessed two different boundary conditions at the injector walls. For the first one, it is indicated that '*the particles reaching the walls slip along the wall at their initial speed*': this is identified as 'SLIP' condition. For the second one, called 'FILM' condition, '*particles reaching the wall form a film. Its depth and speed are calculated using Saint Venant equations*'. The limit cycle observed experimentally was well predicted by using the 'FILM' condition, while the 'SLIP' conditions led to a damped system. This showed that spray-combustion coupling can be a driving mechanism for instabilities.

The dependence of instabilities on the spray-combustion-acoustics coupling is a serious issue for fuel-flexible systems. This means that stable operating conditions for a given fuel are not necessarily stable for another one. The EM2C team [141] established stability maps in the self-unstable MICCA-Spray annular combustor for various fuels, among which n-heptane and dodecane. As shown in Figure 8.1, operating conditions that were unstable with n-heptane were stable with dodecane (*e.g.*, for an equivalence ratio $\phi \leq 1$). The instability amplitude varied greatly when the fuel is changed, but the instability frequency remained in the same range of 770-820 Hz, although it was a little lower with dodecane. In their experiments, the oscillations were coupled with the 1A-1L mode of the combustor, explaining the closeness of the instability frequencies observed for various fuels.

This chapter aims at examining the impact of the liquid fuel on the response of swirl-stabilised spray flames to a transverse acoustic oscillation. For this study, n-heptane and dodecane are chosen due to their physico-chemical characteristics leading to different atomisation properties and evaporation times. In Section 8.2, the operating conditions are detailed. In Section 8.3, the energy system is described without acoustic forcing for the two fuels. Section 8.4 presents the global and local OH^*-intensity oscillations for the two fuels. The consequences on the thermoacoustic coupling are addressed. In Section 8.5, the similarity of the airflow for the two fuels is discussed. Finally, Section 8.6 deals with the responses of the sprays of n-heptane or dodecane to the acoustic modulation.

8.2 Material and methods

The experimental setup is the acoustic cavity TACC-Spray, presented in Section 2.1.1. Its length L_c is set to 880 mm, ensuring that the resonance frequency f_r of the 2T1L mode of the cavity is in the range 710 - 740 Hz. The five-injector linear array is placed in the cavity such that the central flame is located at the central pressure antinode (PAN). The injection system is described in Section 2.1.2. In this chapter, the three central injection units are supplied with either n-

heptane or dodecane as a fuel. These two fuels are chosen for their different atomisation and evaporation properties. The operating points associated to n-heptane and dodecane correspond respectively to $\mathbb{P}_{59}$ and $\mathbb{P}_{59d}$ in Table 8.1. They share the same flame power (5.9 kW per flame), equivalence ratio ($\phi = 0.85$), fuel mass flow rate ($\dot{m}^a = 0.133$ g/s) and air mass flow rate ($\dot{m}^f = 2.35$ g/s). The set of swirler and outlet cup is the K modified set. The flame power of 5.9 kW per flame is chosen in light of the findings of Section 8.6, in which it is shown that this flame power ensures a strong flame response together with the possibility to reach high levels of relative acoustic forcing.

Analysis of the flame intensity is performed with a photomultiplier (PM), equipped with a filter centered on $\lambda = 305$ nm with a FWHM of 24 nm to observe emission of the OH* radical, which is linked to the HRR (see Section 2.2.3.1 for details about the setup). Spray analysis is performed in reacting conditions with a two-component Phase Doppler Anemometry (PDA) system, which allows to obtain the fuel velocity components U_r^f, U_θ^f, U_z^f and the diameter d of the fuel droplets (see Section 2.2.4 for more details). Measurements are performed during 4 seconds for around 40 measurement locations distributed along a radial line cutting the axis of the injector. They are carried out at three heights above the injector: $z = 2.1$ mm, $z = 6.8$ mm and $z = 20.5$ mm, corresponding to $z/D_{exit} = 0.26$, $z/D_{exit} = 0.85$ and $z/D_{exit} = 2.56$ respectively, where D_{exit} is the nozzle exit.

Fuel	flame power (kW)	equivalence ratio	$\dot{m}^f$ (g/s)	$\dot{m}^a$ (g/s)	U_b (m/s)	f_r (Hz)
n-heptane dodecane	5.9	0.85	0.133	2.35	38.9	719-732

Table 8.1: Operating points and experimental characteristics.

8.3 Characterisation of the energy systems without acoustic forcing

We first focus on the system operated with n-heptane or dodecane in steady conditions, *i.e.* without acoustic forcing.

8.3.1 Characterisation of the swirl-stabilised spray flames

The shape of the swirl-stabilised spray flames is first characterised by using 1,000 line-of-sight instantaneous OH* images of the central flame. Time-averaged flame images without acoustic forcing are shown in Figure 8.2 with n-heptane or dodecane, along with vertical and horizontal distributions of the OH*-intensity reduced by its maximum value specific to each fuel, corresponding to the spatial integration of the time-averaged images over $\vec{r}$ and $\vec{z}$ directions respectively (see Section 2.3.2.1). The vertical distributions show the maximum levels of the reduced OH*-intensity are found around $z = 25$ mm for dodecane and $z = 28$ mm for n-heptane. With dodecane, the reduced OH*-intensity is higher than with n-heptane at almost all vertical locations, indicating that the OH*-intensity is more uniformly distributed along z compared to n-heptane, for which it is rather concentrated around $z = 28$ mm. The spread of the vertical OH*-intensity distribution is quantified by calculating their FWHM, which is 27.6 mm with n-heptane

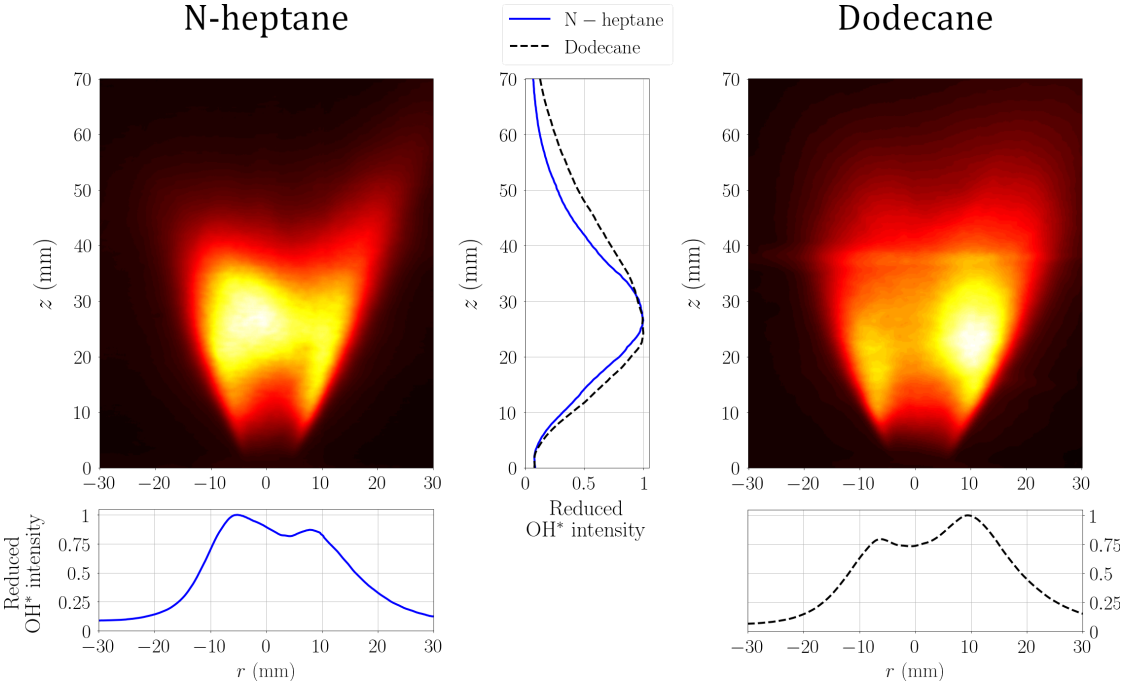

Figure 8.2: Time-averaged OH*-intensity images of the central flame with n-heptane or dodecane fuel without acoustic forcing, and associated vertical and horizontal profiles.

and 36.1 mm with dodecane. The horizontal distributions show that the highest OH*-intensity levels are around $r = 8 - 10$ mm with the two fuels. With the two fuels, one side of the flame is little more intense than the other side. A similar observation was made in the three-injector combustor TICCA-Spray in the thesis work of Rajendram Soundararajan [113] (Section 10.4).

The time-averaged flame base angle, $\overline{\theta}_{flame}$, is determined with a threshold method applied to Abel-transforms of the time-averaged images. With n-heptane, $\overline{\theta}_{flame}$ is 62.1° while with dodecane, it is 68.5°. The time-averaged flame standoff distance, $\overline{h_{base}}$, is 3.3 mm with n-heptane and 3.9 mm with dodecane.

8.3.2 Impact of the fuel on spray characteristics

The impact of the fuel on the spatial droplet distribution is first examined in Figure 8.3, showing the radial data rate profiles with n-heptane and dodecane at $z = 2.1$ mm. At this height, the characteristics of the fuel droplet radial distribution identified with n-heptane in Section 3.1 are retrieved with dodecane: a core region ($|r| < 2$ mm) almost empty of droplets; an annular region (2.5 mm $\leq r \leq 5$ mm) in which the data rate forms a quasi-plateau around 10,000 drops/s and an outer region ($|r| > 5$ mm) in which the data rate decreases up to $|r| = 6$ mm, beyond which no droplets are measured.

Radial profiles of the mean and rms values of the three fuel droplet velocity components, $U_z^f(r)$, $U_\theta^f(r)$ and $U_r^f(r)$, are given in Figure 8.4 at $z = 2.1$ mm for n-heptane and dodecane. The mean profiles for n-heptane and dodecane show a very good agreement. One can nonetheless notice small differences. For instance, in the $\overline{U_z^f}(r)$ profile, an almost perfect agreement is found

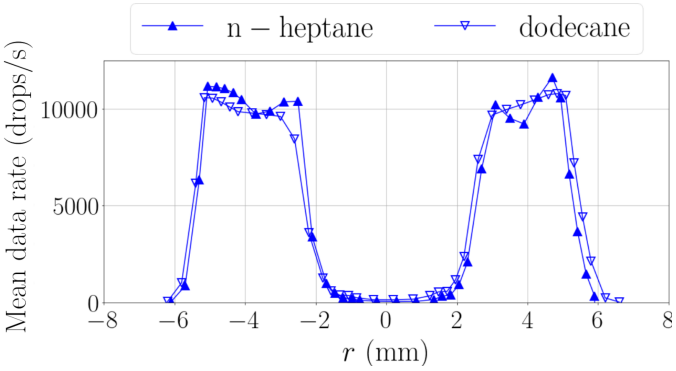

Figure 8.3: Radial profiles of mean fuel droplet data rate, $\overline{N}(r)$, with n-heptane and dodecane at $z = 2.1$ mm. This quantity is calculated by including all the droplets validated by the PDA system.

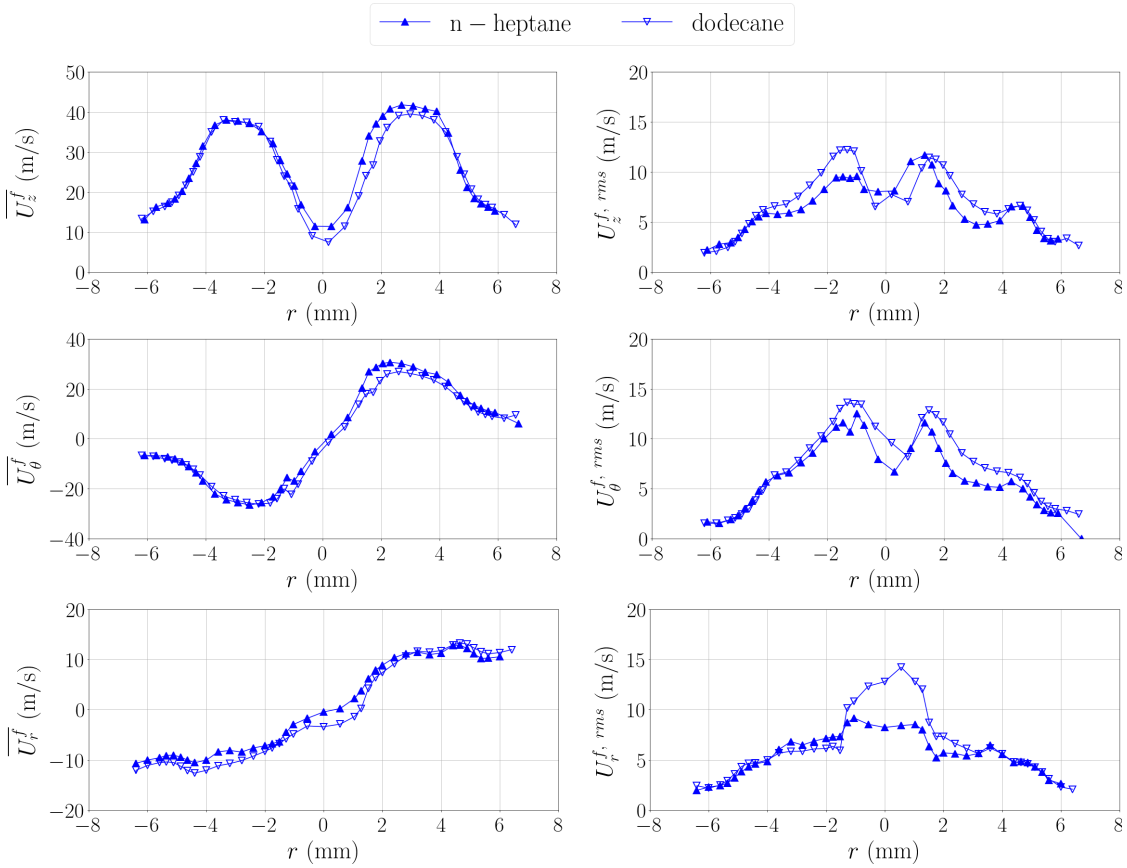

Figure 8.4: Radial profiles of the velocity components at $z = 2.1$ mm without acoustic forcing, for n-heptane and dodecane. Left column: time-averaged velocity components; right column: rms velocity components. Top: axial velocity U_z^f; middle: tangential velocity U_θ^f; bottom: U_r^f. All these quantities calculated by including all the droplets validated by the PDA system.

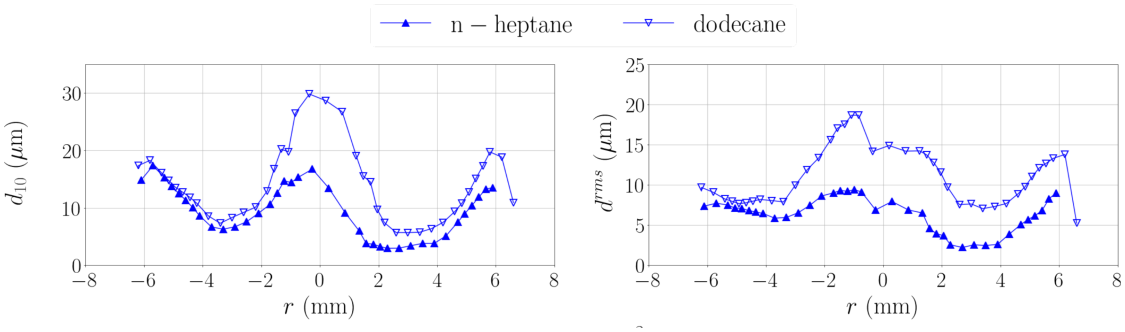

(a) Profiles of the local arithmetic mean droplet diameter and of the local rms droplet diameter

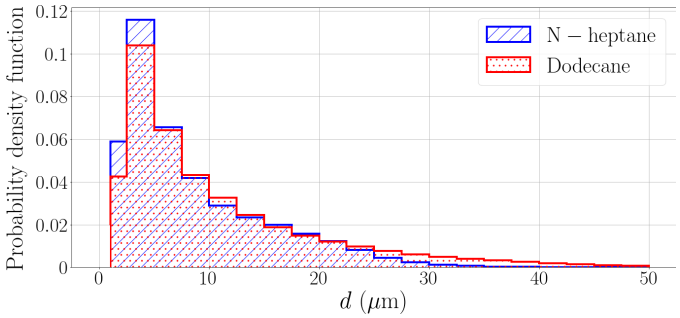

(b) Probability density function of the whole spray

Figure 8.5: Influence of the fuel on the fuel droplet diameter without acoustic forcing. (a) radial profiles at $z = 2.1$ mm for n-heptane and dodecane. Left: local arithmetic mean droplet diameter, $d_{10}(r)$; right: local rms droplet diameter, $d^{rms}(r)$. (b) probability density function of the fuel droplet diameter with n-heptane and dodecane, obtained by integrating the droplets on all a radial line at $z = 2.1$ mm. All these quantities calculated by including all the droplets validated by the PDA system.

for $r < 0$ and $r > 4$ mm, while for $0 < r < 4$ mm, $\overline{U_z^f}(r)$ is lower with dodecane than with n-heptane. The latter feature is explained below. The rms profiles are also similar for both fuels. The only notable exception concerns the rms value of the radial velocity, $U_r^{f,\,rms}(r)$, for $|r| < 1.5$ mm. In this range, $U_r^{f,\,rms}$ suddenly increases for both fuels, but the increase is much more pronounced with dodecane. Nevertheless, this might be linked to the very small droplet-amount in the region.

Radial profiles of the local arithmetic mean droplet diameter, $d_{10}(r)$, and the rms of the local droplet diameter, $d^{rms}(r)$ are shown in Figure 8.5 (a) at $z = 2.1$ mm, for n-heptane and dodecane without acoustic forcing. The profiles of d_{10} and d^{rms}, calculated by including all the droplets validated by the PDA system, present a slight asymmetry for both fuels inherent to this injector: for a same value of $|r|$, d_{10} is generally smaller for $r > 0$ than for $r < 0$. Nevertheless, the profile of d_{10} has the same shape with the two fuels, characterised by maximum values on the injector axis, minimum values for $|r|$ in the range 2-4 mm, beyond which d_{10} increases until r-locations at which no droplet is found. At all locations, d_{10} is higher with dodecane than with n-heptane. This is particularly noticeable for $|r| \lesssim 1.5$ mm, at which the values of d_{10} with dodecane are almost twice those with n-heptane. The profiles of d^{rms} have a very similar shape

with both fuels: it reaches a maximum at $r = 0$ and decreases at further radial locations until $|r| = 4$ mm, beyond which it increases again. The higher values obtained with dodecane indicate a more scattered drop size distribution.

The normalised drop diameter distribution, corresponding to the probability density function (PDF) of the droplet diameter, is obtained by integrating all the fuel droplets measured along the radial direction (-6.5 mm $\leq r \leq 6.5$ mm). It is shown in Figure 8.5 (b). The proportion of droplets of diameter d in the range 1-5 µm is larger with n-heptane ($\sim 39\%$ of the total droplet count) than with dodecane ($\sim 32\%$ of the total droplet count). On the contrary, droplets of diameter larger than 25 µm are very rare with n-heptane and proportionally more numerous with dodecane. The droplets of diameter in the range 5-25 µm are approximately in the same proportion for both fuels.
Statistical mean droplet diameters of the whole spray are calculated. The arithmetic mean droplet diameter, D_{10}, and the Sauter mean diameter (SMD), D_{32}, here calculated at N_{pos} radial locations, for which $N_{drops}(r_i)$ droplets are validated, are expressed by:

$$D_{10} = \sum_{i=1}^{N_{pos}} \sum_{j=1}^{N_{drops}(r_i)} \frac{d_j^1(r_i)}{d_j^0(r_i)} \tag{8.1}$$

$$D_{32} = \sum_{i=1}^{N_{pos}} \sum_{j=1}^{N_{drops}(r_i)} \frac{d_j^3(r_i)}{d_j^2(r_i)} \tag{8.2}$$

At $z = 2.1$ mm, D_{10} is 8.3 µm with n-heptane and 10.6 µm with dodecane, while D_{32} is 20.4 µm with n-heptane and 30.8 µm with dodecane. Since the SMD indicates the ratio of the fuel volume to the surface area, it gives insight into fuel evaporation. For a given fuel and fixed ambient conditions, a lower SMD indicates a faster spray evaporation, thus suggesting a longer evaporation time for the dodecane droplets. This is supported by the higher boiling temperature of dodecane (~ 489 K) than n-heptane (~ 371.5 K).

8.3.3 Impact of the fuel on the air flow

To estimate the ability of the fuel droplets to follow the airflow, radial profiles of the Stokes number Stk^2 (see Equation (3.1)) are shown with the two fuels in Figure 8.6, in which Stk is obtained by including all the droplets validated. **For** -4 **mm** $\leq r \leq -2$ **mm**, Stk is in the range $0.4 - 0.75$ with n-heptane, and in $0.55 - 1$ with dodecane. At each radial location, it is 40% to 60% higher with dodecane than with n-heptane. But, $\overline{U_z^f}$ is similar with both fuels in this range (see Figure 8.4 (top left)). **For** 2 **mm** $\leq r \leq 4$ **mm**, the Stokes number is lower than 0.16 with n-heptane whereas it is higher than 0.34 with dodecane. In this range, $\overline{U_z^f}$ is about 10% higher with n-heptane than with dodecane. Therefore, the twofold increase of the Stokes number with dodecane results in lower values of $\overline{U_z^f}$, which is calculated by including all the droplets validated. **For** $|r| < 2$ **mm**, the Stokes number is significantly affected by the fuel: it can be tripled with dodecane, reaching almost 3 at some specific locations. Despite the increase

[2] μ^a is calculated at $T = 293K$ for $|r| \leq 4$ mm and at $T = 700K$ for $|r| > 4$ mm.

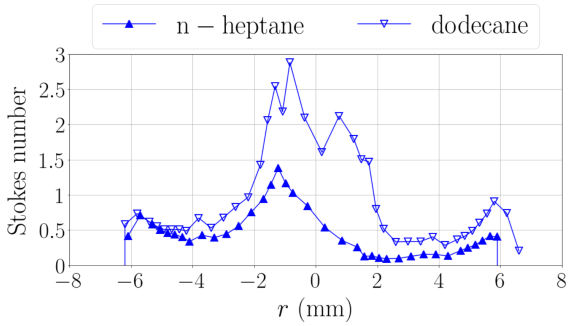

Figure 8.6: Radial profile of the Stokes number Stk, calculated by including all the droplets validated by the PDA system.

of Stk, lower values of $\overline{U_z^f}$ are found with dodecane than with n-heptane for $|r| < 1$ mm, which is contrary to the observations made at other radial locations. This suggests that the CRZ could go closer to the burner with dodecane.

A further investigation focuses on the smallest fuel droplets. To this end, only the droplets of class C_1, corresponding to a diameter d in the range $1-5$ µm are retained during post-processing. The ability of a droplet of diameter $d = 5$ µm to characterise the air flow motion is estimated with the Stokes number, calculated by considering that the axial velocity of this droplet corresponds to the mean axial velocity of the whole class C_1, either with n-heptane or dodecane. The Stokes number thus obtained is a majorant for class C_1 for two reasons: (i) $d = 5$ µm is the maximum diameter in this class; (ii) the mean axial velocity of the droplet of diameter $d = 5$ µm is actually slightly lower than the mean axial velocity of the whole class C_1 at most radial locations[3]. The associated radial profiles of the Stokes number are shown in Figure 8.7 (a). The profiles with the two fuels merge together at all radial locations[4] and Stk is everywhere lower than 0.27. Since this value is a majorant for class C_1, this indicates that droplets of this class can be reasonably considered to estimate the air flow motion. Like Stk, the *acoustic* Stokes number $\mathrm{Stk_{ac}} = \omega\tau_{drop}$ is identical for a droplet of diameter $d = 5$ µm with the two fuels: as indicated in Section 5.3.3.1, it does not exceed 0.25 for droplets of class C_1, showing that air flow oscillations are captured by these droplets. The data rate profiles of C_1 droplets are given in Figure 8.7 (b) to show the spatial distribution of such droplets.

The profiles of the mean and rms air flow axial velocities, $\overline{U_z^a}$ and $U_z^{a,\,rms}$, are displayed in Figure 8.8. For $|r| > 1$ mm, $\overline{U_z^a}$ and $U_z^{a,\,rms}$ are identical, showing that the air flow in this region is unchanged with the two fuels. On the contrary, for $|r| < 1$ mm, $\overline{U_z^a}$ is lower with dodecane, even reaching negative values on the injector axis, while with n-heptane, $\overline{U_z^a}$ decreases only to 8 m/s. There, $U_z^{a,\,rms}$ also differs a little with the two fuels, but it is probably due to the limited data available at these locations. Therefore, while the air flow at $z = 2.1$ mm is identical with n-heptane and dodecane at most radial locations, lower axial velocities found near the injector axis with dodecane suggest that the CRZ is more developed than with n-heptane. Nevertheless,

[3]Indeed, as shown in Section 3.2.1), the mean axial velocity for $|r| \leq 4.5$ mm increases as the mean droplet diameter decreases.

[4]The Stokes number is nonetheless slightly higher at most radial locations due its density of 750 kg/m^3, compared to 684 kg/m^3 for n-heptane.

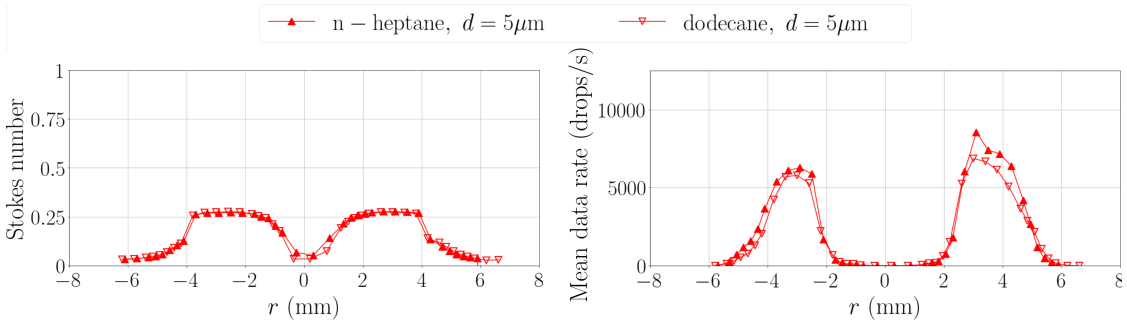

Figure 8.7: Radial profiles at $z = 2.1$ mm for n-heptane and dodecane droplets of class C_1, corresponding to a diameter d in the range $1 - 5$ µm, without acoustic forcing. The Stokes number, shown on the left plot, is calculated for a droplet of diameter $d = 5$ µm, whose axial velocity is assumed to be the mean axial velocity of the C_1 fuel droplets. The data rate is obtained by including all the C_1 droplets.

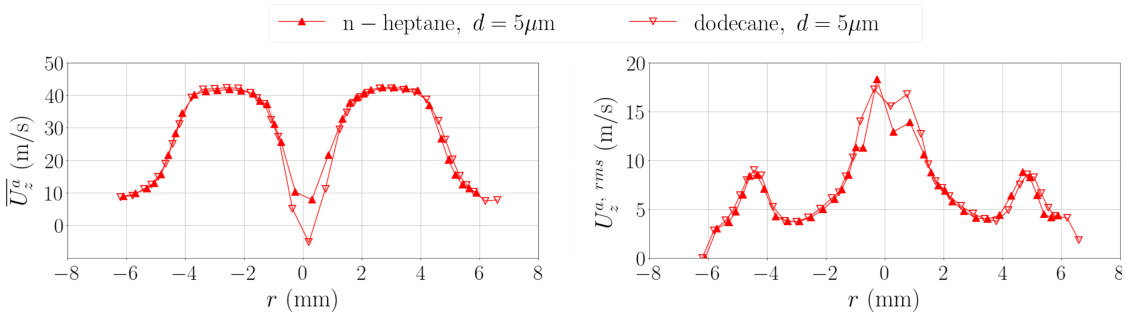

Figure 8.8: Radial profiles of the air flow axial velocity measured at $z = 2.1$ mm without acoustic forcing. Left: mean air flow axial velocity, $\overline{U_z^a}$; right: rms air flow axial velocity, $U_z^{a,\,rms}$. These quantities are measured by including only the fuel droplets of class C_1.

the lower values of $\overline{U_z^a}$ with dodecane are not observed at higher radial locations ($z = 6.8$ mm and $z = 20.5$ mm), at which $\overline{U_z^a}$ is similar with the two fuels. These results further indicate that the CRZ is located closer to the burner with dodecane.

8.4 Flame response to acoustics with n-heptane and dodecane

In this section, the global OH*-intensity oscillation of the central flame and the coupling between combustion and acoustics are first characterised with n-heptane and dodecane. Then, analyses of the local OH*-intensity oscillation are performed to gain deeper insight into the physical mechanisms driving the flame response to acoustics.

8.4.1 Global flame response and thermoacoustic coupling

The global flame response is here evaluated with OH*-intensity measurements of the central flame by using the PM setup described in Section 2.2.3.1. The evolution with Π of the mean OH*-intensity reduced by its value without acoustics, $\overline{I}/\overline{I}^0$, and the reduced rms amplitude of the OH*-intensity oscillation at f_r, $I^{rms}/\overline{I}$, are shown in Figure 8.9 for n-heptane and dodecane.

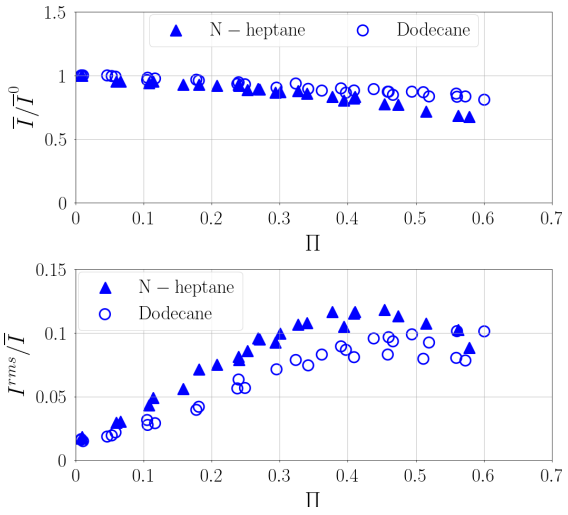

Figure 8.9: Flame response for n-heptane and dodecane obtained with OH* radical. The top plot shows the mean OH*-intensity from the central flame, the middle plot its fluctuation amplitude (rms) at f_r and the bottom plot the fluctuation amplitude reduced by the mean value.

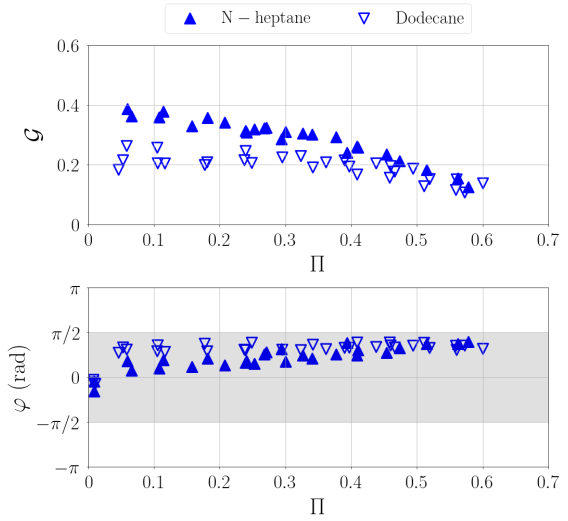

Figure 8.10: Flame Describing Function for n-heptane and dodecane obtained with OH* radical. The gain $\mathcal{G}$ is shown on top and the phase φ on the bottom. The grey band indicates the instability region based on the Rayleigh criterion. The excitation frequency f_r is in the range 714-720 Hz with n-heptane and in the range 725-730 Hz with dodecane.

With n-heptane, $\overline{I}/\overline{I}^0$ decreases slightly until $\Pi = \Pi_{trans} \simeq 0.35$, beyond which the negative slope is steeper. $I^{rms}/\overline{I}$ increases linearly up to $\Pi = \Pi_{trans}$, whereas it stops increasing and even saturates at higher Π (as shown previously in Section 5.2.1).
With dodecane, $I^{rms}/\overline{I}$ follows the same trend as with n-heptane, corresponding to a linear increase until Π_{trans} followed by a roughly constant level up to $\Pi = 0.6$. The fact that the slope break is found at Π_{trans} with both fuels indicates that the nonlinearity is governed by features independent of the fuel here. $\overline{I}/\overline{I}^0$ decreases slightly up to $\Pi = 0.6$. Above $\Pi = \Pi_{trans}$, higher values of $\overline{I}/\overline{I}^0$ are found with dodecane than with n-heptane.

The flame response to acoustics is also evaluated via the Flame Describing Function (FDF) framework, here expressed at freuqency f_r by:

$$\mathcal{F}(f_r, \Pi) = \frac{\breve{I}/\overline{I}}{\breve{P}/\rho^a U_b} = \mathcal{G}(f_r, \Pi) e^{i\varphi_{\mathcal{F}}(f_r, \Pi)} \tag{8.3}$$

FDFs are presented for both fuels in Figure 8.10. **The gain** $\mathcal{G}$ is almost twice higher with n-heptane than with dodecane in the linear zone, indicating a more efficient coupling between acoustics and combustion with n-heptane. With n-heptane, the gain slightly decreases, indicating the presence of weak nonlinearities while with dodecane, it remains roughly constant. For $\Pi > \Pi_{trans}$, the negative slope of the gain with Π is noticeably steeper with both fuels, reflecting in a loss of the efficiency of the combustion-acoustics coupling. Nevertheless, it is steeper with n-heptane, resulting in the same gain around $\Pi = 0.5$. **The phase** has a different behaviour with each fuel. With n-heptane, it increases linearly with the acoustic amplitude, from $\sim 0.1\pi$ at $\Pi = 0.05$ to $\sim 0.4\pi$ at $\Pi = 0.5$. At frequencies $f_r \simeq 720$ Hz encountered here, the increase of 0.3π of the phase corresponds to an increase of 0.2 ms of the time delay between $P^{'}(t)$ and $I^{'}(t)$. With dodecane, the phase remains in the range $0.3\pi - 0.4\pi$ at all Π. In spite of this difference between the two fuels, the phase is always inside the instability region predicted by the Rayleigh criterion, indicating the potential ability of the energy system to drive instabilities. This ability is indicated by the Rayleigh source term (see Section 1.2.2).

The coupling between combustion and acoustics is estimated from the instability index $\mathcal{R}a_1(t) = \xi P^{'} I^{'}(t)$, with $\xi = 1/(\rho^a U_b^2 \overline{I})$. Its time-averaged value, $\overline{\mathcal{R}a_1}$, gives insight about the Rayleigh source term (see Section 1.2.2). $\overline{\mathcal{R}a_1}$ is compared for various Π with n-heptane and dodecane in Figure 8.11. For the two fuels, $\overline{\mathcal{R}a_1}$ is positive at all acoustic amplitudes, indicating the constructive interference between $P^{'}(t)$ and $I^{'}(t)$, thus the potential of those flames to drive self-excited instabilities. Values are larger with n-heptane than with dodecane for $\Pi \leq 0.4$ due to the higher FDF gain and the fact that the FDF phase is closer to 0. For higher Π, the FDF gain and phase merge for the two fuels, resulting in a similar values of $\overline{\mathcal{R}a_1}$.

The rest of this chapter focuses on the flame response in the linear zone and attempts to answer the following questions:

- Why is the FDF gain higher with n-heptane than with dodecane?
- Why does the FDF phase differs between the two fuels?

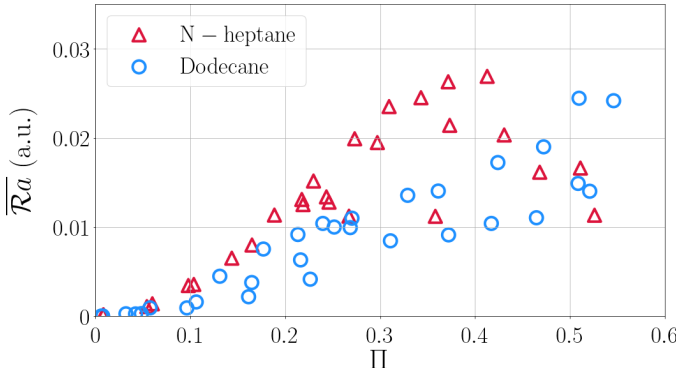

Figure 8.11: Time-averaged value of the instability index $\mathcal{R}a_1 = \xi P^{'} I^{'}(t)$ as a function of reduced acoustic amplitude Π measured at the flame location, with n-heptane or dodecane. $I^{'}(t)$ is measured with OH* radical. The excitation frequency f_r is in the range 714-720 Hz with n-heptane and 725-730 Hz with dodecane.

8.4.2 Local flame response in the linear zone

In this subsection, the local OH*-intensity oscillation is investigated from 2,000 instantaneous OH*-intensity images acquired at 20,000 Hz. The two-dimensional intensity signals obtained from the instantaneous images, $I_{cam}(r, z, t)$, are post-processed with the procedure described in Section 2.3.2.1, giving a phase-averaged local OH*-intensity, $\langle I_{cam} \rangle(\alpha, z)$. For each z-location, the rms amplitude of the phase-averaged OH*-intensity oscillation, $\langle I^{'}_{cam} \rangle^{rms}(z)$, and the phase shift between the phase-averaged acoustic pressure oscillation at the central flame location and the local OH*-intensity oscillation, $\varphi_{\langle P' \rangle - \langle I'_{cam} \rangle(z)}$, are calculated. $\langle I^{'}_{cam} \rangle^{rms}(z)$ and $\varphi_{\langle P' \rangle - \langle I'_{cam} \rangle(z)}$ are shown with n-heptane or dodecane in Figure 8.12, for Π in the linear zone. $\langle I^{'}_{cam} \rangle^{rms}(z)$ is maximum around $z = 30$ mm with both fuels. However, the magnitude of the peak is 67% higher with n-heptane. As shown in Section 6.4.1, the phase delay between the acoustic pressure oscillation and the OH*-intensity oscillation in the middle region of the flame, named R_2, corresponds to the phase of the FDF. In Figure 8.12, R_2 is defined by 18 mm $< z <$ 38.5 mm with n-heptane and 17 mm $< z <$ 41.3 mm with dodecane. In these ranges, the averaged value of $\varphi_{\langle P' \rangle - \langle I'_{cam} \rangle(z)}$ is 2.06π with n-heptane and 2.19π with dodecane. The gap of 0.13π is close to the gap between the FDF phase with the two fuels at $\Pi = 0.2$, which is about 0.15π (see Figure 8.10).

These results thus indicate that the gap between the FDF phases of the two fuels is due to the fact that the OH*-intensity wave propagates with a slight phase lag with dodecane compared to n-heptane. This may be linked to the increased evaporation time with dodecane.

8.5 Air flow axial velocity oscillation

In this subsection, the air flow axial velocity oscillation is compared when the system is operated with n-heptane or dodecane. To this end, the phase-averaged axial velocity of the air flow, $\langle U_z^{a'} \rangle$, is obtained by including the fuel droplets of diameter d in the range $1 - 5$ µm, which have been shown to capture correctly the air flow motion (see Figure 8.7). $\langle U_z^{a'} \rangle$ is obtained at f_r by

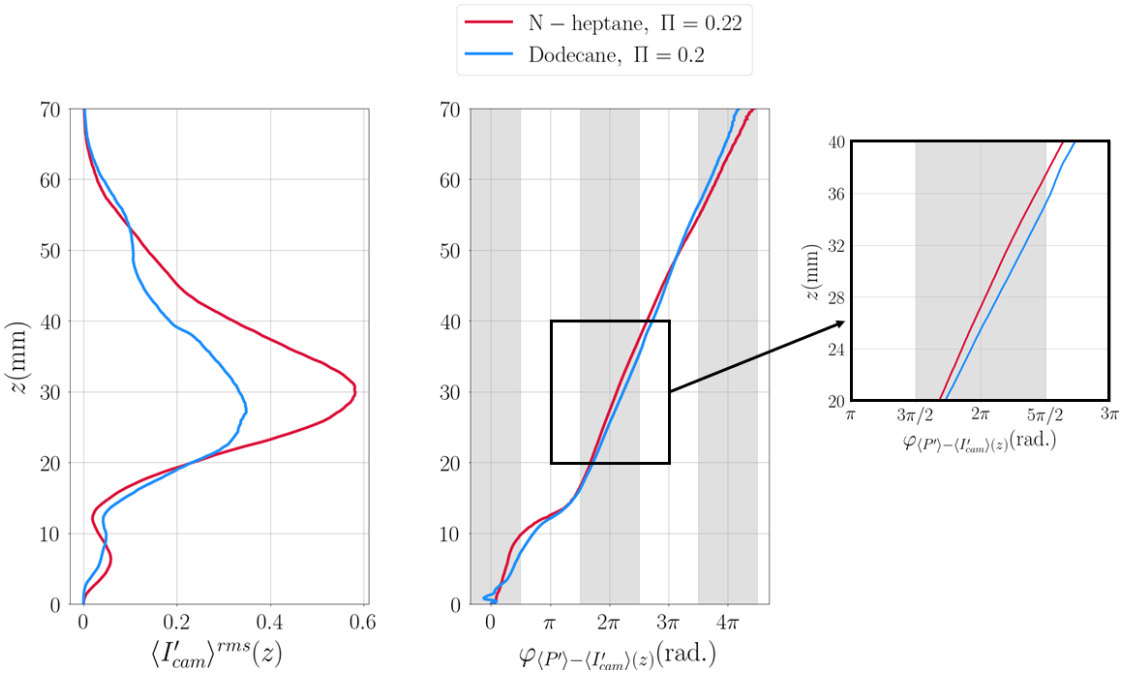

Figure 8.12: Phase-averaged local OH*-intensity oscillation amplitude, $\langle I_{cam} \rangle^{rms}(z)$ (left), and phase shift between the phase-averaged acoustic pressure at the flame location and local OH*-intensity oscillation amplitude, $\varphi_{\langle P' \rangle - \langle I_{cam} \rangle(z)}$ (middle), with n-heptane or dodecane as a fuel in the linear zone of the flame response. A zoomed-in view of the middle plot is shown on the right. With n-heptane, $\Pi = 0.22$, $f_r = 722$ Hz; with dodecane, $\Pi = 0.2$, $f_r = 731$ Hz.

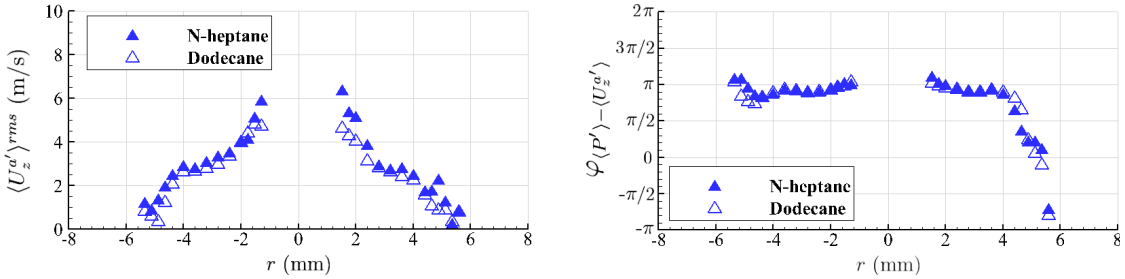

(a) $z = 2.1$ mm

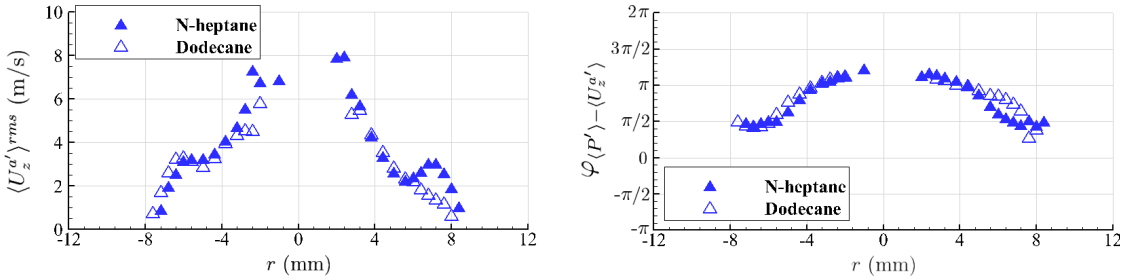

(b) $z = 6.8$ mm

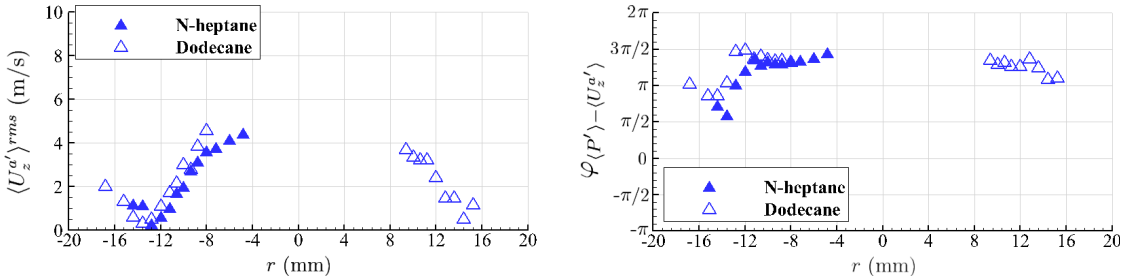

(c) $z = 20.5$ mm

Figure 8.13: Radial profiles of the air flow coherent axial velocity oscillation at f_r with n-heptane or dodecane for three heights $z = 2.1$ mm, $z = 6.8$ mm and $z = 20.5$ mm.

dividing an acoustic cycle in 12 bins of equal width. Its rms oscillation amplitude, $\langle U_z^{a'}\rangle^{rms}$, and the phase delay between $\langle P'\rangle$ and $\langle U_z^{a'}\rangle$, $\varphi_{\langle P'\rangle-\langle U_z^{a'}\rangle}$, are shown at three heights $z = 2.1$ mm, 6.8 mm and 20.5 mm in Figure 8.13. At these three heights, $\langle U_z^{a'}\rangle^{rms}$ and $\varphi_{\langle P'\rangle-\langle U_z^{a'}\rangle}$ are identical with the two fuels, ensuring that the response of the air flow is the same for the two configurations explored here.

8.6 Characterisation of the sprays with acoustic forcing

As shown in Chapter 5, the response of the fuel spray to the acoustic pressure modulation in the chamber is characterised by two main features: (i) the generation of a droplet number wave, later inducing an oscillation of the fuel feeding to the flame through the evaporation and mixing processes, and (ii) the periodic modulation of the fuel spray angle.

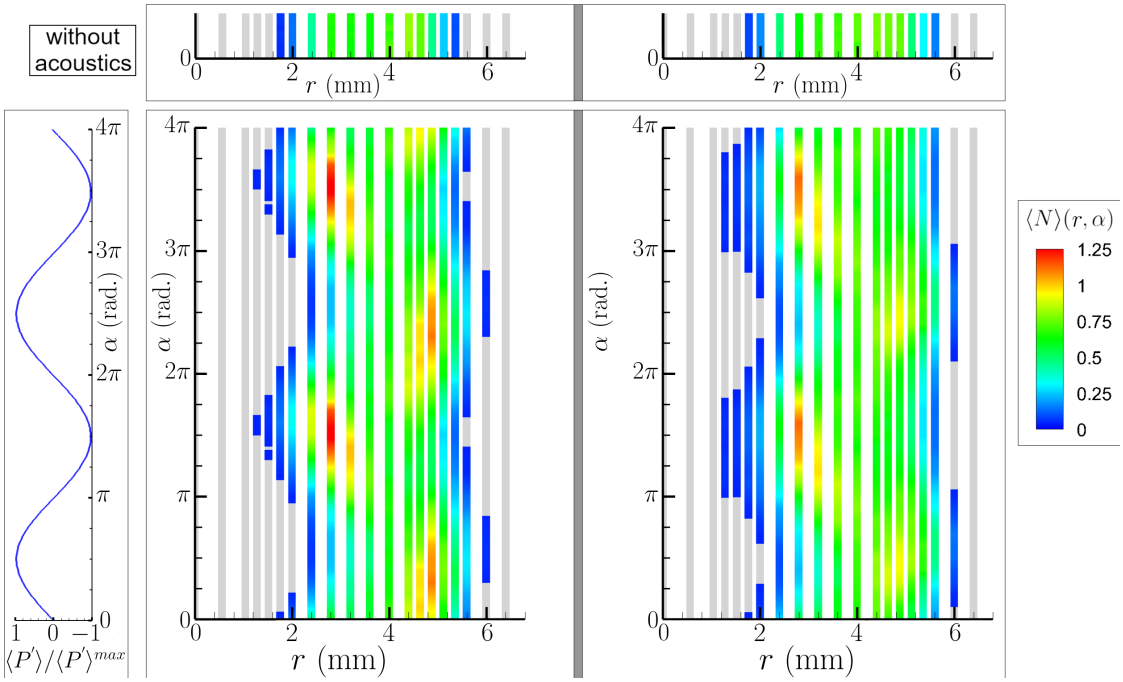

Figure 8.14: Phase-averaged droplet count $\langle N \rangle(r, \alpha)$ over two reconstructed pressure cycles along a radius at $z = 2.1$ mm for $\Pi = 0.22$. Left: n-heptane; right: dodecane. Top: mean droplet count without acoustic forcing, $\overline{N}^0(r)$. Grey: $\langle N \rangle \leq 0.04$ droplet/$\Delta\tau$.

8.6.1 Generation of a droplet number wave

The evolution of the phase-averaged droplet count $\langle N \rangle(r, \alpha)$ is illustrated for both fuels at $z = 2.1$ mm and for $\Pi = 0.22$ in Figure 8.14, with the mean droplet count without acoustic forcing, $\overline{N}^0(r)$. To compare the measurements, $\overline{N}^0(r)$ is averaged during the same duration T/20 as $\langle N \rangle(r, \alpha)$. Grey color indicate zones with a population lower than 0.04 droplet during T/20 (*e.g.* 110 droplets per measurement of duration 4 seconds without forcing), which is too low to validate the corresponding measurements.

Without acoustic forcing, the sprays of n-heptane and dodecane present a core region empty of droplets, which extends from the injector axis to $r \simeq 1.6$ mm. Then, $\overline{N}^0(r)$ increases sharply to reach a plateau that ranges from $r = 2.4$ mm to $r = 4.8$ mm, corresponding to a region where most of the droplets are found. Finally, $\overline{N}^0(r)$ decreases sharply between $r = 4.8$ mm and $r = 5.4$ mm, above which an external region empty of droplets is observed.
With acoustics, a radial oscillation of the envelop of the sprays is visible; it is similar in phase for both fuels. The boundary of the core oscillates between $r = 1.2$ mm at the pressure minimum, and $r = 2.4$ mm at the pressure maximum, but the empty core becomes populated during 50% of an acoustic cycle for dodecane and only 30% for n-heptane. The population of the external region ($r > 4$ mm) is more uniform and its boundary oscillates much less. Moreover, an oscillation of $\langle N \rangle(r, \alpha)$ is induced, giving rise to an inhomogeneous liquid-fuel distribution over space and time, which in turn generates a modulation of the amount of reactants supplied to the flame. The oscillation amplitude of $\langle N \rangle(r, \alpha)$, which is higher with n-heptane than with dodecane, depends

much on r. Consequently, the liquid-fuel distribution evolves with time such that the density of droplets oscillate with a greater amplitude in the inner region of the spray, $\hat{r}_-$ ($r \leq 4$ mm) than in its outer region, $\hat{r}_+$ ($r > 4$ mm). This suggests that effects of the spray dynamics on the flame response are mainly induced by the inner region of the spray.

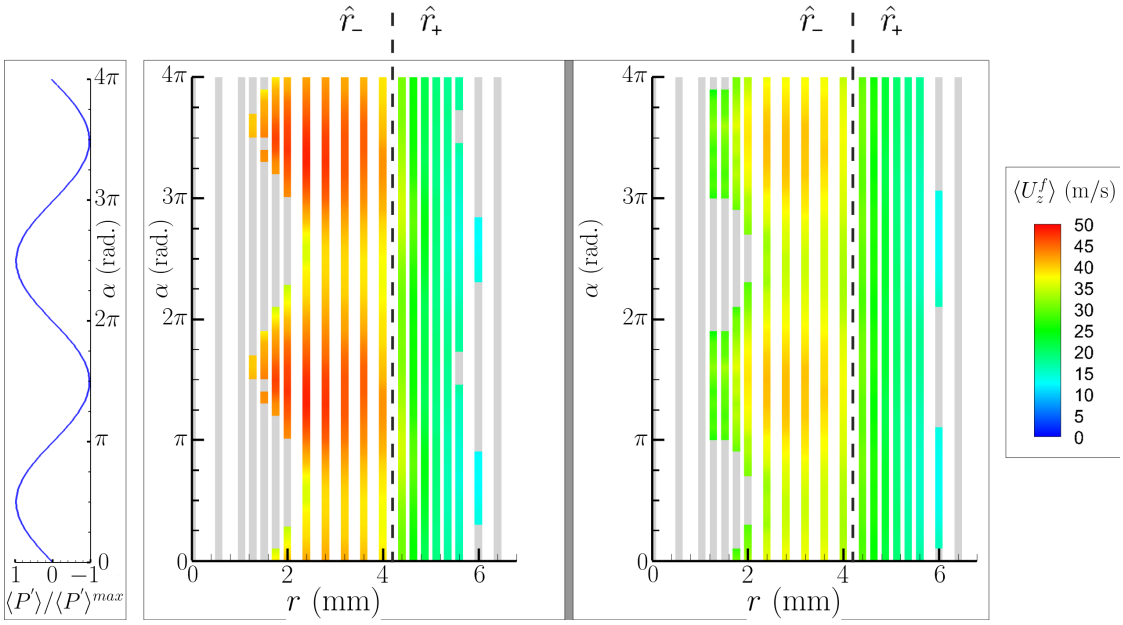

Figure 8.15: Phase-averaged fuel droplet axial velocity $\langle U_z^f \rangle$ over two reconstructed pressure cycles along a radius at $z = 2.1$ mm for $\Pi = 0.22$. Left: n-heptane; right: dodecane. Grey: $\langle N \rangle \leq 0.04$ droplet/$\Delta\tau$.

To create an oscillation of the HRR, the droplet number wave needs to be transported to the flame zone. Figure 8.15 shows the phase-averaged fuel droplet vertical velocity, $\langle U_z^f \rangle(r, \alpha)$, at $z = 2.1$ mm, for n-heptane and dodecane. $\langle U_z^f \rangle(r, \alpha)$ is calculated by including all the fuel droplets validated. At any phase angle, $\langle U_z^f \rangle$ is always higher in $\hat{r}_-$ than in $\hat{r}_+$. Moreover, it oscillates distinctly and in phase with $\langle N \rangle$ in $\hat{r}_-$ (see Figure 8.14), while it oscillates very weakly in $\hat{r}_+$. Therefore, $\hat{r}_-$ is characterised by the injection of many rapid droplets at the pressure minimum, followed by a few droplets that are less rapid at the pressure maximum. Segregation effects (*i.e.* faster droplets reaching the slower ones), could occur and enhance the droplet number waves in the flame zone (as shown in Section 6.6.1.2). Thus, the oscillation amplitude of $\langle U_z^f \rangle$ is of interest to estimate a potential effect of droplet segregation on the flame response. With n-heptane, the oscillation amplitude of $\langle U_z^f \rangle$ can increase by 40% compared to dodecane: for example, at $r = 2.4$ mm, $\langle U_z^f \rangle$ oscillates between 35.7 m/s and 48.4 m/s for n-heptane and between 33 m/s and 42.1 m/s for dodecane. This feature is observed in the entire $\hat{r}_-$ region. Therefore, inhomogeneity in spatial drop distribution is reinforced with n-heptane and may participate in the stronger flame response compared to that with dodecane. In $\hat{r}_+$ region, the weak fluctuation of $\langle U_z^f \rangle$ for both fuels indicates that inhomogeneity is not significant in this region. However, $\langle U_z^f \rangle$ is generally weaker than in $\hat{r}_-$. As a consequence, the dense cloud of droplets, injected in $\hat{r}_+$ near the pressure maximum, needs more time to reach the flame zone than the dense cloud of droplets injected in $\hat{r}_-$ near the pressure minimum. Therefore, oscillations

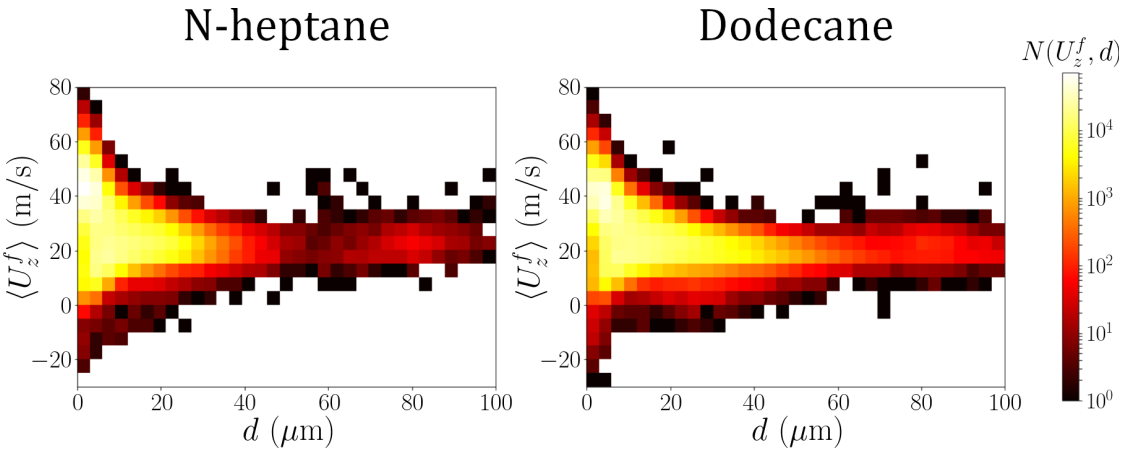

Figure 8.16: Fuel drop size-velocity correlations at $z = 2.1$ mm, $\Pi = 0.22$. $N(U_z^f, d)$ indicates the number of droplets in each class of diameter-width 3 µm and velocity-width 5 m/s. Left: n-heptane; right: dodecane.

of $\langle N \rangle$ measured in $\hat{r}_-$ and $\hat{r}_+$, which were in phase opposition at $z = 2.1$ mm, may interfere constructively for $z > 2.1$ mm due to their different propagation velocity, creating an unsteady fuel feeding to the flame zone. As the oscillation of $\langle N \rangle$ is weaker with dodecane than with n-heptane in $\hat{r}_-$ and $\hat{r}_+$, this effect could participate in the lower gain of the FDF for dodecane.

8.6.2 Size-dependent behaviour of the droplet wave

The phase shift φ is quite similar for n-heptane and dodecane. As shown above, this means that the time delay between the generation of the droplet number wave at the injector exit and its combustion is close for both fuels. The relevance of $\langle U_z^f \rangle$ to estimate the propagation velocity of the droplet number wave is now discussed. Figure 8.16 shows size-velocity correlations integrated throughout the measurement line. Both sprays are polydisperse but the drop size distribution for dodecane is wider since there is a population of diameters $d \geq 30$ µm, whereas it is quasi-inexistent for n-heptane. The range of vertical velocity values covered by droplets with a diameter d decreases when d increases, showing the greater capability of the smallest droplets to follow the velocity fluctuations of the air flow, contrary to the biggest droplets that have a quasi-ballistic behaviour. It is interesting to note that droplets of the same diameter have similar values of U_z^f for both fuels, suggesting that the difference of $\langle U_z^f \rangle$ in $\hat{r}_-$ (see Figure 8.15) between n-heptane and dodecane is mainly due to a difference in drop size distribution, instead of a reduction in vertical velocity of all droplets. This means that several droplet number waves are actually generated with various propagation velocities which decrease when d increases. However, the closeness of φ for the two fuels suggests that the flame response is mainly dominated by droplets of the same size, which are transported to the flame zone in an identical time. In addition, the amount of droplets with a diameter lying in the range 1-5 µm depends considerably on the fuel as it is reduced by more than 30% from n-heptane to dodecane. Consequently, $\mathcal{G}$ may be linked to the number of small droplets: since they are less numerous with dodecane, the modulation of the amount of reactants supplied to the flame may be weaker than with n-heptane.

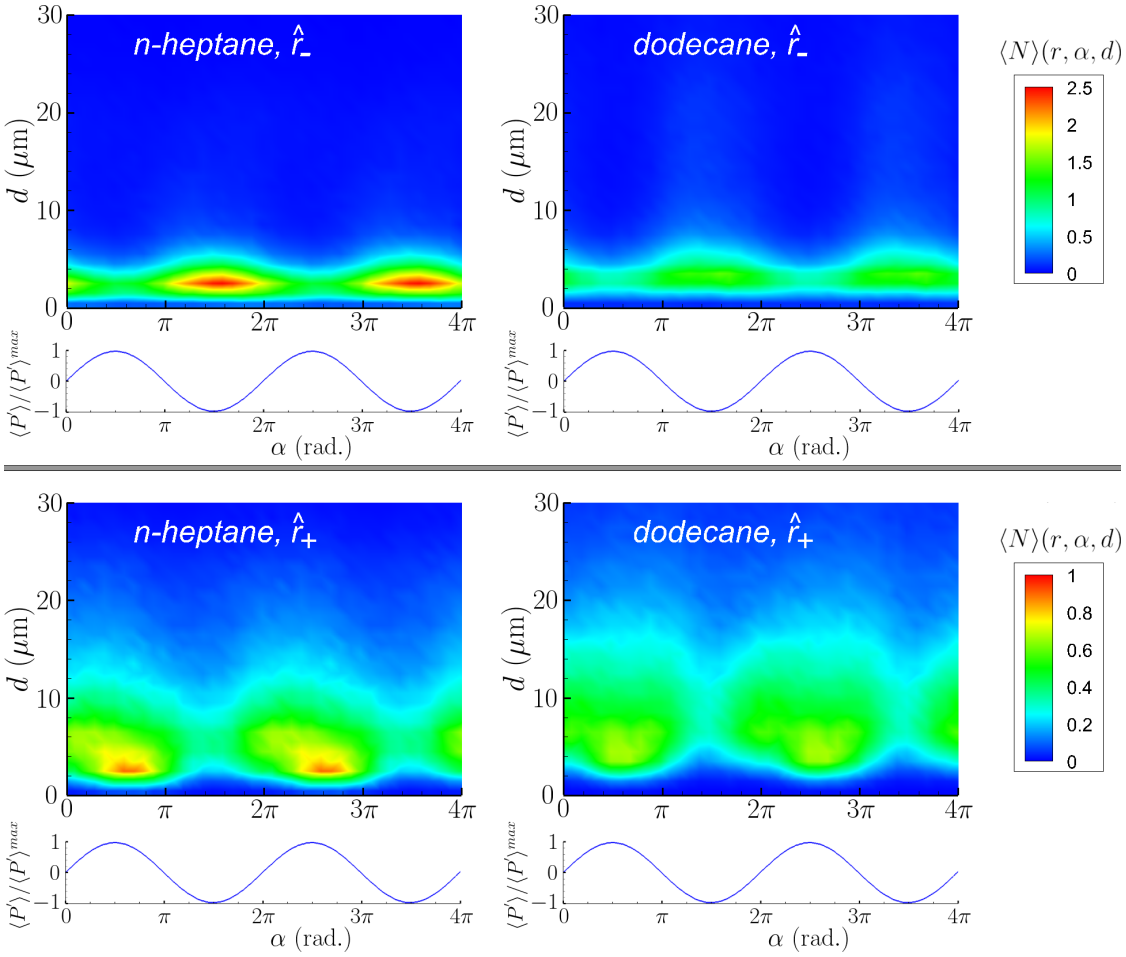

Figure 8.17: Phase-averaged drop size distribution $\langle N \rangle(r, \alpha, d)$ at $z = 2.1$ mm for $\Pi = 0.22$. Left: n-heptane fuel; right: dodecane fuel; top: inner region of the spray, $\hat{r}_-$ ($r \leq 4$ mm); middle: outer region of the spray, $\hat{r}_+$ ($r > 4$ mm); bottom: two reconstructed acoustic cycles.

The phase-averaged drop size distributions can bring information to evaluate the amplitude of the droplet number waves for different values of d. They are presented in Figure 8.17 for both fuels, in $\hat{r}_-$ and in $\hat{r}_+$. The oscillation amplitude of $\langle N \rangle(r, \alpha, d \leq 5$ µm) is more important with n-heptane than with dodecane, both in $\hat{r}_-$ and in $\hat{r}_+$. However, these small droplets are much more numerous in $\hat{r}_-$ than in $\hat{r}_+$. Indeed, for both fuels, they practically disappear in $\hat{r}_+$ when α is around $3\pi/2$, which corresponds to the phase angle at which they are massively injected in $\hat{r}_-$. Consequently, the flame response seems to be dominated by small droplets injected in $\hat{r}_-$. Thus, the atomisation quality is an important parameter in the thermoacoustic coupling. The greater reactivity of small droplets to flow fluctuations make them susceptible to transform acoustic perturbations in HRR oscillations easily. However, the spray quality has a little influence on the phase of FDF.

8.7 Conclusion

Flame, flow and spray analyses are performed on a linear array of swirling spray flames of n-heptane and dodecane. The response of the central flame, which was placed at a pressure antinode of the transverse acoustic field, was studied in the Flame Describing Function (FDF) framework. The gain of the FDF is greater with n-heptane, but it presents the same behaviour as the reduced acoustic pressure amplitude, Π, for the two fuels, characterised by a transition between a linear growth and a nonlinear evolution at Π_{trans}. The same value of Π_{trans} found with the two fuels shows that the appearance of nonlinear processes are independent on the fuel here. The phase of the FDF is affected by the fuel below Π_{trans}, indicating a longer delay between the acoustic pressure oscillation and the OH^*-intensity oscillation with dodecane. Above $\Pi = \Pi_{trans}$, the phase is similar with the two fuels, indicating that the n-heptane flame is more sensitive to the increase of Π. It is verified that the axial velocity oscillation of the air flow for Π in the linear zone is identical with the two fuels. For both fuels, an injection pattern is induced by acoustics at the injector exit, which consists in the alternative injection of many rapid and small droplets in the inner region of the spray, $\hat{r}_-$, and slower and bigger droplets in the outer region of the spray, $\hat{r}_+$. This pattern generates unsteady fuel feeding to the flame zone, which is more intense in $\hat{r}_-$, and in phase opposition between $\hat{r}_-$ and $\hat{r}_+$. Segregation effects can transform this destructive interference in a constructive one in the flame zone. The characteristics of the droplet number waves generated in $\hat{r}_-$ and $\hat{r}_+$ also depend on the fuel: in particular, their amplitude is more intense with n-heptane. The same phase shift of the FDF for n-heptane and dodecane suggests that the flame response is induced by droplets of a similar size for both fuels, which are transported from the injector exit to the flame zone in an identical time. The higher count of small droplets and its stronger modulation with n-heptane than with dodecane indicates that the flame response may be dominated by small droplets.

8.A Additional axial velocity profiles for C_1 fuel droplets

This appendix extends Section 8.3.3 by showing the radial profiles at $z = 6.8$ mm and $z = 20.5$ mm of the mean and rms axial velocity of the air flow, $\overline{U_z^a}$ and $U_z^{a,\,rms}$. These quantities are obtained by including only the velocity of the fuel droplets of class C_1. Results are displayed in Figure 8.18. The radial profiles at $z = 2.1$ mm are shown in Figure 8.8.

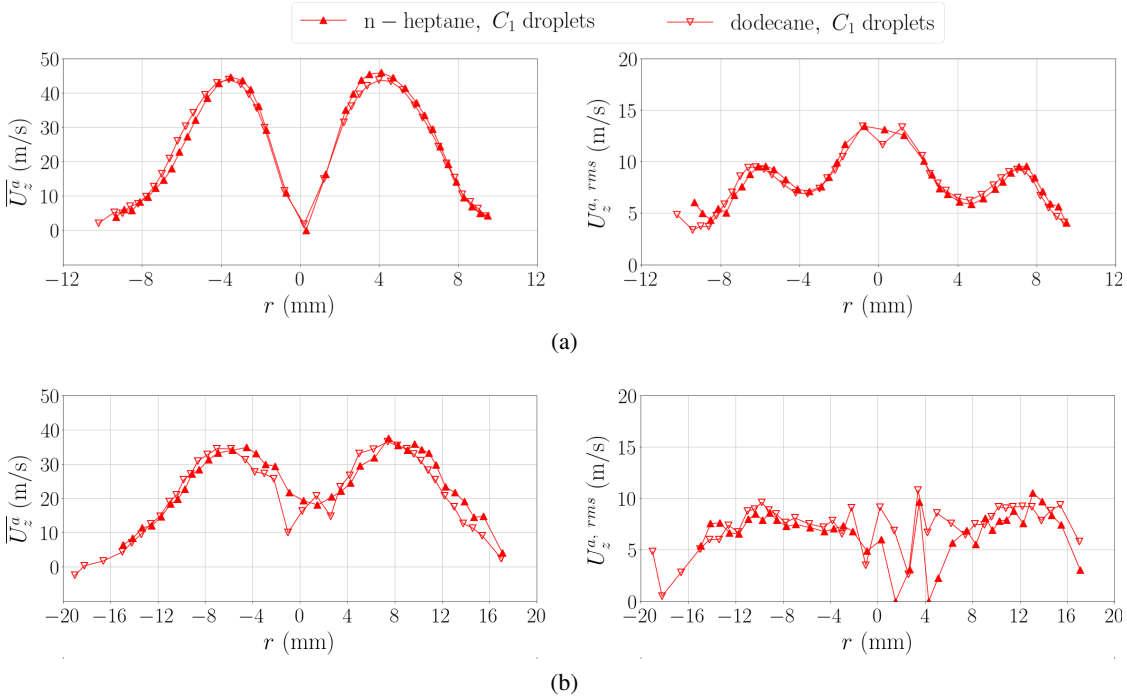

Figure 8.18: Radial profiles of mean and rms axial velocity of C_1 droplets with n-heptane and dodecane without acoustic forcing. These profiles are obtained at: (a) $z = 6.8$ mm; (b) $z = 20.5$ mm.

Part III

Response of the energy system at IAN and VAN

Chapter 9

Impact of the flame location in a standing transverse acoustic field on its response to acoustic perturbations

Contents

Combustion instabilities in annular combustors are likely to couple with an azimuthal mode of the cavity, which can be spinning or standing. In the latter case, the flames are subjected to acoustic pressure or transverse velocity oscillations according to their location in the acoustic field. It is generally observed that the global flame intensity mostly responds to the effects of the acoustic pressure oscillation while it is less sensitive to transverse velocity perturbation. This chapter investigates the behaviour of a linear array of three lean swirl-stabilised spray flames when the central flame is placed at a pressure antinode (PAN), an intensity antinode (IAN) or a transverse velocity antinode (VAN). It is shown that the flame describing function (FDF) is governed by acoustic pressure effects. When subjected to a transverse velocity oscillation, the flame undergoes a lateral motion and local oscillations of the flame intensity are observed.

However, they interfere in a destructive manner in the whole flame, leading to a negligible global flame intensity oscillation. This questions the relevance of the FDF approach for flames located at transverse velocity antinodes. Mechanisms leading to the global flame intensity oscillation, namely air flow axial velocity oscillation and fuel spray modulation, are driven by the acoustic pressure oscillation at the flame location. As a result, flames at PAN and IAN can interfere constructively in a standing transverse acoustic field, helping to sustain self-excited instabilities.

9.1 Introduction

In annular combustors, thermoacoustic instabilities generally couple with azimuthal modes of the cavity since the azimuthal dimension is the largest one. The acoustic field produced inside the cavity can be spinning or standing. In a standing mode, each flame experiences an acoustic perturbation consisting in a combination of an acoustic pressure oscillation and a transverse velocity oscillation, whose amplitudes depend on the location inside the combustor. The main effect of pressure fluctuations is to induce axial flow fluctuations that are symmetric with respect to the injector axis [108]. These axial fluctuations are generally dominant in the gaseous-flame response. However, when located between a pressure antinode and a velocity antinode, a premixed V-flame was shown to undergo dissymmetric perturbations that might be linked to the crossed contribution of the acoustic pressure and its gradient. Indeed, considering only the pressure gradient cannot explain the intensity of the dissymmetry [111]. Transverse velocity oscillations can also lead to a positive thermoacoustic coupling via the flame displacement at a velocity antinode [188]. In addition, other types of flame responses can be observed, *e.g.* high-amplitude instabilities were shown to induce the extinction of swirl-stabilised spray flames near the pressure nodal line [101], showing that transverse velocity fluctuations may have a strong effect on the flames. These results were consistent with other ones obtained for a premixed V-flame [111].

Investigating liquid-fuel combustion in academic configurations is also of major interest since the presence of a fuel spray introduces supplementary complexity, due to the need for the fuel to evaporate and to mix with the air before combustion. Moreover, the presence of two distinct fluid phases implies that their responses to an acoustic perturbation are not identical. For an airblast atomiser used in non-reacting conditions, longitudinal acoustic forcing was shown to generate droplet number density waves [136]. The drop size distribution is modified during the acoustic cycle by the higher sensitivity of small droplets to flow velocity fluctuations [135], but also by the unsteady air momentum. In particular, for an airblast atomiser, a correlation between drop Sauter diameter D_{32} and air velocity was found, indicating that D_{32} diminishes as the air velocity increases [71]. Since evaporation is more efficient for small droplets, the evaporation dynamics is modified with the drop size distribution and the air-fuel mixing can be produced more rapidly with small droplets. Thus, such modulations of the spray may generate fluctuations of the local flame intensity due to the modulation of the amount of reactants supplied to the flame or potential equivalence ratio fluctuations. In particular, the modification of the evaporation dynamics was shown to influence self-excited combustion instabilities [89]. Nevertheless, the evaporation rate could be reduced in regions of high droplet number density through droplet clustering, which would therefore act as a damping effect [189]. A more recent numerical work

showed the capability of a liquid-fuel film created on the walls of the injection system to couple with the thermoacoustic oscillation, leading to self-sustained combustion instability [140]. However, few studies examined the spray flame response to both pressure and velocity perturbations in a transverse acoustic field. Consequently, it is of great interest to investigate the response of swirl-stabilised spray flames by taking the flame location in a standing transverse acoustic field as a parameter.

This chapter aims at investigating the response of lean swirl-stabilised spray flames at several locations in a standing transverse acoustic field, characterised by different acoustic pressure or transverse velocity oscillation amplitudes. A description of the experimental methods relative to this chapter is firstly provided. Then, the behaviour of the flames placed in the same transverse acoustic field is examined, as well as their coupling with the local acoustic pressure oscillation. Finally, the flame response is related to the local pressure oscillation to understand the mechanisms driving the flame intensity oscillation. The modulation of the air flow and that of the fuel spray are also investigated.

9.2 Experimental setup and methods

In this chapter, the injection array is placed at several locations in the standing transverse acoustic field corresponding to the 2T1L mode of the cavity. Three distinct cases are investigated, for which the central flame is located: (i) at a pressure antinode (PAN); (ii) at a intensity antinode (IAN); and (iii) at a velocity antinode (VAN). These three cases are illustrated in Figure 9.1. The theoretical acoustic mode corresponding to the 2T1L mode of the cavity is represented in Figure 9.2, with the fields of the acoustic pressure amplitude P^{rms}, transverse acoustic velocity amplitude U_{ac}^{rms} and acoustic intensity I_{ac}^{rms}. In this work, the central flame is placed at $x/L_c = 0$, 0.125 or 0.25 to evaluate the flame response at PAN, IAN or VAN respectively. The acoustic pressure oscillation is measured at the central flame location, giving $P^{'}(t)$, and at the central PAN, giving $P_{ref}^{'}(t)$. Thus, when the central flame is placed at PAN, $P^{'}(t) = P_{ref}^{'}(t)$. Two non-dimensional parameters are defined to evaluate the rms acoustic pressure amplitude reduced by the bulk aerodynamic pressure: $\Pi = P^{rms}/\rho^a U_b^2$ and $\Pi_{ref} = P_{ref}^{rms}/\rho^a U_b^2$, where ρ^a and U_b^2 are calculated at 20°C.
In theory, pressure oscillations are absent at VAN; however, a weak pressure oscillation is measured at this location. Its amplitude is $9.5\% \pm 3\%$ of that the PAN at the centre of the cavity. At IAN, the amplitude of the pressure oscillation is $59\% \pm 7\%$ of that the PAN at the centre of the cavity. Oscillations of the transverse velocity progressively increase from PAN, where they are theoretically equal to zero, to VAN. Therefore, flames located at various positions in the transverse acoustic field do not experience the same acoustic perturbations. This study focuses on the flame response at the operating point $\mathbb{P}_{59}$, characterised by a flame thermal power of 5.9 kW, an equivalence ratio $\phi = 0.85$, a fuel mass flow rate of 0.133 g/s and an air mass flow of 2.35 g/s (see Table 2.1). The bulk velocity calculated at the injector exit at 20°C is 38.9 m/s and the set of swirler and outlet cup is the K modified set. These conditions are those of the baseline case whose response at PAN is investigated in Chapter 5.

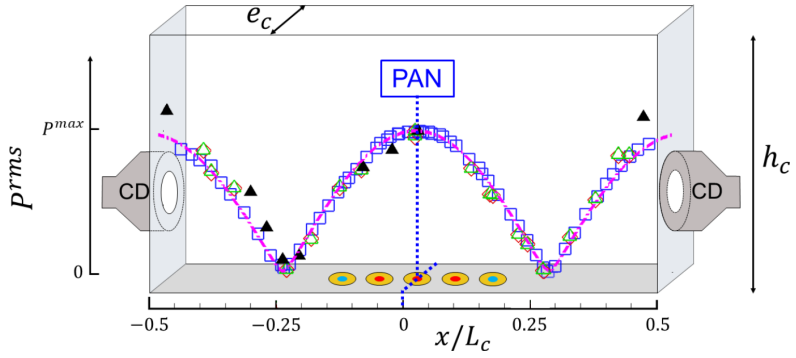

(a) Central flame at a pressure antinode (PAN)

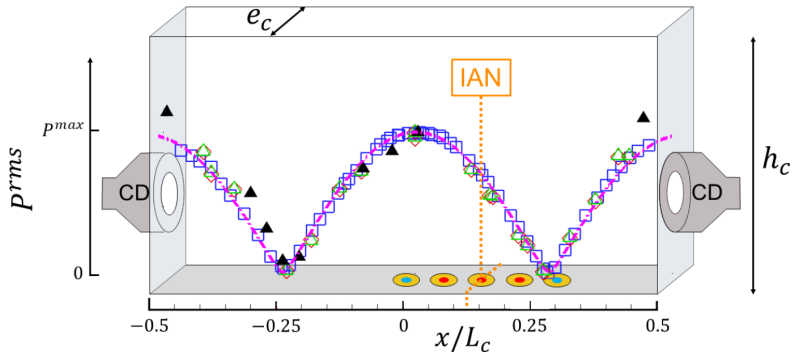

(b) Central flame at an intensity antinode (IAN)

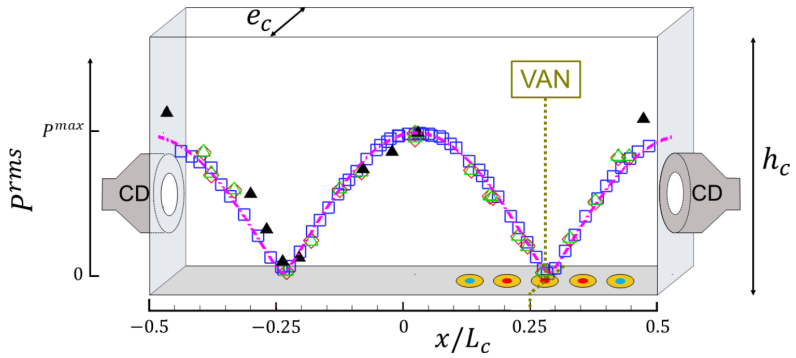

(c) Central flame at a velocity antinode (VAN)

Figure 9.1: 3-dimensional sketch of the acoustic cavity, acoustic pressure field and location of the injector array inside the cavity when the central injector is placed at PAN, IAN or VAN. P^{max} corresponds to the acoustic pressure amplitude measured at the central PAN, $L_c = 880$ mm, $h_c = 200$ mm and $e_c = 55$ mm. The acoustic field is detailed in Figure 2.4. CD: compression drivers.

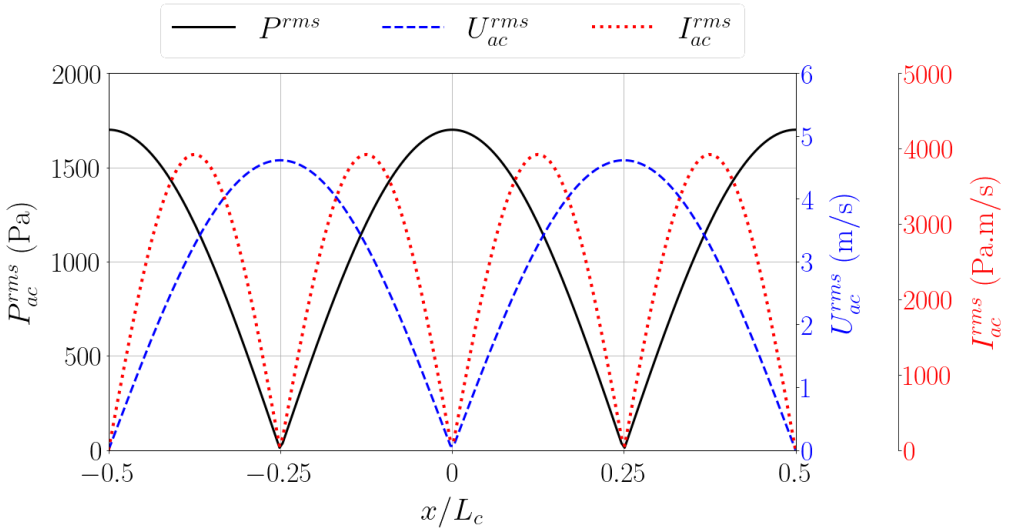

Figure 9.2: Theoretical acoustic pressure field, acoustic velocity field and acoustic intensity field for the 2T1L mode of the TACC-Spray cavity. P_{ac}^{rms} is the acoustic pressure amplitude, U_{ac}^{rms} the transverse acoustic velocity amplitude and I_{ac}^{rms} the acoustic intensity amplitude.

9.3 Response in a same acoustic field

We first focus on the response of the central flame when it is placed at PAN, IAN or VAN of a same acoustic field, which is defined by a same acoustic pressure amplitude measured at the central PAN, *i.e.,* a same Π_{ref}.

9.3.1 Global flame intensity

The mean global OH*-intensity reduced by its value without acoustic forcing, $\overline{I}/\overline{I}^0$, is shown in Figure 9.3 (top) as function of Π_{ref}. At PAN, $\overline{I}/\overline{I}^0$ slightly decreases up to $\Pi_{ref} = 0.2$, while the negative slope is steeper at higher Π_{ref}. At IAN and VAN, $\overline{I}/\overline{I}^0$ remains higher than 0.9 for all the values of Π_{ref} here. This may indicate an effect of the transverse velocity oscillation on $\overline{I}/\overline{I}^0$.

The global OH*-intensity oscillation amplitude reduced by the mean OH*-intensity, $I^{rms}/\overline{I}$, is also shown in Figure 9.3 (bottom) as a function of Π_{ref}. At VAN, $I^{rms}/\overline{I}$ is very low at all the acoustic amplitudes, indicating that the global swirl-stabilised flame intensity responds very weakly even when the acoustic pressure at PAN is such that $\Pi_{ref} = 0.5$. At IAN, $I^{rms}/\overline{I}$ increases linearly up to $\Pi_{ref} \simeq 0.5$, beyond which it remains constant as the acoustic amplitude increases. At PAN, $I^{rms}/\overline{I}$ grows linearly up to $\Pi_{ref} = \Pi_{trans} \simeq 0.3 - 0.35$ and evolves nonlinearly beyond. When $\Pi_{ref} \geq 0.45$, values of $I^{rms}/\overline{I}$ are more scattered than in the linear zone. This characteristic feature of the saturation zone was previously found in TACC-Spray by Cáceres [45] with a lower flame power. One consequence of the saturation is that, for $\Pi_{ref} \leq 0.55$, $I^{rms}/\overline{I}$ is stronger at PAN than at IAN while for $\Pi_{ref} > 0.55$, it is similar at these two locations.

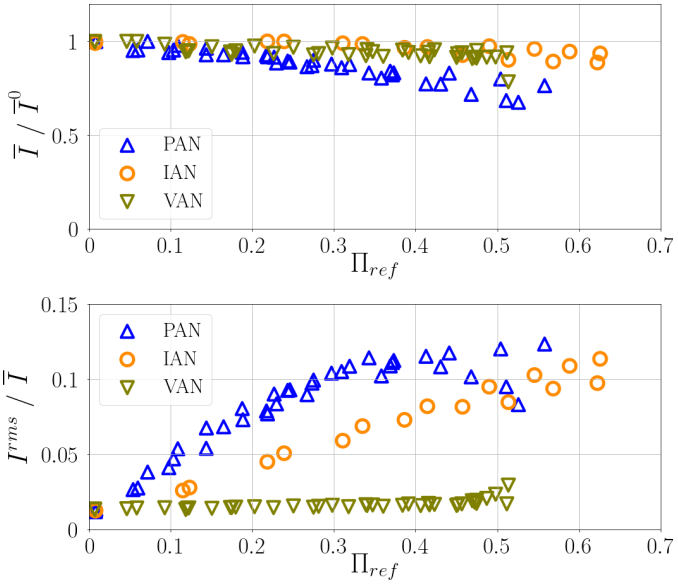

Figure 9.3: Response of the flame OH* intensity as a function of the reduced acoustic amplitude at the central PAN, Π_{ref}, for PAN, IAN and VAN. Top: mean intensity reduced by its value without acoustic forcing; bottom: rms oscillation amplitude reduced by the mean intensity.

9.3.2 Local flame intensity

The local flame intensity oscillation is examined from OH*-intensity images of the central flame by identifying its most energetic dynamic mode with the Dynamic Mode Decomposition (DMD) method[1]. The DMD method reconstructs a signal during one oscillation cycle from instantaneous data. Here, the instantaneous data consists in 740 OH*-intensity images. Figure 9.4 compares the oscillation of the dominant dynamic mode, whose frequency is f_r, at the three locations for a range $\Pi_{ref} = 0.5 - 0.6$. The longitudinal flame intensity wave is well depicted at PAN and at IAN. At PAN, is it almost perfectly axisymmetric while at IAN, a stronger asymmetric oscillation, induced by the local transverse velocity oscillation, is distinguished. At VAN, the flame undergoes a lateral motion accompanied by a lateral flame intensity oscillation, whereas the longitudinal flame intensity wave is not discernible. The lateral intensity oscillation produces a destructive interference between the left and the right sides of the flame (see $\alpha = \pi/2$ and $3\pi/2$), resulting in the very weak global flame intensity oscillation during the acoustic cycle. These behaviours are consistent with the observation at the velocity antinodal line in the self-excited annular combustor MICCA-Spray [142].

Further insight is given by plotting the phase-averaged location of the OH*-intensity barycentre with the method described in Section 2.3.2.3. Results, shown in Figure 9.5 for $\Pi_{ref} = 0.5 - 0.6.$, highlight the dominant axial motion of the barycentre at PAN. The weak lateral motion is induced by the small asymmetries of the axial flame intensity wave. At IAN, the axial motion of the barycentre is also clearly visible and its amplitude is identical to that at PAN. As shown in Figure 9.3, $I^{rms}/\overline{I}$ is similar for the values of Π_{ref} in the range $0.5 - 0.6$ explored in Figure 9.5. This suggests that the axial flame motion is linked to $I^{rms}/\overline{I}$. However, the OH*-intensity

[1]The DMD algorithm used here was provided by the EM2C team [142].

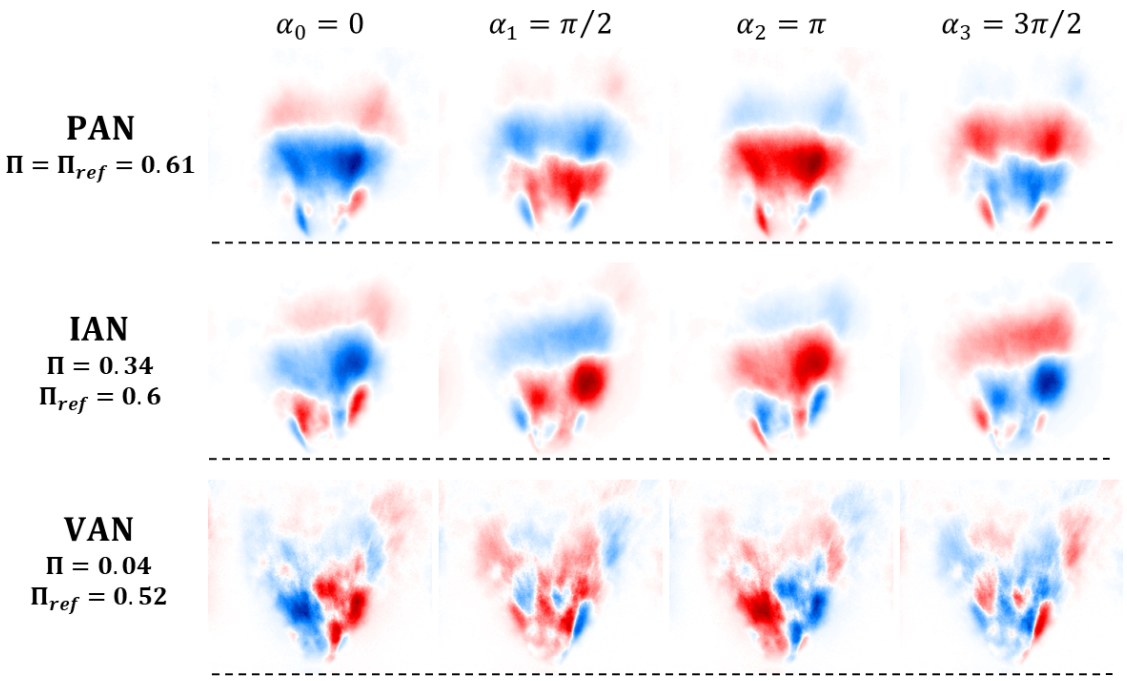

Figure 9.4: Motions of the dominant mode of flame intensity oscillation for a reconstructed acoustic pressure cycle obtained with dynamic mode decomposition via an algorithm provided by the EM2C team [142]. The black dash lines indicate the location of the nozzle exit, $z = 0$.

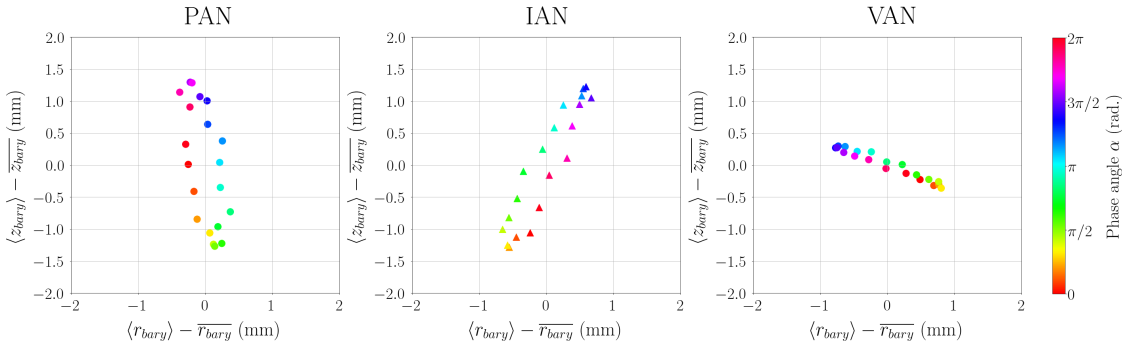

Figure 9.5: Phase-averaged location in the (r, z) plane of the OH*-intensity barycenter when the central flame is placed at (left) PAN, $\Pi = \Pi_{ref} = 0.6$; (middle) IAN, $\Pi_{ref} = 0.52$; $\Pi = 0.32$; (right) VAN, $\Pi_{ref} = 0.51$, $\Pi = 0.07$. The measurements are post-synchronised with the acoustic pressure oscillation.

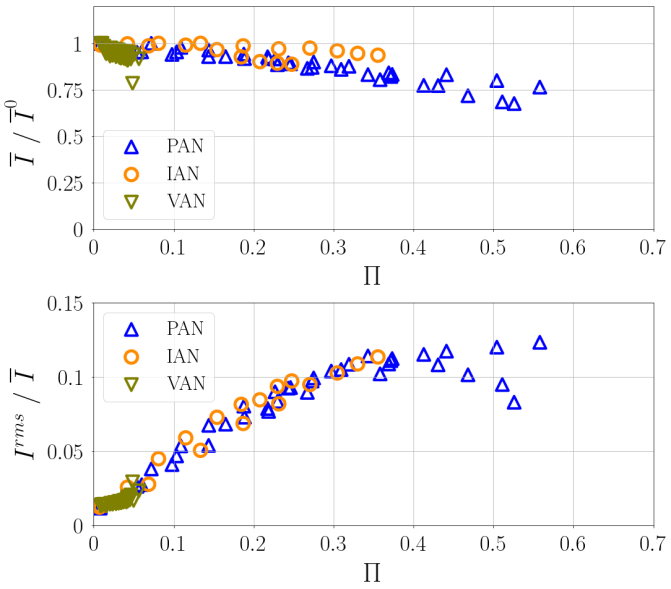

Figure 9.6: Response of the flame OH* intensity as a function of the reduced acoustic amplitude at the central flame location, Π, for PAN, IAN and VAN. Top: mean intensity reduced by its value without acoustic forcing; bottom: rms oscillation amplitude reduced by the mean intensity.

barycentre is subject to a lateral motion between $\langle r_{bary} \rangle = \overline{r_{bary}} - 0.5$ mm and $\langle r_{bary} \rangle = \overline{r_{bary}} + 0.5$ mm. At VAN, the barycentre mainly displays a lateral motion with an amplitude twice as that at IAN, but a weak axial motion is still present due to the local residual acoustic pressure oscillation (corresponding to $\Pi = 0.07$).

These results indicate that the global flame intensity oscillation is related to the axial flame intensity wave, which comes from acoustic pressure effects. The acoustic transverse velocity oscillation induces a lateral motion, but does not modify the global flame intensity during the acoustic cycle.

9.4 Response to a same local pressure perturbation

We now focus on the response of the system for a given acoustic pressure amplitude at the central flame location.

9.4.1 Global flame intensity oscillation

The evolution of $\overline{I}/\overline{I}^0$ and $I^{rms}/\overline{I}$ are now investigated as a function of Π, the reduced acoustic pressure amplitude at the central flame location. Results are shown in Figure 9.6. $\overline{I}/\overline{I}^0$ follows the same trend at PAN and IAN, characterised by a slow decrease up to $\Pi \simeq 0.3$ and a steeper decrease beyond. The measurements at VAN are restricted to low Π, but Figure 9.6 shows that $\overline{I}/\overline{I}^0$ is not significantly altered by the transverse velocity oscillation here. $I^{rms}/\overline{I}$ is very weak and only results from residual acoustic pressure effects. At PAN and IAN, $I^{rms}/\overline{I}$ is identical in the common range of Π explored, indicating that the global flame intensity oscillation is mainly

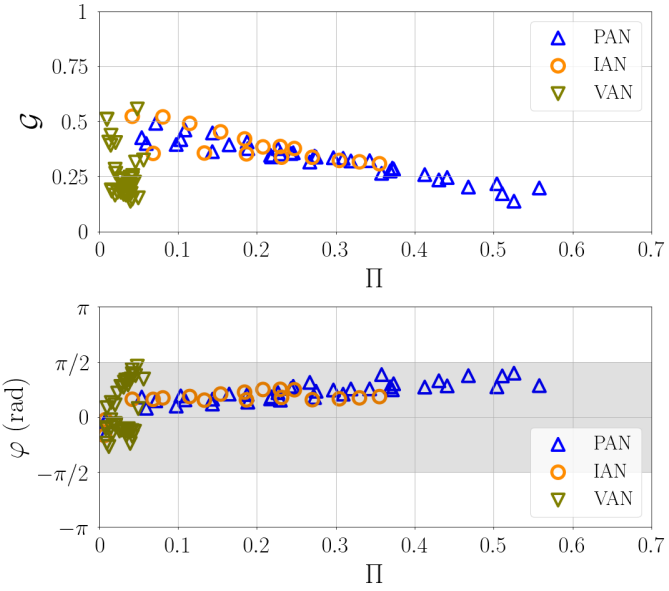

Figure 9.7: Flame Describing Function $\mathcal{F}$ as a function of acoustic amplitude at the central flame location, Π. Top: gain; bottom: phase. The grey band indicates the region of potential instability predicted by the Rayleigh criterion.

induced by acoustic pressure effects, while it is not influenced by effects linked to the transverse velocity oscillation and the pressure gradient. It is also interesting to visualise the FDF for the three locations. The FDF, given by Equation (2.5), uses the acoustic pressure signal at the central flame location as a reference signal, hence, it characterises the response of the global flame intensity to the acoustic pressure oscillation experienced by the central flame. The gain $\mathcal{G}$ is similar at PAN and IAN, showing that the same processes drive the flame intensity oscillation at both locations. At VAN, the very versatile gain indicates the presence of noise, and so that the flame intensity does not respond globally to the local transverse velocity perturbation, as mentioned above The phase φ further supports the previous observations. Indeed, φ is driven by acoustic pressure effects while at VAN, its dispersion results from the fact that the global flame intensity oscillation does not stand out from the noise. At PAN and IAN, the phase lies inside the instability region, identified by the grey band, showing that the flames are able to drive self-excited instabilities at these two locations.

9.4.2 Air flow modulation

It is now worth investigating whether coupling mechanisms are modified when comparing results at PAN and IAN. Here, the air flow axial velocity is estimated through PDA measurements on the fuel droplets, from which the behaviour of the droplets of class C_1 (*i.e.*, with a diameter d in the range $1 - 5$ µm) is extracted. These droplets are shown to describe the air flow motion (see Section 5.3.3.1). The radial profiles of mean air flow axial velocity, $\overline{U_z^a}$, are shown in Figure 9.8 (top) for $\Pi = 0.2$ when the central flame is placed at PAN and IAN. The two profiles match perfectly, demonstrating that the mean axial flow is identical. The axial velocity oscillation at the forcing frequency, $\langle U_z^{a'} \rangle$, is then characterised by its rms amplitude, $\langle U_z^{a'} \rangle^{rms}$, and the

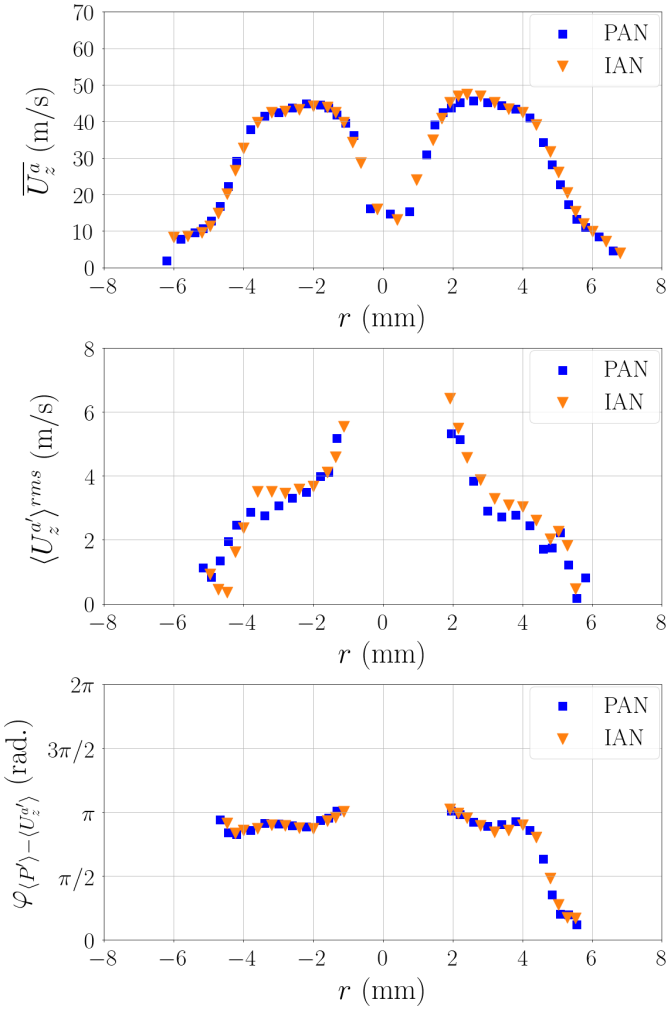

Figure 9.8: Radial profiles of the air flow axial velocity at $z = 2.1$ mm obtained for $\Pi = 0.2$. when the central flame is placed at PAN or IAN. Top: mean air flow axial velocity, $\overline{U_z^a}$; middle: air flow axial velocity oscillation, $\langle U_z^{a\prime} \rangle^{rms}$; bottom: phase shift $\varphi_{\langle P' \rangle - \langle U_z^{a\prime} \rangle}$.

phase shift $\varphi_{\langle P' \rangle - \langle U_z^{a\prime} \rangle}$ between the phase-averaged pressure osillation, $\langle P' \rangle$, and $\langle U_z^{a\prime} \rangle$, . Radial profiles at $z = 2.1$ mm, also shown in Figure 9.8 at PAN or IAN, demonstrate that $\langle U_z^{a\prime} \rangle^{rms}$ and $\varphi_{\langle P' \rangle - \langle U_z^{a\prime} \rangle}$ are similar at all the radial locations. It is interesting to remark that the asymmetry of $\varphi_{\langle P' \rangle - \langle U_z^{a\prime} \rangle}$ betwen $r = +4$ mm and $r = -4$ mm, already observed at PAN with n-heptane or dodecane (see Figure 8.13), is well captured at IAN too. This suggests that this asymmetry is inherent to the injector.

9.4.3 Response of the fuel spray

The response of the fuel spray is now investigated through the space-time modulation of the droplet count, obtained by phase-averaging the droplet count at each radial location at the injector exit ($z = 2.1$ mm). The phase-averaged droplet count, $\langle N \rangle(r, \alpha)$, is shown in Figure 9.9 for $\Pi = 0.2$ when the central flame is placed at PAN or IAN. $\langle N \rangle(r, \alpha)$ corresponds to the droplet

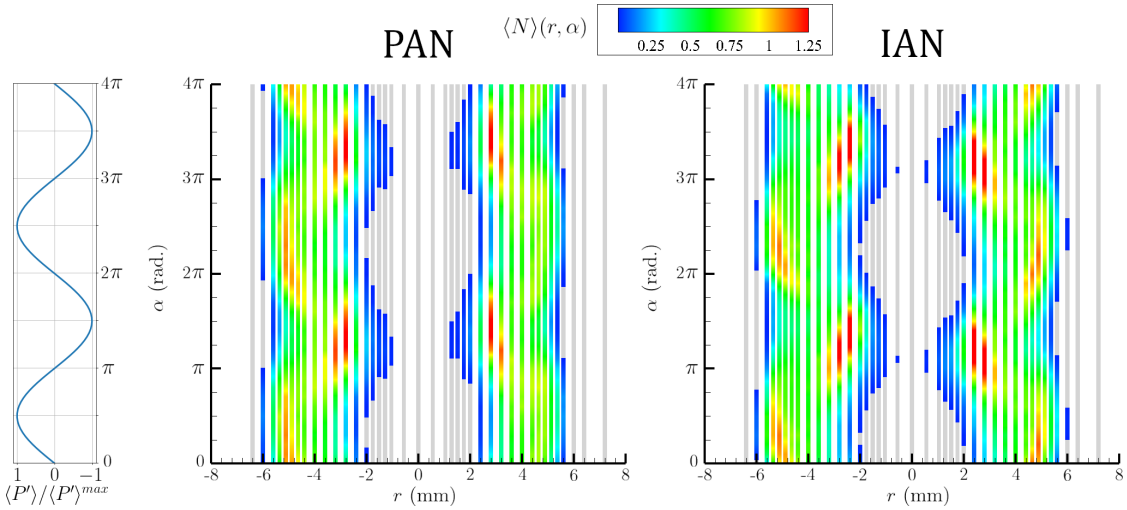

Figure 9.9: Phase-averaged droplet number $\langle N \rangle(r, \alpha)$ at $z = 2.1$ mm when the central flame is placed at PAN (center) or at IAN (left), for $\Pi = 0.2$. The acoustic cycle, reproduced two times, is represented on the left. The grey zones indicate regions where $\langle N \rangle < 0.04$ drops/$\Delta\tau$.

count during a time interval $\Delta\tau = T/20$, where T is the acoustic period. The results highlight the similar space-time modulation as PAN and at IAN, when the central flame is subjected to the same Π, leading to the formation of droplet number waves (see Section 5.3.4.2). At both locations, the spray is modulated such that a large droplet amount is injected in the external part of the spray ($r > 4$ mm) near the pressure maximum while a larger dropelt amount is injected in the internal part of the spray ($r \leq 4$) mm near the pressure minimum. Since these features are identical at PAN and IAN, this indicates that the spray response is mostly dominated by the acoustic pressure effects, further supporting that the same flame intensity oscillation found at both locations results from the same mechanisms. This shows the inability of the transverse velocity oscillation to excite the mechanisms driving the global flame intensity oscillation.

9.5 Thermoacoustic coupling

The thermoacoustic coupling is now examined by using the instability index $\mathcal{R}a_1(t) = \xi P' I'(t)$, with $\xi = 1/(\rho^a U_b^2 \overline{I})$ (previously defined in Section 5.2.3). Its time-averaged value, $\overline{\mathcal{R}a_1}$, gives an indication about the Rayleigh source term. $\overline{\mathcal{R}a_1}$ is evaluated as a function of Π_{ref} in Figure 9.10 for PAN, IAN and VAN. This figure allows to see, at a given Π_{ref}, the strength of the thermoacoustic coupling at the three locations. At VAN, $\overline{\mathcal{R}a_1}$ is near zero due to the non-significant global flame intensity oscillation. At PAN and IAN, $\overline{\mathcal{R}a_1}$ is positive, indicating that flames placed at these two locations could participate in a constructive manner to drive self-excited instabilities. In general, $\overline{\mathcal{R}a_1}$ is stronger at PAN than at IAN, showing that the flames at PAN are those which participate the most to sustain instabilities. This is generally true not only in the linear zone, where both the acoustic pressure amplitude and $I^{rms}/\overline{I}$ are stronger at PAN, but also for Π_{ref} in the range 0.51-0.6. At the latter acoustic amplitude, the higher value of $\overline{\mathcal{R}a_1}$ at PAN is only due to the higher acoustic pressure amplitude at PAN, since $I^{rms}/\overline{I}$ is similar at

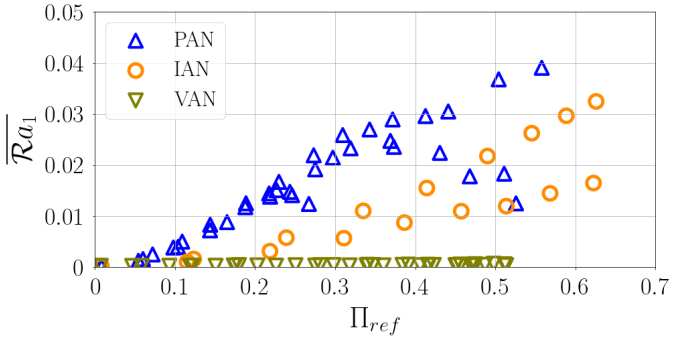

Figure 9.10: Phase-averaged local instability index $\overline{\mathcal{R}a_1}$ based on the Rayleigh criterion as a function of Π_{ref} for a given Π_{ref}.

PAN and IAN due to the saturation of the global flame intensity oscillation.

The phase-averaged local instability index $\langle \mathfrak{Ra} \rangle(\alpha, z)$, defined by Equation (5.5), is also examined to find the flame regions which participate the most to the thermoacoustic coupling. This investigation is made when the central flame is placed at PAN or IAN. Results are shown in Figure 9.11. Two comparisons can be performed. **For a given** $\Pi_{ref} \simeq 0.2$ (Figure 9.11 (a,b)), the spatial distribution of $\langle \mathfrak{Ra} \rangle(\alpha, z)$ is similar at PAN and IAN: it is weak during all the cycle for $z \lesssim 20$ mm, positive for a middle region defined by 20 mm $\lesssim z \lesssim 40$ mm and negative in the upper region, defined by $z > 40$ mm. The positive contribution to the coupling in the middle region of the flame leads to the positive value of the global index $\overline{\mathcal{R}a_1}$ shown in Figure 9.10. But, differences between PAN and IAN are visible: at PAN, both the positive coupling in the middle region and the negative coupling in the upper region are stronger than at IAN. Nevertheless, the positive global thermoacoustic coupling is stronger at PAN than at IAN (see Figure 9.10). **For a given** $\Pi \simeq 0.2$ (Figure 9.11 (a,c)), the spatial distribution of $\langle \mathfrak{Ra} \rangle(\alpha, z)$ remains similar at PAN (where $\Pi_{ref} = 0.2$) and IAN (where $\Pi_{ref} = 0.36$), but the values of $\langle \mathfrak{Ra} \rangle(\alpha, z)$ now agree at all z-locations, suggesting that the thermoacoustic coupling is equally strong at both locations. This is confirmed by Figure 9.10, which shows that the value of $\overline{\mathcal{R}a_1}$ at PAN for $\Pi_{ref} = 0.2$ equals that at IAN for $\Pi_{ref} = 0.36$.

To conclude, this analysis indicates that both flames at PAN and IAN are characterised by a positive thermoacoustic coupling, indicating that they can participate in sustaining a self-excited instability at frequency f_r. At VAN, the weak flame response results in a non-significant contribution to the Rayleigh source term. Since the coupling is driven by acoustic pressure effects, the flames at PAN are the largest contributors to the thermoacoustic coupling.

9.6 Conclusion

This chapter examines the response of swirl-stabilised spray flames of n-heptane or dodecane at three locations inside a standing transverse acoustic field: a pressure antinode (PAN), an intensity antinode (IAN) and a velocity antinode (VAN). The flame describing function (FDF) is governed by effects of the acoustic pressure oscillation, while effects of the transverse velocity

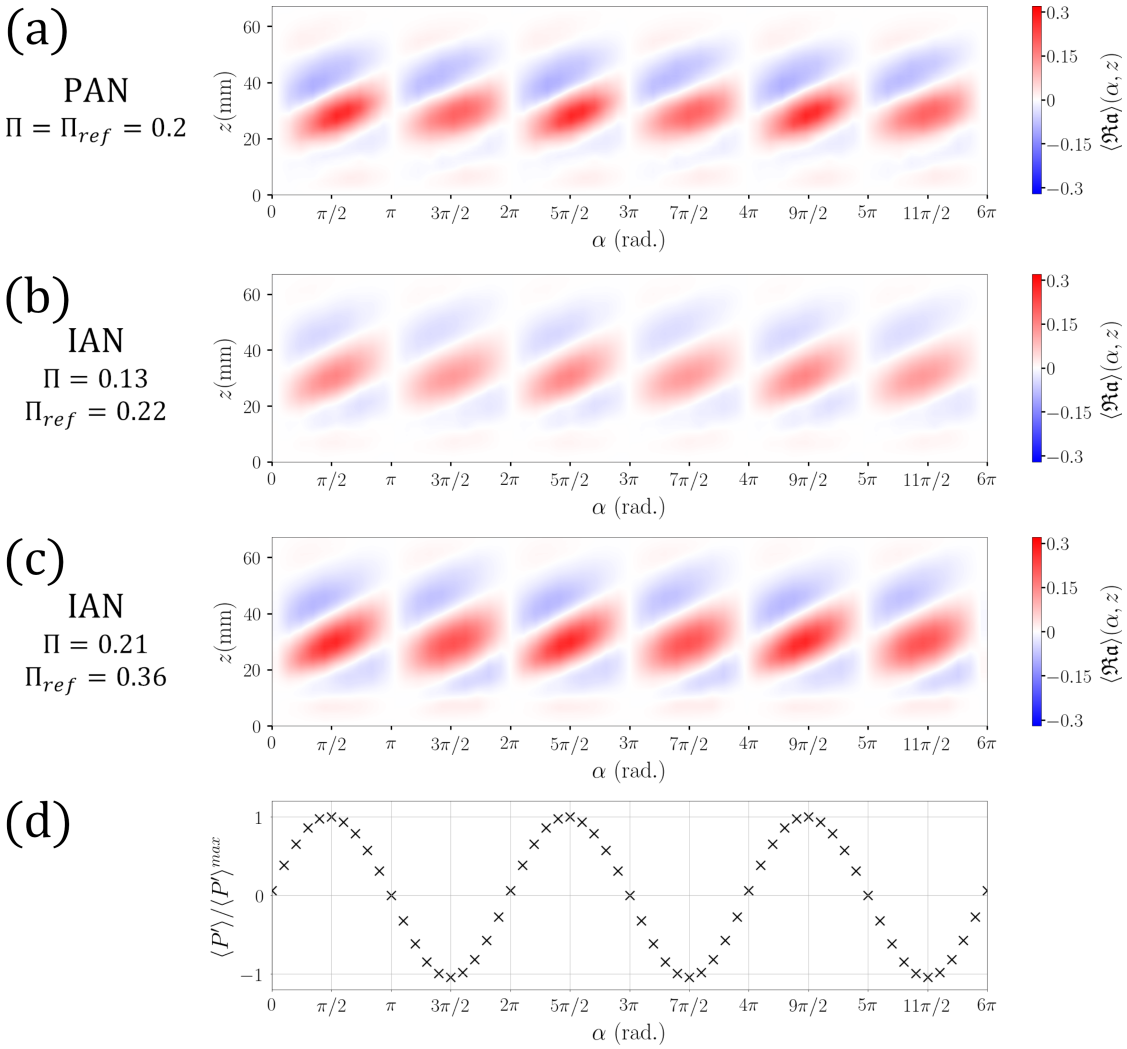

Figure 9.11: Phase-averaged local instability index $\langle \mathfrak{Ra} \rangle(\alpha, z)$ based on the Rayleigh criterion at PAN and IAN for various acoustic amplitudes. The associated reconstructed acoustic pressure cycle, reproduced three times for clarity, is shown at the bottom. Subfigures (a) and (b) compare results at PAN and IAN for a similar $\Pi_{ref} \simeq 0.2$; subfigures (a) and (c) compare results for a similar $\Pi \simeq 0.2$.

oscillation have no impact on it. This questions the relevance of the FDF approach for flames located at transverse velocity antinodes. Nevertheless, the flame at VAN can undergo a lateral motion due to the transverse velocity oscillation, which might perturb a proper flame stabilisation by affecting the central recirculation zone of the swirling flow, thereby increasing its sensitivity to blow-out. The analysis, at PAN and IAN, of mechanisms driving the global flame intensity oscillation, namely air flow axial velocity modulation and space-time fuel droplet number modulation, indicate that these mechanisms are also governed by the acoustic pressure oscillation in the chamber. As a result, it is shown that the thermoacoustic coupling is driven by the same mechanisms at both PAN and IAN. In addition, it is positive at these two locations, showing that flames at PAN and IAN of a standing transverse acoustic field can interfere in a constructive manner, thus helping to sustain thermoacoustic instabilities. This work provides insight that may help to model self-excited instabilities in multiple-injector combustion systems subjected to a standing acoustic wave.

Chapter 10

Dynamical blow-out at velocity antinodes

Contents

This chapter is the result of a joint work between EM2C and CORIA laboratories through the ANR FASMIC program. It has been published as a journal article in Proceedings of the Combustion Institute (2022) after peer-review, under the title 'Swirling spray flames dynamical blow-out induced by transverse acoustic oscillations', by Clément Patat, Françoise Baillot, Jean-Bernard Blaisot, Éric Domingues, Guillaume Vignat, Preethi Rajendram Soundararajan, Antoine Renaud, Daniel Durox and Sébastien Candel. It follows a work presented with the same title by C. Patat at the 39th International Symposium on Combustion, which was held on 24 - 29 July 2022 in Vancouver, Canada. This study exploits the complementarity of the self-unstable sixteen-injector annular combustor MICCA-Spray (EM2C) and the acoustically-forced three-injector linear array TACC-Spray (CORIA). The present work is based on flame extinctions observed around the pressure nodal line during high-amplitudes instabilities coupled by an standing azimuthal mode in the annular combustor MICCA-Spray, a feature called dynamical blow-out (DBO). These extinctions are reproduced in TACC-Spray, equipped with the same injections units, by placing the central swirl-stabilised spray flame of the three-injector linear array at the velocity antinode of a forced standing transverse acoustic field. Experimental observations are compared with a theoretical model initially derived in a previous work [142] but modified in the present study. To this end, DBO limit curves are obtained in TACC-Spray for three air mass flow rates by varying independently the acoustic amplitude and the equivalence ratio. The flame behaviour close to DBO is then explored by examining OH*-emission signals from the flame. Finally, the DBO

mechanisms are investigated by using high-speed line-of-sight OH images.*

10.1 Introduction

When combustion instabilities arise in a real system, they induce high levels of pressure oscillations, mechanical vibrations, cyclic fatigue, enhanced heat fluxes to the combustor walls, and in extreme cases, structural degradation possibly leading to failure. In some instances, the oscillation can be so strong that it gives rise to flame flashback. Understanding, predicting and controlling these dynamical processes have been constant objectives of a considerable amount of fundamental and more applied research (see for example the reviews [30, 108, 185, 190]). One aspect that is less well documented is the possible extinction of flames submitted to high amplitude oscillations accompanying certain types of instabilities. This intriguing phenomenon is the subject of the present investigation. It was recently observed when the coupling between acoustics and combustion involves an azimuthal mode. It is then logical to briefly review the literature specifically dealing with such instabilities. Most of these investigations have been carried out during the more recent period in annular systems. These are typically found in aircraft engines and gas turbines. Since the perimeter is usually the largest dimension in these annular geometries, azimuthal modes feature the lowest eigenfrequencies, which fall in the range where combustion is most sensitive to disturbances. As a consequence, these systems are susceptible to instabilities coupled by azimuthal modes. Experimental studies [142, 191–198] have been accompanied by theoretical investigations [161, 163, 164, 199–204] and by some remarkable large eddy simulations [205, 206].

On the experimental level, much of the data originates from two laboratory scale annular systems with optical access to the combustion region, one of these facilities was initially located in Cambridge and later in NTNU [193, 194], while the other (MICCA-Spray) has been operated at EM2C lab [103, 104, 142, 196, 198]. These two systems reproduce, in an idealized fashion, conditions prevailing in gas turbines and jet engines. They feature multiple injectors arranged in a circular array in the chamber backplane. While the first is essentially fed with premixed reactants (air and ethylene), MICCA-Spray may be operated with premixed air and propane or may be fed with liquid fuel (n-heptane or dodecane) that is injected in the form of sprays. Flame stabilization in the Cambridge-NTNU system is assured by central bluff bodies with a relatively low swirl number. In the MICCA-Spray device, investigations have been carried out with swirling injectors fed by premixed reactants and more recently by liquid fuels atomized as a spray of droplets.

These experimental facilities have provided considerable insight on the processes driving and coupling azimuthal instabilities. Recent combustion instability experiments carried out in MICCA-Spray have shown that flames could be extinguished when the oscillation amplitude was taking large values, typically in excess of 2% to 3% of the chamber pressure [142]. Under these conditions, some of the flames established in the combustor were blown out, as illustrated in Fig. 10.1 for an acoustic pressure amplitude of 4000 Pa. Further analysis indicated that this partial blow out occurred in the vicinity of the pressure nodal line, where the transverse velocities associated with the azimuthal mode reach their maximum level, inducing an intense sweeping motion.

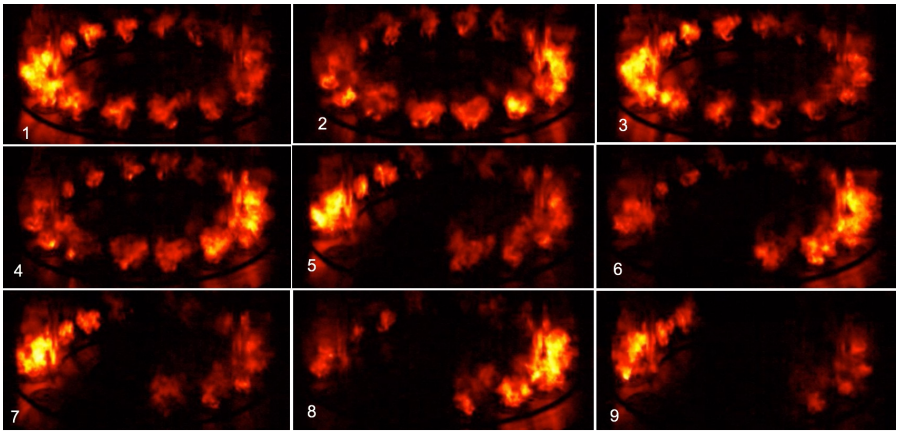

Figure 10.1: Dynamical blow out in the annular combustor MICCA-Spray. Images show the successive extinctions of the flames located near the pressure nodal line of a standing 1A1L azimuthal mode of the system as the acoustic pressure amplitude grows up and reaches 4000 Pa (see [101] for further experimental data).

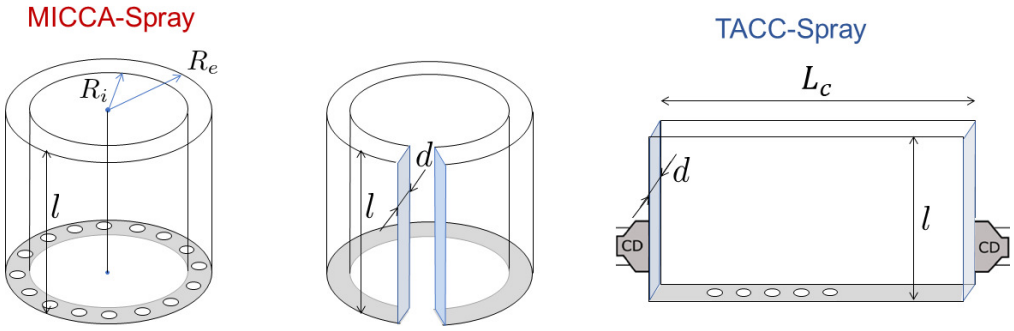

Figure 10.2: Relationship between the annular combustor MICCA-Spray sketched on the left and its equivalent linear array equipped with lateral driver units, TACC-Spray, which consists in an unwrapped sector of the annular combustor. CD: driver units.

Under these conditions, the combustion process is disrupted, inducing a complete extinction of flames established near the nodal line. The time duration of this phenomenon was found to encompass about 100 ms, corresponding to about 70 cycles of oscillation. After this blow out, the amplitude of oscillation in the chamber diminishes and the flames are established again. The process may then be repeated, leading to a new partial blow out. This phenomenon, designated in what follows as dynamical blow out (DBO) was the subject of a further investigation [101], and it was found that the flame extinction was accompanied by a notable distortion of the pressure field and simultaneously by a shift in the resonance frequency. It was also possible to estimate the velocity fluctuation amplitude corresponding to the initial flame extinction.

The objective of the present study is to pursue the analysis of the DBO by making use of a configuration designated as TACC-Spray, in which the acoustic modulations are imposed to the flame by external means. In essence, this consists in placing a linear array of swirl spray injectors in a rectangular chamber, which consists in an unwrapped sector of the annular combustor MICCA-Spray (as explained in Fig. 10.2). A transverse acoustic mode is generated by driver

units located on the lateral boundaries of this facility. The central flame formed in this injector array can then be placed at the pressure nodal line, corresponding to the maximum transverse acoustic velocity. It is then possible to augment the level of oscillation and examine the process leading to flame blow out. One advantage of this procedure is that the acoustic level is fully controlled, thus facilitating the detailed investigation of the DBO. It is in particular possible to decouple the level of the acoustic mode and the combustion operational conditions, a feature that is not available in the annular combustor MICCA-Spray where the acoustic level is governed by the coupling between acoustics and combustion.

The idea of using linear arrays of injectors to represent a sector of an annular system is not new. Such arrays have already been employed by O'Connor and Lieuwen [207, 208], by Kwong and Steinberg [83] or by Lespinasse et al. [111, 126]. In these last references, a premixed "V" flame is submitted to a transverse acoustic field. When placed at the pressure antinodal line, where the pressure reaches maximum levels of fluctuations, the flame executes an axial motion. There are also nonlinear features with lateral ejections of fluid at the injector outlet [126]. In the vicinity of the pressure nodal line, the flame is periodically swept back and forth in the transverse direction. If the injection unit comprises a swirler, helical perturbations result from the interaction of the transverse acoustic velocities with the shear regions and with the vortex breakdown process [207, 208]. Transverse waves acting on the upstream side of the injector unit may also induce a rotational motion of the flames at the injector outlets, associated to asymmetric velocity field perturbations in the injector nozzles [209]. The capacity of flames to maintain the combustion process under intense transverse velocities induced by an acoustic mode was investigated by Lespinasse et al. [111], where it was shown that premixed "V" flames placed at a pressure nodal line are more sensitive to blow off than the same flames placed at a pressure antinodal line. For these flames, stabilized on a cylindrical rod having a diameter $d = 3$ mm placed in a premixed stream at a bulk velocity $U_b = 2$ m.s^{-1}, extinction was obtained, for example, at a pressure amplitude of 100 Pa at two resonance frequencies $f_0 = 506$ Hz and $f_0 = 1012$ Hz. The transverse velocity at the pressure node could be estimated to be about 0.2 m.s^{-1}, corresponding to 10% of the bulk velocity. The response of a linear array of swirling spray flames centered on a pressure antinode of a 2T1L resonant mode was examined in the new facility TACC-Spray [99], where the flames are stabilized aerodynamically and without the help of side walls.

Further references dealing with combustion instabilities and coupling with transverse acoustic modes are reviewed in [108]. It appears that there are no detailed investigations of the DBO process for swirling spray flames subjected to a transverse acoustic field. The objective of the present work is to bring new insight into this process by combining well controlled experiments with a theoretical framework initially proposed in [142] but modified in the present article.

This article begins with a brief description of the experimental configuration. The theoretical framework is introduced next and serves to guide the experimental investigation. Experiments confirm that flame blow out is observed when the pressure amplitude reaches high levels and when the flame is located near the transverse velocity antinodal line. Characteristic features of the dynamical blow out process are then examined in more detail for three mass flow rates of air.

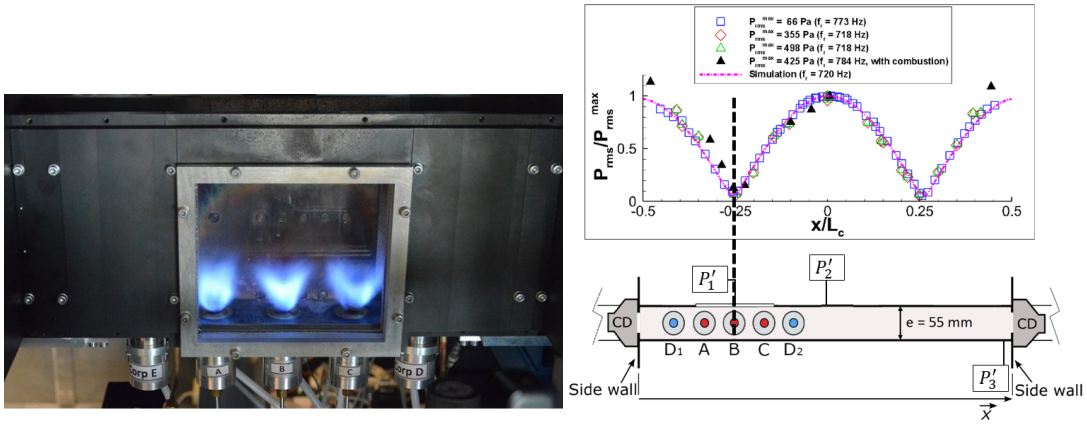

Figure 10.3: TACC-Spray setup. Left: injector array and lateral quartz window with the flames ignited. Right: transverse acoustic field inside the cavity (top) and a schematic of the top view of TACC-Spray (bottom). The central flame (injector B) is at a velocity antinode (VAN). P_1', P_2' and P_3' are simultaneously obtained at VAN, central pressure antinode (PAN) and lateral PAN respectively.

10.2 Experimental setup and diagnostics

The TACC-Spray setup, shown in Fig. 10.3, comprises a rectangular chamber. The top of the chamber is surmounted by a convergent part which prevents the entrainment of surrounding air. Its exhaust is open to the atmosphere. An array of five injection units is mounted at the chamber backplane with a spacing that is equal to that used in the MICCA-Spray experiment. They are equipped with tangential swirlers of type 716, identical to those of MICCA-Spray (see [101] for further details about the swirler). The three central units inject air and a droplet spray of liquid n-heptane while the two lateral injectors only supply air, thus partially reproducing the aerodynamics in the side regions and acting as stabilizers of the lateral flames. This original arrangement where the lateral flames are well anchored far from the side walls, places the central flame in an environment reflecting that of MICCA-Spray at any location of the acoustic field. Two compression drivers Beyma CP850ND (marked as CD in Fig. 10.3) are fixed on the side walls, facing each other such that their common acoustic axis which passes through their centers is at 90 mm from the chamber backplane. They are characterized by a wide frequency range (0.5–20 kHz). The excitation signals are delivered by a Hameg HM8150 signal generator, an IMG Stageline frequency filter and a Peavey PV900 amplifier. Here, the 0-peak acoustic pressure amplitude P' is measured with B&K type 4182 microphones plugged at several positions on the chamber front walls at 8 mm from the chamber backplane, as shown in Fig. 10.3. The vertical side walls holding the driver units are placed on rails and the front walls are made of plates of height $h_c = 200$ mm and different lengths, which allows to vary the chamber length L_c and ensure acoustic resonance at a selected frequency f for a frequency in the range 680-780 Hz, corresponding to the DBO frequency range in MICCA-Spray. A transverse mode is generated in the rectangular chamber, with peak amplitude levels that may reach 1700 Pa. This is used to locate the pressure, velocity or intensity antinode so that it coincides with the central injector. Global flame emission is observed with a photomultiplier Hamamatsu H10721-210 equipped

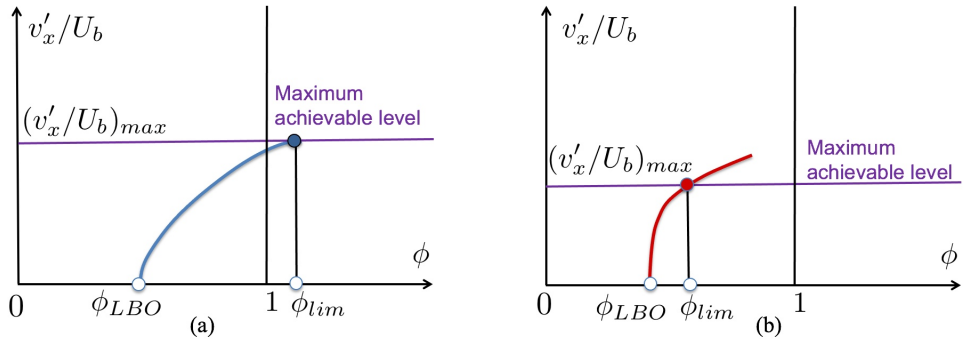

Figure 10.4: Dynamical flame blow out conditions may be determined by changing the equivalence ratio to vary the stability margin. When this ratio reaches the lean blow out limit, the flame is extinguished. The range of equivalence ratios between ϕ_{LBO} and a limit value ϕ_{lim} may be explored and the level of transverse oscillation that leads to extinction may be determined. Beyond ϕ_{lim}, the level of transverse velocity fluctuation exceeds the maximum achievable value and this range cannot be explored. These diagrams only consider lean operating conditions. Left: Low bulk velocity case. The flame is not very well anchored and extinction may be observed over an extended range of equivalence ratios limited by the maximum achievable level of transverse velocity fluctuation. Right: High bulk velocity case. Flame anchoring is improved and the maximum achievable level of relative transverse velocity oscillation is reduced. The range of equivalence ratios in which DBO may be observed is diminished.

with a UV-visible lens and an interference filter centered on OH^* emission in the UV range ($\lambda = 305$ nm, FWHM = 24 nm). High-speed imaging of the OH^* radical is performed at a rate of 10000 fps with a Phantom V2012 camera equipped with a Lambert HiCATT 25 intensifier, a UV-105 mm lens and a UG11 filter.

10.3 Theoretical framework

The general ideas that were followed in [142] to derive a theoretical model for the DBO phenomenon are now used to guide the blow out experiments in TACC-Spray. Blow out takes place when the central injector is located at a pressure node of the resonant acoustic field, where the transverse velocity v'_x reaches maximum values. The data from MICCA-Spray indicate that DBO requires high amplitude oscillations. It is also found that the transverse velocity induced by the acoustic field displaces the flames in the transverse direction. This modifies the heat release rate in the flames located near the pressure nodal line, where the transverse velocity reaches its maximum. In the initial model, the parameters influencing the blow out were as follows: injector exit diameter d, bulk velocity at the injector exit U_b, conversion time τ_c, transverse velocity fluctuation amplitude v'_x, angular frequency $\omega = 2\pi f$, and the swirl number S. Parameter $\tau_c = \tau_m + \tau_v + \tau_{ch}$ includes a mixing time τ_m, a vaporization time τ_v and a chemical time τ_{ch}. Mixing is essentially governed by turbulence, vaporization depends on the droplet diameters and clustering in the spray, while the chemical conversion is a function of the local equivalence ratio ϕ. Dimensional analysis indicates that there are four dimensionless groups that may be written as v'_x/U_b, the relative velocity perturbation amplitude, $v'_x/(\omega d)$, the ratio of the transverse dis-

placement to the injector outlet diameter, $(\tau_c U_b)/d$, the ratio of the chemical conversion time to a mechanical time d/U_b and S, the swirl number measuring the rate of rotation with respect to the axial flow velocity. The flame extinction is then formally governed by a criterion that may be cast in the form:

$$\psi_1 \left(\frac{v'_x}{U_b}, \frac{v'_x}{\omega d}, \frac{\tau_c U_b}{d}, S \right) > 0 \tag{10.1}$$

It was initially considered that the relative transverse displacement amplitude $v'_x/(\omega d)$ was governing the flame extinction process. When this ratio is sufficiently large, the central recirculation zone which anchors the flame is significantly perturbed, destabilizing the flame and inducing blow out. However, $v'_x/\omega d$ is dependent on v'_x/U_b and the inverse of the Strouhal number St defined by $\mathrm{St} = \omega d/U_b$. So, it may be interesting to replace the second dimensionless group by the Strouhal number. The influence of frequency on the process is then reflected by this important dimensionless number. The extinction condition may then be rewritten in the form:

$$\frac{v'_x}{U_b} > \psi_2 \left(\mathrm{St}, \frac{\tau_c U_b}{d}, S \right) \tag{10.2}$$

It is known that the parameter $(\tau_c U_b)/d$ that will be designated from here on by b, typically determines the stability of a combustion system. When this parameter is smaller than a critical value corresponding to static blow out, say b_* of the order of one, the conversion time is shorter than the mechanical time and the flame is stabilized. When b exceeds b_*, the flame is extinguished. This is equivalent to say that the Damköhler number should exceed a critical value for flame stabilization (*i.e.*, $\mathrm{Da} > \mathrm{Da}_c$). The difference $b_* - b$ then measures the stability margin and may be used in place of the dimensionless group b. One may then separate the right hand side in expression (10.2) in two parts, the first reflecting the state of rotation and flow response $\psi_3(S, \mathrm{St})$ while the second represents the stability margin in the form $(b_* - b)^n$. The dynamical blow out criterion then takes the form:

$$\frac{v'_x}{U_b} > \psi_3(S, \mathrm{St})(b_* - b)^n \tag{10.3}$$

This criterion slightly differs from that proposed in [142] in that it puts the accent on the transverse velocity disturbance and on the stability margin of the flame. The function ψ_3 portrays the swirling flow characterized by the swirl number S and its response to external modulations through a Strouhal number. For a fixed injector and a broadband receptivity to incident disturbances, one may consider that ψ_3 is a constant so that the criterion is essentially controlled by the stability margin $(b_* - b)^n$, where n may be obtained from experiments. If the flame is close to blow off, it may be easily perturbed by the external acoustic field. If the stability margin is greater, then the combustion process will be less easily perturbed. In the previous expression, $b = U_b \tau_c / d$ defines the stability of the flame and one may note that v'_x/U_b has to be sufficiently large if the acoustic field is to play a role and induce flame blow off. This analysis may be tested by changing the value of b to vary the stability margin of the flame. For a fixed injector geom-

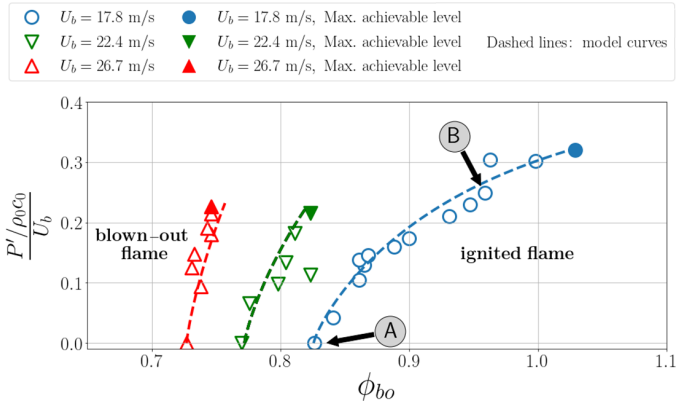

Figure 10.5: Flame blow out boundary for three regimes of operation. Swirler type: 716, liquid n-heptane fuel. The blue symbols correspond to $U_b = 17.8$ m/s, $f = 745 - 760$ Hz, the green symbols to $U_b = 22.4$ m/s, $f = 755$ Hz and the red symbols correspond to $U_b = 26.7$ m/s, $f = 750 - 762$ Hz. Filled symbols indicate the maximum achievable level of $P_2'/(\rho_0 c_0 U_b)$. A and B indicate operating conditions that are analyzed in the text. Theoretical curves shown as dashed lines are obtained with $n = 0.8$.

etry, this may be achieved by changing the bulk velocity U_b or by changing the conversion time τ_c. When τ_c is increased, the stability margin is reduced. It is most convenient to augment the chemical time by operating under leaner conditions, *i.e.*, by reducing the equivalence ratio and operating near the lean blow out limit. This is illustrated in Fig. 10.4.

Diagrams in Fig. 10.4 may be used to guide the exploration of the DBO phenomenon. The central idea is to explore flames that have a narrow margin with respect to the lean blow out limit. The acoustic level is fixed and the equivalence ratio is progressively decreased until flame blow out. This scheme is repeated for higher acoustic levels until the maximum achievable level is reached. The corresponding equivalence ratio ϕ_{lim} is that which requires the highest achievable level of pressure oscillation, *i.e.*, the highest level of transverse velocity fluctuation. Beyond that point, the system cannot provide a level of oscillation that will lead to blow out.

10.4 Flame blow out induced by high amplitude oscillations

It is now interesting to examine results of blow out experiments carried out for three different bulk velocities, calculated by dividing the air mass flow rates by the ambient air density at 20°C and by the injector exit surface area (diameter $d = 8$ mm). The corresponding blow out boundaries are plotted in Fig. 10.5. The transverse velocity amplitude, v_x' corresponds to the theoretical value $P_2'/\rho_0 c_0$, with P_2' obtained from experiments. This correspondence is well verified by evaluating the flame displacement by means of the high-speed OH* images. When the bulk velocity is low ($U_b = 17.8$ m/s) corresponding to the blue line, the maximum level of fluctuation can reach a value of 32 %. The flame is also not very well anchored because atomization produces bigger droplets, increasing the vaporization time and reducing the Damköhler number. In this case, transverse acoustic oscillations induce blow out at equivalence ratios as high as 1.03. This situation corresponds to that shown schematically in Fig. 10.4 (left). When the bulk

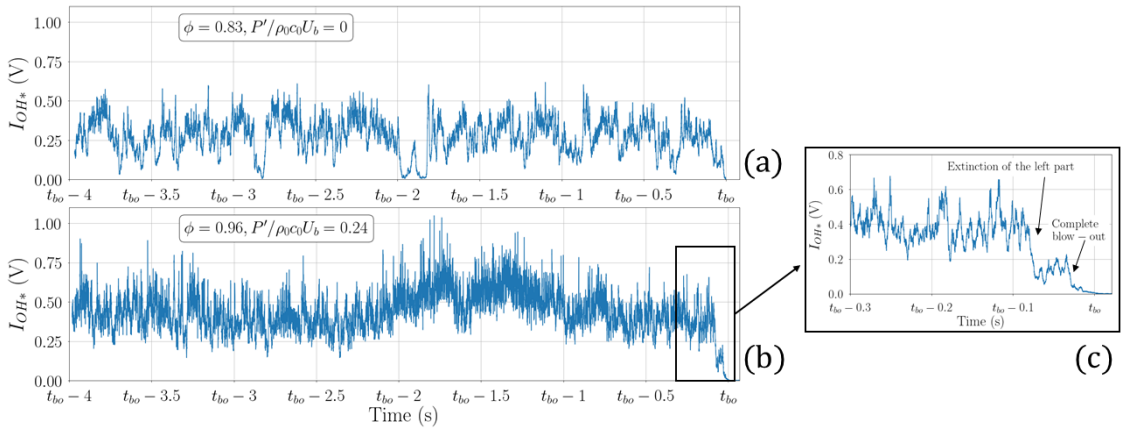

Figure 10.6: OH* signals of the whole central flame during 4 seconds before DBO for $U_b = 17.8$ m/s: (a) Light emission during a typical blow out at $\phi = 0.83$, in the absence of acoustic modulation; (b) Dynamical blow out obtained at $\phi = 0.96$ with an acoustic modulation level $P_2'/(\rho_0 c_0 U_b) = 0.24$ at a frequency $f = 760$ Hz; (c) A detailed view of the last signal during the final period.

velocity is increased, atomization is improved, vaporization time is reduced and flame anchoring is enhanced. The maximum achievable level of velocity fluctuation is reduced to about 20% for $U_b = 26.7$ m/s, so DBO is observable in a more limited range of equivalence ratios, as shown schematically in Fig. 10.4 (right). To assess the theoretical model, b_* (without acoustics), b at the maximum achievable level and ψ_3 of eq. (10.3) are obtained by making use of values of τ_c deduced from flame stabilization experimental data [210], expressed as a function of ϕ. Those data correspond to experiments carried out under premixed conditions in a situation where the flame was anchored by hot gas recirculation behind a buff-body. In that case, the characteristic time τ_c only depended on the equivalence ratio ϕ. In the present case, the flame is stabilized by hot products that are recirculated by the rotating flow, and the characteristic time τ_c also accounts for a delay associated with vaporization. It is then necessary to use the general trends with respect to ϕ defined in [210] but shift the data, thus including a dependency on this vaporization time. This is guided by the fact that flame blow off in the absence of acoustic modulation is a function of the bulk velocity. The curves derived from the model are in good agreement with the experimental data for $n = 0.8$ for the three operating points.

For $U_b = 17.8$ m/s, the DBO limit curve presents a changing slope, showing a limited sensitivity to acoustics for low acoustic amplitudes, which is accentuated when U_b is increased. Indeed, blow out at $U_b = 26.7$ m/s occurs almost at the same equivalence ratio without acoustics and for a relative velocity perturbation of 20%, which is not observed for the lower value of the bulk velocity. The blow out process is detected when the OH* light emission captured by the photomultiplier drops down to zero. This is illustrated in Fig. 10.6 which shows light intensity records for the central flame. The system operates at $U_b = 17.8$ m/s. The signal recorded in the absence of acoustics characterizes a typical blow out event at $\phi = 0.83$. The second signal recorded at an equivalence ratio of $\phi = 0.96$ exemplifies a dynamic blow out induced by a relative pressure fluctuation $P'/\rho_0 c_0 U_b = 24\%$, where the air density ρ_0 and sound velocity c_0

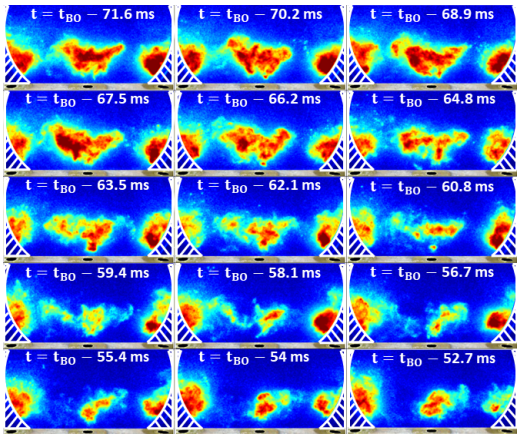

Figure 10.7: Images of step 1 of the flame blow out process extracted from a high speed film recorded at 10000 fps for $U_b = 17.8$ m/s, $\phi = 0.96$, $f = 760$ Hz. Time t is counted down and indicates the time before complete blow out of the central flame. Successive images are presented from left to right and top to bottom. Flames cannot be observed in the white dashed regions.

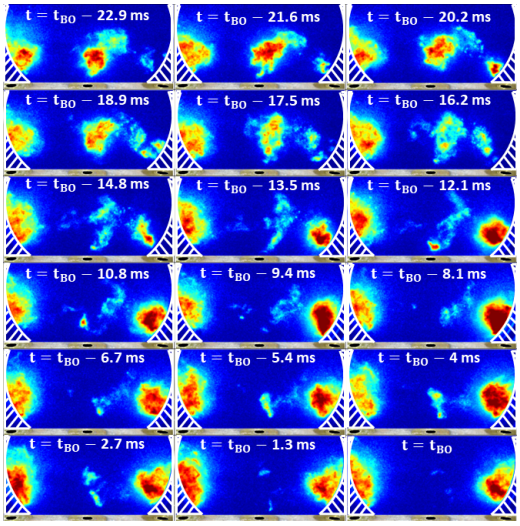

Figure 10.8: Images of the step 3 of the flame blow out process extracted from a high speed film recorded at 10000 fps for $U_b = 17.8$ m/s, $\phi = 0.96$, $f = 760$ Hz. Time t is counted down and indicates the time before complete blow out of the central flame. Successive images are presented from left to right and top to bottom. Flames cannot be observed in the white dashed regions.

are determined at the microphone location. These two signals correspond to points A and B in Fig. 10.5. In the absence of acoustics, blow out of the whole system is induced by the total extinction of any of the three flames, but the partial extinction of any of the three flames does not necessarily provoke the whole system extinction. There, the central flame undergoes many partial extinctions of short duration when the system operates in the vicinity of its stability limit. These events are identified by pronounced reductions of the OH*-intensity, which drops down to zero, as shown at times $t_{BO} - 2.85$ s and $t_{BO} - 1.9$ s. Each partial extinction lasts for less than 70 ms, after which the flame is reignited. Finally, a complete blow-out occurs when the partial extinction exceeds 50 to 70 ms. In the presence of an adequate acoustic level, it is only the central flame at VAN which first blows out, leading to the extinction of the whole system a short time later. Two behaviors are observed in this case, highlighted by the change in the slope of the DBO limit curve. In the region pertaining to the smaller acoustic fluctuation levels, characterized by a nearly vertical boundary between ignited flames and blown-out flames (see Fig. 10.5), the extinction process is quite similar to that observed in the absence of acoustics. For these lower acoustic amplitudes, DBO is mainly induced by standard mechanisms of lean blow out. As the equivalence ratio is increased, stabilization is improved, and a greater acoustic amplitude is required to blow out the flame. In the region corresponding to the weaker slope of the blow out boundary, partial extinctions appear when the point of operation approaches the DBO limit curve. These extinction events are less common as the acoustic amplitude increases, as found by a statistical analysis of the OH* signals during time intervals of 8000 - 10000 acoustic

cycles preceding blow out. This is illustrated in Fig. 10.6 for $\phi = 0.96$, in which a single partial extinction of one part of the flame is detected just before blow out occurs, the PM-signal recorded for 4 seconds showing no other partial extinction event, while for $\phi = 0.83$, five partial extinctions are identified during the same time span. When the equivalence ratio is augmented, flame anchoring is enhanced, and DBO requires higher acoustic amplitudes inducing stronger transverse velocities. The ability of the flame to reignite after undergoing such a strong partial extinction is then impeded, as seen in Fig. 10.6.

The DBO process for the low bulk velocity case is examined by making use of time-resolved high-speed OH*-emission images. All image sequences captured with acoustics show the total extinction of the central flame located at the pressure node, retrieving the DBO phenomenon observed in MICCA-Spray (for $\phi = 1.06$). The DBO process driven by acoustic effects is achieved in three successive steps where the front-interaction between the central flame and one of the lateral flames plays an important role, favored by the transverse flame displacement induced by the acoustic velocity. This is illustrated in Figs. 10.7 and 10.8 for ϕ = 0.96 and $P'/\rho_0 c_0 U_b = 24\%$ (case (b) of Fig. 10.6) where flame interactions take place between the central and lateral right flames. *Step 1* (see Fig. 10.7) corresponds to the partial extinction of the central flame with a net reduction of light emission from its left part, reflecting a reduction in the global heat release rate. This affects the flame stabilization mechanism by facilitating the penetration of a greater amount of burnt gases diluting fresh reactants in the flame anchoring region. Simultaneously, the right part of the central flame becomes weaker, featuring a fragmentation in lumps at $t = t_{BO} - 60.8$ ms. During *step 2*, the weakened flame persists and remains ignited until $t = t_{BO} - 22.9$ ms by interacting here with the left part of the lateral right flame, which is also seen to become less intense during this interval. *Step 3*: from $t = t_{BO} - 22.9$ ms (see Fig. 10.8), the central flame progressively extinguishes by its downstream part. At the same time, the OH*-intensity of the left part of the lateral right flame increases again such that it reaches a similar level to the one observed for $t < t_{BO} - 60$ ms, showing the ability of the lateral flame to fully reignite from a weakened state. This process is facilitated by the strong displacement of the central flame. The central flame stabilization point is occasionally reactivated, as shown by the presence of puffs of OH* at $t = t_{BO} - 12.1$ ms and $t = t_{BO} - 5.4$ ms, but the associated heat release rate is unable to allow reignition of the entire flame and the presence of the lateral flames is not sufficient to maintain the central flame. Therefore, the lower resistance to blow out of the central flame results from the stronger transverse velocity at the pressure node.

10.5 Conclusion

Experiments have been carried out in a system comprising an array of swirling injectors fed with liquid n-heptane and air placed in a rectangular configuration operating at atmospheric pressure. This configuration may be modulated by transverse acoustic modes generated by a set of driver units located on the lateral sides of the system. The pressure oscillation may reach peak values of the order of 1700 Pa peak (about 2% of the chamber pressure). Experiments reveal that these high acoustic levels induce a strong transverse motion in the neighborhood of the pressure nodal line which also corresponds to a maximum in transverse velocity fluctuations. Experiments

indicate that the combustion process markedly changes when the position of the central injector coincides with a pressure antinode or when it corresponds to a nodal line. In this latter case, when the pressure oscillation amplitude exceeds a certain threshold, the flame senses maximum transverse velocity fluctuations that produce a dynamical extinction. A mechanism is proposed for this flame extinction process that defines a critical value for the transverse velocity amplitude with respect to the injection velocity. The blow out limit boundary highlights two extinction regimes, in which blow out is dominated either by standard mechanisms leading to lean blow out, or by transverse velocity oscillations. In the latter case, partial extinctions of the central flame lead to irreversible flame blow out, while lateral flames can be maintained even after complete blow out of the central flame. The data reported in this article provide new insights on the dynamical blow out that results from excessive levels of acoustic oscillation and may serve to guide modeling and simulation of interactions between acoustics and combustion.

Conclusion and perspectives

General conclusion of this work

This research work is intended to provide new knowledge about the dynamics of lean swirl-stabilised spray flames in a standing transverse acoustic field, by using the experimental configuration TACC-Spray. It is chosen to use swirling air flows and liquid fuel to share the main features of practical injection units found in industrial gas turbines or aircraft engines. The selected forced acoustic mode, corresponding to the 2T1L mode of the chamber, aims at simulating combustion dynamics in the presence of standing azimuthal acoustic modes, which are the most detrimental to the proper functioning of annular combustors due to their low damping. The excitation frequency is adapted to the instability frequency found in the laboratory-scale annular combustor MICCA-Spray, located at EM2C laboratory, in which 16 swirl-stabilised spray injection units are equally distributed over an annular surface. In order to best represent the flame dynamics in an annular combustor in TACC-Spray, a linear array of three swirl-stabilised spray flames, is placed inside the acoustic field. The central flame, which is the main object of our study, is therefore located between two stable flames, mimicking the environment of a flame in the laboratory-scale annular combustor. The main conclusions are given below.

Measurement of the flame describing function with downstream transverse forcing

- The flame describing function (FDF) is usually defined by linking the axial velocity oscillation reduced by its mean value, as an input signal, to the heat release rate (HRR) oscillation reduced by its mean value, as an output signal. However, the axial velocity oscillation is highly sensitive to its measurement location at the burner exit, and it may be difficult to measure in experimental configurations. In this work, two FDFs are compared at a given frequency f_r:
  - $\mathcal{F}_{U'}$, linking the reduced axial velocity oscillation to the reduced OH*-intensity oscillation of the flame;
  - $\mathcal{F}_{P'}$, linking the acoustic pressure oscillation reduced by the aerodynamic bulk pressure n to the reduced OH*-intensity oscillation of the flame.

  It is shown that the same evolution of the gain and phase are retrieved with both FDFs. This behaviour is explored by analysing the describing function linking the reduced pressure oscillation to the reduced axial velocity oscillation. It is found that the amplitudes

of both oscillations are proportional, while the phase shift between them is very slightly modified. These characteristics indicate that in the present setup, operated with downstream transverse acoustic forcing, $\mathcal{F}_{P'}$ is suitable to characterise the evolution of flame dynamics with the acoustic amplitude.

Mechanisms driving the flame intensity oscillation at a pressure antinode

- A study with n-heptane fuel shows that the amplitude of the global flame CH^* (or OH^*) intensity oscillation reduced by the mean CH^* (or OH^*) intensity evolves with the non-dimensional acoustic amplitude Π, which reduces the acoustic pressure amplitude by the bulk aerodynamic pressure of the air flow. As Π increases, the reduced global flame intensity oscillation first grows linearly; then, it enters a transition zone characterised by the presence of nonlinearities; and finally, it saturates.

- The global flame intensity oscillation is governed by the middle region of the flame. The flame response mechanisms, explored in the linear zone, involve the periodic simultaneous ejection of a high fuel droplet amount and the roll-up of a coherent vortex at the injector exit, leading to the engulfment of a significant fuel amount and subsequently to an effective air-fuel mixing during transports, and then to a periodic increase of the flame intensity in the flame middle region. This is followed by a decrease of the flame intensity, leading to a pattern corresponding to the generation of an axially-propagating flame intensity wave.

- When the flame power is augmented but the equivalence ratio is kept constant, *i.e.* the fuel and air mass flow rates are proportionally increased, the propagation velocities of the droplet number wave and axial flame-intensity wave increase and, as the flame middle region remains at the same vertical location, the transport time between the injector exit and the flame middle region is reduced. As a consequence, the flame is more compact relatively to the convective waves such as the flame-intensity wave, limiting the destructive interferences between different locations of the flame and therefore increasing the global flame intensity oscillation. In the present case, this is accompanied by a progressive phasing between the acoustic pressure oscillation and the flame intensity oscillation, leading to a strong positive thermoacoustic coupling at the higher flame power, which is consistent with self-excited instabilities found by the EM2C team in the MICCA-Spray annular combustor (EM2C) for the same operating point [174].

- The nature of the fuel impacts the flame response. Results with n-heptane or dodecane indicate that the atomisation quality affects the flame intensity oscillation: a large proportion of small droplets, which are more sensitive to the modulations induced by acoustics, may increase the global flame intensity oscillation. In addition, the evaporation time also influences the time delay between the acoustic pressure oscillation and the global flame intensity oscillation. While in the present case, the thermoacoustic coupling is positive for the two fuels, showing the potential of both fuels to drive self-excited instabilities, the results indicate a weaker thermoacoustic coupling with dodecane. However, this conclusion is not necessarily common to all combustors, since the modification of the time delay with the fuel could lead from a stable system with n-heptane to an unstable system with

dodecane for other operating conditions.

Saturation mechanisms

- The high acoustic levels that can be attained in TACC-Spray ($P^{'} > 1700$ Pa) allow to excite nonlinear mechanisms leading to the saturation of the flame response. Among them, partial extinctions of the flame lead to a significant decrease of the flame intensity oscillation. Such extinctions are induced by the occasional destabilisation of the flame anchoring point. In addition, the saturation of the flame response can result from the generation of strong droplet number waves, which may induce droplet clustering, potentially reducing fuel evaporation and mixing.

Influence of the flame location in a standing transverse acoustic field on its response

- The response of the lean swirl-stabilised spray flames depends on the acoustic perturbation to which they are subjected. Whereas acoustic pressure oscillations induce a periodic axial flame intensity wave, leading to remarkable flame intensity oscillations, transverse velocity oscillations cause the periodic lateral displacement of the flame. It is shown that the modulation of the air flow axial velocity and the generation of droplet number waves, two mechanisms explaining the periodic flame intensity oscillation, result from the acoustic pressure oscillation only. Nevertheless, flames subjected to strong transverse velocity modulations may be blown-out during high-amplitude instabilities. This phenomenon, first observed by the EM2C team [142], is here reproduced in TACC-Spray by placing the central flame at a velocity antinode. Comparison of the experimental results with a theoretical model indicates that flame blow-out is governed by the balance between relative transverse velocity oscillation and the flame stability margin. Experimental observations highlight the mechanisms leading to flame blow-out under strong relative transverse velocity oscillations.

Perspectives for future works

This research work raises issues concerning thermoacoustic instabilities in annular combustors. Some of them are indicated in the following.

Fuel spray modulation

- This work has evidenced the presence of fuel droplet number waves induced by the acoustic pressure oscillation in reacting conditions, and has shown a correlation between the axial location of the maximum droplet amount and the maximum CH^* (or OH^*) intensity. Nevertheless, it is still unclear how the fuel droplets evaporate and mix with the air. For instance, the amplification of the droplet number wave could result from spray segregation [136] or from local droplet clustering, inducing a decrease of the local evaporation rate [189]. In addition, strong droplet clustering at high acoustic amplitudes could be involved into the saturation of the flame response (see Chapter 7). In addition to these

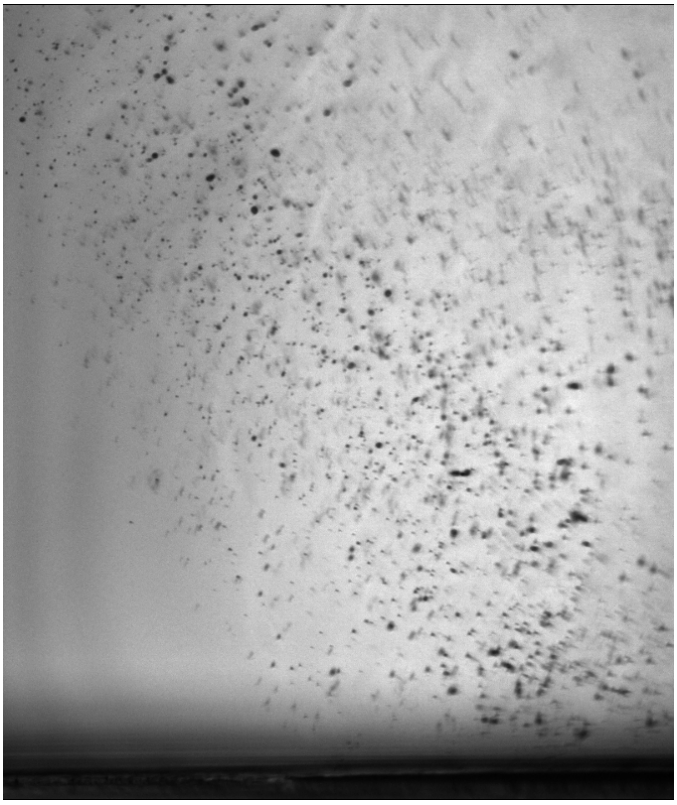

Figure 10.9: Image of the n-heptane spray obtained by Backlight Diffuse Illumination. The separation between the black zone at the bottom of the image and the grey background indicates $z = 0$. The image size is 5.9×5 mm^2 with a spatial resolution of 2.3 µm/pixel.

features, the droplet number waves that are evidenced here cannot give a precise quantitative information about the modulation of the fuel mass flow rate injected into the chamber. Indeed, PDA is a point measurement technique and measures only the spherical droplets, limiting the quantitative estimate. To gain insights about these features, it would be interesting to perform LES on the same configuration.

- The spray behaviour can be further understood by visualising the spray with a high spatial resolution. Backlight Diffuse Illumination images, recently obtained, give insight about the quality of the atomisation. An example shown in Figure 10.9 indicate that with n-heptane, the spray is mainly composed of spherical (or elliptical) droplets at the injector exit, while no liquid ligaments are noticed.

Flame front interactions

- Preliminary works performed during this thesis showed that the response of the swirl-stabilised spray flames is lower in the presence of **flame front interactions**. Such interactions are obtained by reducing the inter-injector distance a_{inj} from 65 mm to 40 mm. Results, shown in Figure 10.10, indicate that nonlinearities arise at at $\Pi \simeq 0.2$ for $a_{inj} = 40$ mm against $\Pi \simeq 0.35$ for $a_{inj} = 65$ mm. Mechanisms have been identified

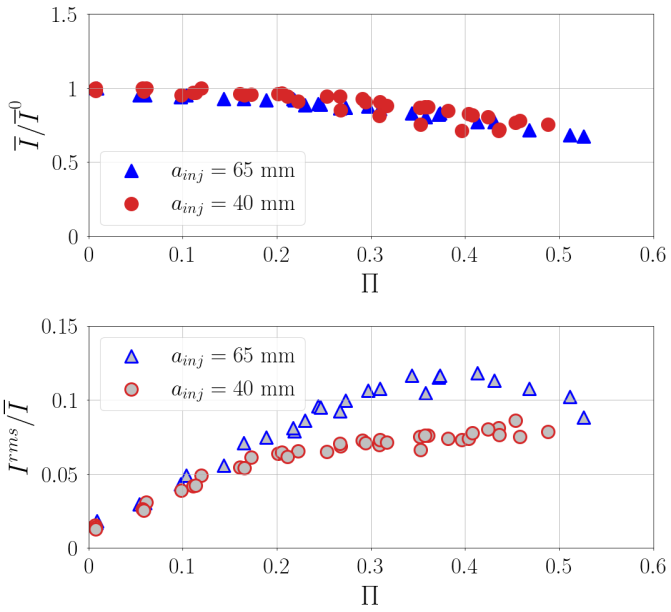

Figure 10.10: Response of the flame OH* intensity as a function of the reduced acoustic amplitude Π for two inter-injector distances, $a_{inj} = 40$ mm and $a_{inj} = 65$ mm. Top: mean intensity, $\overline{I}/\overline{I}^0$; bottom: reduced rms oscillation amplitude: $I^{rms}/\overline{I}$.

in premixed flames without swirl [81, 165], but there is a lack of knowledge concerning swirl-stabilised spray flames. One perspective of this work pertains to the investigation of the mechanisms inducing the modification of the response of such flames with the flame separation distance. These mechanisms could be linked to the air flow (*e.g.*, interaction between vortices from adjacent flames), to the fuel spray (*e.g.*, creation of droplet clusters reducing the local evaporation rate [189]) or to the flame front itself (*e.g.*, flame annihilation events [165]).

- The flame separation distance was also shown to affect the **lean blow-out limit** of the energy system during experiments. It was indeed observed that for $a_{inj} = 40$ mm, the flames extinguish at a higher equivalence ratio than for $a_{inj} = 65$ mm. It would be interesting to extend the analysis performed in Chapter 10 to interacting flames. It is likely that flame-flame interactions modify the stability margin of the flames.

Acoustic response for various fuel compositions

- The **effect of the fuel composition on the flame response** requires further investigation. This is fully in line with the objectives concerning (i) the development of fuel-flexible systems and (ii) those concerning sustainable aviation fuels (SAFs). Regarding the first point, it is important to determine what are the main liquid fuel characteristics involved in self-sustained combustion instabilities, in order to design combustion chambers that can be operated safely and with a high efficiency for a variety of fuels. About the second point, SAFs must meet the requirement of a stable combustion to become a reliable alternative to fossil fuels. As SAFs are produced from other sources than fossil sources, their chemical

composition is different from that of conventional fuels, and thus the physico-chemical fuel characteristics are modified. In addition, SAF properties depend on the production pathway. It is therefore of primary interest to target the physico-chemical characteristics that future SAFs will need to have, in order to develop the production chain. For these purposes, the ANR FlySAFe program, which is a collaboration between CORIA, CERFACS and EM2C laboratories, has started in November 2022. It is a continuation of the ANR FASMIC program with the same three partners, dedicated to bring further knowledge about thermoacoustic instabilities with a surrogate fuel for a SAF. A two-component surrogate of S-8 fuel made of iso-octane and dodecane [211] will be used. One question arises as to whether the differential evaporation of these two fuels play a significant role in the flame response.

- It was also observed that the **lean blow-out limit** is modified when the fuel is changed: dodecane flames could be extinguished at higher equivalence ratios than n-heptane flames. The approach taken in Chapter 10 (dynamical blow-out at a velocity antinode) could be applied to dodecane flames to better understand the role of the conversion time[1] on the blow-out process.

Measurement of flame describing functions with transverse forcing

- An interesting point would be to measure the FDF in TACC-Spray not only as a function of acoustic amplitude, but also for various frequencies, in particular for lower ones than those investigated in this manuscript. As the excited acoustic mode in TACC-Spray is the 2T1L mode, this requires to increase the length or the height of the cavity. The counterparts are (i) a greater acoustic damping and (ii) a modification of the thermal field which could affect the flame stability. To reach the goals, a new acoustic forcing system is being designed to deliver greater acoustic levels.

[1] The conversion time includes the characteristic times for air-fuel mixing, fuel evaporation and chemical reaction.

Appendix

Appendix A

Synchronisation of experimental measurements

A.1 Synchronisation for high-speed flame imaging

Synchronisation between image acquisition, acoustic pressure measurements and PM signal acquisition is performed using a Berkeley Nucleonics (BNC) Model 575 delay/pulse generator with eight outputs. The experimental setup is depicted in Figure A.1. Image acquisition is performed with a camera equipped with an intensifier and acoustic pressure and PM signals are acquired using a National Instruments (NI) acquisition card. The intensifier is equipped with a shutter control system, which is activated manually to open the shutter just before measurements. After shutter opening, four output signals are generated and sent to the different devices. Single-shot trigger signals are sent to the camera to trigger image acquisition and to the NI acquisition card to trigger acquisition of acoustic pressure and PM signals. The signal width, $\Delta t_{trigger}$ has no importance since acquisition starts from the rising edge of the trigger signal. Simultaneously with the trigger signal, synchronisation signals are sent to the camera and to the intensifier. These signals act as a clock that control image acquisition. They consist in rectangular signals of width Δt_{sync} with the same frequency corresponding to the desired acquisition frequency (here, either 10,000 or 20,000 Hz). At each rising edge, intensifier gate opens and the acquisition of one image starts. The intensifier gate width and the image exposure time, which are equal here, are specified on the software associated to each device. Therefore, the width of the synchronisation signal has no influence on these parameters. After acquisition of the data, the intensifier shutter is closed in order to protect the intensifier from too much light emission.

A.2 Synchronisation for high-speed tomography

Synchronisation between the laser pulse generation, image acquisition, acoustic pressure measurements and PM signal acquisition is performed using a Berkeley Nucleonics (BNC) Model 575 delay/pulse generator with eight outputs. The experimental setup is depicted in Figure A.2. Six output signals are generated and sent to the different devices. A ‘gate’ signal is sent to the

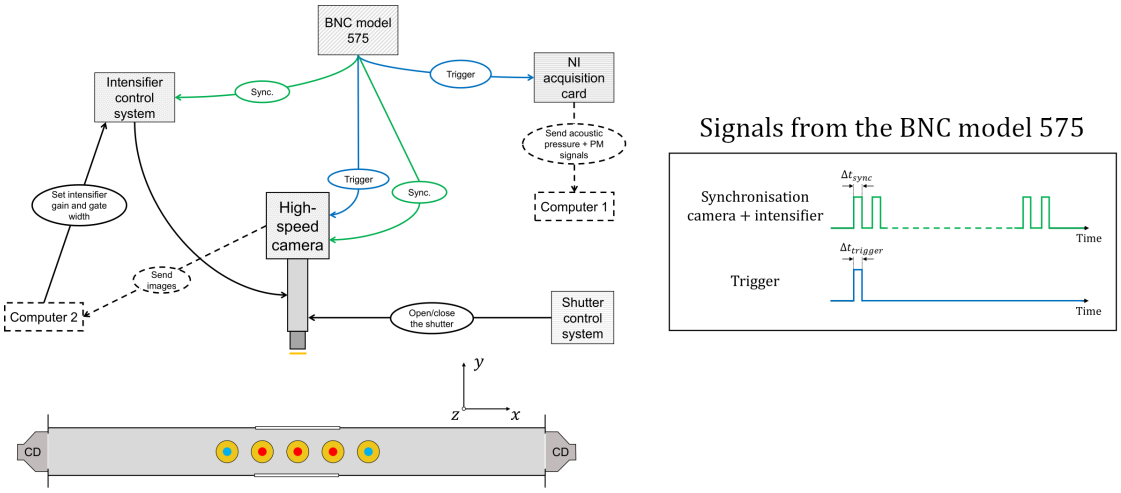

Figure A.1: Signals for synchronisation between image acquisition and acoustic pressure measurements for high-speed imaging of the radical light emission by the flames.

Rate (kHz)	Δt_{sync} (µs)	$\Delta t_{trigger}$ (µs)	t_{expo} (µs)
10	10	10	99
20	10	10	49

Table A.1: Characteristics of the synchronisation and acquisition signals for radical light emission imaging.

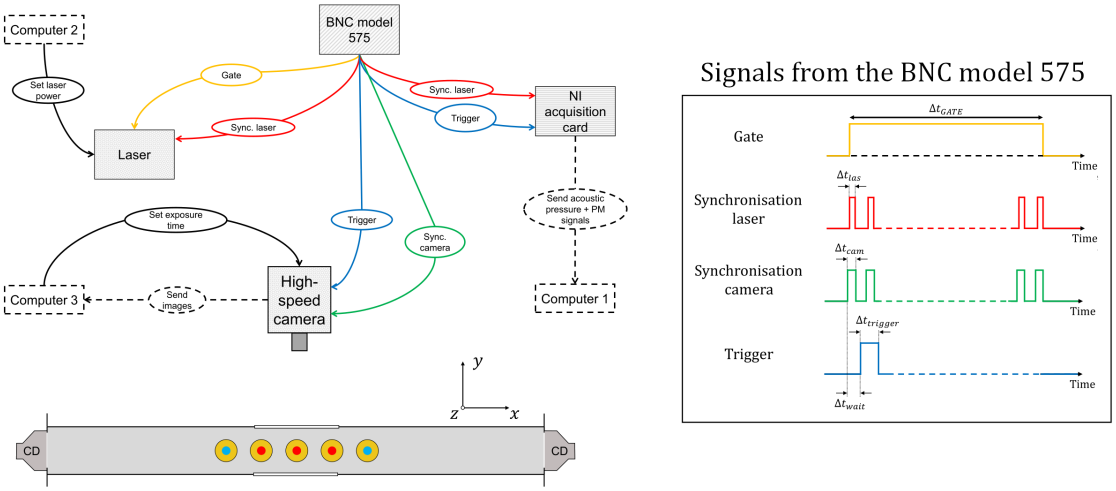

Figure A.2: Signals for synchronisation between laser pulse generation, image acquisition and acoustic pressure measurements for high-speed vertical tomography.

laser to open the gate, allowing to generate the laser shots. This signal has a width Δt_{GATE} which defines the time during which laser shots are emitted. Simultaneously with the beginning of this signal, two synchronisation signals are sent to the camera and to the laser. The laser synchronisation signal is also sent to the National Instruments (NI) acquisition card, in order to be monitored on the computer using Labview. These synchronisation signals consist in rectangular signals with the same frequency corresponding to the desired acquisition frequency (here, in the range 20,000 - 35,000 Hz). At each rising edge, a laser shot is emitted. The falling edge has no influence on the signal, as the duration of the laser pulse is specified by the laser, and the image exposure time is defined with the software associated to the camera. At a time Δt_{wait} after the beginning of the synchronisation signals, a same single-shot signal is sent to the camera to trigger image acquisition and to the NI acquisition card to trigger acquisition of acoustic pressure and PM signals. From this signal, image acquisition is synchronised with the laser shots by the synchronisation signals. The delay Δt_{wait} allows the laser to stabilise and to emit repeatable pulses. Here, Δt_{wait} is chosen such that ten laser pulses are emitted before the trigger is sent. Therefore, acquisition of the images, acoustic pressure and PM signals starts at the eleventh laser shot.

Rate (kHz)	Δt_{GATE} (ms)	Δt_{las} (µs)	Δt_{cam} (µs)	$\Delta t_{trigger}$ (µs)	Δt_{wait} (pulses)	t_{expo} (µs)
20	200	5	20	50	10	49
25	200	5	20	50	10	39
30	200	5	20	50	10	32
35	200	5	20	50	10	28

Table A.2: Characteristics of the synchronisation and acquisition signals for high-speed tomography imaging.

References

[1] BP. Bp statistical review of world energy, 71st edition, 2022. 2, 204

[2] J. Tyndall. On the absorption and radiation of heat by gases and vapours, and on the physical connexion of radiation, absorption, and conduction. *Philosophical Transactions of the Royal Society of London*, 151:1–36, 1861. 2

[3] S. Arrhenius. On the influence of carbonic acid in the air upon the temperature of the ground. *Philosophical Magazine and Journal of Science*, 51(251):237–276, 1896. 2

[4] Intergovernmental Panel on Climate Change (IPCC). Summary for policymakers, in climate change 2021: The physical science basis, 2021. 3

[5] K.L. Ricke and K. Caldeira. Maximum warming occurs about one decade after a carbon dioxide emission. *Environmental Research Letters*, 9:124002, 2014. 2

[6] K. Zickfeld and T. Herrington. The time lag between a carbon dioxide emission and maximum warming increases with the size of the emission. *Environmental Research Letters*, 10:031001, 2015. 2

[7] T.R. Barfknecht. Toxicology of soot. *Progress in Energy and Combustion Science*, 9:199–237, 1983. 2

[8] T. Boningari and P.G. Smirniotis. Impact of nitrogen oxides on the environment and huma, health: Mn-based materials for the nox abatement. *Current Opinion in Chemical Engineering*, 13:133–141, 2016. 2

[9] D. Nuvolone, D. Petri, and F. Voller. The effects of ozone on human health. *Environmental Science and Pollution Research*, 25:8074–8088, 2018. 2

[10] Z. Han, A. Uludogan, G.J. Hampson, and R.D. Reitz. Mechanism of soot and nox emission reduction using multiple-injection in a diesel engine. *SAE Transactions, Section 3: Journal of Engines*, 105:837–852, 1996. 3

[11] L.J. Muzio and G.C. Quartucy. Implementing nox control: research to application. *Progress in Energy and Combustion Science*, 23:233–266, 1997. 3

[12] J. O'Connor and M. Musculus. Post injections for soot reduction in diesel engines: A review of current understanding. *SAE International Journal of Engines*, 6(1):400–421, 2013. 3

[13] Y.B. Zeldovich. The oxidation of nitrogen in combustion explosions. *Acta Physicochimica*, 21:577–628, 1946. 3

[14] M. Cazalens, S. Roux, C. Sensiau, and T. Poinsot. Combustion instability problems analysis for high-pressure jet engine cores. *Journal of Propulsion and Power*, 24(4):770–778, 2008. 3, 5

[15] M. Barrère and F.A. Williams. Comparison of combustion instabilities found in various types of combustion chambers. *Symposium (International) on Combustion*, 12(1):169–181, 1969. 3

[16] A.T. Jones. Singing flames. *The Journal of the Acoustical Society of America*, 16(4):254–266, 1945. 4

[17] J.S.W. Rayleigh. *The Theory of Sound, Vol. 2*. Dover, New York, 1945. 4

[18] J.C. Oefelein and V. Yang. Comprehensive review of liquid-propellant combustion instabilities in f-1 engines. *Journal of Propulsion and Power*, 9(5):657–677, 1993. 4, 5

[19] A. Young. *The Saturn V F-1 Engine*. Springer Praxis Books, 2008. 5

[20] U.S. Departement of Transportation. *Airplane Flying Handbook, FAA-H-8083-3A*, 2004. 5

[21] H.I.H. Saravanamuttoo, H. Cohen, and G.F.C. Rogers. *Gas Turbine Theory*. Pearson, fifth edition, 2001. 6, 7

[22] R. Noroozian and P. Asgharian. *Distributed Generation Systems: Design, Operation and Grid Integration*, chapter 4: MicroTurbine Generation Power Systems, pages 149–219. Butterworth-Heinemann, 2017. 6, 7

[23] P. Kiameh. *Power Generation Handbook: Selection, Applications, Operation, and Maintenance*. McGraw Hill Professiona, 2002. 7

[24] N. Syred and J.M. Beer. Combustion in swirling flows: A review. *Combustion and Flame*, 23:143–201, 1974. 7

[25] S. Candel, D. Durox, T. Schuller, J.-F. Bourgouin, and J.P. Moeck. Dynamics of swirling flames. *Annual Review of Fluid Mechanics*, 46:147–173, 2014. 7, 8, 190

[26] R. Weber, F. Boysan, J. Swithenbank, and P.A. Roberts. Computations of near field aerodynamics of swirling expanding flows. *Symposium (International) on Combustion*, 21(1):1435–1443, 1986. 7

[27] O. Lucca-Negro and T. O'Doherty. Vortex breakdown : a review. *Progress in Energy and Combustion Science*, 27:431–481, 2001. 7

[28] N. Syred. A review of oscillation mechanisms and the role of the precessing vortex core (pvc) in swirl combustion systems. *Progress in Energy and Combustion Science*, 32:93–161, 2006. 7, 9, 71, 133, 193

[29] S. Leibovich. The structure of vortex breakdown. *Annual Reviews of Fluid Mechanics*, 10(1):221–46, 1978. 7

[30] Y. Huang and V. Yang. Dynamics and stability of lean-premixed swirl-stabilized combustion. *Progress in Energy and Combustion Science*, 35:293–364, 2009. 8, 242

[31] K. Manoharan, M. Frederick, S. Clees, J. O'Connor, and S. Hemchandra. A weakly nonlinear analysis of the precessing vortex core oscillation in a variable swirl turbulent round jet. *Journal of Fluid Mechanics*, 884:A29, 2020. 8

[32] B. Vonnegut. A vortex whistle. *The Journal of the Acoustical Society of America*, 26(1):18–20, 1954. 9

[33] R.C. Chanaud. Observations of oscillatory motion in certain swirling flows. *Journal of Fluid Mechanics*, 21(1):111–127, 1965. 9

[34] A.M. Steinberg, C.M. Arndt, and W. Meier. Parametric study of vortex structures and their dynamics in swirl-stabilized combustion. *Proceedings of the Combustion Institute*, 34:3117–3125, 2013. 9

[35] A. Karmarkar, S. Gupta, S. Boxx, I. ans Hemchandra, and J. O'Connor. Impact of precessing vortex core dynamics on the thermoacoustic instabilities in swirl-stabilized combustor. *Journal of Fluid Mechanics*, 946:A36, 2022. 9

[36] H.H. Chiu and T.M. Liu. Group combustion of liquid droplets. *Combustion Science and Technology*, 17:127–142, 1977. 10, 11, 138

[37] H.H. Chiu, H.Y. Kim, and E.J. Croke. Internal group combustion of liquid droplets. *Proceedings of the Combustion Institute*, 19:971–980, 1982. 10

[38] J. Réveillon and L. Vervisch. Analysis of weakly turbulent dilute-spray flames and spray combustion regimes. *Journal of Fluid Mechanics*, 537:317–347, 2005. 10, 29, 138

[39] E.K. Longmire and J.K. Eaton. Structure of a particle-laden round jet. *Journal of Fluid Mechanics*, 236:217–257, 1992. 11, 129

[40] C. Lacour, D. Durox, S. Ducruix, and M. Massot. Interaction of a polydisperse spray with vortices. *Experiments in Fluids*, 51:295–311, 2011. 11

[41] J.B. Greenberg and D. Katoshevski. The influence of droplet grouping on a burke-schumann spray diffusion flame in an oscillating flow field. *Proceedings of the Combustion Institute*, 33:2055–2062, 2011. 11

[42] J. Réveillon and F.-X. Demoulin. Effects of the preferential segregation of droplets on evaporation and turbulent mixing. *Journal of Fluid Mechanics*, 583:273–302, 2007. 11, 138, 174

[43] S. Kotake. On combustion noise related to chemical reactions. *Journal of Sound and Vibration*, 42(3):399–410, 1975. 12, 13

[44] S. Candel, C. Huynh, and T. Poinsot. *Unsteady Combustion*, chapter 5: Some modeling methods of combustion instabilities, pages 83–112. Kluiwer Academic Publishers, 1996. 12

[45] M. Cáceres. *Impact of Transverse acoustic modes on a linearly arranged two-phase flow swirling flames*. PhD thesis, INSA de Rouen Normandie, 2019. 14, 20, 21, 30, 38, 39, 44, 49, 66, 68, 74, 93, 131, 159, 191, 192, 194, 195, 199, 231

[46] B.T. Zinn and T.C. Lieuwen. *Combustion Instabilities in Gas Turbine Engines: Operational Experience, Fundamental Mechanisms, and Modeling*, chapter 1: Combustion Instabilities: Basic Concepts, pages 3–26. American Institute of Aeronautics and Progress in Astronautics and Aeronautics, 2005. 14, 16, 19, 91

[47] T. Poinsot and D. Veynante. *Theoretical and Numerical Combustion*. R.T. Edwards Inc., 2005. 15, 17, 18

[48] B.T. Chu. On the energy transfer to small disturbances in fluid flow (part i). *Acta Mechanica*, pages 215–234, 1965. 15

[49] A.P. Dowling. A kinematic model of a ducted flame. *Journal of Fluid Mechanics*, 394:51–72, 1999. 16, 19

[50] N. Noiray, D. Durox, T. Schuller, and S. Candel. A unified framework for nonlinear combustion instability analysis based on the flame describing function. *Journal of Fluid Mechanics*, 615:139–167, 2008. 16, 190

[51] J. Eckstein and T. Sattelmayer. Low-order modeling of low-frequency combustion instabilities in aeroengines. *Journal of Propulsion and Power*, 22(2):425–432, 2006. 16, 17

[52] R. Gaudron, M. Gatti, C. Mirat, and T. Schuller. Flame describing functions of a confined premixed swirled combustor with upstream and downstream forcing. *Journal of Engineering for Gas Turbines and Power*, 141(5):1–9, 2019. 16, 19, 21, 31, 81, 197

[53] P. Rajendram Soundararajan, D. Durox, A. Renaud, G. Vignat, and Candel S. Swirler effects on combustion instabilities analyzed with measured fdfs, injector impedances and damping rates. *Combustion and Flame*, 238:111947, 2022. 16, 19, 20, 22, 31, 39, 81, 82, 85, 89, 93, 97, 115, 116, 127, 161

[54] F.E.C Culick. *Unsteady Motions in Combustion Chambers for Propulsion Systems*. RTO/NATO, 2006. 16

[55] R. Gaudron. *Acoustic Response of Premixed Flames Submitted to Harmonic Sound Waves*. PhD thesis, Université Paris-Saclay, 2018. 17

[56] A.P. Dowling. The calculation of thermoacoustic oscillations. *Journal of Sound and Vibration*, 180(4):557–581, 1995. 17

[57] T. Sattelmayer. Influence of the combustor aerodynamics on combustion instabilities from equivalence ratio fluctuations. *Journal of Engineering for Gas Turbines and Power*, 125:11–19, 2003. 17, 68

[58] P. Palies, D. Durox, T. Schuller, and S. Candel. Nonlinear combustion instability analysis based on the flame describing function applied to turbulent premixed swirling flames. *Combustion and Flame*, 158:1980–1991, 2011. 17

[59] F. Boudy, D. Durox, T. Schuller, and S. Candel. Nonlinear mode triggering in a multiple flame combustor. *Proceedings of the Combustion Institute*, 33:1121–1128, 2011. 17

[60] F. Boudy, D. Durox, T. Schuller, G. Jomaas, and S. Candel. Describing function analysis of limit cycles in a multiple flame combustor. *Journal of Engineering for Gas Turbines and Power*, 133:061502, 2011. 17

[61] T. Schuller, D. Durox, P. Palies, and S. Candel. Acoustic decoupling of longitudinal modes in generic combustion systems. *Combustion and Flame*, 159:1921–1931, 2012. 17, 80

[62] S. Bomberg, T. Emmert, and W. Polifke. Thermal versus acoustic response of velocity sensitive premixed flames. *Proceedings of the Combustion Institute*, 35:3185–3192, 2015. 17

[63] M. Hoeijmakers, V. Kornilov, I. Lopez Arteaga, P. de Goey, and H. Nijmeier. Intrinsic instability of flame-acoustic coupling. *Combustion and Flame*, 161:2860–2867, 2014. 17

[64] T. Emmert, S. Bomberg, and W. Polifke. Intrinsic thermoacoustic instability of premixed flames. *Combustion and Flame*, 162:75–85, 2015. 17

[65] L. Crocco and S.-I. Cheng. *Theory of combustion instability in liquid propellant rocket motors*. Butterworth Scientific Publications, 1956. 18

[66] K. Oberleithner, S. Schimek, and C.O. Paschereit. Shear flow instabilities in swirl-stabilized combustors and their impact on the amplitude dependent flame reponse: A linear stability analysis. *Combustion and Flame*, 162:86–99, 2015. 19, 26, 134, 138, 173

[67] R. Balachandran, B.O. Ayoola, C.F. Kaminski, A.P. Dowling, and E. Mastorakos. Experimental investigation of the nonlinear response of turbulent premixed flames to imposed inlet velocity oscillations. *Combustion and Flame*, 143:37–55, 2005. 19, 20, 26, 92, 115, 121, 129, 173, 191

[68] S.K. Thumuluru, M.K. Bobba, and T. Lieuwen. Mechanisms of the nonlinear response of a swirl flame to harmonic excitation. *Proceedings of ASME Turbo Expo*, pages GT2007–27932, 2007. 19, 115, 191

[69] A.P. Dowling. Nonlinear self-excited oscillations of a ducted flame. *Journal of Fluid Mechanics*, 346:271–290, 1997. 19

[70] T. Lieuwen. Modeling premixed combustion-acoustic wave interactions: A review. *Journal of Propulsion and Power*, 19(5):765–781, 2003. 19, 170, 190

[71] J. Eckstein, E. Freitag, C. Hirsch, and T. Sattelmayer. Experimental study on the role of entropy waves in low-frequency oscillations in a rql combustor. *Journal of Engineering for Gas Turbines and Power*, 128:264–270, 2006. 19, 29, 190, 204, 228

[72] F.A. Williams. *The Mathematics of Combustion*, chapter 3: Turbulent Combustion, pages 91–131. Society for Industrial and Applied Mathematics, 1985. 19

[73] L. Boyer and J. Quinard. On the dynamics on anchored flames. *Combustion and Flame*, 82:51–65, 1990. 19, 24, 131

[74] F. Baillot, D. Durox, and R. Prud'homme. Experimental and theoretical study of a premixed vibrating flame. *Combustion and Flame*, 88:149–168, 1992. 19, 24, 131, 190

[75] M. Fleifil, A.M. Annaswamy, Z.A. Ghoneim, and A.F. Ghoniem. Response of a laminar premixed flame to flow oscillations: A kinematic model and thermoacoustic instability results. *Combustion and Flame*, 106:487–510, 1996. 19

[76] T. Schuller, D. Durox, and S. Candel. A unified model for the prediction of laminar flame transfer functions: comparisons between conical and v-flame dynamics. *Combustion and Flame*, 134:21–34, 2003. 19

[77] Preetham and T. Lieuwen. Nonlinear flame-flow transfer function calculations: Flow disturbance celerity effects. *40th AIAA/ASME/SAE/ASEE Joint Propulsion Conference and Exhibit*, (AIAA 2004-4035), 2004. 19, 24, 25, 26

[78] Preetham, H. Santosh, and T. Lieuwen. Dynamics of laminar premixed flames forced by harmonic velocity disturbances. *Journal of Propulsion and Power*, 24(6):1390–1402, 2008. 19, 131

[79] V. Acharya, Shreekrishna, D.-H. Shin, and T. Lieuwen. Swirl effects on harmonically excited, premixed flame kinematics. *Combustion and Flame*, 159:1139–1150, 2012. 19, 21, 24

[80] V. Acharya and T. Lieuwen. Nonlinear response of swirling premixed flames to helical flow disturbances. *Journal of Fluid Mechanics*, 896, 2020. 19

[81] N.A. Worth and J.R. Dawson. Cinematographic oh-plif measurements of two interacting turbulent premixed flames with and without acoustic forcing. *Combustion and Flame*, 159:1109–1126, 2012. 20, 81, 257

[82] A. Tyagi, I. Boxx, S. Peluso, and J. O'Connor. Statistics and topology of local flame-flame interactions in turbulent flames. *Combustion and Flame*, 203:92–104, 2019. 20

[83] W.Y. Kwong and A.M. Steinberg. Effect of internozzle spacing on lean blow-off of a linear multinozzle combustor. *Journal of Propulsion and Power*, 236(4):540–550, 2020. 20, 244

[84] X. Han and A.S. Morgans. Non-linear interactions of two premixed flames explored large eddy simulation with external acoustic forcing. *Combustion Science and Technology*, 190(3):425–436, 2017. 20, 81

[85] R.B. Price, I.R. Hurle, and T.M. Sugden. Optical studies of the generation of noise in turbulent flames. *Symposium (International) on Combustion*, 12(1):1093–1102, 1969. 20, 45, 91, 114, 115

[86] C. Külsheimer and H. Büchner. Combustion dynamics of turbulent swirling flames. *Combustion and Flame*, 131:70–84, 2002. 20, 26, 115, 173

[87] A.M. Kypraiou, P.M. Allison, A. Giusti, and E. Mastorakos. Response of flames with different degrees of premixedness to acoustic oscillations. *Combustion Science and Technology*, 190(8):1426–1441, 2008. 20

[88] B. Ćosić, S. Terhaar, J.P. Moeck, and C.O. Paschereit. Response of a swirl-stabilized flame to simultaneous perturbation in equivalence ratio and velocity at high oscillation amplitudes. *Combustion and Flame*, 162:1046–1062, 2015. 20, 27, 28, 190, 191, 196

[89] M. de la Cruz García, E. Mastorakos, and A.P. Dowling. Investigations on the self-excited oscillations in a kerosene spray flame. *Combustion and Flame*, 156:374–384, 2009. 20, 150, 190, 204, 228

[90] C.I. Sevilla-Esparza, J.L. Wegener, S. Teshome, J.I. Rodriguez, O.I. Smith, and A.R. Karagozian. Droplet combustion in the presence of acoustic excitation. *Combustion and Flame*, 161:1604–1619, 2014. 20

[91] K. Prieur, D. Durox, T. Schuller, and S. Candel. Strong azimuthal combustion instabilities in a spray annular chamber with intermittent partial blow-off. *Proceedings of the ASME Turbo Expo*, (GT2017-63343), 2017. 20, 39, 190, 191, 198, 206

[92] V. Fratalocchi and J.B.W Kok. Ethanol turbulent spray flame response to gas velocity perturbation. *Combustion Theory and Modelling*, 22(1):91–109, 2018. 20

[93] X. Han and A.S. Morgans. Simulation of the flame describing function of a turbulent premixed flame using an open-source les solver. *Combustion and Flame*, 162:1778–1792, 2015. 20

[94] H.J. Krediet, C.H. Beck, W. Krebs, S. Schimek, C.O. Paschereit, and J.B.W. Kok. Identification of the flame describing function of a premixed swirl flame from les. *Combustion Science and Technology*, 184:888–900, 2012. 20

[95] D. Pampaloni, A. Andreini, B. Facchini, and C.O. Paschereit. Les modelling of the flame describing function of a lean premixed swirl stabilized flame. *AIAA Propulsion and Energy Forum, July 9-11, Cincinnati Ohio*, pages 2018–4608, 2018. 20

[96] C.O. Paschereit, E. Gutmark, and W. Weisenstein. Control of thermoacoustic instabilities and emissions in an industrial-type gas-turbine combustor. *Symposium (International) on Combustion*, 27(2):1817–1824, 1998. 20

[97] D. Durox, T. Schuller, N. Noiray, and S. Candel. Experimental analysis of nonlinear flame transfer functions for different flame geometries. *Proceedings of the Combustion Institute*, 32:1391–1398, 2009. 20, 24, 25

[98] J. O'Connor, N. Worth, and J. Dawson. Flame and flow dynamics of a self-excited, standing wave circumferential instability in a model annular gas turbine combustor. *Proceedings of the ASME Turbo Expo*, pages GT2013–95897, 2013. 20

[99] F. Baillot, C. Patat, M. Cáceres, J-B. Blaisot, and E. Domingues. Saturation phenomenon of swirling spray flames at pressure antinodes of a transverse acoustic field. *Proceedings of the Combustion Institute*, 38(4):5987–5995, 2020. 20, 244

[100] H.T. Nygård, G. Ghirardo, and N.A. Worth. Azimuthal flame response and symmetry breaking in a forced annular combustor. *Combustion and Flame*, 233:111565, 2021. 20, 91

[101] G. Vignat, D. Durox, A. Renaud, and S. Candel. High amplitude combustion instabilities in an annular combustor inducing pressure field deformation and flame blow off. *Journal of Engineering for Gas Turbines and Power*, 142(1):011016, 2019. 20, 31, 82, 114, 190, 191, 228, 243, 245

[102] M. Mazur, H.T. Nygård, J.R. Dawson, and N.A. Worth. Characteristics of self-excited spinning azimuthal modes in an annular combustor with turbulent premixed bluff-body flames. *Proceedings of the Combustion Institute*, 37:5129–5136, 2019. 20

[103] J.-F. Bourgouin, D. Durox, J.P. Moeck, T. Schuller, and S. Candel. Characterization and modeling of a spinning thermoacoustic instability in an annular combustor equipped with multiple matrix injectors. *Journal of Engineering for Gas Turbines and Power*, 137:021503–1, 2015. 20, 242

[104] J.-F. Bourgouin, D. Durox, J.P. Moeck, T. Schuller, and S. Candel. A new pattern of instability observed in an annular combustor: The slanted mode. *Proceedings of the Combustion Institute*, 35(3):3237–3244, 2015. 20, 190, 242

[105] D. Mejia, M. Miguel-Brebion, A. Ghani, T. Kaiser, F. Duchaine, L. Selle, and T. Poinsot. Influence of flame-holder temperature on the acoustic flame transfer functions of a laminar flame. *Combustion and Flame*, 188:5–12, 2018. 20

[106] H.T. Nygård and N.A. Worth. Flame transfer functions and dynamics of a closely confined premixed bluff body stabilized flame with swirl. *Journal of Engineering for Gas Turbines and Power*, 143:041011, 2021. 20, 115

[107] P. Rajendram Soundararajan, G. Vignat, D. Durox, A. Renaud, and S. Candel. Do flame describing functions suitably represent combustion dynamics under self-sustained oscillations? *Journal of Sound and Vibration*, 534:117034, 2022. 20

[108] J. O'Connor, V. Acharya, and T. Lieuwen. Transverse combustion instabilities: Acoustic, fluid mechanic, and flame processes. *Progress in Energy and Combustion Science*, 49:1–39, 2015. 20, 55, 121, 190, 228, 242, 244

[109] M. Cáceres, F. Baillot, F. Lespinasse, and É. Domingues. Comparative study between transverse and longitudinal acoustic modes on a premixed v-shape flame. *7th European Combustion Meeting (ECM), Budapest (Hungary)*, 2015. 20, 26, 81, 93

[110] A. Saurabh, J.P. Moeck, and C.O. Paschereit. Swirl flame response to simultaneous axial and transverse velocity fluctuations. *Journal of Engineering for Gas Turbines and Power*, 139(061502-1), 2017. 21, 81

[111] F. Lespinasse, F. Baillot, and T. Boushaki. Responses of v-flames placed in an hf transverse acoustic field from a velocity to pressure antinode. *Comptes Rendus Mécanique*, 341:110–120, 2013. 21, 195, 228, 244

[112] K. Truffin and T. Poinsot. Comparison and extension of methods for acoustic identification of burners. *Combustion and Flame*, 142:388–400, 2005. 21, 31, 81

[113] P. Rajendram Soundararajan. *Investigation of combustion instabilities in annular combustors combining injector dynamics and flame describing functions determined in simplified configurations*. PhD thesis, Université Paris-Saclay, 2022. 22, 38, 115, 127, 208

[114] F.A. Williams. *Combustion Theory*. The Benjamin/Cummings Publishing Company, Inc., 1985. 23

[115] P. Dirrenberger, H. Le Gall, R. Bounaceur, O. Herbinet, P.-A. Glaude, A. Konnov, and F. Battin-Leclerc. Measurements of laminar flame velocity for components of natural gas. *Energy and Fuels*, 25:3875–2884, 2011. 23

[116] M. Lawes, M.P. Ormsby, C.G.W. Sheppard, and R. Woolley. The turbulent burning velocity of iso-octane/air mixtures. *Combustion and Flame*, 159:1949–1959, 2012. 23

[117] T. Schuller, T. Poinsot, and S. Candel. Dynamics and control of premixed combustion systems based on flame transfer and flame describing functions. *Journal of Fluid Mechanics*, 894:P1, 2020. 24

[118] S. Ducruix, D. Durox, and S. Candel. Theoretical and experimental determinations of the transfer function of a laminar premixed flame. *Proceedings of the Combustion Institute*, 28(1):765–773, 2000. 24, 115

[119] Q.-V. Nguyen and P.H. Paul. The time evolution of a vortex-flame interactions observed via planar imaging of ch and oh. *Symposium (International) on Combustion*, 26:357–364, 1996. 26

[120] D. Thévenin, P.H. Renard, J.C. Rolon, and S. Candel. Extinction processes during a non-premixed flame-vortex interaction. *Symposium (International) on Combustion*, 27:719–726, 1998. 26

[121] B. Franzelli, A. Vié, and M. Ihme. Characterizing spray flame-vortex interaction: A spray spectral diagram for extinction. *Combustion and Flame*, 163:100–114, 2016. 26

[122] P.-H. Renard, D. Thévenin, J.C. Rolon, and S. Candel. Dynamics of flame/vortex interactions. *Progress in Energy and Combustion Science*, 26:225–282, 2000. 26, 121

[123] T.J. Poinsot, A.C. Trouvé, D.P. Veynante, S.M. Candel, and E.J. Esposito. Vortex-driven acoustically coupled combustion instabilities. *Journal of Fluid Mechanics*, 177:265–292, 1987. 26

[124] B.D. Bellows, M.K. Bobba, A. Forte, J.M. Seitzman, and T. Lieuwen. Flame transfer function saturation mechanisms in a swirl-stabilized combustor. *Proceedings of the Combustion Institute*, 31:3181–3188, 2007. 26, 92, 129, 173

[125] S. Terhaar, B. Ćosić, C.O. Paschereit, and K. Oberleithner. Impact of shear flow instabilities on the magnitude and saturation of the flame response. *Journal of Engineering for Gas Turbines and Power*, 136:071502, 2014. 26

[126] F. Baillot and F. Lespinasse. Response of a laminar premixed v-flame to a high-frequency transverse acoustic field. *Combustion and Flame*, 161:1247–1267, 2014. 26, 115, 129, 244

[127] P. Palies, D. Durox, T. Schuller, and S. Candel. The combined dynamics of swirler and turbulent premixed swirling flames. *Combustion and Flame*, 157:1698–1717, 2010. 26, 27, 173, 178

[128] K.T. Kim. Combustion instability feedback mechanisms in a lean-premixed swirl-stabilized combustor. *Combustion and Flame*, 171:137–151, 2016. 27

[129] T. Komarek and W. Polifke. Impact of swirl fluctuations on the flame response of a perfectly premixed swirl burner. *Journal of Engineering for Gas Turbines and Power*, 132(061503), 2010. 27

[130] V. Caux-Brisebois, A.M. Steinberg, C.M. Arndt, and W. Meier. Thermo-acoustic velocity coupling in a swirl stabilized gas turbine model combustor. *Combustion and Flame*, 161:3166–3180, 2014. 27

[131] M. Frederick, K. Manoharan, J. Dudash, B. Brubaker, S. Hemchandra, and J. O'Connor. Impact of pvc dynamics on shear layer response in a swirling jet. *Journal of Engineering for Gas Turbines and Power*, 140:061503, 2018. 27

[132] F. Lückoff and K. Oberleithner. Excitation of the precessing vortex core by active flow control to suppress thermoacoustic instabilities in swirl flames. *International Journal of Spray and Combustion Dynamics*, 11:1–23, 2019. 27

[133] T. Lieuwen, H. Torres, C. Johnson, and B.T. Zinn. A mechanism of combustion instability in lean premixed gas turbine combustors. *Journal of Engineering for Gas Turbines and Power*, 123:182–189, 2001. 27

[134] A. Huber and W. Polifke. Impact of fuel supply impedance on combustion stability of gas turbines. *Proceedings of ASME Turbo Expo*, pages GT2008–51193, 2008. 28

[135] F. Giuliani, P. Gajan, O. Diers, and M. Ledoux. Influence of pulsed entries on a spray generated by an airblast injection device: an experimental analysis on combustion instability processes in aeroengines. *Proceedings of the Combustion Institute*, 29:91–98, 2002. 29, 138, 173, 204, 228

[136] P. Gajan, A. Strzelecki, B. Platet, R. Lecourt, and F. Giuliani. Investigation of spray behavior downstream of an aeroengine injector with acoustic excitation. *Journal of Propulsion and Power*, 23(2):390–397, 2007. 29, 138, 173, 186, 204, 228, 255

[137] P.D. McCormack. A driving mechanism for high frequency combustion instability in liquid fuel rocket engines. *Journal of the Royal Aeronautical Society*, 68(645):633–637, 1964. 29

[138] D.T. Harrje and F.H. Reardon. *Liquid Propellant Rocket Combustion Instability*. NASA SP-194, 1972. 29

[139] J.B. Greenberg and D. Katoshevski. Spray flame dynamics with oscillating flow and droplet grouping. *Combustion Theory and Modelling*, 16(2):321–340, 2012. 29, 138, 174, 201

[140] E. Lo Schiavo, D. Laera, E. Riber, L. Gicquel, and T. Poinsot. Effects of liquid fuel/wall interaction on thermoacoustic instabilities in swirling spray flames. *Combustion and Flame*, 219:86–101, 2020. 29, 116, 174, 201, 204, 206, 229

[141] P. Rajendram Soundararajan, G. Vignat, D. Durox, A. Renaud, and S. Candel. Effect of different fuels on combustion instabilities in an annular combustor. *Journal of Engineering for Gas Turbines and Power*, 143(3):031007, 2021. 30, 82, 95, 150, 151, 164, 204, 205, 206

[142] K. Prieur, D. Durox, T. Schuller, and S. Candel. Strong Azimuthal Combustion Instabilities in a Spray Annular Chamber With Intermittent Partial Blow-Off. *Journal of Engineering for Gas Turbines and Power*, 140(3):031503, 2018. 33, 232, 233, 241, 242, 244, 246, 247, 255

[143] S. McAllister, J.-Y. Chen, and A. Carlos Fernandez-Pello. *Fundamentals of Combustion Processes*. Springer, 2011. 42

[144] F. Lespinasse. *Réponse de la dynamique d'une flamme prémélangée à des modes acoustiques transverses*. PhD thesis, Université de Rouen, 2014. 44

[145] R.R. John and M. Summerfield. Effect of turbulence on radiation intensity from propane-air flames. *Journal of Jet Propulsion*, 27(2):169–175, 1957. 45

[146] I.R. Hurle, R.B. Price, T.M. Sugden, F.R.S., and A. Thomas. Sound emission from open turbulent premixed flames. *Proceedings of the Royal Society of London. Series A, Mathematical and Physical Sciences*, 303(1475):409–427, 1968. 45, 114

[147] G.J. Bloxsidge, A.P. Dowling, and P.J. Langhorne. Reheat buzz: an acoustically coupled combustion instability. part 2. theory. *Journal of Fluid Mechanics*, 193:445–473, 1988. 45

[148] B. Higgins, M.Q. McQuay, F. Lacas, J.C. Rolon, N. Darabiha, and S. Candel. Systematic measurements of oh chemiluminescence for fuel-lean, high-pressure, premixed, laminar flames. *Fuel*, 80:67–74, 2001. 45, 114

[149] T. Lieuwen and Y. Neumeier. Nonlinear pressure-heat release transfer function measurements in a premixed combustor. *Proceedings of the Combustion Institute*, 29:99–105, 2002. 45

[150] T. Yi and D.A. Santavicca. Flame spectra of a turbulent liquid-fueled swirl-stabilized lean-direct injection combustor. *Journal of Propulsion and Power*, 25(5):1058–1067, 2009. 45, 115

[151] A. Desclaux. *Étude expérimentale du comportement linéaire et non linéaire d'une flamme diphasique soumise à une excitation acoustique*. PhD thesis, Université de Toulouse, 2020. 45, 115

[152] D. Arnal, A. Boutier, L. David, M. Eléna, J. Haertig, B. Lecordier, P. Millan, J.-M. Most, and M. Riethmuller. *Vélocimétrie laser pour la mécanique des fluides*, chapter 3, pages 51–168. Lavoisier Hermès, 2017. 47

[153] D. Sinclair. Light scattering by spherical particles. *Journal of the Optical Society of America*, 37(6):475–480, 1947. 50

[154] A.K.M.F. Hussain and W.C. Reynolds. The mechanics of an organized wave in turbulent shear flows. *Journal of Fluid Mechanics*, 41(2):241–258, 1970. 51, 163

[155] P. Stoica and R. Moses. *Spectral Analysis of Signals*. Prentice Hall. 53, 76

[156] G. Vignat, E. Lo Schiavo, D. Laera, A. Renaud, L. Gicquel, D. Durox, and S. Candel. Dynamics of spray and swirling flame under acoustic oscillations : A joint experimental and les investigation. *Proceedings of the Combustion Institute*, 38:6015–6024, 2021. 55, 121, 126, 127, 181

[157] A.H. Lefebvre and V.G. McDonell. *Atomization and Sprays*. CRC Press, second edition, 2017. 63, 173, 174

[158] C. Brunet, N. Gori, G. Godard, F. Frindt, G. Cabot, B. Renou, and F. Grisch. Étude de l'influence de la viscosité sur la distribution de taille de gouttes par mesure pdpa. *16ème Congrès Francophone de Techniques Laser pour la mécanique des fluides (CFTL)*, pages https://hal.archives–ouvertes.fr/hal–02098287/document, Dourdan, 17-21 septembre 2018. 65

[159] E. Æsoy, J.G. Aguilar, S. Wiseman, M.R. Bothien, N.A. Worth, and J.R. Dawson. Scaling and prediction of transfer functions in lean premixed h2/ch4-flames. *Combustion and Flame*, 215:269–282, 2020. 68

[160] D. Durox, J.P. Moeck, J-F. Bourgouin, P. Morenton, M. Viallon, T. Schuller, and S. Candel. Flame dynamics of a variable swirl number system and instability control. *Combustion and Flame*, 160:1729–1742, 2013. 71

[161] D. Laera, T. Schuller, K. Prieur, D. Durox, S.M. Camporeale, and S. Candel. Flame Describing Function analysis of spinning and standing modes in an annular combustor and comparison with experiments. *Combustion and Flame*, 184:136–152, 2017. 81, 242

[162] N. Noiray, M. Bothien, and B. Schuermans. Investigation of azimuthal staging concepts in annular gas turbines. *Combustion Theory and Modelling*, 15(5):585–606, 2011. 81

[163] N. Noiray and B. Schuermans. On the dynamic nature of azimuthal thermoacoustic modes in annular gas turbine combustion chambers. *Proceedings of the Royal Society A: Mathematical, Physical and Engineering Science*, 469:20120535, 2013. 81, 242

[164] G. Ghirardo, M.P. Juniper, and J. P. Moeck. Weakly nonlinear analysis of thermoacoustic instabilities in annular combustors. *Journal of Fluid Mechanics*, 805:52–87, October 2016. 81, 242

[165] N.A. Worth and J.R. Dawson. Characterisation of flame surface annihilation events in self-excited interacting flames. *Combustion and Flame*, 199:338–351, 2019. 81, 257

[166] C. Mirat, D. Durox, and T. Schuller. Analysis of the spray and transfer function of swirling spray flames from a multi-jet steam assisted liquid fuel injector. *Proceedings of the ASME Turbo Expo 2014*, pages GT2014–25111, 2014. 111, 114, 115, 159, 192

[167] Y. Hardalupas and M. Orain. Local measurements of the time-dependent heat release rate and equivalence ratio using chemiluminescence emission from a flame. *Combustion and Flame*, 139:188–207, 2004. 114, 116

[168] T.M. Muruganandam, B.-H. Kim, M.R. Morrell, V. Nori, M. Patel, B.W. Romig, and J.M. Seitzman. Optical equivalence ratio sensors for gas turbine combustors. *Proceedings of the Combustion Institute*, 30:1601–1609, 2005. 115, 116

[169] G. Vignat. *Injection and combustion dynamics in swirled spray flames and azimuthal coupling in annular combustors*. PhD thesis, Université Paris-Saclay, 2020. 115

[170] V. Kather, F. Lückoff, C.O. Paschereit, and K. Oberleithner. Interaction of equivalence ratio fluctuations and flow fluctuations in acoustically forced swirl flames. *International journal of spray and combustion dynamics*, 13(1-2):72–95, 2021. 116

[171] N. Docquier, F. Lacas, and S. Candel. Closed-loop equivalence ratio control of premixed combustors using spectrally resolved chemiluminescence measurements. *Proceedings of the Combustion Institute*, 29:139–145, 2002. 116

[172] E. Æsoy, J.G. Aguilar, N.A. Worth, and J.R. Dawson. The response of an axisymmetric jet placed at various positions in a standing wave. *Journal of Fluid Mechanics*, 917:A16, 2021. 129

[173] T. Schuller, S. Ducruix, D. Durox, and S. Candel. Modeling tools for the prediction of premixed flame transfer functions. *Proceedings of the Combustion Institute*, 29(1):107–113, 2002. 131

[174] K. Prieur. *Dynamique de la combustion dans un foyer annulaire multi-injecteurs diphasique*. PhD thesis, Université Paris-Saclay, Centrale Supélec, 2017. 164, 254

[175] J. Achury and W. Polifke. Modulation of spray droplet number density and size distribution by an acoustic field. *The Journal of Computational Multiphase Flows*, 9(1):32–46, 2017. 173

[176] M. Birouk and I. Gökalp. Current status of droplet evaporation in turbulent flows. *Progress in Energy and Combustion Science*, 32:408–423, 2006. 173

[177] R. Kumara Gurubaran and R.I. Sujith. Dynamics of spray-swirl-acoustics interactions. *International journal of spray and combustion dynamics*, 3(1):1–22, 2011. 173, 204

[178] M. Gatti, R. Gaudron, C. Mirat, L. Zimmer, and T. Schuller. Impact of swirl and bluff-body on the transfer function of premixed flames. *Proceedings of the Combustion Institute*, 37(4):5197–5204, 2019. 178

[179] A.H. Lefebvre and D.R. Ballal. *Gas turbine combustion: alternative fuels and emissions*. Taylor and Francis, 2010. 190

[180] W. Polifke. Black-box system identification for reduced order model construction. *Annals of Nuclear Energy*, 67:109–128, 2014. 190

[181] L. Tay-Wo-Chong, S. Bomberg, A. Ulhaq, T. Komarek, and W. Polifke. Comparative validation study on identification of premixed flame transfer function. *Journal of Engineering for Gas Turbines and Power*, 134:021502, 2012. 190

[182] G. Staffelbach, L.Y.M. Gicquel, G. Boudier, and T. Poinsot. Large eddy simulation of self excited azimuthal modes in annular combustors. *Proceedings of The Combustion Institute*, 32(2):2909–2916, 2009. 190

[183] J.R. Dawson and N.A. Worth. Flame dynamics and unsteady heat release rate of self-excited azimuthal modes in an annular combustor. *Combustion and Flame*, 161:2565–2578, 2014. 190

[184] M. Bauerheim, G. Staffelbach, N.A. Worth, J.R. Dawson, L.Y.M. Gicquel, and T. Poinsot. Sensitivity of les-based harmonic flame response model for turbulent swirled flame and impact on the stability of azimuthal modes. *Proceedings of the Combustion Institute*, 35(3):3355–3363, 2015. 190

[185] T. Poinsot. Prediction and control of combustion instabilities in real engines. *Proceedings of the Combustion Institute*, 36(1):1–28, 2017. 190, 242

[186] A. Ghani. *Simulation aux grandes échelles des instabilités de combustion transverses des flammes parfaitement prémélangées et swirles diphasiques*. PhD thesis, Université de Toulouse, 2015. 190

[187] G.A. Richards, M.M. McMillian, R.S. Gemmen, W.A. Rogers, and S.R. Cully. Issues for low-emission, fuel-flexible power systems. *Progress in Energy and Combustion Science*, 27:141–169, 2001. 204

[188] J. Schwing and T. Sattelmayer. High-frequency instabilities in cylindrical flame tubes: Feedback mechanism and damping. *Proceedings of ASME Turbo Expo*, pages GT2013–94064, 2013. 228

[189] J. Réveillon and F.-X. Demoulin. Evaporating droplets in turbulent reacting flows. *Proceedings of the Combustion Institute*, 31:2319–2326, 2007. 228, 255, 257

[190] S. Candel. Combustion dynamics and control: Progress and challenges. *Proceedings of the Combustion Institute*, 29(1):1–28, 2002. 242

[191] D. Fanaca, P.R. Alemela, C. Hirsch, and T. Sattelmayer. Comparison of the flow field of a swirl stabilized premixed burner in an annular and a single burner combustion chamber. *Journal of Engineering for Gas Turbines and Power*, 132(7):071502, 2010. 242

[192] J.P. Moeck, M. Paul, and C.O. Paschereit. Thermoacoustic instabilities in an annular rijke tube. In *ASME Conference Proceedings, Paper GT 2010-23577*, 2010. 242

[193] N. A. Worth and J. R. Dawson. Self-excited circumferential instabilities in a model annular gas turbine combustor: Global flame dynamics. *Proceedings of the Combustion Institute*, 34(2):3127–3134, 2013. 242

[194] N.A. Worth and J.R. Dawson. Modal dynamics of self-excited azimuthal instabilities in an annular combustion chamber. *Combustion and Flame*, 160:2476–2489, 2013. 242

[195] J.-F. Bourgouin, D. Durox, T. Schuller, J. Beaunier, and S. Candel. Ignition dynamics of an annular combustor equipped with multiple swirling injectors. *Combustion and Flame*, 160(8):1398–1413, 2013. 242

[196] J.-F. Bourgouin, D. Durox, J.P. Moeck, T. Schuller, and S. Candel. Self-sustained instabilities in an annular combustor coupled by azimuthal acoustic modes. In *Proceedings of ASME Turbo Expo, Paper GT2013-95010*, San Antonio, Texas, USA, June 3-7, 2013. 242

[197] N. A. Worth, J. R. Dawson, J. A. M. Sidey, and E. Mastorakos. Azimuthally forced flames in an annular combustor. *Proceedings of the Combustion Institute*, 36(3):3783–3790, 2016. 242

[198] K. Prieur, D. Durox, T. Schuller, and S. Candel. A hysteresis phenomenon leading to spinning and standing azimuthal instabilities in an annular combustor. *Combustion and Flame*, 175:283–291, 2017. 242

[199] S. Evesque, W. Polifke, and C. Pankiewitz. Spinning and azimuthally standing acoustic modes in annular combustors. In *AIAA Conference Proceedings Paper 2003-3182*, 2003. 242

[200] G. Ghirardo and M.P. Juniper. Azimuthal instabilities in annular combustors: standing and spinning modes. *Proceedings of the Royal Society A: Mathematical, Physical and Engineering Science*, 469:2013032, 2013. 242

[201] M. Bauerheim, J.-F. Parmentier, P. Salas, F. Nicoud, and T. Poinsot. An analytical model for azimuthal thermoacoustic modes in an annular chamber fed by an annular plenum. *Combustion and Flame*, 161:1374–1389, 2014. 242

[202] M. Bauerheim, P. Salas, F. Nicoud, and T. Poinsot. Symmetry breaking of azimuthal thermo-acoustic modes in annular cavities: a theoretical study. *Journal of Fluid Mechanics*, 760:431–465, 2014. 242

[203] M. Bothien, N. Noiray, and B. Schuermans. Analysis of azimuthal thermo-acoustic modes in annular gas turbine combustion chambers. *Journal of Engineering for Gas Turbines and Power*, 137:061505, 2015. 242

[204] J.P. Moeck, D. Durox, T. Schuller, and S. Candel. Nonlinear thermoacoustic mode synchronization in annular combustors. *Proceedings of the Combustion Institute*, 37(4):5343–5350, 2019. 242

[205] P. Wolf, R. Balakrishnan, G. Staffelbach, L.Y.M.Y. M. Gicquel, and T. Poinsot. Using LES to Study Reacting Flows and Instabilities in Annular Combustion Chambers. *Flow, Turbulence and Combustion*, 88(1-2):191–206, 2012. 242

[206] P. Wolf, G. Staffelbach, L.Y.M. Gicquel, J.-D. Müller, and T. Poinsot. Acoustic and large eddy simulation studies of azimuthal modes in annularcombustion chambers. *Combustion and Flame*, 159:3398–3413, 2012. 242

[207] J. O'Connor and T. Lieuwen. Disturbance field characteristics of a transversely excited burner. *Combustion Science and Technology*, 183(5):427–443, 2011. 244

[208] J. O'Connor and T. Lieuwen. Further characterization of the disturbance field in a transversely excited swirl-stabilized flame. *Journal of Engineering for Gas Turbines and Power*, 134:011501, 2012. 244

[209] M. Hauser, M. Lorenz, and T. Sattelmayer. Influence of transversal acoustic excitation of the burner approach flow on the flame structure. *Journal of Engineering for Gas Turbines and Power*, 133:041501, 2011. 244

[210] E.E. Zukoski. *Aerothermodynamics of Aircraft Engine Components*, chapter 2: Afterburners. AIAA, 1985. 249

[211] S. Dooley, S.H. Won, S. Jahangirian, Y. Ju, F.L. Dryer, H. Wang, and M.A. Oehlschlaeger. The combustion kinetics of a synthetic paraffinic jet aviation fuel and a fundamentally formulated, experimentally validated surrogate fuel. *Combustion and Flame*, 159:3014–3020, 2012. 258